

21

FINAL REPORT

to the

**NATIONAL AERONAUTICS AND SPACE
ADMINISTRATION**

in connection with

NASA Grant NGR 47-004-006

Parts 2 through 21

MISCELLANEOUS PROJECT FINAL REPORTS

Virginia Polytechnic Institute & State University
Blacksburg, Virginia

December, 1970

FACILITY FORM 602

N71-71001- N71-71021

(ACCESSION NUMBER)

(THRU)

546

(PAGES)

CR-116415

(NASA CR OR TMX OR AD-NUMBER)

(CODE)

(CATEGORY)



FINAL REPORT

N71-71002

to the

NATIONAL AERONAUTICS AND SPACE ADMINISTRATION

in connection with

NASA Grant NGR 47-004-006

Part 2 of 21 Parts

Final Report
VPI&SU Project 313249

Supersonic Flow of Nonuniform Free-Streams
Past Aerodynamic Decelerators

by

F. G. Moore
F. R. DeJarnette
E. N. Brooks, Jr.
Aerospace Engineering

Virginia Polytechnic Institute & State University
Blacksburg, Virginia

December, 1970

SUPERSONIC FLOW OF NONUNIFORM FREE-STREAMS

PAST AERODYNAMIC DECELERATORS

by

Frankie G. Moore, Fred R. DeJarnette, and Eugene N. Brooks, Jr.

Aerospace Engineering Department

Virginia Polytechnic Institute and State University

Blacksburg, Virginia

for

AIAA AERODYNAMIC DECELERATION SYSTEMS CONFERENCE

Dayton, Ohio

September 14-16, 1970

SUPERSONIC FLOW OF NONUNIFORM FREE-STREAMS
PAST AERODYNAMIC DECELERATORS

Frankie G. Moore^{*}, Fred R. DeJarnette[†], and Eugene N. Brooks, Jr.^{††}
Virginia Polytechnic Institute and State University
Blacksburg, Virginia

ABSTRACT

Flow fields past aerodynamic decelerators immersed in the wake of a primary vehicle are investigated analytically. Inviscid flow fields were computed by the methods of characteristics and integral relations, and laminar boundary layer properties were calculated numerically. Results for pointed wedges and cones showed an adverse pressure gradient on the surface which led to boundary layer separation in some cases and an inviscid surface Mach number going to unity for some wake profiles. Surface pressure distributions were found to correlate very well with the tangent cone approximation and reasonably well with a Newtonian theory applied to nonuniform free streams.

NOMENCLATURE

A = Parameter used in specifying nonuniform freestream velocity defect in equations (1) and (2)

a = Speed of sound

B = Parameter used in specifying nonuniform freestream velocity distribution in equation (1)

\bar{B} = Parameter used in equation (2)

C_D = Drag coefficient, see equation (15)

C_f = Skin friction coefficient based on far freestream conditions

C_p = Surface pressure coefficient based on far free-stream conditions, see equation (11)

C_p^* = Surface pressure coefficient based on local free-stream conditions, see equation (10)

C_v = Specific heat at constant volume

H = Total enthalpy

j = 0 or 1 for wedge or cone, respectively

k = Constant defined by equation (14)

L = Cone length

M = Mach number

p = Pressure

\bar{p} = Nondimensional pressure, $\bar{p} = p/\rho_\infty V_\infty^2$

q_w = Heat transfer rate at the wall, Btu/ft²-sec

Re = Reynolds number based on far free-stream conditions

S = Entropy

V = Total velocity

x, y = Coordinate along and normal to body axis of symmetry, see Figure 1

y^* = Shock-wave position on initial-data line, see Figure 2

β = Shock wave angle

γ = Ratio of specific heats (1.4)

δ = Body inclination angle with respect to body axis

θ = Direction of velocity vector with respect to body axis of symmetry

μ = Mach angle

ρ = Density

Subscripts

b = Body point

s = Shock point

N = Conditions at the nose ($y_1 = 0$)

∞ = Far free-stream condition at $y = \infty$

1 = Local free-stream condition at $y = y_1$

* Graduate Student on leave from Naval Weapons Laboratory, Dahlgren, Virginia.

† Associate Professor, Aerospace Engineering Department; presently Associate Professor, North Carolina State University at Raleigh; Associate Fellow, AIAA

†† Former Graduate Student, presently Aerospace Engineer, Naval Ship Research and Development Center, Washington, D. C.; Associate, AIAA

This research was partially supported by NASA Grant 47-004-006.

INTRODUCTION

One of the problems associated with the re-entry of a space vehicle into a planetary atmosphere is the design of a decelerator to slow the vehicle down to tolerable speeds. Aerodynamic decelerators, composed of light-weight high-drag bodies towed behind the primary vehicle, have been proposed to solve this problem. Since the decelerator follows in the wake of the primary vehicle, the free stream approaching the decelerator is nonuniform and similar to that shown in Figure 1. The nonuniformity of this free stream has a substantial effect on both the drag and stability of a decelerator when compared to the corresponding results for a uniform free stream.

Various experimental and theoretical studies have been performed on towed right-circular cones¹⁻⁶ to assess their feasibility as a decelerator. These experimental results confirm that the static pressure in the far wake is nearly constant even though the velocity varies significantly. Campbell¹ found that the measured transverse velocity profile for wakes behind cones in supersonic flow can be accurately represented by the relation

$$\frac{V_1}{V_\infty} = 1 - A \exp(-By_1^2) \quad (1)$$

where V_∞ is the wake velocity as $y_1 \rightarrow \pm \infty$, y_1 is the distance perpendicular to the body axis (see Figure 1), and A and B are parameters depending on the primary body shape and axial position relative to the wake.

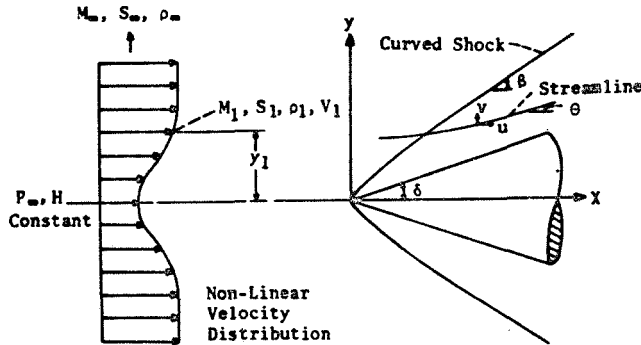


FIG. 1 Coordinate System and Freestream Properties

Another velocity profile of the form⁶

$$\frac{V_1}{V_\infty} = 1 - A [1 - (\sqrt{B} y_1)^{3/2}]^2 \quad \text{for } \sqrt{B} y_1 \leq 1 \quad (2)$$

$$\frac{V_1}{V_\infty} = 1 \quad \text{for } \sqrt{B} y_1 > 1$$

was found to be representative of the velocity profile in the turbulent far-wake of typical vehicles at supersonic speeds. However, equations (1) and (2) yield nearly the same profile when the parameters B and \bar{B} are appropriately related,

and the first author⁷ found that equations (1) and (2) yielded similar results for flow-fields over wedges and cones.

Although the static pressure in the wake is nearly constant, the velocity variation causes other flow field properties like Mach number (M_1), density (ρ_1), and entropy (S_1) to be nonuniform.

In particular, a strong entropy layer exists which, in turn, passes over the decelerator as it moves through the wake. On the other hand, the total enthalpy (H) may be considered to be approximately constant in the wake⁶.

Nerem⁸ has shown that the tow cable changes the velocity profiles near the axis since there is a viscous layer associated with the cable itself. In addition, the tow cable may cause flow separation just upstream of the nose of the decelerator⁵. These effects are not considered in the present analysis which is concerned with the calculation of flow fields past decelerators immersed in wake-like nonuniform free streams.

Sullivan, et al⁹, used a linearized method of characteristics to solve the inviscid flow-field past small-angle wedges with a free-stream Mach-number profile similar to that approaching the flare on a cone-cylinder-flare configuration. However, this linearized solution is limited to very small wedge angles. George¹⁰ obtained linearized perturbation solutions for plane and axisymmetric entropy layers over small angle wedges and flares.

In an unpublished M. S. Thesis, the third author¹¹ used the first approximation (one strip) of Dorodnitsyn's Method of Integral Relations¹² to calculate the flow field of the nonuniform free-stream given by equation (1) past wedges and cones. Some of these results appear herein for comparison purposes. In an independent analysis, Barteneu and Shirshou¹³ also used the one-strip method of integral relations to calculate nonuniform supersonic flows past pointed bodies of revolution. Since the flow fields produced by nonuniform free-streams are highly nonlinear, the results from the method of integral relations are questionable.

Inoyue¹⁴ used a combined inverse method - method of characteristics to calculate the inviscid flow field past blunt axisymmetric bodies in a supersonic spherical source flow. Patterson and Lewis¹⁵ used a somewhat similar approach to investigate nonuniform hypersonic free-streams about blunt axisymmetric bodies. However, the free stream velocity profiles for both of these analyses had the maximum velocity along the axis of symmetry, and the velocity decreased in the transverse direction. These velocity profiles are quite different from the wake-like profiles considered here.

The present paper applies the method of characteristics to calculate two-dimensional and axisymmetric flow-fields past pointed bodies in nonuniform supersonic free-streams. Modifications are required, however, to the standard method of characteristics¹⁶ to account for the nonuniform free-stream properties at the shock wave and the entropy layer on the surface. Free streams with wake-like profiles given by equation (1) are used

for a perfect gas ($\gamma = 1.4$) with the static pressure and total enthalpy constant in the free stream. Laminar boundary-layer properties are computed to check for boundary-layer separation and to determine skin friction coefficients and heat transfer rates. Approximate methods, based on tangent cone and Newtonian impact theories, are developed for the surface pressure coefficients. Results are presented for wedges in two-dimensional free-stream profiles and cones in axisymmetric free-stream profiles.

ANALYSIS

Determination of Free-Stream Properties

The nonuniform free-stream velocity profile given by equation (1) is used here with the parameters A and B held constant. Since the pressure and total enthalpy are constant in the free stream, the adiabatic energy equation yields

$$\frac{\gamma}{\gamma-1} \frac{p_\infty}{\rho_1} + \frac{v_1^2}{2} = \frac{\gamma}{\gamma-1} \frac{p_\infty}{\rho_\infty} + \frac{v_\infty^2}{2} = H \quad (3)$$

where again the subscript 1 refers to conditions at a position $y = y_1$ in the free stream, and subscript ∞ refers to conditions in the far free-stream ($y_1 \rightarrow \infty$). For a perfect gas the speed of sound is simply

$$a_1^2 = \frac{\gamma p_\infty}{\rho_1} \quad (4)$$

Equations (3) and (4) may be combined to yield

$$M_1^2 = M_\infty^2 \frac{v_1^2}{v_\infty^2} \left\{ 1 + \frac{\gamma-1}{2} M_\infty^2 \left(1 - \frac{v_1^2}{v_\infty^2} \right) \right\}^{-1} \quad (5)$$

and the density follows from equation (3) as

$$\frac{\rho_1}{\rho_\infty} = \left\{ 1 + \frac{\gamma-1}{2} M_\infty^2 \left(1 - \frac{v_1^2}{v_\infty^2} \right) \right\}^{-1} \quad (6)$$

Since $p_1 = p_\infty$ the expression for the entropy S_1 reduces to

$$\frac{S_1 - S_\infty}{C_V} = -\gamma \ln \left(\frac{\rho_1}{\rho_\infty} \right) \quad (7)$$

Equation (1) along with equations (5) through (7) are sufficient to determine the nondimensional free-stream properties $\frac{v_1}{v_\infty}$, M_1 , $\frac{\rho_1}{\rho_\infty}$, and $\frac{S_1 - S_\infty}{C_V}$ for any y_1 position in the free stream.

Inviscid Flow-Field Solution

There are several methods which could be used

for the inviscid flow-field solution, depending on whether the shock wave is attached or not. If it is assumed that M_1 at $y_1 = 0$ is large enough so that the shock wave is attached to the body, then the most accurate and well-known method for the solution is the method of characteristics. This is the method used here.

In order to apply the method of characteristics, the flow-field properties must be known along an initial data line. To determine this data, a small region of the free stream at the nose, of height y^* , is assumed to be uniform and have the same properties as those at $y_1 = 0$ (see Figure 2).

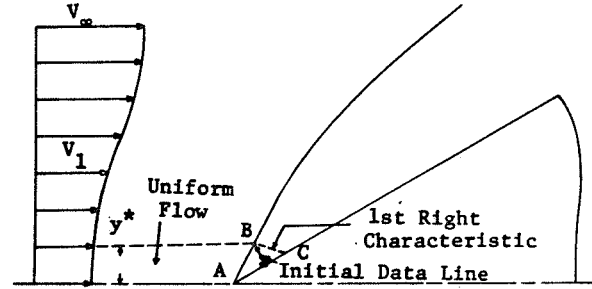


Fig. 2 Calculation of Initial Data

This means that the small region near the nose bounded by the shock wave from point A to B in Figure 2, by the right-running characteristic from B to C, and by the body from A to C is not affected by the nonuniform part of the free stream, and hence the usual flow-field properties for a cone (or wedge) exist in this region. In this manner the flow-field properties are determined along an initial data line constructed from point B at the shock along a line normal to the body.

Due to the small uniform flow region used at the nose, the nonuniform free-stream velocity or Mach number profiles given by equations (1) and (2) are modified by replacing y_1 with $(y_1 - y^*)$. Then the transition from the small uniform region to the nonuniform region occurs smoothly, and as $y^* \rightarrow 0$ the free-stream profile again assumes the original nonuniform profile. From a practical standpoint, this means that once a sufficiently small value of y^* is attained such that a further decrease in y^* causes no discernible change in the downstream flow-field solution, the effect of a finite value of y^* is negligible.

Since the method of characteristics appears in many references it will not be derived here. Using the approach given by Shapiro¹⁶, the characteristics lines are determined by

$$\left(\frac{dy}{dx} \right)_{I,II} = \tan(\theta \mp \mu) \quad (8)$$

with compatibility conditions

$$\begin{aligned} \frac{1}{v} \left(\frac{dv}{d\theta} \right)_{I,II} &= \mp \tan \mu - \frac{\sin^2 \mu}{\gamma(\gamma-1)} \left(\frac{dS}{d\theta} \right) \\ &+ j \frac{\sin^0 \mu \sin^2 \mu}{\cos \mu \sin(\theta \mp \mu)} \frac{1}{v} \frac{dv}{d\theta} \end{aligned} \quad (9)$$

where θ is the slope of the local velocity vector, μ is the Mach angle, and j is zero for two-dimensional flows and unity for axisymmetric flows. The subscript I refers to a right-running characteristic line and II refers to a left-running characteristic line. The derivatives in equations (8) and (9) are replaced with finite-difference quotients, and the solution proceeds downstream of the initial data line in a manner similar to that described by Shapiro¹⁶. However, modifications are required at the shock wave and body, which are explained below.

Boundaries

The boundaries for the method of characteristics are the body surface and the shock wave. A mesh point on the surface is located by the simultaneous solution of the right-running characteristic line (equation (8)) from a known mesh point off the surface and the equation of the body $y_b = f(x)$. Since the entropy on the surface and the flow inclination angle θ are known, the velocity can be found from the finite-difference form of equation (9). This is the usual approach used in the method of characteristics; however, the strong entropy layer adjacent to the surface in the problems considered here caused large differences to exist for some properties between the surface and the next mesh point off the surface. When this occurs, linear and even quadratic interpolation of properties between these two points are not adequate, and hence additional mesh points must be added to the characteristic mesh near the body surface. This problem is discussed more thoroughly in the Results and Discussion Section.

Calculation of shock points requires special attention, and since the method differs from the usual method of calculation, it is discussed in detail here. In essence, calculation of the shock point amounts to a double iteration for the non-uniform free-stream as opposed to a single iteration in the uniform free-stream case. The first iteration is performed as though the free stream were uniform. That is the shock wave is first extrapolated until it intersects the left-running characteristic drawn from point B in Figure 3. However, in order to avoid the intersection from occurring too far downstream, a point C is generally found by linearly interpolating the properties between points A and B. Then the left-running characteristic is drawn from point C until it intersects the extrapolated shock wave at point D. Knowing the value of y_1 at point D, the free stream properties can be calculated from the equations derived above. Next, the velocity V_3 , flow-inclination angle θ_3 , and entropy S_3 just behind the shock wave are calculated from the shock jump conditions. Using θ_3 and S_3 and the finite-difference form of equation (10), a new velocity just behind the shock, say V_s , is calculated and compared with V_3 . If V_s does not agree with V_3 within the accuracy desired, the velocity behind the shock is given the value

$$V_3' = (V_3 + V_s)/2$$

and this velocity and the free-stream velocity V_1 at point D are used to calculate a new shock-wave angle β' . Then the remaining flow-field properties are computed from the shock jump conditions corresponding to β' and the free-stream conditions at point D on Figure 3. This procedure is then repeated until the desired accuracy between V_3 and V_s is obtained. However, the new location of the shock point is point E on Figure 3, and unless point E is very close to point D the free-stream properties at E are different from those at point D.

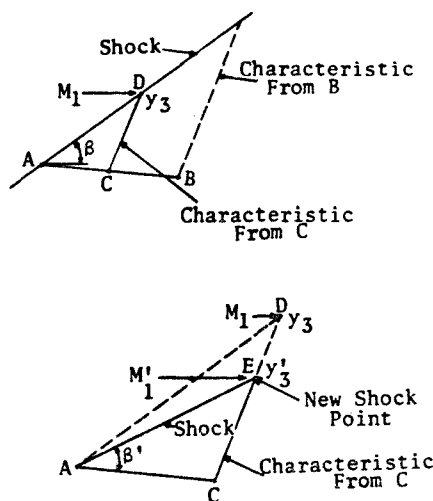


FIG. 3 Calculation of Shock Point

For the second part of the iteration scheme, if point E is not sufficiently close to point D, new free-stream properties are computed at D using $y_1 = y_3'$ in Figure 3. The entire iteration scheme is then repeated until the desired accuracy between points D and E in the second part of the iteration is obtained. Although a double iteration scheme is required, the technique converges very rapidly, and usually two or three iterations give an accuracy within 10⁻³% on velocity and shock location.

Tangent Cone Approximation

As noted by Nerem⁸ the tangent cone approximation¹⁷, modified for the nonuniform free stream, should provide a reasonably accurate pressure distribution for pointed bodies in supersonic flows. If C_p^* is defined as the pressure coefficient based on local free stream conditions,

$$C_p^* = \frac{P - P_\infty}{\frac{1}{2} \rho_1 V_1^2} \quad (10)$$

then C_p^* in the tangent cone approximation can be determined from Sim's cone tables¹⁸ for the local value of δ and M_1 . Then the pressure coefficient based on far free stream conditions is

$$C_p = \frac{p - p_\infty}{\frac{1}{2} \rho_\infty V_\infty^2} = C_p^* \frac{M_1^2}{M_\infty^2} \quad (11)$$

This technique can be used to determine C_p at each body position.

Approximate Pressure Distribution from Newtonian Theory

At hypersonic speeds the Newtonian impact theory¹⁷ has been found to yield reasonably accurate pressure distributions. Unlike the tangent cone approximation, it may be used for blunted as well as pointed bodies. The Newtonian Theory gives

$$C_p^* = 2 \sin^2 \delta$$

and hence the pressure coefficient based on far free-stream properties is

$$C_p = 2 \sin^2 \delta \frac{M_1^2}{M_\infty^2}$$

Love¹⁹ has shown that a better approximation may be obtained by requiring the equation above to yield the correct value at the nose. The result here is

$$C_p = C_{p_N}^* \frac{\sin^2 \delta}{\sin^2 \delta_N} \frac{M_1^2}{M_\infty^2} \quad (12)$$

where N refers to conditions at the nose ($y_1 = 0$). For blunt-nosed bodies $\sin \delta_N = 1$ and $C_{p_N}^*$ is the

stagnation pressure coefficient based on free stream properties at $y_1 = 0$. In the case of pointed bodies with attached shock waves, $C_{p_N}^*$ is the wedge or cone C_p^* at the nose.

Equation (12) is used herein to compare with the method of characteristics and tangent cone pressure distributions over wedges and cones. However, it is more accurate for the blunt-nosed bodies than the pointed ones.

The Newtonian pressure drag-coefficient for the special case of a cone in the free-stream velocity profile given by equation (1) is determined by integrating the pressure coefficient (equation (12)) as shown below:

$$C_D = \frac{2}{L^2} \int_0^L C_p x dx = C_{p_N}^* \left\{ 1 + \frac{1}{2BL^2 \tan^2 \delta} \left[k(k+1) \ln \left(\frac{Ae^{-BL^2 \tan^2 \delta_{1+k}}}{A-1+k} \right) + k(k-1) \ln \left(\frac{Ae^{-BL^2 \tan^2 \delta_{-1-k}}}{A-1-k} \right) \right] \right\} \quad (13)$$

where

$$k = \left[1 + \frac{2}{(\gamma-1)M_\infty^2} \right]^{1/2} \quad (14)$$

L is the cone length, and $C_p = 0$ is used for the base of the cone.

Laminar Boundary Layer Computations

As will be shown in the next section, wake-like velocity profiles produce adverse pressure gradients on the surfaces of wedges and cones. Therefore, solutions to the first-order laminar boundary layer equations were obtained, using the finite-difference method described by Blottner²⁰, to check for possible boundary-layer separation and to determine skin friction coefficients and heat transfer rates. The fact that the pressure gradient normal to the surface of a wedge or cone is zero gives some justification for using the first-order boundary layer equations. All of the results were obtained for a perfect gas ($\gamma = 1.4$) with a Prandtl number of 0.70 and using Sutherland's viscosity formula. The wall temperature has a significant effect on the separation point, but the Reynolds number does not affect separation.

RESULTS AND DISCUSSION

In order to start the method of characteristics, the height of the uniform flow region y^* (discussed above) and the flow-field properties along the initial data-line must be known. For a given value of y^* , the flow-field properties may be computed from the shock jump conditions (for a wedge) or the cone solution¹⁸.

A numerical study was performed to determine the effect of y^* on the solutions. For the free-stream velocity profiles given by equations (1) and (2), it was found that when $B = 10$ the solutions with $y^* = 0.01$ and $y^* = 0.001$ differed very little. However, significant differences were noted for the computational times since y^* establishes the height of the initial data line. Therefore, all the solutions presented here used $B = 10$ and $y^* = 0.01$.

The number of points on the initial data line must be chosen large enough to insure that the size of the characteristic mesh remains sufficiently small downstream, yet small enough to keep the computational time from being excessive. The number of points on the initial data line varied from 4 to 11 for the cases considered. As any of the parameters M_∞ , A , or δ are increased the entropy difference between the body and the next mesh point off the surface increases, and the method of characteristics will not converge unless a finer mesh scale is used. The method of characteristics discussed previously has V and S as dependent variables and uses linear interpolation between mesh points. Since the entropy variation is large in the problems considered here, several cases were also computed

using the method of characteristics developed by Rakich²¹, which has p and θ as dependent variables and uses quadratic interpolation near the body. However, the results were very close to those obtained here, and that method also would not converge near the body unless more mesh points are added.

To illustrate the highly nonlinear nature of some flow-field properties, Figure 4 shows the Mach number, pressure, and density profiles normal to a cone for $M_\infty = 8.5$, $A = 0.091$, and $\delta = 20^\circ$ at three streamwise positions. It is seen that the Mach number and density profiles are reasonably linear near the nose, but downstream these profiles become highly nonlinear. This nonlinearity is encompassed in an entropy layer near the surface which becomes progressively thinner downstream until finally as $x \rightarrow \infty$ an entropy singularity exists on the surface. On the other hand, Figure 4 shows that the pressure profile has little variation, and in fact the pressure gradient normal to the surface is zero.

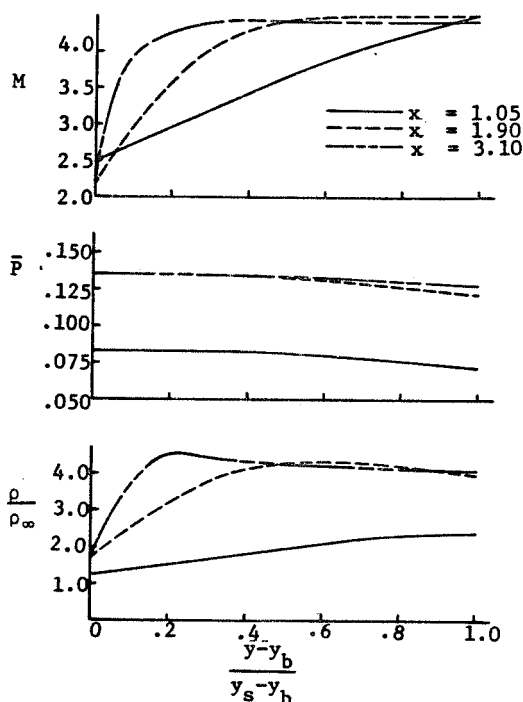


Fig. 4 Profiles of Flow-Properties Normal to Cone. $M_\infty = 8.5$, $\delta = 20^\circ$, $A = 0.091$

Another problem which arises, particularly for the larger values of δ and A , is that near the body the characteristic mesh size tends to increase in a direction normal to the body, whereas near the shock wave it increases in a direction parallel to the body (see Figure 5). The local Mach number explains why, because the Mach number on the body is generally decreasing as x increases which means the Mach angle is increasing. Conversely, the Mach number just behind the shock wave increases as x increases which causes the slope of the Mach line there to decrease. These two problems can be solved by again adding more mesh points to the flow-field.

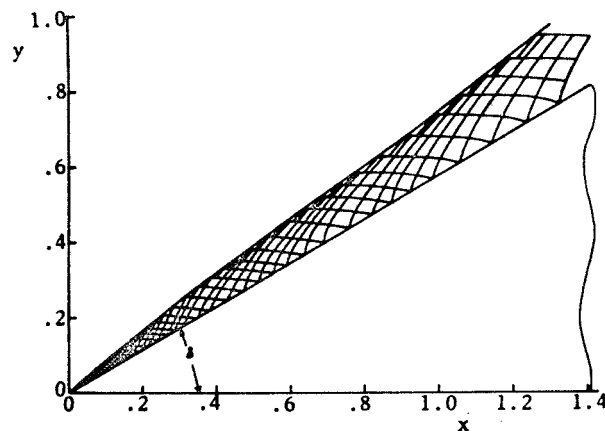


FIG. 5 Characteristics net for the flow over a Cone. $M_\infty = 4$; $\delta = 30^\circ$; $A = 0.1$.

Several flow fields were computed for wedges and cones to determine the effect of M_∞ and the parameter A on the solution. The parameter B has no effect on the free-stream nonuniformity other than to change the scale in the y_1 -direction, so a value of 10 was used for all the cases herein. This value is completely arbitrary, however, since B always occurs in the product By_1^2 , and a change in B is compensated by a change in y_1 .

Figure 6 shows the nondimensional surface pressure, surface Mach number, and shock wave shape for a cone with $\delta = 20^\circ$, $A = 0.1$ and several values of M_∞ . Figure 7 gives the nondimensional pressure and surface Mach number for $M_\infty = 4$, $\delta = 20^\circ$, and several values of A . In both of these cases the shock-wave angle β initially decreases as x increases until it reaches a minimum value and then increases and asymptotically approaches the value one would calculate for a completely uniform free-stream at that value of M_∞ . Although the shock-wave shapes are not shown for the cases given in Figure 7 they follow the same general trends as those in Figure 6. The nondimensional pressure increases along the surfaces and approaches an asymptotic value corresponding to that for a completely uniform free-stream. It is noticed that as M_∞ or A increases the adverse pressure gradients increase which may cause the boundary layer to separate; this point is discussed later. Since the surface pressure increases and the surface entropy for the inviscid solution is constant, the Mach number decreases along the surface until it too approaches an asymptotic value. However, this asymptotic value does not correspond to the Mach number for a completely uniform free-stream because the surface entropy is determined from the shock-wave angle and free-stream properties at the nose where $y_1 = 0$. On the other hand, the correct asymptotic value of the surface Mach number can be calculated from the asymptotic pressure and the surface entropy; these Mach-number asymptotes are indicated on the figures.

Figure 8 presents the Mach number and nondimensional pressure along the surface of a wedge for $M_\infty = 4$, $A = 0.1$, and various wedge angles.

It is interesting to note that the surface Mach-number decreases as δ increases, and finally for $\delta = 30^\circ$ the Mach number approaches unity at $x = 0.75$. Since the method of characteristics cannot compute subsonic flow-fields, the solution was terminated at this point.

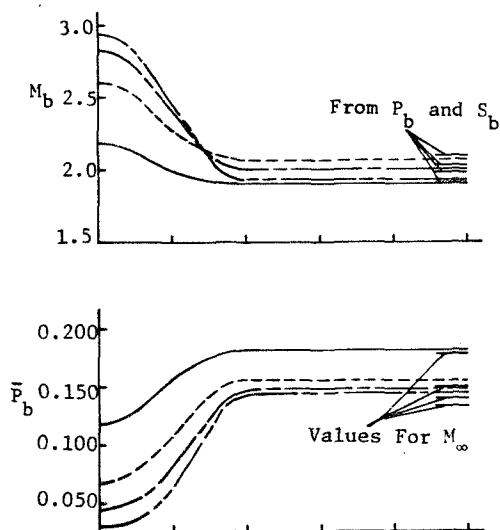


Fig. 6 Surface Mach Number and Pressure Distribution and Shock Wave Shape For a Cone. $\delta = 20^\circ$, $A = 0.10$

As an attempt to examine the flow field more closely in cases where the inviscid flow-field appeared to have embedded subsonic regions, the one-strip method of integral relations was used since it is applicable to both subsonic and supersonic regions. However, it was found that for the cases in which the method of characteristics indicated a surface Mach number of one the profiles

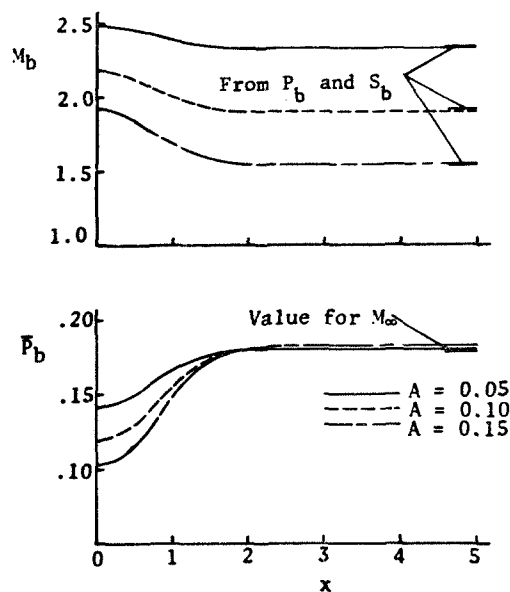


FIG. 7 Surface Mach Number and Pressure Distributions for a Cone. $M_\infty = 4$; $\delta = 20^\circ$; $A = 0.05, 0.10, 0.15$.

of flow-field properties normal to the surface were so nonlinear that the one-strip method of integral relations would not give adequate results. For example, consider the case of a wedge with $M_\infty = 10$, $\delta = 10^\circ$, and $A = 0.2$. The surface Mach number went to unity for the method of integral relations,

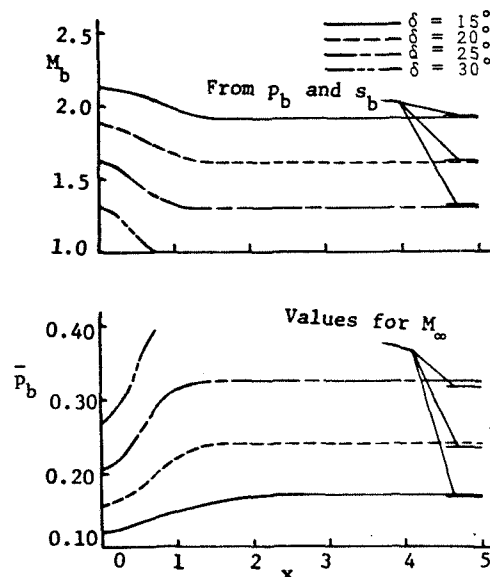
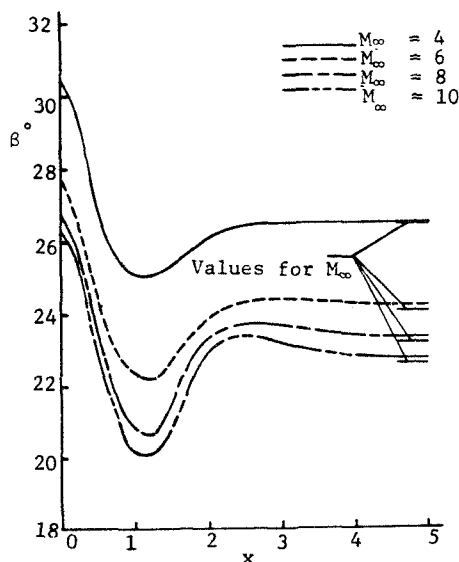


Fig. 8. Surface Mach Number and Pressure Distributions for Wedges. $M_\infty = 4$; $\delta = 15^\circ, 20^\circ, 25^\circ, 30^\circ$; $A = 0.10$

whereas the results from the method of characteristics did not. On the other hand, for a cone with $M_\infty = 4$, $\delta = 15^\circ$, and $A = 0.1$, the surface pressure and shock-wave shape compare well with the method of characteristics, but the surface Mach number compares poorly. However, this particular case produced nearly linear profiles of properties normal to the surface in the method of characteristics solution, and thus one would expect good results for the surface pressure and shock-wave shape from the method of integral relations. The Mach number predicted on the surface by the method of integral relations should be disregarded since the entropy is not held constant on the surface in that approach.

The third author¹¹ found that by holding entropy constant on the body (while disregarding the streamwise momentum equation), the one-strip method of integral relations yielded entirely different results than when the streamwise momentum equation was used and the entropy on the body allowed to vary. Comparing these results with the present method in Figure 9 it is seen that much better agreement in shock shape and surface pressure is obtained if the entropy is allowed to vary on the body; however, the surface Mach number compares more favorably with the present method if the entropy on the body is constrained to be constant.

For all the cases computed, the computational time required by the method of characteristics was highly dependent on the number of points on the initial data line. Typical cases with four points on the initial data line required less than 3 minutes on an IBM 7040 computer, whereas cases with eleven points on the initial data line required up to 30 minutes. However this computer is relatively slow and much faster computational times could be obtained with the newer models of computers.

Now to show what a large effect these non-uniform free-streams have on the drag, and hence on the deceleration capabilities of a towed decelerator, the pressure distribution was numerically integrated over a cone of various lengths. If the base pressure coefficient is assumed to be zero then the pressure drag - coefficient is

$$C_D = \frac{2}{L} \int_0^L C_p x dx \quad (15)$$

where L is the length of the cone considered. Figure 10 shows the pressure distribution and the resulting drag coefficient obtained by numerically integrating the above integral by Simpson's rule for $M_\infty = 4.47$, $A = 0.1667$, and $\delta = 25^\circ, 27.5^\circ, 30^\circ$. The asymptotic values that the drag coefficients approach for large L are those that would be obtained for a cone in a uniform flow with the freestream conditions being those of the far-freestream. It is seen that a detrimental reduction in drag by as much as 65% is encountered as a result of the nonuniform freestream and hence must certainly be accounted for in any design of a towed decelerator.

Also shown in Figure 10, for comparison with the method of characteristics, are the tangent cone and Newtonian approximations to the pressure

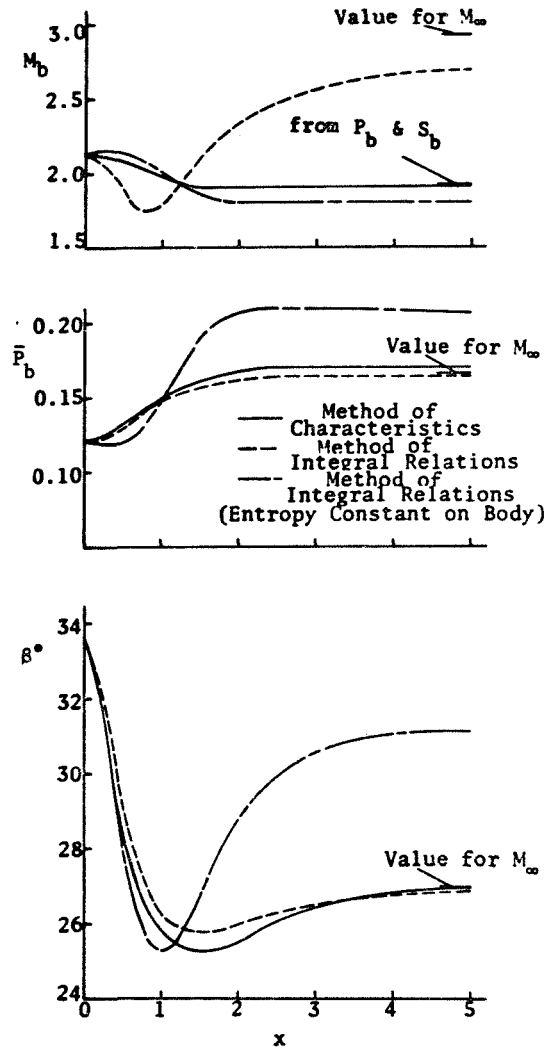


FIG. 9 Surface Mach Number and Pressure Distribution and Shock Wave Shape for a Wedge. $M_\infty=4$; $\delta=15^\circ$; $A=0.1$.

distribution and drag. It is seen that the tangent cone approximation gives very accurate results. This is quite significant because one can compute the remaining surface properties from the pressure and entropy and hence obtain an accurate solution for these properties with a minimum of computations. Moreover, computational time on the computer is approximately two percent of that for a corresponding case using the method of characteristics. A method such as this could be used very effectively in a boundary layer program where the inviscid pressure along the body is required to compute the flow field properties in the boundary layer.

On the other hand, the Newtonian approximations are not as accurate as the tangent cone method far back on the body. However, better results could be obtained by requiring the Newtonian pressure coefficient approach the asymptotic value far back on the body rather than that at the nose. This could

be done by simply replacing $C_{p_N}^*$ in equation (12) with the C_p^* in the far freestream.

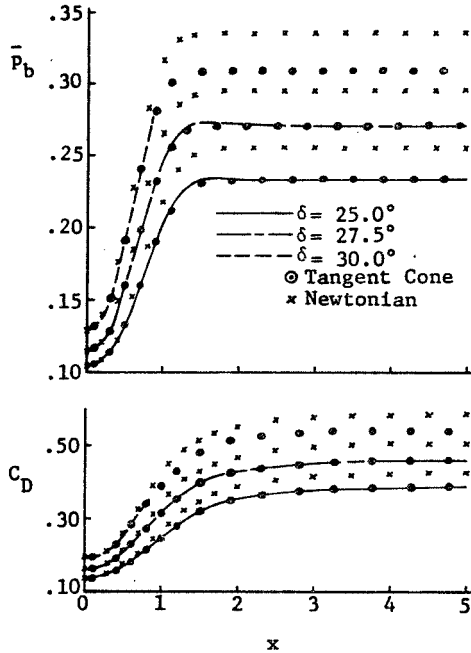


Fig. 10. Surface Pressure and Drag Coefficient For Cones. $M_\infty = 4.47$, $A = 0.1667$.

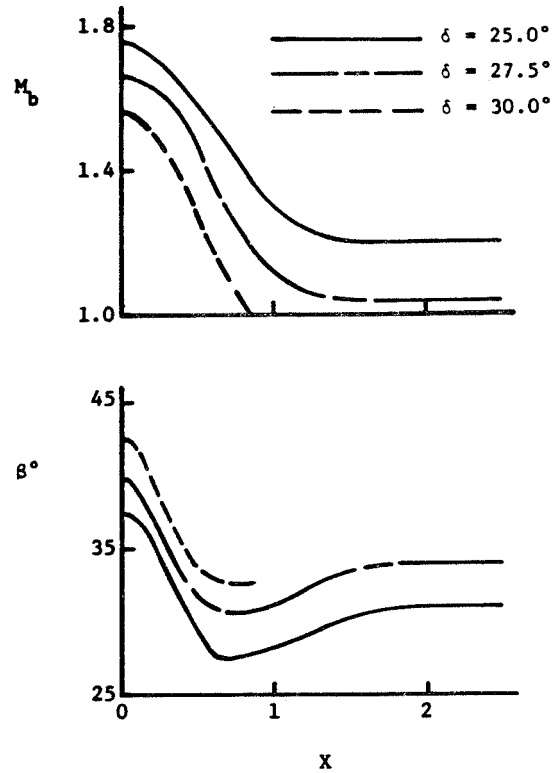


Fig. 11. Surface Mach Number and Shock Wave Shape For Cones. $M_\infty = 4.47$; $A = 0.1667$

Figure 11 shows the surface Mach number and shock wave shape for the above case. The same general trends in the Mach number and shock shape were obtained here by varying the cone half angle, δ , as was found in Figures 6 and 7 where the free-stream Mach number, M_∞ , and velocity defect parameter, A , were varied. Note that the Mach number goes to unity at $x = 0.86$ for the 30° cone. Hence the method of characteristics cannot continue beyond this point, but the tangent cone and Newtonian methods can still be applied. Also worth mentioning is the fact that although the tangent cone approximation gives excellent results on the surface it can not be used to compute the remainder of the flow field and shock shape whereas the method of characteristics gives the whole flow field solution.

As mentioned previously, the adverse pressure gradient on the surface of wedges and cones may cause boundary-layer separation. The laminar boundary-layer equations were solved numerically for several cases, using the method described previously, to investigate this possibility. For these computations, the units on x and y would be feet if the units on B were considered $(ft)^{-1/2}$, because (By^2) is dimensionless. Consider the cases presented in Figure 8 for wedges with $M_\infty = 4$, $A = 0.1$, and an adiabatic wall. The boundary layer for the thirty degree wedge was found to separate at $x \approx 0.70$, which is upstream

of the point where the surface inviscid Mach-number went to unity ($x \approx 0.75$). On the other hand, the wedges for $\delta = 15^\circ$ and 20° did not experience boundary-layer separation. Another case of a wedge with $M_\infty = 10$, $\delta = 20^\circ$, $A = 0.1$, and an adiabatic wall was found to separate at $x = 1.14$. It is important to note that for all the wedge solutions in which the inviscid surface Mach-number went to unity, the boundary layer separated upstream of the sonic point for the adiabatic wall condition. This means that the inviscid flow-field computations should be disregarded downstream of this point where separation occurs although the inviscid surface Mach numbers has not reached unity.

Boundary layer properties were also computed for several cone cases. Figure 12 shows the skin friction coefficient for the same three cone angles ($\delta = 25^\circ, 27.5^\circ, 30^\circ$) presented in Figure 11 and for an adiabatic wall. Note that the boundary layer not only separates on the 30° cone ($M_b = 1$ at $x = 0.86$) but on the 27.5° cone as well, even though an inviscid Mach number of unity was not reached on the surface. This verifies that one can indeed have boundary layer separation in these nonuniform flow fields without the inviscid surface Mach number going to one.

In an effort to determine what effect a non-adiabatic wall would have on boundary layer separation, solutions were obtained for the 30°

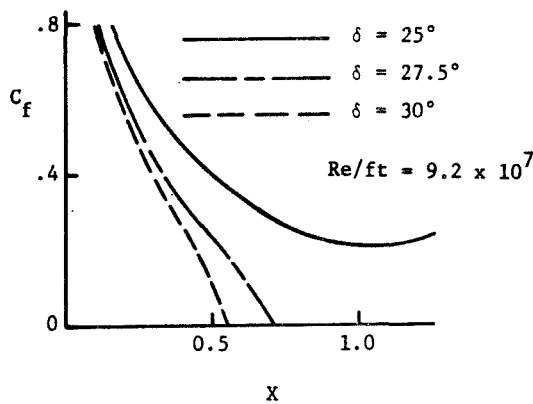


Fig. 12. Skin Friction Coefficient For Cones with Adiabatic Wall. $M_\infty = 4.47$; $A = 0.1667$.

cone with $\frac{T_w}{T_o} = 1.00, 0.75, 0.50$, and 0.25 where

T_w is the wall temperature and T_o the free stream stagnation temperature. In this particular case the adiabatic wall corresponded to a value

of $0.75 < \frac{T_w}{T_o} < 1.0$ so that the above four values

for $\frac{T_w}{T_o}$ represents successively colder values of

the wall temperature. Figure 13 presents the heat transfer at the wall, q_w , where positive heat transfer is taken to be into the wall, and the local skin friction coefficient, C_f . It is

seen that for the hot wall ($\frac{T_w}{T_o} = 1.0$) and re-

latively cool wall ($\frac{T_w}{T_o} = 0.75$) the boundary layer

separates, whereas for the cold wall ($\frac{T_w}{T_o} = 0.5$)

and very cold wall ($\frac{T_w}{T_o} = 0.25$) the boundary layer

remains attached. As might be expected the relatively hot wall dissipates heat into the free-stream (q_w negative) whereas in the other three

cases ($\frac{T_w}{T_o} = 0.75, 0.5$, and 0.25), the wall is

being heated. Thus, here, as in the case of a wedge, the boundary layer is seen to separate upstream of the point where the inviscid surface Mach number went to unity for an adiabatic wall and also for a relatively cool wall.

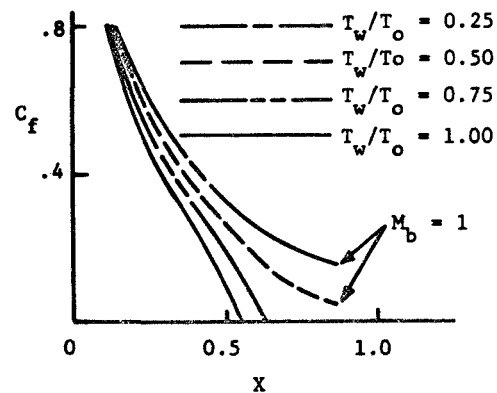
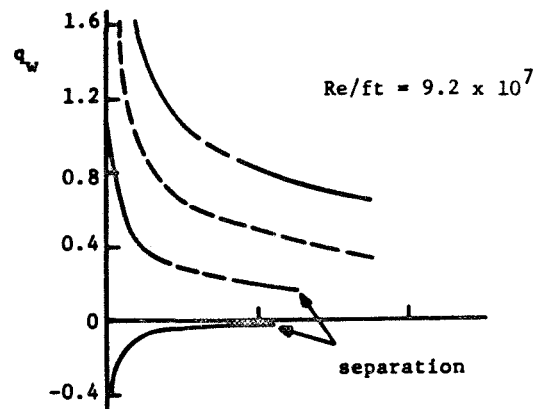


Fig. 13. Heat Transfer and Skin Friction Coefficient For a Cone. $M_\infty = 4.47$; $A = 0.1667$, $\delta = 30^\circ$.

CONCLUSIONS

1. The method of characteristics can be used to solve the inviscid flow-field past pointed bodies with attached shock waves in non-uniform free-streams representative of wakes. Modifications are required, however, at the shock wave to account for the nonuniform free-stream and also near the body due to a strong entropy layer.
2. Typical results for wedges and cones show that the shock-wave angle decreases near the nose until it reaches a minimum value, then it increases and asymptotically approaches the angle corresponding to a completely uniform free-stream. An adverse pressure gradient occurs along the surface in the nose region, after which the pressure asymptotically approaches the value for a uniform free-stream. The surface Mach number decreases and asymptotically approaches a value much lower than that of the completely uniform free-stream.
3. For some of the inviscid wedge and cone solutions the surface Mach number went to unity.

4. Due to the adverse pressure gradient, the laminar boundary layer separated on several of the wedge and cone cases. In addition, all cases where the inviscid Mach number went to unity were found to experience boundary-layer separation upstream of that point if the wall was assumed to be either adiabatic or relatively cool ($\frac{T_w}{T_o} = 0.75$).
5. Compared with the method of characteristics, the one-strip method of integral relations yields accurate results for the shock shape and surface pressure for free streams with a weak nonuniformity. However, the surface Mach number is not accurate using that approach; and when highly nonuniform free-streams are used, all the flow-field properties are inaccurate.
6. The tangent cone approximation gave excellent results for properties on the body and at a reduction in computational time of about 98% over the method of characteristics.
7. An approximate equation for the pressure coefficients derived from Newtonian theory for nonuniform free-streams, was found to yield reasonably accurate results for wedges and cones. However, more accurate results could be obtained for blunt-nosed bodies.
8. For cones used as decelerators, large drag reductions can be realized due to the wake-like nonuniform free-streams.
9. Sullivan, R. P.; Donaldson, C. duP.; and Hayes, W. D., "Linearized Pressure Distribution with Strong Supersonic Entropy Layers", J. Fluid Mech. 16, 1963, pp. 481-496.
10. George, A. R., "Perturbations of a Plane and Axisymmetric Entropy Layers", AIAA J., Vol. 5, No. 12, Dec. 1967, pp. 2155 - 2159.
11. Brooks, E. N., "Application of the Method of Integral Relations to Supersonic Non-uniform Flow Past Wedges and Cones", M. S. Thesis, Virginia Polytechnic Institute, Blacksburg, Virginia, 1967.
12. South, J. C., Jr., "Calculation of Axisymmetric Supersonic Flow Past Blunt Bodies with Sonic Curves, Including a Program Description and Listing", NASA TN D-4563, 1968.
13. Barteneu, D. A. and Shishou, V. P., "Calculation of a Non-uniform Supersonic Axisymmetric Gas Flow Past a Pointed Body of Revolution", Aviatsonnaia Tekhnika, No. 1, 1968, pp. 3-9, in Russian.
14. Inouye, M., "Numerical Solutions For Blunt Axisymmetric Bodies in a Supersonic Spherical Source Flow", NASA TN D-3383, 1966.
15. Patterson, J. L. and Lewis, A. B., "An Investigation of Nonuniform Hypersonic Free-Stream Flows About Blunt Axisymmetric Bodies", AFFDL-TR-69-57, Nov. 1969.
16. Shapiro, A. H., The Dynamics and Thermodynamics of Compressible Fluid Flow, Vol. I & II, The Ronald Press Company, New York, 1953, pp. 516-522 and 676-688.
17. Truitt, R. W., Hypersonic Aerodynamics, The Ronald Press Company, New York, 1959.
18. Sims, J. L., "Tables for Supersonic Flow Around Right Circular Cones at Zero Angle of Attack", NASA SP-3004, 1964.
19. Love, E. S., "Generalized - Newtonian Theory," Journal of the Aero/Space Sciences, Vol. 26, No. 5, 1959, pp. 314-315.
20. Blottner, F. G., "Finite-Difference Methods of Solution of the Boundary-Layer Equations", AIAA J., Vol. 8, No. 2, 1970, pp. 193-205.
21. Rakich, J. V., "Three-Dimensional Flow Calculation by the Method of Characteristics", AIAA J., Vol. 5, No. 10, Oct. 1967. pp. 1906-1908.

REFERENCES

1. Campbell, J. F. and Graw, J. W., "Experimental Flow Properties in the Wakes of a 120° Cone at Mach number 2.20", NASA TN D-5365, July 1969.
2. Charzenko, Nickolai and McShera, J. T. "Aerodynamic Characteristics of Towed Cones Used as Decelerators at Mach numbers from 1.57 to 4.65", NASA TN D-994, 1961.
3. Coats, J. D., "Static and Dynamic Testing of Conical Decelerators for the Pershing Re-Entry Vehicle", AEDC-TN-60-188, U. S. Air Force, Oct. 1960.
4. McShera, J. T., "Aerodynamic Drag and Stability Characteristics of Towed Inflatable Decelerators at Supersonic Speeds", NASA TN D-1601, 1963.
5. Reding, J. P. and Ericsson, L. E.: "Loads on Bodies in Wakes", AIAA Aerodynamic Deceleration Systems Conference, 1966.
6. "Performance of and Design Criteria for Deployable Aerodynamic Decelerators", ASD-TR-61-579, Dec. 1963.
7. Moore, F. G., "Calculation of Nonuniform Flow Fields Over Wedges and Cones by the Method of Characteristics", Thesis, Virginia Polytechnic Institute, Blacksburg, Virginia, 1968.
8. Nerem, R. M., "Pressure and Heat Transfer on High-Speed Aerodynamic Decelerators of the Ballute Type", AIAA Aerodynamic Deceleration Systems Conference, 1966.

N 71 - 71003

FINAL REPORT
to the
NATIONAL AERONAUTICS AND SPACE ADMINISTRATION
in connection with
NASA Grant NGR 47-004-006

Part 3 of 21 Parts

Final Report
VPI&SU Project 313142

Harmonic Vibrations of Viscoelastic Layered Media

by

D. Frederick
Engineering Mechanics

Virginia Polytechnic Institute & State University
Blacksburg, Virginia

December, 1970

TABLE OF CONTENTS

	<u>Page</u>
I. LIST OF SYMBOLS	1
II. SUMMARY	3
III. VIBRATIONS OF VISCOELASTIC MEDIA	4
A. Introduction	4
B. Governing Equations	5
C. Forced Harmonic Vibrations	7
D. Free Vibrations	11
E. Circular Cylinder in Torsional Oscillation	13
IV. SHEAR DEFORMATION OF A BEAM	18
A. Basic Analysis	18
B. Segmented Normals	21
V. REFERENCES	27

I. LIST OF SYMBOLS

σ_{jk}	stress tensor
ϵ_{jk}	strain tensor
s_{jk}	stress deviator tensor
e_{jk}	strain deviator tensor
u_j	displacement vector
f_j	forcing function
δ_{jk}	Kronecker delta
ρ	density
ω	frequency
t	time
G	complex shear modulus
K	complex bulk modulus
E	complex tensile modulus
ν	complex Poisson's ratio
G', \dots	real part of G, \dots
G'', \dots	imaginary part of G, \dots
G_R	stress relaxation modulus in shear
K_R	stress relaxation modulus in bulk
g	intensity of the relaxation spectrum for shear
b	intensity of the relaxation spectrum for bulk
P, Q, P', Q'	linear time operators
δ	damping factor
i	$\sqrt{-1}$
Re	means take real part of
Im	means take imaginary part of
r, θ, z	radial, angular, and axial coordinates of cylinder, resp.

T	torque
x, y, z	coordinates of beam
u_x, u_y, u_z	deformations of beam
κ	Timoshenko shear coefficient
W	average deflection of cross section of beam
Q	transverse shear force
M	moment
U	displacement of cross section in axial direction
Φ	total angle of rotation of cross section
ϕ	angle of rotation of cross section due to transverse shear
A	area of cross section of beam
I	moment of inertia
$\bar{}$	a bar over a function indicates a complex function of coordinates

Subscripts:

j, k, m, \dots	indices for rectangular Cartesian coordinates
r, θ, z	indices for cylindrical coordinates
δ	means quantity is for free vibration case
x, y, z	indices for coordinates of beam

II. SUMMARY

The purpose of the investigation was to study vibrations of structures made of alternate layers of elastic and viscoelastic materials. Many approaches have been taken by numerous researchers to solve vibrations of the viscoelastic materials, and the various approaches are discussed later in this report. Most authors seem to prefer handling free vibration rather than forced vibration of lossy materials but their methods have been found here to be approximately correct for small damping only. The theory of forced vibration is verified here and the torsional pendulum is solved using damped traveling waves which gives a physical picture of what is occurring in the bar. In addition a study of shear deformation is made using the recent and very lucid paper on the Timoshenko beam written by Cowper [31].

III. VIBRATIONS OF VISCOELASTIC MATERIAL

A. Introduction

A viscoelastic material converts mechanical energy of loading into heat. Because of this property, viscoelastic layers may be applied to elastic layers to damp out free vibrations and to decrease the amplitude of forced vibrations. Such multilayered media have been analyzed in the forms of beams, plates, and shells. The viscoelastic material has been treated by many investigators by assuming that it obeys the stress-strain laws of a spring-dashpot model [6], [7], [8], [9], [10], [11]. But a fairly simple model describing the behavior of a real material gives good results over only a narrow frequency range, and taking a larger number of springs and dashpots becomes mathematically unwieldy. In solving forced harmonic vibrations, some authors such as Henry and Freudenthal [12] and Biot and Pohle [13] under certain conditions correctly substitute complex moduli for the elastic moduli in the elastic solution and consequently solve the viscoelastic problem of the same shape and loading as the elastic problem. However, most authors seem to prefer treating free vibration [14], [15], [16], [17], [18], [19], rather than forced vibration. The usual procedure for free vibration is to select the time dependence for all stresses and displacements as $\exp(i\omega t - \delta t)$. This amounts to changing the frequency ω in the elastic solution to a complex frequency in addition to changing the elastic moduli to complex values. This procedure seems to be approximately correct for small damping only.

In attempts to simplify solutions, authors have made the assumption that the material is viscoelastic in shear but elastic in bulk [13], [24], or, alternately, the shear and bulk moduli have the same phase angle [13], [25].

Experiments have shown that neither of these assumptions is accurate. Kolsky [26] and Lifshitz and Kolsky [29] have shown experimentally for three familiar polymers that the tangent of the phase angle of the bulk modulus should be taken as two-tenths of the phase angle of the shear modulus. Another common assumption is that the material is incompressible [25], [27], [28].

Investigators such as Lee [20], Hunter [21], and Ward and Pinnock [22] who are interested primarily in the presentation of the theory of deformation of a three-dimensional linear viscoelastic body give only a one-dimensional theory for harmonic vibration. In reality, it appears that the three-dimensional vibration theory can be formulated by extending the one-dimensional case. The three-dimensional case appears in Bland's book [2], and is also presented here.

B. Governing Equations

The material considered is assumed to be isotropic, homogeneous, and to obey the linear viscoelastic laws. The stress-strain laws in integral form are [5], [21]

$$\begin{aligned} \sigma_{ijk} = & 2 \int_{-\infty}^t G_R(t-u) \frac{d\varepsilon_{ijk}}{du} du \\ & + \delta_{ijk} \int_{-\infty}^t \left[K_R(t-u) - \frac{2}{3} G_R(t-u) \right] \frac{d\varepsilon_{mm}}{du} du \end{aligned} \quad (1)$$

where

$$G_R(t) = \int_0^{\infty} g(\tau) e^{-t/\tau} d\tau \quad (2a)$$

$$K_R(t) = \int_0^{\infty} b(\tau) e^{-t/\tau} d\tau \quad (2b)$$

$G_R(t)$ and $K_R(t)$ are the stress relaxation moduli in shear and bulk, respectively, $g(\tau)$ and $b(\tau)$ are the intensities of the relaxation spectrums for shear and bulk, respectively, t is the time, and $(t - u)$ is the elapsed time.

The differential forms of the stress-strain laws are [20]

$$P s_{jk} = Q e_{jk} \quad (3a)$$

$$P' \sigma_{mm} = Q' \varepsilon_{mm} \quad (3b)$$

where

$$P = \sum_{n=0}^{\infty} \rho_n D^n, \quad Q = \sum_{n=0}^{\infty} q_n D^n$$

$$P' = \sum_{n=0}^{\infty} \rho'_n D^n, \quad Q' = \sum_{n=0}^{\infty} q'_n D^n \quad (3c)$$

and

$$D^n = \frac{\partial^n}{\partial t^n}$$

Also, s_{jk} and e_{jk} are the deviator tensors for stress and strain, respectively.

They are related to the stress and strain tensors by the following equations.

$$s_{jk} = \sigma_{jk} - \frac{1}{3} \sigma_{mm} \delta_{jk} \quad (4a)$$

$$e_{jk} = \varepsilon_{jk} - \frac{1}{3} \varepsilon_{mm} \delta_{jk} \quad (4b)$$

The strain-displacement relations for infinitesimal strains are

$$\varepsilon_{jk} = \frac{1}{2} (u_{j,k} + u_{k,j}) \quad (5)$$

where the comma means partial differentiation with respect to the coordinates.

The equations of motion are

$$\sigma_{jk,k} + f_j = \rho \frac{\partial^2 u_j}{\partial t^2} \quad (6)$$

where f_j is the forcing function or, alternately, a function describing a source of traveling waves. In simplifying the governing equations, the following

lemma from Harrington [1] is needed. If $\text{Re}(Ae^{i\omega t}) = \text{Re}(Be^{i\omega t})$ where Re means to take the real part, and A and B are independent of time, then $A = B$. This is easily verified by letting $t = 0$ for which $\text{Re}(A) = \text{Re}(B)$, and then letting $\omega t = \frac{1}{2}\pi$ for which $\text{Im}(A) = \text{Im}(B)$ where Im means to select the imaginary part.

C. Forced Harmonic Vibration

If a linear viscoelastic material experiences forced harmonic vibration for a long enough time, a steady state will exist in which transient effects have died out and the stresses, strains and displacements vary harmonically in time. This statement has been used by Bland [2] in formulating the general three-dimensional equations of wave propagation in a linear viscoelastic media. To show the validity of the statement and therefore of Bland's work, the type of transient term involved is derived in the following analysis taken from Albrecht and Freudenthal [3]. It is assumed that the body is at rest for all negative time, and that a shearing strain

$$\epsilon_{12} = \frac{\gamma_0}{2} \sin \omega t \quad (7a)$$

is imposed at zero time at some point in the material. The resulting shear stress from equations (1) and (2a) is

$$\begin{aligned} \tau_{12} &= 2 \int_0^t G_R(t-u) \frac{d\epsilon_{12}}{du} du \\ &= \int_0^t \left[\int_0^\infty g(\tau) e^{(-t+u)/\tau} d\tau \right] \gamma_0 \omega \cos \omega u du \\ &= \gamma_0 \left[G' \sin \omega t + G'' \cos \omega t \right] \\ &\quad - \gamma_0 \int_0^\infty g(\tau) e^{-t/\tau} \frac{\tau \omega}{1 + \tau^2 \omega^2} d\tau \end{aligned} \quad (7b)$$

where

$$G'(\omega) = \int_0^\infty g(\tau) \frac{\tau^2 \omega^2}{1 + \tau^2 \omega^2} d\tau \quad (8a)$$

$$G''(\omega) = \int_0^\infty g(\tau) \frac{\tau \omega}{1 + \tau^2 \omega^2} d\tau \quad (8b)$$

The quantities G' and G'' are the storage and loss moduli in shear, respectively.

The third term of (7b) is nonharmonic and exponentially damped in time. Denoting this transient term as $f(t)$ where

$$f(t) = \int_0^\infty g(\tau) e^{-t/\tau} \frac{\tau \omega}{1 + \tau^2 \omega^2} d\tau,$$

it is noted that $f(0) = G''$ and $f(t)$ approaches zero as t approaches infinity.

Therefore, after a sufficient length of time has passed, (7b) may be written as

$$\tau_{12} = \tau_0 (G' \sin \omega t + G'' \cos \omega t) \quad (9)$$

Thus ϵ_{12} and σ_{12} may be taken in the following more convenient form after steady state conditions are attained.

$$\epsilon_{12} = \text{Re} (\bar{\epsilon}_{12} e^{i\omega t}) \quad (10a)$$

$$\tau_{12} = \text{Re} (\bar{\tau}_{12} e^{i\omega t}) \quad (10b)$$

where the value of $\epsilon_{12} = -\frac{1}{2}i\gamma_0$ gives the previously defined strain. Equations (10) are the type of definitions used in the equations of wave propagation and they are valid for time large enough.

The forcing function for the case of steady state forced vibration may be considered as a source of traveling waves of a single frequency equal to the frequency of the forcing function. In the following, the governing equations for motion in a linear viscoelastic medium are simplified for wave propagation and, in a later section, it is shown how traveling waves may be added together to construct solutions to forced vibration problems. Following Bland [2], the forcing function (or source), displacements, strains, and stresses for linear viscoelastic media are taken in the forms

$$f_j = \text{Re} (\bar{f}_j e^{i\omega t}) \quad (12a)$$

$$u_j = \text{Re} (\bar{u}_j e^{i\omega t}) \quad (12b)$$

$$\varepsilon_{ijk} = \text{Re}(\bar{\varepsilon}_{ijk} e^{i\omega t}) \quad (12c)$$

$$\tau_{ijk} = \text{Re}(\bar{\tau}_{ijk} e^{i\omega t}) \quad (12d)$$

$$e_{ijk} = \text{Re}(\bar{e}_{ijk} e^{i\omega t}) \quad (12e)$$

$$s_{ijk} = \text{Re}(\bar{s}_{ijk} e^{i\omega t}) \quad (12f)$$

where the functions having a bar are complex functions of the coordinates and are independent of time. Substituting (12e) and (12f) into (3a),

$$P \text{Re}(\bar{s}_{ijk} e^{i\omega t}) = Q \text{Re}(\bar{\varepsilon}_{ijk} e^{i\omega t})$$

$$\text{Re}\left[\bar{s}_{ijk} e^{i\omega t} \sum_{n=0}^{\infty} p_n(i\omega)^n\right] = \text{Re}\left[\bar{e}_{ijk} e^{i\omega t} \sum_{m=0}^{\infty} g_m(i\omega)^m\right]$$

The differential forms of the stress-strain laws have been used here because they are much simpler when used with (12) than the integral forms. Applying the lemma and then dividing by the series in p_n ,

$$\bar{s}_{ijk} = \left[\frac{\sum_{m=0}^{\infty} g_m(i\omega)^m}{\sum_{n=0}^{\infty} p_n(i\omega)^n} \right] \bar{e}_{ijk} \quad (13a)$$

or,

$$\bar{s}_{ijk} = 2G \bar{e}_{ijk} \quad (13b)$$

where $2G$ is defined as the quantity in brackets in (13a). Also,

$$G(\omega) = G'(\omega) + i G''(\omega)$$

The quantity G is the complex shear modulus; its components G' and G'' are the same as those defined by (8). Substituting (12c) and (12d) into (3b) and proceeding as before, the complex equation governing the dilatation is obtained,

$$\bar{\tau}_{mmm} = 3K \bar{\varepsilon}_{mmm} \quad (15)$$

where

$$3K = \frac{\sum_{m=0}^{\infty} g'_m(i\omega)^m}{\sum_{n=0}^{\infty} p'_n(i\omega)^n}$$

and

$$K(\omega) = K'(\omega) + iK''(\omega) \quad (16)$$

K' and K'' are the storage and loss moduli in bulk, respectively, for forced vibration. Applying the lemma and the definitions (12) to equations (4), (5), and (6), the corresponding complex equations are obtained.

$$\bar{S}_{ijk} = \bar{V}_{ijk} - \frac{1}{3} \bar{V}_{mm} S_{ijk} \quad (17a)$$

$$\bar{E}_{ijk} = \bar{E}_{ijk} - \frac{1}{3} \bar{E}_{mm} S_{ijk} \quad (17b)$$

$$\bar{E}_{ijk} = \frac{1}{2} (\bar{u}_{j,k} + \bar{u}_{k,j}) \quad (18)$$

$$\bar{V}_{ijk,k} + \bar{S}_j + \rho \omega^2 \bar{u}_j = 0 \quad (19)$$

Define

$$\nu = \frac{3K - 2G}{2(G + 3K)} \quad (20)$$

and

$$E = 2G(1 + \nu) \quad (21)$$

where ν is the complex Poisson's ratio and E is the complex tensile modulus for forced vibration. Equations (13) and (17) can be solved to give

$$\bar{V}_{ijk} = 2G \bar{E}_{ijk} + (K - \frac{2}{3}G) \bar{E}_{mm} S_{ijk} \quad (22)$$

Substituting (20) and (21) into (22),

$$\bar{V}_{ijk} = \frac{E}{1 + \nu} \left[\bar{E}_{ijk} + \frac{\nu}{1 - 2\nu} \bar{E}_{mm} S_{ijk} \right] \quad (23)$$

Equation (23) may be solved for the complex strain. The result is

$$\bar{E}_{ijk} = \frac{1 + \nu}{E} \bar{V}_{ijk} - \frac{\nu}{E} \bar{V}_{mm} S_{ijk} \quad (24)$$

Equations (18), (19), and (23) may be solved together to get the governing equation for the complex displacements.

$$\bar{u}_{j,kk} + \frac{1}{1-2\nu} \bar{u}_{m,mj} + \frac{1}{G} \bar{f}_j + \frac{\rho\omega^2}{G} \bar{u}_j = 0 \quad (25)$$

The forcing function may be dropped from the governing equation and applied instead through the boundary conditions. If this is done, (25) becomes

$$\bar{u}_{j,kk} + \frac{1}{1-2\nu} \bar{u}_{m,mj} + \frac{\rho\omega^2}{G} \bar{u}_j = 0$$

or, in vector notation,

$$(\nabla^2 + \frac{\rho\omega^2}{G}) \bar{u}_j \vec{e}_j + \frac{1}{1-2\nu} \nabla (\nabla \cdot \bar{u}_j \vec{e}_j) = 0 \quad (26)$$

where \vec{e}_j is a unit vector in the direction of the coordinate x_j .

D. Free Vibration

An exact solution to the equations of viscoelasticity for free vibration appears to be much more difficult to obtain than for forced vibration. The standard procedure in solving free vibration problems in viscoelasticity is to assume the time dependence to be of the form $\exp(i\omega t - \delta t)$ which may also be written as $\exp(i[\omega + i\delta]t)$. This assumed time dependence can be imposed on the equations for forced harmonic vibration by substituting $\omega + i\delta$ for ω in the governing equations. However, this procedure results in a shear modulus for free vibration, G_δ , which is different from the one for forced vibration. This is demonstrated in the following example. It is assumed first that a specimen is forced to vibrate at a natural frequency until all transient effects have become negligibly small. Then zero time is taken as the time when the load is removed after which the specimen is allowed to vibrate freely. The deflection for this motion is

$$u_j = \begin{cases} \operatorname{Re}(\bar{u}_j e^{i\omega t}) & , -\infty < t < 0 \\ \operatorname{Re}(\bar{u}_j e^{i\omega t - \delta t}) & , t > 0 \end{cases} \quad (27)$$

Hence the shearing strain ϵ_{12} is

$$\epsilon_{12} = \begin{cases} \operatorname{Re}(\bar{\epsilon}_{12} e^{i\omega t}) & , -\infty < t < 0 \\ \operatorname{Re}(\bar{\epsilon}_{12} e^{i\omega t - \delta t}) & , t > 0 \end{cases} \quad (28)$$

The corresponding stress may be found by substituting (2a) and (28) into (1).

$$\tau_{12} = \operatorname{Re} \left\{ \int_{-\infty}^0 2G_R(t-u) \frac{d}{du} (\bar{\epsilon}_{12} e^{i\omega u}) du + \int_0^t 2G_R(t-u) \frac{d}{du} (\bar{\epsilon}_{12} e^{i\omega u - \delta u}) du \right\} \quad (29)$$

or,

$$\tau_{12} = \operatorname{Re} \left\{ 2G_S \bar{\epsilon}_{12} e^{i\omega t - \delta t} \right\} + \operatorname{Re} \left\{ 2 \int_0^\infty g(\tau) e^{-\delta \tau} \bar{\epsilon}_{12} \left[\frac{\tau \omega (\tau \omega + i)}{1 + \tau^2 \omega^2} - \frac{\tau^2 \omega^2 - \delta \tau (1 - \delta \tau) + i \tau \omega}{(1 - \delta \tau)^2 + \tau^2 \omega^2} \right] d\tau \right\} \quad (30)$$

where

$$G_S = G'_S + i G''_S \quad (31)$$

$$G'_S = \int_0^\infty g(\tau) \left[\frac{\tau^2 \omega^2 - \delta \tau (1 - \delta \tau)}{(1 - \delta \tau)^2 + \tau^2 \omega^2} \right] d\tau \quad (32a)$$

$$G''_S = \int_0^\infty g(\tau) \left[\frac{\tau \omega}{(1 - \delta \tau)^2 + \tau^2 \omega^2} \right] d\tau \quad (32b)$$

A comparison of equations (8) with (32) reveals that G may be obtained from G_S in theory by setting δ equal to zero in (32). But the shear modulus is a material property and is independent of the nature of the loading applied. Thus the assumed time dependence for free vibration leads to the erroneous conclusion that the shear modulus for free vibration is different from the one for forced vibration. However, when δ is small, G_S is nearly equal to G , and $\exp(i\omega t - \delta t)$ may then be valid approximately for damping small enough.

No exact solutions for free vibration of a viscoelastic specimen have been found in a search of the literature, and all efforts to find such a solution under this project have so far been fruitless.

E. Circular Cylinder in Torsional Oscillation

For forced torsional oscillations of a circular cylinder, all normal strains are zero in the usual circular cylindrical coordinates (r, θ, z) . Thus the dilatation vanishes, and (26) becomes

$$\left(\nabla^2 + \frac{\rho\omega^2}{G}\right) \bar{u}_i \vec{e}_i = 0 \quad (33)$$

Furthermore, only the angular displacement u_θ has a value in this case. Therefore, (33) reduces to

$$\left(\nabla^2 + \frac{\rho\omega^2}{G}\right) \bar{u}_\theta \vec{e}_\theta = 0 \quad (34)$$

Equation (34) is known as a vector wave equation. Complex equations of this form occur in the study of electromagnetic wave propagation in lossy media[1]. Thus the well-developed electromagnetic wave theory may be used as a guide in constructing solutions to (34).

Torsional waves in a circular cylinder travel in the axial, or z , direction. A plane torsional wave traveling in the positive z direction is given by

$$\bar{u}_\theta = V(r) e^{-ikz} \quad (35)$$

where

$$k = k' - ik'' \quad (36)$$

In electromagnetic wave theory, k' is called the propagation constant, and k'' is known as the attenuation constant. These quantities have the same names in linear viscoelasticity even though they are in reality not constants, but

functions of frequency. The same wave as (35) traveling in the negative z direction is expressed as

$$\bar{u}_0 = V(r) e^{-ikz} \quad (37)$$

Consider an infinitely long cylindrical bar with a source of plus z traveling waves of torsion located at a large negative value of z and an identical source of negative z traveling waves located at a large positive value of z. The waves will interact to produce a displacement-free surface at the origin when the displacement is the difference of (35) and (37),

$$\bar{u}_0 = V(r) (e^{ikz} - e^{-ikz}) \quad (38)$$

For k'' not equal to zero, there are no other displacement-free surfaces. The complex stress $\sigma_{z\theta}$ from (22) and (18) is

$$\bar{\tau}_{z\theta} = G \frac{\partial \bar{u}_0}{\partial z} \quad (39)$$

Substituting (38) into (39)

$$\bar{\tau}_{z\theta} = G V(r) ik (e^{ikz} - e^{-ikz}) \quad (40)$$

It can be shown with this equation that for k'' not equal to zero, there are no surfaces free of this stress. Substituting (38) into (34) and simplifying, the relationship for $V(r)$ is obtained.

$$\frac{\partial}{\partial r} \left[\frac{1}{r} \frac{\partial}{\partial r} (rV) \right] + (ik)^2 V + \frac{\rho\omega^2}{G} V = 0 \quad (41)$$

Let

$$\alpha^2 = \frac{\rho\omega^2}{G} - k^2 \quad (42)$$

Then

$$\frac{\partial}{\partial r} \left[\frac{1}{r} \frac{\partial}{\partial r} (rV) \right] + \alpha^2 V = 0 \quad (43)$$

The solution for $\alpha = 0$ is

$$V = Ar + \frac{B}{r} \quad (44)$$

For a solid bar, $B = 0$, and

$$V = Ar \quad (45)$$

Substituting (45) into (38)

$$\bar{u}_\theta = Ar(e^{ikz} - e^{-ikz}) \quad (46)$$

For $\alpha = 0$, (42) gives

$$k^2 = \frac{\rho\omega^2}{G} \quad (47)$$

The shear modulus may be expressed in terms of its magnitude, $|G|$, and phase angle, γ , by

$$G = |G| e^{i\gamma}$$

This can be used to solve for k' and k'' from (47). The result is

$$k' = \omega \sqrt{\frac{\rho}{|G|}} \cos \frac{\gamma}{2} \quad (48a)$$

$$k'' = \omega \sqrt{\frac{\rho}{|G|}} \sin \frac{\gamma}{2} \quad (48b)$$

The shear stress $\bar{\sigma}_{r\theta}$ must vanish on the surface of the bar. Equations (18) and (22) expressed in cylindrical coordinates and solved with (46) yield

$$\begin{aligned} \bar{\sigma}_{r\theta} &= 2G\bar{\epsilon}_{r\theta} \\ &= G\left[\frac{2\bar{u}_\theta}{r} - \frac{\bar{u}_\theta}{r}\right] \\ &= 0 \end{aligned}$$

It can be shown that all stresses vanish except $\sigma_{z\theta}$.

Since (46) gives no displacement at $z = 0$, it is also the solution for a semi-infinite circular bar built in at $z = 0$ if the portion of the bar along the negative z axis is discarded. The solution may then be interpreted physically as a train of waves emanating from a source at a large value of positive z and reflecting from the fixed end at the origin. The solution for forced oscillation

of a torsional pendulum in terms of the torque applied at one end may also be obtained from (46). A plane perpendicular to the z-axis is passed through the semi-infinite bar at $z = L$, and the portion of the bar beyond $z = L$ is discarded. A forcing function placed at $z = L$ exactly duplicates the stress distribution occurring before the cut was made. From (40) and (45), this stress distribution is

$$\bar{T}_{z\theta} \Big|_{z=L} = GA\tau ik (e^{ikz} - e^{-ikz}) \quad (49)$$

The applied torque is

$$T = \text{Re} (\bar{T} e^{i\omega t}) \quad (50)$$

$$\bar{T} = \int_{\theta=0}^{2\pi} \int_{r=0}^a r \bar{T}_{z\theta} \Big|_{z=L} r dr d\theta \quad (51)$$

where a is the radius of the cylinder. Substituting (49) into (51) and solving for the constant A ,

$$A = \frac{2\bar{T}}{\pi a^4} \left[G ik (e^{ikL} - e^{-ikL}) \right]^{-1} \quad (52)$$

The deflection from (46) and (52) is

$$\bar{u}_\theta = \frac{2\bar{T} r (e^{ikz} - e^{-ikz})}{\pi a^4 ik G (e^{ikL} + e^{-ikL})} \quad (53)$$

Since the deflection varies linearly with r , it may be duplicated experimentally by attaching a rigid disk to the end at $z = L$ and forcing the disk to oscillate.

For an elastic material, (53) becomes

$$\bar{u}_\theta = \frac{2\bar{T} r \sin kz}{\pi a^4 k G \cos kL} \quad (54)$$

The viscoelastic deflection could have been obtained from the elastic solution (54) by making k and G complex. A third technique is used by Berry [4] who

seems to be the first to have solved torsional oscillation of a viscoelastic pendulum. He used a separation of variables technique and applied the forcing function through the boundary conditions. The advantage of using traveling waves to construct a solution is that it gives a physical picture of what is occurring in the bar.

IV. SHEAR DEFORMATION OF A BEAM

A. Basic Analysis

In the following, a study is made of the Timoshenko beam which includes the effects of rotary inertia and shear deformation in the governing equations. Shear deformation and rotary inertia also occur in a shell, but a study of these effects in a beam gives all the information necessary to understand the same effects in a shell and has the advantage of involving only one coordinate in the governing equations. The ultimate application of the derived theory presented here will be to vibration of multilayered shells.

The initial analysis is taken from Cowper's [31] derivation of the beam equations by integrating the equations of elasticity over the cross section of the beam. The beam coordinates x , y , z have directions as shown in figure 1.

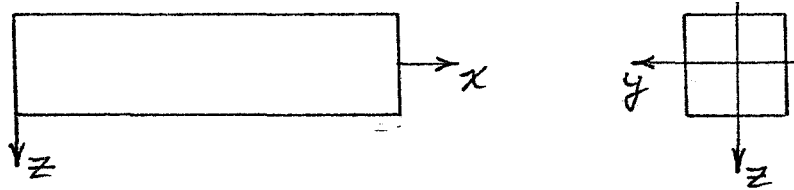


Figure 1

The deflections u_z and u_x in the z and x directions, respectively, are written as

$$u_z = W + v_z \quad (55a)$$

$$u_x = U + z\Phi + v_x \quad (55b)$$

where

$$W = \frac{1}{A} \iint u_z dy dz \quad (56a)$$

$$U = \frac{1}{A} \iint u_x dy dz \quad (56b)$$

$$\Phi = \frac{1}{I} \iint z u_x dy dz \quad (56c)$$

W is the average deflection of the cross section in the z direction, U is the average displacement of the cross section in the x direction, Φ is the average angle of rotation of the cross section about the neutral axis, A is the area of the cross section, and v_x and v_z are residuals. Integrating equations (55) over the cross section and applying equations (56) yields

$$\iint v_z dy dz = \iint v_x dy dz = \iint z v_x dy dz = 0 \quad (57)$$

The equations (55) are substituted into the following stress-strain relation from elasticity.

$$\frac{\partial u_z}{\partial x} + \frac{\partial u_x}{\partial z} = \frac{\nabla x z}{G} \quad (58)$$

The result is

$$\frac{\partial W}{\partial x} + \Phi = \frac{\nabla x z}{G} - \frac{\partial v_x}{\partial z} - \frac{\partial v_z}{\partial x} \quad (59)$$

This is integrated over the cross section to obtain

$$\frac{\partial W}{\partial x} + \Phi = \frac{Q}{AG} - \frac{1}{A} \iint \frac{\partial v_x}{\partial z} dy dz \quad (60)$$

Cowper assumes that the distribution of the residual, v_x , for a vibrating beam is the same as the distribution for a static load on the beam. This allows him to evaluate the last term in (60) as a constant times the factor $\frac{Q}{AG}$. After performing the integration, (60) becomes

$$\frac{\partial W}{\partial x} + \Phi = \frac{Q}{\kappa AG} \quad (61)$$

where κ is called the Timoshenko shear coefficient. It is easily seen that if v_x is neglected in (60), the result is

$$\frac{\partial W}{\partial x} + \Phi = \frac{Q}{AG} \quad (62)$$

which is the same as setting κ equal to unity in (61). For elementary beam theory, the shear deformation is neglected and (60) becomes

$$\frac{\partial W}{\partial x} + \Phi = 0 \quad (63)$$

Three other equations derived by Cowper are

$$\frac{\partial Q}{\partial x} + p = \rho A \frac{\partial^2 W}{\partial t^2} \quad (64a)$$

$$\frac{\partial M}{\partial x} - Q = \rho I \frac{\partial^2 \Phi}{\partial t^2} \quad (64b)$$

$$EI \frac{\partial \Phi}{\partial x} = M \quad (64c)$$

where

$M = \iint z \tau_{xx} dy dz$ is the bending moment acting at a section, I is the moment of inertia of the cross section, p is the total force acting in the z direction on the beam, E is the tensile modulus, and ρ is the density. The governing equation on W can be obtained by eliminating the unknowns Q , M , and Φ in (61) and (64). The deflection W may further be written as

$$W = W_H + W_p$$

where W_H is the homogeneous solution to the governing equation on W , and W_p is the particular solution. Assuming a harmonic time dependence, the equation governing W_H is

$$\frac{\partial^4 W_H}{\partial x^4} + \left[\frac{\rho \omega^2}{\kappa G} + \frac{\rho \omega^2}{E} \right] \frac{\partial^2 W_H}{\partial x^2} + \frac{\rho \omega^2}{E} \left[\frac{\rho \omega^2}{\kappa G} - \frac{A}{I} \right] W_H = 0 \quad (65)$$

A quantity which is needed later is ϕ which is the rotation of the cross section due to transverse shear. Its relationship to previously defined quantities is

$$\frac{\partial W}{\partial x} + \Phi = \phi \quad (66a)$$

Φ and ϕ are positive when measured counterclockwise, but $\frac{\partial W}{\partial x}$ is positive when measured clockwise in the coordinate system used here. Equations (66a) and (62) lead to

$$\phi = \frac{Q}{AG} \quad (66b)$$

B. Segmented Normals

The warped surfaces of certain statically loaded beams are known functions of the beam coordinates, and Cowper assumed that these surfaces were the same as the warped surfaces when a vibratory load was applied. This led to an equation for the shear coefficient as a function of Poisson's ratio. For an elastic shell, the shear coefficients have been found by means of a free vibration solution, but this is not practical at this time for viscoelastic materials since free vibration of these materials has not been satisfactorily described mathematically as yet. Another procedure which in effect gives a better approximation than unity for the shear coefficient is to divide the normal into segments each of which can rotate independently of the other segments but each of which remains straight after deformation. This procedure is applied here to the Timoshenko beam in order to show the kind of accuracy that may be expected from this method.

The solid beam is first divided into three layers of equal thicknesses as shown in figure 2 for the purpose of assigning a number to each of the segments

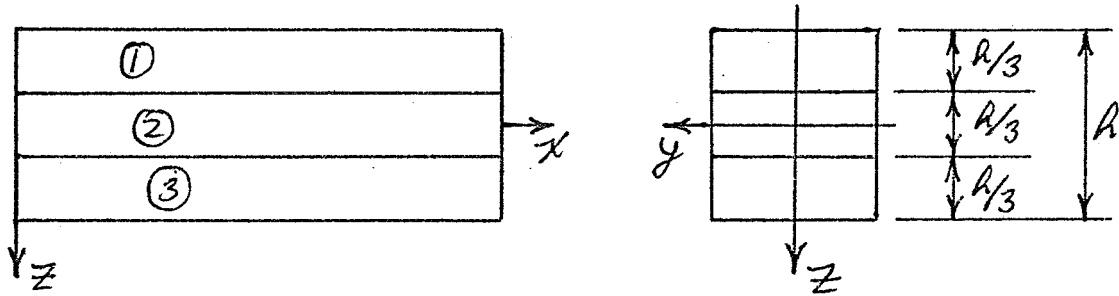


Figure 2

of the normal. A subscript on a variable will refer to the corresponding layer, and the same variable without a subscript indicates a quantity which describes the beam as a single unit. The deflections will be taken as follows:

$$u_{z_1} = u_{z_2} = u_{z_3} = W \quad (67a)$$

$$u_{x_1} = U_1 + \left(z + \frac{H}{3}\right) \Phi_1 \quad (67b)$$

$$u_{x_2} = U_2 + z \Phi_2 \quad (67c)$$

$$u_{x_3} = U_3 + \left(z - \frac{H}{3}\right) \Phi_3 \quad (67d)$$

U_1 , U_2 , and U_3 are shown in figure 3.

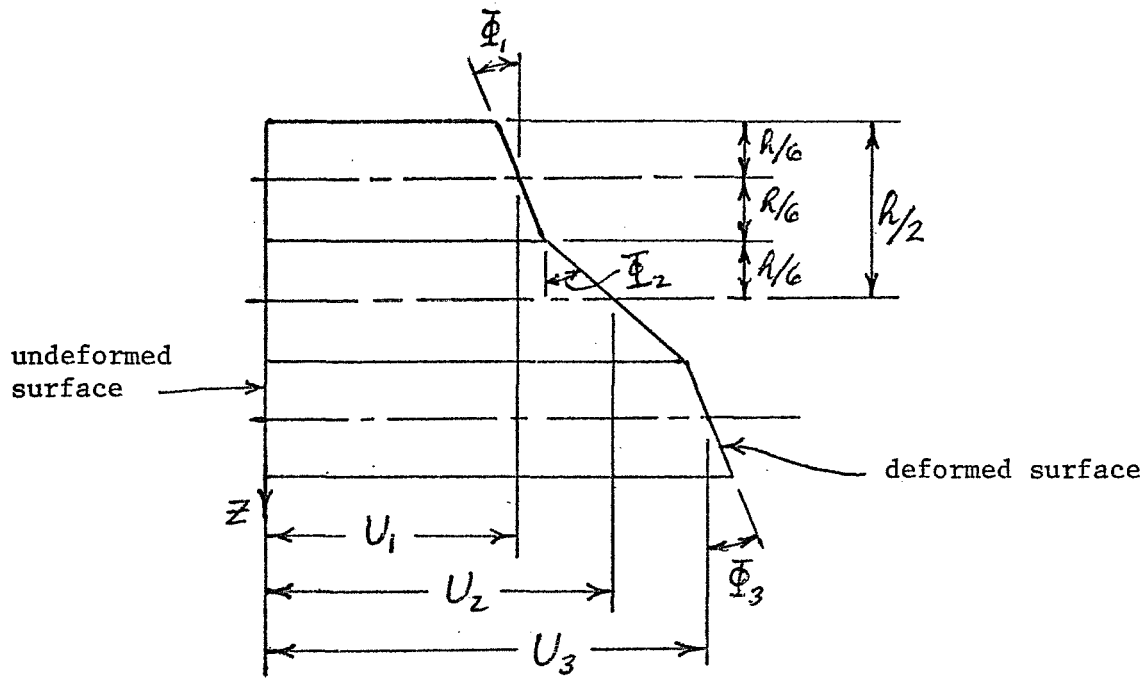


Figure 3

Equation (58) integrated over each layer yields the following three equations.

$$\Phi_1 + \frac{\partial W}{\partial x} = \frac{Q_1}{A_1 G} \quad (68a)$$

$$\Phi_2 + \frac{\partial W}{\partial x} = \frac{Q_2}{A_2 G} \quad (68b)$$

$$\Phi_3 + \frac{\partial W}{\partial x} = \frac{Q_3}{A_3 G} \quad (68c)$$

where

$$Q_1 + Q_2 + Q_3 = Q \quad (69a)$$

$$A_1 = A_2 = A_3 = \frac{1}{3} A \quad (69b)$$

Also, the following assumption is made.

$$\Phi_1 = \Phi_3 \quad (70a)$$

which leads to

$$Q_1 = Q_3 \quad (70b)$$

The result of adding the equations (68) and applying (69) and (70) is

$$\frac{1}{3}(2\Phi_1 + \Phi_2) + \frac{\partial W}{\partial x} = \frac{Q}{AG} \quad (71a)$$

The three following equations are derived similarly.

$$\frac{\partial Q}{\partial x} + p = \rho A \frac{\partial^2 W}{\partial t^2} \quad (71b)$$

$$\frac{\partial M}{\partial x} - Q = \frac{\rho A L^2}{324} \left[38 \frac{\partial^2 \Phi_1}{\partial t^2} + 13 \frac{\partial^2 \Phi_2}{\partial t^2} \right] \quad (71c)$$

$$M = \frac{EAL^2}{324} \left[38 \frac{\partial \Phi_1}{\partial x} + 13 \frac{\partial \Phi_2}{\partial x} \right] \quad (71d)$$

The four equations (71) involve the five unknowns Φ_1 , Φ_2 , W , Q , and M . Thus another relationship between these variables must be found.

From (66), (68), and (69b),

$$\phi_1 = \Phi_1 + \frac{\partial W}{\partial x} \quad (72a)$$

$$\phi_2 = \Phi_2 + \frac{\partial W}{\partial x} \quad (72b)$$

and

$$\phi_1 = \frac{3Q_1}{AG} \quad (73a)$$

$$\phi_2 = \frac{3Q_2}{AG} \quad (73b)$$

Also, (70) and (68) yield $\phi_3 = \phi_1$. The angles ϕ_1 and ϕ_2 are the rotations of the segments of normal due to transverse shear. A relationship between ϕ_1 and ϕ_2 can be chosen to make the shearing stresses have the best fit to a parabolic distribution in the z-direction. This is accomplished by first writing a parabolic distribution for σ_{xz} . The correct result is

$$\tau_{xz} = \frac{3Q}{2h^2A} (h^2 - z^2) \quad (74)$$

Next, the average of σ_{xz} is taken over each layer.

$$\iint_{\text{LAYER \#1}} \tau_{xz} dy dz = Q_1 \quad (75a)$$

$$\iint_{\text{LAYER \#2}} \tau_{xz} dy dz = Q_2 \quad (75b)$$

The final result of evaluating equations (75) and using (73) is

$$\phi_1 = \frac{7}{13} \phi_2 \quad (76)$$

The functions ϕ_1 , ϕ_2 , ϕ_1 , ϕ_2 , M, and Q may be eliminated from equations (71), (72), and (76) resulting in the governing equation on W. The result for W_H assuming a harmonic time dependence is

$$\begin{aligned} \frac{d^4 W_H}{dx^4} + \left[\frac{81}{89} \frac{\rho \omega^2}{G} + \frac{\rho \omega^2}{E} \right] \frac{d^2 W_H}{dx^2} \\ + \frac{\rho \omega^2}{E} \left[\frac{81}{89} \frac{\rho \omega^2}{G} - \frac{A}{I} \right] W_H = 0 \end{aligned} \quad (77)$$

This is the same equation as (65) with κ taking the value

$$\kappa = \frac{81}{89} = 0.912 \quad (78)$$

for three segments of normal. Cowper's value for κ which allows the normal to warp is (for a rectangular beam)

$$\kappa = \frac{10(1+\nu)}{12 + 11\nu} \quad (79a)$$

where ν is Poisson's ratio. (79a) gives

$$\kappa = 0.833 \quad \text{for } \nu = 0 \quad (79b)$$

$$\kappa = 0.857 \quad \text{for } \nu = 0.5 \quad (79c)$$

For a single straight normal with warping neglected,

$$\kappa = 1.00 \quad (80)$$

A comparison of (78), (79) and (80) reveals that dividing the normal into three segments decreases by more than 50% the difference between the shear coefficient for a single straight normal with no warpage and the best known value of the shear coefficient as determined by Cowper. Dividing the normal into more than three segments should improve the accuracy further. As mentioned previously, the purpose of applying this analysis to a beam was to evaluate the accuracy of the method before applying it to a shell.

REFERENCES

1. Harrington, R. F., Time-Harmonic Electromagnetic Fields, McGraw-Hill, New York, 1961
2. Bland, D. R., The Theory of Linear Viscoelasticity, Pergamon Press, London, 1960
3. Albrecht, B., and Freudenthal, A. M., "Second-Order Visco-Elasticity in a Filled Elastomer," International Journal of Solids and Structures, Vol. 2, No. 4, Oct. 1966, pp. 555-571
4. Berry, D. S., "Stress Propagation in Visco-Elastic Bodies," Journal of the Mechanics and Physics of Solids, Vol. 6, 1958, pp. 177-185
5. Staverman, A. J., and Schwarzl, F., "Linear Deformation Behaviour of High Polymers," chapter one of Die Physik der Hochpolymeren, edited by H. A. Stuart, Springer, Berlin, 1956
6. Achenbach, J. D., and Chao, C. C., "A Three-Parameter Viscoelastic Model Particularly Suited for Dynamic Problems," Journal of the Mechanics and Physics of Solids, Vol. 10, 1962, pp. 245-252
7. Maybee, J. S., "Normal and Quasi-Normal Modes in Damped Linear Dynamic Systems," Journal of Applied Mechanics, Vol. 33, No. 2, June 1966, pp. 413-416
8. Newman, J. K., "Viscous Damping in Flexural Vibrations of Bars," Journal of Applied Mechanics, Vol. 26, No. 3, Sept. 1959, pp. 367-376
9. Williams, M. L., "Structural Analysis of Viscoelastic Materials," AIAA Journal, Vol. 2, No. 5, May 1964, pp. 785-808
10. Eller, S. A., and Cohen, L., "Investigation of the Vibration Damping Properties of Viscoelastic Materials Using a Delay Angle Technique," Shock and Vibration Bulletin, No. 35, Part 5, Feb. 1966, The Shock and Vibration Information Center, U. S. Naval Research Lab, Washington, D. C., pp. 159-168
11. Pan, H. H., "Vibration of Viscoelastic Plates," Journal de Mecanique, Vol. 5, No. 3, Sept. 1966, pp. 355-374
12. Henry, L. A., and Freudenthal, A. M., "Standing Waves in a Viscoelastic Cylinder Case Bonded to a Thin Shell," AIAA Journal, Vol. 4, No. 2, Feb. 1966, pp. 313-319
13. Biot, M. A., and Pohle, F. V., "Validity of Thin-Plate Theory in Dynamic Viscoelasticity," Journal of the Acoustical Society of America, Vol. 36, No. 6, June 1964, pp. 1110-1117

14. Parke, S., "Logarithmic Decrements at High Damping," British Journal of Applied Physics, Vol. 17, No. 2, pp. 271-273
15. Jones, I. W., Salerno, V. L., and Savacchio, A., "An Analytical and Experimental Evaluation of the Damping Capacity of Sandwich Beams with Viscoelastic Cores," Trans. ASME, Series B, Vol. 89, No. 3, Aug. 1967, pp. 438-444, Journal of Engineering for Industry
16. Yu, Y.-Y., "Damping of Flexural Vibrations of Sandwich Plates," Journal of Aerospace Sciences, Vol. 29, No. 7, July 1962, pp. 790-803
17. DiTaranto, R. A., "Theory of Vibratory Bending for Elastic and Viscoelastic Layered Finite-Length Beams," Journal of Applied Mechanics, Vol. 32, No. 4, Dec. 1965, pp. 881-886
18. DiTaranto, R. A., and Blasingame, W., "Composite Damping of Vibrating Sandwich Beams," Journal of Engineering for Industry, Trans. ASME, Series B, Vol. 89, No. 4, Nov. 1967, pp. 633-638
19. Nicholas, T., and Heller, R. A., "Determination of the Complex Shear Modulus of a Filled Elastomer from a Vibrating Sandwich Beam," Experimental Mechanics, J. Soc. Exp. Stress Analysis, Vol. 7, No. 3, March 1967, pp. 110-116
20. Lee, E. H., "Viscoelastic Stress Analysis," Structural Mechanics, Proc. First Symposium Naval Structural Mechanics, Stanford U., Calif., 1958, edited by J. N. Goodier and N. J. Hoff, Pergamon Press, New York, 1960, pp. 456-482
21. Hunter, S. C., "The Solution of Boundary Value Problems in Linear Viscoelasticity," Mechanics and Chemistry of Solid Propellants, Proc. Fourth Symposium Naval Structural Mechanics, April 1965, edited by A. C. Eringen, et al., Pergamon Press, New York, 1967, pp. 257-295
22. Ward, I. M., and Pinnock, P. R., "The Mechanical Properties of Solid Polymers," British Journal of Applied Physics, Vol. 17, No. 1, Jan. 1966, pp. 3-32
23. Love, A. E. H., A Treatise on the Mathematical Theory of Elasticity, Dover, New York, 1944
24. Lockett, F. J., "Interpretation of Mathematical Solutions in Viscoelasticity Theory Illustrated by a Dynamic Spherical Cavity Problem," Journal of the Mechanics and Physics of Solids, Vol. 9, 1961, pp. 215-229
25. Pan, H. H., "Vibration of a Viscoelastic Timoshenko Beam," Journal of the Engineering Mechanics Division, Proc. ASCE, Vol. 92, No. EM 2, April 1966, pp. 213-234
26. Kolsky, H., "Experimental Studies in Stress Wave Propagation," Proc. of the Fifth U. S. Nat. Congress of Applied Mechanics, 1966, pp. 21-36

27. Achenbach, J. D., "Dynamic Response of a Long Viscoelastic Cylinder," AIAA Journal, Vol. 3, April 1965, pp. 673-677
28. Pilkey, W. D., "Vibrations of a Viscoelastic Timoshenko Beam," Journal of the Engineering Mechanics Division, Proc. ASCE, Vol. 92, EM 6, Dec. 1966, pp. 254-257
29. Lifshitz, J. M., and Kolsky, H., "The Propagation of Spherically Divergent Stress Pulses in Linear Viscoelastic Solids, Journal of the Mechanics and Physics of Solids, Vol. 13, No. 6, Dec. 1965, pp. 361-376
30. Sokolnikoff, I. S., Mathematical Theory of Elasticity, McGraw-Hill, New York, 1956
31. Cowper, G. R., "The Shear Coefficient in Timoshenko's Beam Theory," Journal of Applied Mechanics, Vol. 33, June 1966, pp. 335-340

' N71-71004 '

FINAL REPORT

to the

NATIONAL AERONAUTICS AND SPACE ADMINISTRATION

in connection with

NASA Grant NGR 47-004-006

Part 4 of 21 Parts

Final Report

VPI&SU Project 313241

Preparation of Glass-Ceramic Composites
by Controlled Crystallization Techniques

by

J. J. Brown, Jr.

Metals & Ceramics Engineering

Virginia Polytechnic Institute & State University
Blacksburg, Virginia

December, 1970

PREPARATION OF GLASS-CERAMIC COMPOSITES
BY CONTROLLED CRYSTALLIZATION TECHNIQUES

ABSTRACT

A method of strengthening glass by liquid phase separation is presented using the $\text{Li}_2\text{O-TiO}_2\text{-SiO}_2$ system as an example. The transverse bending strength of annealed bulk glasses prepared on the 70 weight % SiO_2 isopleth increases from 18,320 to 30,775 psi as phase separation develops. This effect is observed prior to loss of transparency of the composite. Glasses once strengthened by liquid immiscibility formation are successfully strengthened still further by conventional chill tempering. The experimental results are presented and discussed and an explanation of the combined strengthening effect is offered.

This paper was presented before the Glass Division at the 72nd Annual Meeting of the American Ceramic Society, Philadelphia, Pennsylvania May 6, 1970.

I. Introduction

Liquid immiscibility is a phenomenon that exists stably in many molten ceramic systems. It has been investigated in considerable depth from both experimental and theoretical standpoints. It is, however, very surprising that so few practical engineering applications have been developed which make use of liquid phase separation in oxide systems. It is, for example, used as an intermediate step in the manufacture of high silica glass (Vycor-brand)⁽¹⁾ and as a source of opaque glazes.⁽²⁾ Liquid immiscibility appears to offer a very convenient approach to the preparation of glass-in-glass, crystal-in-glass, and even crystal-in-crystal composites. Of special interest in the present paper is strengthening provided by properly prepared glass-in-glass composites. When the disperse phase is discontinuous and the individual droplets are too small to scatter visible electromagnetic radiation, the approach seems to be a potentially useful method of strengthening some glasses while retaining visible transparency. Moreover, it is of interest to consider the possibility of using liquid immiscibility strengthening in combination with other conventional strengthening techniques.

II. Mechanical Strength of Glass

Most bulk commercial glasses in the "as-formed" condition possess nominal transverse bending strengths of 10,000 to 15,000 psi. This strength level can be increased to perhaps 30,000 psi by chill tempering. With special chemical and/or physical treatments some glasses can be strengthened up to 400,000 psi. Even this value, however, is far short of the typical theoretical strength of glass which is in the neighborhood of 2,000,000 psi.

This theoretical limit, which can be calculated by using atomistic considerations, has been approached experimentally by preparing and testing thin glass fibers under carefully controlled laboratory conditions.

Although many factors are responsible for reducing the actual strength of glasses to values so far below their theoretical limit, one of the most important is the effect of surface flaws. These can range from the sub-microscopic Griffith flaws⁽³⁾ to major surface abrasions such as would be encountered in rough handling.

III. Methods of Strengthening Glass

It is possible to strengthen glass by rapid quenching. Basically this procedure sets up a system of high compressive stresses on the surface with a corresponding set of tensile stresses in the interior of the glass. This system will provide high strength as long as the compressive layer is not pierced. This concept forms the basis for chill tempering, probably the most widely used glass strengthening process in commercial use at this time. There are several serious handicaps associated with this strengthening mechanism. It is, for example, sometimes difficult to get uniform stress distribution especially if the article has a complex shape. Sharp reentrant angles are virtually impossible to temper. Because the resultant stress system is dependent on thermal expansion, for each desired strengthening level there exists a definite minimum thickness required before strengthening can be achieved.

There are a number of techniques involving chemical methods of strengthening glass. A composite material may be formed in which the outer glass or glass-ceramic has a lower thermal expansion coefficient than the interior. The composite may consist of two different glasses or only one parent glass whose outer layer has been changed by ion exchange and/or surface crystallization.⁽⁴⁾

Nordberg et al.⁽⁵⁾ describe a method of strengthening at low temperatures which involves ion exchange. By replacing a small cation (viz., Na^+) by a larger cation (viz., K^+) in the surface of a glass, high surface compressive stress develops with consequent strengthening.

Because most of the present techniques use a compressive surface layer to provide the strengthening effect in glasses, it is easy to see why once this surface layer is penetrated, the strength of the glass decreases to its nominal level. By using a liquid immiscibility approach it would seem reasonable to expect these compressive stresses to be distributed throughout the matrix phase and that a compressive surface layer would not be a critical factor in controlling the strength of the glass.

None of the current strengthening techniques appears to take advantage of phase separation. It is well known that liquid immiscibility exists in equilibrium in many oxide melts and that the phase separation can be retained in the glassy state. It is also known that one way to strengthen glass is to incorporate a second high expanding (contracting) discontinuous disperse phase in the matrix glass.⁽⁴⁾ The resulting stresses developed by the mismatch in thermal expansion coefficients can provide a significant degree of strengthening.

It is unlikely that liquid phase separation as a means of strengthening glass has not been considered by someone previously. However, no reference demonstrating this technique could be found in the literature.

IV. Selection of System

It seemed desirable to select a silicate system to demonstrate liquid immiscibility strengthening. Apart from the fact that many glass-forming silicate systems contain liquid immiscibility, a high silica matrix glass could be expected to have a relatively low thermal expansion coefficient and a reasonably high softening point.

After a preliminary study, the $\text{Li}_2\text{O}-\text{TiO}_2-\text{SiO}_2$ system was chosen for study (Figure 1). The extent of liquid immiscibility in this system in the vicinity of 1400°C has been previously established⁽⁶⁾ and the two phase region does not extend completely across the ternary system except in the vicinity of the high SiO_2 apex. This offers the opportunity to start with a single phase (miscible) glass and gradually move into the immiscibility region by composition variations. The tie lines across the immiscibility dome indicate equilibrium between a high silica phase and a phase rich in Li_2O and TiO_2 . They indicate the possibility of forming a low expanding silica rich matrix containing a high expanding disperse phase. This situation can occur only when the dome is penetrated on the high silica side of the critical point. Penetration of the dome on the TiO_2 -rich side of the critical point would provide a composite with a high expanding matrix and low expanding disperse phase. Upon cooling, this matrix would exist in a state of tension and the resultant mechanical strength would probably be very low.

Because of the above reasons, major attention in this investigation was focused on the 70 weight % SiO_2 isopleth to demonstrate the strengthening effect.

V. Related Literature

The phase relations in the $\text{Li}_2\text{O}-\text{SiO}_2$ system were determined by Kracek.⁽⁷⁾ A tendency for liquid immiscibility formation in melts between $\text{Li}_2\text{Si}_2\text{O}_5$ and SiO_2 was noted. DeVries, Roy, and Osborn⁽⁸⁾ established the phase relationships in the $\text{TiO}_2-\text{SiO}_2$ system. An extensive region of immiscibility was found to exist above 1780°C and from approximately 7 to 82 weight % SiO_2 . Ternary liquid phase separation in the $\text{Li}_2\text{O}-\text{TiO}_2-\text{SiO}_2$ system was investigated by Kim and Hummel⁽⁶⁾ where the immiscibility regions present in the two boundary systems were found to be connected.

The effect of metastable phase separation in silicate systems was briefly examined by Phillips and Roy.⁽⁹⁾ No evidence of strengthening of glasses was noted. Ohlberg, Golob, and Hollabough⁽¹⁰⁾ described various fracture surfaces of glasses as related to the suppression of crack front propagation by liquid-in-liquid colloidal immiscibility.

A number of investigations of the strength of viscoelastic substances containing embedded crystalline particles have been conducted.⁽¹¹⁾ Tummala and Friedberg⁽¹²⁾ recently investigated the effect of shape of the disperse phase on strength of glass- ZrO_2 composites. Their results support the "prestress theory"⁽¹¹⁾ which suggests that high expansion particles embedded in a low expansion glass puts the glass into a state of compression and provides a degree of strengthening. Binnig⁽¹³⁾ has indicated a relationship

between the strength and elasticity of the disperse phase and the corresponding properties of the composite. Hasselman and Fulrath⁽¹⁴⁾ presented results that suggest fracture stresses of glass-crystal composites are dependent on size and volume fraction of the dispersed phase because of their interrelationships with the size of Griffith flaws.

VI. Experimental Procedure

Chemically pure grades of Li_2CO_3 , TiO_2 , and silicic acid were used to prepare the compositions listed in Table I and Figure 1. 500 to 1000 gram batches were prepared by weighing appropriate proportions of the raw materials to an accuracy of 0.5 grams, mixing in a "V"-shell blender for two hours, and calcining in fireclay crucibles at 800°C for 2 to 6 hours. Approximately 100 gram charges were melted in an electrical resistance furnace at 1315°C . Each preparation was allowed to fine until a homogeneous melt was obtained. Rods 1/2 inch in diameter and 4 inches long were formed by casting in graphite molds preheated to 400°C . After casting, each sample was annealed by cooling to room temperature in the graphite mold.

For each composition approximately ten samples were selected by visual inspection for strength testing. The transverse bending strengths were obtained using a Tinius-Olson tensile testing apparatus with central loading applied over a three inch span. A constant loading rate of approximately 500 pounds/minute was used. The transverse bending strength for each specimen was calculated using the standard Mc/I relationship. The values were then averaged to obtain a representative strength for the composition.

Refractive indices of the glasses were measured within ± 0.002 with sodium (D) light at 25°C by the Becke line method. The glasses were quenched from approximately 1315°C or higher depending on the temperature of the liquidus surface. Linear thermal expansion measurements were made using a fused silica dilatometer. Electron micrographs of freshly fractured surfaces were obtained using the preshadow carbon replica technique and a Siemens Elmiskop IA Electron Microscope.

VII. Experimental Results

The results for five glass compositions prepared on the 70 weight % SiO_2 isopleth are summarized in Table I. The variation of modulus of rupture as a function of composition is illustrated in Figure 1b. Figure 2 shows representative electron micrographs for compositions 1, 2, 3, and 5.

Composition 1, containing a single phase glass (Figure 2a), yielded an average bending strength of 18,320 psi. This was considered to be the typical nominal strength of bulk glasses in the system examined. Because thermal history of all samples examined was held constant, this was not considered to be a variable parameter. These samples were completely transparent.

Composition 2, prepared in the vicinity of the two phase boundary, contained very fine phase separation (Figure 2b). The discontinuous disperse phase appears as droplets. Although this glass was transparent, a slight amber discoloration was evident. This could be caused by phase separation and/or the larger TiO_2 content. The average modulus of rupture for composition 2 was 25,590 psi, markedly higher than for composition 1, the miscible glass.

TABLE I. COMPOSITIONS AND EXPERIMENTAL DATA FOR $\text{LiO}_2\text{-TiO}_2\text{-SiO}_2$ GLASSES

No.	Composition (Wt. %)		Modulus of Rupture (psi)	Modulus of Elasticity (psi)	Linear Thermal Expansion Coefficient (mm/mm/°C)	Visual Appearance
	Li_2O	TiO_2	Test Values			
1	25	5	70			
			16,875	3.01×10^6	150×10^{-7}	Clear
			22,265			
			25,170			
			9,705	18,320		
			20,910			
			15,870			
			17,445			
2	20	10	70			
			22,665	2.89×10^6	117×10^{-7}	Light Amber
			24,185			
			26,290			
			26,810			
			34,745	25,590		
			21,100			
			24,865			
			24,080			
3	15	15	70			
			28,860	4.00×10^6	91×10^{-7}	Amber
			26,690			
			36,880			
			37,530			
			25,505			
			27,445	30,775		
			25,980			
			34,435			
			27,740			
			36,665			
4	13	17	70			
			24,080	3.07×10^6	-	Opalescent
			35,700			
			25,195			
			36,020			
			30,160			
			30,790			
			26,450			
5	10	20	70			
			625	-	96×10^{-7}	Opalescent
			9,245			
			4,355	4,740		

All of the previously observed trends were continued by composition 3. The phase separation became more pronounced (Figure 2c), the discoloration became increasingly evident, and the strength increased sharply to 30,775 psi.

As expected, composition 5 showed considerable phase separation (Figure 2d) and large decrease in strength. The disperse phase, however, was observed to still be discontinuous. Considerable difficulty was encountered in forming glass rods. Apparently the high TiO_2 content promoted recrystallization when the cooling rate was too slow. Numerous cracks appeared in the bars upon cooling and these are reflected in the very low strength levels.

Figure 3 shows the linear thermal expansion curves for samples 1, 2, 3, and 5. The softening temperature for composition 1 is in the vicinity of 450°C and this characteristic temperature increases as expected as the TiO_2 content increases (the liquidus surface temperature increases as shown by Kim and Hummel⁽⁶⁾). Figure 4 shows the thermal expansion coefficients passing through a minimum near composition 3. This reflects the change of the composition of the matrix towards a higher silica (lower expansion) glass as the glass compositions penetrate the immiscibility dome more deeply (Figure 1). At composition 5, the expansion increases again, possibly due to the larger influence of the disperse phase which, being rich in TiO_2 , is high expanding and/or to the thermal enlarging of the numerous microfractures suspected to be present in this composition.

VIII. Discussion

The strengthening mechanism evidenced in this study does not appear to involve any surface stresses as is the case in chill tempering (Figure 5b). Instead, it seems reasonable to visualize liquid immiscibility strengthening

as producing compressive stresses throughout the matrix phase and confining the tensile stresses to the disperse phase as illustrated schematically in Figure 5b. If this is indeed the case, it should be possible to strengthen the glass still further by chill tempering phase separated glasses and thereby taking advantage of surface compressive stresses (Figure 5c).

A qualitative test of this idea was achieved by heating four samples of composition 3 to temperatures near their softening points and rapidly quenching them in air. The strengths of these four samples were found to average approximately 70,000 psi. Assuming that the pretempered strengths of these bars were about 31,000 psi as Table I would suggest, the tempering treatment increased the strength level two-fold. This brief test clearly indicates the possibility of obtaining very attractive strength levels in bulk glasses by combining liquid immiscibility strengthening with tempering. Other secondary strengthening treatments also appear to be attractive.

The data presented in this investigation indicate that liquid immiscibility strengthening is primarily caused by the mismatch in the thermal expansion coefficients of the two phases. This supports the prestress theory of strengthening glass composites as advocated by Tummala and Friedberg⁽¹²⁾ and others⁽¹¹⁾. The strengthening effect is only observed until the disperse phase becomes too prevalent and internal cracks begin to appear. Warshaw and Seider⁽¹⁵⁾ observed a similar phenomena in crystalline composites.

Apart from thermal expansion considerations, a number of other factors can possibly contribute to liquid immiscibility strengthening of glasses. Hasselman and Fulrath⁽¹⁴⁾ have shown that strengths of crystal-in-glass composites are dependent on the disperse phase size and volume fraction. Their argument points out that these two factors limit the size of the

Griffith flaws and thereby increase the strength of the composite. Other considerations regarding this strengthening effect must include the bonding between the phases (in order to transmit stresses), the formation and propagation of cracks, and the viscoelastic nature of the system under stress. These considerations are presently under investigation and will be the subject of future publications.

IX. Summary

By examining compositions on the 70 weight % SiO_2 isopleth in the $\text{Li}_2\text{O}-\text{TiO}_2-\text{SiO}_2$, it has been demonstrated that liquid immiscibility can lead to significant strengthening of bulk glasses. For the system examined here, the transverse bending strength increased from 18,320 psi to 30,775 psi as microscopic and sub-microscopic liquid phase separation developed. Too much phase separation is detrimental to the high strength levels. Evidence for secondary strengthening (to 70,000 psi) by conventional chill tempering of glasses containing phase separation has also been obtained.

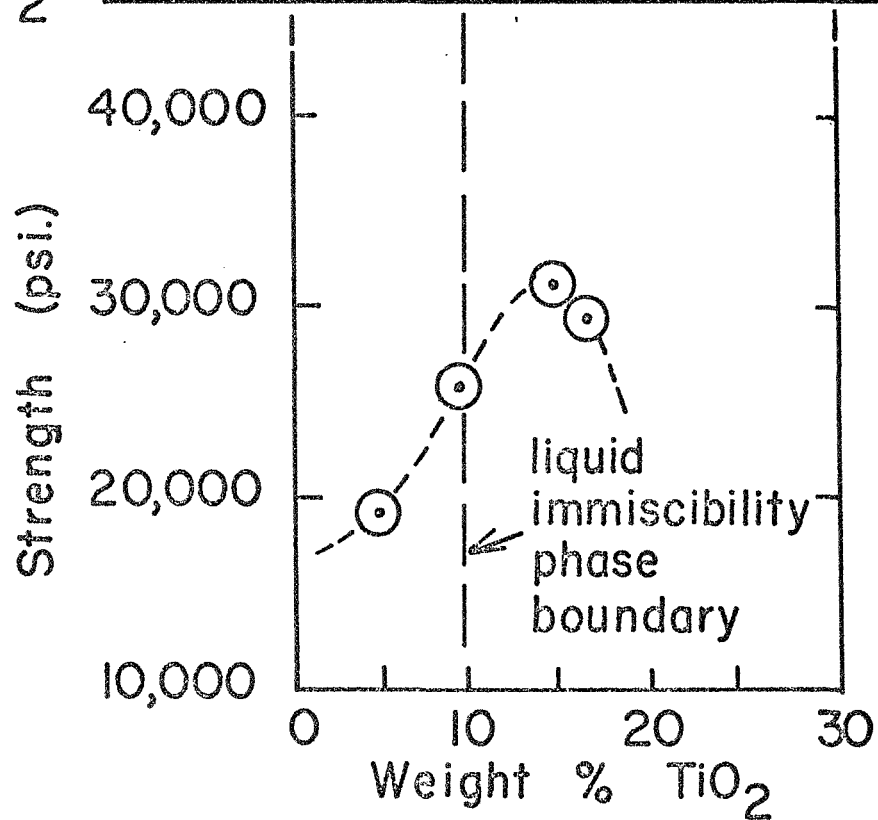
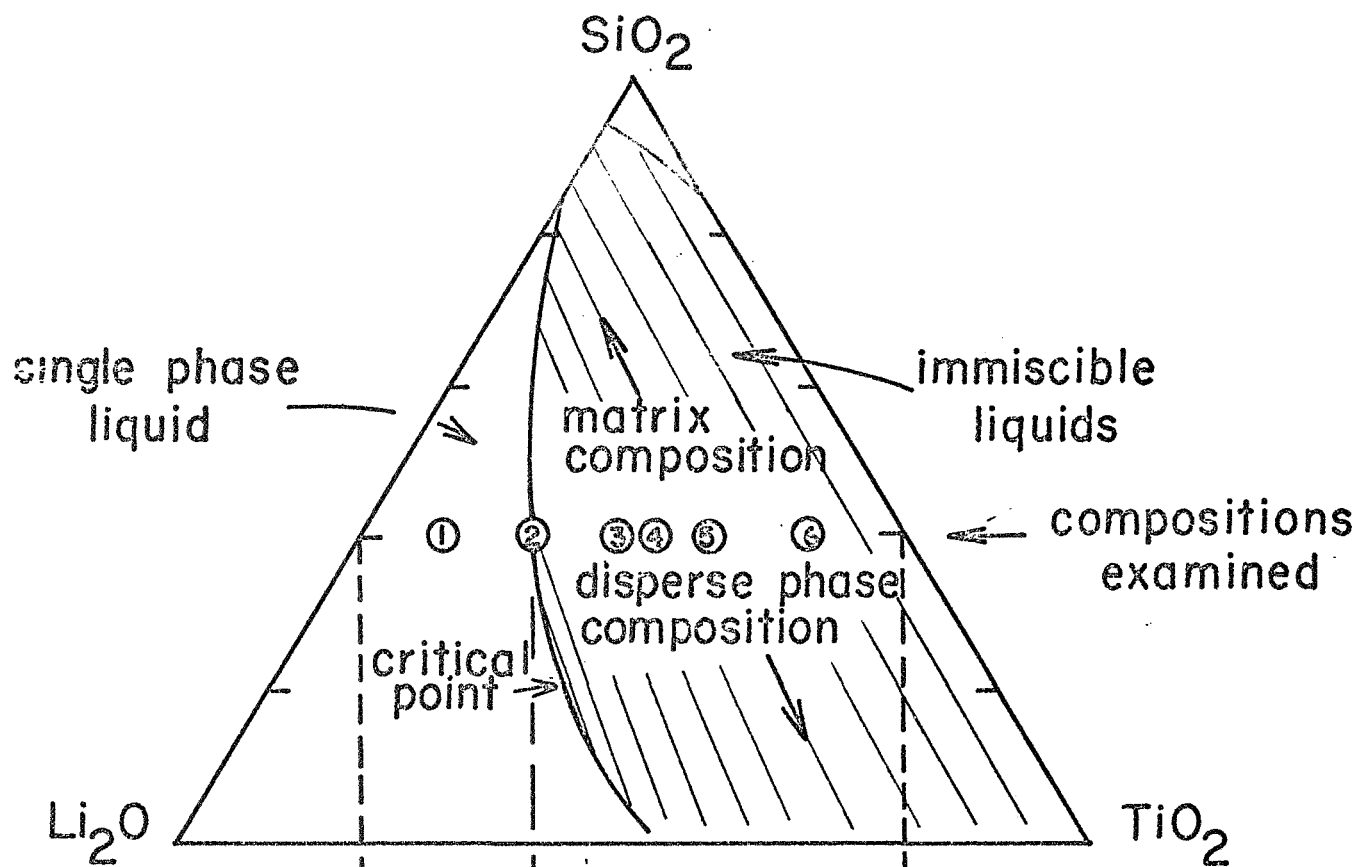
References Cited

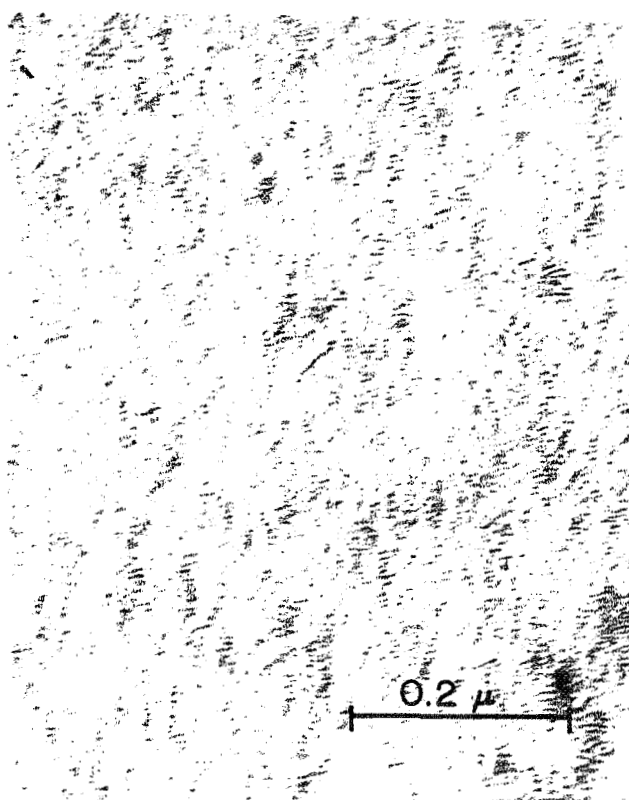
1. H. P. Hood and M. E. Nordberg, "Treated Borosilicate Glass," U. S. Patent 2, 106, 744. February 1, 1938 Ceram. Abstr., 17 (4) 141 (1938).
2. F. A. Hummel, T. Y. Tien, and K. H. Kim, "Studies in Lithium Oxide Systems: VIII, Applications of Silicate Liquid Immiscibility to Development of Opaque Glazes," J. Am. Ceram. Soc., 43 (4) 192-97 (1960).
3. A. A. Griffith, "Phenomena of Rupture and Flow in Solids," Phil. Trans. Roy. Soc. London, A221, 163-98 (1920). Ceram. Abstr., 4 (6) 513 (1921).
4. (a) J. S. Olcott and S. D. Stookey, "Strengthening by Surface Crystallization," Advances in Glass Technology, pp. 400-403 Plenum Press, New York (1962).
(b) H. M. Garfinkel, D. L. Rothermel, and S. D. Stookey, "Strengthening by Ion Exchange," ibid., 404-411.
(c) A. Sendt, "Ion Exchange and Diffusion Processes in Glass," ibid., 307-32.
5. M. E. Nordberg, E. L. Mochel, H. M. Garfinkel, and J. S. Olcott, "Strengthening by Ion Exchange," J. Am. Ceram. Soc., 47 (5) 215 (1964).
6. K. H. Kim and F. A. Hummel, "Studies in Lithium Oxide Systems: VI Progress Report on the System $\text{Li}_2\text{O}-\text{SiO}_2-\text{TiO}_2$," J. Am. Ceram. Soc., 42 (6) 286 (1959).
7. F. C. Kracek, "The Binary System $\text{Li}_2\text{O}-\text{SiO}_2$," J. Phys. Chem., 34 (12) 2641-50 (1930). Ceram. Abstr., 10 (2) 150 (1931).
8. R. C. DeVries, Rustum Roy, and E. F. Osborn, "The System $\text{TiO}_2-\text{SiO}_2$," Trans. Brit. Ceram. Soc., 53 (9) 525-40 (1954).

9. B. Phillips and R. Roy, "Controlled Phase Separation Due to Metastable Liquid Immiscibility in Simple Silicate Systems," Phys. Chem. Glasses, 5 (6) 172 (1964).
10. S. M. Ohlberg, H. R. Golob, and M. Hollabough, "Fractography of Glasses Evidencing Liquid-in-Liquid Colloidal Immiscibility," J. Am. Ceram. Soc., 45 (1) 1 (1962).
11. (a) L. A. Jacobson, "Strength of Two-Phase Model System," M.Sc. Thesis, Univ. of Calif. at Berkeley (1962).
(b) D. G. Hanes, "Residual Stress Systems Created by Inclusions in Multiphase Materials," Ph.D. Thesis, Washington Univ., St. Louis (1963). University Library, microfilm.
(c) A. Winterling, "Structure Stress as a Cause of Increasing Strength in Porcelain," Ber. Deut. Keram. Ges., 38 (1) 9-22 (1961).
(d) J. de Jong; pg. 379-91 (in English) in Transactions of the VIIIth International Ceramic Congress, Copenhagen, 1962. The Organizing Committee of the VIIIth International Ceramic Congress, Copenhagen, 1962.
12. R. R. Tummala and A. L. Friedberg, "Strength of Glass-Ceramic Composites," J. Am. Ceram. Soc., 52 (4) 228 (1969).
13. D. B. Binnis; pg. 315-34 in Science of Ceramics, Vol. 1. Edited by G. H. Stewart. Academic Press, London and New York, (1962).
14. D.P.H. Hasselman and R. M. Fulrath, "Proposed Fracture Theory of a Dispersion Strengthened Glass Matrix," J. Am. Ceram. Soc., 49 (2) 68 (1966).
15. S. I. Warshaw and R. Seider, "Comparison of Strength of Triaxial Porcelains Containing Alumina and Silica," ibid., 50 (7) 337-43 (1967).

List of Figures

- Figure 1a (top) Liquid Immiscibility Region in the High-Silica Portion of $\text{Li}_2\text{O-TiO}_2\text{-SiO}_2$ System (after Kim and Hummel⁽⁴⁾).
- Figure 1b (bottom) Strength of Glasses as a Function of Composition on 70 Weight % SiO_2 Isopleth in the $\text{Li}_2\text{O-TiO}_2\text{-SiO}_2$ System.
- Figure 2 Electron Micrographs of Compositions 1, 2, 3, and 5.
- Figure 3 Linear Thermal Expansion Curves for Compositions 1, 2, 3, and 5.
- Figure 4 Variation of Linear Thermal Expansion Coefficient with Composition.
- Figure 5 Schematic Illustrations of Glass Strengthening by Surface Stresses, Liquid Immiscibility, and a Combination of the Two Effects.





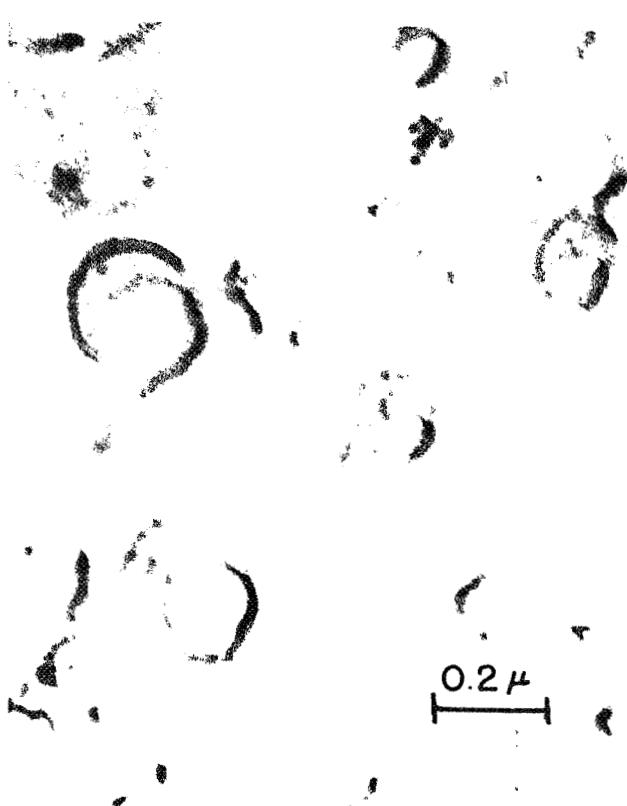
Composition 1 (5% TiO_2)



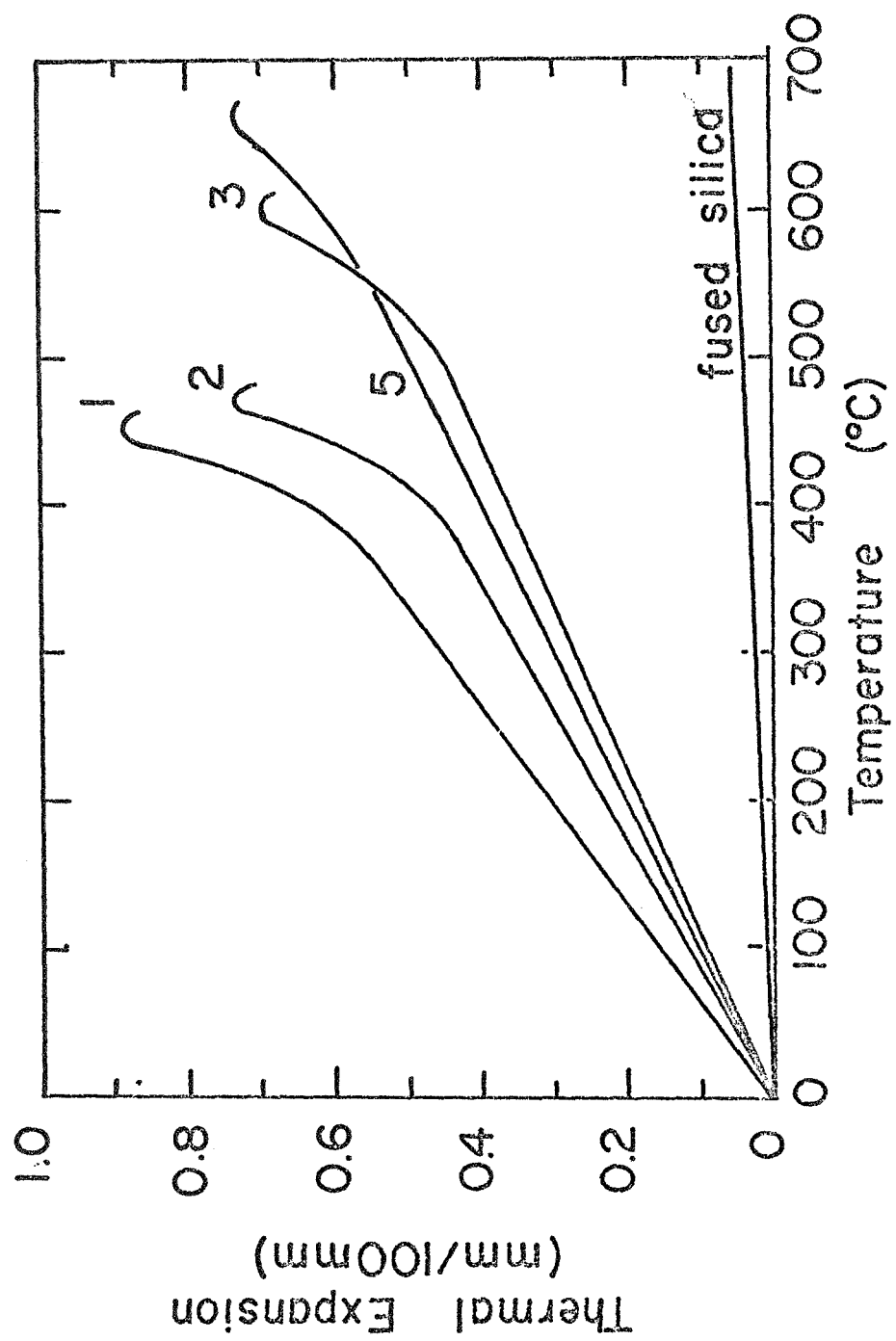
Composition 2 (10% TiO_2)

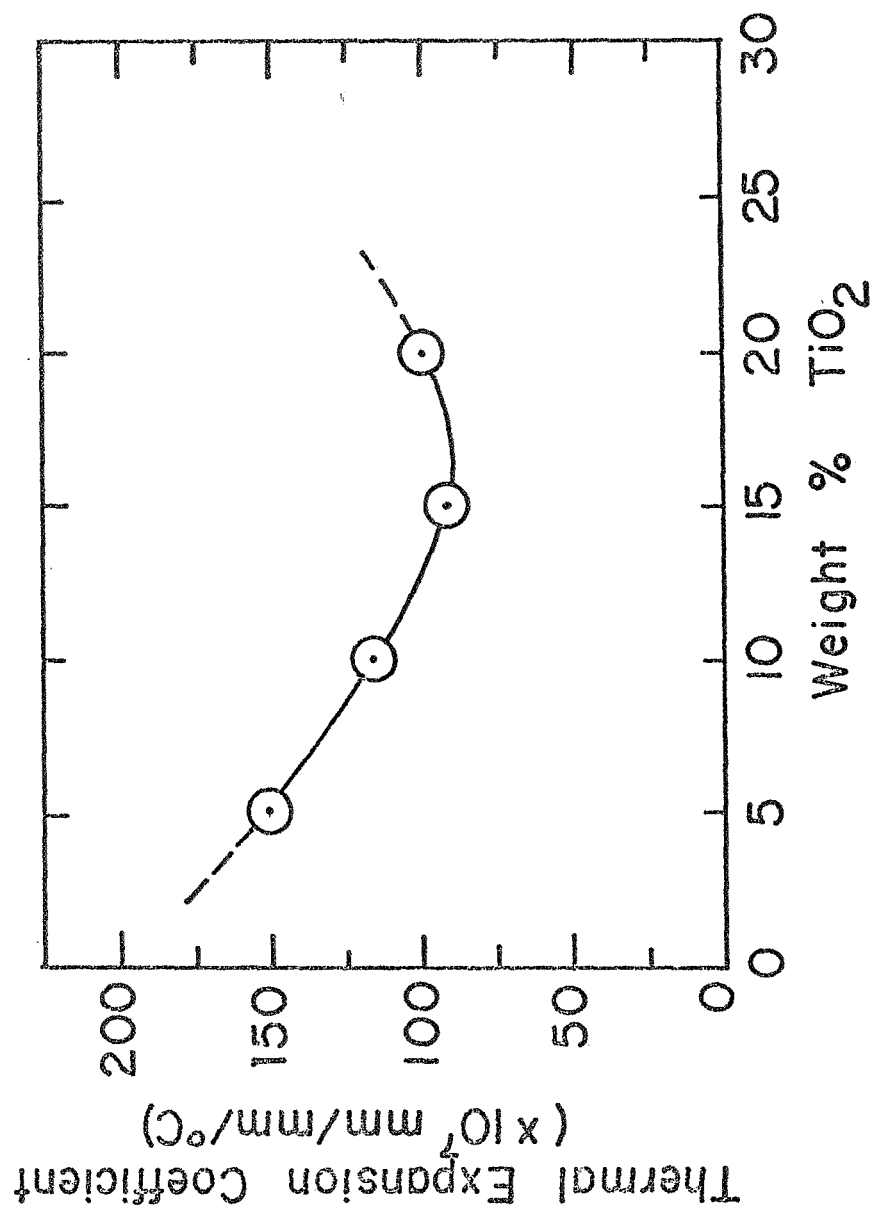


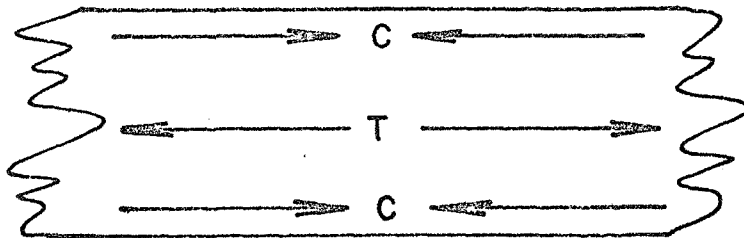
Composition 3 (15% TiO_2)



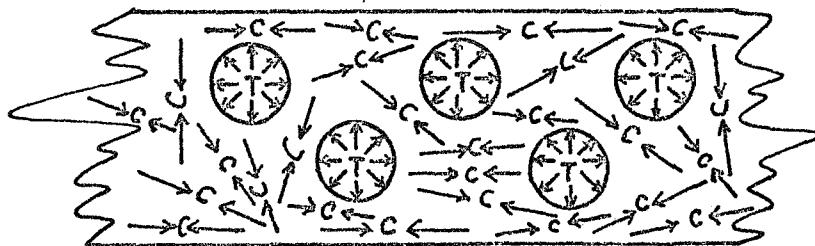
Composition 5 (20% TiO_2)



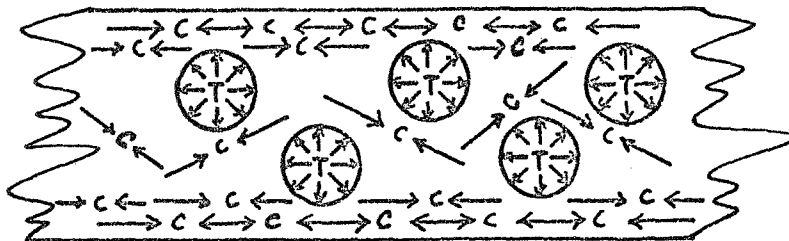




Normal glass strengthened by developing surface compressive stresses (via chill tempering, ion exchange, etc.)



Glass strengthened by liquid immiscibility formation ($\alpha_d > \alpha_m$)



Glass strengthened by liquid immiscibility formation followed by chill tempering

N71-71005

FINAL REPORT

to the

NATIONAL AERONAUTICS AND SPACE ADMINISTRATION

in connection with

NASA Grant NGR 47-004-006

Part 5 of 21 Parts

Final Report
VPI&SU Project 313242

Rotational Locks for Gravity Gradient Satellites

by

F. H. Lutz, Jr.
M. W. Abbitt, Jr.
Aerospace Engineering

Virginia Polytechnic Institute & State University
Blacksburg, Virginia

December, 1970

ROTATIONAL LOCKS FOR GRAVITY GRADIENT SATELLITES

Abstract

Locked-in planar rotational motion for satellites moving in a gravity gradient field is examined using both analytical and numerical techniques. It is shown that rotational locks at spin rates of $n/2$ (where n is an integer) satellite rotations per orbit revolution exist for specific combinations of satellite inertia properties and orbital eccentricity.

For nearly axial symmetric satellites, the maximum and minimum instantaneous rates which permit the satellite to remain in a particular rotational lock are found analytically by applying the averaging techniques of Kryloff and Bogoliuboff and that of Symon. For these cases, it is found that the strength of the higher rotational locks ($n > 3$) are greater than the strength of the $n = 2$ or $1/1$ rotational lock for proper combinations of lock number, n , and orbital eccentricity. Comparison of the results for the case of the planet Mercury are shown to be in good agreement with both observations of the planet and the numerical calculations of Liu.

Numerical results were obtained for representative values throughout the range of satellite inertia properties. Periodic solutions of periods 2π and 4π are found and their variational stability investigated by Floquet analysis. The results which are presented on

stability charts show that for satellites that deviate appreciably from axial symmetry, the stable periodic solutions occur at eccentricities which tend to increase as the absolute value of the lock number $|n|$ increases.

Estimates of the strength of these rotational locks are found by applying the phase space technique of Brereton and Modi. For nearly axially symmetric satellites, the results of this technique agreed favorably with the analytical results. Rotational locks for satellites that are not nearly axial symmetric were found in general to be considerably weaker than the more frequently investigated 1/1 lock.

TABLE OF CONTENTS

	PAGE
LIST OF FIGURES	iii
LIST OF TABLES	vii
LIST OF SYMBOLS	viii
1. INTRODUCTION	1
1.1 1/1 Rotational Lock	1
1.2 3/2 Rotational Lock	3
2. THE EQUATIONS OF MOTION	5
3. NEARLY AXIAL SYMMETRIC SATELLITES	8
3.1 Conditions for Rotational Lock	8
3.2 Small e Considerations	11
3.3 Results	13
4. PERIODIC SOLUTIONS	14
4.1 Numerical Determination of Periodic Solutions	14
4.2 Variational Stability	18
5. PHASE SPACE ANALYSIS	22
5.1 Invariant Surfaces	22
5.2 Small α Verification	27
5.3 Large α	30
6. CONCLUSIONS	31
6.1 Summary of Results	31
6.2 Physical Explanation	33
REFERENCES	35

LIST OF FIGURES

FIGURE	PAGE
1. Geometry of the Problem	38
2. Variation of $\Phi_2(e)$ with Eccentricity	39
3. Lock Strength vs. Orbital Eccentricity for the Rotational Lock $n/2$	40
4. Variation of $\phi_1'(0)$ with $\phi_1(\pi)$ ($n=4$, $\alpha=2.0$)	41
5. Odd 2π Periodic Solutions ($n=5$, $\alpha=3.0$)	42
6. Odd 2π Periodic Solutions ($n=-4$, $\alpha=2.0$)	43
7. Initial Derivative Required to Produce 2π Periodic Solutions ($n = -10$)	44
8. Initial Derivative Required to Produce 2π Periodic Solutions ($n = -5$)	45
9. Initial Derivative Required to Produce 2π Periodic Solutions ($n = -4$)	46
10. Initial Derivative Required to Produce 2π Periodic Solutions ($n = -2$)	47
11. Initial Derivative Required to Produce 2π Periodic Solutions ($n=0$)	48
12. Initial Derivative Required to Produce 2π Periodic Solutions ($n=1$)	49
13. Initial Derivative Required to Produce 2π Periodic Solutions ($n=2$)	50
14. Initial Derivative Required to Produce 2π Periodic Solutions ($n=3$)	51
15. Initial Derivative Required to Produce 2π Periodic Solutions ($n=4$)	52
16. Initial Derivative Required to Produce 2π Periodic Solutions ($n=5$)	53

FIGURE	PAGE
17. Initial Derivative Required to Produce 2π Periodic Solutions (n=9)	54
18. Initial Derivative Required to Produce 2π Periodic Solutions (n=10)	55
19. Initial Derivative Required to Produce 2π Periodic Solutions (n=20)	56
20. Initial Derivative Required to Produce 2π Periodic Solutions (n=40)	57
21. Odd 4π Periodic Solutions (n=3, $\alpha=3.0$, $e=0.3$).	58
22. Initial Derivative Required to Produce 4π Periodic Solutions (n=2)	59
23. Initial Derivative Required to Produce 4π Periodic Solutions (n=3)	60
24. Typical Variations of the Error Found in the Numerical Determination of Periodic Solutions ($e=0.9$, $\alpha=3.0$)	61
25. Variational Stability Chart (n=-10, m=1)	62
26. Variational Stability Chart (n=-5, m=1)	63
27. Variational Stability Chart (n=-4, m=1)	64
28. Variational Stability Chart (n=-2, m=1)	65
29. Variational Stability Chart (n=0, m=1)	66
30. Variational Stability Chart (n=1, m=1)	67
31. Variational Stability Chart (n=2, m=1)	68
32. Variational Stability Chart (n=3, m=1)	69
33. Variational Stability Chart (n=4, m=1)	70
34. Variational Stability Chart (n=5, m=1)	71
35. Variational Stability Chart (n=9, m=1)	72
36. Variational Stability Chart (n=10, m=1)	73
37. Variational Stability Chart (n=20, m=1)	74
38. Variational Stability Chart (n=40, m=1)	75

FIGURE	PAGE
39. Variational Stability Chart ($n=2$, $m=2$)	76
40. Variational Stability Chart ($n=3$, $m=2$)	77
41. Schematic of an Invariant Surface	78
42. Effect on $ \phi_1 $ After $ \phi_1 $ Becomes Greater Than $\pi/2$	79
43. Nesting of Invariant Curves at $f=0$ ($n=10$), $\alpha=1.5$, $e=0.3$	80
44. Location of the Periodic Solution ($n=10$, $\alpha=1.5$, $e=0.6$	81
45. Cross-sections of the Limiting Invariant Surfaces ($n=10$, $\alpha=1.5$, $e=0.3$)	82
46. Location of the Periodic Solution ($n=-5$, $\alpha=1.5$, $e=0.6$) ...	83
47. Cross-sections of the Limiting Invariant Surfaces ($n=-5$, $\alpha=1.5$, $e=0.6$)	84
48. Conservative and Liberal Estimates of Invariant Surfaces ..	85
49. Change in Absolute Angular Velocity for Maximum Values of Φ_n	86
50. Conservative Estimate of Momentum Change at $f=0$ ($\alpha=0.05$) ..	87
51. Liberal Estimate of Momentum Change Throughout the Orbit ($n=2$, $\alpha=0.05$)	88
52. Liberal Estimate of Momentum Change Throughout the Orbit ($n=3$, $\alpha=0.05$)	89
53. Liberal Estimate of Momentum Change Throughout the Orbit ($n=5$, $\alpha=0.05$)	90
54. Liberal Estimate of Momentum Change Throughout the Orbit ($n=10$, $\alpha=0.05$)	91
55. Liberal Estimate of Momentum Change Throughout the Orbit ($n=20$, $\alpha=0.05$)	92
56. Conservative Estimate of Momentum Change at $f=0$ ($n \geq 2$)	93
57. Conservative Estimate of Momentum Change at $f=0$ ($n \leq 2$)	94

FIGURE	PAGE
58. Liberal Estimate of Momentum Change Throughout the Orbit ($\alpha=1.0$, $n \geq 2$)	95
59. Liberal Estimate of Momentum Change Throughout the Orbit ($\alpha=2.0$, $n \geq 2$)	96
60. Liberal Estimate of Momentum Change Throughout the Orbit ($\alpha=3.0$, $n \geq 2$)	97
61. Liberal Estimate of Momentum Change Throughout the Orbit ($\alpha=1.0$, $n \leq 2$)	98
62. Liberal Estimate of Momentum Change Throughout the Orbit ($\alpha=2.0$, $n \leq 2$)	99
63. Liberal Estimate of Momentum Change Throughout the Orbit ($\alpha=2.0$, $n \leq 2$)	100
64. Satellite Position for 2π Periodic Solution ($n=10$, $\alpha=1.0$, $e=0.4$)	101
65. Angular Rate of the Orbit as a Function of Orbital Eccentricity	102

LIST OF TABLES

TABLE	PAGE
I Properties of the Parameter $\Phi_n(e)$ for Lock Numbers 1-28	103
II The Numerical Results of Liu (21) Compared to the Analytical Results of the Small e and Arbitrary e Cases for $e=0.206$ and $n=3$	104
III Comparison of Analytical to Numerical Results	105

LIST OF SYMBOLS

a	Satellite inertia parameter = $\sqrt{\frac{B-A}{C}} = \sqrt{\frac{\alpha}{3}}$
a_{11}	Constant = $x_1(2\pi m)$
a_{21}	Constant = $x_2(2\pi m)$
a_{12}	Constant = $x_1'(2\pi m)$
a_{22}	Constant = $x_2'(2\pi m)$
A	Minimum principal moment of inertia of the satellite
b	On stability charts - indicates that $x_1(2\pi)$ was in the range $0.99 < x_1(2\pi) < 1.01$ for one periodic solution
B	Median principal moment of inertia of the satellite
C	Maximum principal moment of inertia of the satellite
d	Semi-major axis of the elliptic orbit
e	Orbital eccentricity
f	True anomaly (Figure 1)
G	Gravitational constant
k	Integer or zero (Figure 1), indicates the rotational position of the satellite
m	Positive integer which indicates solutions of period $2\pi m$
M	Mean anomaly
n	Integer or zero, usually the lock number
N	Indicates no periodic solution found
o	On Stability charts - variational stability for one periodic solution
p	Mean daily motion = $2\pi/T_o$

P	Period of small oscillations
\bar{r}	Position vector of the mass center of the satellite with respect to the mass center of the attracting body (Figure 1)
t	Time
T_o	Period of the orbit
w_o	Constant which specifies the rotational rate of the satellite ($w_o/1$)
x	Throughout text - perturbation from a periodic solution On stability charts - indicates variational instability for one periodic solution
X, Y, Z	Coordinate system rotating about the Z axis such that the X axis remains aligned with the radius vector \bar{r} . (Figure 1)
X_r, Y_r, Z_r	Coordinate system rotating about the Z axis where X_r is rotated $kf/2$ radians from the X axis (Figure 1)
X_p, Y_p, Z_p	Principal axes of the satellite
α	Satellite inertia parameter $= 3(\frac{B-A}{C}) = 3a^2$
δ	Increment in the initial derivative $\phi_1'(0)$,
ε	Error function, defined in equation (4.2)
η	Angular displacement in equation (3.2)
η_1	Angular displacement $= \eta - \frac{n\pi}{2}$
θ	Angle measured from the line of apses to the X_p axis in a counter-clockwise direction (Figure 1)
θ_o	Constant depending on initial conditions at pericenter
Λ	Positive conservative estimate (Figure 48)
μ	Negative conservative estimate (Figure 48)
ν	Positive liberal estimate (Figure 48)

ρ	Constant which indicates the range of investigation for the initial derivative $\dot{\phi}_1(0)$ in equation (4.1)
σ_i	Characteristic multipliers, equation (4.21)
τ	Negative liberal estimate (Figure 48)
ϕ	Angle measured from position vector \bar{r} to the X_p axis in a counter-clockwise direction (Figure 1)
ϕ_1	Angle measured from X_r axis to X_p axis in a counter-clockwise direction (Figure 1)
ϕ_1^*	Periodic solution
Φ_n	Lock strength defined in equation (3.4)
(\cdot)	Differentiation with respect to time (t)
$(\)'$	Differentiation with respect to the true anomaly (f)

1. INTRODUCTION

Recent developments in the application of earth satellites to scientific programs require special attention regarding their orientation in space. Over a long satellite lifetime, it is desirable to use passive rather than active methods of maintaining satellite orientation since the former does not require the consumption of power. The most frequently used passive method of attitude control is the gravity gradient effect which occurs when a body is immersed in a non-uniform gravitational field. This effect exists because the center of mass and the center of gravity of the satellite do not generally coincide, thus creating a torque about the mass center of the satellite. Proper distribution of satellite mass provides the desirable torque to allow passive orientation to be achieved.

The motion of a satellite may be considered to consist of two components; the motion of the mass center of the satellite about the attracting body called orbital motion, and the motion of the satellite about its mass center called rotational motion. Rotational motion only in the plane of the orbit is called planar rotational motion, a special case of which is librational or oscillatory motion. Of the above types of motion, this report is primarily concerned with planar rotational motion.

1.1 1/1 Rotational Lock

The first satellite placed into orbit in 1957 greatly stimulated

research in the area of rotational satellite motion. Lunar motion as well as the motion of communication and observation satellites, which perform most efficiently when one side of the satellite is always facing the earth, motivated particular interest in the case where the satellite rotates in the orbital plane once per orbit revolution or in a 1/1 rotational lock. This principal lock has been the subject of several investigations (1-16). References (1-9) discuss the preliminary concepts of planar rotational analysis and are primarily concerned with the planar librations of various shaped satellites whose orbits are either circular or of small eccentricity.

Beletskii (10) in a comprehensive work summarized all the pertinent papers on rotational motion of satellites in the Russian literature through 1965. One of these papers, Chernous'ko (11), developed a method for investigating higher rotational locks for nearly axial-symmetric satellites, but his results were limited to the 1/1 rotational lock for orbits of arbitrary eccentricity. In Section 3 of this report his results will be extended to include higher rotational locks.

Torzhevshiz (12) mathematically proved the existence of $2\pi m$, $m = 1, 2, \dots$, odd periodic solutions to the 1/1 planar rotational equation of motion. Using this fact, Zlatoustov et al (13) investigated the 1/1 rotational lock by numerically finding 2π periodic solutions to the equation of motion. The stability of these periodic solutions were then investigated by using the theory of Floquet (27). The above method due to Zlatoustov et al will be extended to include higher rotational locks in Section 4.

Brereton and Modi (14, 15, 16, 23) numerically analyzed the stability of the 1/1 rotational lock for orbits of arbitrary eccentricity and satellites of various shapes by using phase space analysis. Their technique involved the numerical integration of the equation of motion over many orbits. By tracing the solution trajectories in the phase space, a stability surface was formed. The largest of these stability surfaces or integral manifolds, defines a region, inside of which, initial values of angular velocity and displacement produce a stable 1/1 rotational lock. In Section 5, the method due to Brereton and Modi (23) will be modified to investigate a large number of higher rotational locks.

1.2 3/2 Rotational Lock

Studies of the rotational motion of the planet Mercury led to investigations of possible "locked in" motion at other spin rates, in particular that of three satellite rotations for every two orbit revolutions or a 3/2 rotational lock. Locks which would explain Mercury's motion were found by Liu and O'Keefe (20) by numerically integrating the equation of motion with an orbit eccentricity of 0.2 and assuming Mercury to be nearly axially symmetric. They found that Mercury would lock at an average rotational period of 58.65 days with small librations which have a period of 25 years about this average period. These values are in excellent agreement with radar (17) and visual (18) observations of the planet Mercury which indicate that the period of rotation of the planet is 58.4 ± 0.4 days. Since Mercury's orbital period of revolution is 87.97 days, it appears that a 3/2

rotational lock caused by gravity gradient stabilization is indeed possible.

Liu (21) extended his initial computer results by finding the upper and lower limit for the rotational period of the planet required for it to remain in a $3/2$ rotational lock. The period of librations about these periods for orbit eccentricity of 0.206 and for various assumed shapes of the planet were also calculated. These results appear in Table II.

Laslett and Sessler (22) analytically investigated the case of nearly axial-symmetric satellites in nearly circular orbits by employing an averaging method discussed by Symon et al (24). Their work will be extended to include higher rotational locks in Section 3.

The investigations discussed in this Section tend to indicate that rotational locks other than the $1/1$ and $3/2$ are possible for satellites of various shapes in orbits of arbitrary eccentricity. The purpose of this report is to determine the conditions under which such higher rotational locks are possible and to evaluate the strength of these locks.

2. THE EQUATIONS OF MOTION

The equations of motion which describe the planar rotational motion of a satellite about an attracting body are indeed complex. However the utilization of appropriate assumptions and the selection of a proper axes system reduces the equations of motion to a deceptively simple form. The nomenclature of the problem along with the pertinent assumptions are presented below.

Consider a satellite whose principal moments of inertia about the principal axis system X_p, Y_p and Z_p are A, B, and C respectively. Furthermore let the mass distribution be such that $A \leq B \leq C$. The problem is shown schematically in Figure 1 where:

\bar{r} -	position vector of the mass center of the satellite with respect to the mass center of the attracting body
k -	positive or negative integer
X, Y, Z -	coordinate system rotating about the Z axis such that the X axis remains aligned with the radius vector r .
X_r, Y_r, Z_r -	coordinate system rotating about the Z axis where X_r is rotated $\frac{k}{2} f$ radians from the X axis.
X_p, Y_p, Z_p -	principal axes of the satellite
ϕ -	angle measured from position vector r to the X_p axis in a counter-clockwise direction

- f - true anomaly
- θ - angle measured from the line of apses to
the X_p axis in a counter-clockwise direction

The assumptions involved in obtaining the planar equation of motion of the satellite are:

- A. The rotation of the satellite about its center of mass is restricted to the orbital plane about the Z_p axis. (i.e. the satellite has equatorial symmetry)
- B. The body about which the satellite is orbiting (attracting body) is spherically homogeneous and is the only body which exerts forces on the satellite.
- C. The characteristic length of the satellite is small compared to the dimensions of the orbit.
- D. The influences of atmospheric drag, magnetic fields, solar radiation, and other extraneous effects are ignored. For a discussion of the relative magnitudes of these phenomena see (25), (10, p. 26), and (23, p. 6.)
- E. The motion of the satellite about its mass center has no effect on the motion of the mass center itself which therefore moves in accordance with Kepler's laws (28).

As a consequence of these assumptions, the equation of motion reduces to the form given by Beletskii (10),

$$(1 + e \cos f) \frac{d^2 \phi}{df^2} - 2e \sin f \left[\frac{d\phi}{df} + 1 \right] + 3a^2 \cos \phi \sin \phi = 0 \quad (2.1)$$

where $a^2 = \frac{B-A}{C}$

An equivalent form of equation (2.1) where θ is the dependent variable and M , the mean anomaly, is the independent variable is given by

$$\frac{d^2 \theta}{dM^2} + \frac{3}{2} a^2 \left(\frac{1 + e \cos f}{1 - e^2} \right)^3 \sin 2(\theta - f) = 0 \quad (2.2)$$

If ϕ in equation (2.1) is replaced by $\frac{k}{2}f + \phi_1$, as is shown in Figure 1, equation (2.1) becomes,

$$(1 + e \cos f) \frac{d^2 \phi_1}{df^2} - 2e \sin f \left[\frac{d\phi_1}{df} + \frac{k+2}{2} \right] + 3a^2 \cos \left(\phi_1 + \frac{k}{2}f \right) \sin \left(\phi_1 + \frac{k}{2}f \right) = 0 \quad (2.3)$$

Equations (2.1), (2.2), and (2.3) are the three forms of the rotational equation of motion of the satellite which will be investigated throughout the remainder of this report.

3. NEARLY AXIAL SYMMETRIC SATELLITES

For the case where $a^2 = 0$ (axially symmetric satellite) the solution of equation (2.2) is that of a constant angular rate given by

$$\theta = w_o M + \theta_o \quad (3.1)$$

where w_o and θ_o are constants which depend upon the initial conditions at pericenter. The form of equation (3.1) suggests that for " a^2 " equal to a small non-zero constant (nearly axial symmetric) the solution would take the form

$$\theta = w_o M + \eta \quad (3.2)$$

where η is some function of M not necessarily small. Several methods for investigating such cases are presented below.

3.1 Conditions for Rotational Lock

Chernous'ko (11) has shown that for the case where " a " is small, the averaging techniques of Kryloff and Bogoliuboff can be applied to equation (2.2) utilizing the form of solution given in equation (3.2). For the case where $2w_o$ is not an integer, Chernous'ko (11, page 709) showed that to a first approximation the satellite is not influenced by the gravitational perturbing moment. However, for the more interesting

case $2w_0 = n$, where n , the lock number is an integer, equation (2.2) becomes periodic and can be averaged over its period (2π) to give the equation

$$\frac{d^2(2\eta)}{dM^2} + 3a^2 \Phi_n(e) \sin 2\eta = 0 \quad (3.3)$$

where $\Phi_n(e)$ is given by

$$\Phi_n(e) = \frac{1}{\pi(1-e^2)^{3/2}} \int_0^\pi (1 + e \cos f) \cos (nM - 2f) df \quad (3.4)$$

and M is given exactly in terms of f by

$$M = 2 \tan^{-1} \left[\left(\frac{1-e}{1+e} \right)^{1/2} \tan \frac{f}{2} \right] - \frac{e(1-e^2)^{1/2} \sin f}{1+e \cos f} \quad (3.5)$$

Equation (3.3) is that of a simple pendulum and consequently the solution of equation (2.2) is given in the form of equation (3.2) which describes either slow rotations or oscillations superimposed on a constant angular rate where the constant angular rate is given by

$w_0 = \frac{n}{2}$ satellite rotations for each orbit revolution. For "locked-in" rotational motion the solutions must be oscillatory about a stable

equilibrium state which determined from equation 3.3 are,

$$\eta = \frac{s\pi}{2} \quad (3.6)$$

where

$$s = 0, \pm 2, \pm 4, \dots \text{ for } \phi_n(e) > 0$$

$$s = 1, \pm 3, \pm 5, \dots \text{ for } \phi_n(e) < 0$$

The requirement for the motion to be oscillatory allows approximate upper and lower bounds of the angular rate of a satellite to be determined for any given rotational lock. These bounds are determined by evaluating the first integral associated with the pendulum equation at the critical points $\eta = 0$ and $\eta = \frac{\pi}{2}$ and can easily be shown to be

$$\left. \frac{d\eta}{dt} \right|_{\substack{\max \\ \min}} = \pm \frac{2\pi}{T_o} \left(3a^2 \left| \phi_n(e) \right| \right)^{1/2} \quad (3.7)$$

where T_o is the period of the satellite orbit. In terms of the absolute angular velocity equation (3.7) becomes.

$$\left. \frac{d\theta}{dt} \right|_{\substack{\max \\ \min}} = \frac{2\pi\omega_o}{T_o} \pm \frac{2\pi}{T_o} \left(3a^2 \left| \phi_n(e) \right| \right)^{1/2} \quad (3.8)$$

Consequently the extreme values for the instantaneous period of the satellite for a given rotational lock are

$$T_{\min}^{\max} = \frac{T_o}{w_o \pm \left(3a^2 \left| \Phi_n(e) \right| \right)^{1/2}} \quad (3.9)$$

where the rotational lock is given by $n/2$ or $w_o/1$.

From equation 3.9 it can be shown that it is possible for identical satellites in the same orbit but with different rotational locks to have the same instantaneous period provided the following condition is satisfied

$$\left(\left| \Phi_n(e) \right|_2 \right)^{1/2} + \left(\left| \Phi_n(e) \right|_1 \right)^{1/2} \geq \frac{w_{o2} - w_{o1}}{(3a^2)^{1/2}}, \quad w_{o2} > w_{o1} \quad (3.10)$$

In addition the period of small oscillations of the satellite about it's mean angular rate is easily obtained from the pendulum equation (3.3) and is given by

$$P = \frac{T_o}{\left(3a^2 \left| \Phi_n(e) \right| \right)^{1/2}} \quad (3.11)$$

3.2 Small e Considerations

For the case where the orbits are nearly circular, several analytic results can be obtained by expanding the appropriate terms in powers of

the small eccentricity e . For example the integrand of equation (3.4) can be expanded in powers of " e " and the resulting expression integrated. Alternatively the governing equation (2.2) can be expanded in powers of " e " with the true anomaly given by (29):

$$f = M + 2 e \sin M + \frac{5}{2} e^2 \sin (2M) + o(e^3) \quad (3.12)$$

If the solutions in the form of equation (3.2) are substituted into the expanded form of equation (2.2), the resulting differential equation in η is to $O(e^2)$,

$$\begin{aligned} \frac{d^2 \eta}{dM^2} + \frac{3}{2} a^2 \left[\left((1 - 5/2 e^2) \cos 2M (w_o - 1) + \frac{7}{2} e \cos M (2w_o - 3) \right. \right. \\ \left. \left. - \frac{e}{2} \cos M (2w_o - 1) + \frac{17}{2} e^2 \cos 2M (w_o - 2) \right) \sin 2\eta \right. \\ \left. + \left((1 - 5/2 e^2) \sin 2M (w_o - 1) + \frac{7}{2} e \sin M (2w_o - 3) \right. \right. \\ \left. \left. - \frac{e}{2} \sin M (2w_o - 1) + \frac{17}{2} e^2 \sin 2M (w_o - 2) \right) \cos 2\eta \right] = 0 \end{aligned} \quad (3.13)$$

A method developed by Symon et al (24) and used by Laslett and Sessler (22) assumes that terms averaging to zero in the coefficients of terms containing η can be ignored if their period is much smaller

than the period of the solution found without these averaged terms, if $2w_0 = n$, $n = 1, 2, 3, 4, \dots$ these coefficients contain one non zero constant term and terms of period T_0 which can be ignored. Consequently equation (3.13) takes the form of equation (3.3).

The results of carrying out either operations outlined above, averaging then expanding or expanding and then averaging lead to the same results, to $o(e^2)$, which are present below. For small e , $\phi_n(e)$ can be approximated by

$$\begin{aligned}
 \phi_0(e) &= 0 \\
 \phi_1(e) &= -\frac{1}{2} e + o(e^2) \\
 \phi_2(e) &= 1 - \frac{5}{2} e^2 + o(e^2) \\
 \phi_3(e) &= \frac{7}{2} e + o(e^2) \\
 \phi_4(e) &= \frac{17}{2} e^2 + o(e^2) \\
 \phi_n(e) &= o(e^2) \quad n \neq 1, 2, 3, 4
 \end{aligned} \tag{3.14}$$

3.3 Results

Since the sign and magnitude of $\phi_n(e)$ are imperative to the investigation, equation (3.4) has been numerically integrated for several values of n , the results of which are presented in Figures 2 and 3. An indication of the strength of a rotational lock is given by the magnitude of $\phi_n(e)$. The greater $\phi_n(e)$ the larger the allowable deviation from the mean angular rate before relative tumbling occurs as

indicated by equation (3.8). Figure 3 indicates that for each rotational lock there is a particular value of e which gives the strongest lock. These values of e and their associated maximum positive values of Φ_n as well as the values of e at which $\Phi_n = 0$ are given for each rotational lock in Table I. Contrary to the implications of the literature, the strengths of these higher locks, with the exception of the 3/2 lock, are greater for certain ranges of eccentricity than the 1/1 lock case in a circular orbit.

Values of the lock number, n , less than zero were found to give very small values of $\Phi_n(e)$ eliminating the possibility of strong retrograde rotational locks for nearly axial symmetric satellites.

Table II shows several results obtained from the arbitrary e and small e techniques as compared to those of Liu (21) who numerically integrated the equation of motion over a time period of 100 years.

The period of small amplitude oscillations given by equation (3.11) and the upper and lower limits in the instantaneous periods of the satellite given by equation (3.9) were used for this comparison.

The discussion thus far has been limited to nearly axial symmetric satellites. The remaining sections will consider the more general case of arbitrary satellite parameter, a^2 , and arbitrary orbit eccentricity, e .

4. PERIODIC SOLUTIONS

4.1 Numerical Determination of Periodic Solutions

The existence of odd $2\pi m$ periodic solutions of equation (2.3) was

was indicated by Torzhevskiz (12) and may be explained physically for k equal to an integer by noting the symmetry of the central force field about the line of apses. For equation (2.1), oscillatory solutions which are periodic in ϕ define a rotational rate of lock number $n = 2$. In an analogous manner, oscillatory periodic solutions in ϕ_1 of equation (2.3) define a rotational rate of lock number $n = k + 2$ since the satellite rotates $\frac{k+2}{2}$ times about its mass center for each orbit revolution (see Figure 1).

These odd $2\pi m$ periodic solutions were obtained numerically by integrating equation (2.3) with the initial conditions $\phi_1(0) = 0$ for a wide range of $\phi_1'(0)$ values. An illustration of the results of this numerical technique is shown in Figure 4 for the case of $m = 1$, $k = 2$, $\alpha = 2.0$ where α is defined as $\alpha = 3a^2$ and consequently satisfies the limits of $-3 \leq \alpha \leq 3$. The values of $\phi_1'(0)$ where the curve crosses the $\phi_1'(0)$ axis yield odd periodic solutions since odd $2\pi m$ periodic solutions satisfy the condition

$$\phi_1(0) = \phi_1(m\pi) = 0$$

The range over which these $\phi_1'(0)$ roots lie varies considerably depending on the particular rotational lock investigated and the eccentricity of the orbit. However from the definition of the variables ϕ_1 , M , w_0 and f , the approximate range of $\phi_1'(0)$ can be determined to be

$$\phi_1'(0) = w_0 \left[\frac{(1 - e^2)^{3/2}}{(1 + e)^2} - 1 \right] \pm \rho \quad (4.1)$$

where the value of $\rho = 3.0$ was found to be adequate for finding periodic solutions for all rotational locks investigated. For the case where $\alpha = 0$ (axially symmetric satellite), equation (4.1) with $\rho = 0$ is exact and served as a check on the numerical calculations.

For a representative sampling of rotational locks, solutions of period 2π were found for 130 uniformly distributed points in the region $[-3 \leq \alpha \leq 3 : 0 \leq e \leq 0.9]$. Additional points for the case of small e as well as for the case of small α were also investigated. The region of $e > 0.9$ was not included since the numerical integration of equation (2.3) becomes inaccurate because of the singularity at $e = 1$. Some typical examples of these odd 2π -periodic solutions are shown in Figures 5 and 6. For rotational locks other than the 1/1, it is interesting to note that the $e = 0$ case does not result in $\phi_1(f) = 0$. The solutions are $2\pi/k$ periodic because of the pendulum like motion about the $X_r - Y_r$ axis system (Figure 1) which rotates with respect to the radius vector at the constant angular rate $\frac{k}{2} M$.

The initial angular velocities $\phi_1'(0)$ which produce 2π periodic solutions of equation (2.3) for 14 rotational locks are shown in Figures 7-20. Figure 13 agrees with that of Zlatoustov et al (13) and is presented here for comparison with the other locks.

Certain points of Figure 14 can be checked analytically by using an exact solution. Beletskii (10) observed that equation (2.1) has the exact solution $\phi = f/2$, when the particular relationship, $a^2 = 2e$ exists between the satellite parameter and the orbit eccentricity. By examining equation (2.3) it is seen that this solution is equivalent to $\phi_1 = 0$ when

$e = \frac{\alpha}{6}$ for the 3/2 rotational lock. Consequently, points at which the curves of Figure 14 intersect the e axis must satisfy the relationship $e = \frac{\alpha}{6}$.

For particular values of α and e , it is interesting to note that as many as three 2π periodic solutions were found for the $n \geq 2$ rotational locks where for $n \leq 1$ there is no trend indicating the existence of more than one 2π periodic solution for each combination of e and α .

Solutions of periods other than that of the satellite's period of revolution on its orbit were also investigated. For the 1/1 and 3/2 rotational locks, 4π periodic solutions were found for various combinations of α and e . Typical examples of these solutions are shown in Figure 21 and the initial angular velocities $\dot{\phi}_1(0)$ necessary to produce these solutions are shown in Figures 22 and 23. Figure 22 represents a more complete investigation than a similar figure by Brereton (23) since many additional 4π periodic solutions are found. Investigation of the usual 130 uniformly distributed points in the region $[-3 \leq \alpha \leq 3 : 0 \leq e \leq 0.9]$ for the 0/1 and 5/1 rotational locks resulted in finding no 4π periodic solutions for either lock.

The numerical integration was carried out by using double precision, fourth order, Runge Kutta on an IBM system 360/65 digital computer. Since the exact $2m\pi$ periodic solutions are odd about the point $m\pi$ for all rotational locks, the error estimate

$$\epsilon(f) = \frac{1}{2} [\phi_1(m\pi + f) + \phi_1(m\pi - f)] \quad (4.2)$$

similar to that used by Brereton (23), may be utilized in these cases. If the numerically determined solutions were exact, the function $\varepsilon(f)$ would be identically zero in the interval $0 \leq f \leq m\pi$. It was found that the accuracy of the solutions became worse with increasing α and e . Typical values of $\varepsilon(f)$ for several rotational locks with $e = 0.9$ and $\alpha = 3.0$ are shown in Figure 24.

4.2 Variational Stability

The stability of $2\pi m$ periodic solutions of equation (2.3) can be investigated by constructing the variational equation (31 p. 121). Let

$$\phi_1 = \phi_1^* + x \quad (4.3)$$

where ϕ_1^* is known periodic solution and x is a linear perturbation. By substituting equation (4.3) into equation (2.3), retaining terms to $O(x)$, and subtracting from it the original periodic solution ϕ_1^* , the variational equation becomes

$$\begin{aligned} (1 + e \cos f) x'' - (2e \sin f) x' + \\ + \alpha \cos 2\left(\frac{k}{2} f + \phi_1^*\right) x = 0 \end{aligned} \quad (4.4)$$

Equation (4.4) is a linear differential equation with $2\pi m$ periodic coefficients where the integer m depends on the period of ϕ_1^* . For such a system, Floquet theory (27) is applicable and will be applied to the particular equation (4.4).

The characteristic equation of equation (4.4) is given by (31)

$$\sigma^2 - (a_{11} + a_{22}) \sigma + (a_{11}a_{22} - a_{12}a_{21}) = 0 \quad (4.5)$$

where the constants are given by

$$\begin{aligned} a_{11} &= x_1(2\pi m) & a_{12} &= x_1'(2\pi m) \\ a_{21} &= x_2(2\pi m) & a_{22} &= x_2'(2\pi m) \end{aligned} \quad (4.6)$$

and the functions $x_1(f)$ and $x_2(f)$ are linearly independent solutions of equation (4.4) obtained utilizing the two sets of initial conditions

$$\begin{aligned} x_1(0) &= 1 & x_2(0) &= 0 \\ x_1'(0) &= 0 & x_2'(0) &= 1 \end{aligned} \quad (4.7)$$

Since equation (4.4) remains invariant when the independent variable f is replaced by $-f$, and is also invariant when x is replaced by $-x$, the initial conditions on x_1 and x_2 indicate that $x_1(f)$ must be an even function of f and $x_2(f)$ must be an odd function of f . In addition the constant term in equation (4.5) is the Wronskian determinant of x_1 and x_2 evaluated at $f = 2\pi m$ and is given by (31, p 131)

$$W(2\pi m) = a_{11}a_{22} - a_{12}a_{21} = \exp \left[- \int_0^{2\pi m} - \frac{2e \sin f}{1 + e \cos f} df \right] = 1 \quad (4.8)$$

Combining all this information leads to the result that

$$a_{11} = a_{22} \quad (4.9)$$

and hence the characteristic equation reduces to the form

$$\sigma^2 - 2a_{11}\sigma + 1 = 0 \quad (4.10)$$

Then from Floquet theory (31), for stability it is required that $|a_{11}| < 1$. Consequently the variational stability of the odd $2\pi m$ periodic solutions, ϕ_1^* , depends only on the value of a_{11} which is found by examining the x_1 type of solution at $2\pi m$.

By numerically finding the values of the $x_1(2\pi)$ for the 2π periodic solutions indicated in Figures 7-20, the stability charts 25-38 were constructed. The notation used in these and subsequent stability charts is:

- "o" - variational stability for one periodic solution
- "x" - variational instability for one periodic solution
- "N" - no periodic solution found
- "b" - $x_1(2\pi)$ was in the range $0.99 < |x_1(2\pi)| < 1.01$
for one periodic solution

The existence of more than one of the above letters for any particular combination of α and e indicates the presence of more than one periodic solution. The stability chart in Figure 31 agrees with the

results of Zlatoustov (13) and Brereton (23) and is presented here for the purpose of comparing it with the other rotational locks.

For all rotational locks investigated, the value of $x_1(2\pi)$ for the line $\alpha = 0$ (i.e. axial symmetric satellite) was found to be unity. This phenomenon occurs because for $\alpha = 0$ there is no torque on the satellite. With the exception of the 1/1 rotational lock, the line $e = 0$ also resulted in $|x_1(2\pi)| = 1$. The reason for this can be seen by examining equation (2.3) with $e = 0$ and written in the following form

$$\frac{d^2 2(\phi_1 + \frac{k}{2}f)}{df^2} + \alpha \sin 2(\phi_1 + \frac{k}{2}f) = 0 \quad (4.11)$$

Equation (4.11) is the equation of a simple pendulum with dependent variable $2(\phi_1 + \frac{k}{2}f)$ and for $k \neq 0$ the solution is that of a rotating simple pendulum.

An examination of the small α region for the $n > 1$ stability charts indicates that the stable region crosses the e axis in the interval $0.6 < e < 1.0$ depending on the rotational lock considered. By examining points on the stability charts in the vicinity of the crossing points indicated by Table II, complete agreement between the analytical results of Section 3 and the numerically determined variational results of the present chapter were found.

It is interesting to note that the stability charts with $n > 1$ contain stable regions other than those near the e axis. These stable regions exist for positive α and appear to be approximately vertical

and narrow in width. As the lock number, n , for these stability charts increases, the eccentricity of these narrow stability regions increases. Note also the similar effect for the stability charts with lock numbers $n \leq 0$.

By examining the $3/2$ rotational lock, Figure 32, for values of the planet Mercury's eccentricity, $e = 0.206$, it was determined that the largest stable value α was 0.197. This value indicates that the ratio of the principal moments of inertia, $\frac{B-A}{C}$, of Mercury may have a maximum value of 0.065.

The variational stability of the 4π periodic solutions ($m = 2$) indicated in Figures 22 and 23 is given by the stability charts shown in Figures 39 and 40. Figure 39 shows that the stability regions are larger for the 4π periodic solutions of the $1/1$ rotational lock than the investigation by Brereton (23) indicates. The additional 4π periodic solutions found in the present investigation are the explanation for this discrepancy. In Figure 40, it is interesting to note that none of the 4π periodic solutions investigated were stable.

5. PHASE SPACE ANALYSIS

5.1 Invariant Surfaces

Many rotational locks in the preceeding chapter were found to have regions which were variationally stable. These regions were determined by considering only displacements or disturbances infinitesimal in nature. In order to investigate the stability of rotational locks for

the case of finite disturbances, a technique used by Brereton and Modi (14) which they applied to the 1/1 rotational lock, will be extended to include the wide range of rotational locks considered in this report.

Equation (2.3) can be written as two first order equations as shown:

$$\frac{d\phi_1}{df} = \phi_1'$$

$$\frac{d\phi_1'}{df} = \frac{1}{1 + e \cos f} \left[2e \sin f \left(\phi_1' + \frac{k+2}{2} \right) + \frac{\alpha}{2} \sin 2 \left(\frac{k}{2}f + \phi_1 \right) \right] \quad (5.1)$$

Consequently the state of the system can be represented by a point in the phase space defined by the three orthogonal co-ordinates ϕ_1 , ϕ_1' , f . A particular rotational lock can be investigated in this phase space by assuming initial conditions $\phi_1(0)$ and $\phi_1'(0)$ and numerically integrating equation (2.3), or equivalently equation (5.1), from $f = 0$ to $f = 2\pi$. Since the coefficients of equation (2.3) are 2π periodic, the integration need only be carried out over this interval. The final point, $\phi_1(2\pi)$ and $\phi_1'(2\pi)$, is taken as the new initial point at $f = 0$ and the integration again carried out to $f = 2\pi$. Equation (2.3) therefore can be thought of as a transformation which transforms points in the phase space from $f = 0$ to $f = 2\pi$.

For the case of the 1/1 rotational lock ($k = 0$) Brereton and Modi (14), using the above method, demonstrated that the locus of points in the plane $f = 0$ form a closed curve provided $|\phi|$ remains less than $\frac{\pi}{2}$.

These closed curves are invariant (i.e. they are the same at multiples of 2π) and the infinite number of trajectories which connect them define an invariant surface or integral manifold. Invariant surfaces for the case $k \neq 0$ were numerically found to exist and were constructed in the following manner.

The initial conditions

$$\phi_1(0) = 0$$

$$\frac{d\phi_1(0)}{df} = \frac{d\phi_1^*(0)}{df} + \delta \quad (5.2)$$

were selected, where $\frac{d\phi_1^*(0)}{df}$ is the initial angular velocity of the periodic solution under investigation at $f = 0$ and δ is a small increment. Equation (2.3) can then be numerically integrated from $f = 0$ to $f = 2\pi$ repeatedly for a large number of orbits as explained previously. If the absolute value of $|\phi_1|$ at $f = 0$ remains less than $\frac{\pi}{2}$ for each orbit, it was found that an invariant closed curve was formed by these trajectories at $f = 0$. The value of δ in equation (5.2) was then increased and the procedure repeated. If the $|\phi_1|$ of one of the trajectories becomes greater than $\frac{\pi}{2}$ at $f = 0$, the value of δ in equation (5.2) was decreased and the procedure restarted. By varying δ according to the above procedure, the largest invariant closed curve was formed. Such invariant closed curves and associated invariant surface are shown schematically in Figure 41.

The limiting value of $|\phi_1| < \frac{\pi}{2}$ at $f = 0$ was not arbitrarily selected. For the $k \neq 0$ cases, the value of $|\phi_1|$ that can be tolerated before the satellite "tumbles" out of a particular lock, is not evident. Consequently, a numerical study was conducted to investigate the invariant curves in the neighborhood of $|\phi_1| = \frac{\pi}{2}$ at $f = 0$. In this study, a variety of rotational locks, orbit eccentricities, and satellite parameters were selected from the points shown to be variationally stable in Section 4. For each of these cases, initial conditions (5.2) were found that produced the maximum invariant surface inside the bounds $|\phi_1| \leq \frac{\pi}{2}$ at $f = 0$. Initial conditions slightly larger than these invariant surfaces were selected and values of ϕ_1 were studied carefully for many orbits. The results indicated that once $|\phi_1|$ exceeded $\frac{\pi}{2}$ at $f = 0$, the satellite left the particular rotational lock investigated since $|\phi_1|$ at subsequent values of $f = 0$ became greater than 2π for every case examined. Figure 42 shows the values of $|\phi_1|$ at $f = 0$ versus the number of orbits for several typical cases where δ was chosen slightly larger than the maximum or limiting invariant curves at $f = 0$. It is interesting to note that one case was found, $n = 10$, $\alpha = 3$, $e = 0.3$, in which the satellite clearly left the 5/1 lock and several orbits later actually returned momentarily to the same "lock". It should also be pointed out that for each case investigated the angular velocities $\dot{\phi}_1$ at $f = 0$ for the orbits where $|\phi_1| > \frac{\pi}{2}$ were in the same general region as for the orbits where $|\phi_1| < \frac{\pi}{2}$.

There is a definite relationship between invariant surfaces and periodic solutions. A point whose initial values lie inside an invariant

surface will generate another invariant surface. The property of uniqueness which specifies that no two trajectories intersect, requires that the inner invariant surface must lie completely within the outer invariant surface. By generating smaller and smaller invariant surfaces, it becomes apparent that the limiting invariant surface must have zero cross-sectional area and be a periodic solution. Figure 43 illustrates the nesting of invariant surfaces for a particular case by showing their cross-sections at $f = 0$.

A point outside an invariant surface was found to generate another invariant surface completely encompassing the first provided $|\phi_1|$ remained less than $\frac{\pi}{2}$ at $f = 0$. The significance of the limiting invariant surface is that it represents all possible angular displacements ϕ_1 and angular velocities $\dot{\phi}_1$ throughout the orbit to which a satellite can be subjected and still remain in the same rotational lock.

Typical examples of the cross-sections of maximum invariant surfaces at $f = 0, 90, 180, 270$ degrees are shown in Figures 44, 45, 46, and 47. As indicated by these two cases, the cross-sections of the maximum invariant surfaces for the higher rotational locks at various values of f are not approximately elliptical as was the case for the 1/1 rotational lock. It was also noticed that the deviation from an elliptical cross-section increased as the satellite parameter α increased.

Throughout a satellite's lifetime many types of disturbances may influence its motion. At a particular position in orbit impulsive

type loadings possibly caused by meteorite collisions would tend to increment the satellites velocity where the angular displacement would remain essentially constant. On the other hand, disturbances from other bodies, solar radiation effects, and other less impulsive type forces may have the effect of incrementing both the angular velocity and angular displacement of the satellite. As indicated by Figures 45 and 47, the stability of a satellite performing periodic motion in a rotational lock therefore depends not only on the particular rotational lock, n , the orbit eccentricity, e , the satellite parameter, α , and position in orbit f , but also on the type of disturbance encountered.

In order to convey as concisely as possible a meaningful evaluation of the size of the various maximum invariant surfaces constructed, a conservative and liberal estimate of their respective sizes will be presented. The conservative estimate was found by measuring the positive and negative increment from the periodic solution along the ϕ_1' axis to the maximum invariant surface at $f = 0$. These values were found to be as small or smaller than the values found throughout the orbit in the same manner and consequently represent a conservative estimate of the size of the invariant surfaces. The liberal estimates of the size of the maximum invariant surfaces were found by measuring the positive and negative distances from the periodic solution to the farthest extremities of the invariant surface. An illustration of these measurements appears in Figure 48.

5.2 Small α Verification

The change in angular velocity, $\Delta \frac{d\phi_1}{df}$, indicated by either of the

above estimates can be discussed more effectively if $\Delta \frac{d\phi_1}{df}$ is converted to the change in absolute angular velocity $\Delta \frac{d\theta}{dt}$. Using the definitions expressed in Section 2, the change in absolute angular velocity divided by p can be written

$$\frac{\Delta \left(\frac{d\theta}{dt} \right)}{p} = \frac{df}{dM} \Delta \left(\frac{d\phi_1}{df} \right) = \frac{(1 + e \cos f)^2}{(1 - e^2)^{3/2}} \Delta \left(\frac{d\phi_1}{df} \right) \quad (5.3)$$

where $p = \frac{2\pi}{T_o}$ is the mean daily motion.

Since the change in absolute angular velocity times the moment of inertia C and the change in angular momentum, H , are identical, the change in angular momentum divided by Cp can also be written in the form of equation (5.3).

Equation (3.8) indicates that for small α the maximum positive or negative change in absolute angular velocity from a constant absolute angular rate which allows the satellite to remain in a specific rotational lock can be written

$$\frac{\Delta \left(\frac{d\theta}{dt} \right)}{p} = \left(3a^2 |\phi_n| \right)^{1/2} = \left(\alpha |\phi_n| \right)^{1/2} \quad (5.4)$$

For small values of α , a comparison between the numerical phase space analysis and the analytical results of Section 3 can be made using equations (5.3) and (5.4). For this comparison, the values of orbit eccentricity which produced the strongest lock from Table I were

selected for several rotational locks. It was found that the conservative and liberal estimates of the maximum invariant surfaces for the cases $\alpha = 0.0015$ and 0.00015 were approximately the same throughout the orbit indicating near constant elliptical type cross-sections. Figure 49 indicates the positive and negative changes in absolute angular velocity obtained from the maximum invariant surface and equation (5.3) for the values 0.0015 and 0.00015 . Figures 49 and 3 compare favorably taking into account that equation (5.4) involves the square root of ϕ_n . Table III indicates the percent error found between the phase space and analytical results for the three α values of 0.015 , 0.0015 , and 0.00015 . For the $\alpha = 0.015$ case, the maximum invariant surface deviated from an elliptical type cross-section. The error is given by the average value of the conservative and liberal estimates at $f = 0$. Also from Table III, an estimate of the size of α can be obtained for the analytical results to remain valid.

The variational stability analysis of Section 4 indicated that all rotational locks investigated with $n \geq 2$ had a narrow region near the e axis for which periodic solutions were variationally stable. To obtain an estimate of the strength of rotational locks in this region, conservative and liberal estimates of the size of the maximum invariant surfaces for several rotational locks at $\alpha = 0.05$ were investigated. Figure 50 illustrates the conservative estimates of the positive and negative changes in angular momentum versus the orbit eccentricity for the rotational locks $n = 2, 3, 5, 10$, and 20 . Figures 51-55 on the other hand show the liberal estimates of the positive and negative changes in

momentum for various orbit eccentricities throughout the orbit for the rotational locks $n = 2, 3, 5, 10, \text{ and } 20$. Although many trends of the analytical results of Section 3 are still present, it is apparent from these figures that for the case of $\alpha = 0.05$, the analytical results are not valid. These figures also indicate that for $\alpha = 0.05$, the strengths of the higher locks for various values of eccentricity and orbit position are of approximately the same strength as the 1/1 rotational lock.

5.3 Large α

For $\alpha \geq 0.1$, the variational stability charts of Section 4, Figures 25-38, indicate that all rotational rates investigated, with the exception of the $n = 1$ case, have regions that are variationally stable. These stability regions can, in general, be represented by areas about lines of constant eccentricity. Consequently, it was felt that a phase space analysis of points lying along these lines of constant eccentricity for various rotational locks would serve as representative estimates of the strengths of these rotational locks. The lines of constant eccentricity and associated rotational locks, n , examined were $n = 20, e = 0.5$; $n = 10, e = 0.3$; $n = 5, e = 0.1$; and $n = 2, e = 0.1$ for the $n \geq 2$ cases and $n = 0, e = 0.4$; $n = 2, e = 0.5$; and $n = -10, e = 0.7$ for the $n < 2$ cases.

Figures 56 and 57 show the conservative estimates of the positive and negative changes in momentum for the cases $n \geq 2$ and $n < 2$ respectively. The liberal estimates of the changes in momentum are shown in Figures 58-60 for $n \geq 2$ and in Figures 61-63 for $n < 2$. The case $n = 2$ (1/1 rotational lock) with $e = 0.1$ is presented on each figure for comparison with the other rotational locks.

These figures indicate that for the cases investigated, the 1/1 rotational lock is in general stronger than the higher rotational locks particularly for very large values of α . However under certain circumstances, the higher rotational locks can be as strong as the 1/1 rotational lock. Care must be taken when making this observation by noting that for orbits of higher eccentricity, the strength of the 1/1 rotational lock is greatly reduced (23).

A large number of points which were shown to be variationally unstable ($|a_{11}| > 1$) in Section 4 were investigated using the phase space analysis presented in the current section. The stability of all points investigated using the phase space analysis (with the exception of two) were found to be unstable as anticipated (i.e. no invariant surface could be constructed for values of $\delta \leq 0.00004$).

The two contradictory cases mentioned above were for $n = 10$, $\alpha = 0.05$, $e = 0.8$ and $n = 20$, $\alpha = 0.05$, $e = 0.7$ for which $|a_{11}|$ was 1.17 and 1.13 respectively. For these cases invariant surfaces were found about their respective periodic solutions. The behavior of these two cases appears to be exceptional and at present difficult to explain. The discovery of these two cases led to further investigations where $1.0 \leq |a_{11}| < 1.20$ for many combinations of α , e , and n . All of these additional cases were found to corroborate the results of the variational analysis.

6. CONCLUSIONS

6.1 Summary of Results

Stable or locked-in planar rotational motion at spin rates of $n/2$

(where n is an integer) satellite rotations per orbit revolution are shown to exist for specific combinations of satellite parameter, α , and orbit eccentricity, e . Analytic results were obtained for the case of small α which indicated that the strength of the higher rotational locks ($n > 3$) are greater than the strength of the 1/1 rotational lock for proper combinations of lock number, n , and orbit eccentricity. Comparison of the results for the case of the planet Mercury are shown to be in good agreement with both observations of the planet and the numerical results of Liu.

Numerical results were obtained for representative values throughout the range of the satellite parameter α . Odd 2π and 4π periodic solutions are found for various combinations of α , e , and n and the stability of these solutions presented. In general, it is shown that for values of α not small, the stable periodic solutions occur at eccentricities which tend to increase as the absolute value of the lock number $|n|$ increases. Conservative and liberal estimates of the strengths of these locks are presented which indicate that for larger values of α the lock strength is in general considerably less than that of the 1/1 rotational lock.

When regions of investigation for the various analytical and numerical techniques employed overlapped, the results were compared and found to agree. The numerical programs written, when reduced to the case of the 1/1 rotational lock, substantiated other published results.

6.2 Physical Explanation

For small α , the curves of Figure 3 indicate that for each rotational lock there is a particular eccentricity associated with the strongest lock. For larger values of α , Figures 32-38 show that the rotational locks ($n > 3$) occur only for specific intervals of eccentricity. In both cases, these values of eccentricity tend to increase as the value of the lock number, n , increases. A possible explanation for this motion could be that the absolute angular velocity of the satellite attempts to match the angular rate of the orbit at some point, especially near pericenter where the interaction between the satellite and the attracting body is strongest. This apparent interaction at pericenter is shown in Figure 64 for the 2π periodic solution found for the case $n = 10, \alpha = 1.0, e = 0.4$.

The angular rate of the radius vector to the satellite can be expressed as (30)

$$\frac{df}{dM} = \frac{(1 + e \cos f)^2}{(1 - e^2)^{3/2}}$$

Figure 65 is a plot of the angular rate of the radius vector $\frac{df}{dM}$ versus the eccentricity of the orbit, e , for the value of true anomaly $f = 0$. Also plotted for each rotational lock are the particular values of eccentricity which produce the strongest lock from Table 1 for small α , and the approximate intervals of eccentricity from Figures 32-38 for larger values of α . Figure 65 indicates that neither of the above

cases coincides identically with the $f = 0$ curve, but that the trends for both cases are similar to that of the angular rate of the orbit at pericenter.

REFERENCES

1. Klemperer, W.B. and Baker, R.M., "Satellite Librations," Astronautica Acta, vol. 3, pp. 16-27, 1957.
2. Schindler, G.M., "On Satellite Librations," ARS Journal, vol. 29, pp. 368-370, May 1959.
3. Schindler, G.M., "Satellite Librations in the Vicinity of Equilibrium Solutions," Astronautica Acta, vol. 6, Fasc. 5, pp. 233-240, 1960.
4. Klemperer, W.B., "Satellite Librations of Large Amplitude," ARS Journal, vol. 30, pp. 123-4, Jan. 1960
5. Baker, R.M.L., "Plane Libration of a Prolate Ellipsoidal Shell," ARS Journal, vol, 30, pp. 126-8, Jan. 1960.
6. Auelmann, R.R., "Regions of Libration for a Symmetrical Satellite," AIAA Journal, vol. 1, No. 6, pp. 1445-7, June 1963.
7. Moran, J.P., "Effects of Plane Librations on the Orbital Motion of a Dumbbell Satellite," American Rocket Society Journal, vol. 31, No. 8, pp. 1089-1096, Aug. 1961.
8. Baker, R.M.L., "Librations on a Slightly Eccentric Orbit," ARS Journal, vol. 30, pp. 124-6, Jan. 1960.
9. Schechter, H.B., "Dumbbell Librations in Elliptic Orbits," AIAA Journal, vol. 2, No. 6, pp. 1000-1003, June 1964.
10. Beletskii, V.V., "Motion of an Artifical Satellite About its Center of Mass," NASA TT F-429, pp. 1-58, 1966.
11. Chernous'ko, F.L., "Resonance Phenomena in the Motion of a Satellite Relative to its Mass Center," U.S.S.R. Computational Mathematics and Mathematical Physics, vol. 3, No. 3, pp. 528-538, 1963.

12. Torzhevskiz, A.P., "Periodic Solutions to the Equation of Plane Oscillations of a Satellite on an Elliptical Orbit," Cosmic Research, Vol. 2, No. 5, pp. 17-34, 1964.
13. Zlatoustov, V.A., Okhotsimskiy, D.Y., Sarychev, V.A., and Torzhevshiz, "A Study of the Oscillation of a Satellite in the Plane of an Elliptical Orbit," Cosmic Research, vol. 2, No. 5, pp. 1-15, 1964.
14. Brereton, R. C. and Modi, V.J., "On the Stability of Planar Librations of a Dumbbell Satellite in an Elliptic Orbit," Journal of the Royal Aeronautical Society, vol. 70, pp. 1098-1102, Dec. 1966.
15. Modi, V.J., and Brereton, R.C., "Planar Librational Stability of a Flexible Satellite," AIAA Journal, vol. 6, No. 3, pp. 511-517, March 1968.
16. Brereton, R.C. and Modi, V.J., "Stability of the Planar Librational Motion of a Satellite in an Elliptic Orbit," Proceedings of the XVII International Astronautical Congress, International Astronautical Federation, Madrid, Spain, 1966 (in press).
17. Pettengill, C.H. and Dyce, R. B., "A Radar Determination of the Rotation of the Planet Mercury," Nature, vol. 206, pp. 1240, June 1965.
18. McGovern, W.E., Gross, S.H. and Rasool, S.I., "Rotation Period of the Planet Mercury," Nature, vol. 208, pp. 375, 1965.
19. Colombo, G., "Rotational Period of the Planet Mercury," Nature, pp. 575, Nov. 6, 1965.
20. Liu, H.S. and O'Keefe, J.A., "Theory of Rotation for the Planet Mercury," Science, vol. 150, pp. 1717, 1965.

21. Liu, H.S., "The Libration of Mercury," Journal of Geophysical Research, vol. 71, No. 12, June 1966.
22. Laslett, L.J. and Sessler, A.M., "Rotation of Mercury: Theoretical Analysis of the Dynamics of a Rigid Ellipsoidal Planet," Science vol. 151, pp. 1384-5, 1966.
23. Brereton, R.C., Stability Study of Gravity Oriented Satellites, Thesis (Ph.D. in Mechanical Engineering), The University of British Columbia, 1967.
24. Symon, Kerst, Jones, Laslett and Terwilliger, Physical Review, Appendix A. vol. 103, pp. 1858-9, 1956.
25. Wiggins, L.E., "Relative Magnitudes of the Space Environment Torques on a Satellite," AIAA Journal, vol. 2, No. 4, pp. 770-771, April 1964.
26. Danby, J.M.A., Fundamentals of Celestial Mechanics, Macmillan, New York, pp. 97-98, 1962.
27. Cesari, L., Asymptotic Behavior and Stability Problems in Ordinary Differential Equations, Springer-Verlag, Berlin, 1959, pp. 55-65.
28. Yu, E.Y., "Long-Term Coupling Effects between Librational and Orbital Motions of a Satellite," AIAA Journal, vol. 2, No. 3, pp. 553-555, March 1964.
29. Smart, W.M., Celestial Mechanics, John Wiley, New York, 1953, pp. 38.
30. Roy, A.E., The Foundations of Astrodynamics, Macmillan, New York, 1965, pp. 110.
31. Minorsky, N., Nonlinear Oscillations, D. Van Nostrand Co., New York, 1962.
32. Stoker, J.J., Nonlinear Vibrations in Mechanical and Electrical Systems, Interscience, New York, 1966, pp. 193.

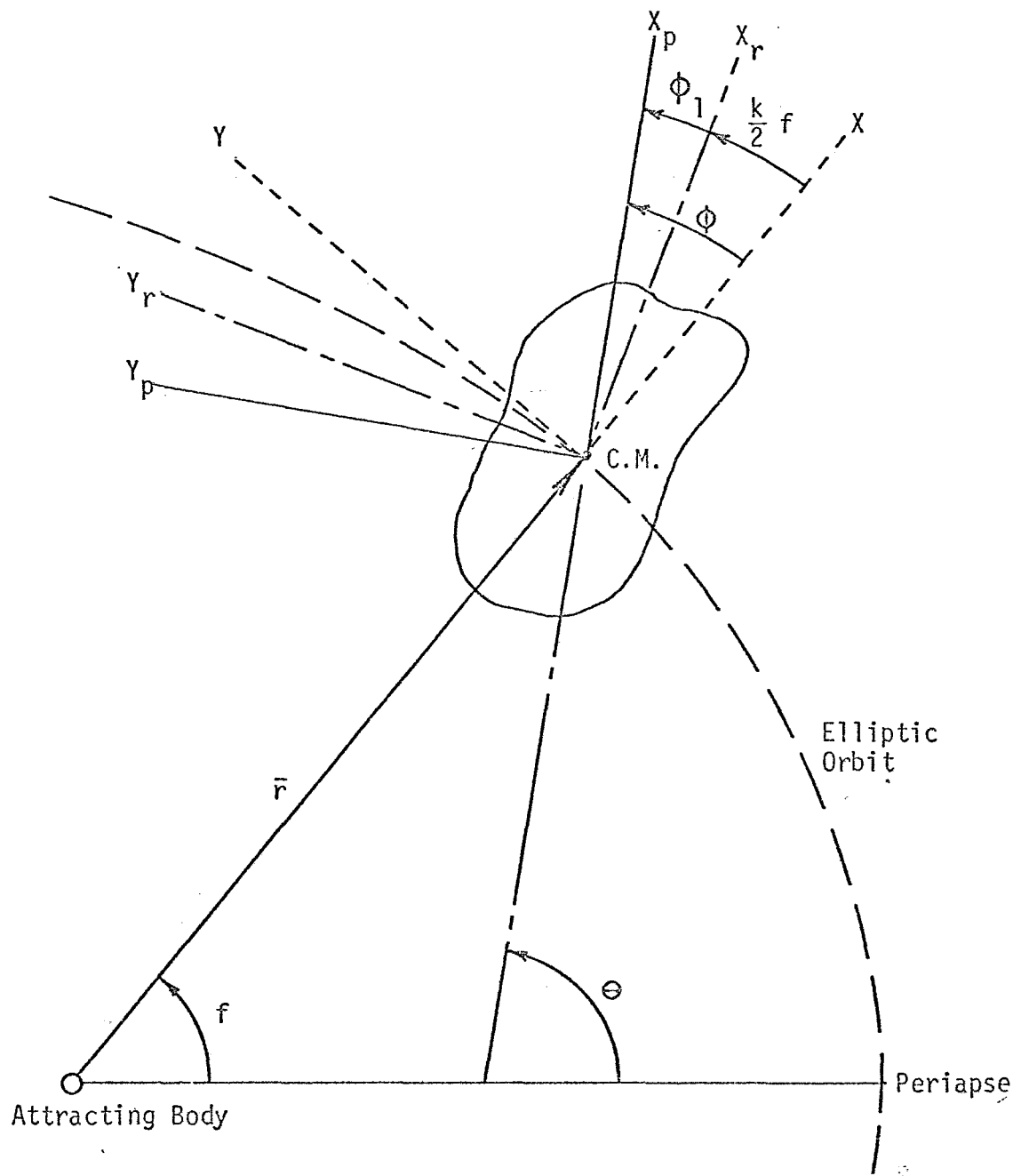


Figure 1 - Geometry of the Problem

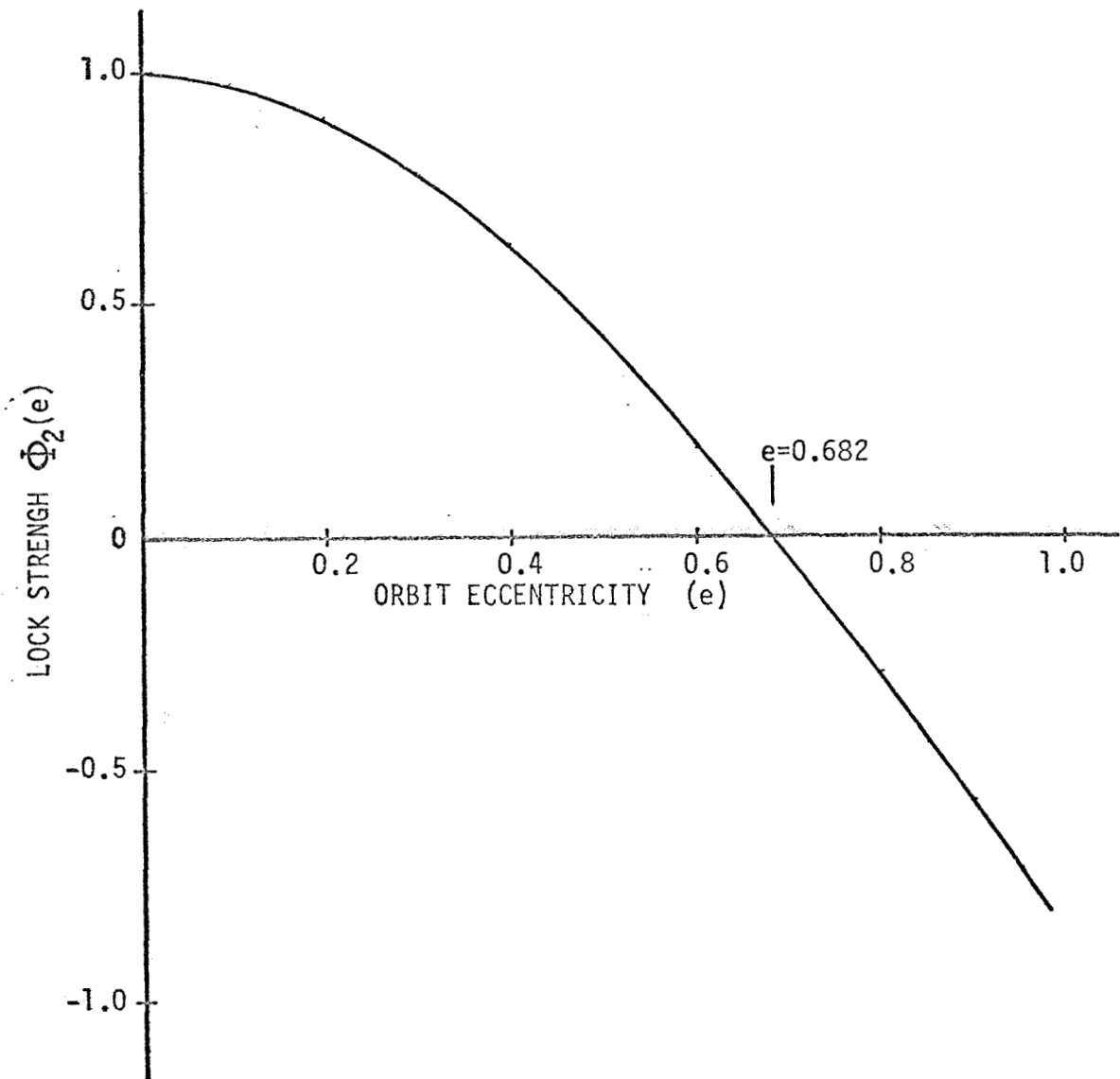
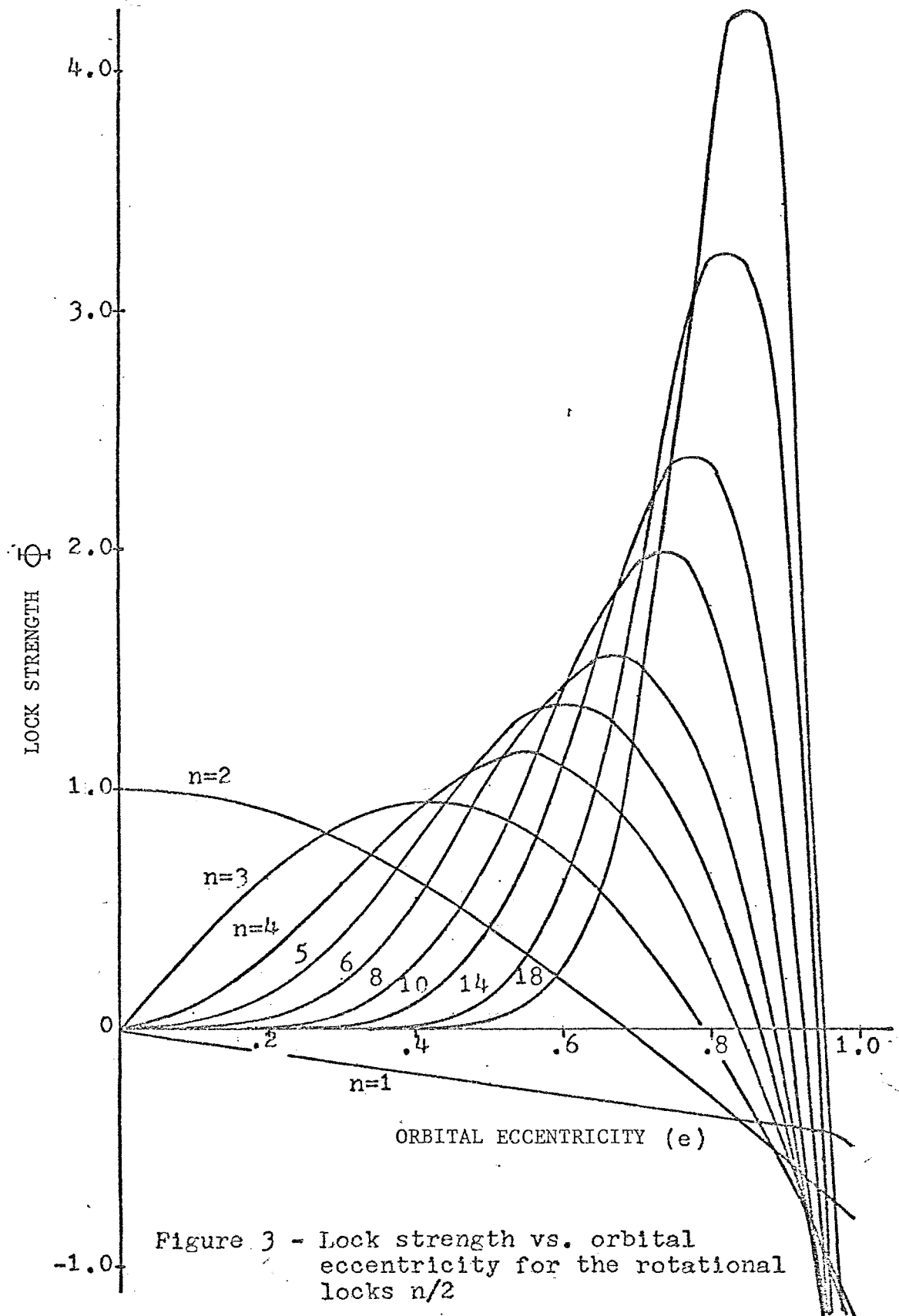


Figure 2 - Variation of $\Phi_2(e)$ with Eccentricity



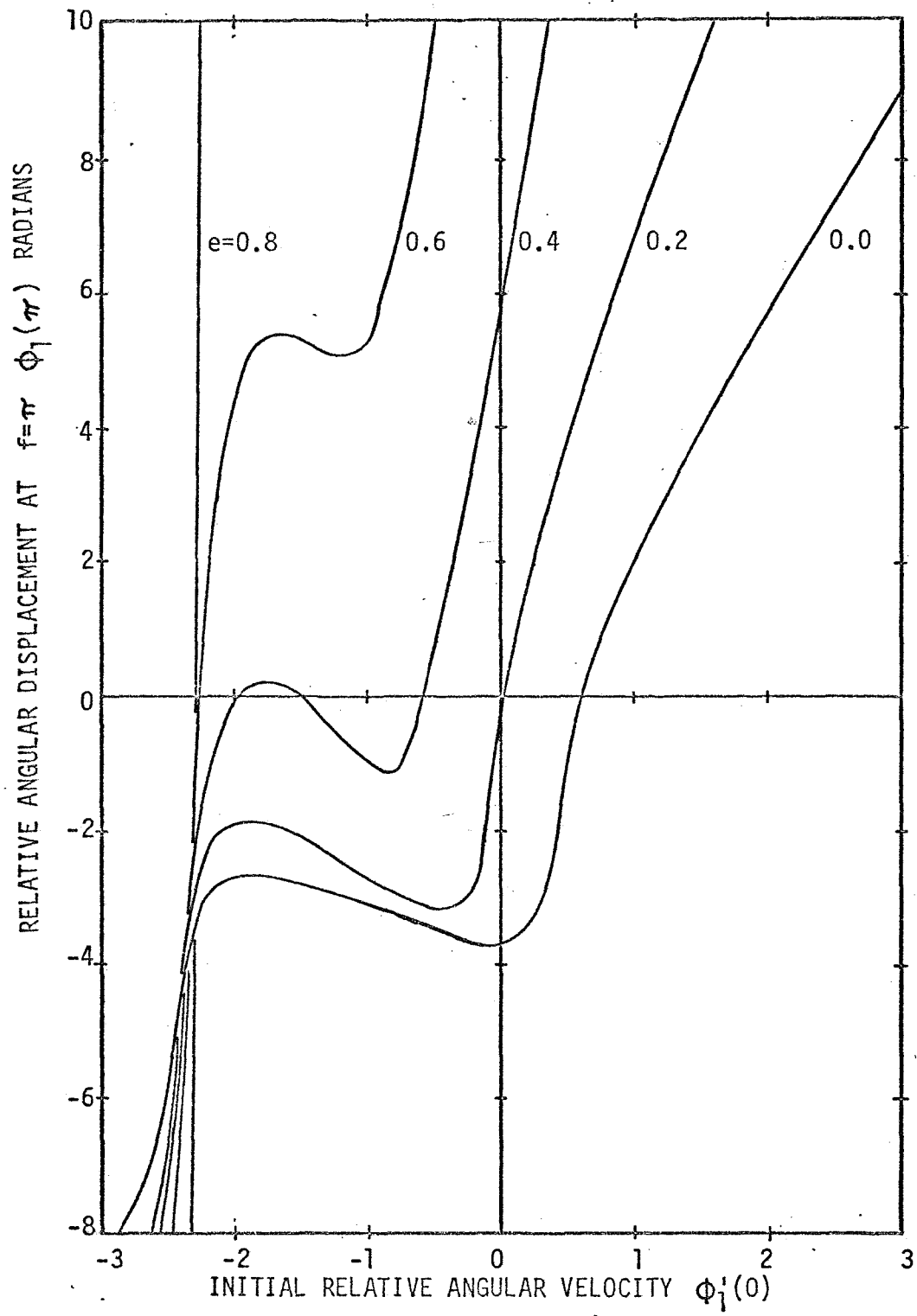


Figure 4 - Variation of $\phi_1'(0)$ with $\phi_1(\pi)$ ($n = 4$, $\alpha = 2.0$)

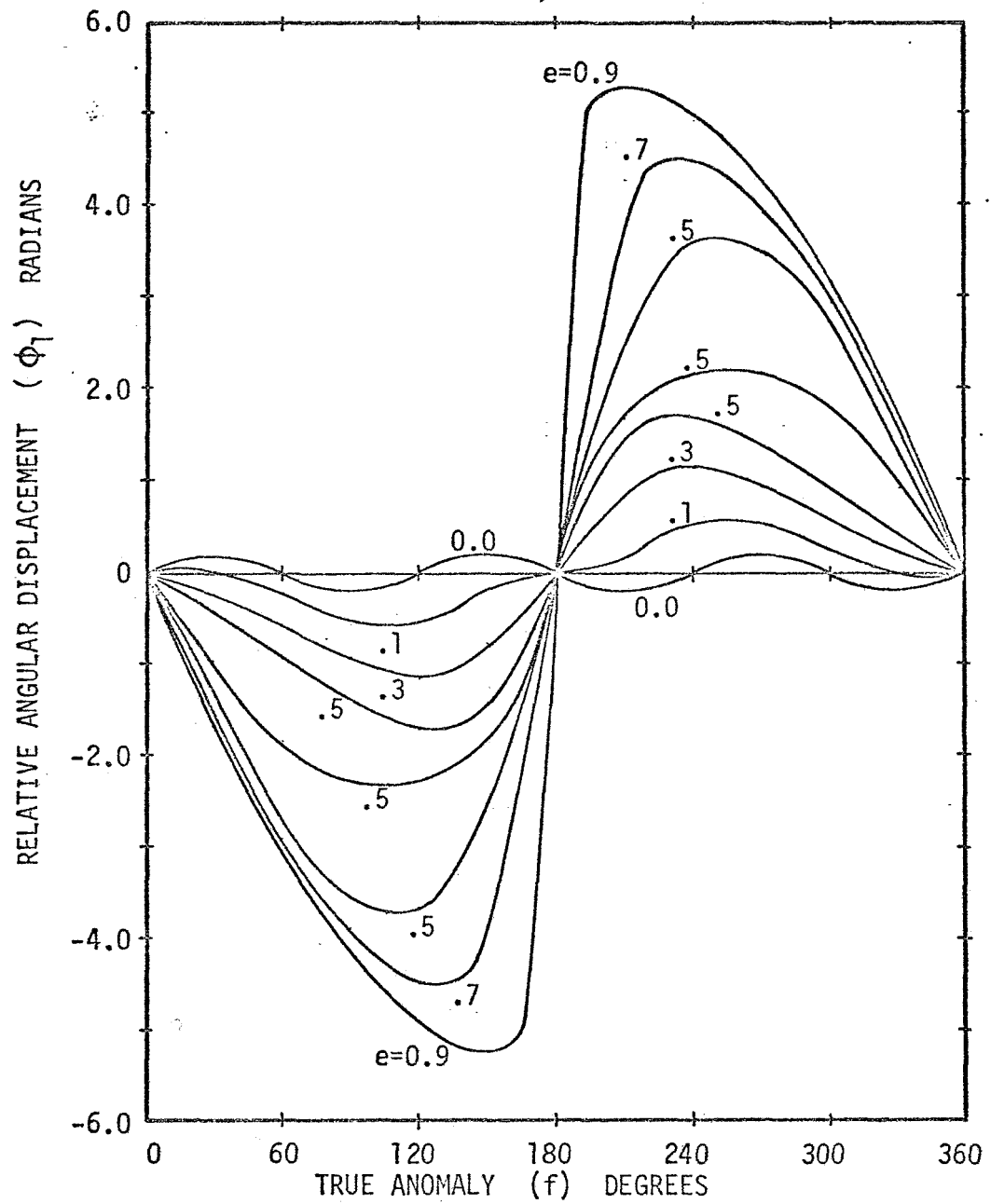


Figure 5 - Odd 2π Periodic Solutions ($n = 5$, $\alpha = 3.0$)

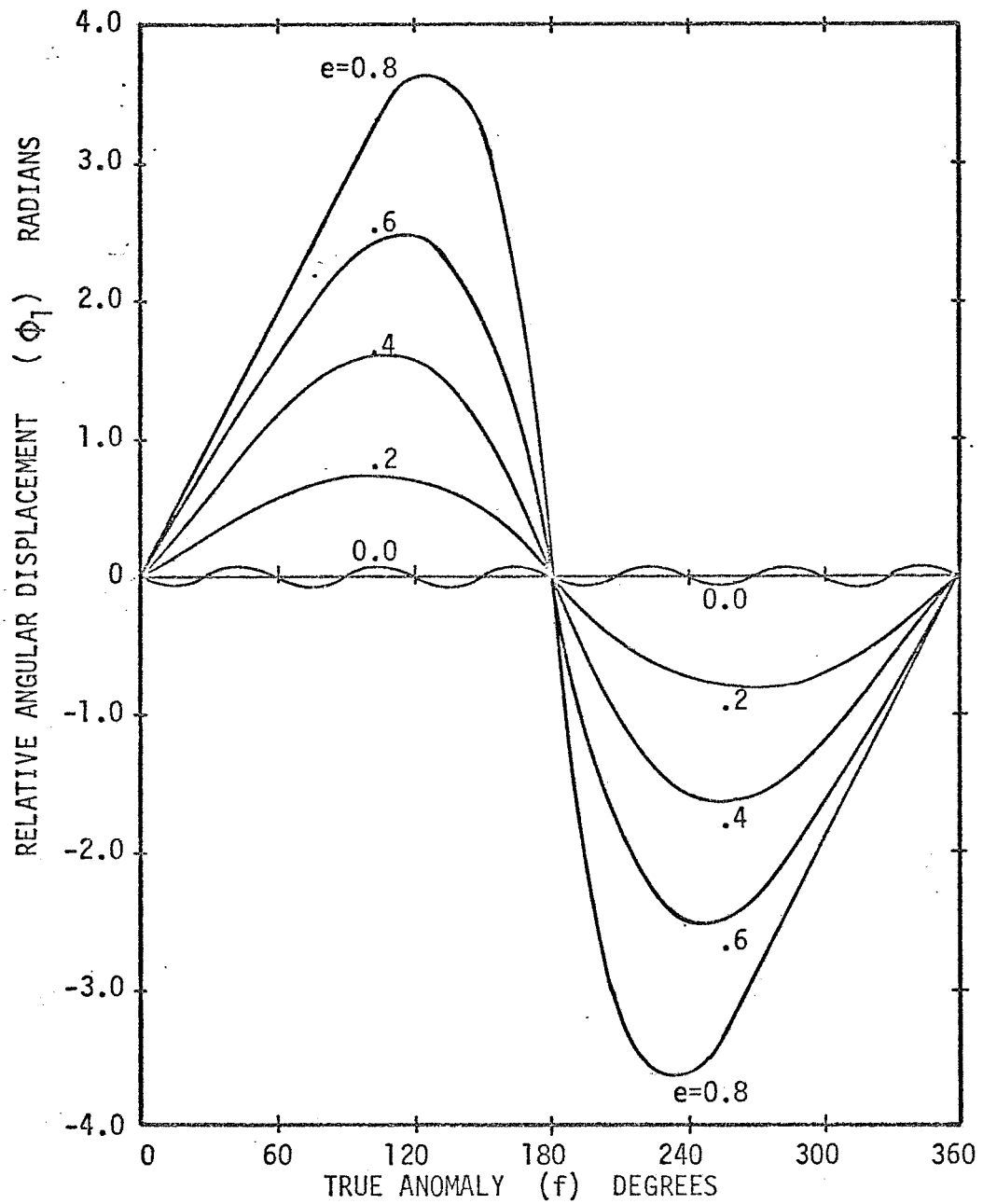


Figure 6 - Odd 2π Periodic Solutions ($n = -4, \alpha = 2.0$)

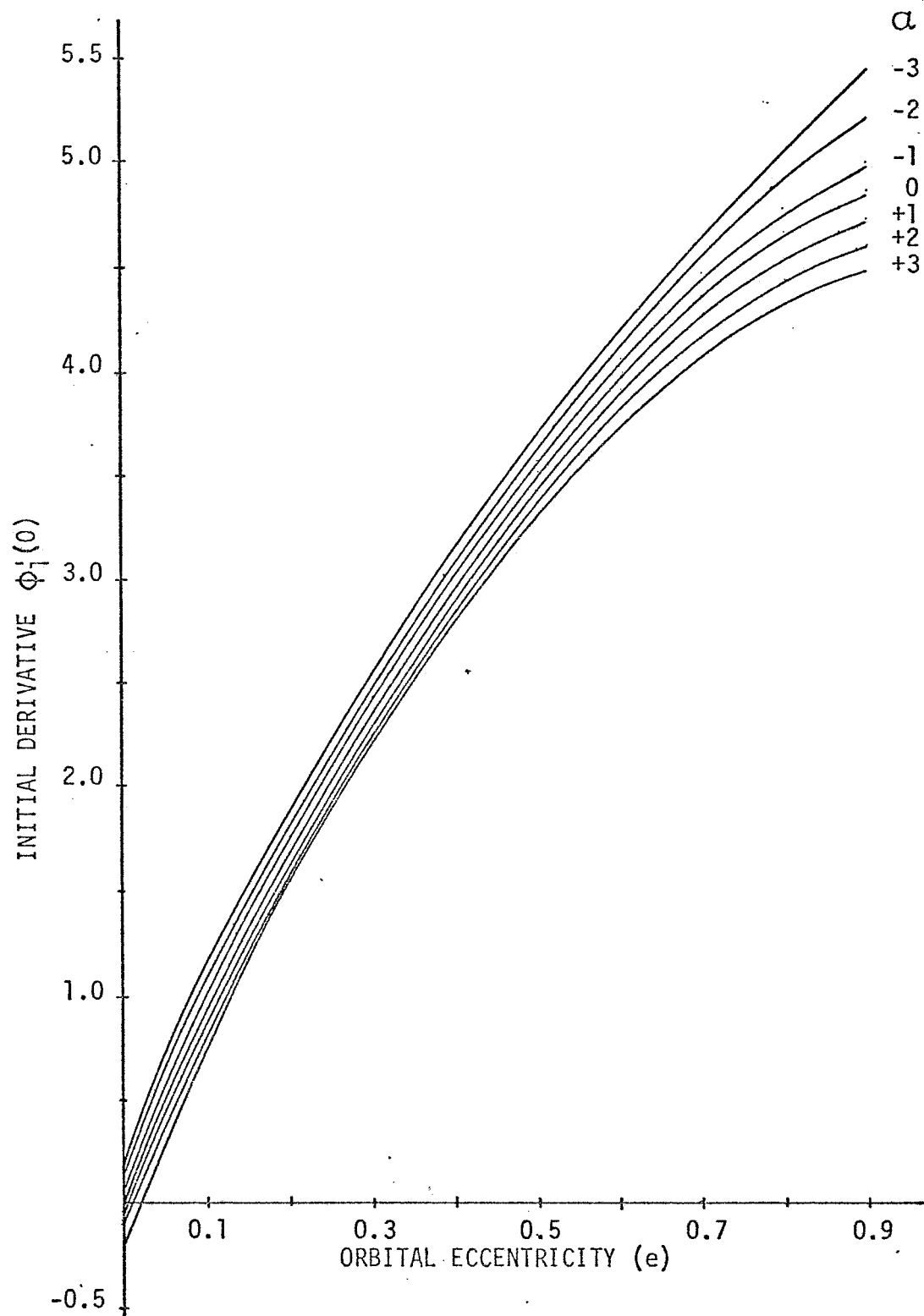


Figure 7 - Initial Derivative Required to Produce 2π Periodic Solutions ($n = -10$)

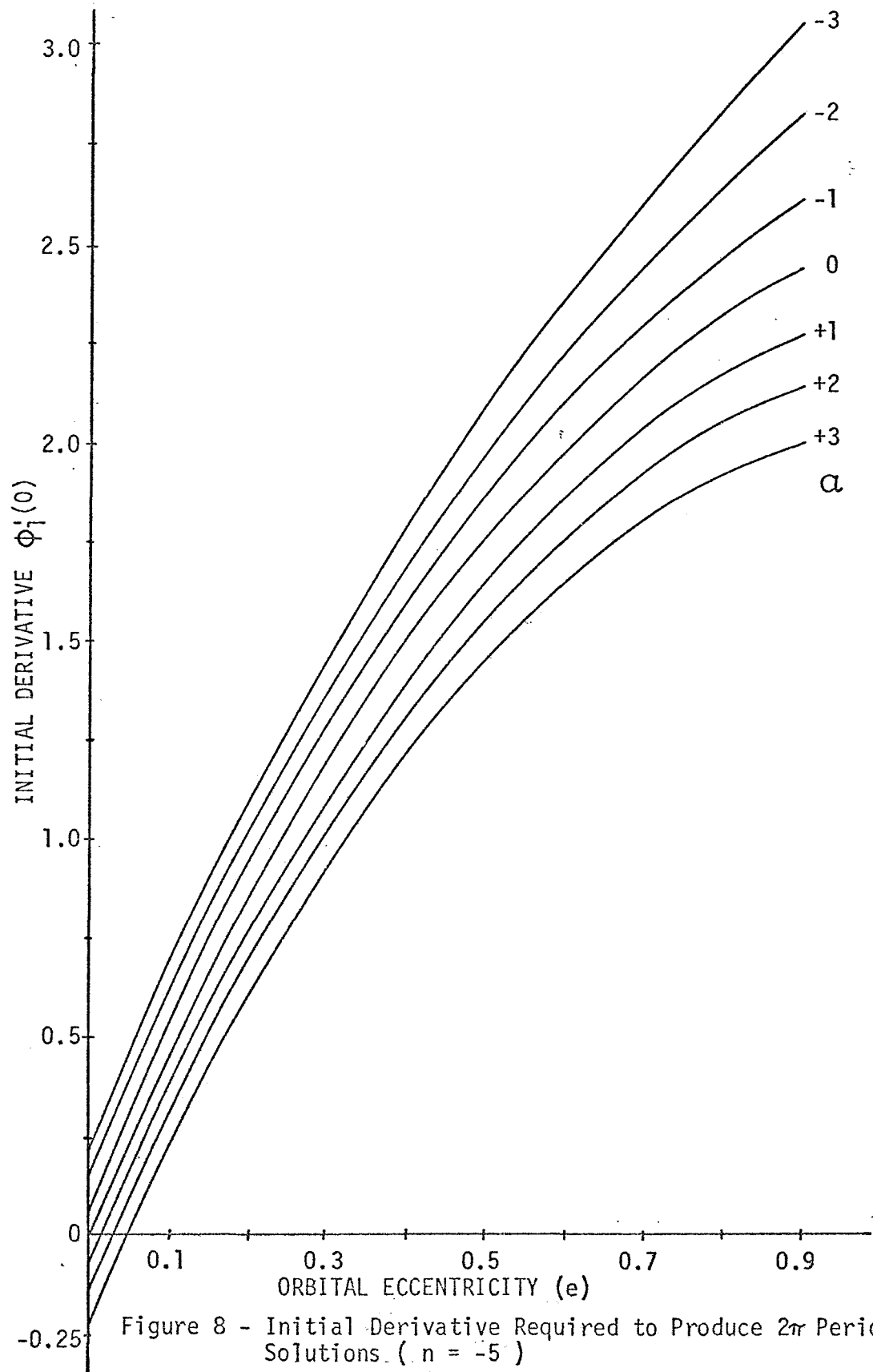


Figure 8 - Initial Derivative Required to Produce 2π Periodic Solutions. ($n = -5$)

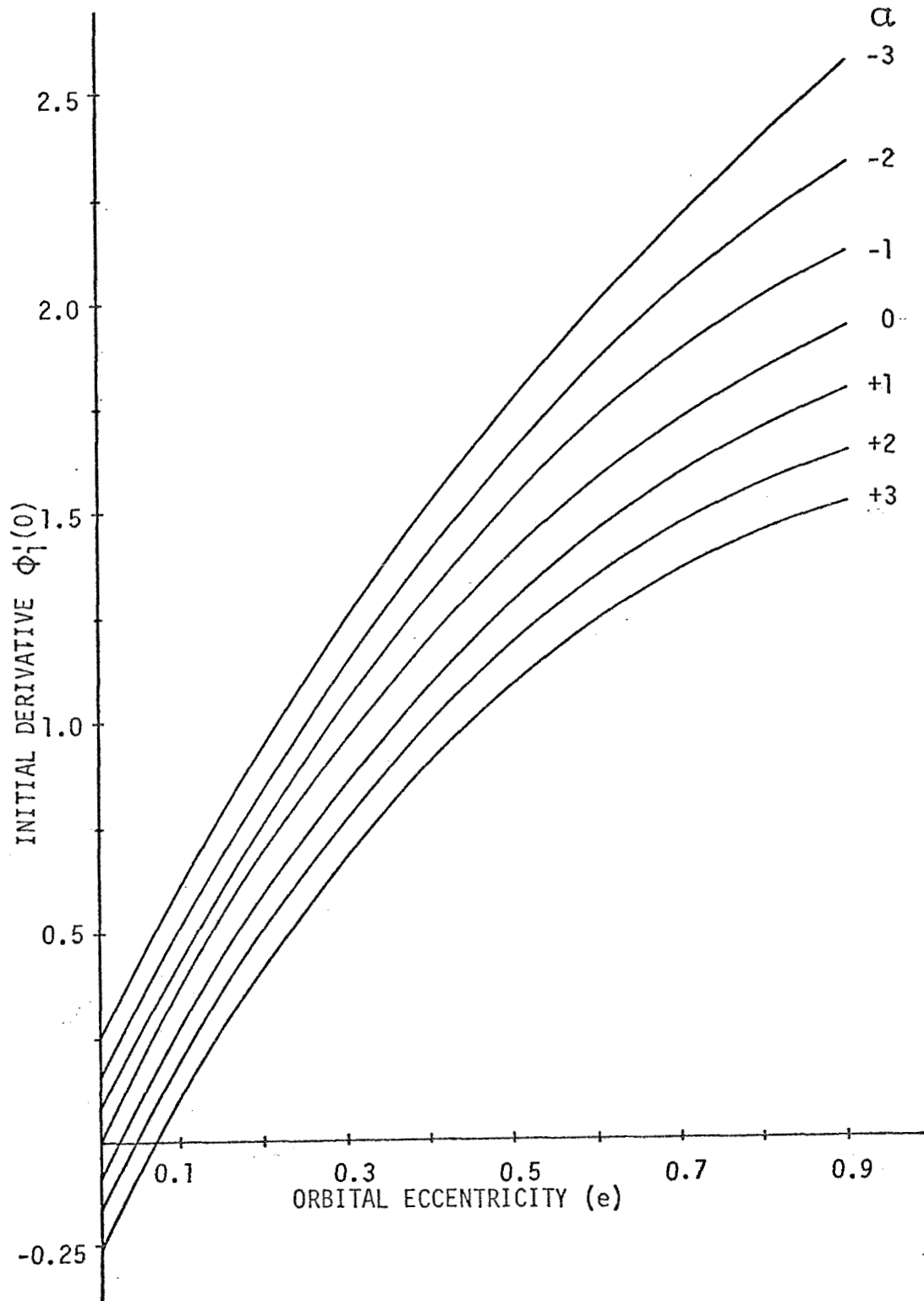


Figure 9 - Initial Derivative Required to Produce 2π Periodic Solutions ($n = -4$)

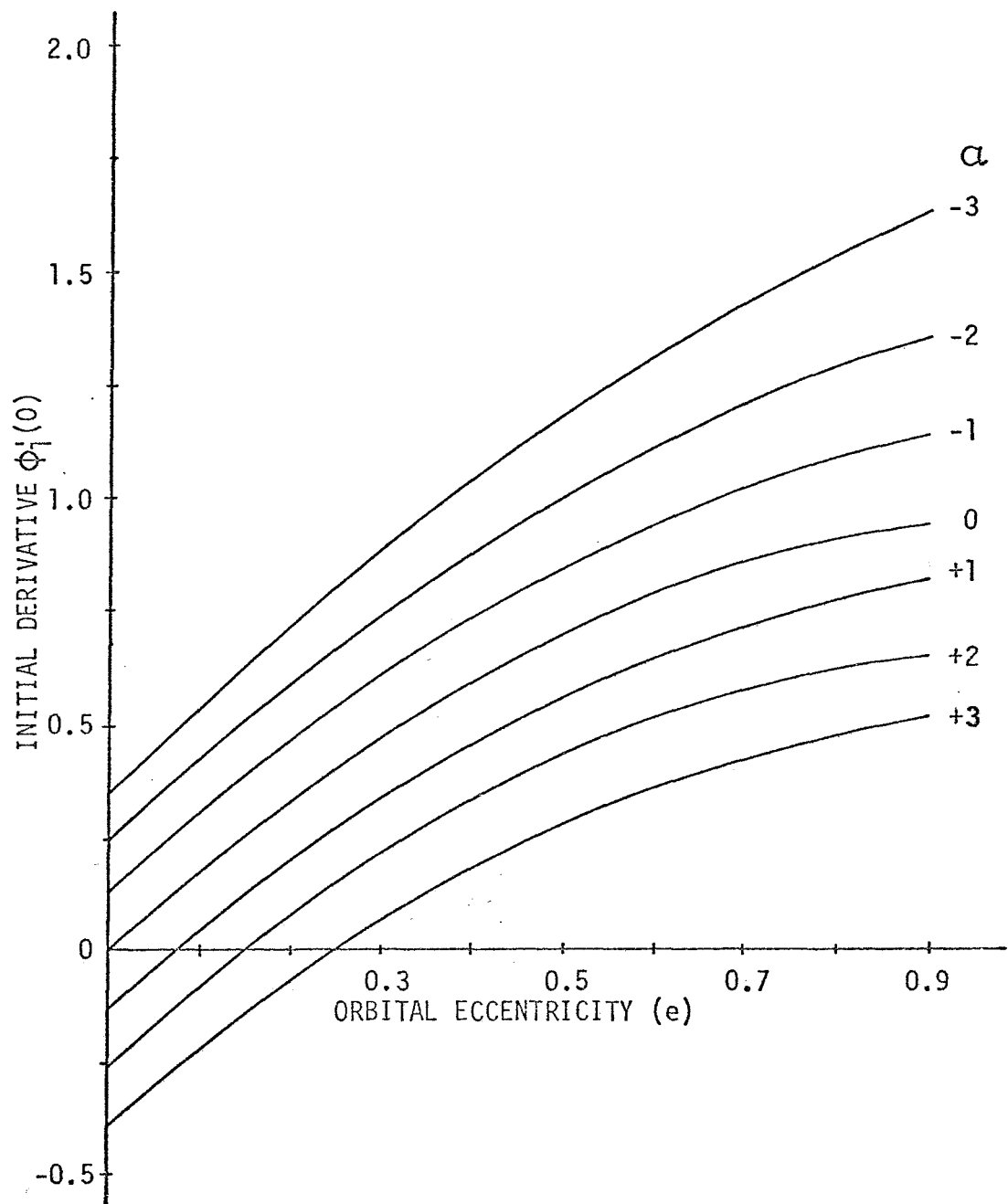


Figure 10 - Initial Derivative Required to Produce 2π Periodic Solutions ($n = -2$)

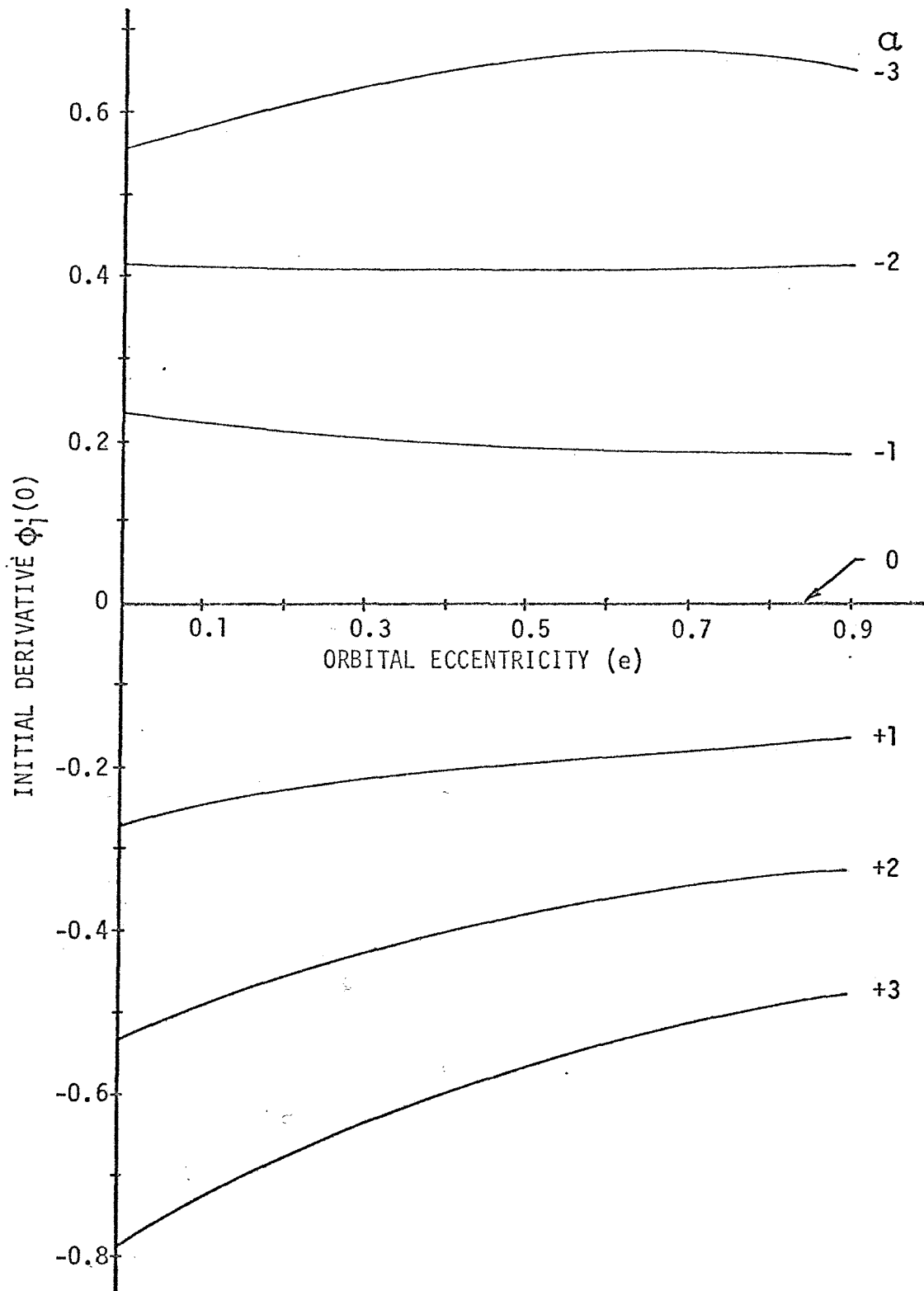
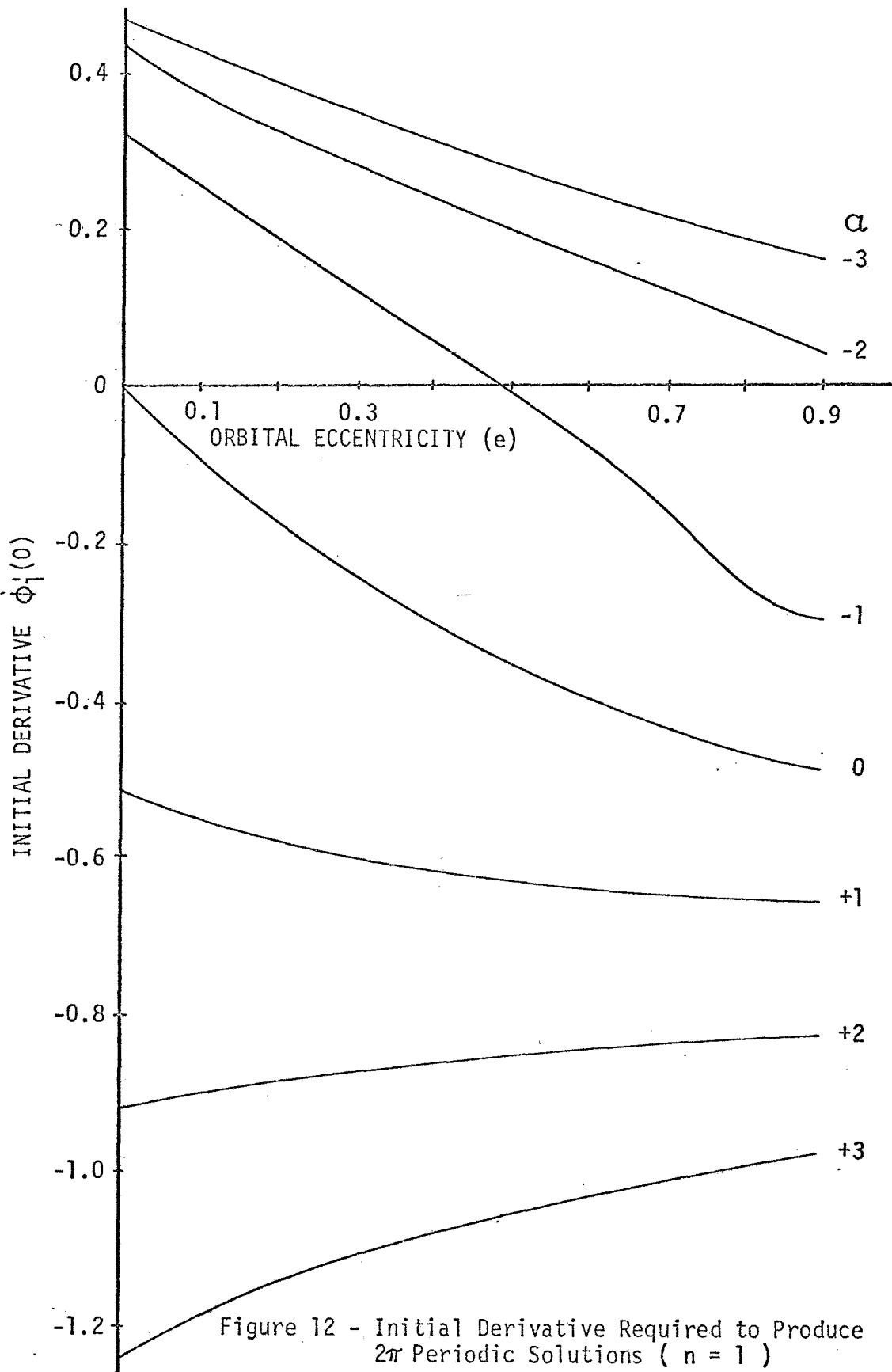
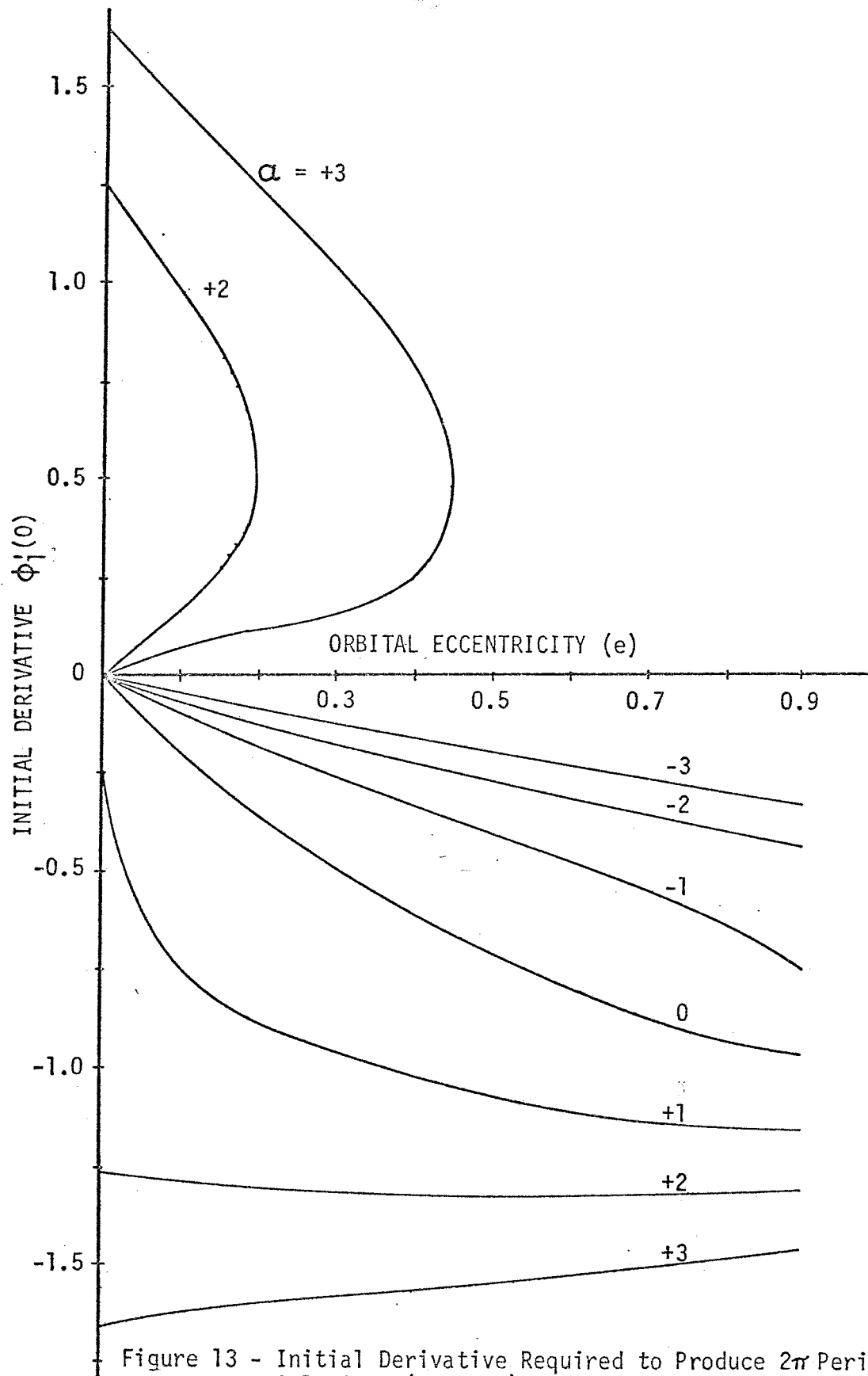


Figure 11 - Initial Derivative Required to Produce 2π Periodic Solutions ($n = 0$)





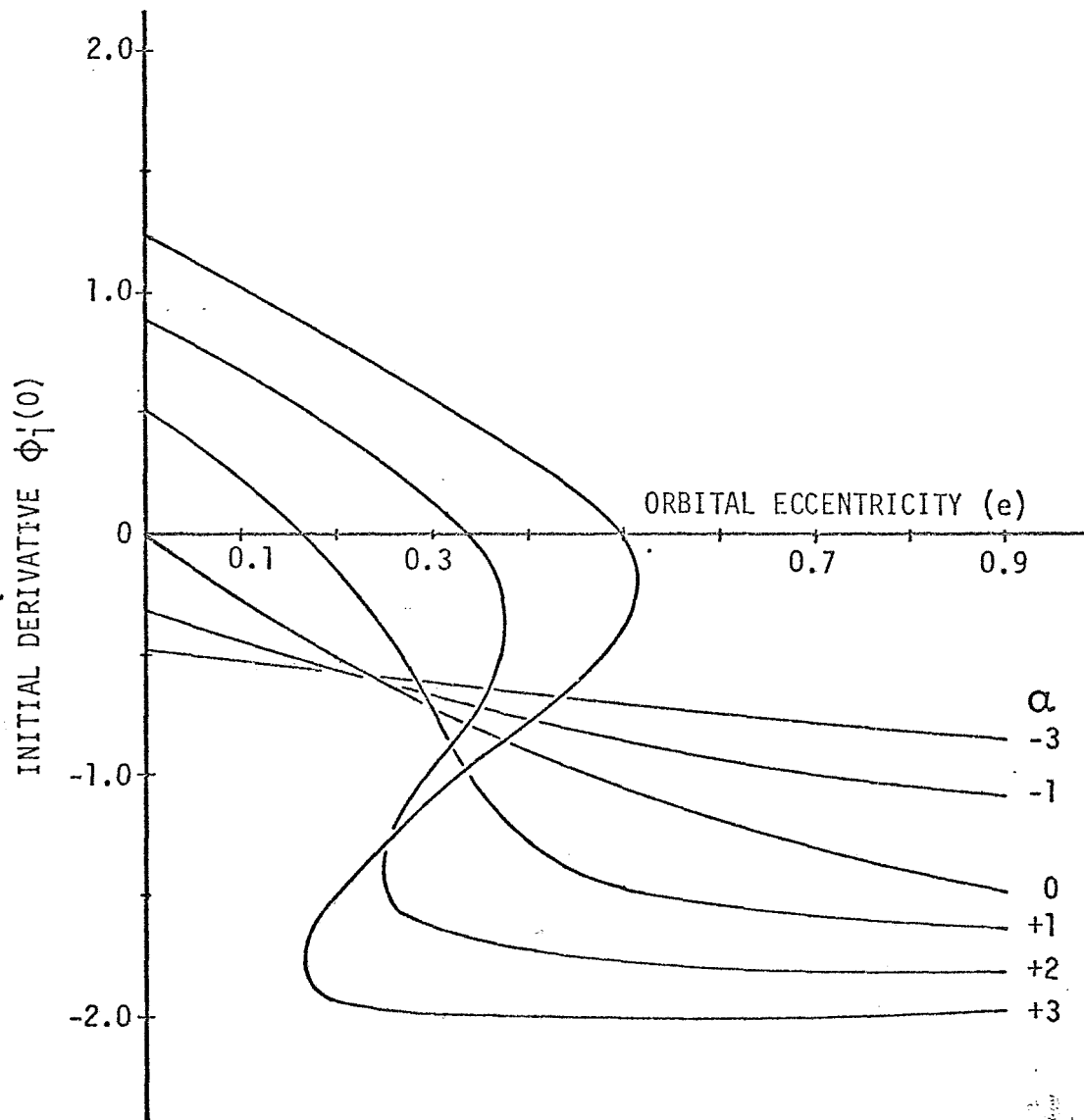


Figure 14 - Initial Derivative Required to Produce 2π Periodic Solutions ($n = 3$)

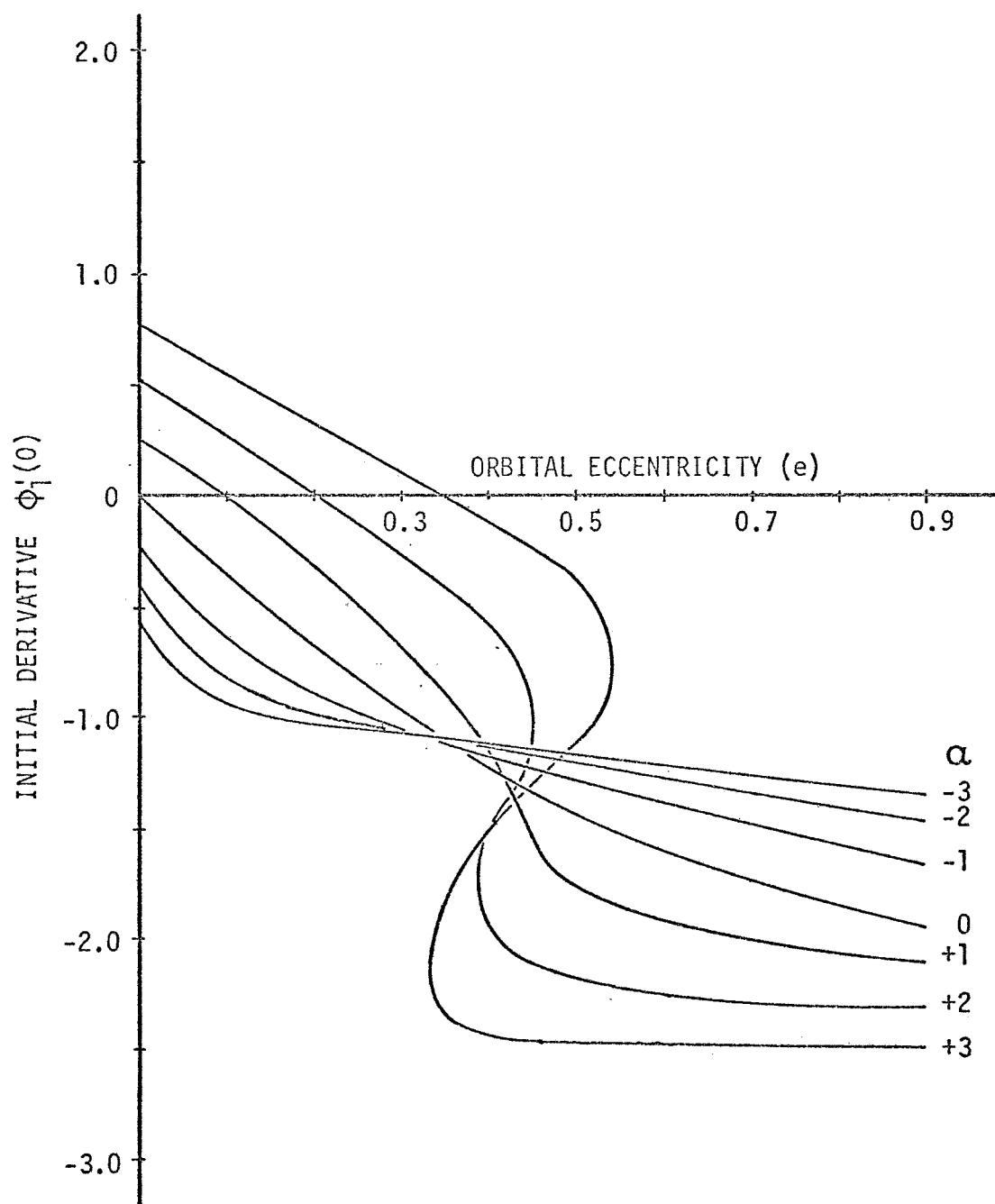


Figure 15 - Initial Derivative Required to Produce 2π Periodic Solutions ($n = 4$)

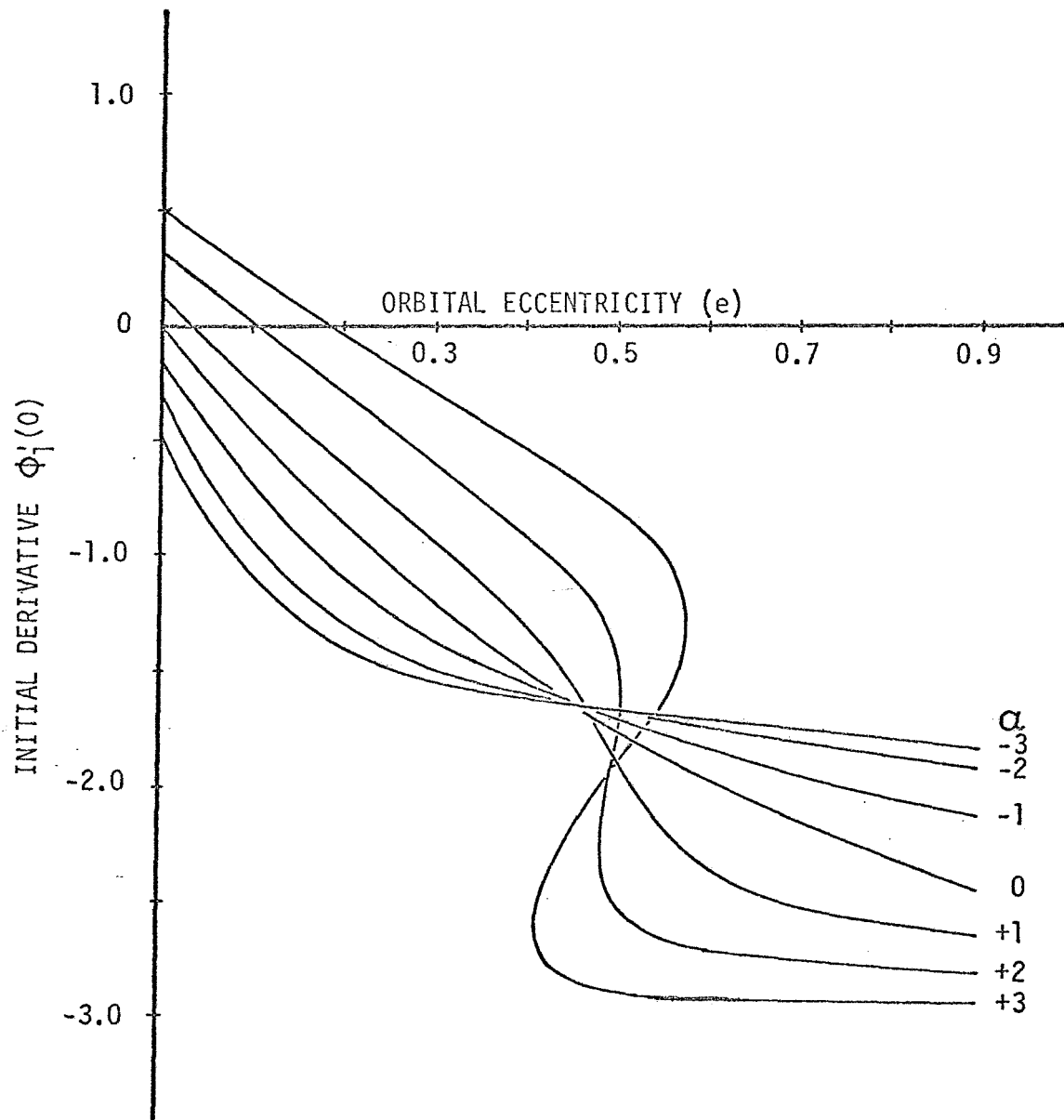


Figure 16 - Initial Derivative Required to Produce 2π Periodic Solutions ($n = 5$)

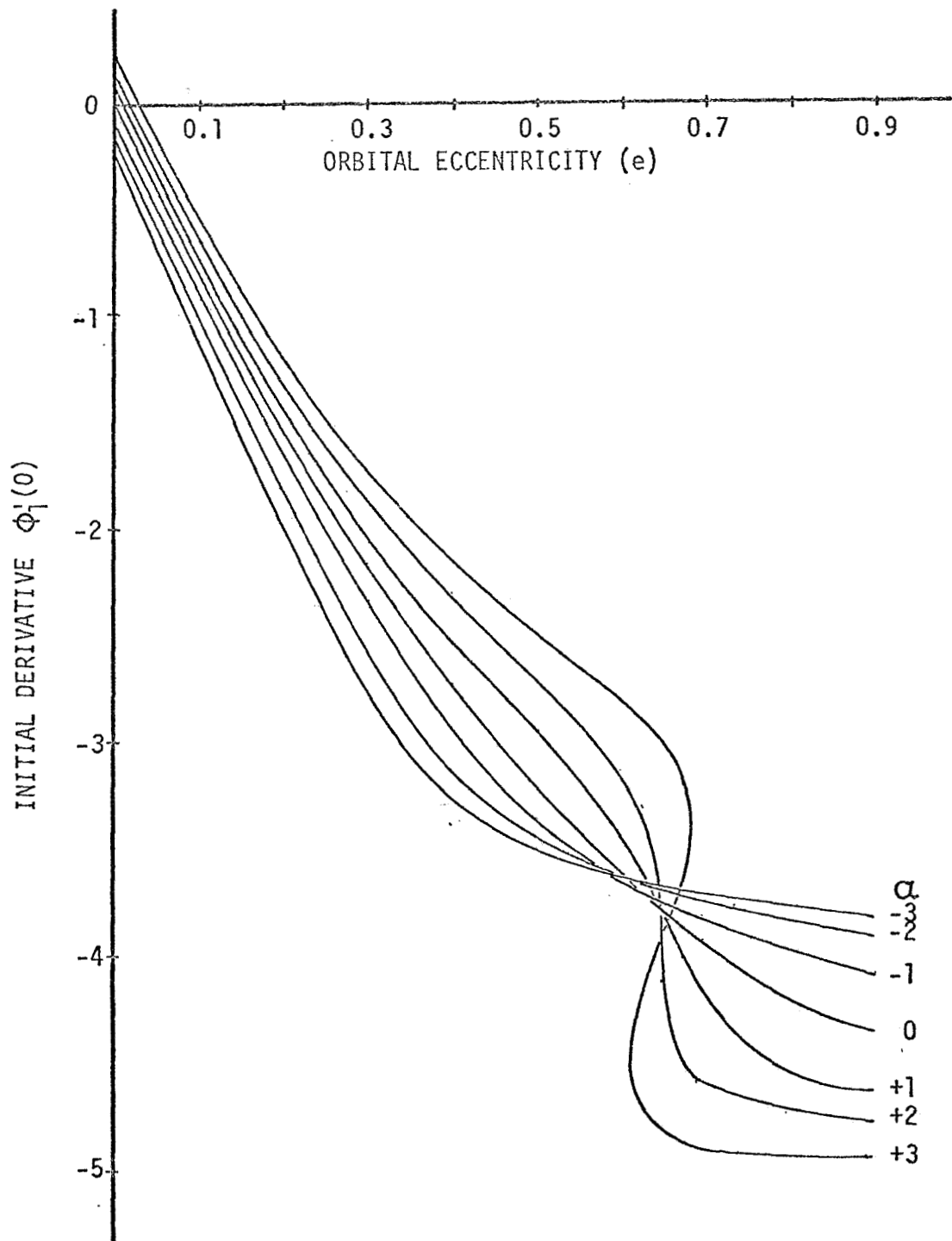


Figure 17 - Initial Derivative Required to Produce 2π Periodic Solutions ($n = 9$)

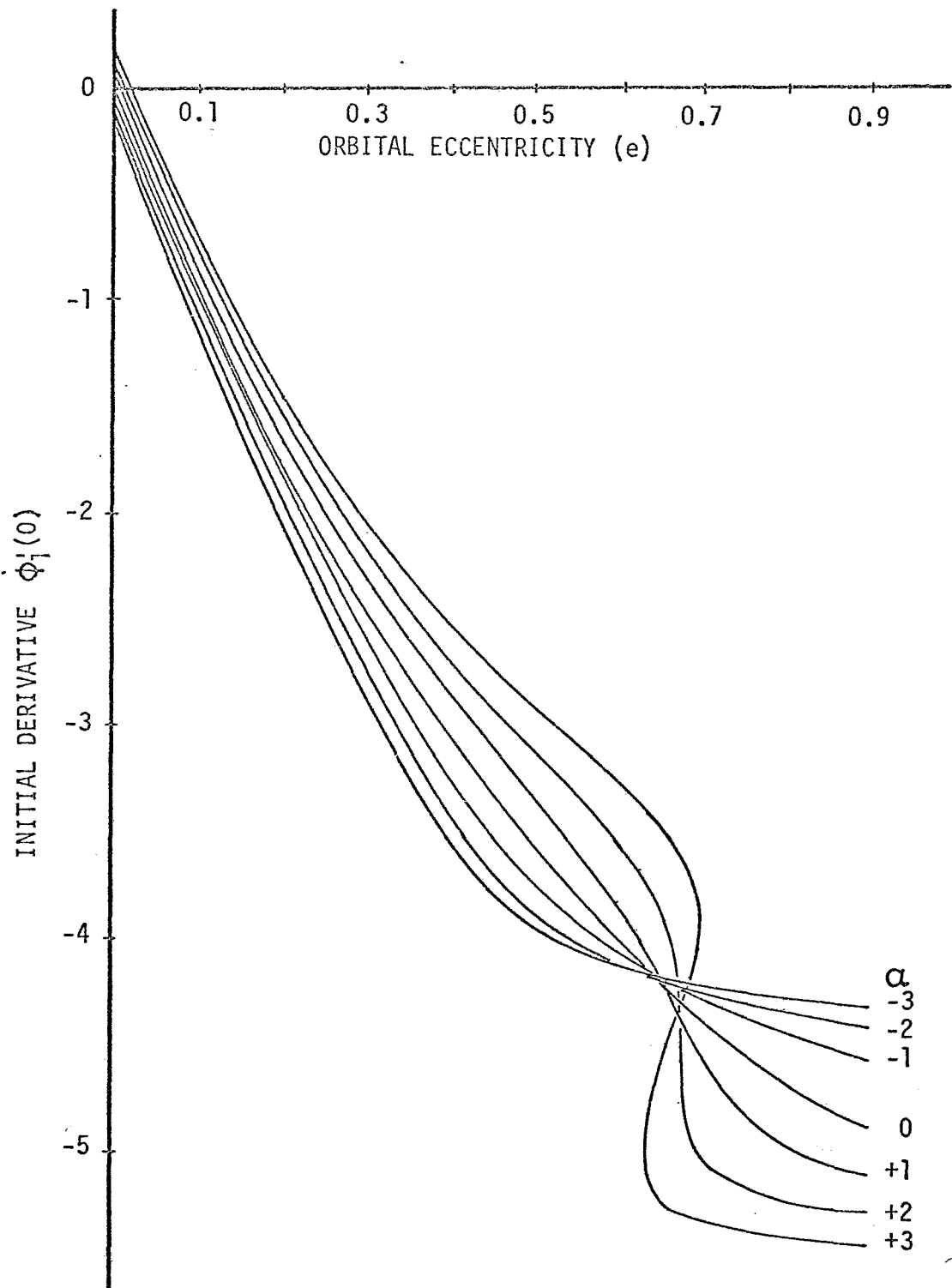


Figure 18 - Initial Derivative Required to Produce 2π Periodic Solutions ($n = 10$)

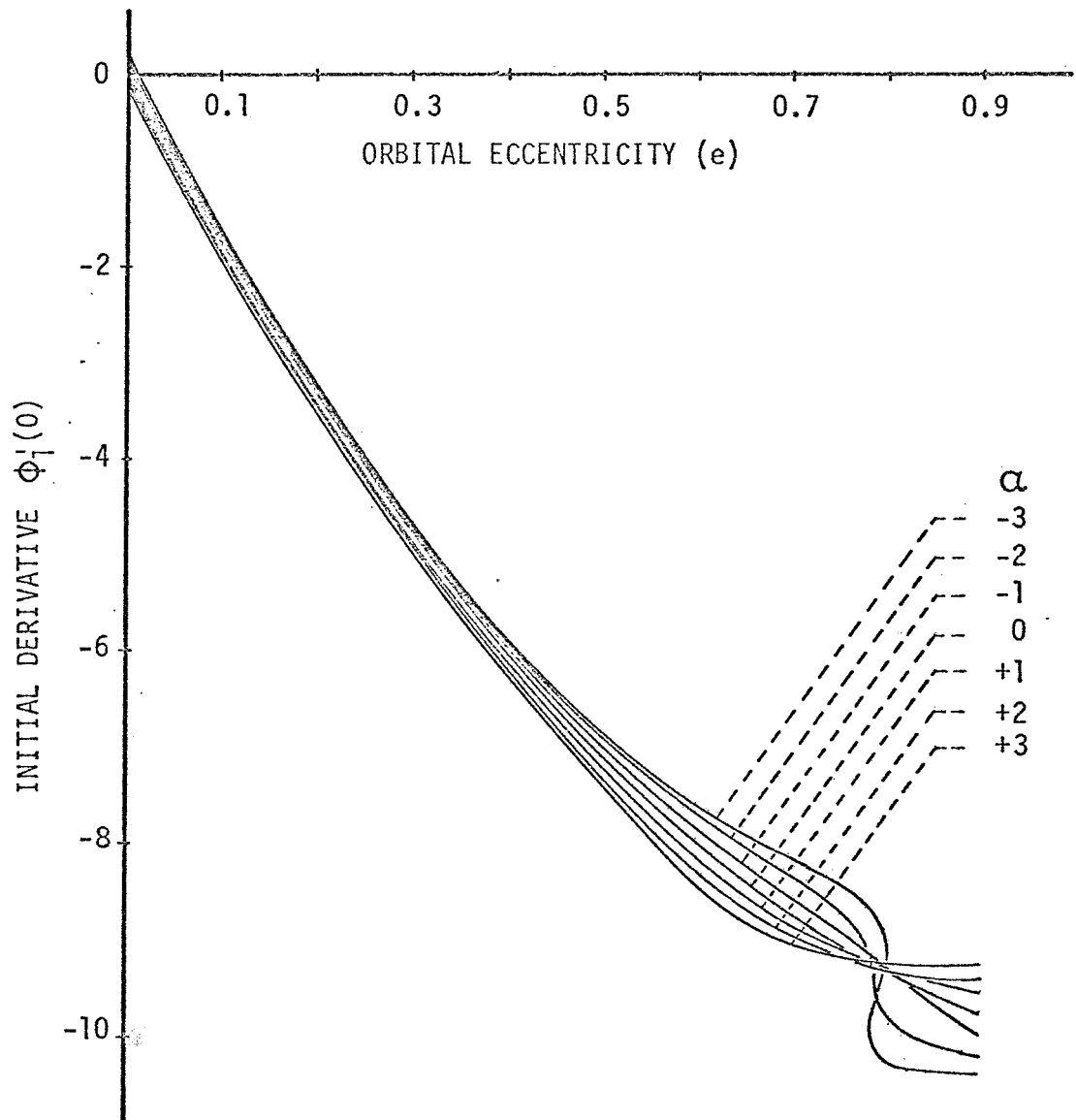


Figure 19 - Initial Derivative Required to Produce 2π Periodic Solutions ($n = 20$)

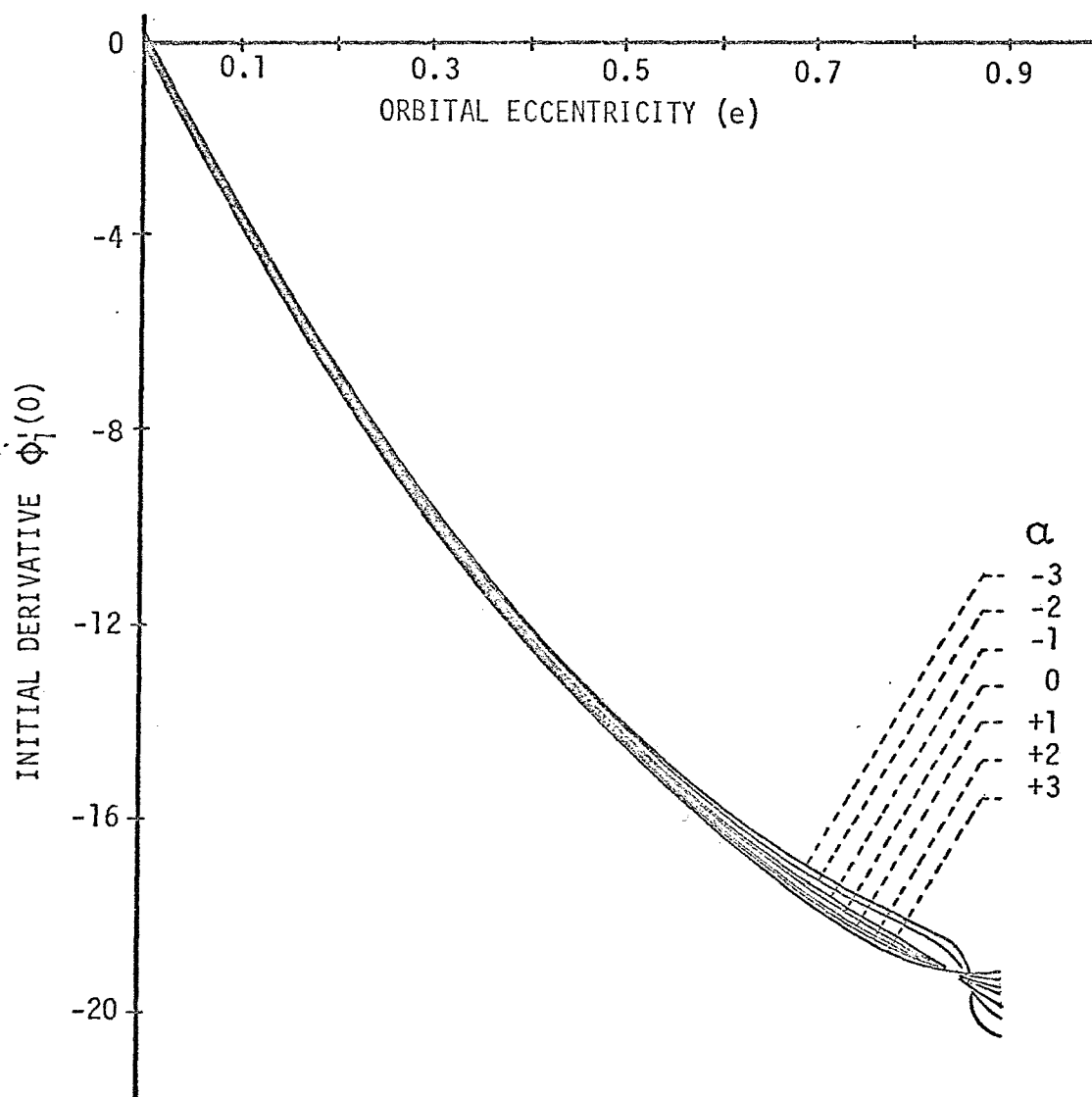


Figure 20 - Initial Derivative Required to Produce 2π Periodic Solutions ($n = 40$)

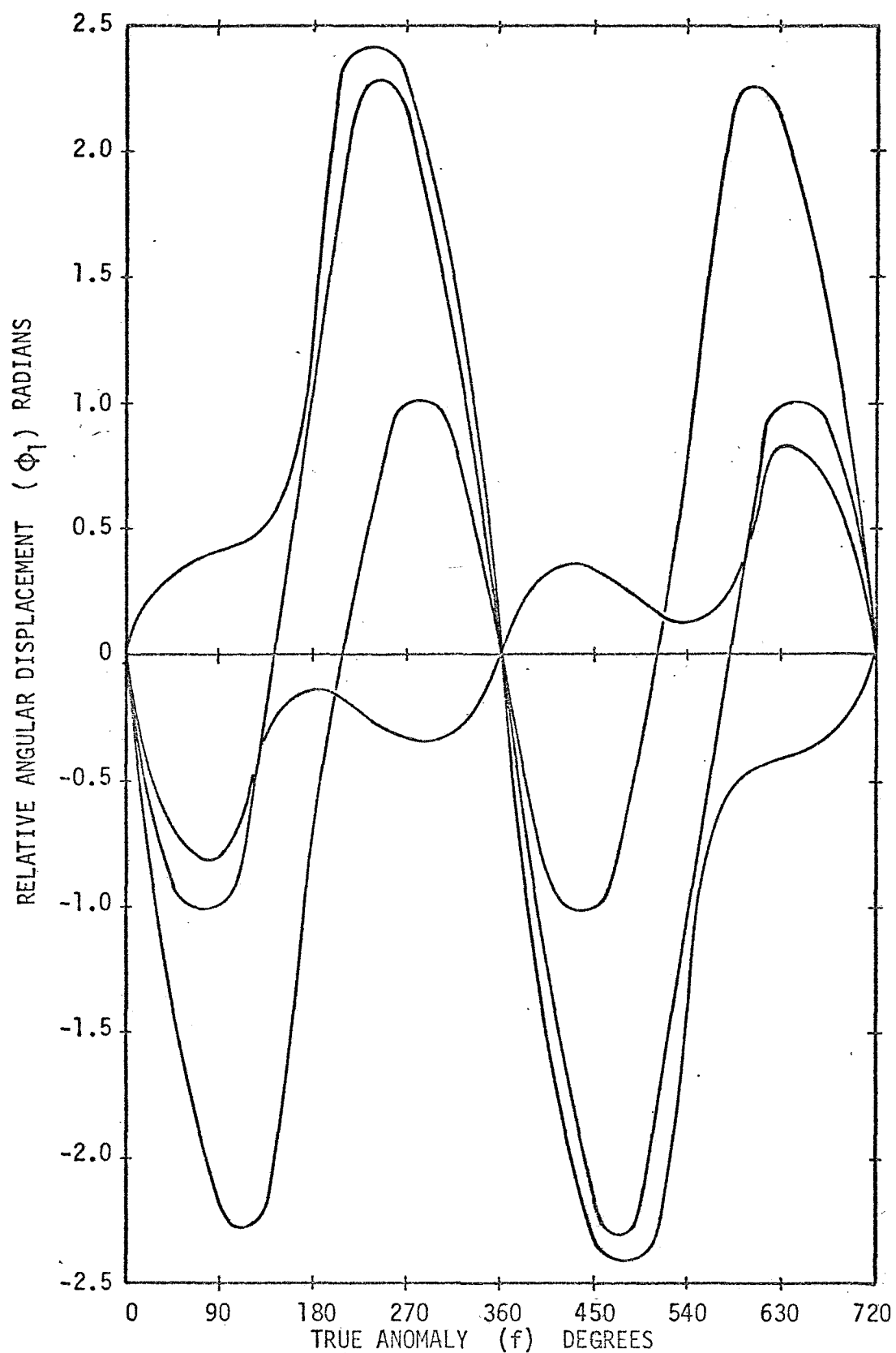


Figure 21 - Odd 4π Periodic Solutions ($n = 3, \alpha = 3.0, e = 0.3$)

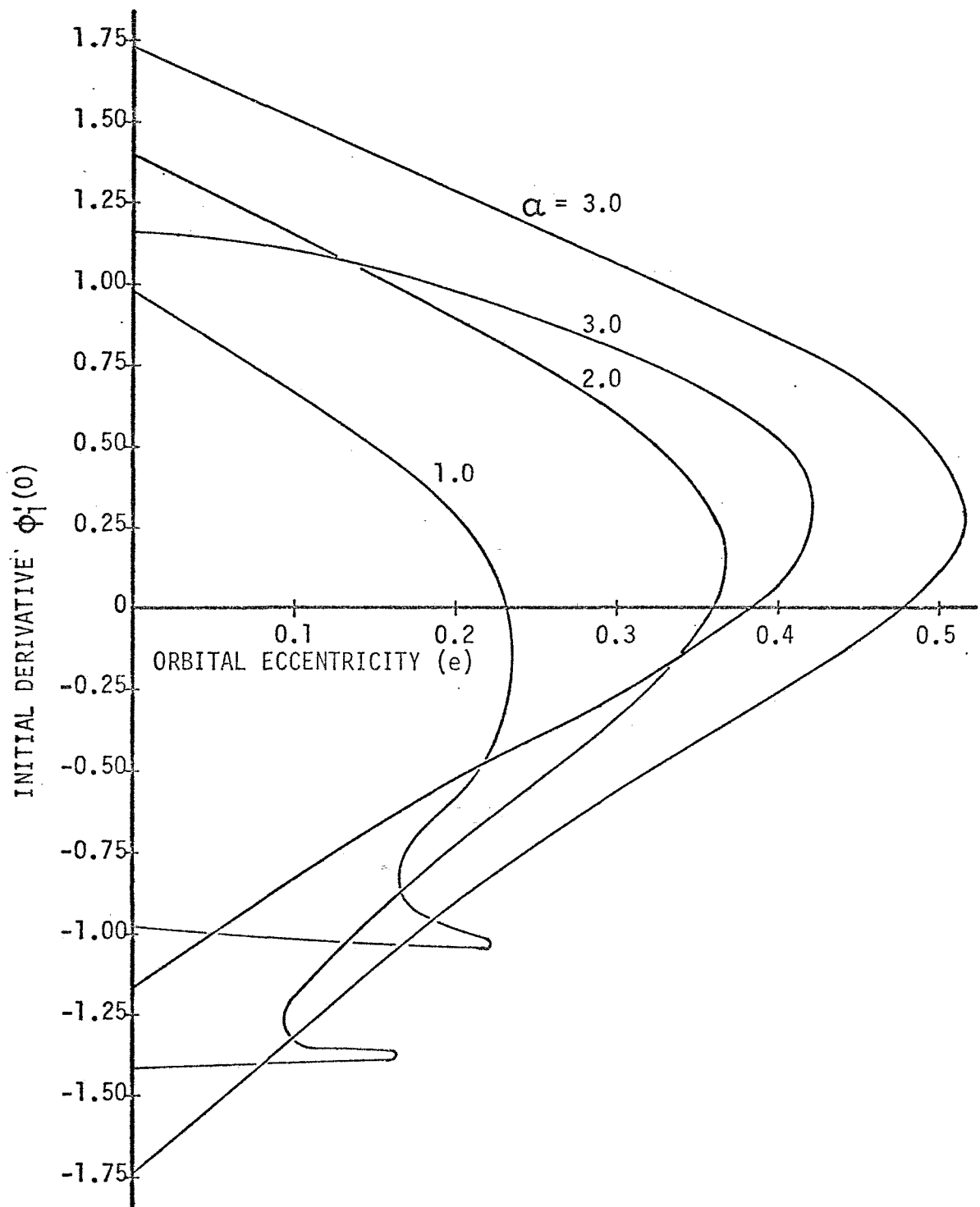


Figure 22 - Initial Derivative Required to Produce 4π Periodic Solutions ($n = 2$)

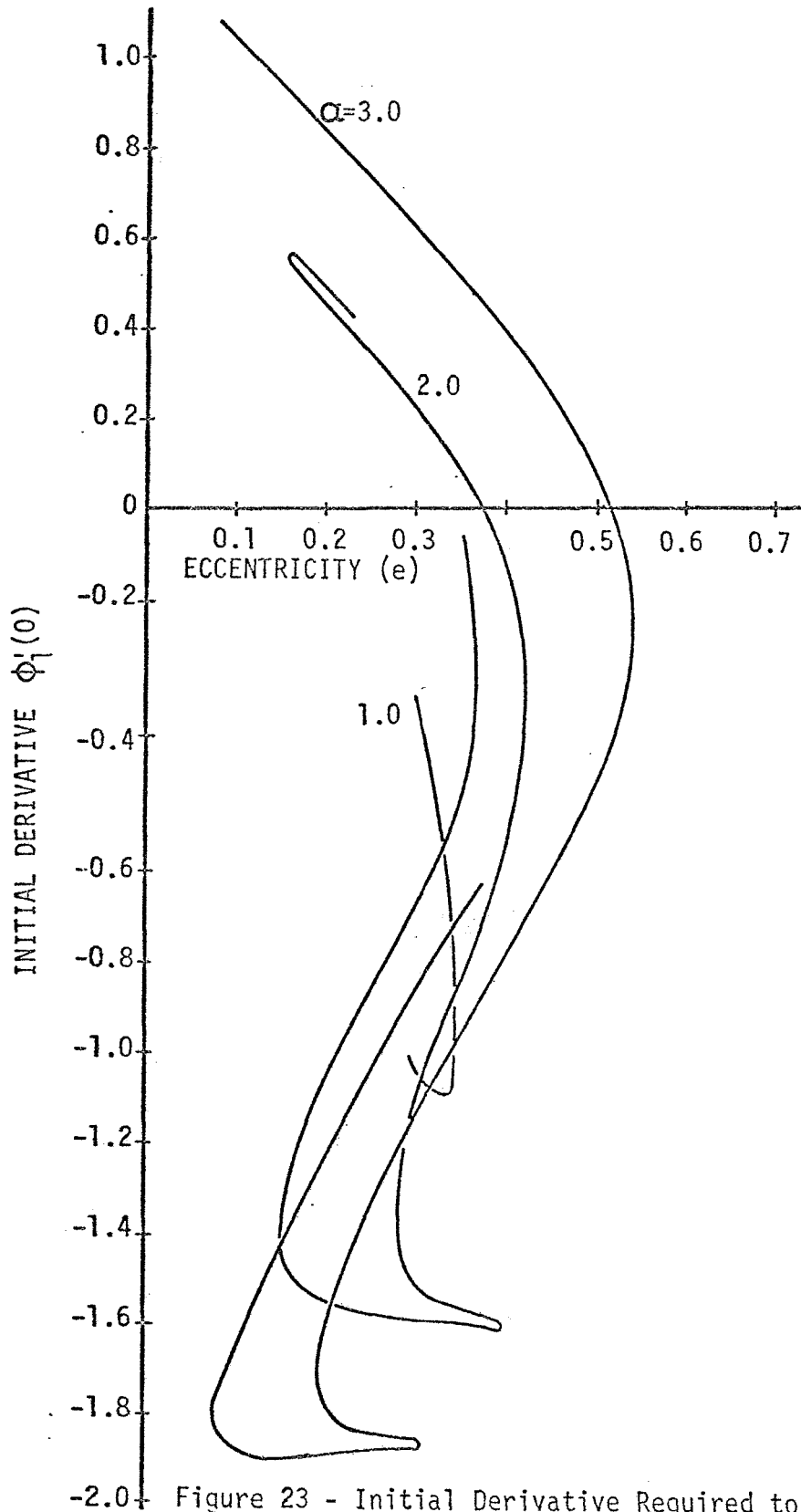


Figure 23 - Initial Derivative Required to Produce 4π Periodic Solutions ($n = 3$)

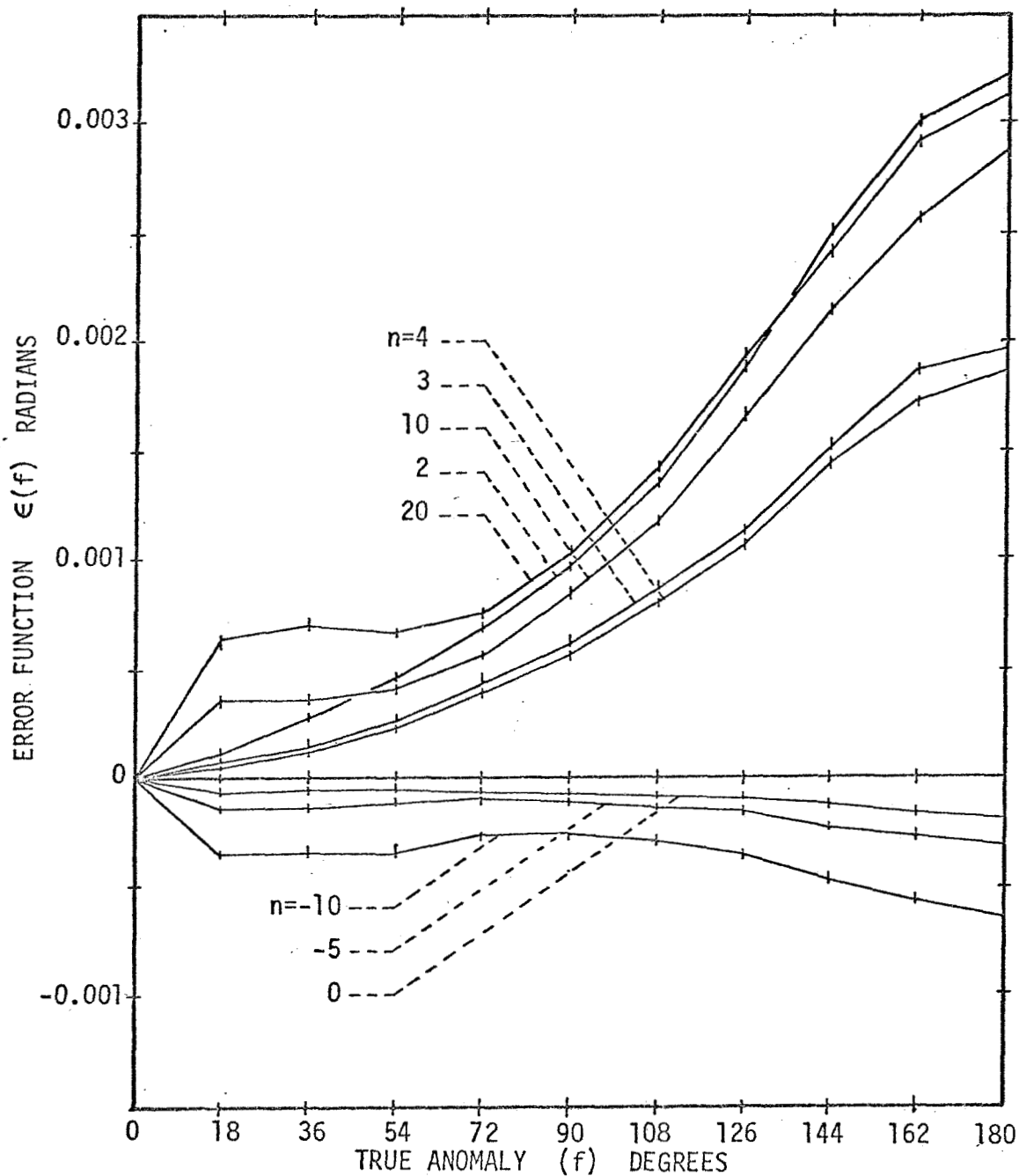
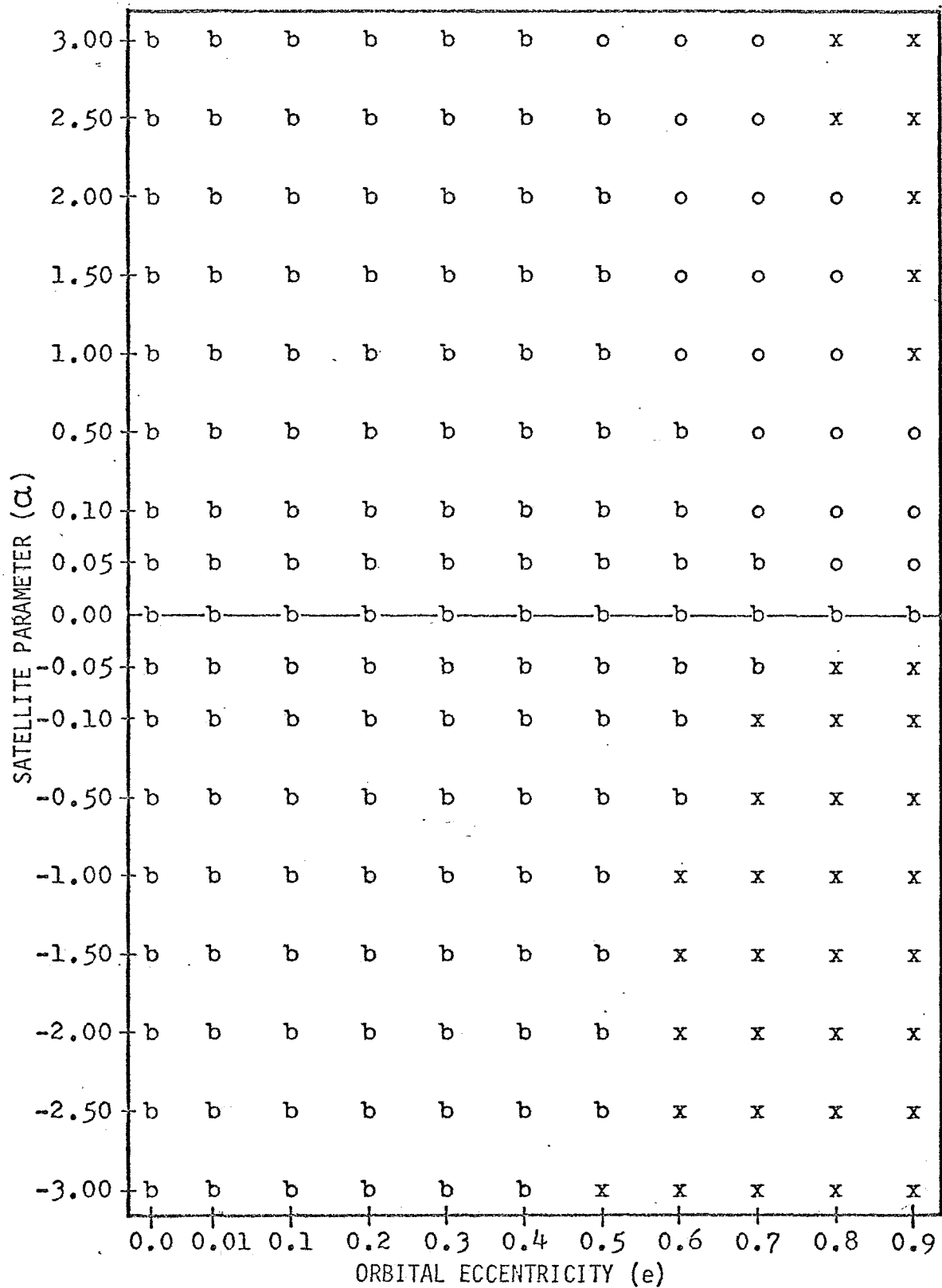
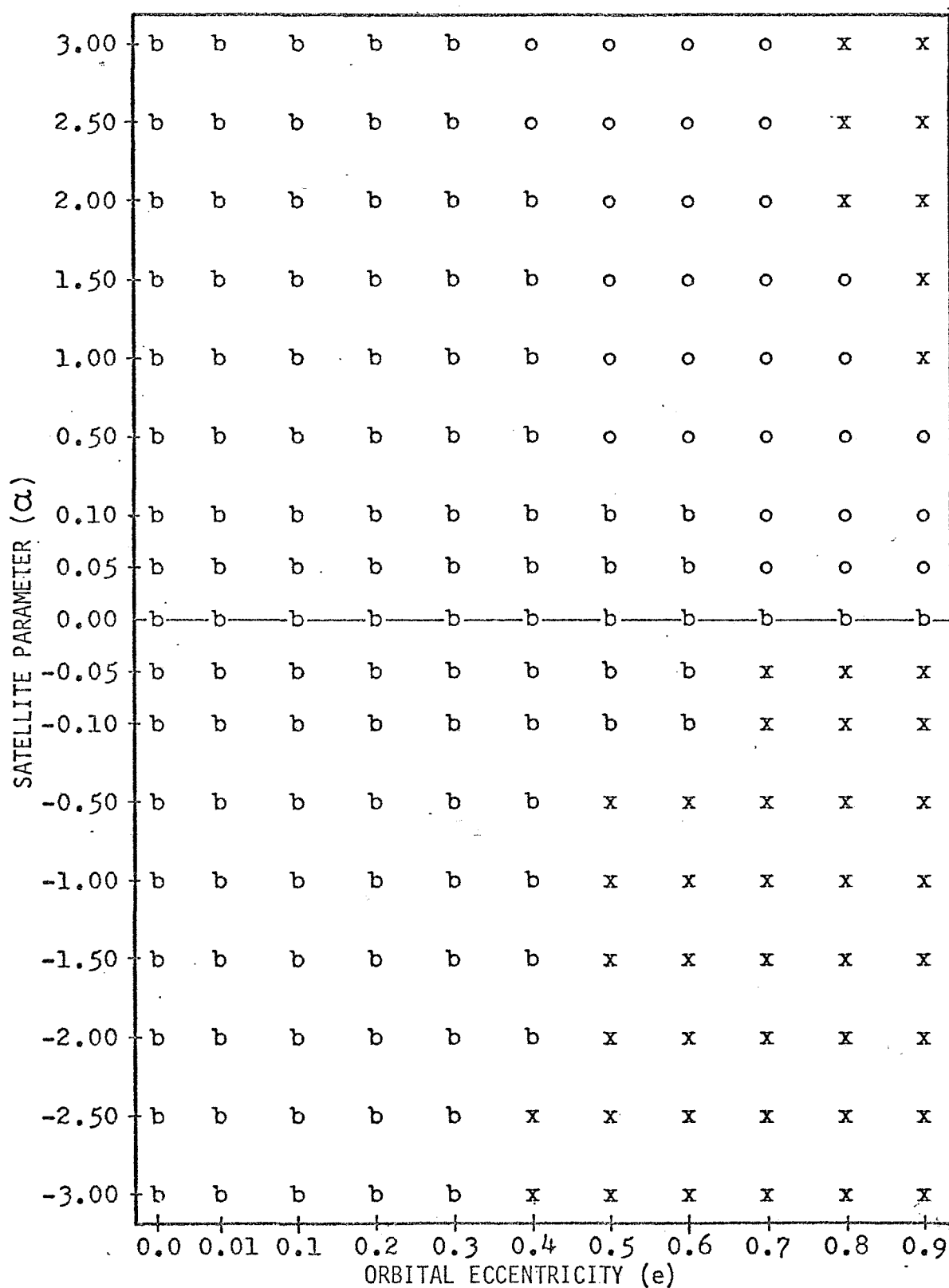


Figure 24 - Typical Variations of the Error Found in the Numerical Determination of Periodic Solutions ($e = 0.9$, $\alpha = 3.0$)

Figure 25 - Variational Stability Chart ($n = -10, m = 1$)

Figure 26 - Variational Stability Chart ($n = -5, m = 1$)

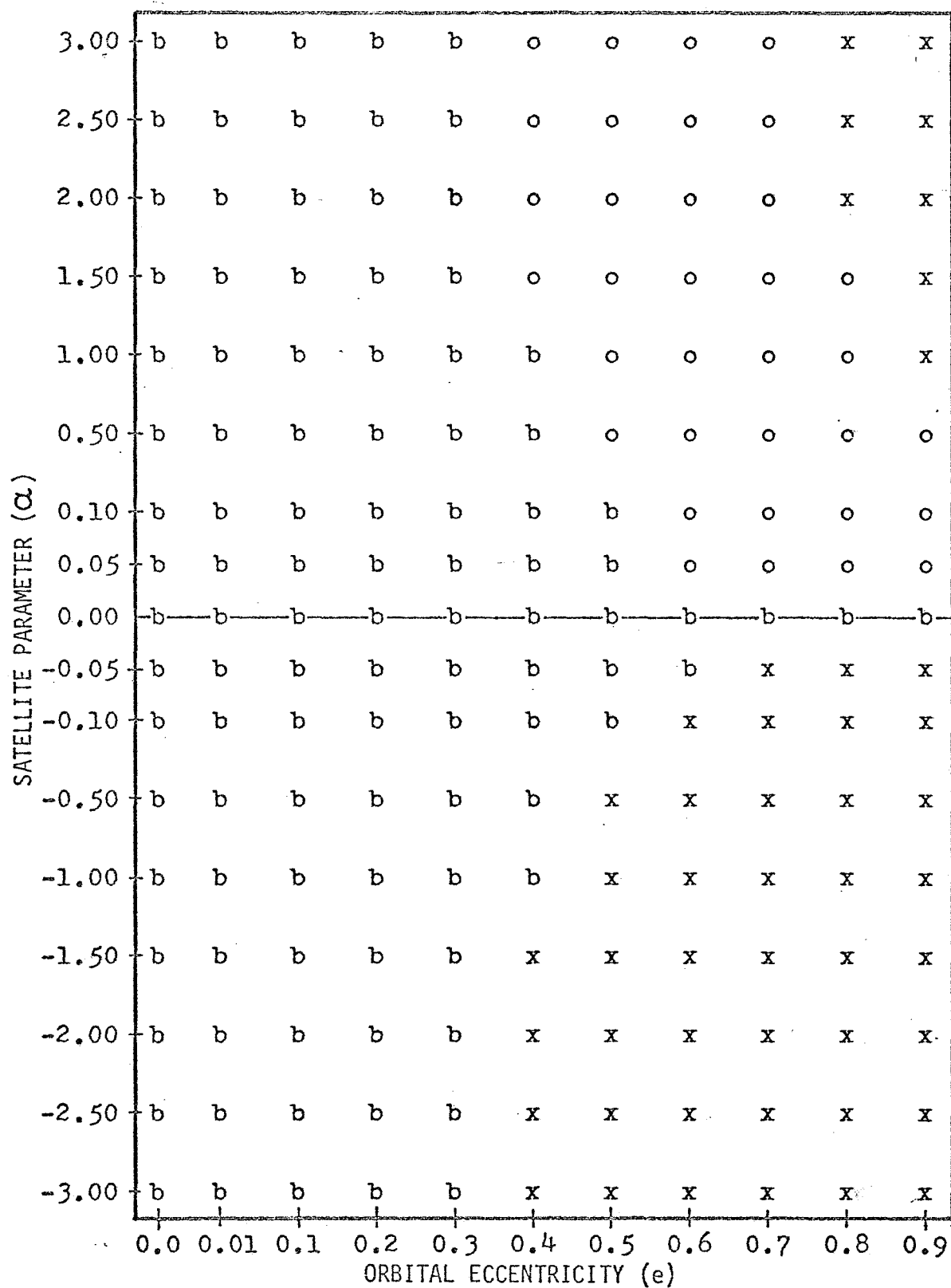
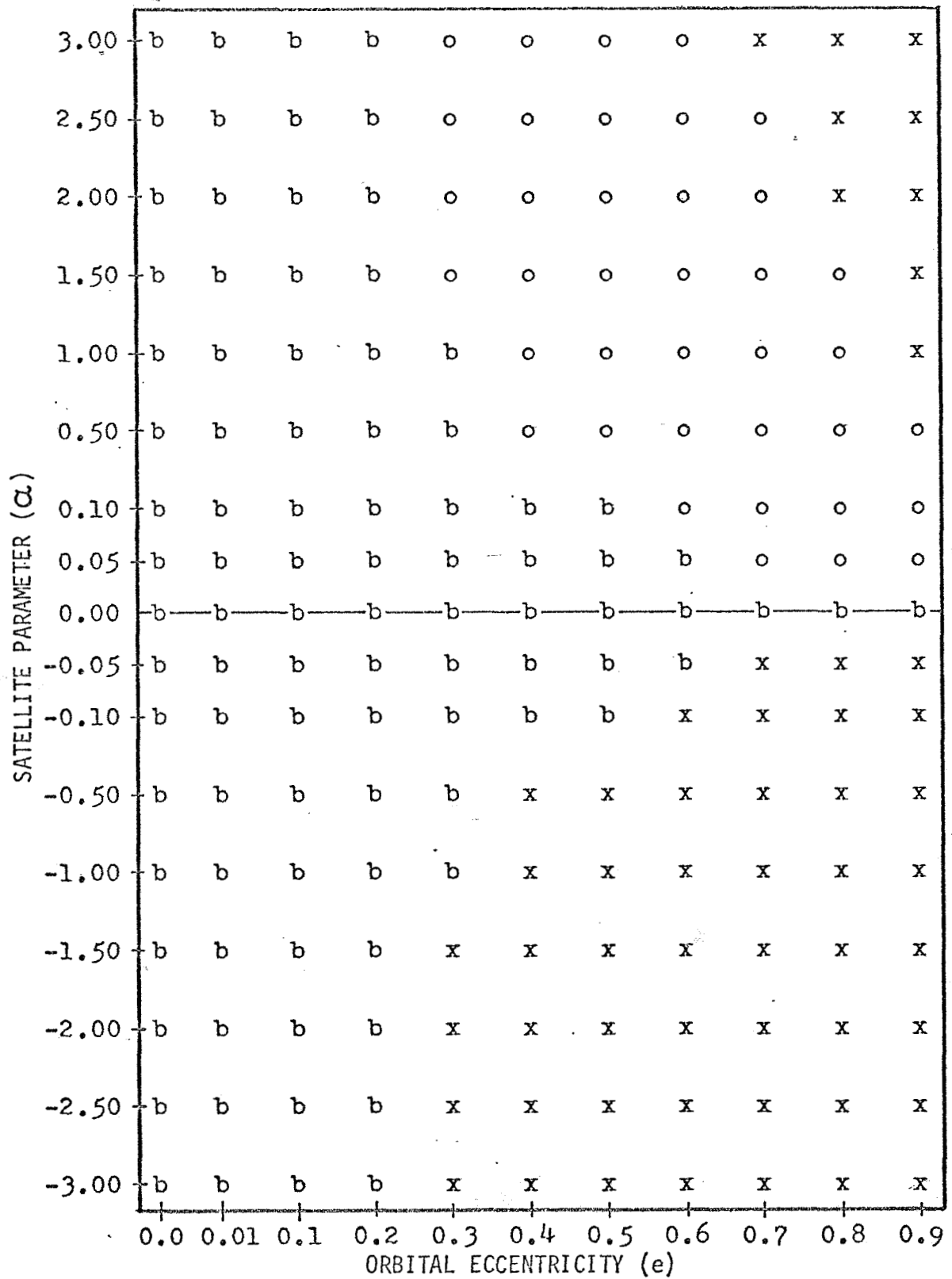
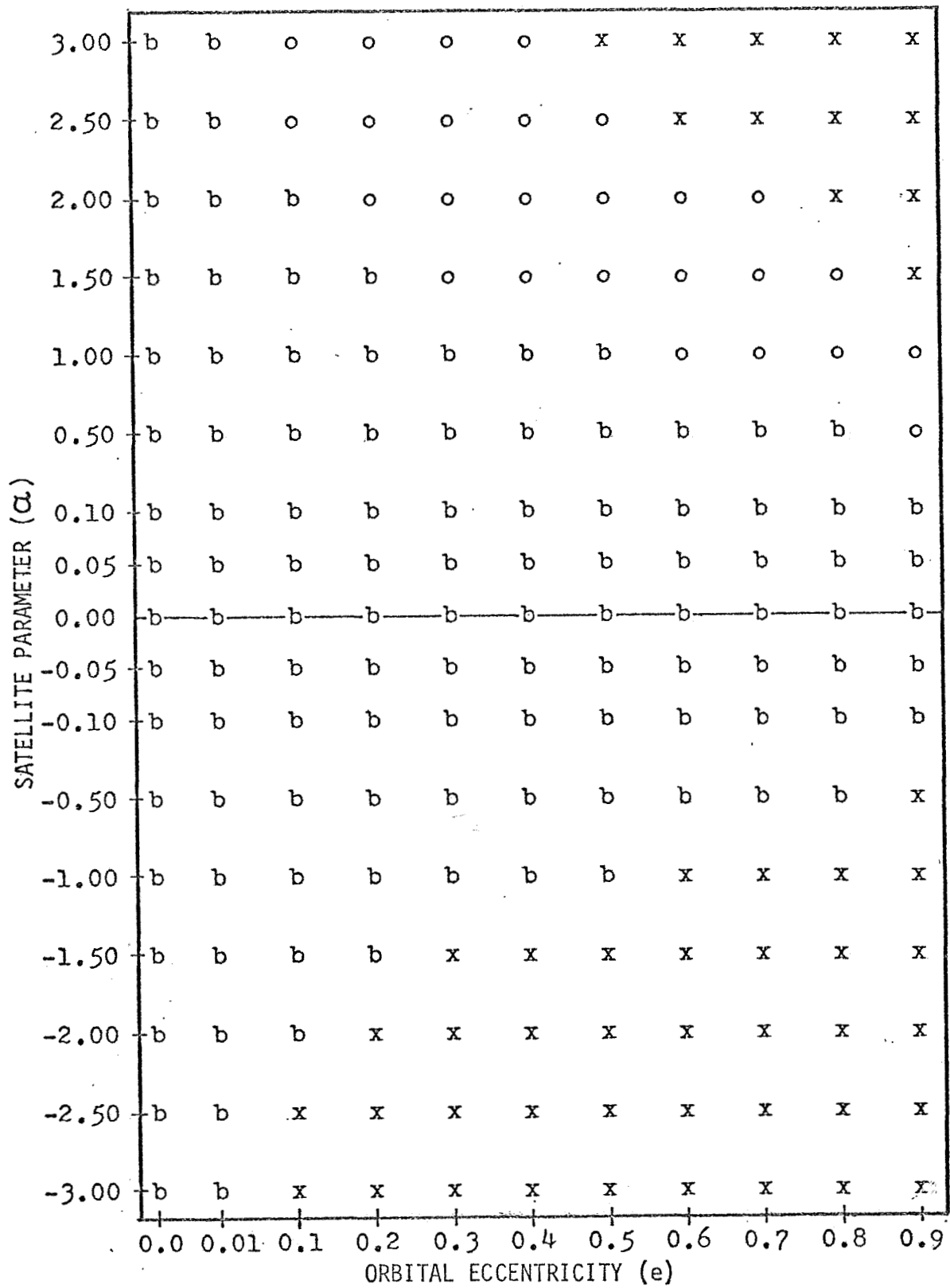
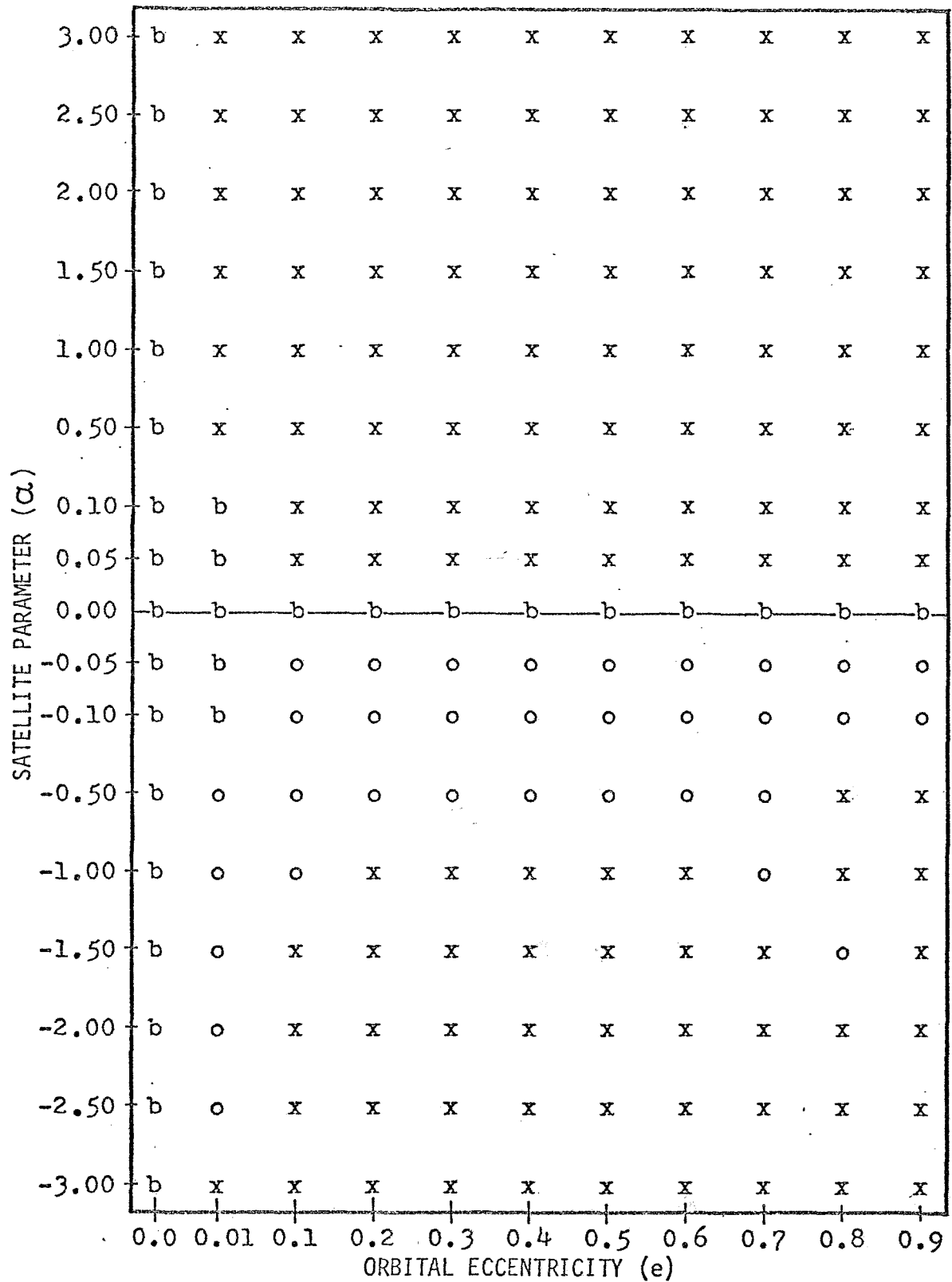
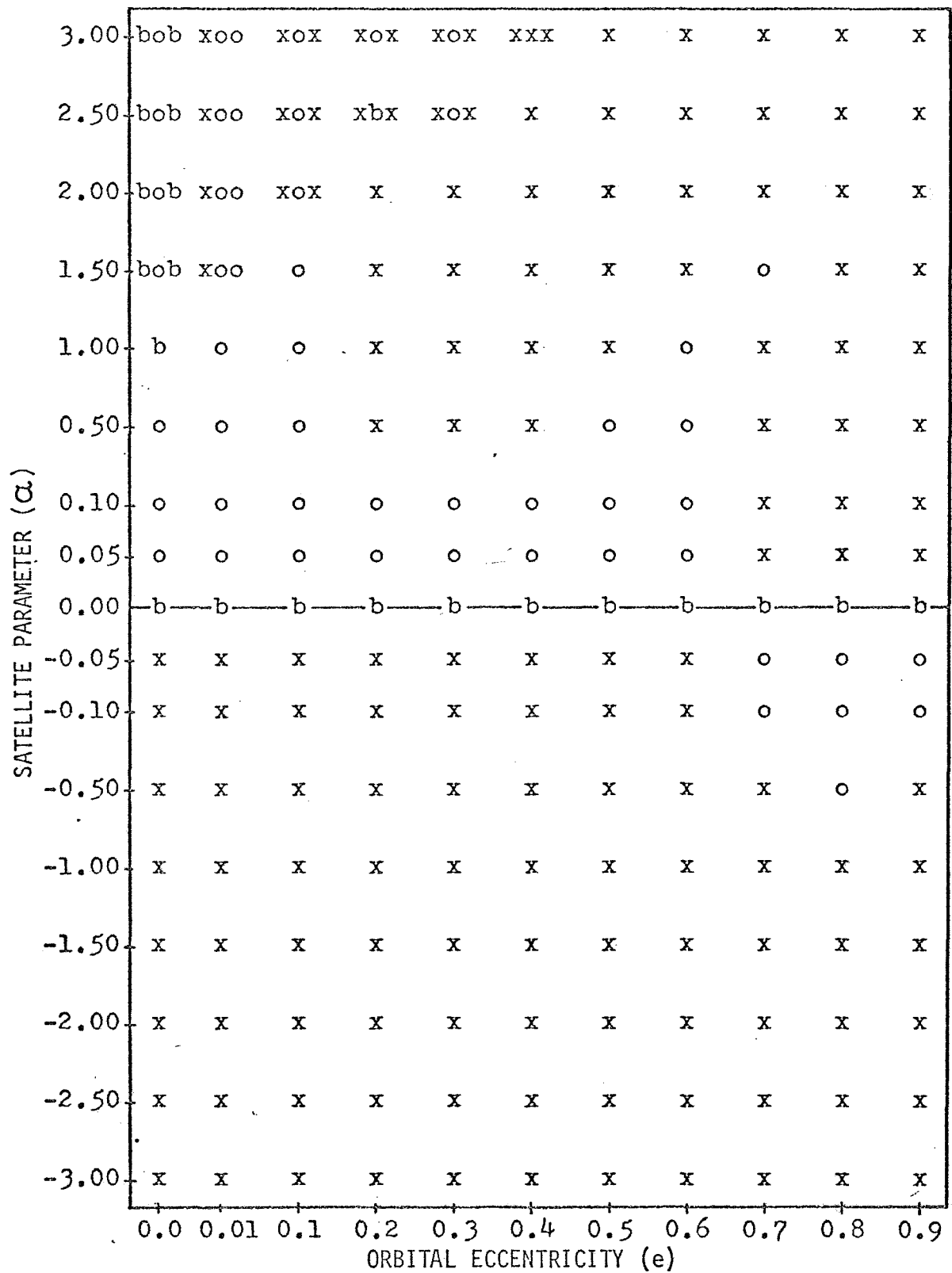


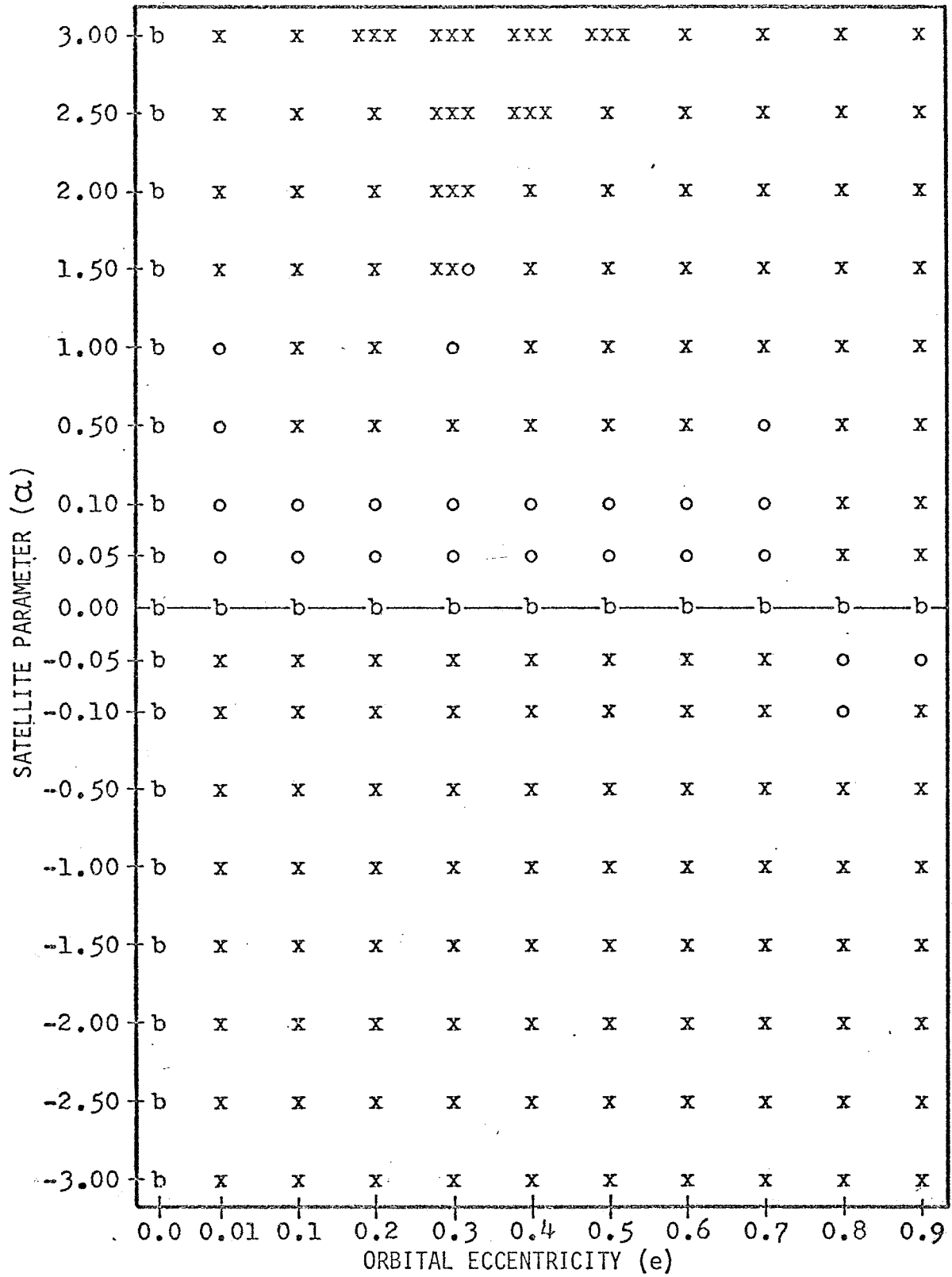
Figure 27 - Variational Stability Chart ($n = -4$, $m = 1$)

Figure 28 - Variational Stability Chart ($n = -2$, $m = 1$)

Figure 29 - Variational Stability Chart ($n = 0, m = 1$)

Figure 30 - Variational Stability Chart ($n = 1, m = 1$)

Figure 31 - Variational Stability Chart ($n = 2, m = 1$)

Figure 32 - Variational Stability Chart ($n = 3, m = 1$)

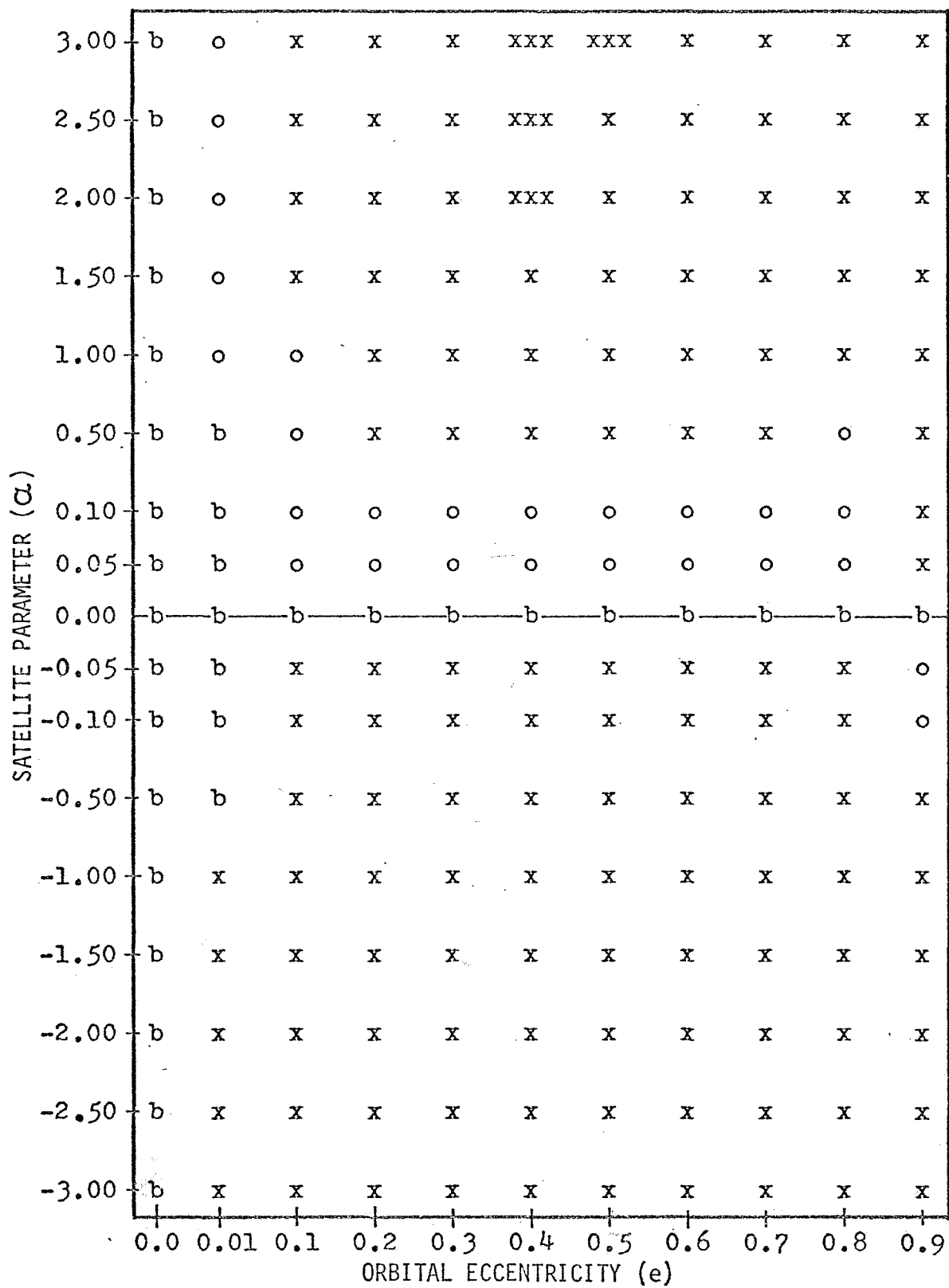
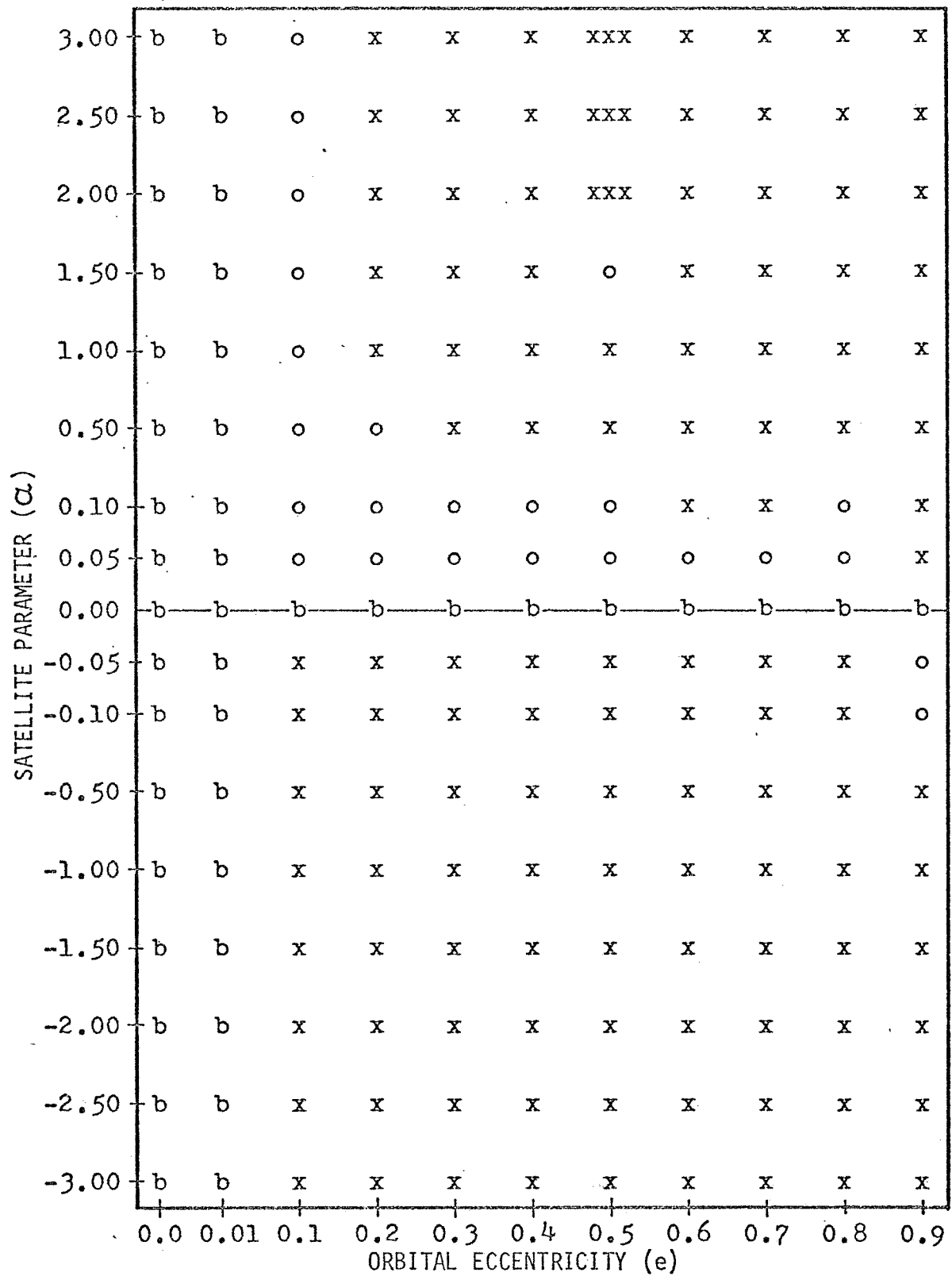
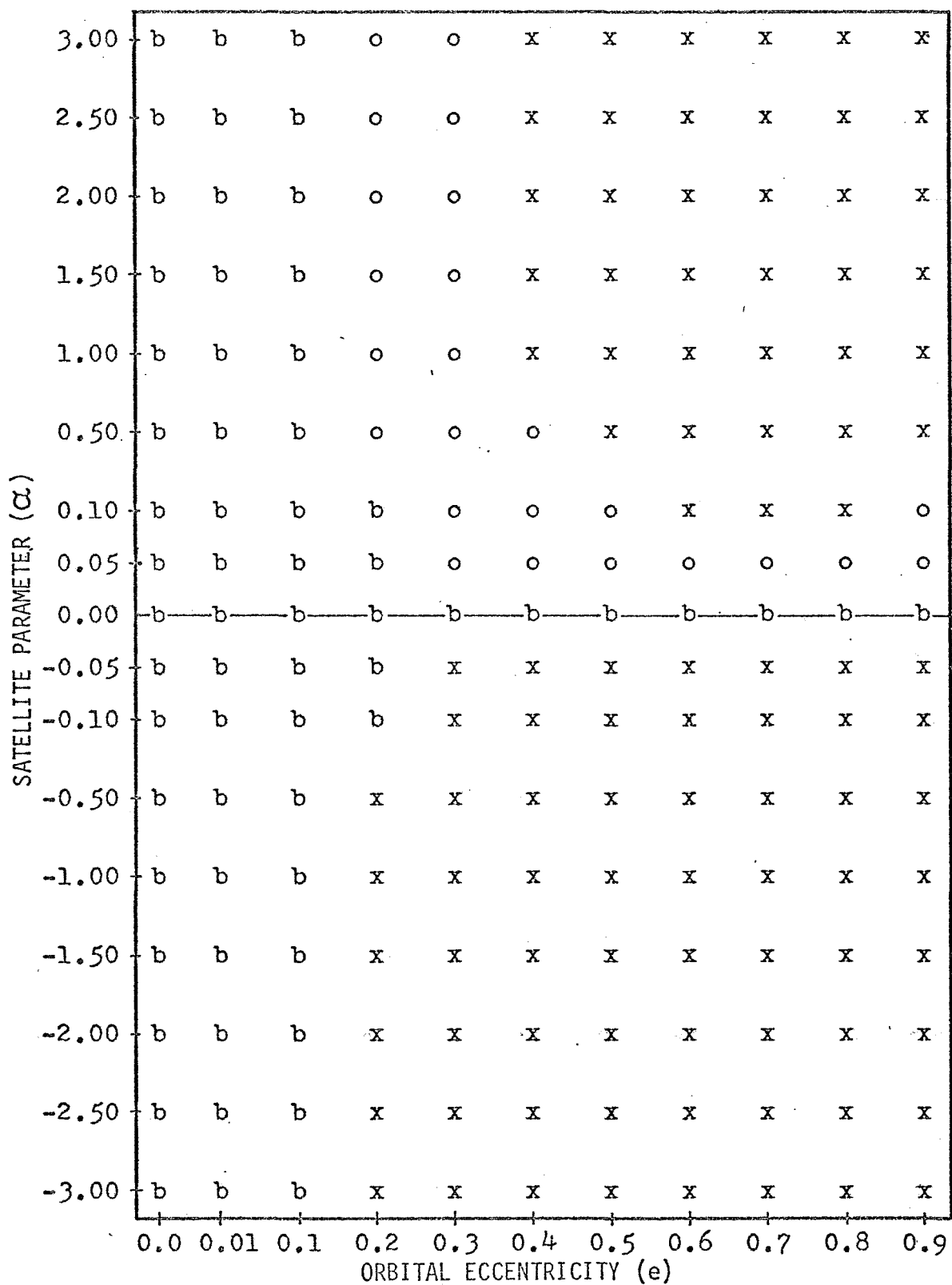
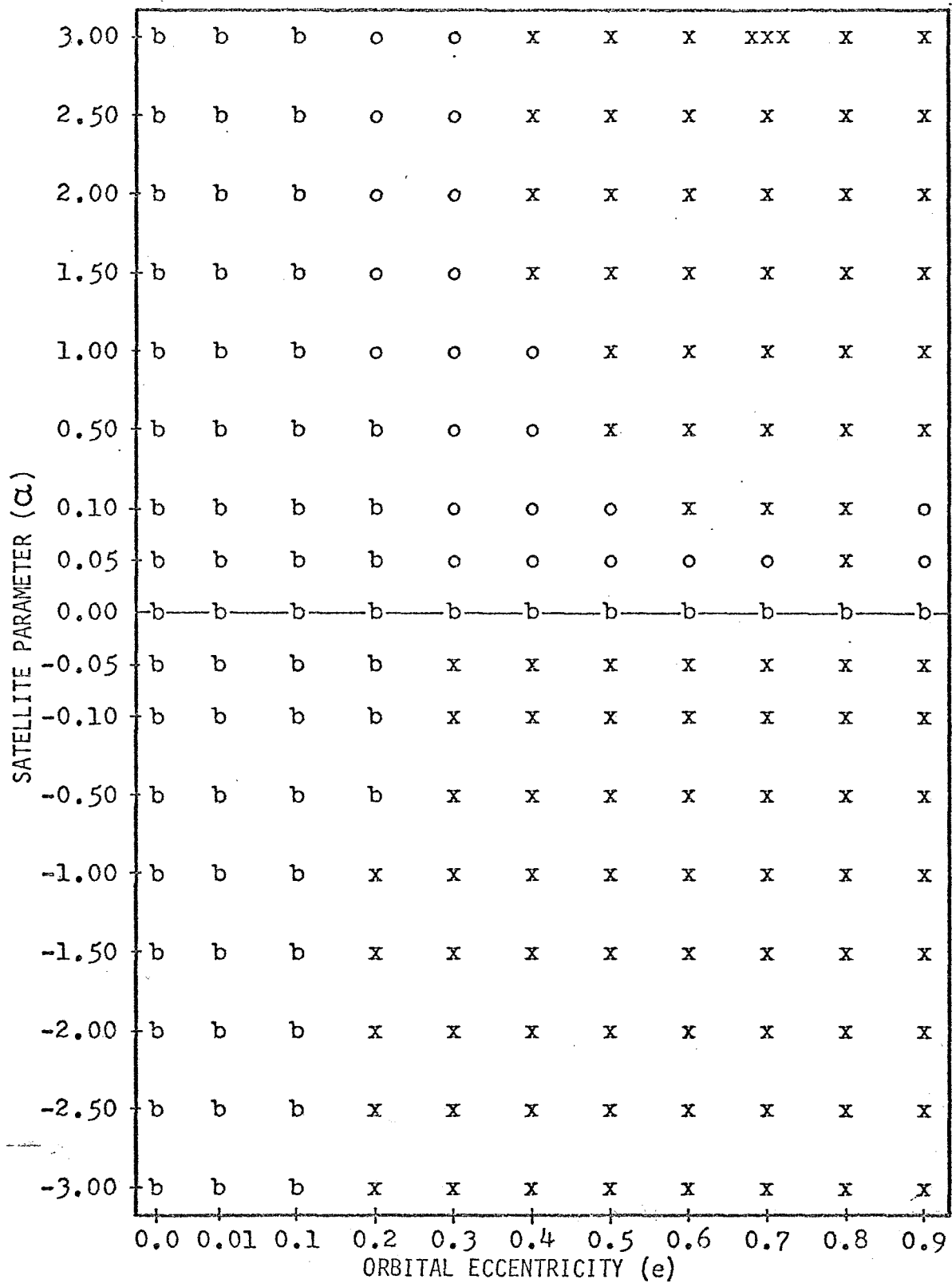


Figure 33 - Variational Stability Chart ($n = 4$, $m = 1$)

Figure 34 - Variational Stability Chart ($n = 5$, $m = 1$)

Figure 35 - Variational Stability Chart ($n = 9$, $m = 1$)

Figure 36 - Variational Stability Chart ($n = 10, m = 1$)

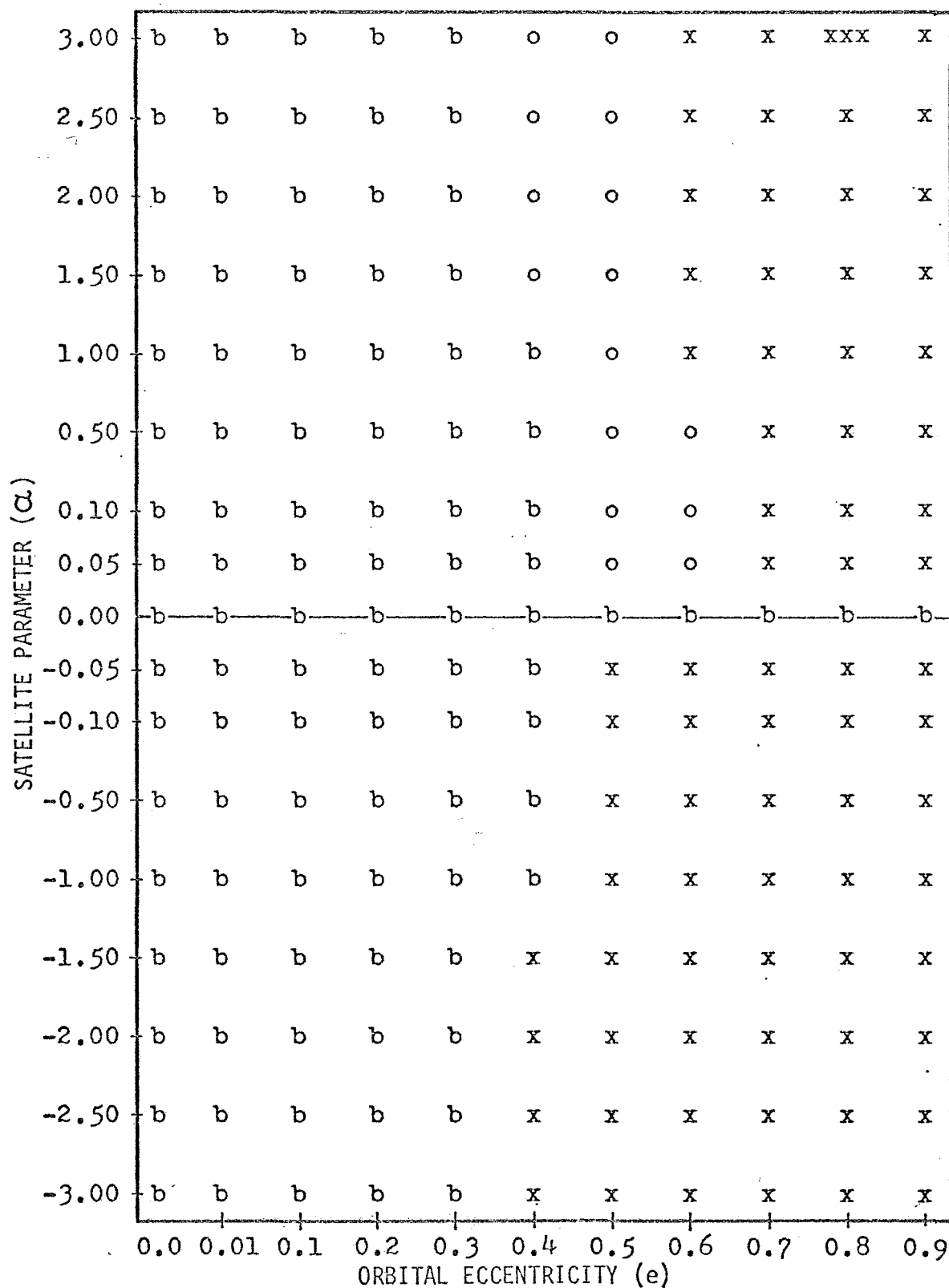
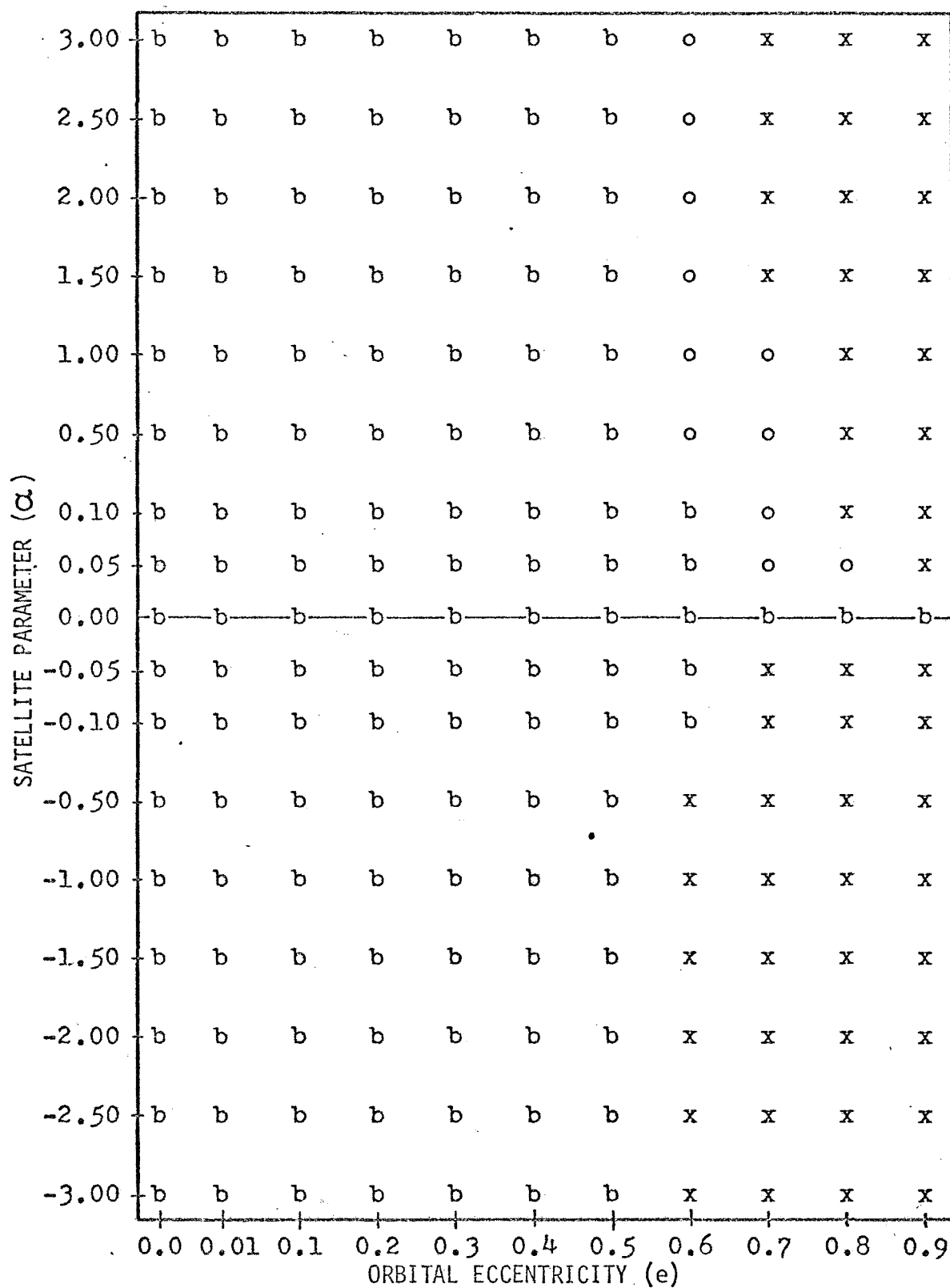
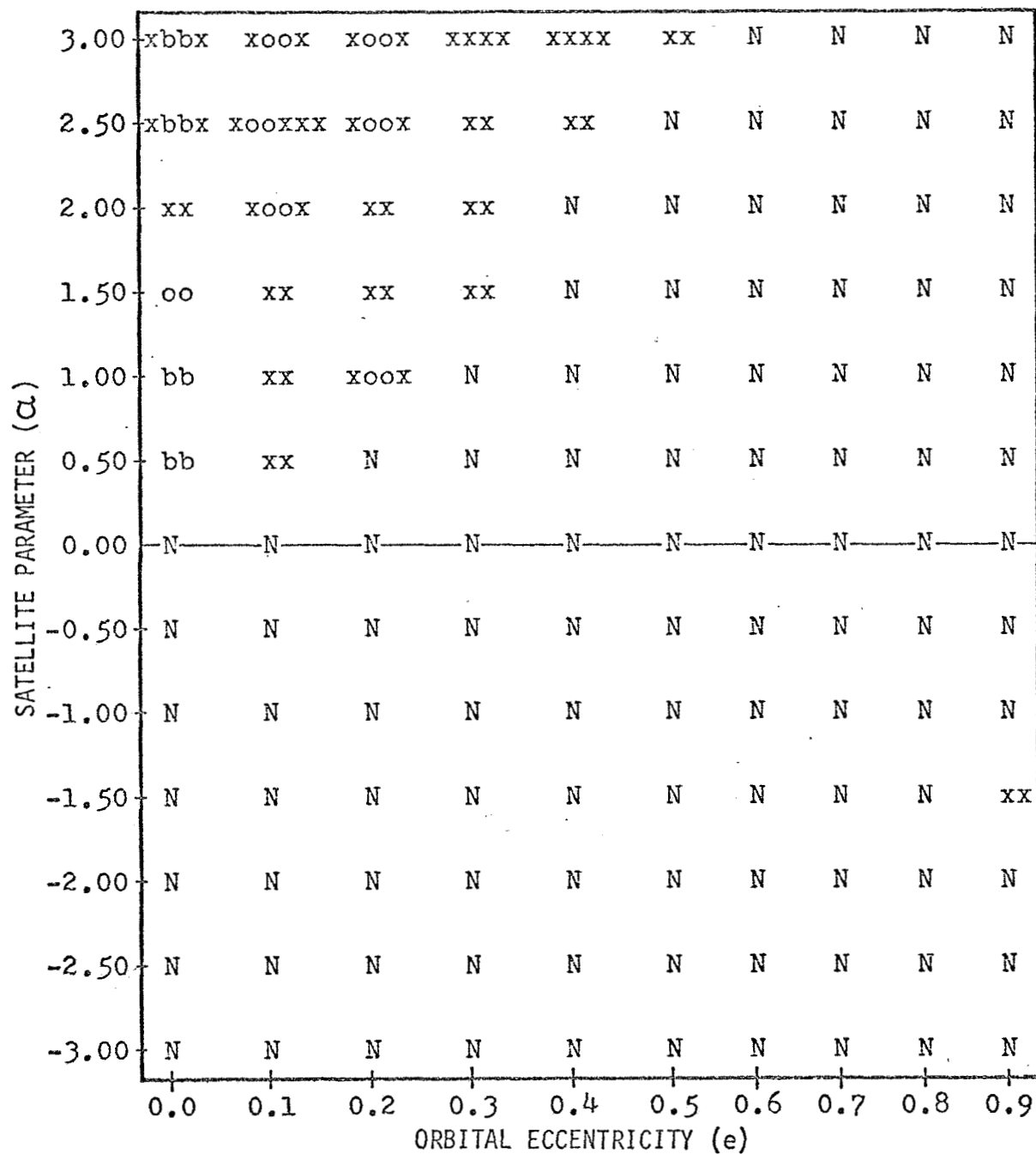


Figure 37 - Variational Stability Chart ($n = 20, m = 1$)

Figure 38 - Variational Stability Chart ($n = 40, m = 1$)

Figure 39 - Variational Stability Chart ($n = 2$, $m = 2$)

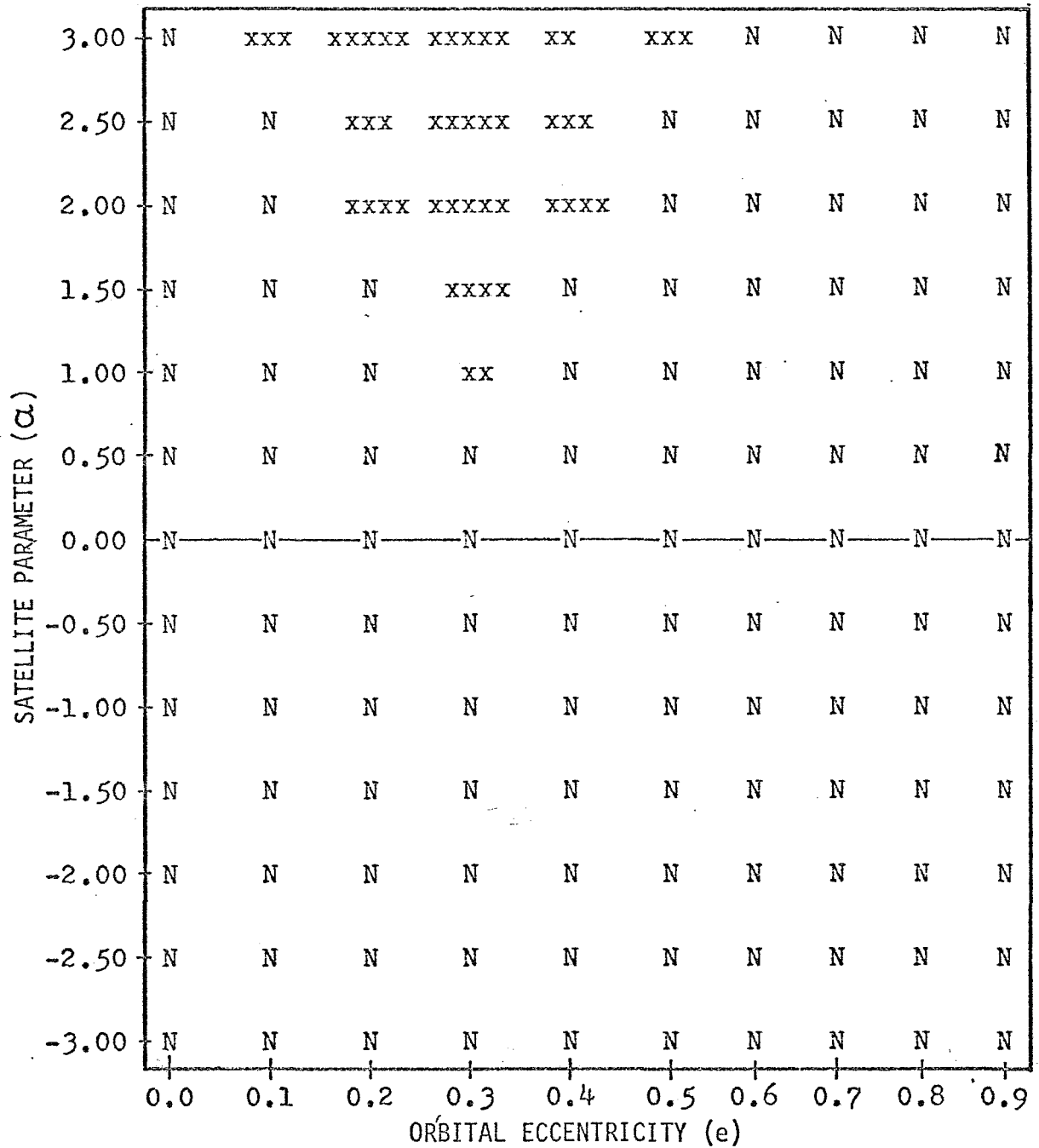


Figure 40 - Variational Stability Chart ($n = 3, m = 2$)

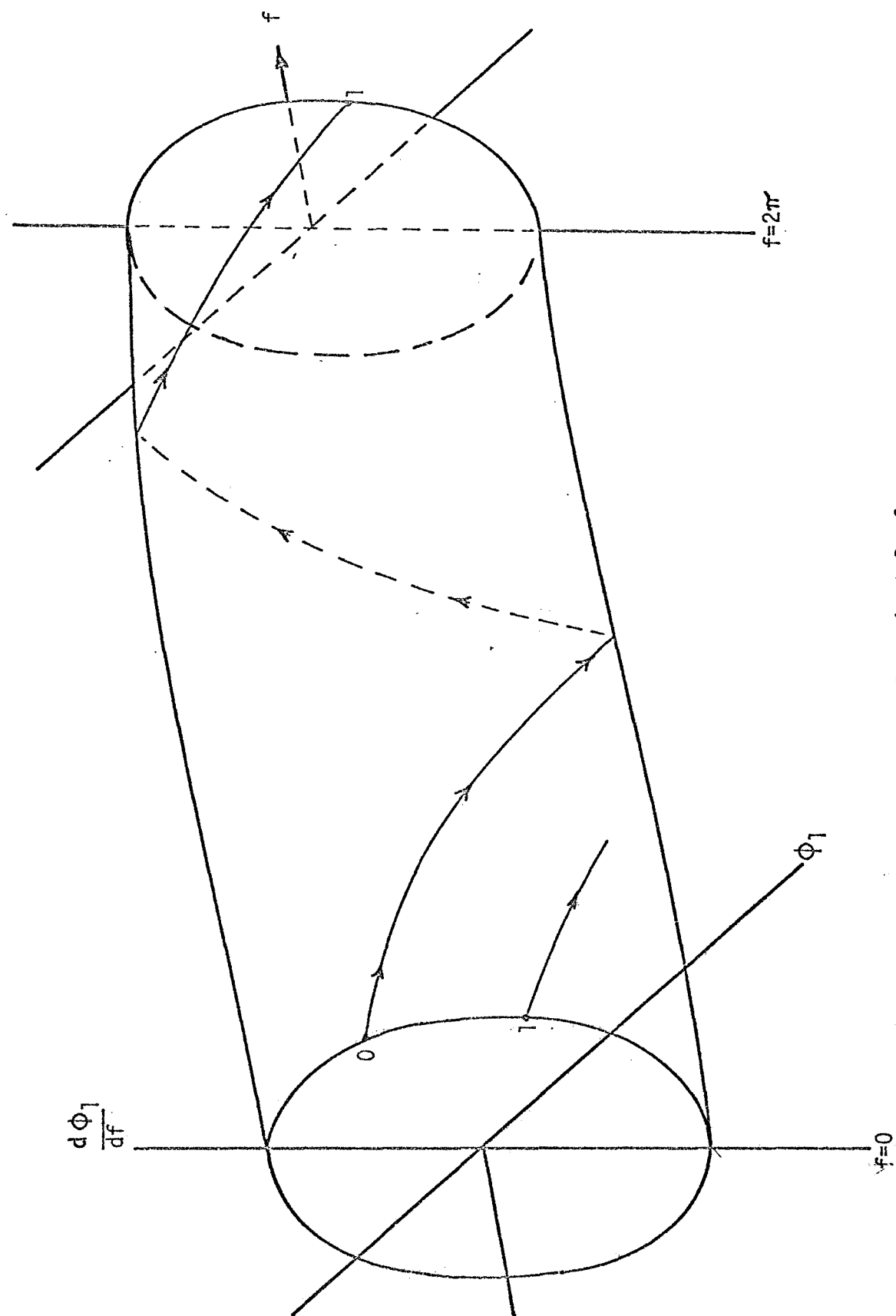


Figure 41 - Schematic of an Invariant Surface

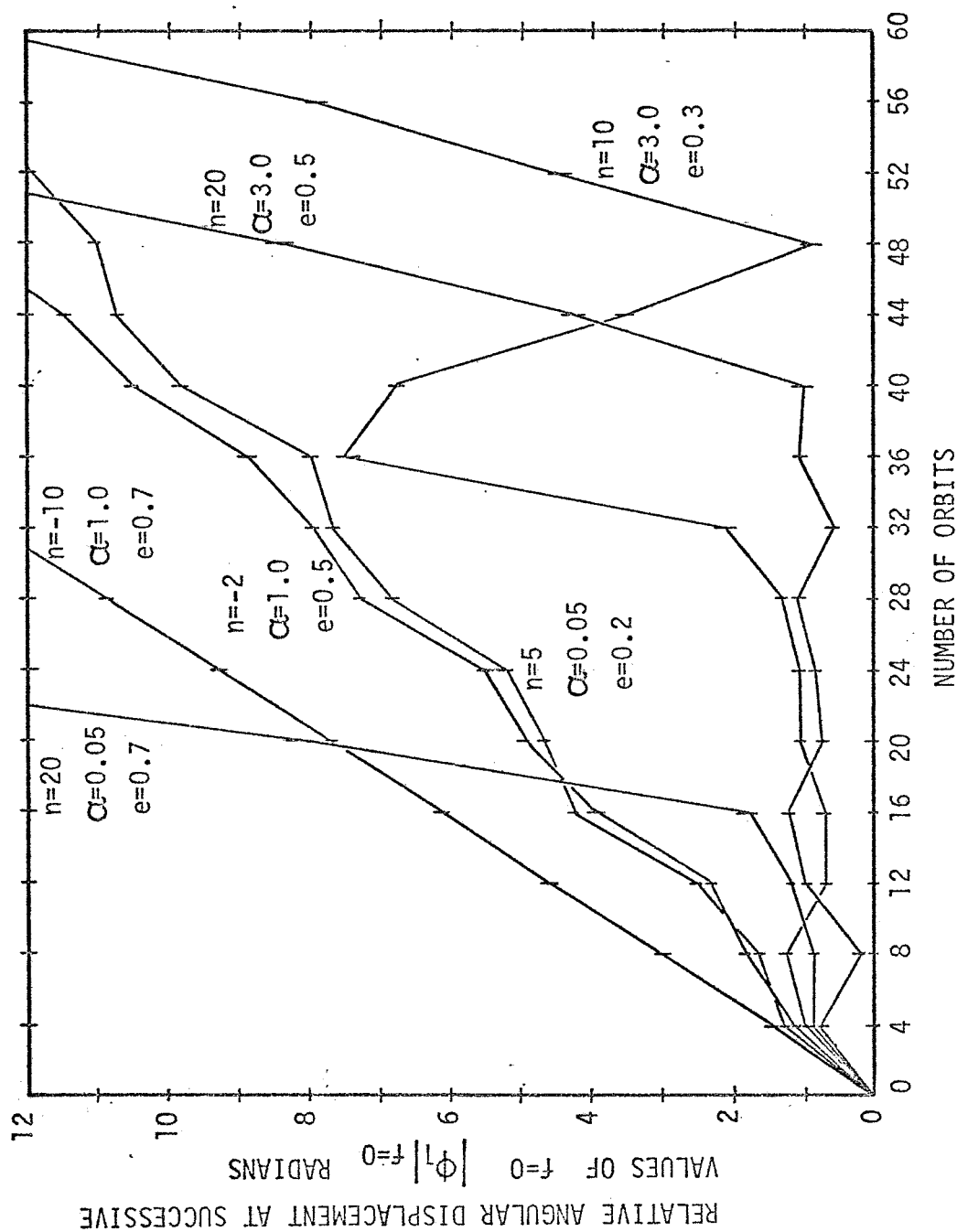


Figure 42 -- Effect on $|\Phi_1|$ After $|\Phi_1|$ Becomes Greater Than $\pi/2$

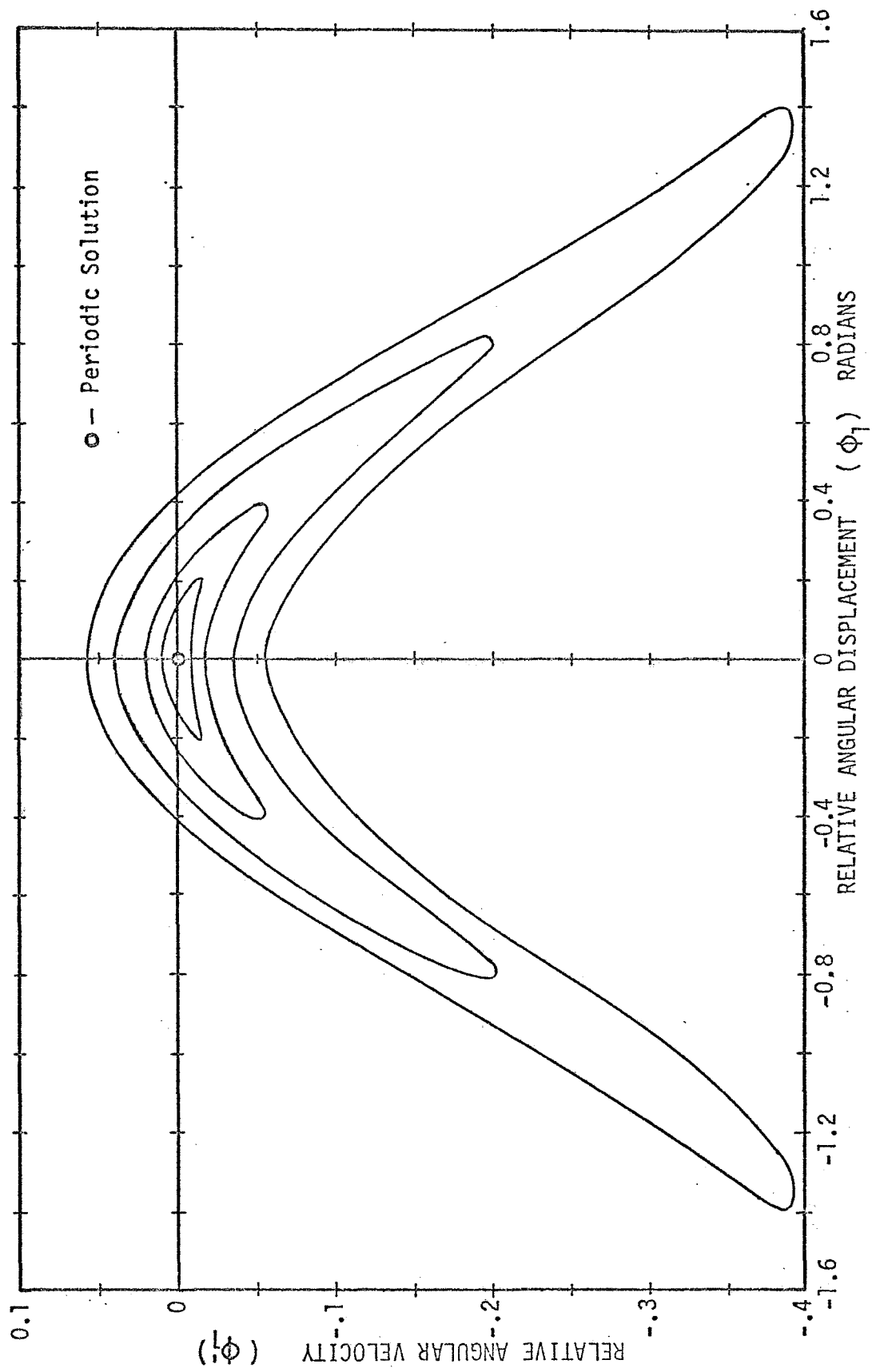


Figure 43 - Nesting of Invariant Curves at $f=0$ ($n = 10$, $\alpha = 1.5$, $e = 0.3$)

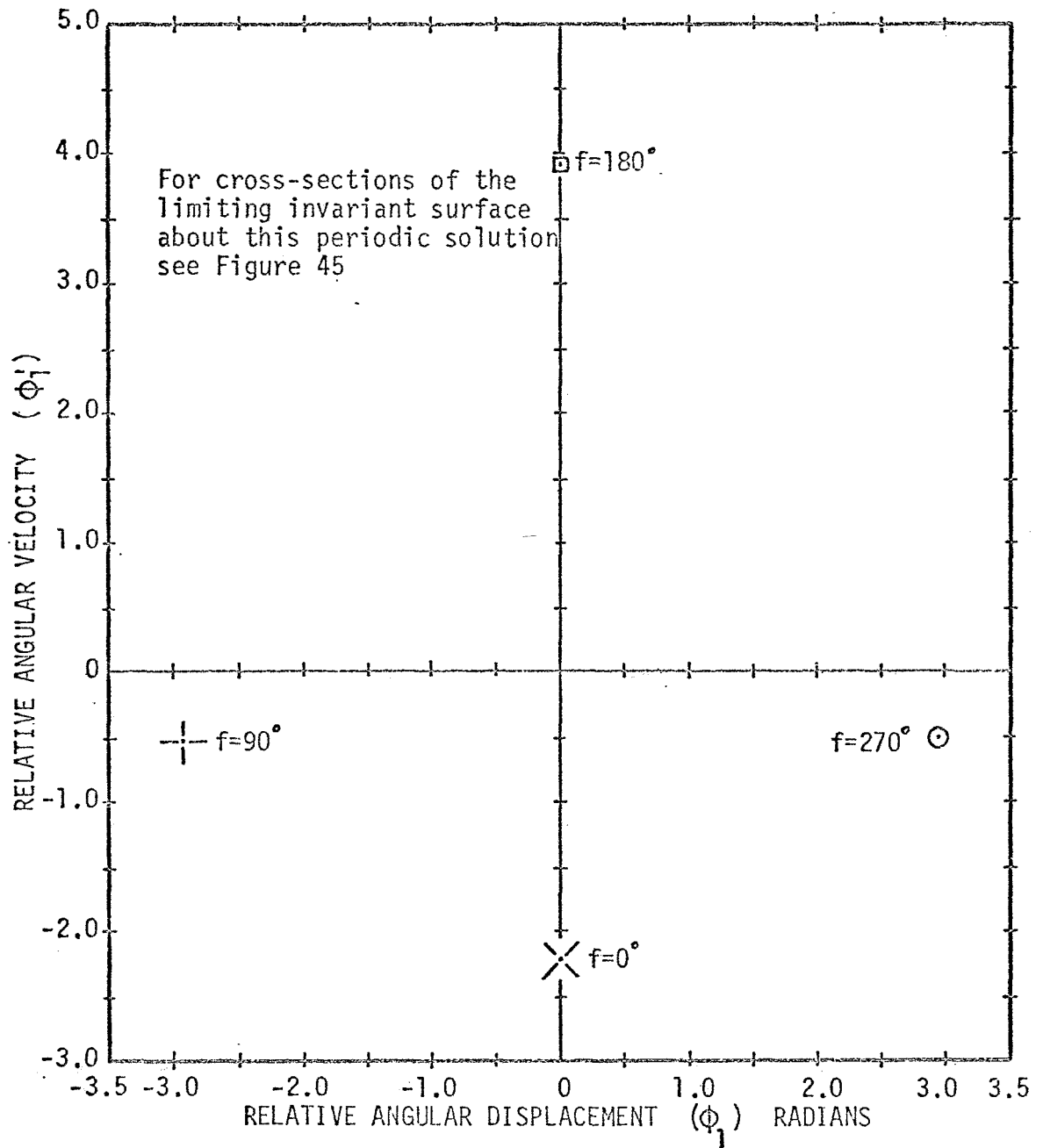


Figure 44 - Location of the Periodic Solution ($n = 10$, $\alpha = 1.5$, $e = 0.3$)

Location of the
periodic solution
is shown on
Figure 45

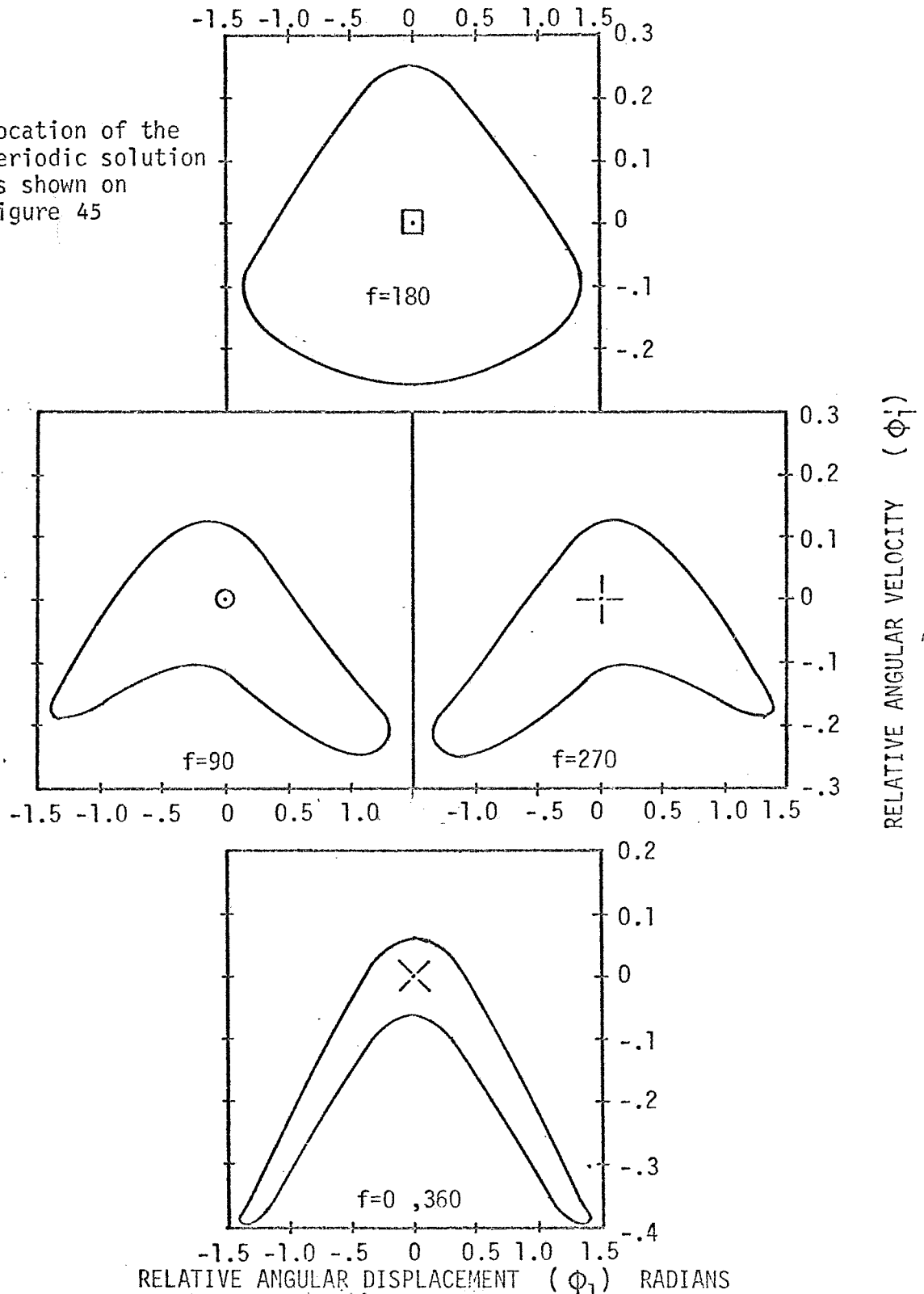


Figure 45 - Cross-sections of the Limiting Invariant Surface
($n = 10$, $\alpha = 1.5$, $e = 0.3$)

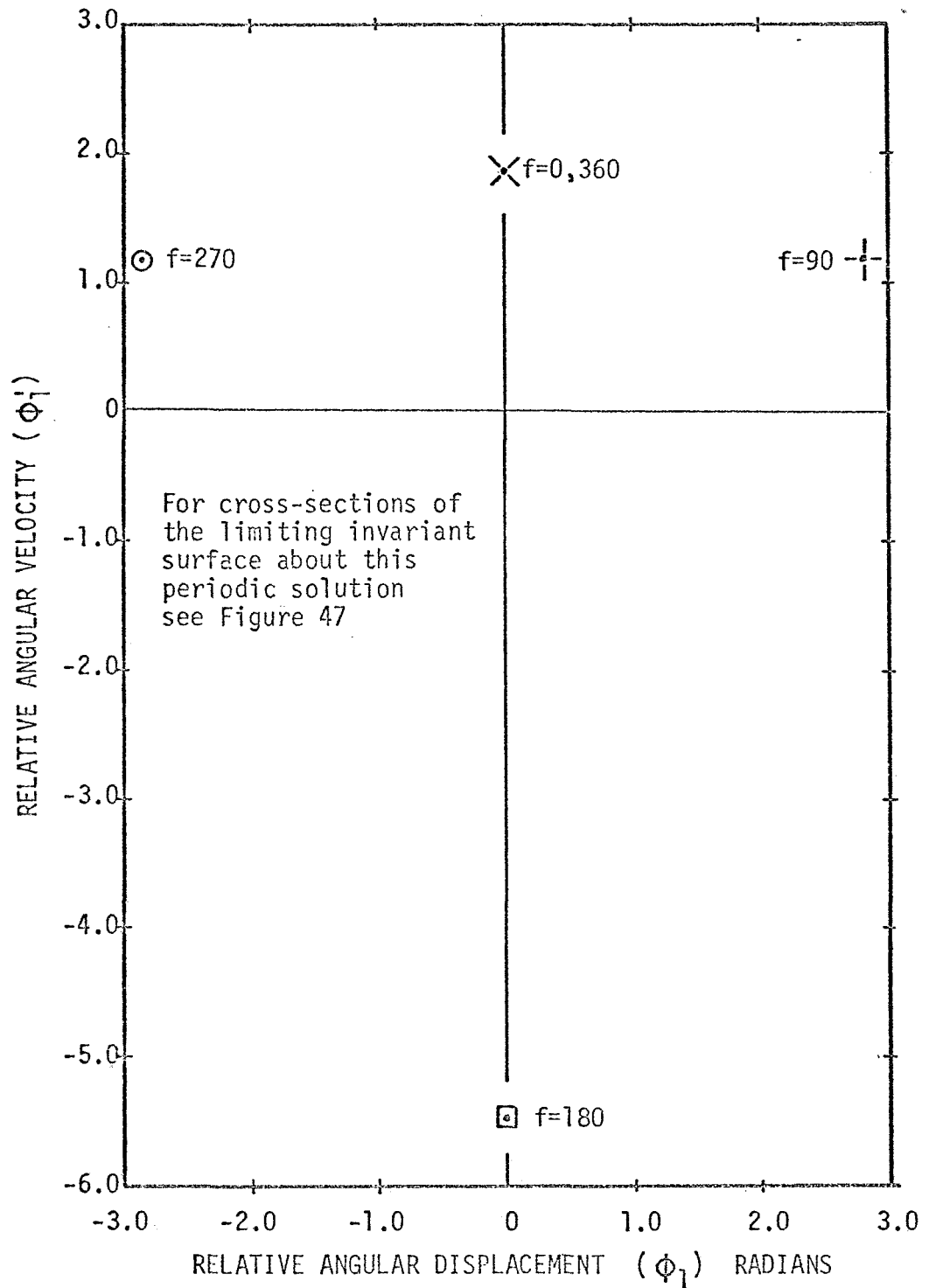


Figure 46 - Location of the Periodic Solution
 ($n = -5$, $\alpha = 1.5$, $e = 0.6$)

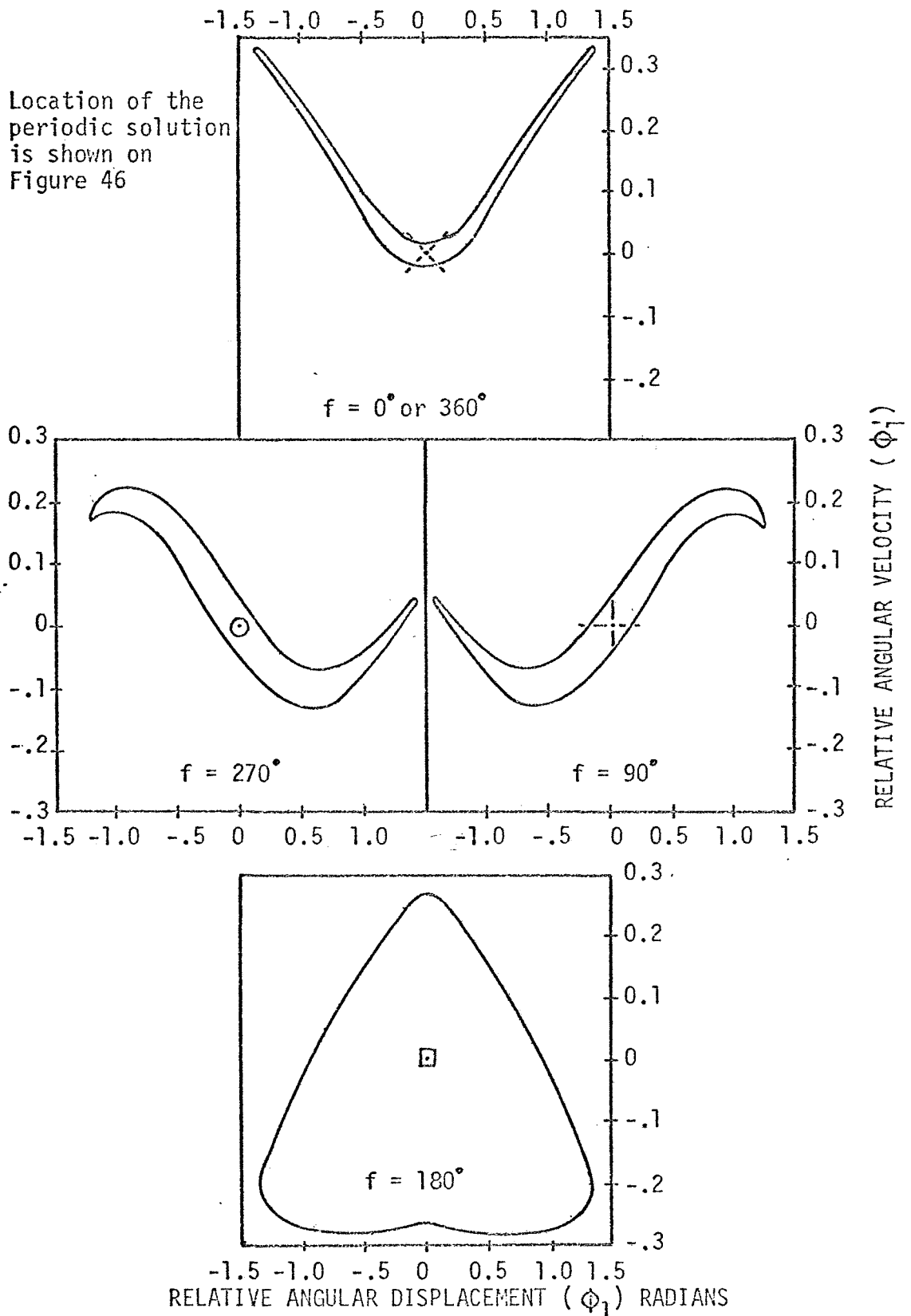


Figure 47 - Cross-sections of the Limiting Invariant Surface
($n = -5$, $\alpha = 1.5$, $e = 0.6$)

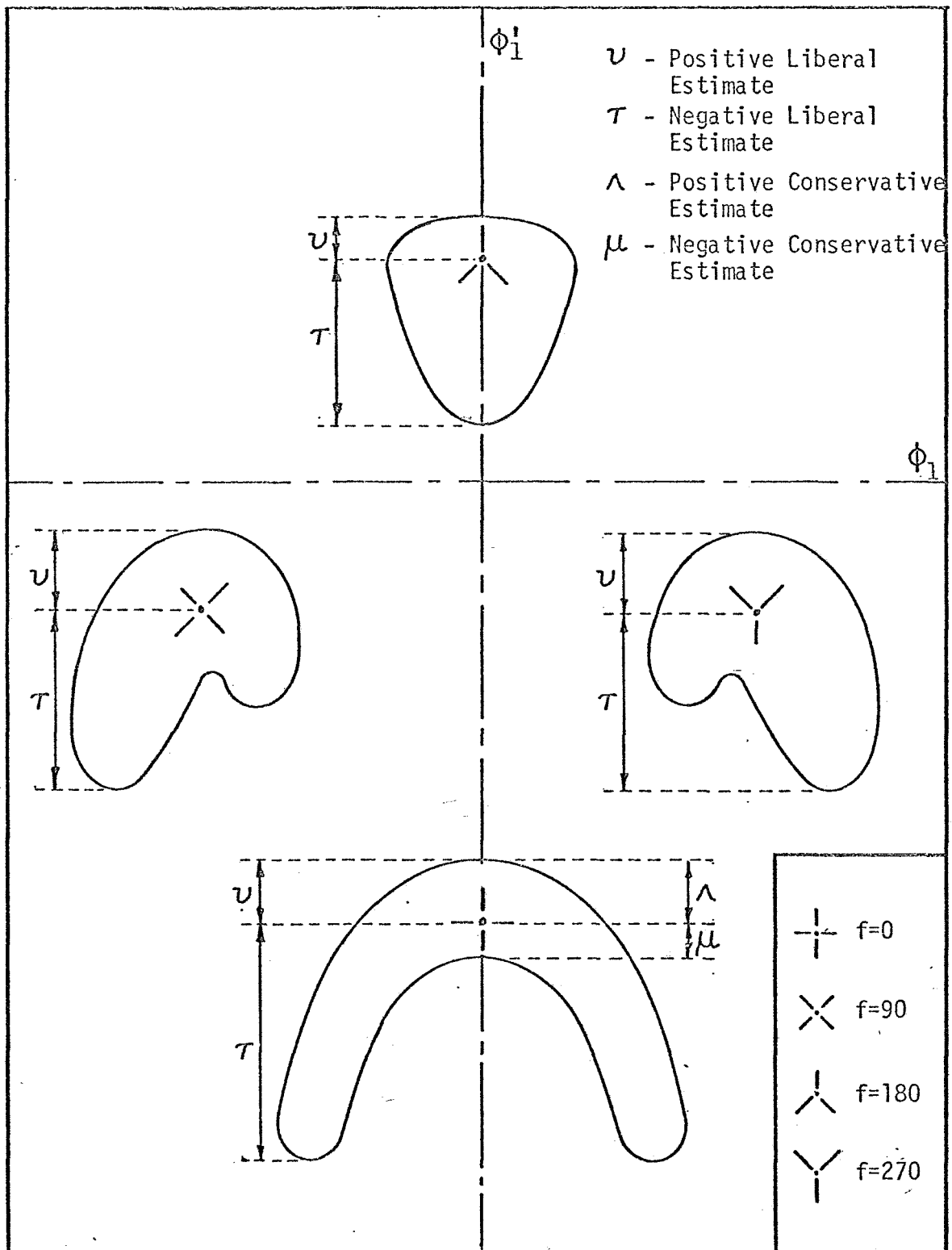


Figure 48 - Conservative and Liberal Estimates of Invariant Surfaces

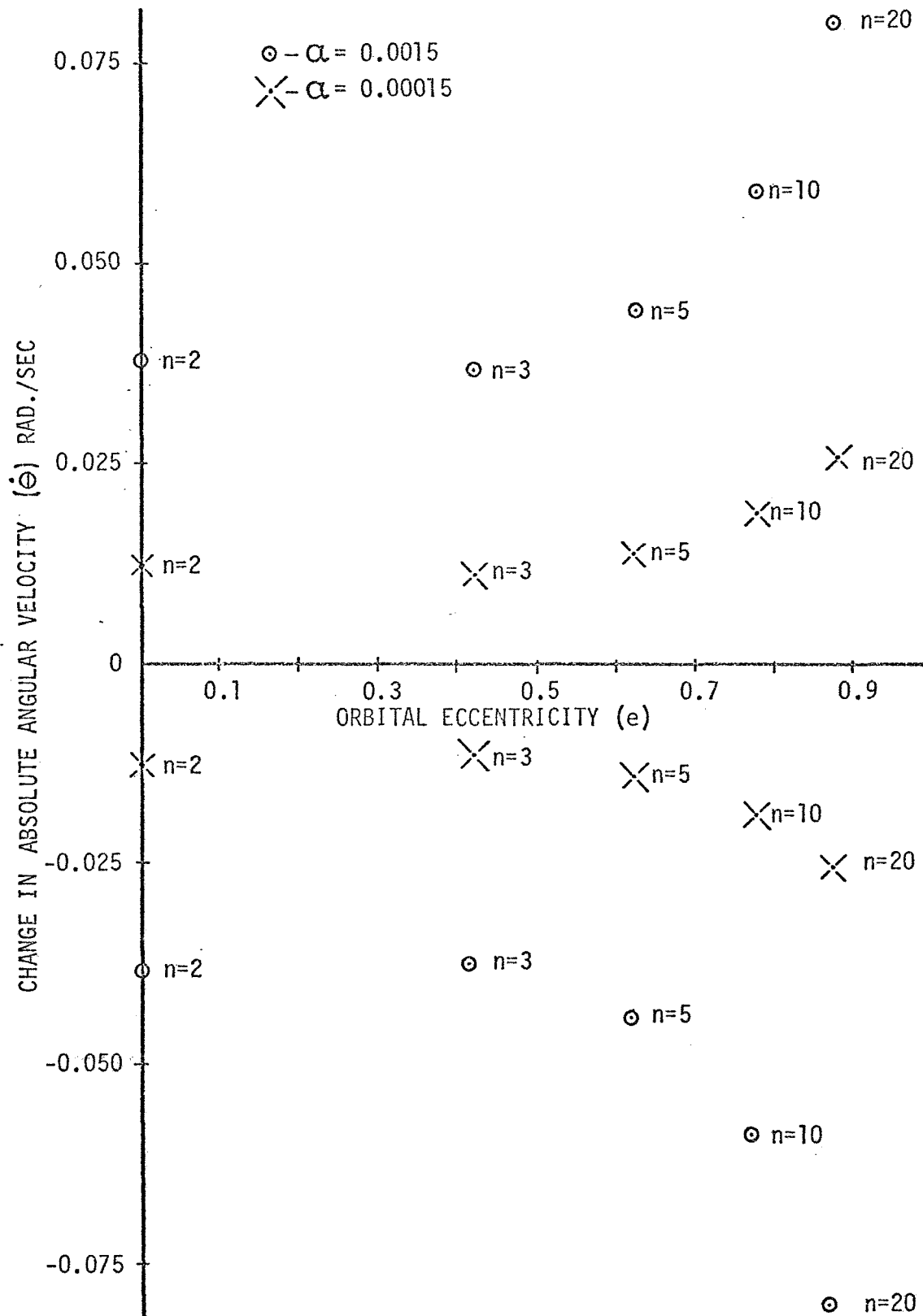


Figure 49 - Change in Absolute Angular Velocity for Maximum Values of Φ_n

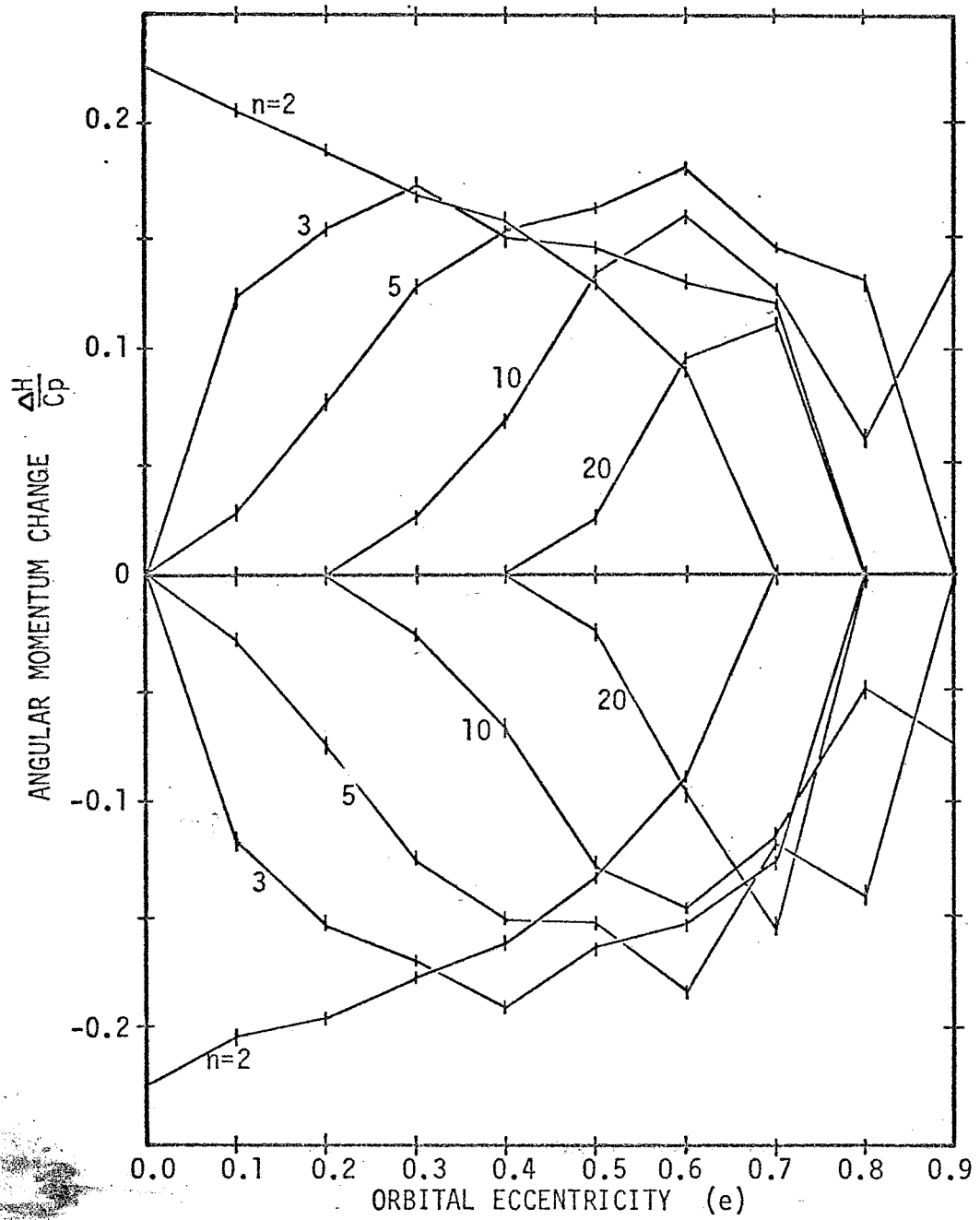


Figure 50 - Conservative Estimate of Momentum Change
at $f=0$ ($\alpha = 0.05$)

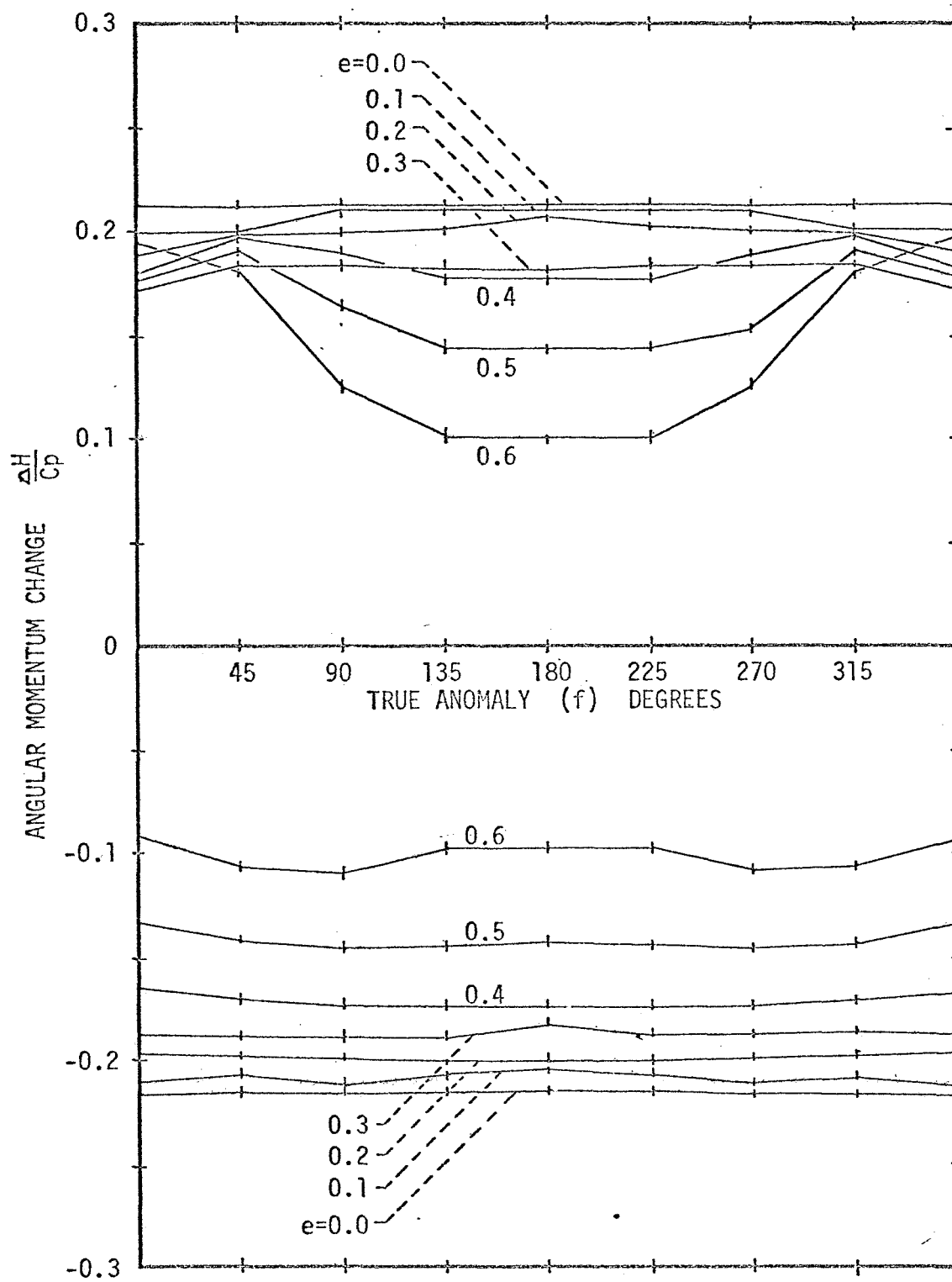


Figure 51 - Liberal Estimate of Momentum Change Throughout the Orbit ($n = 2$, $\alpha = 0.05$)

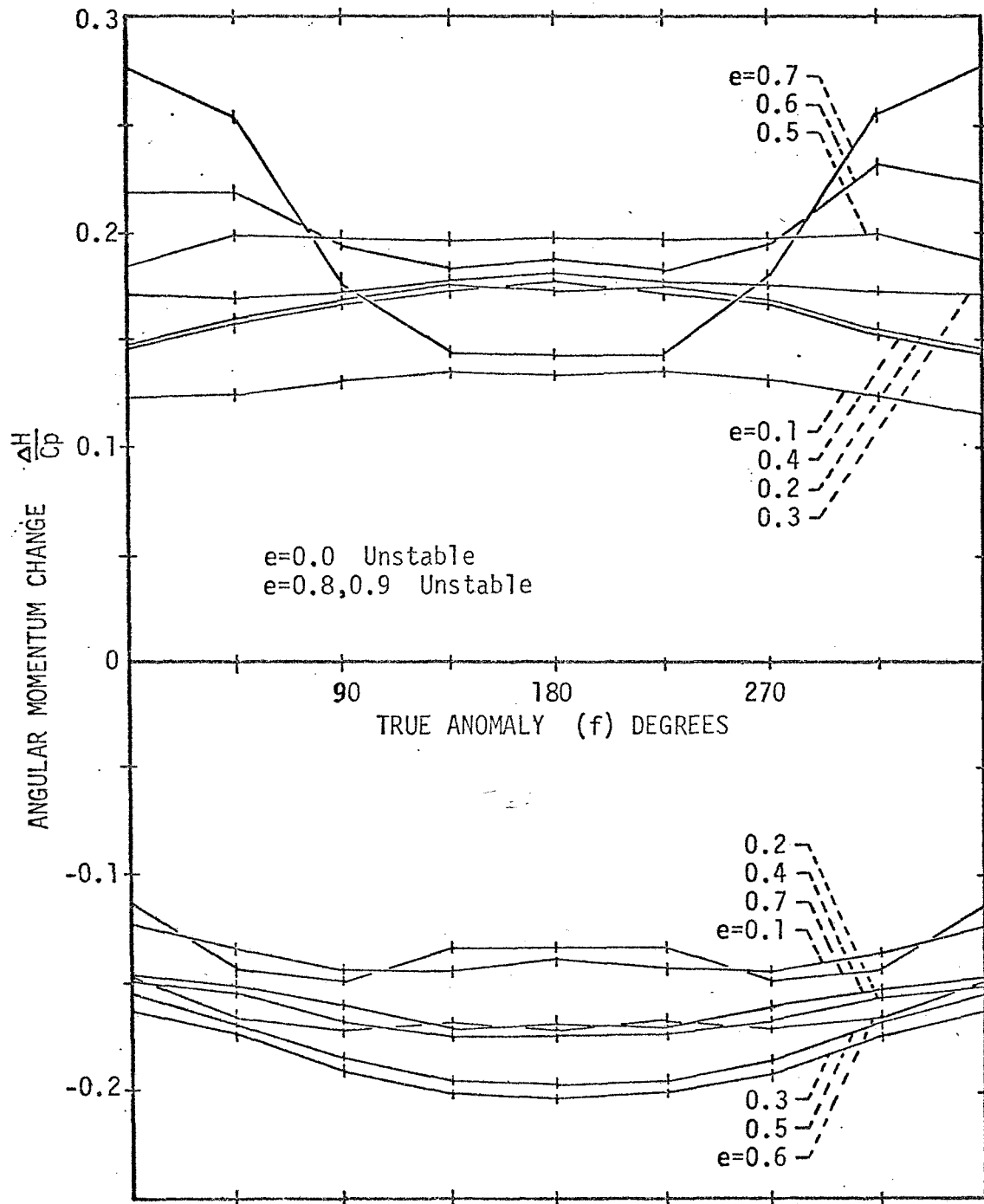


Figure 52 - Liberal Estimate of Momentum Change Throughout the Orbit. ($n = 3$, $\alpha = 0.05$)

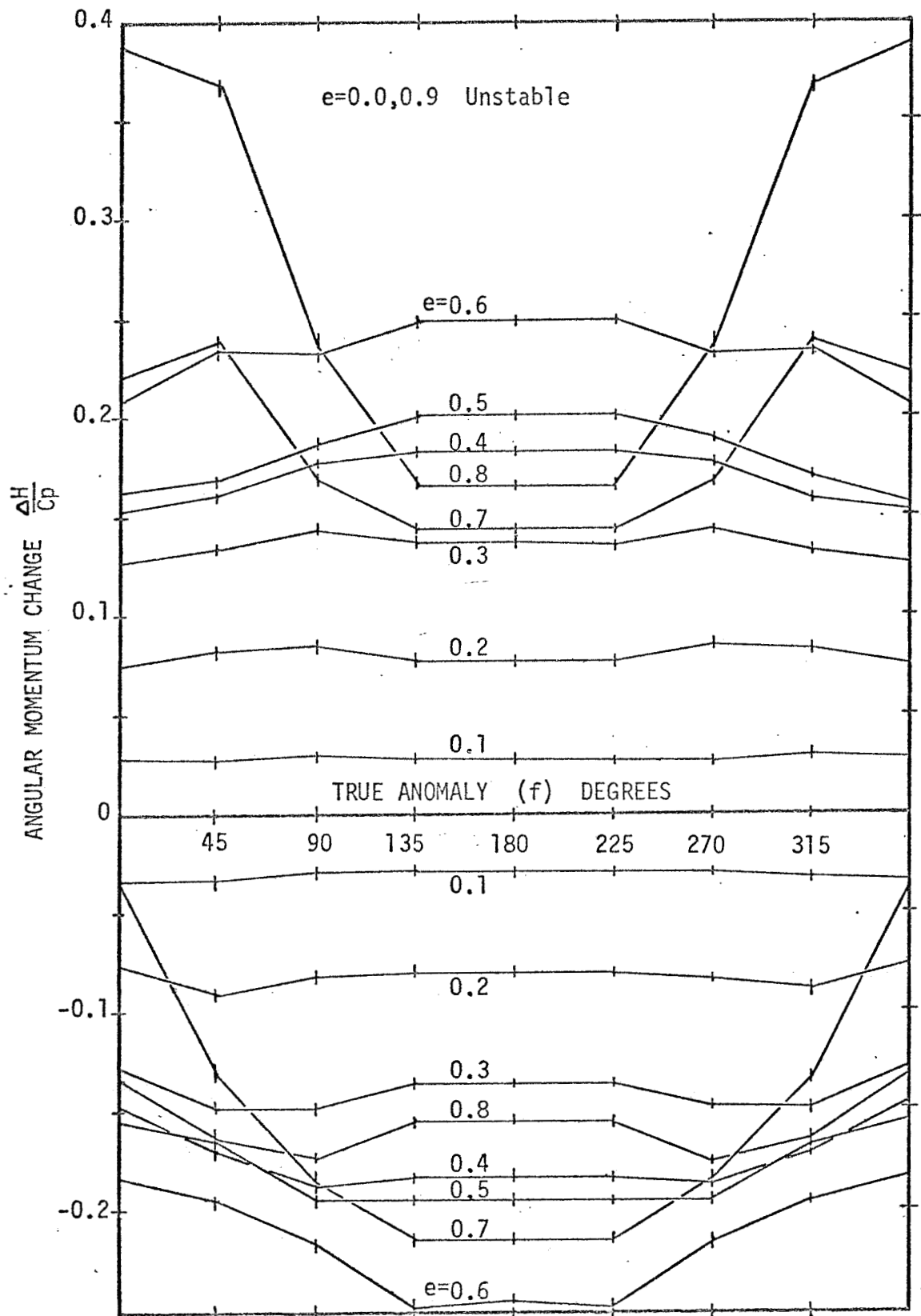


Figure 53 - Liberal Estimate of Momentum Change Throughout the Orbit ($n = 5$, $\alpha = 0.05$)

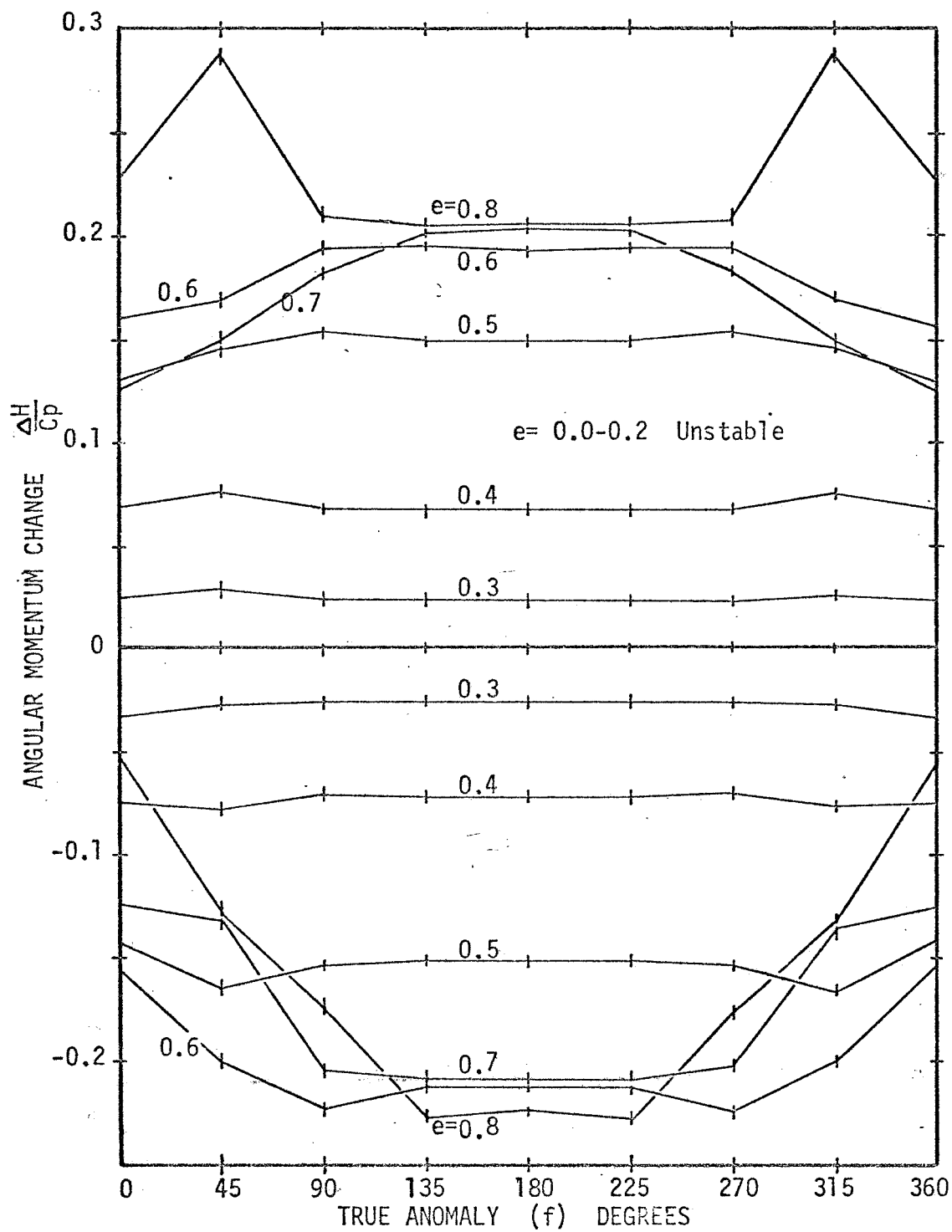


Figure 54 - Liberal Estimate of Momentum Change Throughout the Orbit ($n = 10$, $\alpha = 0.05$)

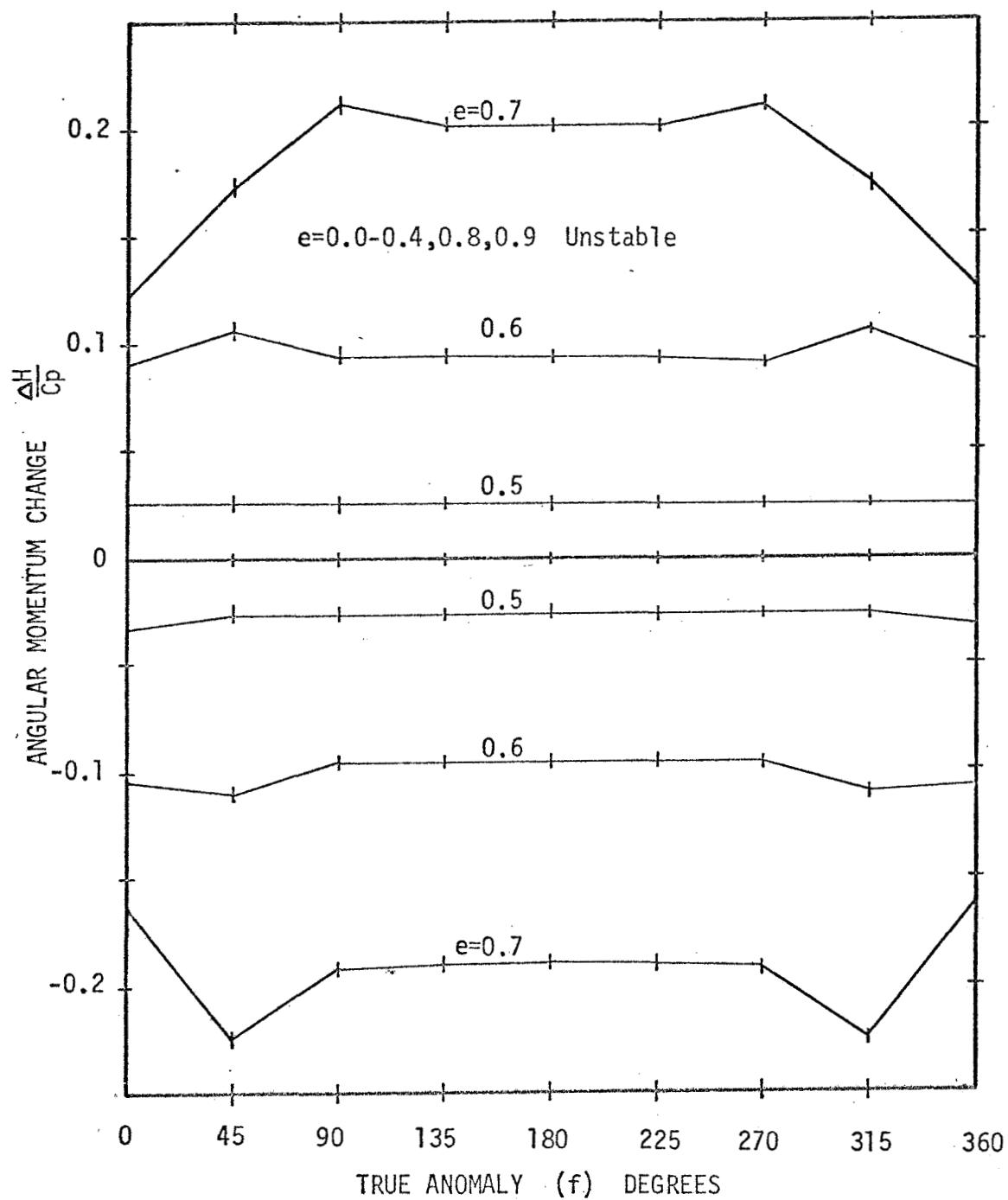


Figure 55 - Liberal Estimate of Momentum Change Throughout the Orbit ($n = 20$, $\alpha = 0.05$)

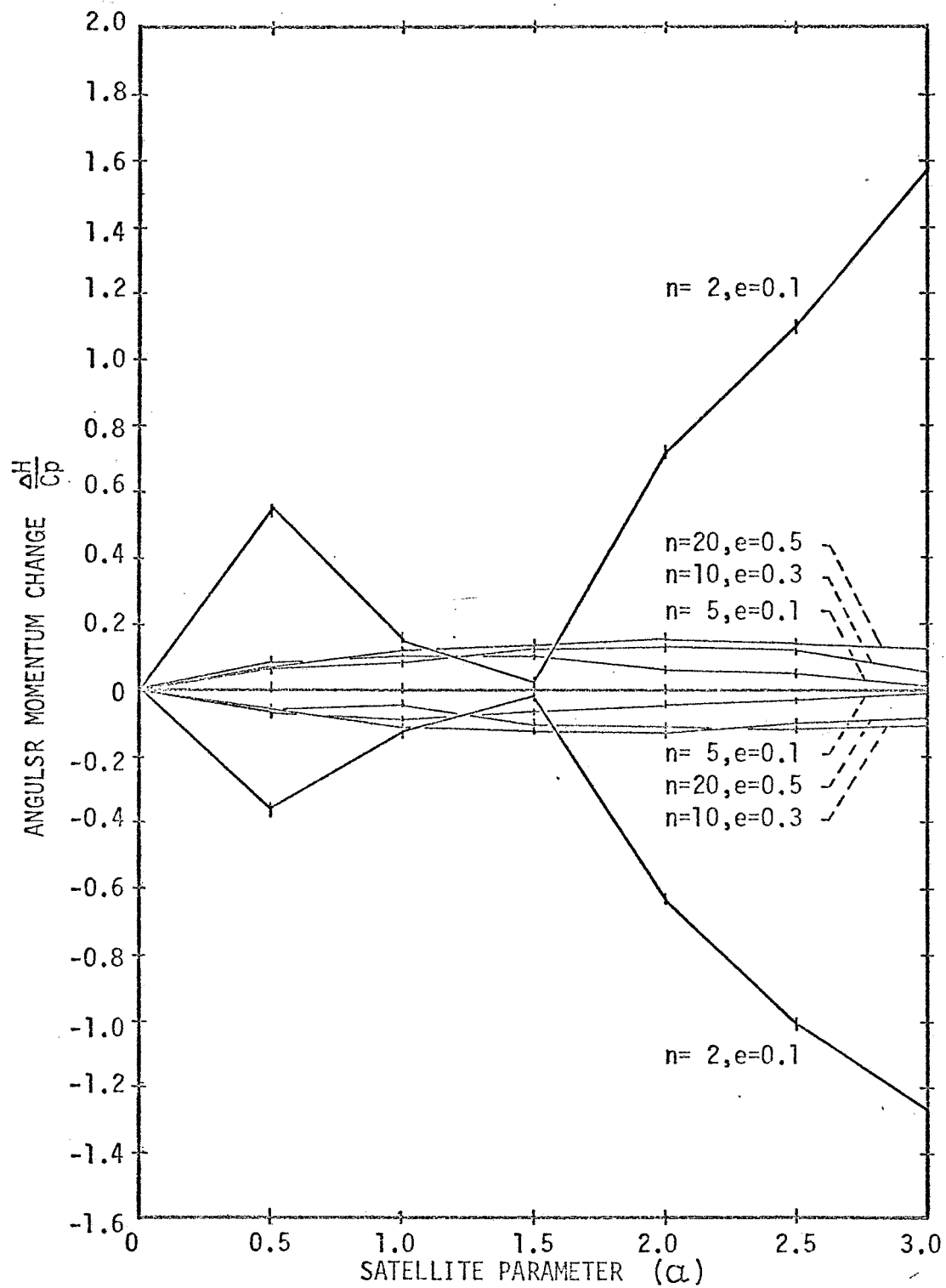


Figure 56 - Conservative Estimate of Momentum Change at $f = 0$ ($n \geq 2$)

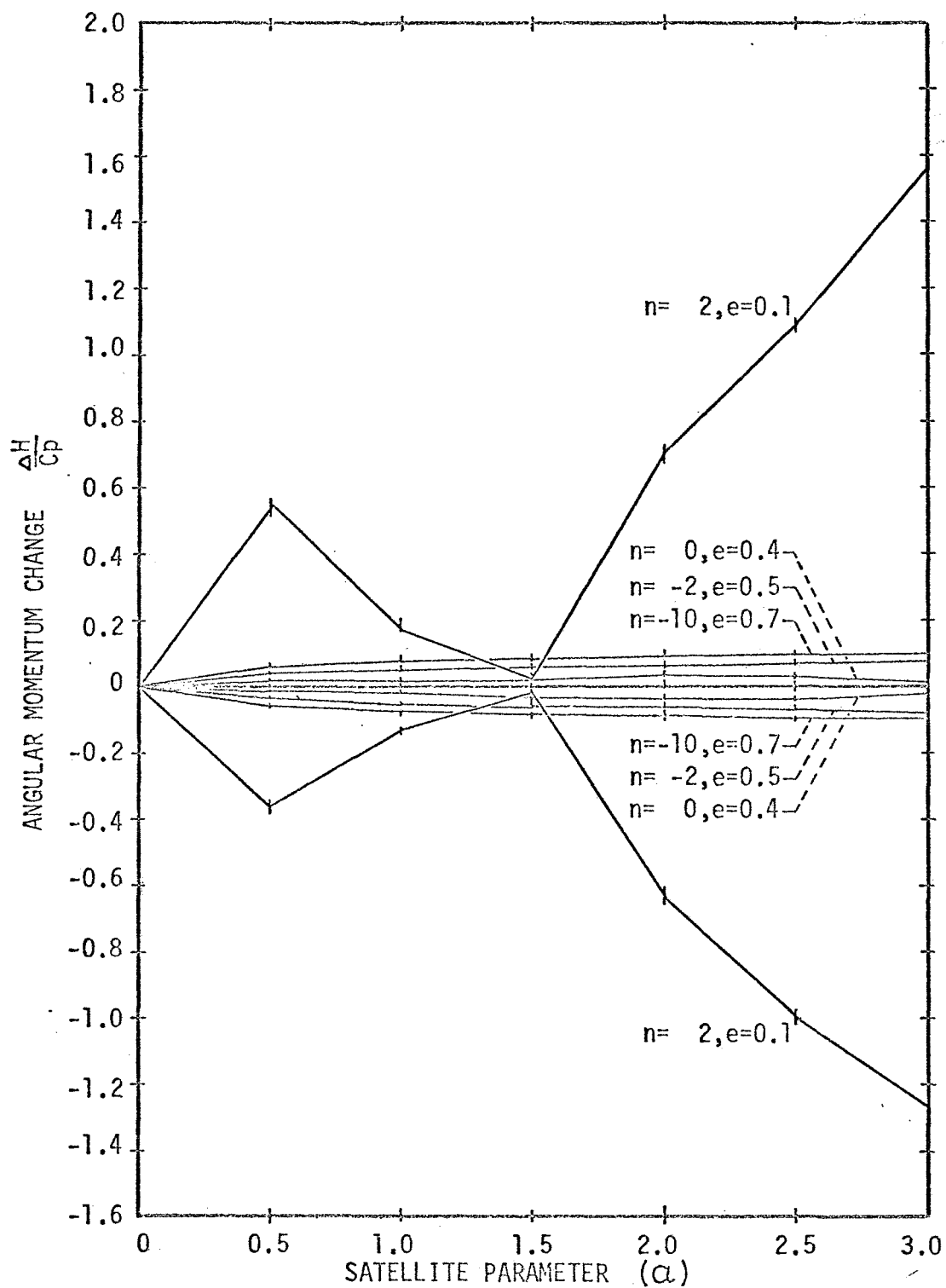


Figure 57 - Conservative Estimate of Momentum Change at $f = 0$ ($n \leq 2$)

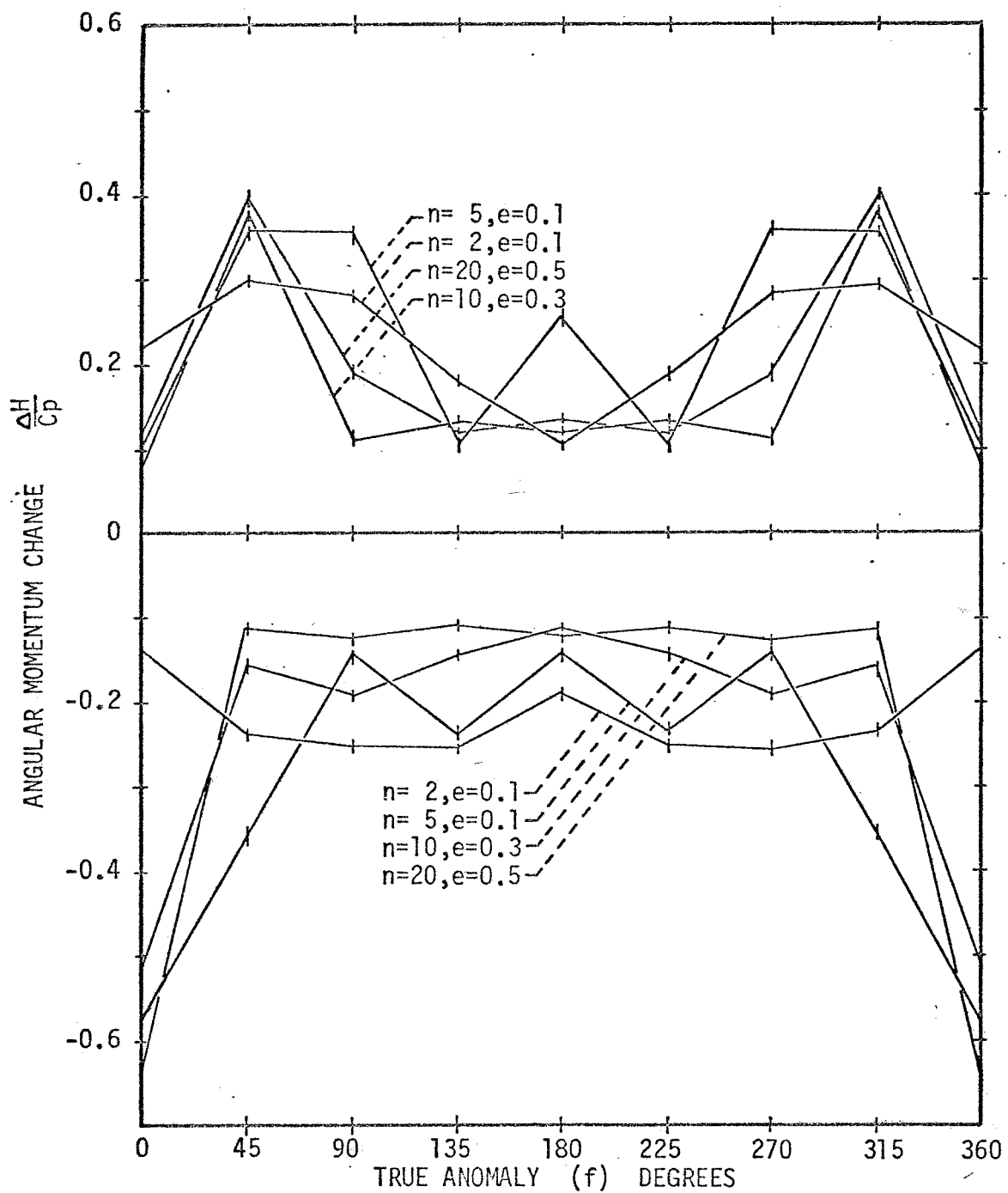


Figure 58 - Liberal Estimate of Momentum Change Throughout the Orbit ($\alpha = 1.0$, $n = 2$)

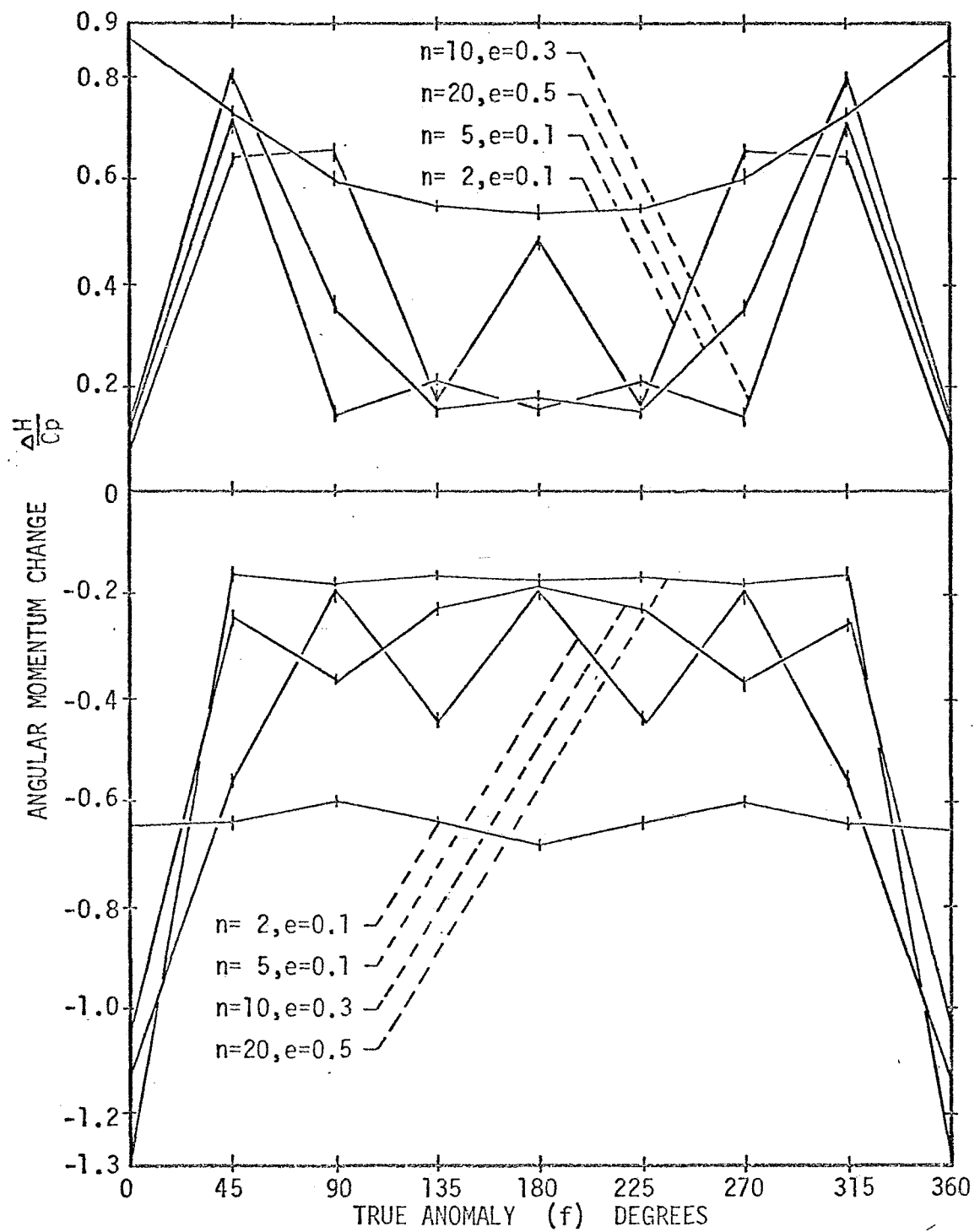


Figure 59 - Liberal Estimate of Momentum Change Throughout the Orbit ($\alpha = 2.0$, $n \geq 2$)

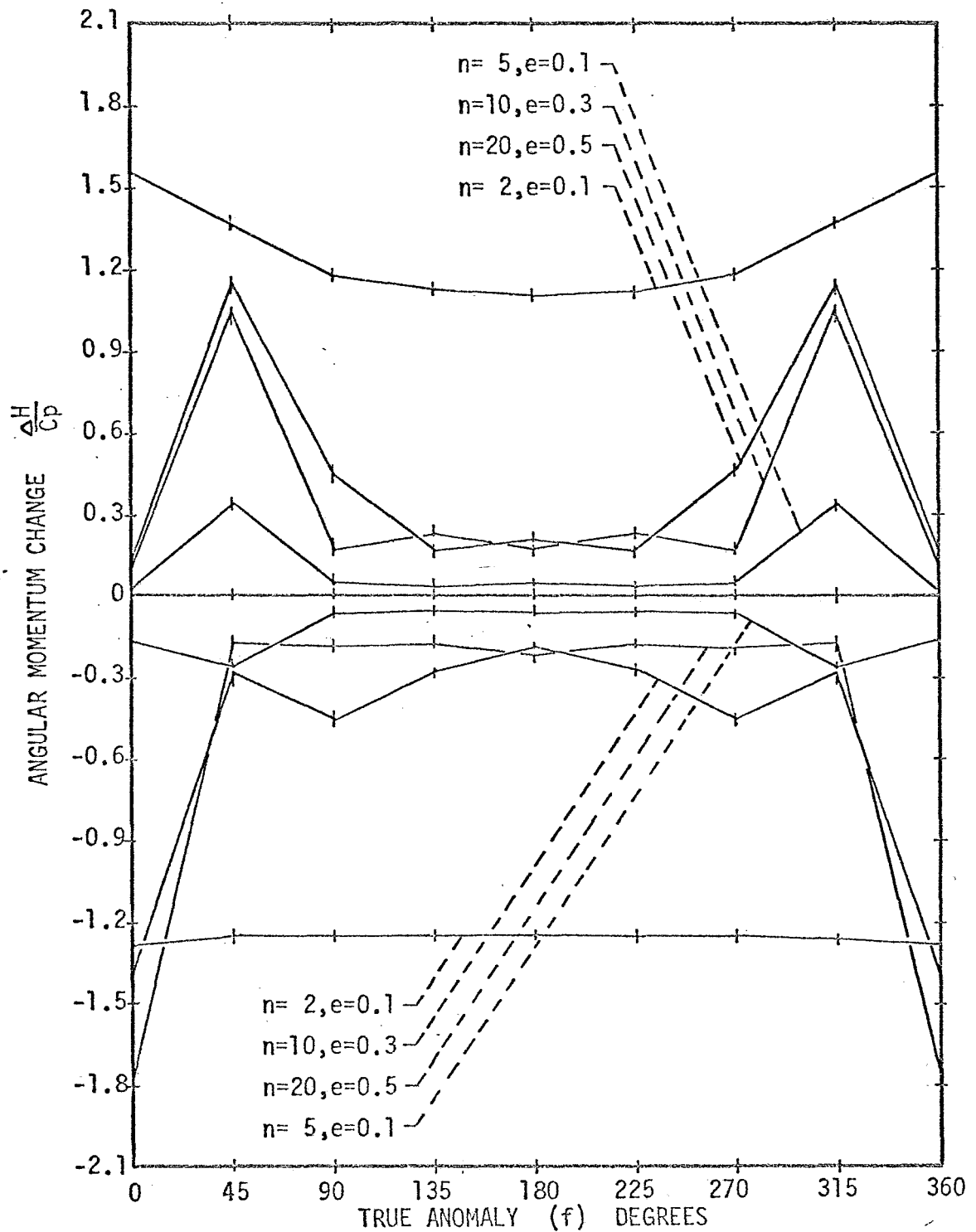


Figure 60 - Liberal Estimate of Momentum Change Throughout the Orbit ($\alpha = 3.0$, $n \geq 2$)

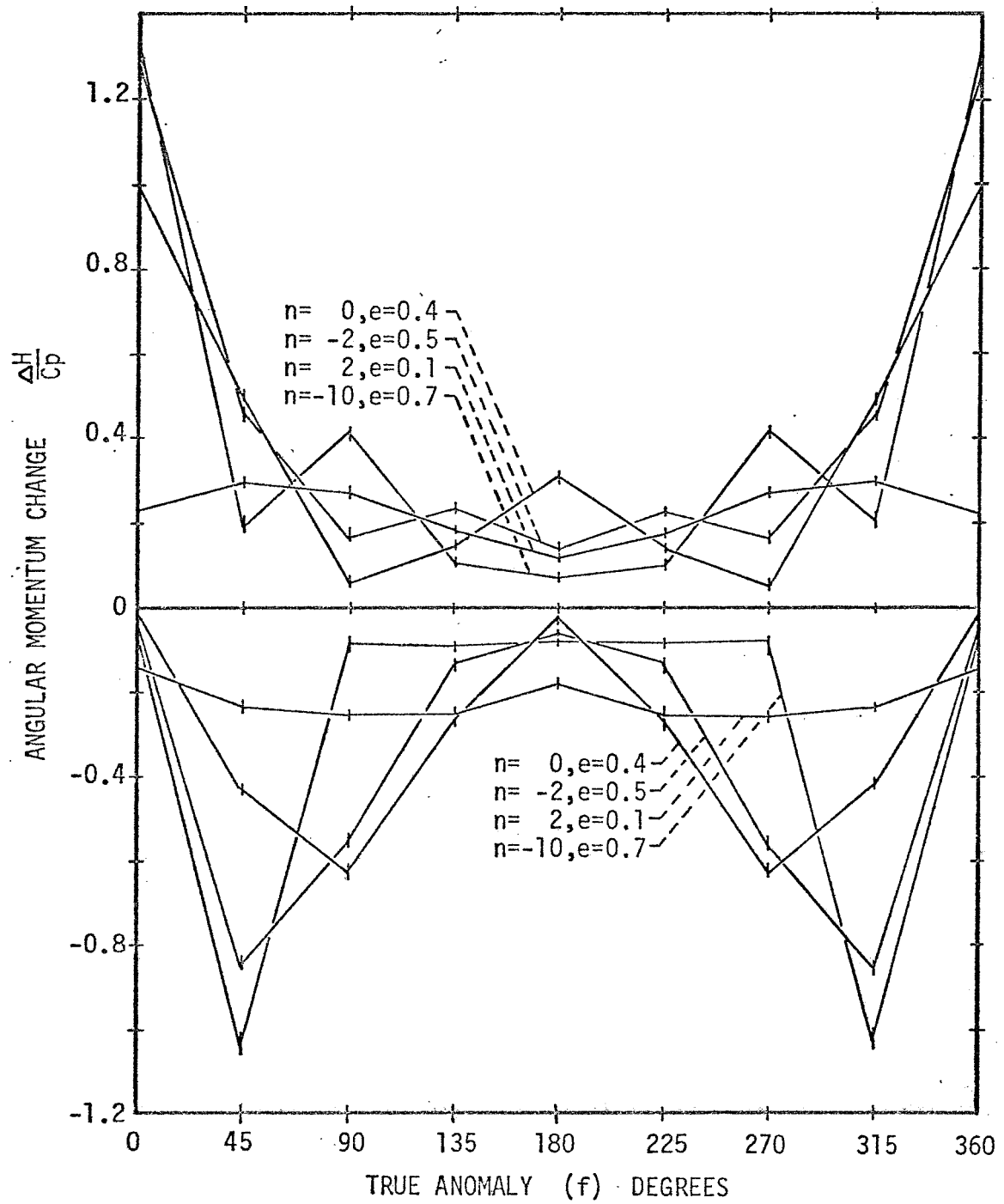


Figure 61 - Liberal Estimate of Momentum Change Throughout the Orbit ($\alpha = 1.0$, $n = 2$)

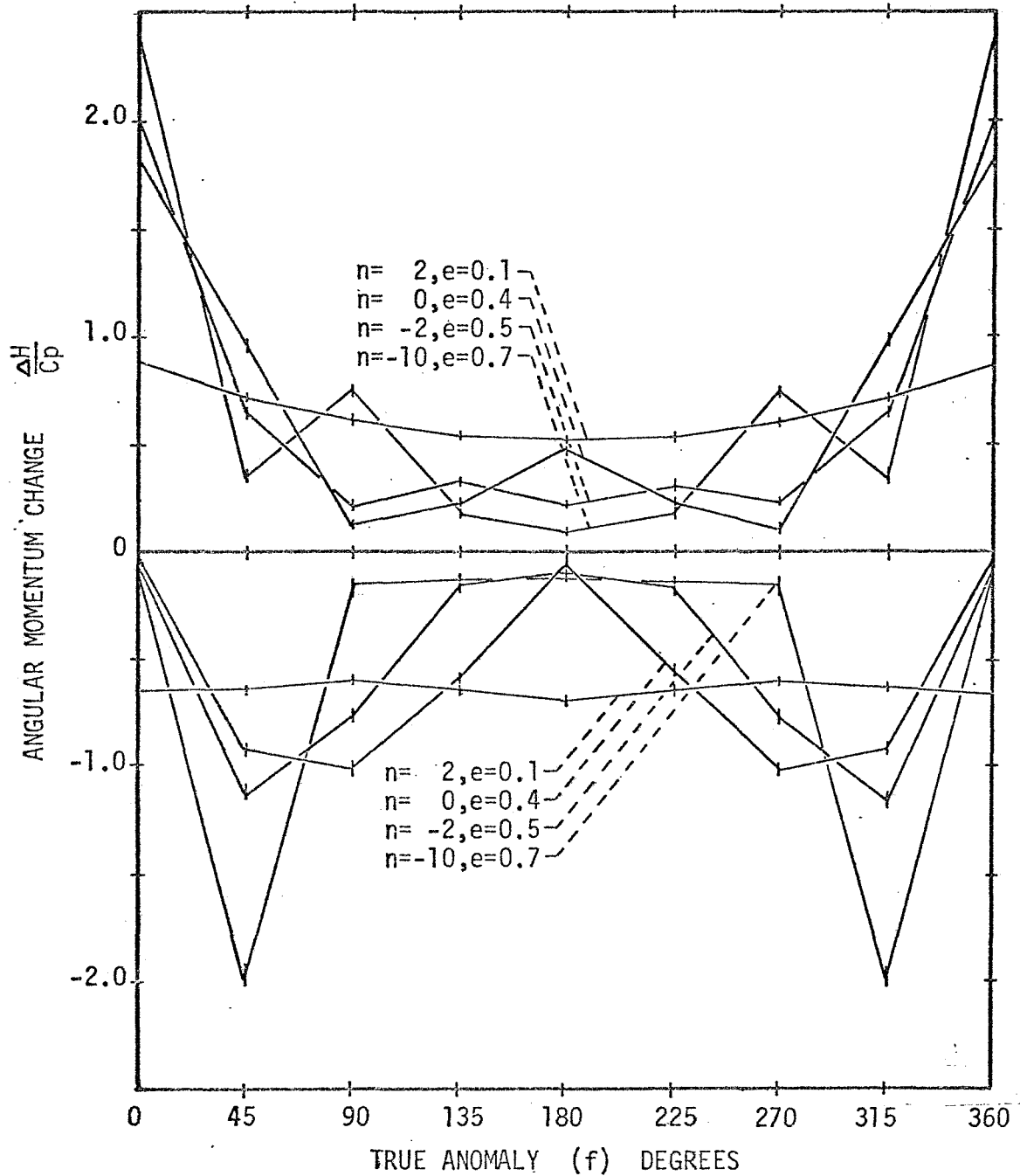


Figure 62 - Liberal Estimate of Momentum Change Throughout the Orbit ($\alpha = 2.0$, $n = 2$)

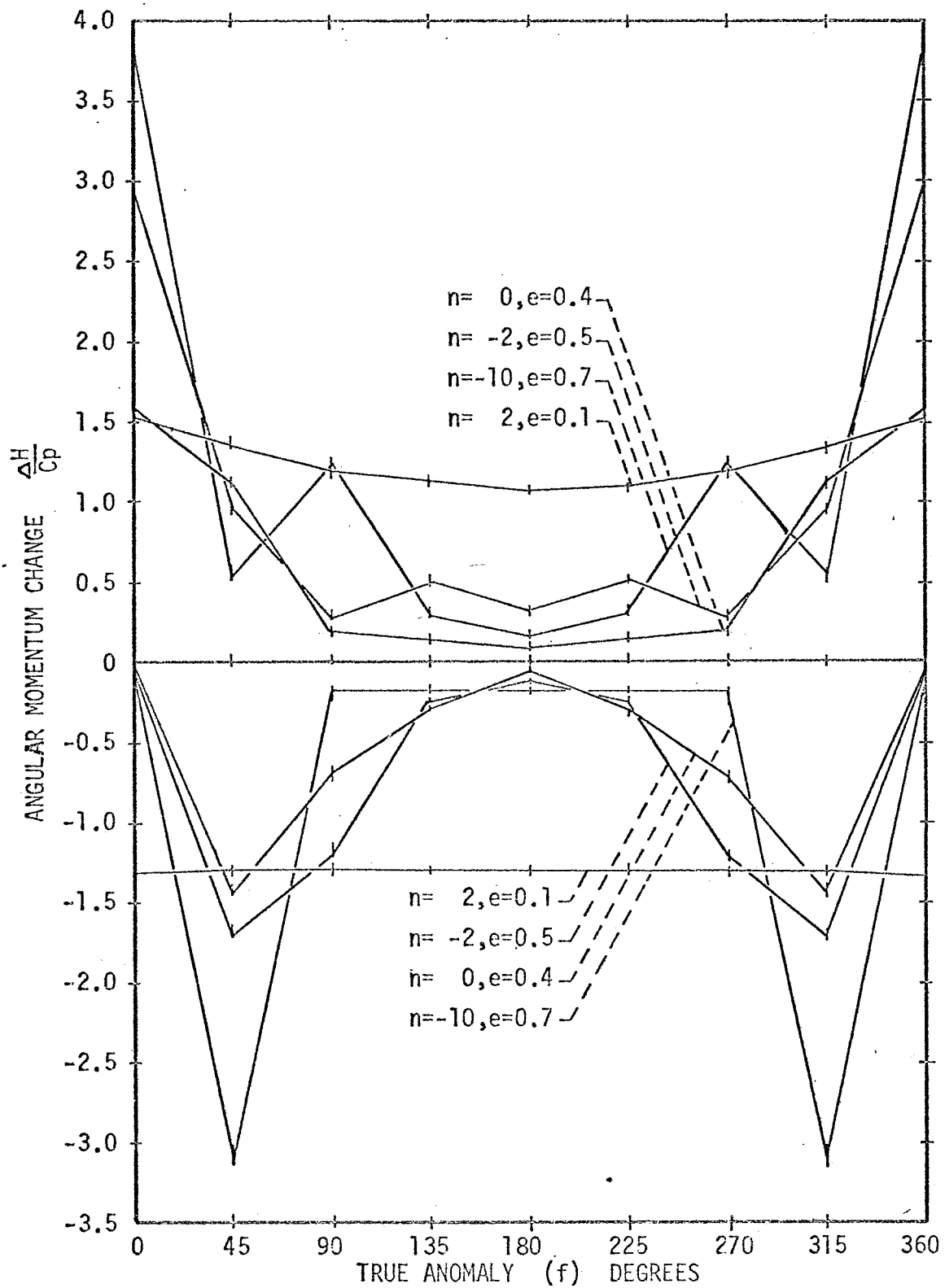


Figure 63 - Liberal Estimate of Momentum Change Throughout the Orbit ($\alpha = 3.0$, $n \leq 2$)

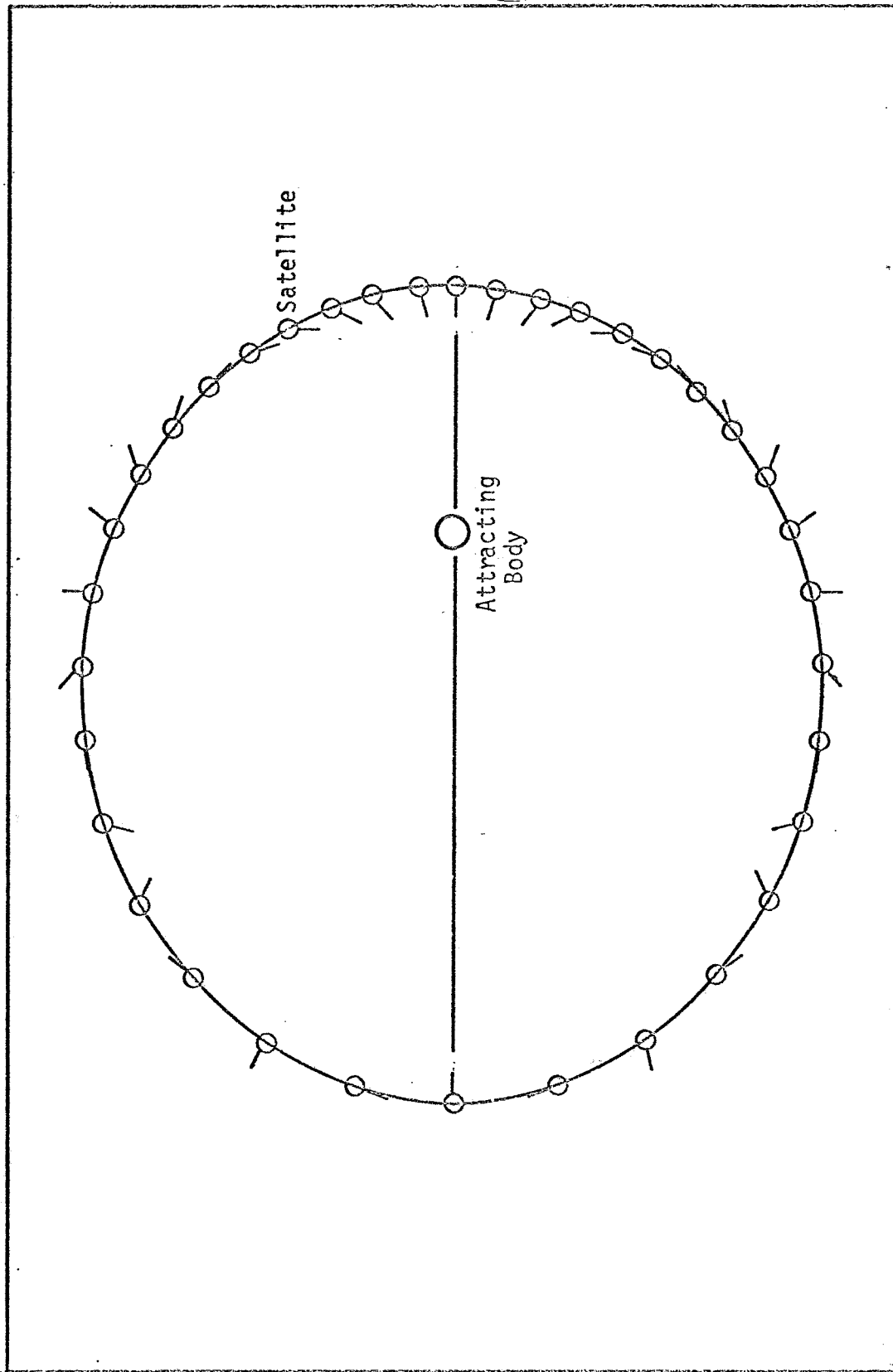


Figure 64 - Satellite Position for 2π Periodic Solution ($n = 10$, $\alpha = 1.0$, $e = 0.4$)

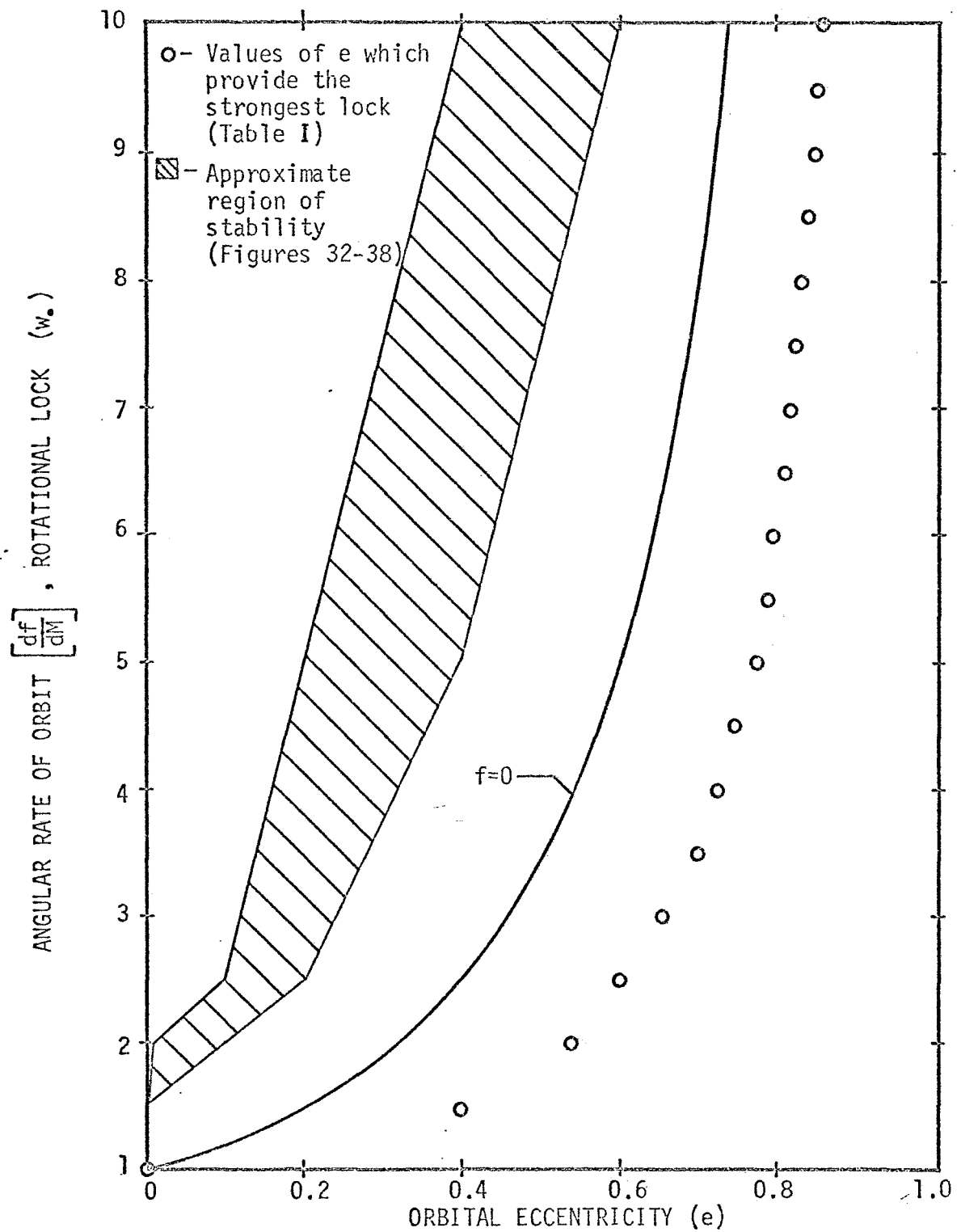


Figure 65 - Angular Rate of the Orbit vs. Orbital Eccentricity

TABLE I - Properties of the Parameter $\Phi_n(e)$ for
Lock Numbers 1-28

n	e for $\Phi_n = 0$	e for $\Phi_n = \text{MAX}$	$\Phi_n \text{ MAX}$
1	0.000	0.000	0.000
2	0.682	0.000	1.000
3	0.788	0.420	0.948
4	0.837	0.547	1.133
5	0.866	0.622	1.339
6	0.885	0.672	1.551
7	0.900	0.708	1.767
8	0.909	0.736	1.984
9	0.916	0.759	2.204
10	0.924	0.774	2.406
11	0.928	0.792	2.668
12	0.934	0.810	2.854
13	0.939	0.817	3.047
14	0.942	0.820	3.278
15	0.945	0.828	3.511
16	0.947	0.840	3.786
17	0.948	0.846	3.911
18	0.952	0.851	4.241
19	0.954	0.863	4.477
20	0.955	0.872	4.646
21	0.957	0.879	4.823
22	0.959	0.867	4.984
23	0.960	0.873	5.281
24	0.962	0.881	5.515
25	0.963	0.886	5.706
26	0.963	0.892	5.978
27	0.964	0.896	6.100
28	0.966	0.897	6.369

TABLE II - The numerical results of Liu (21) compared to the analytical results of the small e and arbitrary e cases for $e = 0.206$ and $n = 3$.

	period of oscillation years	lower limit of rotational period-days	upper limit of rotational period-days
numerical	80	58.583	58.745
small e (K_n)	73.31	58.518	58.726
arbitrary e (Φ_n)	77.91	58.524	58.769
$a^2 = 0.000005$			
numerical	25	58.260	59.032
small e	23.18	58.243	59.056
arbitrary e	24.32	58.262	59.037
$a^2 = 0.000050$			
numerical	8	57.381	59.911
small e	7.33	57.388	59.961
arbitrary e	7.69	57.446	59.898
$a^2 = 0.000500$			

numerical - Liu (21)

small e - Equations (3.27) and (3.28)

arbitrary e - Equations (3.14) and (3.20)

TABLE III - Comparison of Analytical to Numerical Results

	Analytical change in angular momentum equation (5.5)	Numerical change in angular momentum equation (5.4)	% Error
$\alpha = 0.00015$			
n=2, e=0.0	0.012247	0.01220	0.4
n=3, e=0.4196	0.011927	0.01185	0.6
n=5, e=0.6216	0.014170	0.01400	1.2
n=10, e=0.7744	0.018999	0.01889	0.6
n=20, e=0.8720	0.026398	0.02569	2.7
$\alpha = 0.0015$			
n=2, e=0.0	0.038740	0.03840	0.8
n=3, e=0.4196	0.037718	0.03719	1.4
n=5, e=0.6216	0.044808	0.04420	1.3
n=10, e=0.7744	0.060079	0.05910	1.6
n=20, e=0.8720	0.083478	0.08006	4.2
$\alpha = 0.015$			
n=2, e=0.0	0.12247	0.12118*	1.1
n=3, e=0.4196	0.11927	0.11429*	4.4
n=5, e=0.6216	0.14170	0.13219*	7.2
n=10, e=0.7744	0.18999	0.15951*	19.1
n=20, e=0.8720	0.26398	0.17372*	52.0

* Average of the positive and negative conservative and positive and negative liberal estimates, at $f = 0$.

N71-71006

FINAL REPORT
to the
NATIONAL AERONAUTICS AND SPACE ADMINISTRATION
in connection with
NASA Grant NGR 47-004-006

Part 6 of 21 Parts

Final Report
VPI&SU Project 313247

A Study of Spacecraft Powerplant Condensers

by

W. P. Goss
Mechanical Engineering

Virginia Polytechnic Institute & State University
Blacksburg, Virginia

December, 1970

A STUDY OF SPACECRAFT POWERPLANT CONDENSERS

FOREWORD

One proposed spacecraft power generation technique is a nuclear reactor/rankine cycle system. Since a rankine cycle must reject heat to its surrounding environment, an efficient spacecraft condenser to accomplish this heat rejection is necessary. The condenser should be relatively light-weight, thus necessitating high heat transfer coefficients for the condensation process. One method of achieving high heat transfer coefficients is to have the working fluid condense at high velocities inside of small diameter, externally cooled tubes. The analysis of the turbulent, two-phase, annular-mist flow regime which normally occurs in this situation is of major concern in this report. The results of the analysis show the effect of various parameters on the turbulent condensation of steam in small tubes. It was also anticipated that analytical results could also be provided for working fluids other than water, however, they were not complete at the time of this report.

For the reader interested in further details on the analytical work reported here, and on some related experimental work carried out on another grant, the following Masters Theses and Ph.D. Dissertation would be useful.

Taliaferro, O.B., Jr., "A Study of Interfacial Waves and Heat Transfer for Turbulent Condensation in Vertical Tubes", M.S. Thesis, Virginia Polytechnic Institute, April, 1970.

Kammula, K., "An Integral Technique for Predicting Wall and Interfacial Shear Stresses in Turbulent, Condensing, Annular-Mist Flow", M.S. Thesis, Virginia Polytechnic Institute, May, 1970.

Boyer, C.T., Jr., "An Experimental Investigation of the Radial Distribution of Velocity in Turbulent, Condensing, Annular-Mist Flow in Vertical Tubes", M.S. Thesis, Virginia Polytechnic Institute, December, 1970.

Berry, M.R., Jr., "An Integral Analysis of Two-Phase, Annular-Mist Condensing Flows", Ph.D. Dissertation, Virginia Polytechnic Institute, August, 1970.

TABLE OF CONTENTS

	PAGE
LIST OF FIGURES	v
NOMENCLATURE	vii
I. INTRODUCTION.	1
A. Two-Phase Liquid-Gas Flows.	1
B. Review of Literature.	2
C. Statement of the Problem	8
II. THEORETICAL ANALYSIS	12
A. Assumptions.	12
B. Development of Equations	15
1. Resulting Integral Equations.	15
2. Correlations	19
3. Assumed Profiles.	29
4. Simplification of the Equations.	31
C. Starting Equations	32
D. Method of Solution	38
III. RESULTS AND DISCUSSION	41
A. Correlation with Experimental Data	41
B. Heat Transfer Results	52
C. The Effect of Varying the Slip Ratio and the Entrainment Correlation.	54
D. The Effects of Varying the Shear Stress Correlations	57
IV. CONCLUSIONS AND RECOMMENDATIONS	68
V. REFERENCES	70

	PAGE
VI. APPENDICES	75
Appendix A - Derivation of the Integral Equations	75
Appendix B - Correlations	80
Appendix C - Simplification of the Integral Equations.	85

LIST OF FIGURES

	PAGE
Figure 1. Actual Two-Phase, Annular-Mist Flow Pattern . . .	9
Figure 2. Control Volumes for the Theoretical System . . .	16
Figure 3. University of Connecticut Entrainment Correlation .	21
Figure 4. Interfacial Shear Stress Correlation	28
Figure 5. Control Volumes at the Inlet	34
Figure 6. Axial Pressure Distribution for UCONN Run 62364. .	42
Figure 7. Axial Pressure Distribution for UCONN Run 72764. .	43
Figure 8. Axial Pressure Distribution for VPI Run 22 . . .	44
Figure 9. Axial Pressure Distribution for VPI Run 32 . . .	45
Figure 10. Axial Pressure Distributions for NASA Runs 171 and 172	49
Figure 11. Axial Gas Velocity Distributions.	51
Figure 12. Heat Transfer Correlations.	53
Figure 13. Entrainment Flow Rate Variations for UCONN Run 72764.	55
Figure 14. Wall Shear Stress Variations for UCONN Run 72764 .	56
Figure 15. Effects of S_E and γ on the Pressure Distribution for UCONN Run 72764	58
Figure 16. Variation of Interfacial Shear Stress Correlation .	60
Figure 17. Effect of Varying the Interfacial Shear Stress Correlation.	61
Figure 18. Effect of Varying the Interfacial Shear Stress Correlation for UCONN Run 72764	63

	PAGE
Figure 19. Variations of the Wall Shear Stress Correlation. .	64
Figure 20. Effect of Varying the Wall Shear Stress Correlation for UCONN Run 72764	66
Figure 21. Effect of Varying the Wall Shear Stress Correlation on the Axial Pressure Distribution for UCONN Run 72764.	67

NOMENCLATURE

A	Area (ft^2)
a_i	Parameters in the Entrainment Correlation, Equation (II-9)
a_{ij}	Coefficient Matrix Defined by Equation (II-27)
b_i	Column Matrix Defined by Equation (II-27)
c_j	Coefficients Defined by Equation (B-14)
c_p	Specific Heat ($\text{B}/\text{lb}_m \text{F}$)
D	Inside Diameter of the Condensing Tube (ft)
Δx	Increment in the Axial Direction (ft)
d_{ij}	Coefficient Matrix Defined by Equation (C-8)
e_i	Coefficients Defined by Equation (C-8)
g_c	Universal Constant ($32.174 \text{ lb}_m \text{ft}/\text{lb}_f \text{sec}^2$)
h	Enthalpy (B/lb_m)
h_{coef}	Annular Liquid Film Heat Transfer Coefficient ($\text{B}/\text{hr ft}^2 \text{F}$)
J	Conversion Factor ($778.26 \text{ ft lb}_f/\text{B}$)
K	Modified von Karman Constant as Used in the Wall Shear Stress Correlation
k	Constant in the Entrainment Correlation, Equation (II-9)
k_p	Square Root of the Ratio of the Vapor to the Liquid Momentum Fluxes, $(\rho_g V_G^2 / \rho_f V_L^2)^{1/2}$
P	Absolute Static Pressure (lb_f/ft^2)
\dot{q}''	Total Radial Heat Transfer Rate Per Unit Surface Area of the Condensing Tube ($\text{B}/\text{ft}^2 \text{sec}$)
R	Radius of Constant Area Duct (ft)
S_E	Entrainment Slip Ratio
T	Temperature (F)

T_w	Inside Wall Temperature (F)
t	Nondimensional Parametric Variable in the Entrainment Correlation
u	Local Velocity in the Axial Direction (ft/sec)
V	Velocity at a Specific Point or Average Velocity (ft/sec)
W	Flow Rate (lb_m/hr)
X	Entrainment Dynamic Quality
x	Distance from the Tube Entrance in the Axial Direction (ft)
y	Distance from the Tube Wall in the Radial Direction (ft)
α	Core Void Fraction
β	Ratio of the Liquid to the Vapor Density
γ	Variable in the Entrainment Correlation
δ	Time-Averaged Thickness of the Annular Liquid Film (ft)
θ	Dynamic Quality
μ	Dynamic Viscosity ($lb_f \text{sec}/ft^2$)
ψ_j	Column Matrix Defined by Equation (II-27)
ρ	Density (lb_m/ft^3)
τ	Shear Stress (lb_f/ft^2)

Subscripts

c	Core, Coolant
cl	Centerline
E	Entrained Liquid
f	Liquid at Saturation Conditions
G	Gas, Vapor
g	Vapor at Saturation Conditions
I	Interface between the Gaseous Core and the Annular Liquid Film
i	Index Notation ($i=1, 4$)

j	Index Notation (j=1,4)
L	Liquid in the Annular Film
o	Entrance Conditions
T	Total
w	Wall
x	In the Flow Direction

Superscripts

+	Dimensionless Quantity used in the Wall Shear Stress Correlation (Quantity Times $\sqrt{\tau_w \rho_f / g_c} / \mu_L$)
---	--

I. INTRODUCTION

Any combination - solid-liquid, solid-gas, or liquid-gas - in motion constitutes a two-phase flow. Recently, considerable emphasis has been placed on liquid-gas flow since a thorough understanding of this type flow is necessary in the design and analysis of refrigeration cycles, condensers, evaporators, boilers, and, more recently, to space technology and nuclear reactor research. In these investigations, the calculation of two-phase pressure drop and heat transfer characteristics are of utmost importance.

A. Two-Phase Liquid-Gas Flows

Several possible flow regimes are known to exist for the flow of a liquid and gas in a duct. Of the many types listed in the literature, the flows are, in general, classified as one or a combination of several of five main regimes - stratified flow, bubble flow, slug flow, annular flow, and mist flow.

Two-phase flows may also be categorized as one-component or multi-component flows. The term multi-component is used to describe flows in which there are more than one molecular species, such as air-water or oil-natural gas flows. Furthermore, two-phase flows may be either diabatic where heat is exchanged with the surroundings or adiabatic.

The particular flow studied in this report is a diabatic one-component flow, and it is a combination of the annular flow and mist flow regimes termed two-phase, annular-mist flow. It may be described as the confined concurrent flow of a vapor and a liquid in a circular duct where a portion of the liquid flows in a low velocity annular film in contact

with the duct wall, while the remainder of the liquid flows as entrained particles in a relatively high velocity gaseous core. The flow enters the duct as a pure vapor. Due to the cooling at the duct wall, the vapor begins to condense and the two-phase, annular-mist pattern forms. The condensation process continues until that point where liquid flows alone in the duct.

The design of high performance, high vapor velocity internal flow tube condensers will depend on how accurately the two-phase pressure drop and heat transfer characteristics can be calculated. Many analytical predictions of two-phase, annular-mist flow have been proposed to date. Most models offer simplicity at the expense of sufficient accuracy. It is the purpose of this report to present a model that accurately predicts the two-phase, annular-mist flow system described previously. Also, it is hoped that parts of this thesis will stimulate further developments in this area which is still lacking in useful analytical and experimental techniques.

B. Review of Literature

Most of the two-phase flow literature presently available is based on two-component, gas-liquid systems with no condensation or mass transfer. The traditional flow maps of Baker [1], Vohr [2], and Alves [3] are generally accepted for predicting the conditions under which various flow patterns occur. Although there is some discrepancy in the flow maps of the various authors, the annular-mist regime for an air-water mixture flowing adiabatically in a tube is associated with gas velocities in excess of 100 feet per second and annular liquid velocities in the range 0.1

to 10 feet per second. The effect of heat transfer on the system is not reported. Most investigators assume the condensing process will not alter the flow regime maps. It seems possible, for example, that the liquid may not wet the surface macroscopically. The condensate would then form liquid droplets which would be swept off the surface by the high velocity gas stream. If this dropwise condensation were to predominate, a mist type flow could exist where annular flow would normally be predicted. A discussion of dropwise condensation may be found in reference [4].

Much of the early literature in two-phase flow is devoted to predicting two-phase pressure drop without regard to the type of flow pattern. The pioneer publications of Lockhart and Martinelli [5] and Martinelli and Nelson [6] are good examples where semi-empirical frictional pressure drop correlations are presented without reference to flow patterns. Some investigators [7, 8, 9] report that it is not uncommon to encounter errors of $\pm 100\%$ while applying these correlations to two-phase annular flows. As with any method which leads the way in a particular field, much effort is spent on modifications and improvements of that method to apply to a specific problem. For example, McMillan et al. [9] proposed a modification of the Lockhart-Martinelli correlation which includes the interfacial shear stress for use in annular flows. Wallis [10] introduces a modification for hydrostatic pressure forces. However, the fact that numerous investigators are still applying the original correlation to any number of flow patterns clearly points out that improved methods are needed for the determination of two-phase pressure drop.

More recently, most of the literature published in the field of two-phase flow has been concerned with either one flow pattern or, at

the most, two related flow patterns. Within the specialty of two-phase, annular-mist flow itself, there is a wealth of literature, especially adiabatic two-component flows. Rather than try to list all sources, it is suggested that the reader refer to the literature surveys of Gouse [11] and Caughron [7] and the texts of Tong [12] and Wallis [13]. Nevertheless, several of the more significant references should be mentioned, especially those pertaining to condensing flows, many of which will be discussed in detail in the remaining sections of this report.

The pressure drop and heat transfer in annular two-phase flow systems are affected by three factors - friction, momentum, and gravity. Soliman et al. [14], Andeen and Griffith [15], and Carpenter and Colburn [16] discuss the relative contribution of these factors to the two-phase pressure drop in condensing flows. Friction dominates at high and intermediate qualities, while the contribution due to the momentum flux becomes increasingly important at high density ratios (liquid to vapor) and can dominate in the low quality region. The effect of gravity will naturally depend on the orientation of the system. For vertical downward flows, the contribution of gravity is normally negligible for all but low qualities [14, 16, 17]. For vertical upward condensing flows, it is known that slugging and plugging of the tube can occur due to folding and run-back of the liquid film. The effect of gravity on horizontal systems is discussed by Pletcher and McManus [18]. As long as the gas velocity is high enough to maintain the annular-mist flow pattern, gravity effects are negligible in horizontal systems.

Of utmost importance in determining the two-phase pressure drop and heat transfer characteristics in annular flow is the ability to predict

accurate wall and interfacial shear stresses. Analytical predictions of these shear stresses are complicated, since the interaction of the slow moving liquid and the high speed gas results in interfacial wave characteristics which are not well understood. The presence of interfacial waves has been verified by many investigators. Hewitt and Roberts [19] present photographs of the interfacial waves for an air-water mixture. For single-component condensing flow, the recent experimental investigation of Taliaferro [20] presents wave amplitude and frequency measurements. Further investigations of this nature may eventually lead to methods for predicting interfacial wave characteristics. Until that time, analyses must be based on models that assume a time-averaged annular liquid film with a smooth gas-liquid interface. The existing wall and interfacial shear stress correlations are based on this type of model. The wall shear stress correlation of Kammula [21] is based on the equations normally used in single-phase flow modified to account for high interfacial shear stress and mass transfer. Dukler [22] and Hilding [23] have presented semi-empirical wall shear stress correlations which account for the high turbulent intensities in the time-averaged liquid film that are a consequence of the interfacial behavior.

An interfacial shear stress correlation is presented by Levy [24]. The correlation is based on adiabatic two-component annular flow data, and correlates only a limited amount of data [8, 35].

Several investigators have tried to avoid the problem of determining wall and interfacial shear stresses by incorporating equivalent friction factors in their analyses of pressure drop in two-phase annular flows. These friction factors are determined in a variety of ways.

Hoffman [26] and Wrobel and McManus [27] use the well-known Blasius friction factor by varying the constants to fit two-phase annular flow pressure drop data. The friction factor used by Wallis [28] is assumed to be given by the equivalent value for vapor flowing alone in the duct. Chien and Ibele [29] present experimental techniques for determining superficial friction factors for vertical flows.

With the exception of the data of Hilding [30], the available entrainment data are taken from the adiabatic flow of a two-component mixture flowing annularly. Cousins et al. [31] shows that for air-water flow, a minimum "length" is necessary before entrainment takes place. The experimental procedure was to extract the annular liquid film and measure the amount of entrainment by measuring a new liquid film growth. The entrainment correlation of Paleev and Filippovich [32] is based on a similar technique. Wicks and Dukler [33] and Magiros and Dukler [34], using a sampling probe, found that the rate of flow of the entrained phase was fairly constant over the tube cross-section. Hilding's data [30] was taken from condensing steam flowing in an annular-mist pattern. The data was taken at the centerline of the tube. Goss [35] presents a correlation of this data.

There is a wealth of experimental data for pressure drop of a two-component mixture (usually air-water) flowing adiabatically in an annular-mist pattern. For condensing flows, however, the experimental data is somewhat limited. Hilding [36], Taliaferro [20], and Goodykoontz and Dorsch [37,38] present data for pressure drop and heat transfer coefficients for the flow of condensing steam. In all cases, the condensing tubes were cooled by water flowing annularly in a coaxial tube.

An annular-mist flow pattern was observed visually for the data of Hilding while the annular film measurements of Taliaferro strongly suggest a similar pattern. No mention of a flow pattern is made by Goodykoontz et al. [37,38]. Complete condensation data is reported for all tests except for those of Taliaferro where the steam was extracted at a point 11.4 feet from the entrance and condensed externally. Also, with the exception of Taliaferro, the data at the condenser entrance is questionable. The Goodykoontz data must be back-extrapolated in order to determine the entrance pressure. Furthermore, an unexplained stability problem was reported with this data [37]. In some cases, static pressure fluctuations were reported which were an order of magnitude higher than the overall pressure drop. These experimental investigations will be discussed further in the Results section of this report.

Goodykoontz and Brown [39] present data for the vertical-downward flow of condensing Freon-113. This data was taken from the same condensing facility as the condensing steam data of Goodykoontz and Dorsch [37], and the same entrance effects and stability problems are noted.

Due to its application to the design of condensers for Rankine cycle space power systems, there are some data available for condensing liquid metals. Sawochka [40] reports performance data for potassium during condensation inside single tubes. Nemkoong et al. [41] and Lottig et al. [42] present similar data for condensing mercury flows. Fenn et al. [43] present data for potassium condensing in a multitube heat exchanger. No mention is made as to the type flow patterns obtained for the majority of the data. One exception is the data of Nemkoong [41] where a glass condensing tube was used for condensing mercury. It was found that the

mercury condensate did not wet the tube surface and appeared as entrained particles and small patches on the tube walls. The ratio of the observed average velocity of the drops in the vapor stream to the local vapor velocity varied from 0.3 at the inlet to 1.0 at approximately three-fourths of the condensing length.

C. Statement of the Problem

The purpose of this investigation is to develop an analysis which can be used to predict pressure drop and heat transfer characteristics for two-phase, annular-mist condensing flows. A high-speed, pure fluid in a saturated gaseous state is introduced into a tube which is externally cooled. There is no restriction on the means of cooling. The inlet gas will condense into a radially symmetric, slow-moving, thin annular film on the tube wall. Due to the shearing action of the high-speed gas, traveling waves will form at the gas-liquid interface; and eventually the gas begins to shear off the wave peaks. The liquid entrained in this manner is carried along in the gas and subsequently redeposited on the wavy liquid film. This process of liquid particle interchange continues up to the point where complete condensation occurs. The actual flow pattern is shown in figure (1).

A complete analytical description of the flow must include the unsteady behavior of the waves at the liquid-vapor interface and the accompanying mass transfer across the interface due to both the macroscopic particle interchange and molecular condensation. Since it is not feasible at this time to include a wavy interfacial region, an analysis is presented which attempts to account for the wavy interface without

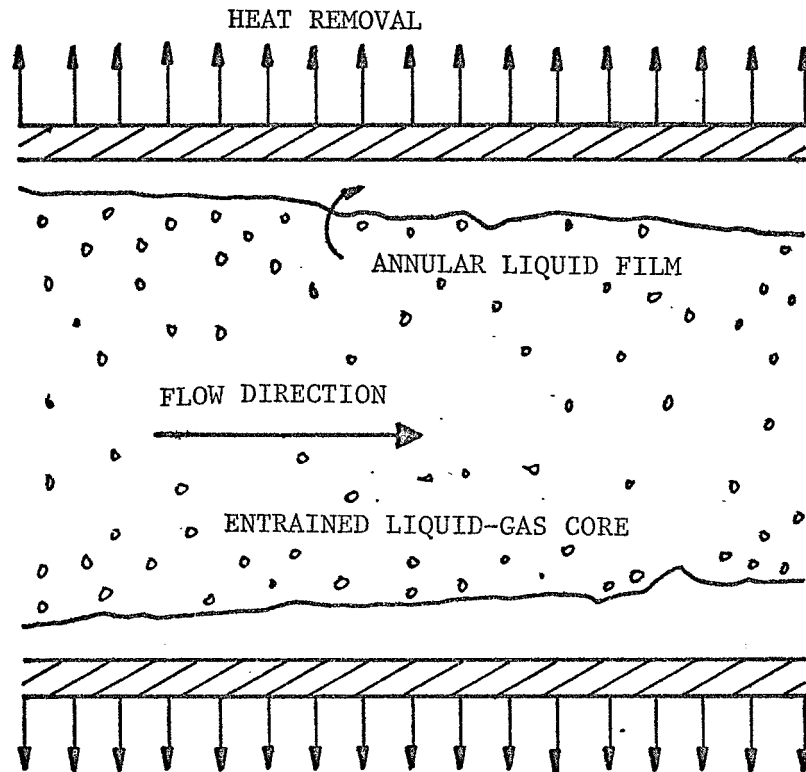


Figure 1. Actual Two-Phase, Annular-Mist Flow Pattern

actually analyzing the interface itself. The analysis is based on a time-averaged annular liquid film with a smooth gas-liquid interface. The interfacial waves affect the mass, momentum, and energy transfer mechanisms between the core and the annulus. These effects are included in this analysis in the following ways:

1. Mass Transfer - An entrainment correlation which predicts the amount of entrained liquid flowing in the gaseous core is employed.
2. Momentum Transfer - This effect must be determined at both the interface and the wall. The high-velocity, entrainment-laden, gas core tends to drag the liquid annulus along while the rigid tube wall tends to retard it. Therefore, effective interfacial and wall shear stresses are included at the gas-liquid interface and the tube wall, respectively.
3. Energy Transfer - The energy transferred at the liquid-gas interface is related to both the mass and the momentum transfer. When vapor is condensed, there is a change in enthalpy which gives rise to a large energy change. Also, there is a large change in kinetic energy associated with the momentum transfer process at the interface.

The inclusion of the interfacial effects in the above manner reduces the analysis to a two-dimensional axisymmetric system with an entrained liquid-gas core region and an annular liquid film region, the thickness of which is the time-averaged value of the actual unsteady liquid film. From this system, it is possible to start with the pure gas inlet conditions and the external cooling configuration and,

subsequently, completely describe the flow at each point throughout the tube up to the point of complete condensation.

II. THEORETICAL ANALYSIS

A. Assumptions

The following assumptions are made in developing the theoretical analysis of the two-phase, annular-mist flow system:

1. The fundamental laws which describe the system are: the conservation of mass, Newton's Second Law, and the conservation of energy.
2. The flow is steady. This assumption is possible since the quantities associated with the core and the liquid annulus are assumed as time and area average quantities, as discussed in the Introduction.
3. The flow is two-dimensional and axisymmetric. The flow pattern is a vapor core containing entrained liquid particles surrounded by a uniform liquid annulus of which the thickness varies with the axial direction only. This follows from assumption (2) and the discussion in the Introduction on gravity forces.
4. The total flow area is a constant. A cylindrical duct of uniform internal diameter is assumed as the flow passage.
5. Body forces are negligible. The only body force that warrants mention is that due to gravity. A discussion of gravity forces is included in the Introduction.
6. A variation in the radial direction of the axial component of velocity is allowed in both the core and the annular regions.

7. The core is homogeneous and its associated thermodynamic properties are assumed at the saturation conditions corresponding to the static pressure. A discussion of this is given by Collier et al. [44]. Radial variation in a property is allowed when passing from one phase to another.
8. In the liquid annulus, a radial variation in the enthalpy is allowed. The liquid enthalpy at the core-annulus interface is assumed at saturation conditions and varies in the axial direction. The liquid enthalpy at the wall is determined from the wall temperature. The density of the liquid annulus varies in the axial direction only. The effect of subcooling on the density near the wall is neglected.
9. The static pressure varies in the axial direction only. This is not truly rigorous since there are small inertial forces in the radial direction. Inasmuch as there are no body forces in the radial direction, the radial pressure gradient is assumed negligible. Similar reasoning is used in the boundary layer approximations.
10. The contribution of the dynamic portion to the total enthalpy of the liquid flowing in the annulus is neglected. For the range of temperatures and velocities anticipated, the effect of the dynamic portion on both the total enthalpy and the change of total enthalpy with respect to axial position is always less than one percent.
11. The hydrodynamics of the liquid-vapor interface controls the entrainment mechanism. There is a continual interchange

of liquid particles being entrained into the core and redeposited onto the interface. It is therefore assumed that the flow of liquid crossing the liquid-vapor interface includes the effects of entrainment and condensation.

12. A constant ratio of local entrained liquid velocity to local gas velocity (S_E) is assumed throughout the core. This leads to an unrealistic phenomenon near the core-annulus interface for all entrainment slip ratios less than unity; namely, entrainment velocities less than interfacial velocities. In actuality, the entrainment slip ratio varies in the radial and axial directions; but at the present time, this variation is not known. From the available data on the entrainment slip ratio, the general opinion is that its value is near unity [34, 46].
13. The heat transferred out of the system by the external cooling mechanism is the dominant mode of heat transfer. Any thermal radiation within the system or heat transfer due to the axial temperature gradient is negligible compared to that due to the radial temperature gradient.
14. The wall heat flux and the wall temperature are known functions of axial position. In much of the experimental data, the external cooling mechanism is cooling water flowing annularly in a coaxial tube. In this case, since the cooling water flow rate, thermal properties, and temperature are known, the wall heat flux is determined from an energy balance on the coolant flow. If only the external

thermal environment is known, a local heat transfer balance in the radial direction must be made in order to determine the wall heat flux. The correlation of Goodykoontz and Dorsch [37] may be useful in determining the local heat transfer coefficient in terms of the local parameters of the system. This correlation is discussed in the Results section of this report.

B. Development of Equations

1. Resulting Integral Equations

Applying the fundamental laws stated in assumption (1) to the control volumes illustrated in figure (2) and utilizing assumptions (2-13) result in the following set of integral equations. The details of the derivations are shown in Appendix A.

Conservation of mass of the total flow yields:

$$\begin{aligned} \frac{d}{dx} \left[\rho_{cc} \int_{\delta}^R u_c (R-y) dy \right] \\ + \frac{d}{dx} \left[\rho_f \int_0^{\delta} u_L (R-y) dy \right] = 0. \end{aligned} \quad (\text{II-1})$$

Newton's Second Law applied to the total flow yields:

$$\begin{aligned} -\frac{R^2}{2} \frac{dP}{dx} - R \tau_w = \frac{d}{dx} \left[\rho_f \int_0^{\delta} u_L^2 (R-y) dy \right] \\ + \frac{d}{dx} \left[\rho_{cm} \int_{\delta}^R u_c^2 (R-y) dy \right]. \end{aligned} \quad (\text{II-2})$$

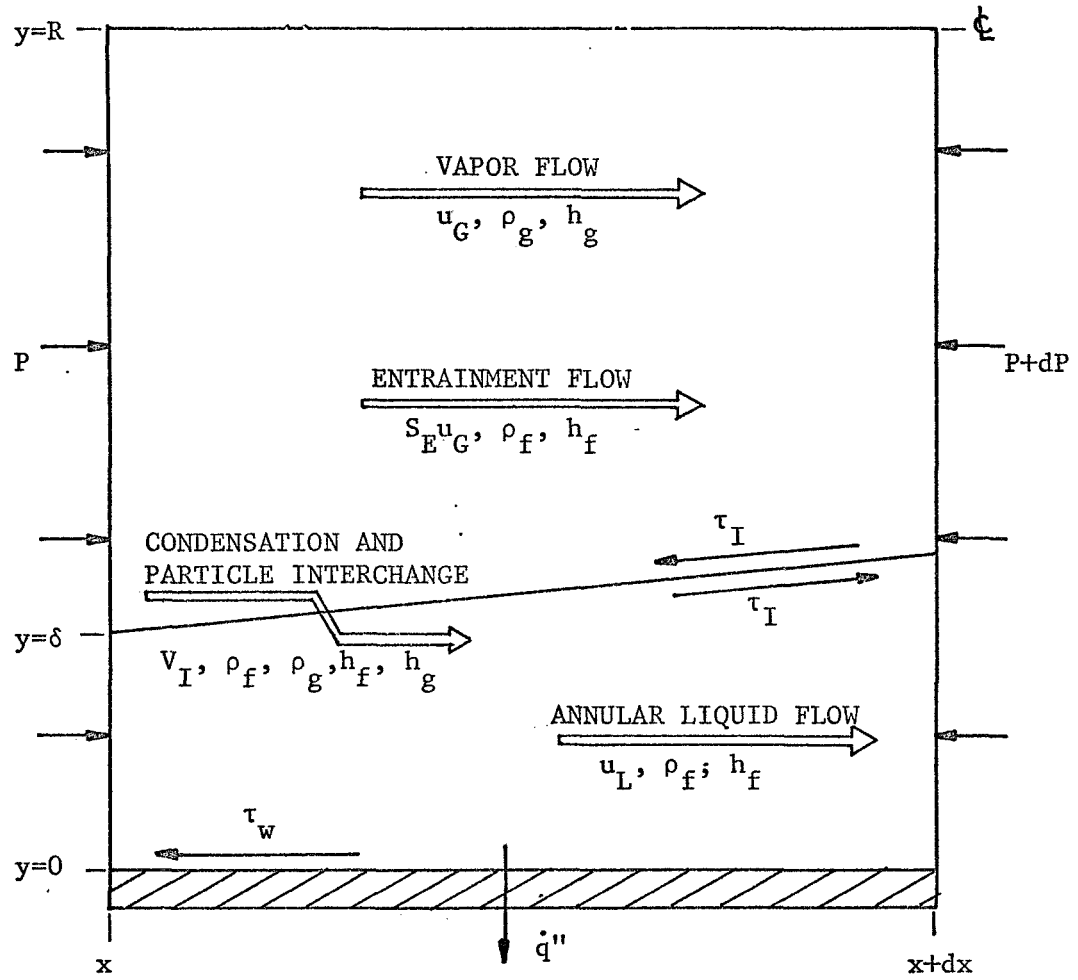


Figure 2. Control Volumes for the Theoretical System

Newton's Second Law applied to the liquid annulus yields:

$$\tau_I (R - \delta) - \delta \left(R - \frac{\delta}{2} \right) \frac{dP}{dx} - \tau_w R =$$

$$\frac{d}{dx} \left[\rho_f \int_0^\delta u_L^2 (R - y) dy \right] - V_I \frac{d}{dx} \left[\rho_f \int_0^\delta u_L (R - y) dy \right]$$

(II-3)

and, applying the conservation of energy to the total flow yields:

$$\frac{d}{dx} \left[\rho_c h_c \int_\delta^R u_G (R - y) dy \right] + \frac{d}{dx} \left[\rho_{ce} \int_\delta^R \frac{u_G^3}{2} (R - y) dy \right]$$

$$+ \frac{d}{dx} \left[\rho_f \int_0^\delta u_L h_L (R - y) dy \right] + R \dot{q}'' = 0$$

(II-4)

where the effective core densities are defined as:

$$\rho_{cc} \equiv \alpha \rho_g + (1 - \alpha) S_E \rho_f \quad (II-5)$$

$$\rho_{cm} \equiv \alpha \rho_g + (1 - \alpha) S_E^2 \rho_f \quad (II-6)$$

$$\rho_{ce} \equiv \alpha \rho_g + (1 - \alpha) S_E^3 \rho_f \quad (II-7)$$

and

$$\rho_c h_c \equiv \alpha \rho_g h_g + (1 - \alpha) S_E \rho_f h_f. \quad (II-8)$$

The above equations (II-1 through II-4) form a set of independent integral equations which must be solved simultaneously to describe the flow system.

There are various methods of solving these integral equations, all of which involve assuming suitable profiles in the radial direction and integrating these profiles, thus reducing the integral equations to ordinary differential equations. Naturally, the closer the assumed profiles come to matching all boundary conditions in the radial direction, the more accurate the solution will be. When the boundary conditions are rather simple, good results may be obtained by applying simple relations for the profiles. An example would be laminar, forced convection flow over a flat plate [47]. As the complexity of the boundary conditions increases, the complexity of the assumed profiles would also increase. However, good results may also be obtained from integral equations when the boundary conditions are complex by assuming algebraically simple profiles and employing empirical or semi-empirical relations to satisfy the complex boundary conditions. This technique is used by Eckert [48] for turbulent, free convection flows. Due to the complexity of the boundary conditions that exist at the vapor-liquid interface for the two-phase, annular mist flow system and also to the limited information available on velocity and temperature profiles, the technique that is used in this analysis is similar to that of Eckert. The following steps will be taken to reduce the set of integral equations into a set of four non-linear, first order, ordinary differential equations with dependent variables V_I , V_L , δ , and P and independent variable x :

- 1) Employ empirical or semi-empirical correlations for the wall shear stress, the interfacial shear stress, and the entrainment flow rate in terms of the dependent variables. At this point, it is noted that the entrainment flow rate does not appear as such in the set of integral equations (II-1 through II-4). This is a consequence of the assumptions made in their derivation (see Appendix A). Since the velocity of the entrained liquid is assumed as a constant (S_E) times the gas velocity, and the density of the entrained liquid is assumed at saturation conditions, the correlation which is needed is one of the entrainment area (or core void fraction, α) in terms of the dependent variables.
- 2) Assume velocity and enthalpy profiles for the core and annular liquid regions in terms of the dependent variables δ , V_I , and V_{ϕ} .
- 3) Perform the necessary integration and differentiation to reduce the equations to a set of four non-linear, first order, ordinary differential equations into a form suitable for solving by numerical techniques.

2. Correlations

In this section, empirical or semi-empirical correlations are presented for entrainment flow rate and wall and interfacial shear stresses.

Entrainment Correlation

As mentioned in the Introduction, there has been no successful analysis on the breakup of the interfacial waves on the liquid annulus in

two-phase, single-component condensing flows. It is generally agreed that droplets are formed from wave instabilities on the film and then entrained in the gas stream. Since the process is basically a dynamic one, it would be anticipated that the axial forces would control the entrainment mechanism, the dominant forces being the gas inertial forces and viscous shear forces. Other forces which may or may not have an appreciable effect are liquid inertial forces, pressure forces, and surface tension.

The majority of the available correlations [31, 32, 33] are based on two-phase, annular-mist flow data of two components flowing adiabatically in a tube, usually air and water. Data taken at equilibrium conditions, or when the entrainment rate equals the redistribution rate, might well be less than that which would occur in condensing flows of a single component when equilibrium conditions are highly unlikely. Grace [49] indicates that most entrainment data is taken at non steady-state conditions; and thus it is not surprising that these values differ from experiment to experiment.

Due to the scatter in the available entrainment correlations and the question of applying air-water data, taken under adiabatic conditions, to condensing flows, a modification of the approximate correlation presented by Goss [35] will be used in this analysis. The correlation is based on experimental data taken at the University of Connecticut [30] from two-phase, annular-mist flow of condensing steam using a Dussourd probe [50]. The correlation is illustrated in figure (3) along with the effect of the modification. The correlation is given in parametric form by the following expressions:

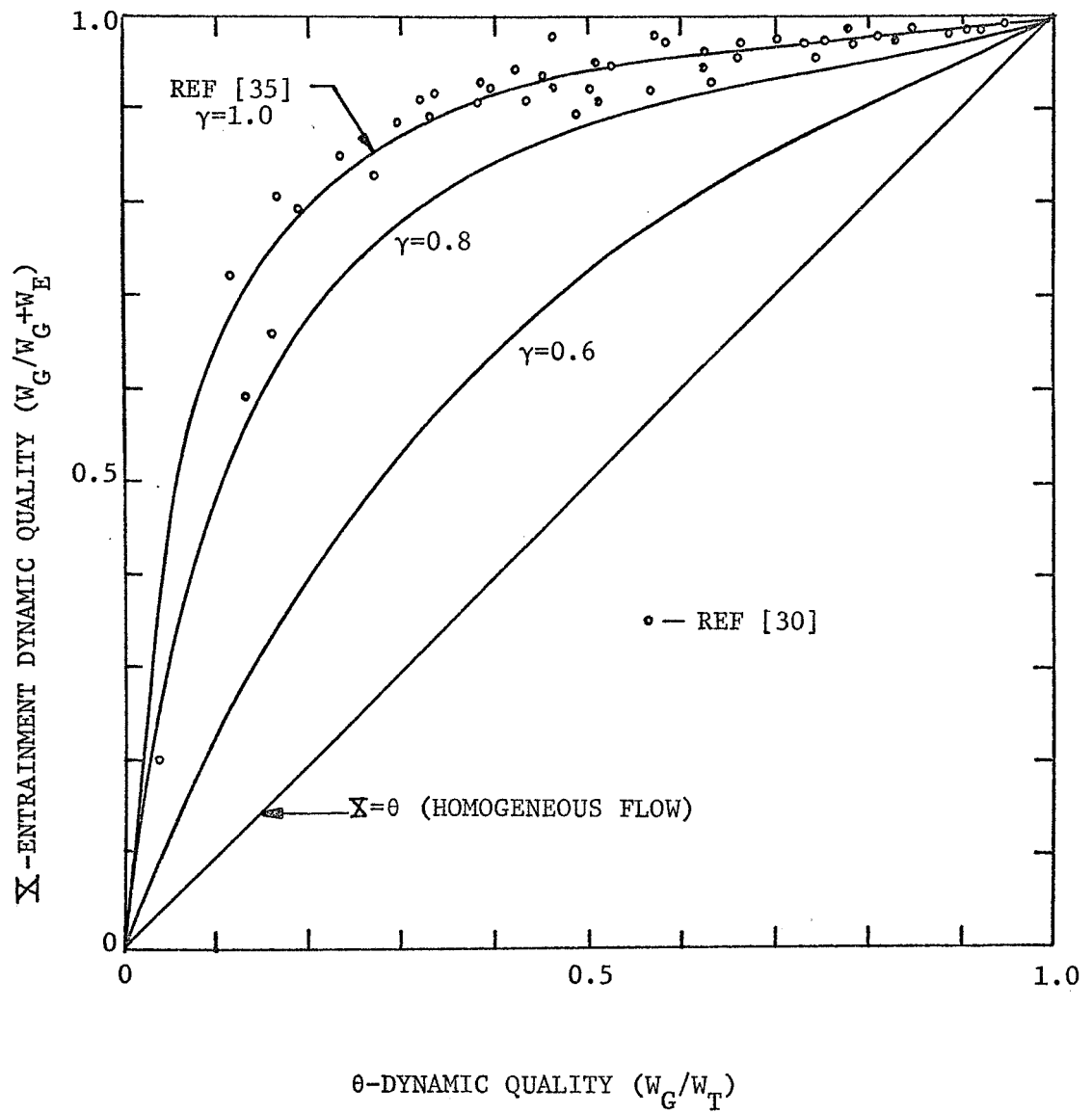


Figure 3. University of Connecticut Entrainment Correlation

$$\theta = k[(1-a_1)t - a_2t^2 - a_3t^3 - a_4t^4] \quad (\text{II-9})$$

$$\bar{X} = 2kt - \theta \quad (\text{II-10})$$

where

$$\begin{aligned} k &= 0.707107 \\ a_1 &= 0.638377\gamma \\ a_2 &= 1.137108\gamma \\ a_3 &= -2.246910\gamma \\ a_4 &= 0.794244\gamma \end{aligned}$$

It is noted [35] that the experimental entrainment flow data was calculated by assuming that the entrainment slip ratio was unity, whereas, if it had been assumed less than unity, the entrained liquid flow would have been higher. For entrainment slip ratios greater than 0.5, the variable γ approximately allows for a deviation in the entrainment flow rates due to including a variable entrainment slip ratio in the data reduction analysis used to obtain the University of Connecticut data [30]. Also, if the entrained particles were not distributed evenly throughout the core, as they probably are not, it is expected that the point of least concentration would be at the center. This is precisely where the probe used to obtain the data was located. These may be reasons why this correlation gives lower values than those obtained by Taliaferro [20] at Virginia Polytechnic Institute. If indeed the concentration of particles is greatest near the interface, they would be moving at a somewhat lower velocity than those near the center of the core and the effect of using an underprediction of entrainment in the analysis should be small.

The area of entrainment flow (or core void fraction, α) is related to the entrainment dynamic quality (X) by the following expression:

$$\alpha = \frac{X \beta S_E}{1 + X \beta S_E - X} \quad (\text{II-11})$$

The details of the use of the entrainment correlation in the analysis are given in Appendix B.

Wall Shear Stress

The determination of the wall shear stress for two-phase, annular-mist flows is a formidable task. Compared to the determination of wall shear stress for turbulent single-phase flows, which has been a point of discussion for several years, there are further complications that arise on account of the interfacial phenomena. Based on an order of magnitude analysis, Hilding [23] indicates very high turbulence intensities in the liquid film; and over the major portion of the condensing length, fluctuating velocity components are of the same order of magnitude as the mass average axial liquid velocity. Because of the high turbulence intensities in the film, it is expected that transition would occur much sooner. Carpenter and Colburn [16] suggest transitional Reynolds numbers, based on the liquid thickness, as low as 240. Also, as a consequence of the deep penetration of the surface waves, it is expected that the laminar sublayer adjacent to the tube wall is quite small. From the above discussion, it is obvious that any valid correlation for wall shear stress for two-phase, annular flow must depend on the interfacial phenomena.

Dukler [22] and Hilding [23] have presented semi-empirical wall shear stress correlations which account for the high turbulent intensities in the liquid film for the case of large interfacial shear stress. Dukler's analysis does not include the inertial effects of the annular liquid film. Hilding assumes a flat average velocity distribution in the turbulent portion of the annular liquid film along with a small laminar sublayer which has a linear distribution. The parameter which accounts for the interfacial shear conditions is the ratio of the gas to liquid momentum fluxes.

The wall shear stress correlation which is used in this analysis is the semi-empirical correlation of Kammula [21] with slight modifications. The equations normally used to predict the velocity distributions and eddy viscosities in single-phase flow are adapted to fit condensing annular-mist flows with high interfacial drag by including a term which accounts for the interfacial shear stress and mass transfer. The procedure involves assuming a value for the wall shear stress and numerically integrating through the liquid film to determine the resulting flow rate in the liquid film. An iteration procedure is used to adjust the wall shear stress until the actual liquid film flow rate is attained.

The liquid film flow rate is given by the expression

$$\omega_L = \pi D \mu_L \int_0^{\delta^+} \left(1 + \frac{2 \delta / D}{\delta^+} y^+ \right) dy^+ \quad .$$

$$\int_0^{y^+} \frac{\tau / \tau_w}{1 + \frac{1}{2} \left\{ -1 + \sqrt{1 + 4 \frac{\tau}{\tau_w} K^2 y^{+2} [1 - \exp(-y^+/A^+)]^2} \right\}} dy^+ dy^+ \quad (II-12)$$

where the shear stress distribution is given by

$$\frac{\tau}{\tau_w} = \frac{R}{R-y} \left[1 - \left(\frac{2R-y}{2R-\delta} \right) \frac{y}{\delta} \left\{ 1 - \frac{\tau_I}{\tau_w} \left(\frac{R-\delta}{R} \right) \right\} \right] \quad (\text{II-13})$$

In eq. (II-12), K is the von Karman constant modified for annular-mist flow and A^+ is the Van Driest turbulent damping constant which has a value of 26 for fully developed turbulent flow.

Kammula [21] suggests several correlations for obtaining the modified von Karman constant (K) as a function of other system properties. Unfortunately, these correlations are based on only one set of data; that of Hilding [36]. It was found from the present investigation that the expressions suggested in [21] do fit the University of Connecticut data [36] quite well. However, the expressions which correlate more of the data with which this analysis will be compared, including that of Hilding, are given as follows:

$$\begin{aligned} \text{for } k_p < 28 \\ K &= 0.4 (1 + k_p)^{1.43} \\ \text{for } k_p > 28 \\ K &= 6.63 (1 + k_p)^{0.6} \end{aligned} \quad (\text{II-14})$$

Also, it was found that Kammula's wall shear stress correlation could be used near the entrance region where the flow in the annular liquid film is laminar by modifying the turbulent damping constant (A^+). Increasing this constant has the effect of increasing the thickness of the laminar sublayer. Near the entrance, where the liquid film is thin, increasing the damping constant tends to make the majority of the liquid film laminar. The variation of the turbulent

damping constant used in this analysis for liquid film Reynolds numbers less than 500 is expressed as

$$A^+ = 43 - \frac{17 R_{eL}}{500} \quad (\text{II-15})$$

where the liquid film Reynolds number is based on the annular film thickness. A further discussion of the wall shear stress correlation is presented in Appendix B.

Interfacial Shear Stress

There is very little information, either experimental or analytical, available in the literature on the shear stress at the gas-liquid interface of a turbulent two-phase system. A number of investigators have assumed that the slow moving, wavy, annular liquid layer may be treated, insofar as the gas is assumed, as a rough cylindrical solid boundary. The interfacial shear stress is then correlated with the gas kinetic energy and a roughness parameter associated with the wave dimensions. This method has the obvious drawback that the literature is also lacking in the area of interfacial wave characteristics in two-phase annular systems. Also, an analysis for shear stress which may be valid for turbulent flow in the vicinity of a solid boundary should not be expected to hold for turbulent flow in the vicinity of a gas-liquid interface. This is because the liquid, although essentially incompressible, is a fluid which can transmit shear through turbulent fluctuations, while a solid cannot due to no slip condition at the gas-solid interface.

Levy [24] has developed a correlation for interfacial shear stress by starting with the basic parameters of the problem, those of

the turbulent fluctuations or the Reynolds stresses. His procedure is similar to that of Prandtl and von Karman in determining the well-known logarithmic velocity distribution function but differs in that density fluctuations are included. The final correlation was based on experimental data of water or alcohol and argon or nitrogen flowing annularly. Goss [35] compared the experimental data for single component flows taken at the University of Connecticut to Levy's correlation. Levy's correlation predicted higher interfacial shear stresses in general; however, the same trend was present. A recent publication of Linehan et al. [52] emphasizes the necessity for including the effect of mass transfer on the interfacial shear during annular film condensation and concludes that a model including this effect must be used but that further work must be done in this area before such a model can be developed.

An interesting result is obtained as a by-product of the wall shear stress work of Kammula [21]. The ratio of interfacial to wall shear stresses is correlated as a function of the ratio of momentum fluxes (k_p) and the dynamic quality (θ). However, when compared to Hilding's data [36], much scatter is seen to exist. In the present investigation, it was found that when the quantity $(1 + \tau_I \theta / \tau_w)$ was plotted versus the dynamic quality (θ) as shown in figure (4), a useful correlation resulted.

The following expressions correlate the data very well for qualities between 10 and 95 percent:

for $1.0 > \theta > 0.745$

$$1 + \tau_I \theta / \tau_w = 2.0 \theta^{0.589}$$

for $0.745 > \theta > 0.1$

$$1 + \tau_I \theta / \tau_w = 1.735 \theta^{0.111} \quad (\text{II-16})$$

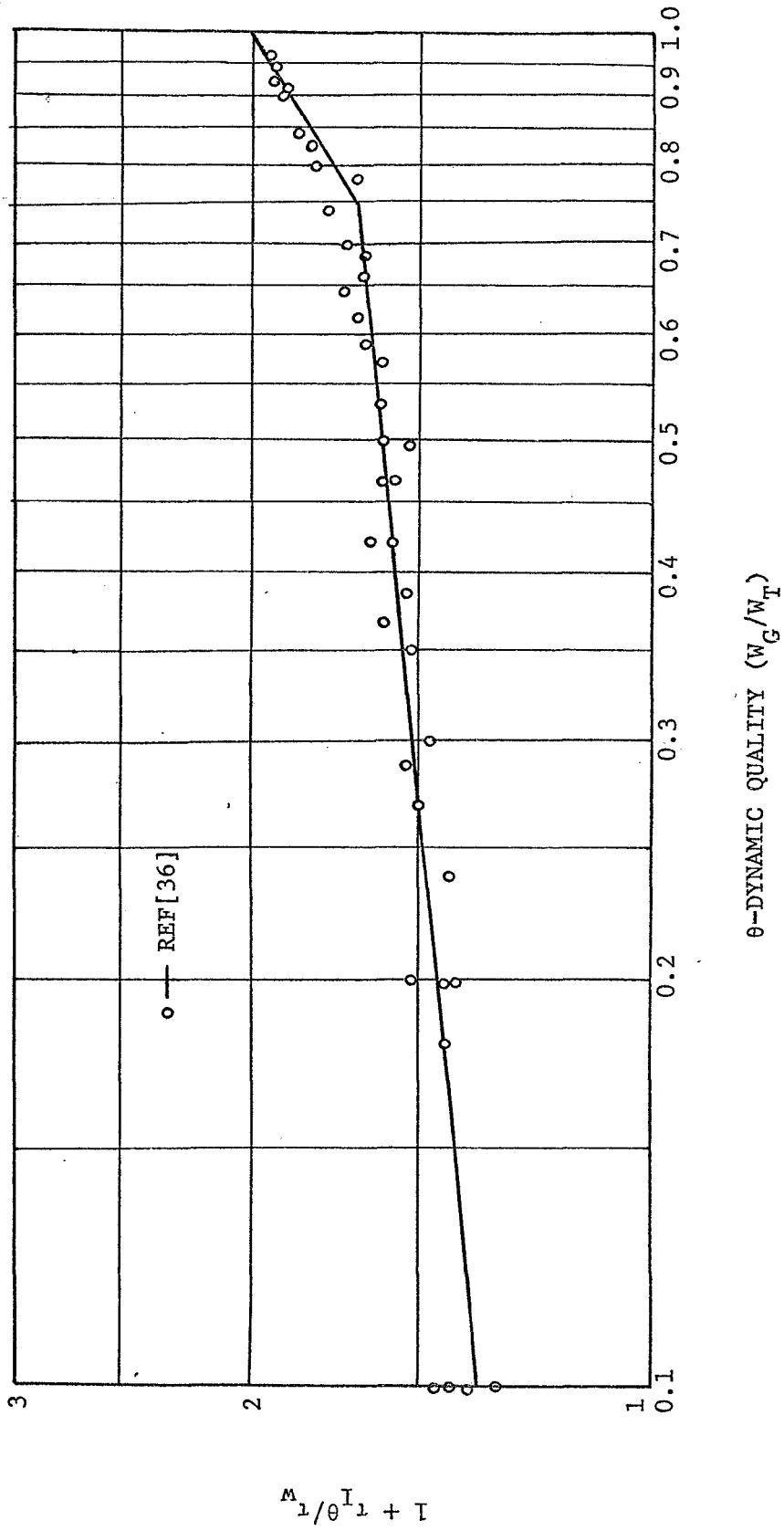


Figure 4. Interfacial Shear Stress Correlation

The above expressions are solved for the ratio of interfacial to wall shear stress and used as an input to the wall shear stress correlation of Kammula [21]. Once the wall shear stress is obtained from this correlation, the interfacial shear stress is determined from equation (II-16). Appendix B contains a discussion of the use of this interfacial shear stress correlation.

3. Assumed Profiles

The experimental measurements of velocity and temperature profiles in two-phase annular flow is an area of the literature where very limited information can be obtained. As yet, there appears to be no successful technique for making local velocity measurements in the annular liquid region. This is due mainly to the random fluctuations of the wavy interface and the relatively small thickness of the stable portion of the liquid film. Virtually no data was found on temperature distributions in the annular region of single-component condensing flows.

Several investigators [53, 54, 55] have probed the core region of an adiabatic two-component mixture flowing annularly. There is a general agreement that the velocity profiles appear similar to those of fully-developed, single-phase turbulent flows but more peaked. Gill [55] indicates that due to the presence of the annular liquid flow, the velocity profiles are strikingly different, having an almost parabolic shape. Also, his results suggest that the velocity profile and turbulence characteristics of the disperse-phase core in annular flow is primarily controlled by the roughness of the film-covered wall, and so far, there is no evidence of any direct effect of the spray. He concludes that

there is not enough data available at this time to model accurately the core velocity profile. Cravarolo [53] indicates a similar trend based on data taken at a point 140 diameters from the entrance of an adiabatic two-component system. The profiles were in general steeper than single-component flow and became more flattened as the gas flow rate increased. A more detailed discussion of velocity distributions in two-phase annular flow may be found in references [12] and [13].

Because of the lack of experimental data on velocity and temperature distributions, there have been numerous hypotheses made on the analytical description of the profiles. In general, these fall into two classes - modifications of the Prandtl-Nikuradse universal profiles and the power-law type. While these profiles are shown to work well for the particular cases where they are employed, there are no universally accepted analytical models. For this reason, the velocity profile models to be used in this analysis are of the power-law type with the exponents left as independent variables. They are given by the following expressions:

$$u_L = V_I (y/\delta)^n \quad (\text{II-17})$$

$$u_G = V_I + (V_E - V_I) \left[\frac{y - \delta}{R - \delta} \right]^m \quad (\text{II-18})$$

The assumed profiles satisfy the boundary conditions for velocity that

$$\text{at } y = 0, u_L = 0 \quad (\text{II-19})$$

$$\text{at } y = \delta, u_L = u_G = V_I \quad (\text{II-20})$$

$$\text{and, at } y = R, u_G = V_{\zeta} \quad (\text{II-21})$$

Since it is assumed in this analysis that the thermal properties are functions of the local saturation temperature only, specifying a temperature profile will also specify the enthalpy distribution. By the nature of equation (II-4), enthalpy is a convenient parameter, and the following distributions are assumed:

$$h_L = h_{fw} + (h_f - h_{fw})(y/\delta)^\ell \quad (\text{II-22})$$

$$h_G = h_g \quad (\text{II-23})$$

The boundary conditions that are satisfied are that

$$\text{at } y = 0, h_L = h_{fw} \quad (\text{II-24})$$

$$\text{at } y = \delta, h_L = h_f \text{ and } h_G = h_g \quad (\text{II-25})$$

$$\text{at } y = R, h_G = h_g \quad (\text{II-26})$$

The assumed profiles allow the freedom of arbitrarily varying the shape of the profile as a function of the distance from the condenser entrance, thereby allowing developing flows and determining the effect of velocity and enthalpy distribution on the dependent variables P , δ , V_I , and V_{ζ} . Also, by assuming the exponents m , n , and ℓ equal to zero, the analysis reduces to a one-dimensional analysis similar to that of Goss [35].

4. Simplification of the Equations

Upon substitution of the assumed profiles into the set of integral equations (II-1 through II-4) and performing the integration in the radial direction, followed by the differentiation with respect to the independent variable (x), with much rearranging and combining,

the following set of non-linear, first order, ordinary differential equations, written in index notation, results:

$$a_{ij} \frac{d\psi_j}{dx} = b_i \quad (\text{II-27})$$

where

$$\begin{aligned} a_{ij} &= a_{ij} (V_I, V_{\ell}, \delta, P) \\ b_i &= b_i (V_I, V_{\ell}, \delta, P, x) \\ \psi_1 &= V_I \\ \psi_2 &= V_{\ell} \\ \psi_3 &= \delta \\ \psi_4 &= P \end{aligned}$$

The details of the simplification, along with the definitions of the coefficient matrix (a_{ij}) and the column matrix (b_i) are given in Appendix C.

C. Starting Equations

The equations (II-27) form a set of non-linear, first order, ordinary differential equations which may be solved by numerical techniques at any axial position other than at the inlet of the condenser. At this point, assuming the annular film has not formed, the equation derived from Newton's Second Law applied to the annular liquid region (II-3) reduces to a zero identity. Since it is impossible to solve the three remaining equations for the four dependent variables, a set of algebraic equations which apply at the entrance only will be developed.

Applying the same fundamental laws used to derive the integral equations (II-1 through II-4) to the control volumes shown in figure (5) yields a set of four non-linear algebraic equations which may be applied at the inlet of the condenser, provided an annular liquid region has not formed. The assumptions made in the development of this set of equations are:

1. The flow is one-dimensional.
2. If the dynamic quality is less than unity (i.e., some condensate enters the tube), all of the liquid flow is assumed as entrainment. This entrainment flow rate and the associated entrainment flow area are assumed to remain constant over the increment.
3. The interfacial velocity is equal to twice the average liquid film velocity.
4. The densities and enthalpies of each phase remain constant over the increment.
5. The wall and interfacial shear stresses are known.
6. The wall heat flux is known.
7. The static pressure, the total flow rate, the total area, and the dynamic quality at the inlet are given.

Mass

Applying the conservation of mass to the control volume (figure 5) for the entire flow results in

$$W_T = \rho_g V_G A_G + \rho_f V_L A_L + W_E \quad (\text{II-28})$$

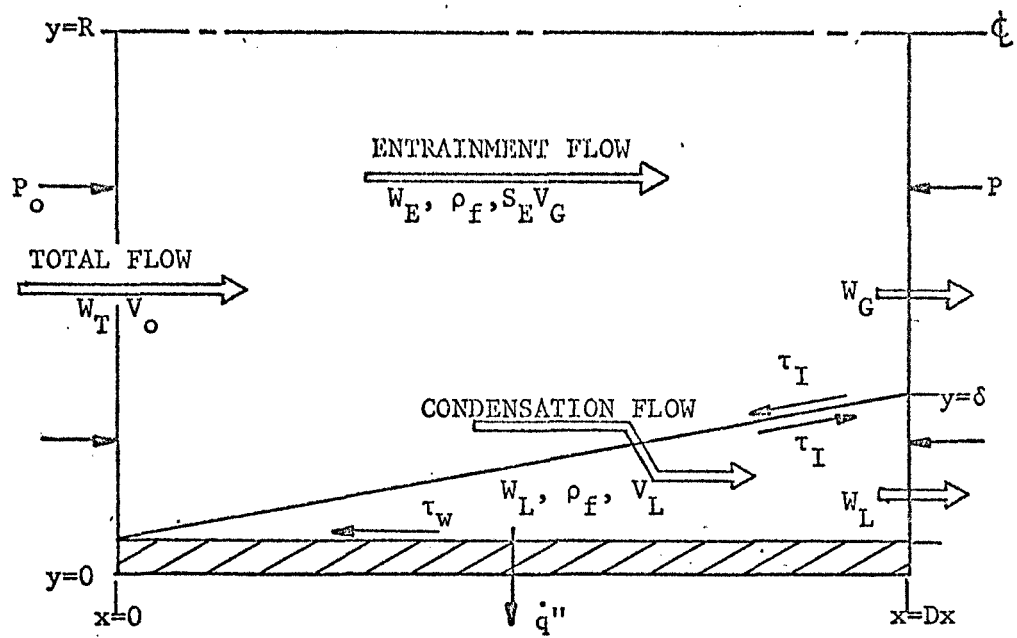


Figure 5. Control Volumes at the Inlet

which, when solved for the gas velocity at the point Dx, yields:

$$V_G = \frac{W_T - W_E}{\rho_g A_G} - \frac{\rho_f V_L (A_T - A_G - A_E)}{\rho_g A_G} \quad (\text{II-29})$$

Momentum

As in the development of the integral equations, Newton's Second Law is applied to both the control volume for the entire flow and the control volume for the liquid annulus only (figure 5). When applied to the total flow, the result is

$$\begin{aligned} P_o A_T - P A_T - 2\pi R D x \tau_w &= -V_o (W_T - W_E) - V_o S_E W_E \\ &+ \rho_f V_L^2 (A_T - A_G - A_E) + \rho_g V_G^2 A_G + V_G S_E W_E \end{aligned} \quad (\text{II-30})$$

which, when solved for the static pressure at the point Dx, yields:

$$\begin{aligned} P &= \frac{1}{A_T} \left[P_o A_T - 2\pi R \tau_w D x + V_o (S_E W_E + W_T + W_E) \right. \\ &\quad \left. - \rho_f V_L^2 (A_T - A_G - A_E) - \rho_g A_G V_G^2 - V_G S_E W_E \right] \end{aligned} \quad (\text{II-31})$$

Newton's Second Law applied to the annular liquid film yields:

$$\begin{aligned} -P A_L + \left(\frac{P + P_o}{2} \right) A_L + 2\pi (R - \delta/2) D x \tau_I \\ - 2\pi R D x \tau_w &= \rho_f A_L V_L^2 - V_I (\rho_f A_L V_L) \end{aligned} \quad (\text{II-32})$$

or, by rearranging and recalling assumption 3,

$$\rho_f V_L^2 = 2\pi \tau_I \left(\frac{\delta}{2} \right) \frac{D\chi}{A_L} - \left(\frac{P_o - P}{2} \right) - 2\pi R \frac{D\chi}{A_L} (\tau_I - \tau_w) \quad (\text{II-33})$$

The area and thickness of the annular liquid film may be written as:

$$A_L = A_T - A_G - A_E \quad (\text{II-34})$$

and

$$\delta = R - \sqrt{\frac{A_G - A_E}{\pi}} \quad (\text{II-35})$$

Substitution of equations (II-34) and (II-35) into equation (II-33), and solving for the liquid velocity, results in:

$$V_L = \left\{ \frac{1}{\rho_f} \left[\frac{\pi \tau_I D\chi}{A_T - A_G - A_E} \left(R - \sqrt{\frac{A_G - A_E}{\pi}} \right) - \left(\frac{P_o - P}{2} \right) - \frac{2\pi R (\tau_I - \tau_w)}{A_T - A_G - A_E} \right] \right\}^{1/2} \quad (\text{II-36})$$

Energy

Applying the conservation of energy to the control volume for the total flow (figure 5) results in

$$\begin{aligned} -2\pi R D\chi \dot{q}'' = & - \left(h_o + \frac{V_o^2}{2} \right) (W_T - W_E) - S_E^2 \frac{V_o^2}{2} W_E \\ & + \left(h_g + \frac{V_g^2}{2} \right) (\rho_g V_g A_G) + h_f \rho_f V_L A_L + S_E^2 \frac{V_g^2}{2} W_E \end{aligned} \quad (\text{II-37})$$

which, when solved for the area of the gas at the point Dx , yields:

$$A_G = \left[\left(h_o + \frac{V_o^2}{2} \right) (W_T - W_E) + S_E^2 \frac{V_o^2}{2} W_E \right. \\ \left. - 2\pi R Dx \dot{q}'' - S_E^2 \frac{V_G^2}{2} W_E - h_f \rho_f V_L (A_T - A_E) \right] \\ \div \left[\left(h_g + \frac{V_G^2}{2} \right) \rho_g V_G - h_f \rho_f V_L \right] \quad (\text{II-38})$$

From the area of the gas, the annular liquid film thickness may be obtained from equation (II-35).

The above equations (II-29, II-31, II-36, and II-38) form a set of non-linear, algebraic equations in the variables V_L , V_G , A_G , and P . Given the inlet pressure, the dynamic quality, the total area, and the total flow rate, these equations can be solved by an iterative method of successive substitutions. The procedure is as follows:

1. Assume values for the liquid velocity (V_L), the gas area (A_G), and the wall and interfacial shear stresses.
2. Solve equation (II-29) for the gas velocity (V_G) and equation (II-31) for the static pressure (P).
3. From these quantities, calculate new values for the liquid velocity from equation (II-36) and the gas area from equation (II-38).
4. Repeat steps (2) and (3) until the difference between successive approximations is less than one percent of the

latest approximation.

5. Calculate the liquid film thickness from equation (II-35).

D. Method of Solution

As stated in the assumptions, it is assumed that the wall temperature and wall heat flux are known as a function of axial position. Given the inlet conditions of pressure, total flow rate, and dynamic quality, the complete flow pattern can be solved from the inlet to the point of complete condensation by using the equations and correlations developed in the previous sections of this report. Due to the complex form of the equations, a closed-form solution is not feasible at this time. To solve the equations numerically, the following steps were carried out:

1. Choose an increment in the axial direction. The best choice of an increment size is a function of many variables. The two main functions are the algorithm used to solve the equations and the accuracy of the digital computer used. A thorough discussion of numerical techniques for solving ordinary differential equations may be found in reference [28].
2. Apply the starting equations (II-29, II-31, II-36, and II-38) to the first increment to obtain the variables at the point Dx . If an annular pattern exists at the inlet and the variables V_I , V_t , δ , and P are known, this step may be omitted.

3. Solve for the numerical values of the derivatives in equations (II-27). Since all variables are known at an axial position x , equations (II-27) may be solved numerically as a set of simultaneous linear equations for the numerical values of the derivatives $(d\psi_j/dx)$ at this position. The method used in this report is the IBM Scientific Subroutine SIMQ [56].
4. Euler's method of numerical integration is then utilized to determine values of the dependent variables at a position $x + Dx$.

$$\psi_j \Big|_{x+Dx} = \psi_j \Big|_x + \frac{d\psi_j}{dx} \Big|_x Dx \quad (\text{II-39})$$

It was decided to use Euler's method even though it is a first order procedure since most higher order methods require several recalculations of the derivatives in equations (II-27). Inasmuch as the calculations in step (3) are rather lengthy, the use of Euler's method along with a small increment size is actually more feasible. A step size of 0.05 ft was found to be optimum for the data presented in this report. There was a negligible change in the results when the increment was reduced, until a value of 0.005 ft where round-off error began to distort the solution. Further discussion on this point is contained in reference [57].

5. Determine the remainder of the parameters at the axial position $x + Dx$ from the variables $\psi_j \Big|_{x+Dx}$.
6. Repeat steps (3 through 5) until the point of complete condensation occurs.

III. RESULTS AND DISCUSSION

The analysis presented in the previous sections of this report was programmed for use on the Virginia Polytechnic Institute Computer Center's I.B.M. 360/65 Digital Computer..

A. Correlation with Experimental Data

The analytical results were compared with data from three experimental investigations. The specific runs chosen for comparison were numbers 62364 and 72764 of the data reported by Hilding [36], numbers 22 and 32 of Taliaferro [20], and numbers 171 and 172 of Goodykoontz and Dorsch [37]. Hereafter, these data will be referred to as UCONN, VPI, and NASA, respectively. The parameters compared were the static pressure distributions for all six runs and the average gas velocities for the UCONN runs. Static pressure distributions for the UCONN and VPI data are shown in figures (6) through (9). Although not illustrated graphically, dynamic quality distributions and total condensation lengths compared extremely well in all cases where experimental data was available. For the particular cases tested, the dynamic quality remained approximately a linear function of axial position and was not affected substantially by varying other parameters in the analysis.

There are five main parameters which may be varied in the analysis. These are the three profile exponents (m , n , and l), the entrainment slip ratio (S_E), and the entrainment flow correlation variable (γ). In most cases, the variation of the velocity and enthalpy profile exponents had a negligible effect on the axial static pressure

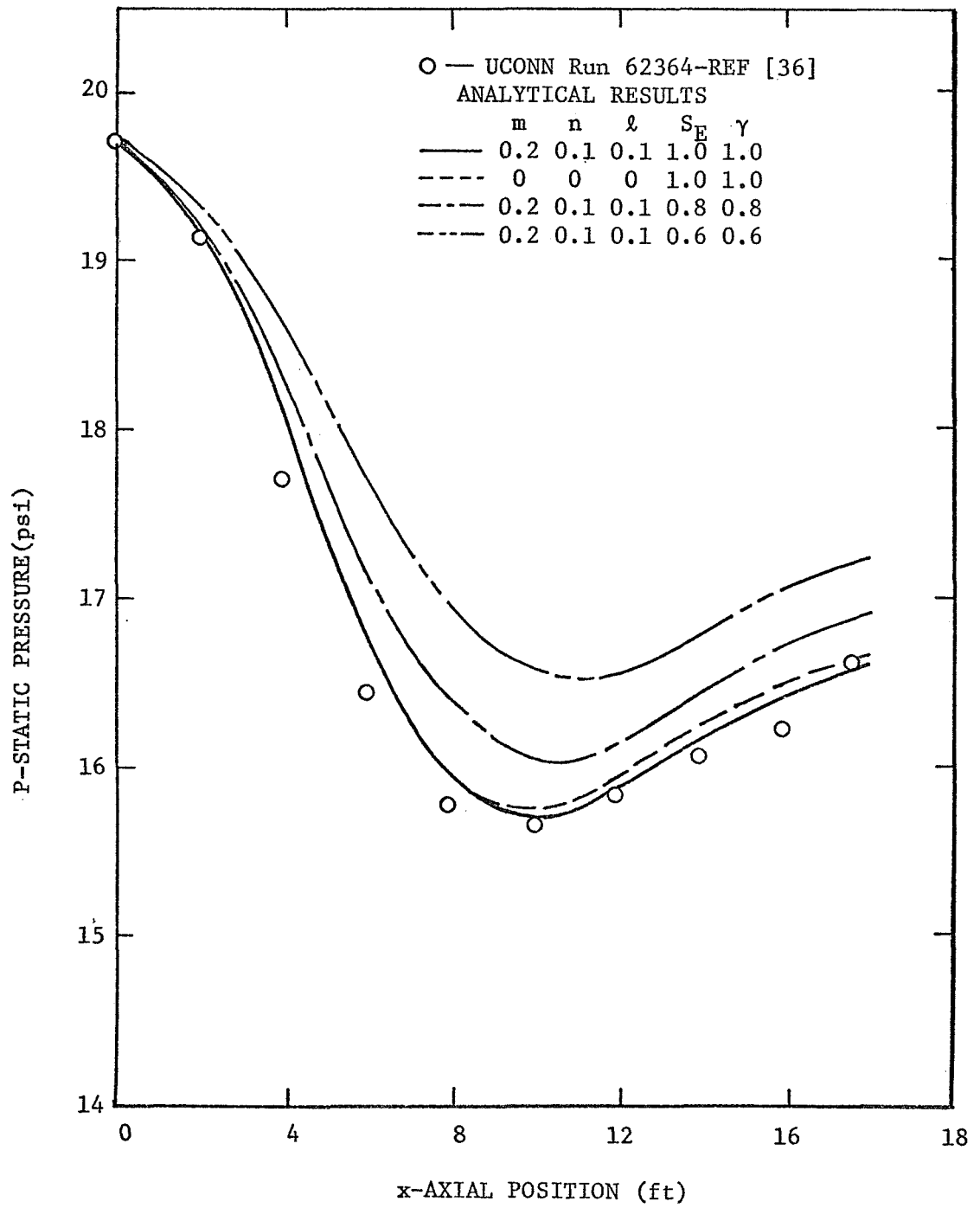


Figure 6. Axial Pressure Distribution for UCONN Run 62364

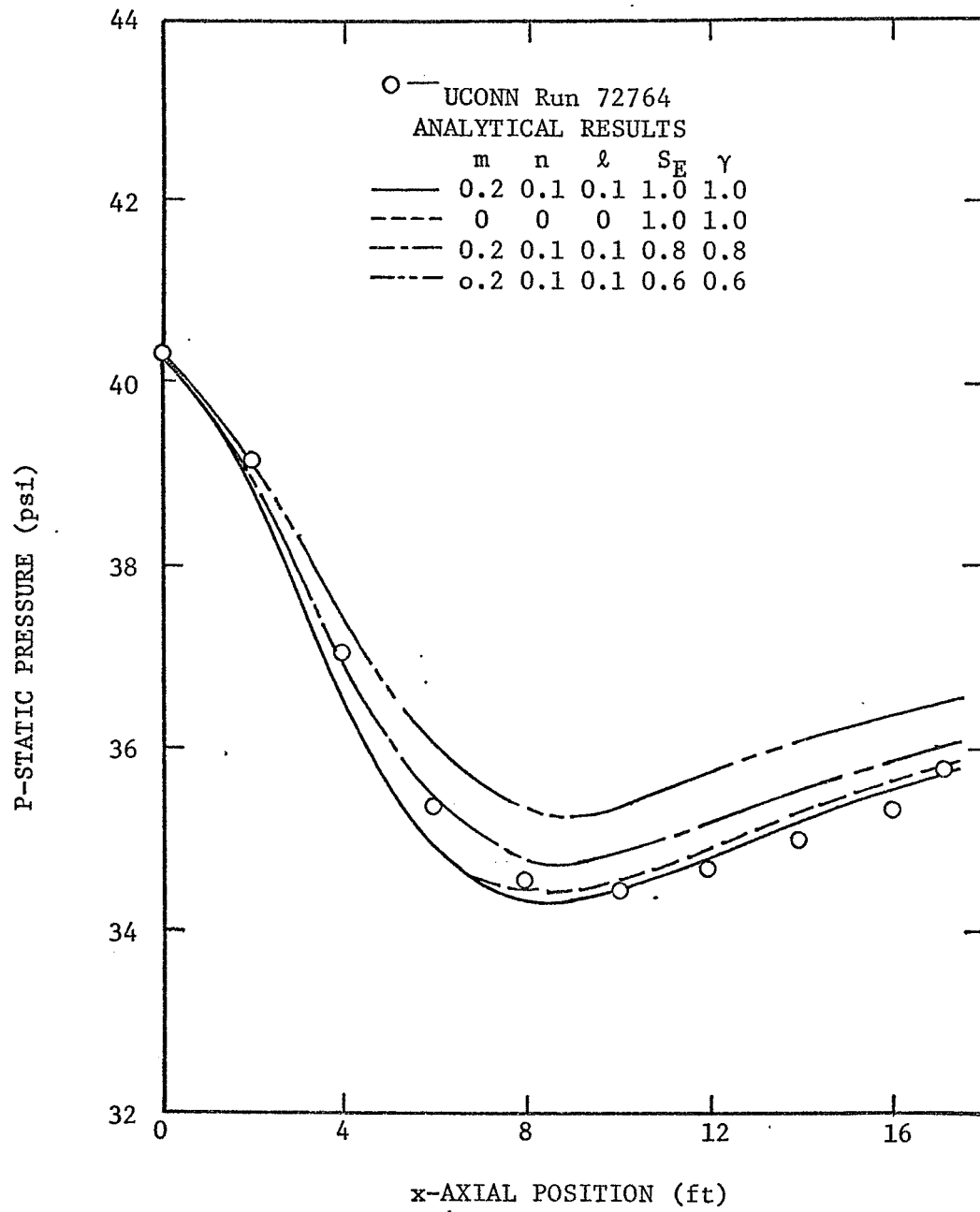


Figure 7. Axial Pressure Distribution for UCONN Run 72764

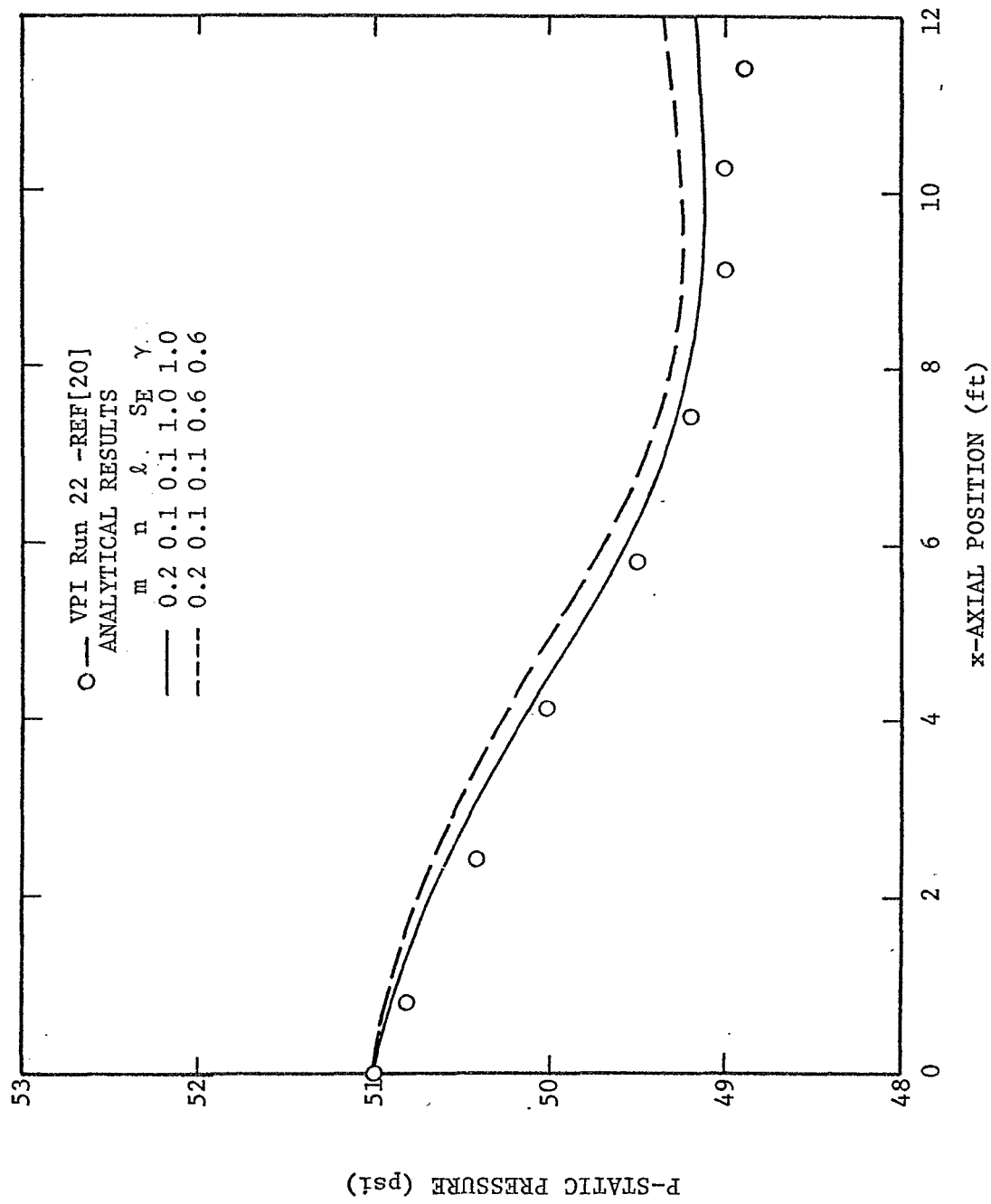


Figure 8. Axial Pressure Distribution for VPI Run 22

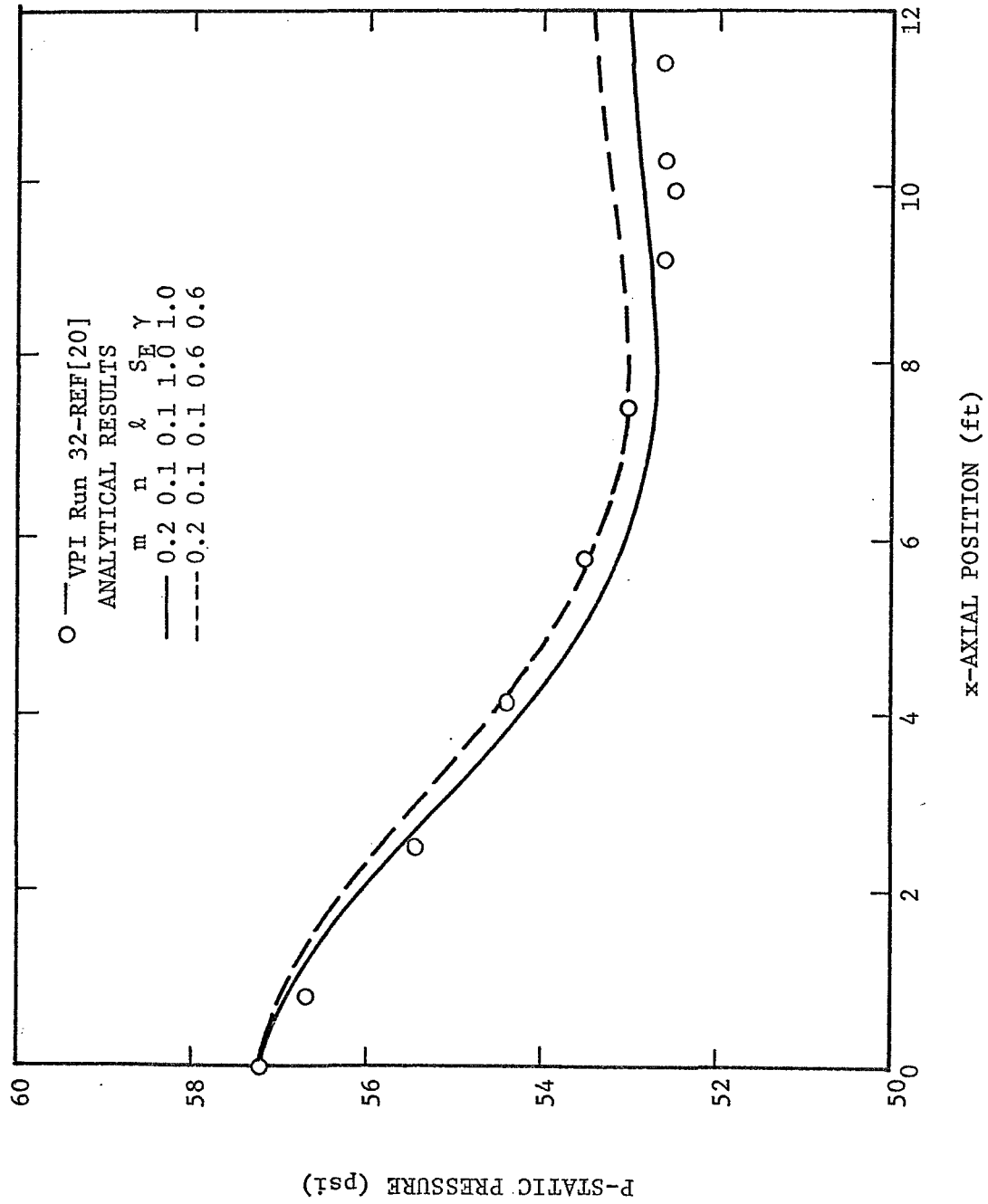


Figure 9. Axial Pressure Distribution for VPI Run 32

distributions and the other variables in the analysis. The UCONN data is, in general, for high-velocity condensing steam (entrance velocities in excess of 600 fps), and a variation in the shape of the velocity profiles alters the momentum contribution to the static pressure change more (figures 6 and 7) than for the lower velocity VPI runs (figures 8 and 9). A difference is seen in figures (6) and (7) between the two-dimensional and one-dimensional (all exponents equal to zero) models for γ and S_E equal to unity.

Since the shape of the profiles seem to have very little effect on the analytical results, the profiles which were used to obtain the remainder of the results were a one-fifth velocity profile for the core and one-tenth profiles for the velocity and the enthalpy distributions in the annular liquid film. These profiles agree with the general trends reported in the rather limited experimental data which is discussed in the previous sections of this thesis. Analytical solutions for developing type flows (i.e., profiles which vary from zero at the entrance as a function of axial position) show no appreciable difference as compared to fully developed flows; again, any difference being for the higher velocity runs.

The effect of varying the entrainment slip ratio (S_E) and the entrainment correlation variable (γ) on the axial static pressure distribution is also illustrated in figures (6) through (9). In all cases, a reduction in S_E and γ below a value of unity reduces the overall static pressure drop. The effect is not as great on the lower velocity VPI runs. As discussed previously, the entrainment correlation variable (γ) is included to account approximately for a variable entrainment slip ratio

in the experimental data reduction analysis. This data reduction analysis [35] was used to obtain the data from which the entrainment correlation was derived. For this reason, the analytical results are normally presented with S_E and γ being equal. In a later section of this chapter, the separate effects of varying S_E and γ on the static pressure distributions and other variables in the analysis will be illustrated.

The axial static pressure distributions shown in figures (6) through (9) have the same general shapes. After some maximum static pressure drop, the frictional pressure drop becomes less than the pressure recovery due to the change in momentum. At that point, the static pressure begins to increase. This is due primarily to the decrease in the wall shear stress which is a consequence of the thickening of the annular liquid film. In all cases, no appreciable deviations between the one- and two-dimensional results were observed until the pressure recovery, due to the change in momentum, significantly offset the frictional pressure drop.

As discussed in the Review of Literature, there are certain limitations to each of the sets of experimental data to which the analytical results are compared. All three experimental facilities were cooled externally by cooling water flowing in a co-axial tube. The UCONN facility consisted of a horizontal 1 1/16-inch i.d. copper tube. The system was not well instrumented in the entrance region. The analytical results shown in figures (6 and 7) cannot be considered as typical results. Of the six sets of UCONN data correlated, figures (6 and 7) show the closest comparison with experimental static pressure data. For other runs, the analysis predicted overall pressure drops which were larger

than those reported in reference [36].

The VPI facility consisted of a 3/4-inch i.d. copper tube oriented for vertical downward flow. The data is subject to the limitation that complete condensation does not occur in the tube. Dynamic qualities at the exit ranged from 18 to 72 percent. The general agreement between analytical and experimental results shown in figures (8 and 9) for the static pressure distributions are typical of the four sets of VPI data correlated for this investigation. The effect of varying the profile exponents and the entrainment slip ratio was much less for the lower velocity VPI runs than for the UCONN data.

For the NASA data, a 0.293-inch i.d. copper tube oriented for vertical downward flow was used as a condenser. The annular gap between the condenser tube and the cooling water jacket was only 0.064 inch. The small gap induced high coolant velocities at low coolant mass flow rates. Figure (10) illustrates the agreement obtained between analytical results and experimental data for the NASA data. In general, the NASA data can be categorized into two classes - those similar to run 172 in which the static pressure remained fairly constant or, as in run 171, where the overall pressure drop is quite large. Runs 171 and 172 were chosen as examples since they are actually quite similar runs. At the entrance for both runs, the dynamic quality, the total steam flow rate, the static pressure, and, as a result, the vapor velocity and Reynolds number, were equal. NASA runs 171 and 172 differ only in external thermal environments. The difference was that the coolant flow rate for run 172 was approximately 65 percent higher. It was also

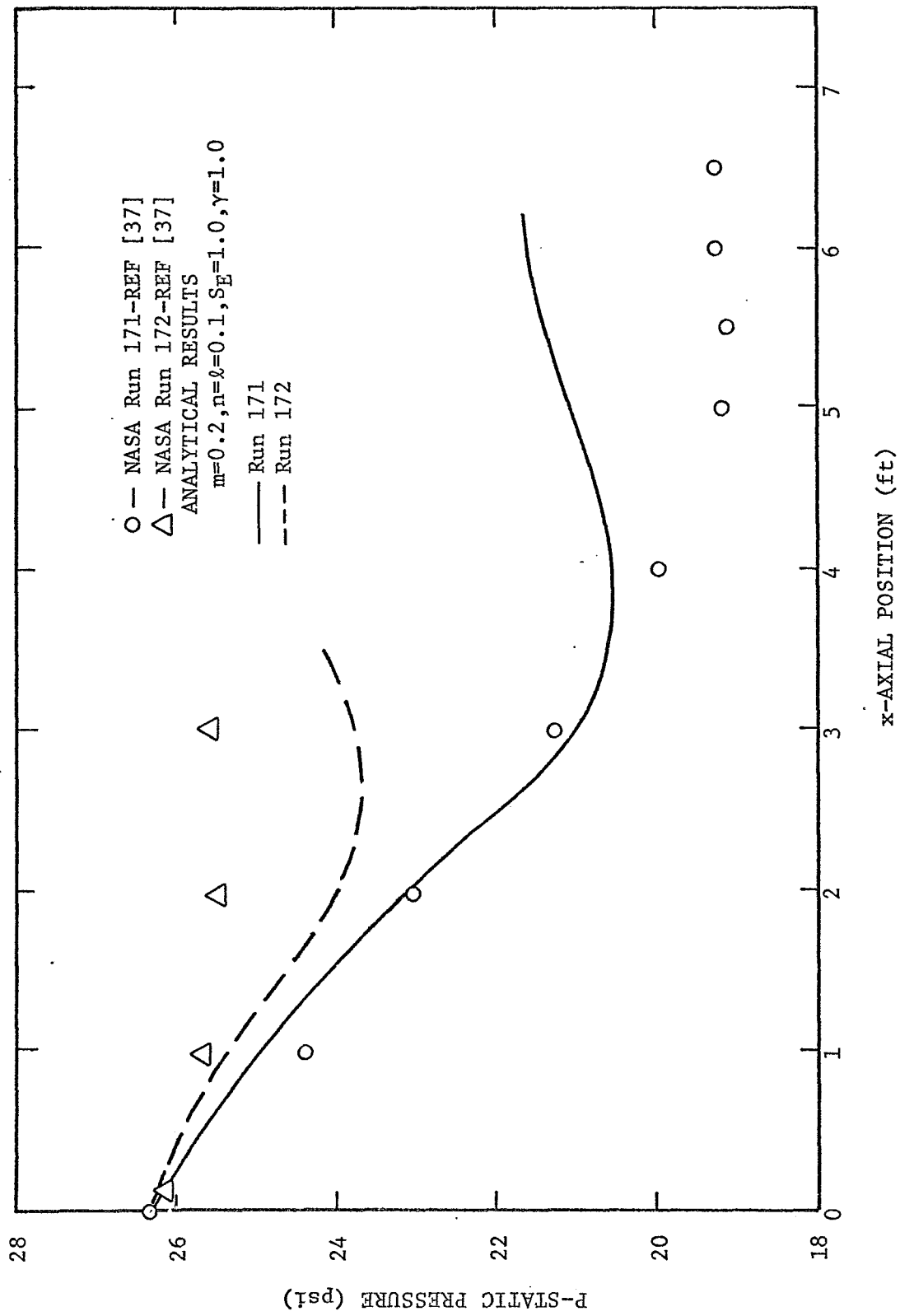


Figure 10. Axial Pressure Distribution for NASA Runs 171 and 172

indicated [37] that for the same entrance conditions, a further increase in the coolant flow rate resulted in runs in which the static pressure increased throughout the run. The analytical results repeatedly predicted too large a pressure drop for the small pressure drop runs and vice versa, as illustrated in figure (10). As mentioned previously, the inlet region of the NASA condenser was not completely instrumented, and accurate inlet conditions are difficult to obtain. Also, it should be emphasized that even though the NASA flow parameters lie well within the region normally observed as the annular-mist flow regime, no indication is made [37] as to the flow pattern obtained during the actual runs. Furthermore, some of the NASA data was subject to pressure fluctuations. This was probably due to the presence of the boiler and superheater in the condensation loop, whereas the steam was supplied from an external source for the UCONN and VPI facilities.

Figure (11) illustrates a comparison of analytical results and experimental data for mass average gas velocity for UCONN runs 62364 and 72764. The results agree with the trend of the data. The major problem with this comparison is that the accuracy of the present methods for measuring gas velocities in two-phase, annular-mist flows is not known. Also shown in figure (11) are the predicted average gas velocities for the VPI data which are considered as relatively low-velocity, two-phase, annular-mist runs in this investigation. Variations of the profile exponents or the entrainment parameters (S_E and γ) have a negligible effect on the average gas velocities. This is discussed further in a subsequent section.

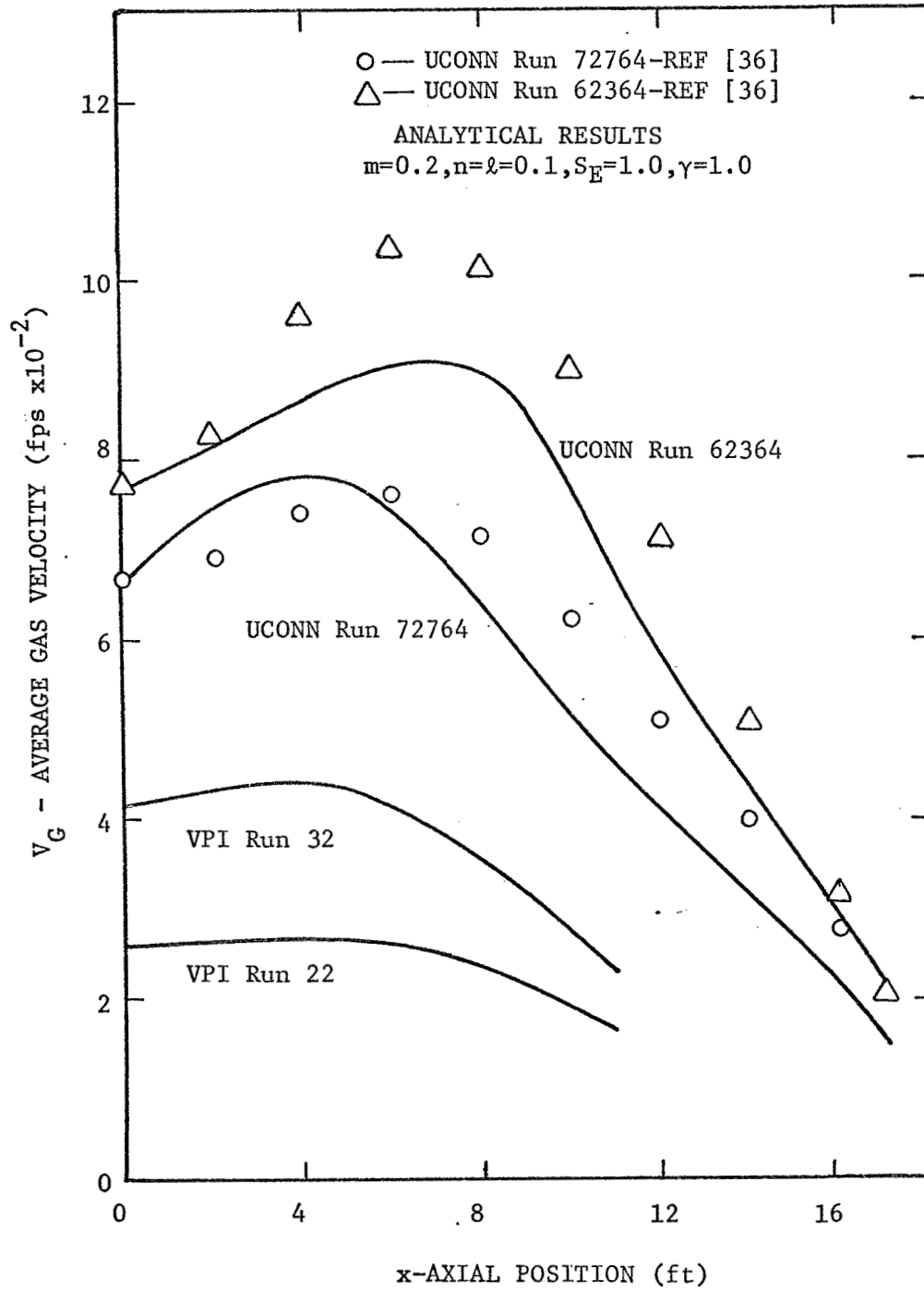


Figure 11. Axial Gas Velocity Distributions

Other trends noted were that the annular liquid layer thickness increased sharply near the entrance and also as the point of complete condensation was approached, while increasing at a lesser rate for intermediate positions. In general, the average liquid layer velocity approached a maximum (never exceeding two feet per second) in this intermediate region.

B. Heat Transfer Results

Normally, in the design of condensers, only the external thermal environment and the vapor entrance conditions are specified. Therefore, energy removed from the condenser in the form of heat must be determined with the aid of a local condensing heat transfer coefficient correlation. The three sets of experimental data (UCONN, VPI, and NASA) with which this analysis is compared specify both the condenser wall temperature and the temperature and flow rate of the cooling water flowing in the annulus of a co-axial tube. Therefore, the wall heat flux may be determined by applying an energy balance to an increment in the axial direction of the condensor tube. The local heat transfer coefficient may then be obtained as a result of the analysis using the experimental wall heat flux and wall temperature distribution as inputs.

Figure (12) compares a representation of the local heat transfer coefficients obtained analytically with experimental data. Essentially all of the NASA experimental data lies within the solid lines shown in figure (12). Similar lines indicate the UCONN and VPI data as shown in the figure. It should be emphasized that the range shown for the VPI data is representative of the heat transfer coefficient at a point five

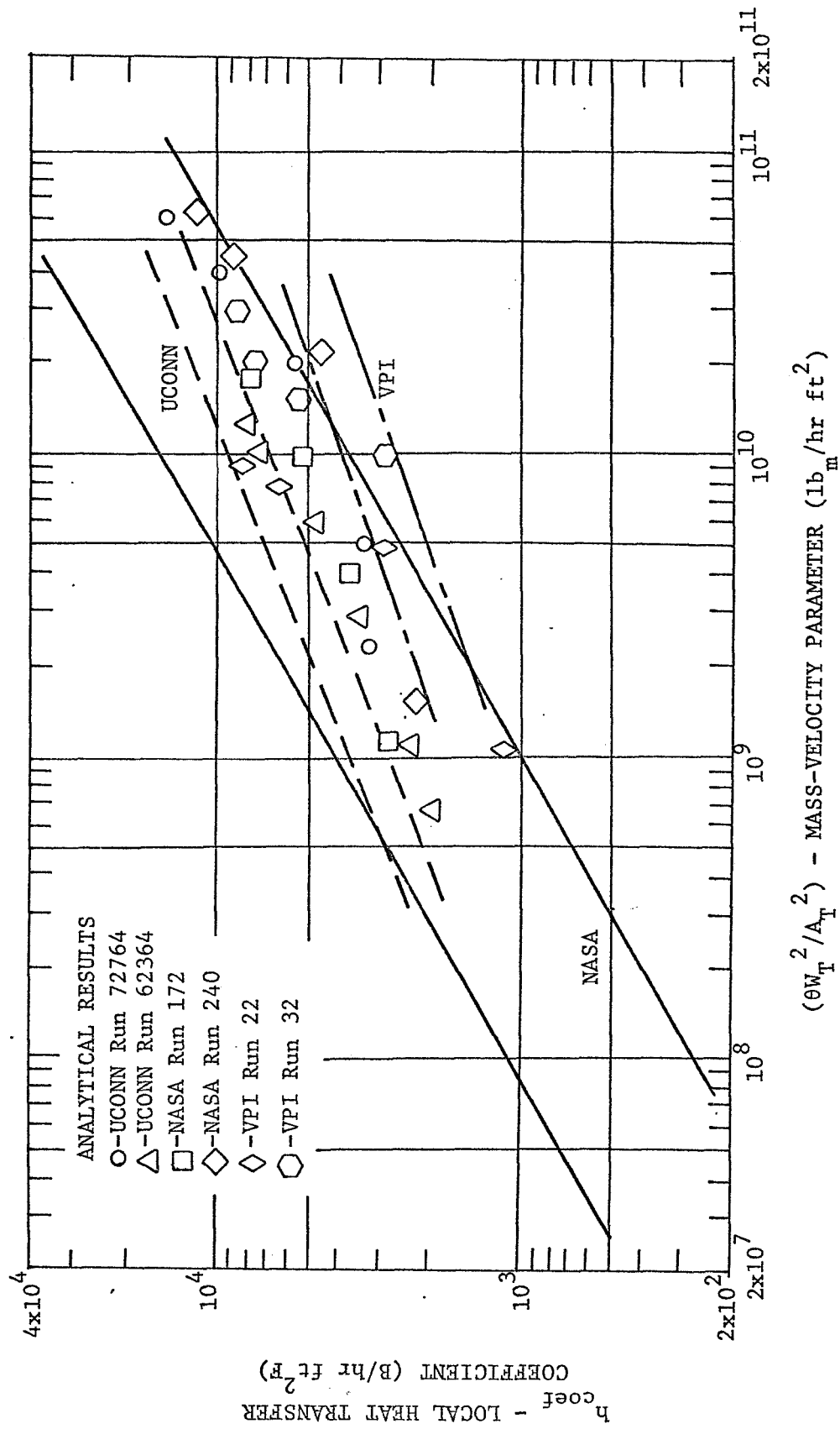


Figure 12. Heat Transfer Correlations

inches upstream of the steam extraction point only. It is therefore not a true representation of local heat transfer coefficient as a function of axial position or dynamic quality. The correlation, as suggested by Goodykoontz and Dorsch [37], is basically one of the local heat transfer coefficient versus the dynamic quality. The analytical results exhibit a similar trend and, in general, the local heat transfer coefficients are slightly lower than the experimental data.

C. The Effect of Varying the Slip Ratio and the Entrainment Correlation

The effect of simultaneously varying the entrainment slip (S_E) and the entrainment correlation variable (γ) on the static pressure distributions has been illustrated in figures (6) through (9). In all cases, S_E and γ are equal and decreasing them below unity tends to decrease the overall static pressure drop. This result is a combination of two factors. First, decreasing the entrainment slip ratio decreases the velocity of the entrained liquid particles and, therefore, alters the contribution of the momentum change to the static pressure drop. Secondly, decreasing the entrainment correlation variable increases the entrainment flow rate as shown in figure (13) for run 72764. The increased entrainment flow rate reduces the amount of liquid flowing in the annular liquid film, which in turn affects the wall shear stress distribution as shown in figure (14). In addition to the direct effect of the lower wall shear stress on the pressure drop, the increased entrainment flow rate also alters the momentum pressure drop since the additional entrainment flow has effectively been moved from the relatively slow moving annular film into the high-

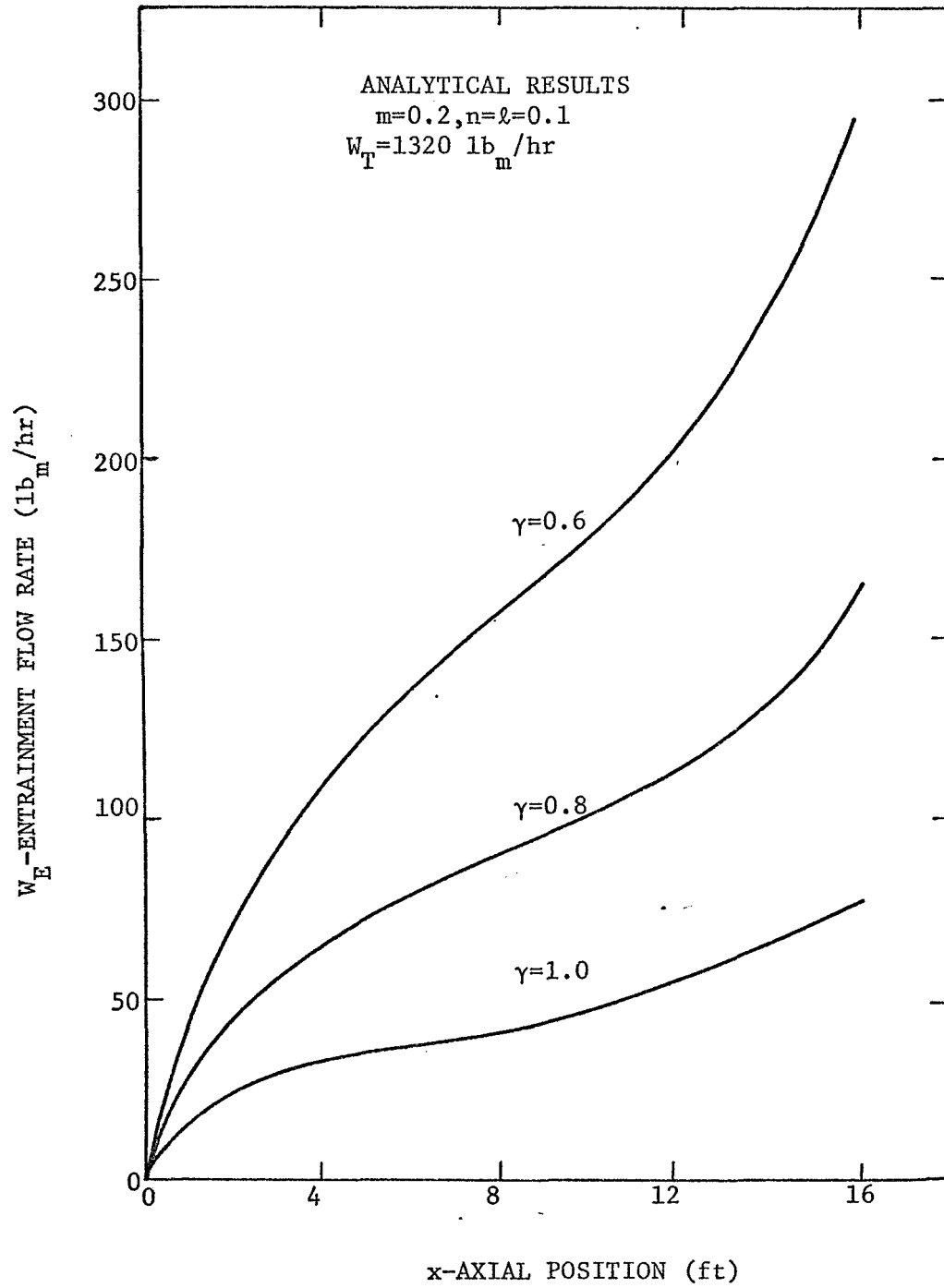


Figure 13. Entrainment Flow Rate Variations for UCONN Run 72764

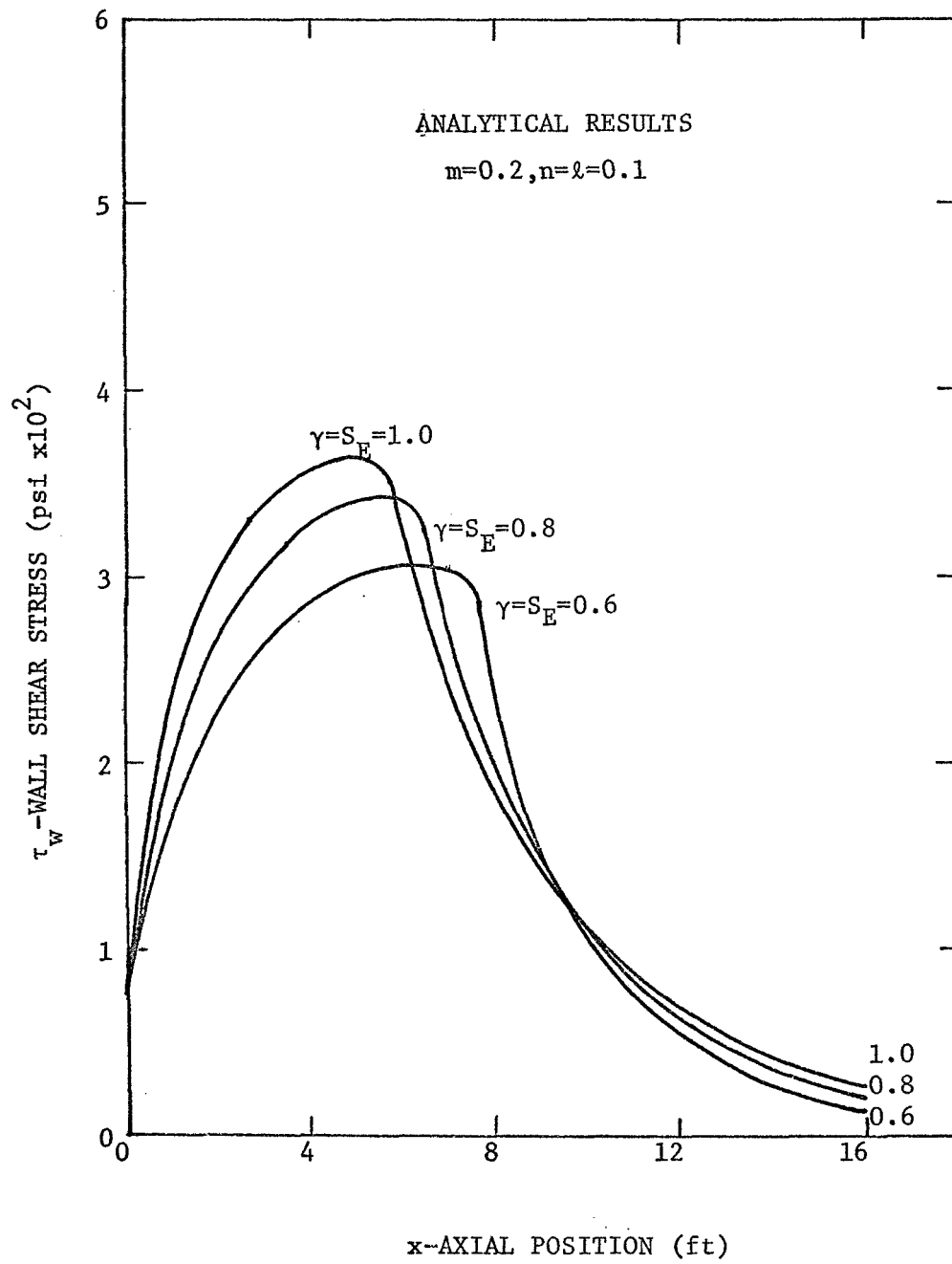


Figure 14. Wall Shear Stress Variations for UCONN Run 72764

velocity core.

The two effects mentioned above on the static pressure distribution are illustrated separately in figure (15) for run 72764. Of the two effects, the second effect (i.e., that effect of increased entrainment flow rate) proved to account for about ninety percent of the variation of the static pressure drop. The increased entrainment flow rate also accounted for the majority of the change in the wall shear stress shown in figure (14).

Based on the above results, it appears that the amount of liquid flowing as entrained particles in the gaseous core has a significant influence on the prediction of the overall pressure drop for two-phase, annular-mist flow systems, whereas, the relative velocity of the entrained particles has much less of an effect on the results. This effect is less significant for the lower velocity VPI data than for the high velocity UCONN data. This is because the momentum effects are much less for the VPI data.

D. The Effect of Varying the Shear Stress Correlations

Both the interfacial shear stress correlation presented in this investigation and the wall shear stress correlation of Kammula [21] contain parameters which are based on experimental data. Since the experimental data on wall and interfacial shear stresses for annular-mist condensing flows is essentially limited to the UCONN data, it is difficult to determine the accuracy of these correlations which are based on this data. One can, however, determine what influence variations of the wall

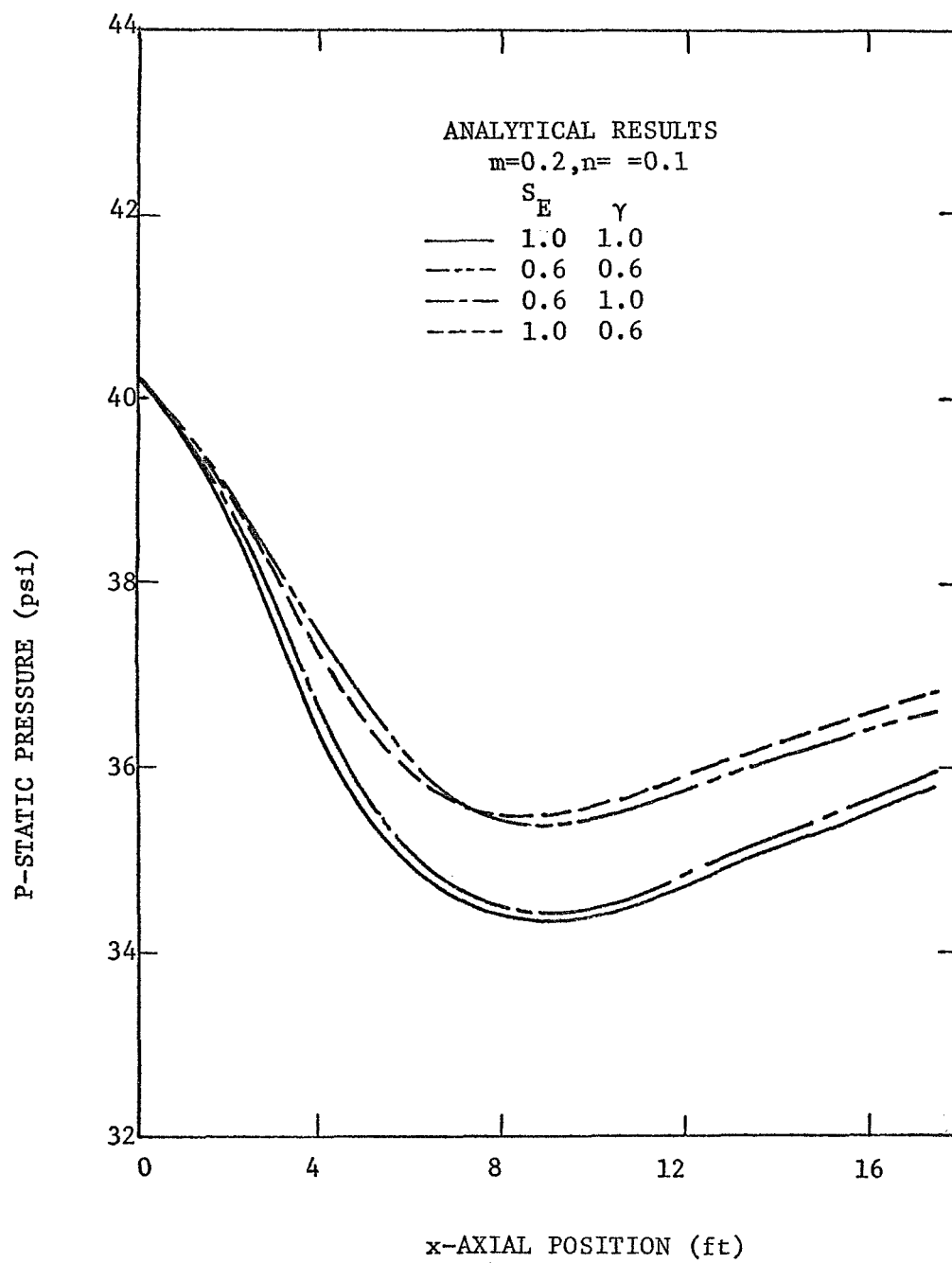


Figure 15. Effects of S_E and γ on the Pressure Distribution for
UCONN Run 72764

and interfacial shear stress correlations would have on the results of the analysis. Before pursuing the effects of varying these parameters, the interdependence of the wall and interfacial shear stress correlations must be recalled.

The interfacial shear stress correlation presented in this investigation is one of dynamic quality versus the ratio of the interfacial shear stress to the wall shear stress. Before a numerical value of the interfacial shear stress can be obtained, the wall shear stress must be determined. This ratio (τ_I/τ_w) is an input to the wall shear stress correlation and is, therefore, necessary in determining the wall shear stress. Once τ_w is known, the interfacial shear stress follows from the interfacial shear stress correlation. It is obvious that a change in the interfacial shear stress correlation will have an influence on the wall shear stress and vice versa.

In the following sections, variations of the parameters which are based on experimental data in the shear stress correlations will be introduced. The influence of these variations on the two-phase, annular-mist flow system are discussed.

Interfacial Shear Stress Correlation

The interfacial shear stress correlation used to obtain the previously reported results is reproduced in figure (16) as the solid lines. In general, this correlation gives the best results for the three sets of data (UCONN, VPI, and NASA). A variation of the interfacial shear stress correlation is shown as the dashed line in the figure. The influence of this variation on the axial static pressure distributions for three runs is shown in figure (17) as the dashed curves. In all cases,

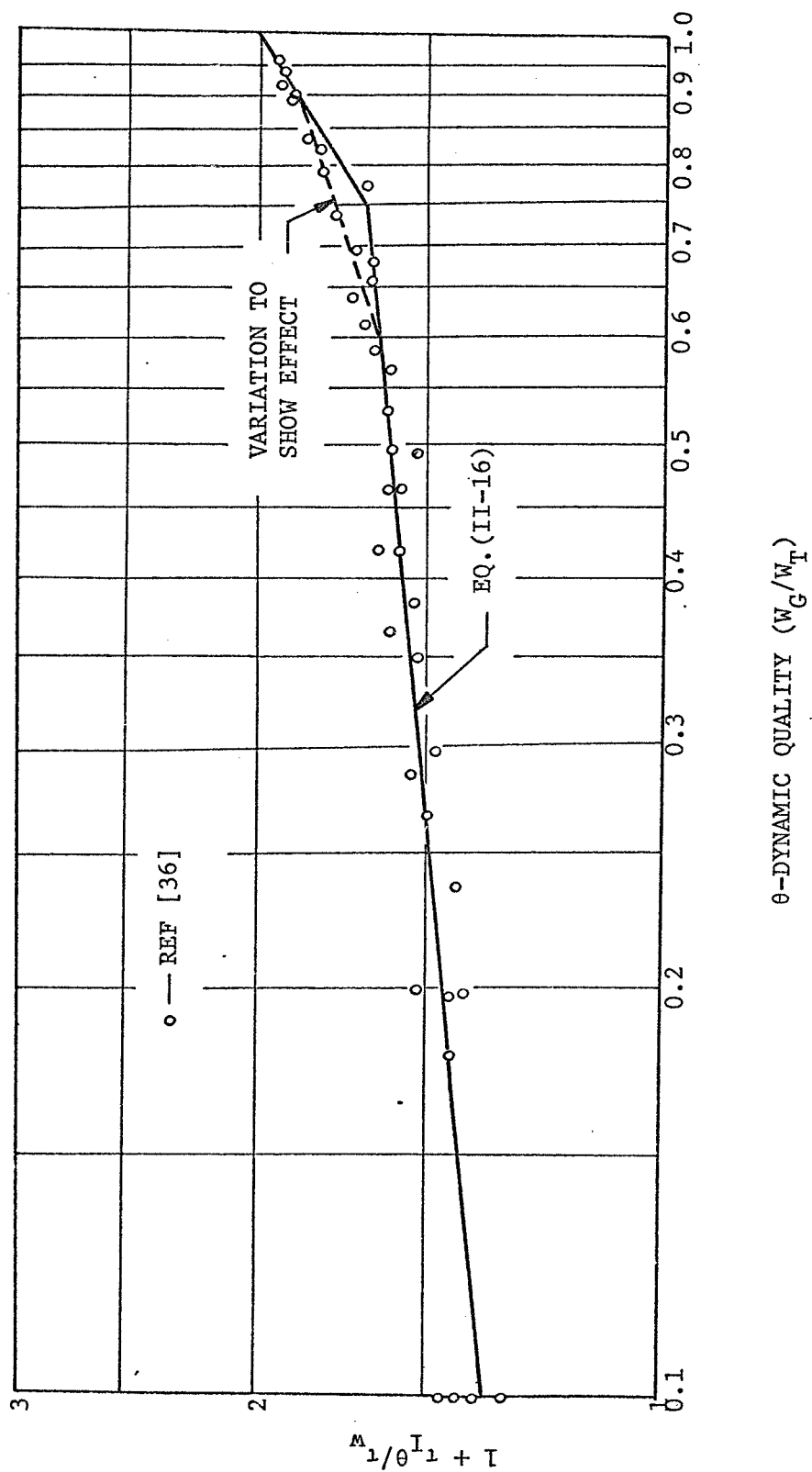


Figure 16. Variation of the Interfacial Shear Stress Correlation

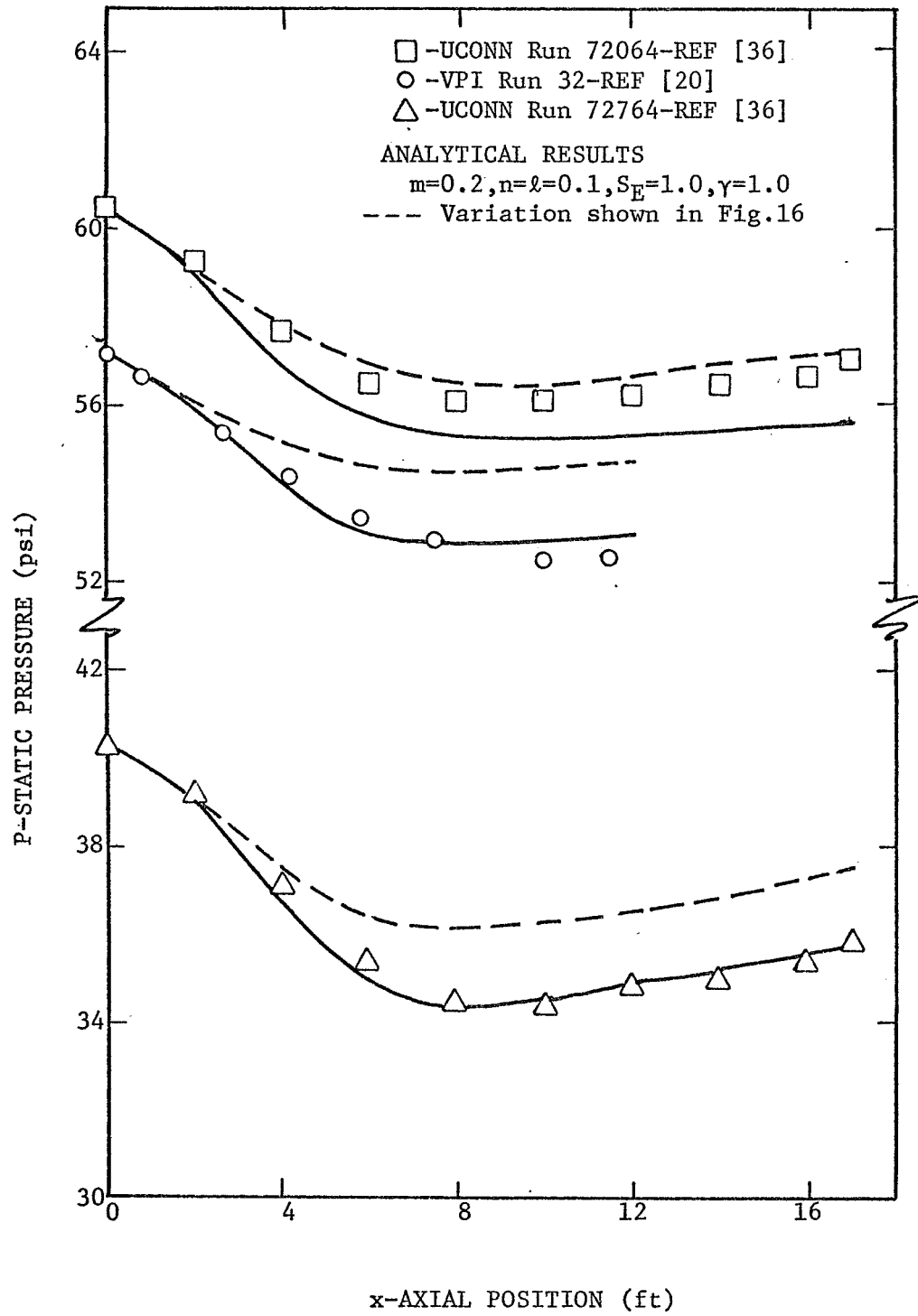


Figure 17. Effect of Varying the Interfacial Shear Stress Correlation

the static pressure drop is decreased due to this variation. Due to the interdependence between the wall and interfacial shear stress correlations, the wall shear stress distribution is also influenced by this variation. This influence on UCONN run 72764 is shown in figure (18). The wall shear stresses are, in general, lower. The effect of the variation of the interfacial shear stress correlation shown in figure (16) should be to increase τ_I , assuming no change in the wall shear stress. However, since the wall shear stress is essentially lower, the net effect on τ_I itself is quite small.

For some runs, the variation of the interfacial shear stress correlation discussed above reduces the static pressure drop such that the experimental results are better correlated. An example is UCONN run 72064 as illustrated in figure (17).

With the present available experimental data for annular-mist condensing flows, accurate interfacial shear stress correlations are quite difficult to obtain.

Wall Shear Stress Correlation

The modified von Karman constant suggested by Kammula [21] that is shown in figure (19) is based on the UCONN data only. The solid curve in figure (19) was used to obtain all analytical results presented previously in this investigation. The curves correspond except for high values of the momentum flux ratio. For certain runs, the analytical results in the high quality regions (greater than 0.9) showed closer agreement with the experimental data when the solid curve was used in lieu of the one suggested in reference [21]. Also shown in figure (19) as the dashed curve is an arbitrary variation of the modified von Karman

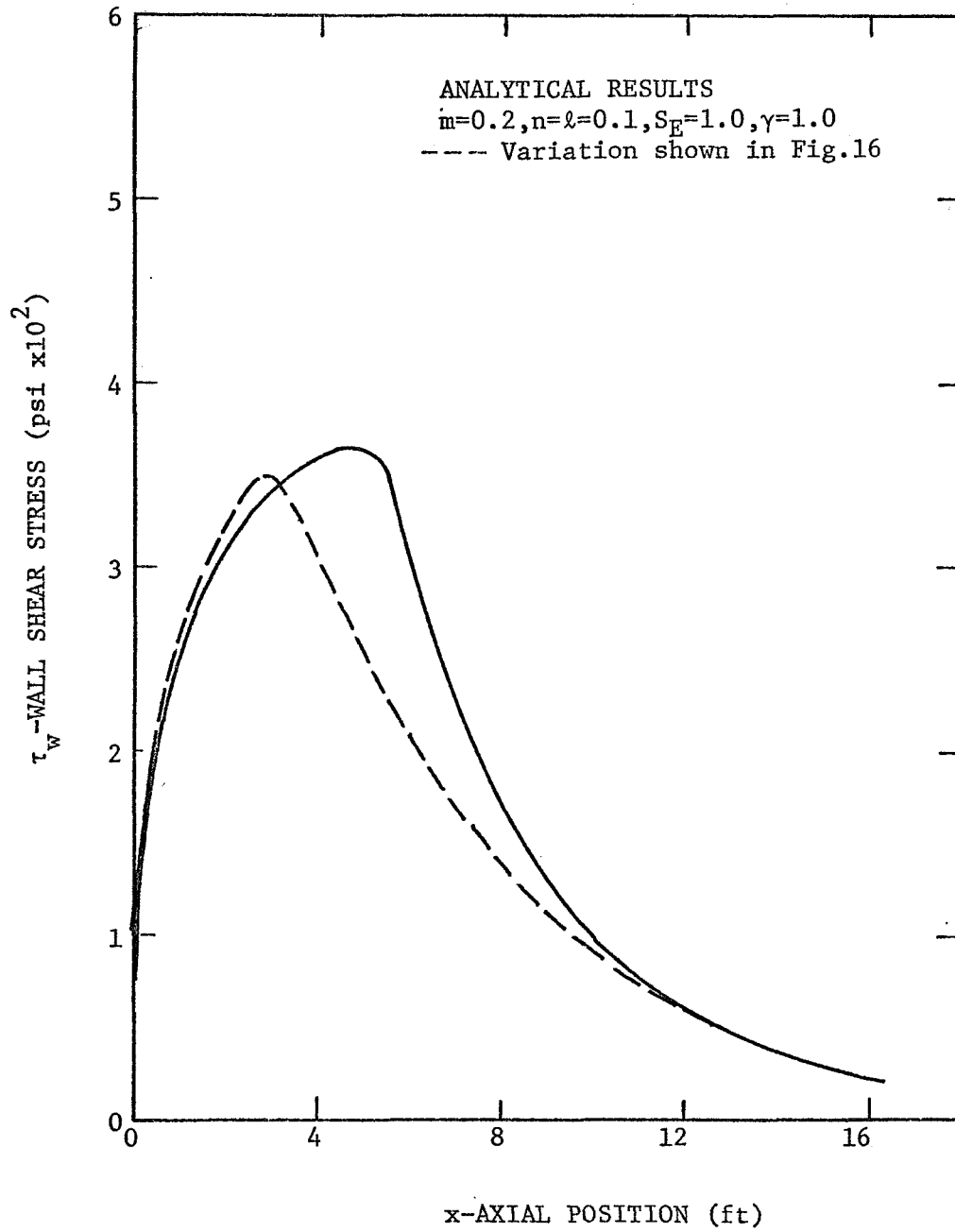


Figure 18. Effect of Varying the Interfacial Shear Stress Correlation for UCONN Run 72764

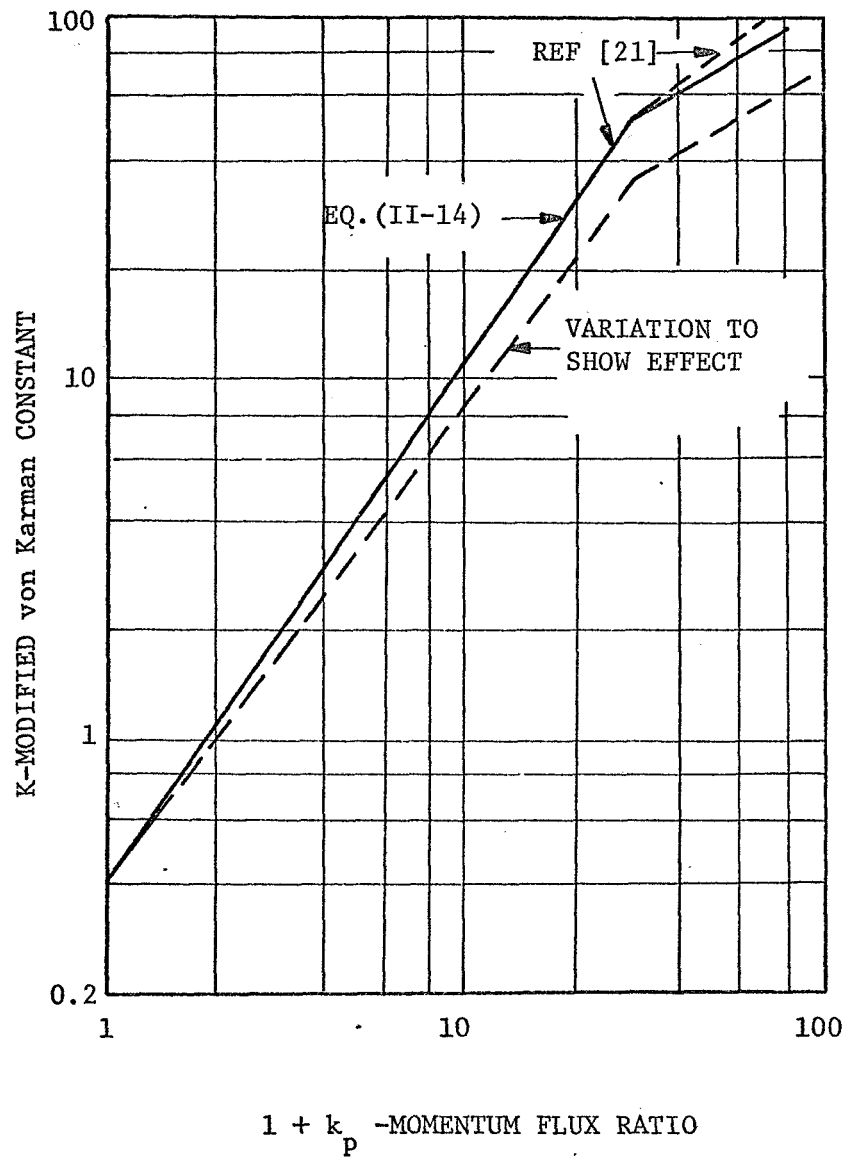


Figure 19. Variations of the Wall Shear Stress Correlation

constant which is employed in the analysis to show the effect of varying the wall shear stress correlation. The effect of varying this parameter on the wall shear stress for UCONN run 72764 is shown in figure (20). It is seen that the magnitude of the wall shear stress is affected significantly by the variation. As expected, this decreased the static pressure drop as illustrated by the dashed curve in figure (21). The accuracy of the overall static pressure drop is not appreciably altered (4.0 psi compared to 4.6 psi). However, the maximum pressure drop is considerably lower (4.4 psi at 13.5 ft compared to 6.0 psi at 8.5 ft) and occurs at a point farther from the condenser entrance. Since the wall and interfacial shear stresses are uniquely related, the interfacial shear stress varied by an amount proportional to the difference shown in figure (20) for the wall shear stress. In other words, the interfacial shear stress was lower for the first eight feet and higher for the remainder of UCONN run 72764.

Although similar results were obtained for other runs, there were certain sets of data for which slight variations in the wall shear stress correlation tended to reduce the discrepancy between analytical and experimental results. Again, the need for more accurate and extensive experimental data is indicated.

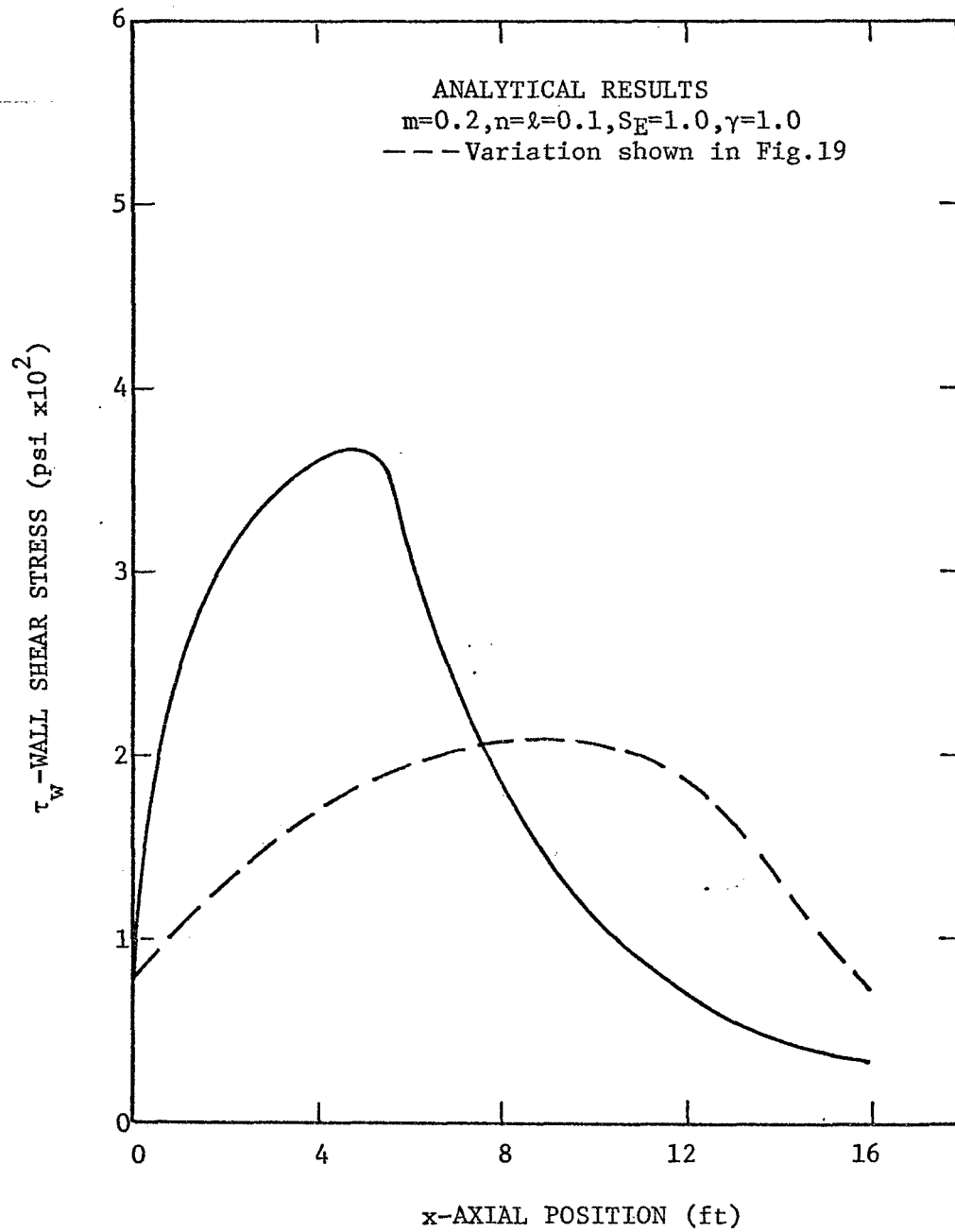


Figure 20. Effect of Varying the Wall Shear Stress Correlation
for UCONN Run72764

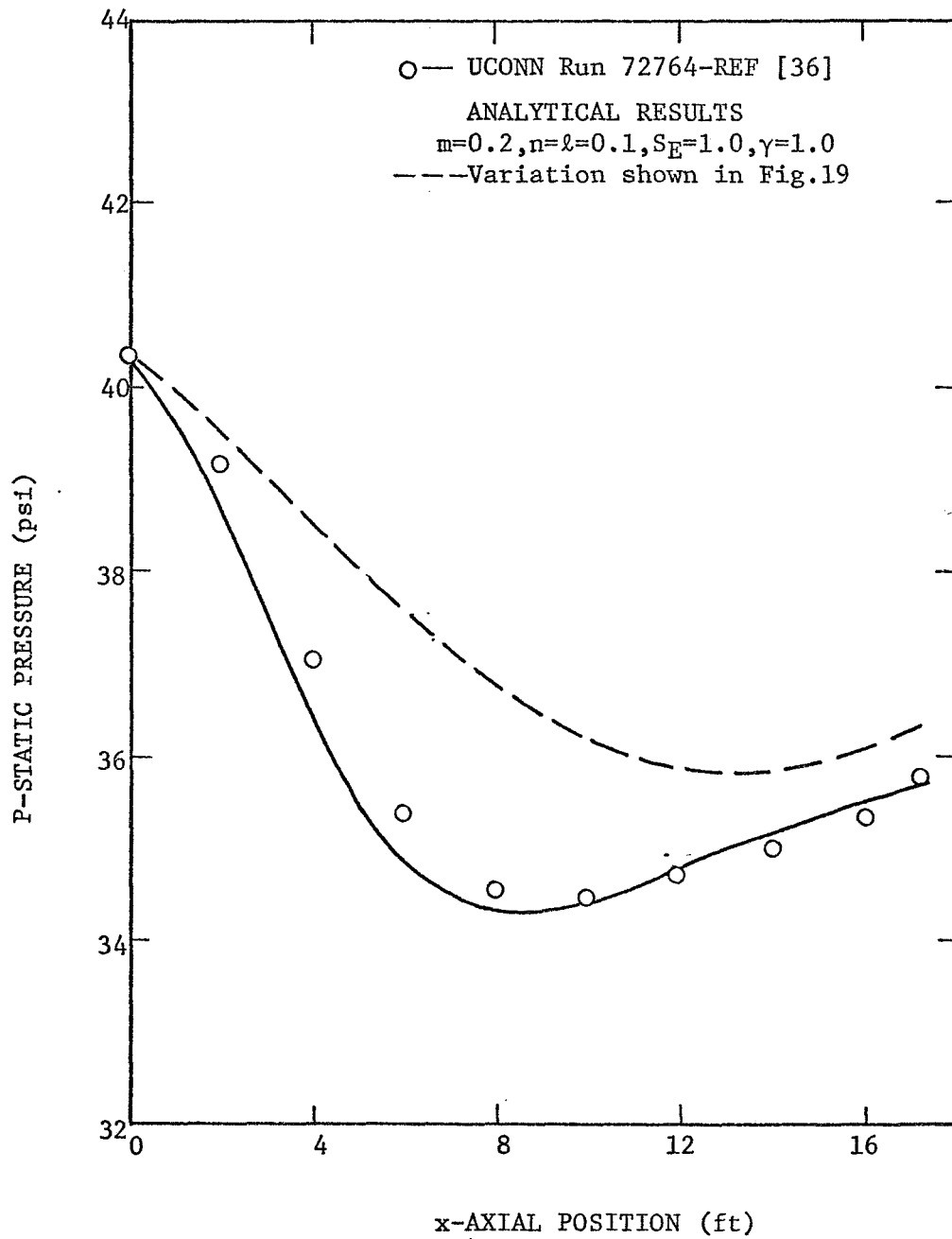


Figure 21. Effect of Varying the Wall Shear Stress Correlation on the Axial Pressure Distribution for UCONN Run 72764

IV. CONCLUSIONS AND RECOMMENDATIONS

In this investigation of the two-phase, annular-mist flow of a condensing vapor, the following significant conclusions are drawn. The conclusions are based on the numerical results obtained from the theoretical analysis. Where appropriate, recommendations for future studies are included:

1. The analytical model accurately predicts the condenser length necessary for complete condensation and, with a reasonable degree of accuracy, the dynamic quality, heat transfer characteristics, and static pressure distribution.
2. An integral analysis is presented for which the assumed velocity and enthalpy profiles are the power-law type. For the range of temperatures and pressures encountered in this investigation, varying the profile shapes has a negligible effect on the dynamic quality and static pressure distributions at all except high vapor velocities.
3. The analysis accounts for the slip between the entrained particles and the vapor in the gas core. A constant entrainment slip ratio (S_E) is assumed. Reducing the ratio below unity has an effect of the static pressure drop. The effect, however, is comparatively small.
4. Due to the lack of entrainment flow rate data available for two-phase, annular-mist, condensing flows, a variable entrainment correlation is included in the analysis.

Changing the entrainment correlation variable (γ) influences the amount of liquid entrained as particles in the core. Increasing the entrainment flow rate significantly decreases the static pressure drop.

5. Varying the interfacial shear stress correlation and the modified von Karman constant in the wall shear stress correlation has a significant influence on the results of the analysis.
6. More accurate and extensive experimental data for annular-mist condensing flows are needed before the wall and interfacial shear stress correlations and the entrainment correlation used in this analysis can be improved upon. Improved experimental techniques are also needed for measuring vapor and liquid film velocity and temperature distributions in both the radial and axial directions for a two-phase, annular-mist flow system.

The analysis presented is an improvement over existing methods for predicting pressure drop, condensation length, and heat transfer characteristics for two-phase, annular-mist condensing flows. Ultimately, however, before accurate predictions for two-phase, annular-mist flows can be made, an analysis which includes the wavy interfacial phenomena at the liquid-gas interface must be developed. Undoubtedly, this will be a two-dimensional or three-dimensional, and possibly an unsteady state, analysis.

V. REFERENCES

1. Baker, O., "New Pipeline Techniques. Designing for Simultaneous Flow of Oil and Gas, Full Report on Magnolia's Research on Two-Phase Pipeline Design, " Oil and Gas Journal, Vol. 53, 1954, p. 185.
2. Vohr, J. H., "Flow Patterns of Two-Phase Flow - A Survey of Literature," Columbia University, Department of Chemical Engineering, December 15, 1960.
3. Alves, G. E., "Co-Current Liquid-Gas Flow in a Pipe-Line Contractor," Chem. Eng. Progress, Vol. 50, 1954, p. 449.
4. Rohsenow, W. M., Editor, Developments in Heat Transfer, The M.I.T. Press, 1964, Chapter 10.
5. Lockhart, R. W., and R. C. Martinelli, "Proposed Correlation of Data for Isothermal Two-Phase, Two-Component Flow in Pipes," Chem. Eng. Progress, Vol. 45, No. 1, 1949, pp. 39-48.
6. Martinelli, R. C., and D. B. Nelson, "Prediction of Pressure Drop During Forced Circulation Boiling of Water," Trans. A.S.M.E., Vol. 70, 1948, pp. 695-702.
7. Caughron, R. D., "Two-Phase Pressure Drop - A Literature Survey and Correlation Analysis," University of California, UCRL-50123, 1966.
8. Dukler, A. E., M. Wicks, III, and R. G. Cleveland, "Frictional Pressure Drop in Two-Phase Flow: A Comparison of Existing Correlations for Pressure Loss and Holdup," A.I. Ch.E. Journal, Vol. 10, No. 1, 1964, pp. 38-43.
9. McMillan, H. K., W. E. Fontaine, and J. B. Chaddock, "Pressure Drop in Isothermal Two-Phase Flow - A Modification of the Lockhart-Martinelli Correlation," A.S.M.E. Paper No. 64-WA/FE-4, 1964.
10. Wallis, G. B., "Two-Phase Flow and Boiling Heat Transfer," U. S. Atomic Energy Commission Rept. NYO-3114-14, 1966.
11. Gouse, S. W., Jr., "An Index to the Two-Phase Gas-Liquid Flow Literature," M.I.T. Rept. No. 9, M.I.T. Press, 1966.
12. Tong, L. S., Boiling Heat Transfer and Two-Phase Flow, Wiley, 1965, pp. 67-72.
13. Wallis, G. B., One-Dimensional Two-Phase Flow, McGraw-Hill, 1969, Chapters 1, 5, and 11.

14. Soliman, M., J. R. Schuster, and P. J. Berenson, "A General Heat Transfer Correlation for Annular Flow Condensation," A.S.M.E. Paper No. 67-WA/HT-12, 1967.
15. Andeen, G. B., and P. Griffith, "Momentum Flux in Two-Phase Flow," A.S.M.E. Paper No. 67-HT-32, 1967.
16. Carpenter, E. F., and A. P. Colburn, "The Effect of Vapor Velocity on Condensation Inside Tubes," Proceedings of the General Discussion on Heat Transfer, Inst. Mech. Engr. and A.S.M.E., 1951, pp. 20-26.
17. Kunz, H. R., "Theoretical Study of Heat Transfer for Annular Two-Phase Flow," Ph.D. Thesis, Rensselaer Polytechnic Institute, 1966.
18. Pletcher, R. H., and H. N. McManus, Jr., "An Analytic Study of Film Behavior in Horizontal Annular Two-Phase Flow," Cornell University, 1965.
19. Hewitt, G. F., and D. W. Roberts, "Investigations on Interfacial Phenomena in Annular Two-Phase Flow by Means of Axial Viewing Techniques," United Kingdom Atomic Energy Authority Report AERE-R6070.
20. Taliaferro, B., "A Study of Interfacial Waves and Heat Transfer for Turbulent Condensation in a Vertical Tube," M. S. Thesis, Virginia Polytechnic Institute, 1970.
21. Kammula, K., "An Integral Technique for Predicting Wall and Interfacial Shear Stresses in Turbulent, Condensing, Annular-Mist Flow," M. S. Thesis, Virginia Polytechnic Institute, 1970.
22. Dukler, A. E. "Fluid Mechanics and Heat Transfer in Vertical Falling-Film Systems," Chem. Engr. Prog., Vol. 55, No. 10, 1959, pp. 62-67.
23. Hilding, W. E., "A Study of Local Wall Shear Stress Variation for High Velocity Vapors Condensing in Tubes," Japan Society of Mechanical Engineers Semi-International Symposium, Paper No. 266, Tokyo, September, 1967.
24. Levy, S., "Prediction of Two-Phase Annular Flow with Liquid Entrainment," Int. J. Heat and Mass Transfer, Vol. 9, 1966, pp. 171-188.
25. Gadbois, S. E., "Droplet Studies in Supersonic Two-Phase Steam Flow with Normal Shocks," Ph.D. Thesis, University of Connecticut, 1965.

26. Hoffman, E. J., "Pressure Drop in Condensation" A.S.M.E. Paper 68-WA/HT-28.
27. Wrobel, J. R., and H. N. McManus, Jr., "An Analytic Study of Film Depth, Wave Height, and Pressure Drop in Annular Two-Phase Flow," Dev. in Mechanics, Vol. 1, Plenum Press, 1961.
28. Wallis, G. B., "Use of the Reynolds Flux Concept for Analysing One-Dimensional Two-Phase Flow, Part II - Applications to Two-Phase Flow," Int. J. Heat and Mass Transfer, Vol. 11, 1968, pp. 459-472.
29. Chien, S. F., and W. Ibele, "Pressure Drop and Liquid Film Thickness of Two-Phase Annular and Annular-Mist Flows," Trans. A.S.M.E., J. Heat Transfer, Vol. 86, No. 1, 1964, pp. 89-96.
30. Hilding, W. E., and Staff, "Interim Progress Report on Heat Transfer Studies of Vapor Condensing at High Velocities in Straight Tubes," Report to N.A.S.A. from the University of Connecticut, June, 1965.
31. Cousins, L. B., W. H. Denton, and G. F. Hewitt, "Liquid Mass Transfer in Annular Two-Phase Flow," United Kingdom Atomic Energy Authority, A.E.R.E.-R4926, 1965.
32. Paleev, I. I., and B. S. Filippovich, "Phenomena of Liquid Transfer in Two-Phase Dispersed Annular Flow," Int. J. Heat and Mass Transfer, Vol. 9, 1966, pp. 1089-1093.
33. Wicks, M., III, and A. E. Dukler, "Entrainment and Pressure Drop in Concurrent Gas-Liquid Flow: 1. Air-Water in Horizontal Flow," A.I.Ch.E. Journal, Vol. 6, No. 3, 1960, pp. 463-468.
34. Magiros, P. G., and A. E. Dukler, "Entrainment and Pressure Drop in Concurrent Gas-Liquid Flow - II. Liquid Property and Momentum Effects," Developments in Mechanics, Vol. 1, Plenum Press, 1961.
35. Goss, W. P., "Two-Phase, Annular-Mist Flow," Ph.D. Thesis, University of Connecticut, 1967.
36. Hilding, W. E., and Staff, "An Analytical and Experimental Investigation of the Two-Phase Flow of a High Velocity Vapor Condensing in a Tube - Part II," Report to N.A.S.A. from the University of Connecticut, August, 1967.
37. Goodykoontz, J. H., and R. G. Dorsch, "Local Heat-Transfer Coefficients and Static Pressures for Condensation of High-Velocity Steam Within a Tube," N.A.S.A. TN D-3953, 1967.

38. Goodykoontz, J. H., and R. G. Dorsch, "Local Heat-Transfer Coefficients for Condensation of Steam in Vertical Downflow Within a 5/8-Inch-Diameter Tube," N.A.S.A. TN D-3326, 1966.
39. Goodykoontz, J. H., and W. F. Brown, "Local Heat-Transfer and Pressure Distributions for Freon-113 Condensing in Downward Flow in a Vertical Tube," N.A.S.A. TN D-3952, 1967.
40. Sawochka, S. G., "Thermal and Hydraulic Performance of Potassium During Condensation Inside Single Tubes," N.A.S.A. CR-851, 1967.
41. Nemkoong, D., H. B. Block, R. P. Macosko, and C. C. Crabs, "Photographic Study of Condensing Mercury Flow in 0- and 1-G Environments," N.A.S.A. TN D-4023, 1967.
42. Lottig, R. A., R. W. Vernon, and W. D. Kenney, "Experimental Heat-Transfer Investigations of Nonwetting, Condensing Mercury Flow in Horizontal, Sodium-Potassium-Cooled Tubes," N.A.S.A. TN D-3998, 1967.
43. Fenn, D. B., L. W. Acker, and H. H. Coe, "Steady-State Performance of a Seven-Tube NaK-Cooled Potassium Condenser," N.A.S.A. TN D-4020, 1967.
44. Collier, J. G., P.M.C. Lacey, and D. J. Pulling, "Heat Transfer to Two-Phase Gas-Liquid Systems, Part II. Further Data on Steam/Water Mixtures in the Liquid Dispersed Region in an Annulus," Trans. Instn. Chem. Engrs., Vol. 42, 1964, pp. T127-T139.
45. Bruges, E. A., B. Latto, and A. K. Ray, "New Correlations and Tables of the Coefficient of Viscosity of Water and Steam Up to 1000 Bar and 1000 DEG-C," Int. J. Heat and Mass Transfer, Vol. 9, 1966, pp. 465-480.
46. Quandt, E. R., "Measurements of Some Basic Parameters in Two-Phase Annular Flow," A.I.Ch.E. Journal, Vol. 11, No. 2, 1965, pp. 311-318.
47. Kays, W. M., Convective Heat and Mass Transfer, McGraw-Hill, 1966.
48. Eckert, E.R.G., and R. M. Drake, Heat and Mass Transfer, McGraw-Hill, 1959.
49. Grace, T. M., "The Mechanism of Burnout in Initially Sub-Cooled Forced Convective Systems," Ph.D. Thesis, University of Minnesota, 1963.
50. Dussourd, J. L., "A Theoretical and Experimental Investigation of a Deceleration Probe for Measurement of Several Properties of a Droplet Laden Stream," Sc.D. Thesis, Massachusetts Institute of Technology, 1954.

51. Keenan, J. H., and F. G. Keyes, "Thermodynamic Properties of Steam," John Wiley and Sons, 1936.
52. Linehan, J. H., M. Petrick, and M. M. El-Wakil, "On the Interface Shear Stress in Annular Flow Condensation," Trans. A.S.M.E., J. Heat Transfer, Vol. 91, 1969, pp. 450-452.
53. Cravarolo, L., and A. Hassid, "Phase and Velocity Distributions in Two-Phase Adiabatic Dispersed Flow," Centro Informazioni Studi Esperienze, Milan, Italy, CISE Report No. 98, August, 1963.
54. Gill, L. E., G. F. Hewitt, and P.M.C. Lacey, "Sampling Probe Studies of the Gas Core in Annular Two-Phase Flow - Part II, Studies of the Effect of Phase Flow Rates on Phase and Velocity Distributions," United Kingdom Atomic Energy Authority, Harwell, England, AERE-R3955, 1963. (N64-15225)
55. Gill, L. E., G. F. Hewitt, J. W. Hitchon, and P.M.C. Lacey, "Sampling Probe Studies of the Gas Core in Annular Two-Phase Flow - Part I, The Effect of Length on Phase and Velocity Distributions," Chemical Engineering Science, Vol. 18, 1963, pp. 525-535.
56. System 360 Scientific Subrouting Package, (360A-CM-03X) Version III Programmer's Manual, International Business Machines Corporation, White Plains, New York, 1968, p. 120.
57. Henrici, P., Discrete Variable Methods in Ordinary Differential Equations, John Wiley and Sons, 1962.

VI. APPENDICES

Appendix A. Derivation of the Integral Equations

In this appendix, the integral equations (II-1 through II-4) will be derived in accordance with the assumptions stated in section II-A of this report.

Mass

Applying the conservation of mass to the control volume for the entire flow (figure 2) gives:

$$W_T = W_G + W_E + W_L$$

Differentiating this expression with respect to the axial position gives the following equation:

$$\frac{d}{dx}(W_G) + \frac{d}{dx}(W_E) + \frac{d}{dx}(W_L) = 0 \quad (A-1)$$

Defining the core void fraction,

$$\alpha \equiv \frac{A_G}{A_c} = \frac{A_G}{A_G + A_E} \quad (A-2)$$

results in the following integral expressions for flow rate at any axial position:

$$W_L = 2\pi\rho_f \int_0^{\delta} u_L (R-y) dy \quad (A-3)$$

$$W_G = 2\pi\alpha\rho_g \int_{\delta}^R u_G (R-y) dy \quad (A-4)$$

$$W_E = 2\pi (1-\alpha) S_E \rho_f \int_{\delta}^R u_G (R-y) dy \quad (A-5)$$

where the entrainment slip ratio is defined as:

$$S_E \equiv \frac{u_E}{u_G} \quad (A-6)$$

Substitution of the expressions for the flow rates into equation (A-1) yields the integral continuity equation (II-1):

$$\frac{d}{d\chi} \left[\rho_{cc} \int_{\delta}^R u_G (R-y) dy \right] + \frac{d}{d\chi} \left[\rho_f \int_0^{\delta} u_L (R-y) dy \right] = 0 \quad (A-7)$$

where the apparent mass density of the core is given by:

$$\rho_{cc} \equiv \alpha \rho_g + (1-\alpha) S_E \rho_f \quad (A-8)$$

Momentum

The forces on the control volume (figure 2) for the entire flow are:

$$\Sigma F_x = P A_T - (P + dP) A_T - \tau_w dA_w$$

or

$$\Sigma F_x = -\pi R^2 dP - 2\pi R \tau_w d\chi$$

Applying Newton's Second Law to the control volume gives:

$$\begin{aligned} & -\pi R^2 dP - 2\pi R \tau_w d\chi \\ & = d(W_L u_L) + d(W_G u_G) + d(W_E u_E) \end{aligned} \quad (A-9)$$

Substituting the integral expressions (A-3 through A-5) for the flow rates and dividing through by $2\pi dx$ yields the integral momentum equation (II-2):

$$\begin{aligned}
 -\frac{R^2}{2} \frac{dP}{dx} - R\tau_w &= \frac{d}{dx} \left[\rho_f \int_0^\delta u_L^2 (R-y) dy \right] \\
 &+ \frac{d}{dx} \left[\rho_{cm} \int_\delta^R u_G^2 (R-y) dy \right]
 \end{aligned}
 \tag{A-10}$$

where the apparent momentum density of the core is given by:

$$\rho_{cm} \equiv \alpha \rho_g + (1-\alpha) S_E^2 \rho_f \tag{A-11}$$

Similarly, the forces on the control volume for the liquid annulus only (figure 2) are:

$$\begin{aligned}
 \Sigma F_x &= PA_L + (P + dP/2) dA_L - (P + dP)(A_L + dA_L) \\
 &+ \tau_I dA_{Ix} - \tau_w dA_w
 \end{aligned}$$

Neglecting differentials of higher order gives:

$$\Sigma F_x = -A_L dP + 2\pi(R-\delta)\tau_I dx - 2\pi R\tau_w dx$$

The area of the liquid annulus normal to the flow direction is given by:

$$A_L = \pi \delta (2R - \delta). \tag{A-12}$$

Applying Newton's Second Law to this control volume gives:

$$\begin{aligned}
 &- \pi \delta (2R - \delta) dP + 2\pi(R-\delta)\tau_I dx - 2\pi R\tau_w dx \\
 &= d(w_L u_L) - V_I d(w_L)
 \end{aligned}
 \tag{A-13}$$

Substituting (A-3) into (A-13) and dividing by $2\pi dx$ yields the integral momentum equation (II-3):

$$\begin{aligned} \tau_I (R-\delta) - \delta (R - \delta/2) \frac{dP}{d\chi} - \tau_w R \\ = \frac{d}{d\chi} \left[\rho_f \int_0^\delta u_L^2 (R-y) dy \right] - V_I \frac{d}{d\chi} \left[\rho_f \int_0^\delta u_L^2 (R-y) dy \right] \end{aligned} \quad (A-14)$$

Energy

The conservation of energy applied to the control volume (figure 2) for the entire flow gives:

$$d(W_G h_{TG}) + d(W_E h_{TE}) + d(W_L h_{TL}) = -\dot{q}'' dA_w \quad (A-15)$$

As stated in the assumptions, the total enthalpies are assumed as:

$$h_{TG} = h_g + \frac{u_g^2}{2} \quad (A-16)$$

$$h_{TE} = h_f + \frac{s_E^2 u_g^2}{2} \quad (A-17)$$

$$h_{TL} = h_L \quad (A-18)$$

Substitution of equations (A-16 through A-18), along with equations (A-3 through A-5), into the energy equation (A-15) and rearranging yields the integral energy equation (II-4):

$$\begin{aligned} \frac{d}{d\chi} \left[\rho_c h_c \int_\delta^R u_g (R-y) dy \right] + \frac{d}{d\chi} \left[\rho_{ce} \int_\delta^R \frac{u_g^3}{2} (R-y) dy \right] \\ + \frac{d}{d\chi} \left[\rho_f \int_0^\delta u_L h_L (R-y) dy \right] + R \dot{q}'' = 0 \end{aligned} \quad (A-19)$$

where the apparent kinetic energy density and apparent enthalpy of the core are given by:

$$\rho_{ce} \equiv \alpha \rho_g + (1-\alpha) S_E^3 \rho_f \quad (\text{A-20})$$

$$\rho_c h_c \equiv \alpha \rho_g h_g + (1-\alpha) S_E \rho_f h_f \quad (\text{A-21})$$

Appendix B. Correlations

Entrainment Correlation

As discussed in section II-B of this report, the variable that describes the entrainment flow rate is the core void fraction α . In order to use the entrainment correlation presented by Goss (equations II-9 and II-10), an expression relating entrainment flow rate and core void fraction must be developed. This is accomplished by using the definitions of the dynamic quality θ , the entrainment dynamic quality \bar{X} , and the core void fraction α , which are:

$$\theta \equiv \frac{W_G}{W_T} \quad (B-1)$$

$$\bar{X} \equiv \frac{W_G}{W_G + W_E} \quad (B-2)$$

$$\alpha \equiv \frac{A_G}{A_G + A_E} \quad (B-3)$$

From equation (B-2),

$$\bar{X} = \frac{\rho_g A_G V_G}{\rho_g A_G V_G + \rho_f A_E V_E} = \frac{\rho_g A_G}{\rho_g A_G + \rho_f A_E S_E}$$

and with equation (B-3)

$$\bar{X} = \frac{\alpha}{\alpha + \beta(1-\alpha)S_E} \quad (B-4)$$

where

$$\beta \equiv \frac{\rho_f}{\rho_g} \quad (B-5)$$

Solving for the core void fraction in (B-4) yields:

$$\alpha = \frac{X\beta S_E}{1 + X\beta S_E - X} \quad (\text{B-6})$$

In the integral equations (II-1 through II-4), the axial derivative of the core void fraction α must be known as a function of the axial derivatives of the primary dependent variables V_I , V_E , δ , and P . Differentiating equation (B-6) results in:

$$\frac{d\alpha}{dX} = \frac{S_E}{(1 + X\beta S_E - X)^2} \left[X(1-X) \frac{d\beta}{dX} + \beta \frac{dX}{dX} \right] \quad (\text{B-7})$$

Using the appropriate equations of state [51],

$$\rho_f = \rho_f(P) \quad \rho_g = \rho_g(P)$$

results in an expression for the change in the density ratio with respect to x as:

$$\frac{d\beta}{dX} = \frac{1}{\rho_g} \left[\frac{d\rho_f}{dP} - \beta \frac{d\rho_g}{dP} \right] \frac{dP}{dX} \quad (\text{B-8})$$

The change in entrainment quality with respect to axial position is obtained from

$$\frac{dX}{dX} = \frac{dX}{d\theta} \frac{d\theta}{dX} \quad (\text{B-9})$$

where, from equations (II-9 and II-10),

$$\frac{dX}{d\theta} = \frac{1 + a_1 + 2a_2t + 3a_3t^2 + 4a_4t^3}{1 - a_1 - 2a_2t - 3a_3t^2 - 4a_4t^3} \quad (B-10)$$

and from equation (B-1),

$$\frac{d\theta}{d\chi} = \frac{1}{W_T} \frac{dW_G}{d\chi} \quad (B-11)$$

The gas flow rate is given by

$$W_G = 2\pi\rho_g \alpha (R-\delta)^2 \left[\frac{V_I}{2} + \frac{V_k - V_I}{(m+2)(m+1)} \right] \quad (B-12)$$

Substitution of equations (B-8, B-11, and B-12) into equation (B-7), and solving for the axial derivative of the core void fraction yields:

$$\begin{aligned} \frac{d\alpha}{d\chi} = & 2\pi S_E \alpha \rho_f (R-\delta)^2 \frac{dX}{d\theta} \left\{ \left[\frac{1}{2} - \frac{1}{(m+2)(m+1)} \right] \frac{dV_I}{d\chi} \right. \\ & + \left[\frac{1}{(m+2)(m+1)} \right] \frac{dV_k}{d\chi} - \frac{2}{(R-\delta)} \left[\frac{V_I}{2} + \frac{V_k - V_I}{(m+2)(m+1)} \right] \frac{d\delta}{d\chi} \\ & + \left[\frac{1}{\rho_g} \left[\frac{V_I}{2} + \frac{V_k - V_I}{(m+2)(m+1)} \right] \frac{d\rho_g}{dP} + \frac{X(1-X)W_T}{2\pi\rho_f\rho_g\alpha(R-\delta)^2} \frac{dX}{d\theta} \left[\frac{d\rho_f}{dP} \right. \right. \\ & \left. \left. - \beta \frac{d\rho_g}{dP} \right] \right\} \frac{dP}{d\chi} \Bigg/ \left\{ W_T (1 - X\beta S_E - X)^2 \right. \\ & \left. - 2\pi\rho_f (R-\delta)^2 \left[\frac{V_I}{2} + \frac{V_k - V_I}{(m+2)(m+1)} \right] \frac{dX}{d\theta} \right\} \quad (B-13) \end{aligned}$$

or, written in index notation form

$$\frac{d\alpha}{dx} = \sum_j c_j \frac{d\psi_j}{dx} \quad (B-14)$$

where $c_j = c_j(V_I, V_{\text{L}}, \delta, P)$ as defined by equation (B-13)

$$\psi_1 = V_I$$

$$\psi_2 = V_{\text{L}}$$

$$\psi_3 = \delta$$

$$\psi_4 = P$$

Equation (B-14) is an expression for the change of core void fraction with respect to the axial position as a function of the primary dependent variables.

Wall and Interfacial Shear Stress Correlations

Kammula [21] has proposed a semi-empirical correlation for determining wall shear stress in annular two-phase flow. This correlation yields values of the wall shear stress from an iterative solution of equations (II-12 through II-14), presented previously, given the following parameters:

τ_{wig} - an initial guess of the wall shear stress

δ - liquid film thickness

W_L - liquid film flow rate

R - tube radius

μ_L - liquid viscosity

θ - dynamic quality

ρ_f - liquid density

V_L - liquid film velocity

k_p - square root of the ratio of the gas to liquid momentum
fluxes

$\frac{\tau_I}{\tau_w}$ - ratio of the interfacial to the wall shear stress

A correlation for the ratio of the interfacial to wall shear stress as a function of dynamic quality is given by equation (II-16). It is therefore possible to obtain the wall shear stress from the correlation of Kammula as described in Section II-B-2. Once the wall shear stress is obtained, the interfacial shear stress is determined from equation (II-16).

Appendix C. Simplification of the Integral Equations

In this appendix, the integral equations (II-1 through II-4), derived in Appendix A, will be simplified to a set of four, non-linear, first order, ordinary differential equations (II-27) suitable for solution by numerical techniques. The simplification involves substituting the assumed velocity and enthalpy profiles

$$u_L = V_I \left(\frac{y}{\delta} \right)^n \quad (\text{II-17})$$

$$u_G = V_I + (V_E - V_I) \left(\frac{y - \delta}{R - \delta} \right)^m \quad (\text{II-18})$$

and,

$$h_L = h_{fw} + (h_f - h_{fw}) \left(\frac{y}{\delta} \right)^l \quad (\text{II-22})$$

into the integral equations and performing the necessary integration and differentiation. With the use of the entrainment correlation in the form of equation (B-13, Appendix B), a set of non-linear, ordinary differential equations with dependent variables V_I , V_E , δ , and P and independent variable χ are obtained.

Mass

Substitution of the assumed profiles (II-17 and II-18) into the integral continuity equation (II-1) and integrating between the indicated limits yields:

$$\begin{aligned} \frac{d}{d\chi} \left\{ \rho_{cc} (R - \delta)^2 \left[\frac{V_I}{2} + \frac{(V_E - V_I)}{(m+2)(m+1)} \right] \right\} \\ + \frac{d}{d\chi} \left\{ \frac{\rho_f V_I \delta}{(n+2)} \left[\frac{(n+2)}{(n+1)} R - \delta \right] \right\} = 0. \end{aligned} \quad (\text{C-1})$$

Differentiation of the equations of state for the properties ρ and h with respect to axial position yield the following expressions

$$\frac{d\rho}{d\chi} = \frac{d\rho}{dP} \frac{dP}{d\chi} \quad (C-2)$$

$$\frac{dh}{d\chi} = \frac{dh}{dP} \frac{dP}{d\chi} \quad (C-3)$$

which are applicable to both the liquid and vapor phase using the appropriate equation of state data.

Performing the indicated differentiation in equation (C-1) with the use of equation (C-2) yields the differential equation for the conservation of mass

$$\begin{aligned} & \left\{ \frac{\rho_{cc} (R-\delta)^2 [(m+2)(m+1) - 2]}{2(m+2)(m+1)} + \delta \rho_f \left[\frac{R}{(n+1)} - \frac{\delta}{(n+2)} \right] \right\} \frac{dV_I}{d\chi} \\ & + \left\{ \frac{\rho_{cc} (R-\delta)^2}{(m+2)(m+1)} \right\} \frac{dV_E}{d\chi} + \left\{ \rho_f V_I \left[\frac{R}{(n+1)} - \frac{\delta}{(n+2)} \right] \right. \\ & \left. - 2\rho_{cc} (R-\delta) \left[\frac{V_I}{2} + \frac{V_E - V_I}{(m+2)(m+1)} \right] \right\} \frac{d\delta}{d\chi} + \left\{ V_I \delta \left[\frac{R}{(n+1)} - \frac{\delta}{(n+2)} \right] \frac{d\rho_f}{dP} \right. \\ & + (R-\delta)^2 \left[\frac{V_I}{2} + \frac{V_E - V_I}{(m+2)(m+1)} \right] \left[a \frac{d\rho_g}{dP} + (1-a) S_E \frac{d\rho_f}{dP} \right] \left\} \frac{dP}{d\chi} \\ & + \left\{ (R-\delta)^2 \left[\frac{V_I}{2} + \frac{V_E - V_I}{(m+2)(m+1)} \right] (\rho_g - S_E \rho_f) \right\} \frac{da}{d\chi} = 0. \end{aligned} \quad (C-4)$$

Momentum

Applying a similar procedure to the integral momentum equation for the entire flow (II-2) yields

$$\begin{aligned}
 & 2 \left\{ \rho_f \delta V_I \left[\frac{R}{(n+1)} - \frac{\delta}{(n+2)} \right] + \rho_{cm} (R-\delta)^2 \left[\frac{V_I}{2} + \frac{V_I}{(m+2)(m+1)} \right. \right. \\
 & \left. \left. + \frac{V_E - V_I}{(m+2)(m+1)} - \frac{V_E - V_I}{(2m+2)(2m+1)} \right] \right\} \frac{dV_I}{d\chi} + \left\{ 2 \rho_{cm} (R-\delta)^2 \right. \\
 & \left. \left[\frac{V_I}{(m+2)(m+1)} + \frac{V_E - V_I}{(2m+2)(2m+1)} \right] \right\} \frac{dV_E}{d\chi} + \left\{ \rho_f V_I^2 \left[\frac{R}{(2n+1)} - \frac{2\delta}{(2n+2)} \right] \right. \\
 & \left. - 2 \rho_{cm} (R-\delta) \left[\frac{V_I^2}{2} + \frac{2V_I(V_E - V_I)}{(m+2)(m+1)} + \frac{(V_E - V_I)^2}{(2m+2)(2m+1)} \right] \right\} \frac{d\delta}{d\chi} \\
 & + \left\{ \frac{R^2}{2} + \delta V_I \frac{d\rho_f}{dP} \left[\frac{R}{(2n+1)} - \frac{\delta}{(2n+2)} \right] + (R-\delta)^2 \left[\frac{V_I^2}{2} \right. \right. \\
 & \left. \left. + \frac{2V_I(V_E - V_I)}{(m+2)(m+1)} + \frac{(V_E - V_I)^2}{(2m+2)(2m+1)} \right] \right\} \alpha \frac{d\rho_g}{dP} \\
 & + (1-\alpha) S_E^2 \frac{d\rho_f}{dP} \left. \right\} \frac{dP}{d\chi} + \left\{ (\rho_g - S_E^2 \rho_f) (R-\delta)^2 \right. \\
 & \left. \left[\frac{V_I^2}{2} + \frac{2V_I(V_E - V_I)}{(m+2)(m+1)} + \frac{(V_E - V_I)^2}{(2m+2)(2m+1)} \right] \right\} \frac{d\alpha}{d\chi} \\
 & = -R\tau_w
 \end{aligned}
 \tag{C-5}$$

and, for the integral momentum equation for the liquid annulus (II-3) the result is

$$\begin{aligned}
 & \left\{ \rho_f \delta V_I \left[\frac{R}{(2n+1)(n+1)} - \frac{2\delta}{(2n+2)(n+2)} \right] \right\} \frac{dV_I}{dx} \\
 & + \left\{ \rho_f V_I^2 n \left[\frac{2\delta}{(2n+2)(2n+1)} - \frac{R}{(2n+1)(n+1)} \right] \right\} \frac{d\delta}{dx} \\
 & + \left\{ \delta(R - \delta/2) - V_I^2 \delta n \left[\frac{R}{(2n+1)(n+1)} - \frac{\delta}{(2n+2)(n+2)} \right] \frac{d\rho_f}{dP} \right\} \frac{dP}{dx} \\
 & = \tau_I (R - \delta) - \tau_w R.
 \end{aligned} \tag{C-6}$$

Energy

Substitution of the assumed profiles (II-17, II-18, and II-22) into the integral energy equation (II-4), performing the integration and differentiation and rearranging yields the differential equation for the conservation of energy

$$\begin{aligned}
 & \left\{ \rho_c h_c (R - \delta)^2 \left[\frac{1}{2} - \frac{1}{(m+2)(m+1)} \right] + \frac{\rho_{ce} (R - \delta)^2}{2} \left[\frac{3}{2} V_I^2 \right. \right. \\
 & + \frac{3V_I (2V_k - 3V_I)}{(m+2)(m+1)} + \frac{3(V_I - V_k)(3V_I - V_k)}{(2m+2)(2m+1)} - \left. \left. \frac{3(V_k - V_I)^2}{(3m+2)(3m+1)} \right] \right\} \\
 & + \rho_f \delta \left[h_{fw} \left(\frac{R}{n+1} - \frac{\delta}{n+2} \right) + (h_f - h_{fw}) \left(\frac{R}{n+1+1} - \frac{\delta}{n+1+2} \right) \right] \frac{dV_I}{dx}
 \end{aligned}$$

$$\begin{aligned}
& + \left\{ \frac{\rho_c h_c (R-\delta)^2}{(m+2)(m+1)} + \frac{\rho_{ce} (R-\delta)^2}{2} \left[\frac{3V_I^2}{(m+2)(m+1)} + \frac{6V_I (V_k - V_I)}{(2m+2)(2m+1)} \right. \right. \\
& \left. \left. + \frac{3(V_k - V_I)^2}{(3m+2)(3m+1)} \right] \right\} \frac{dV_k}{d\chi} + \left\{ \rho_f V_I \left[h_{fw} \left(\frac{R}{n+1} - \frac{2\delta}{n+2} \right) \right. \right. \\
& \left. \left. + (h_f - h_{fw}) \left(\frac{R}{n+l+1} - \frac{2\delta}{n+l+2} \right) \right] - 2\rho_c h_c (R-\delta) \left[\frac{V_I}{2} \right. \right. \\
& \left. \left. + \frac{V_k - V_I}{(m+2)(m+1)} \right] - \rho_{ce} (R-\delta) \left[\frac{V_I^3}{2} + \frac{3V_I^2 (V_k - V_I)}{(m+2)(m+1)} \right. \right. \\
& \left. \left. + \frac{3V_I (V_k - V_I)^2}{(2m+2)(2m+1)} + \frac{(V_k - V_I)^3}{(3m+2)(3m+1)} \right] \right\} \frac{d\delta}{d\chi} \\
& + \left\{ (R-\delta)^2 \left[\frac{V_I}{2} + \frac{V_k - V_I}{(m+2)(m+1)} \right] \left[\alpha \frac{d(\rho_g h_g)}{dP} + (1-\alpha) S_e \frac{d(\rho_f h_f)}{dP} \right] \right. \\
& \left. + \frac{(R-\delta)^2}{2} \left[\frac{V_I^3}{2} + \frac{3V_I^2 (V_k - V_I)}{(m+2)(m+1)} + \frac{3V_I (V_k - V_I)^2}{(2m+2)(2m+1)} + \frac{(V_k - V_I)^3}{(3m+2)(3m+1)} \right] \right. \\
& \left. \left[\alpha \frac{d\rho_g}{dP} + (1-\alpha) S_e^3 \frac{d\rho_f}{dP} \right] + V_I \delta \left[\rho_f \left(\frac{R}{n+l+1} - \frac{\delta}{n+l+2} \right) \frac{dh_f}{dP} \right. \right. \\
& \left. \left. + \left[h_{fw} \left(\frac{R}{n+1} - \frac{\delta}{n+2} \right) + (h_f - h_{fw}) \left(\frac{R}{n+l+1} - \frac{\delta}{n+l+2} \right) \right] \frac{d\rho_f}{dP} \right] \right\} \frac{dP}{d\chi}
\end{aligned}$$

$$\begin{aligned}
& + (R-\delta)^2 \left\{ \left[\frac{V_I}{2} + \frac{V_L - V_I}{(m+2)(m+1)} \right] (\rho_g h_g - S_E \rho_f h_f) \right. \\
& + \frac{1}{2} (\rho_g - S_E^3 \rho_f) \left[\frac{V_I^3}{2} + \frac{3V_I^2 (V_L - V_I)}{(m+2)(m+1)} + \frac{3V_I (V_L - V_I)^2}{(2m+2)(2m+1)} \right. \\
& \left. \left. + \frac{(V_L - V_I)^3}{(3m+2)(3m+1)} \right] \right\} \frac{d\alpha}{d\chi} = -\rho_f V_I \delta \left[\left| \frac{R}{n+1} - \frac{\delta}{n+2} \right| \right. \\
& \left. - \left| \frac{R}{n+l+1} - \frac{\delta}{n+l+2} \right| \right] \frac{dh_{fw}}{d\chi} - R \ddot{q}_f'' \quad (C-7)
\end{aligned}$$

The four differential equations (C-4 through C-7) may be written in index notation as:

$$d_{ij} \frac{d\psi_j}{d\chi} + e_i \frac{d\alpha}{d\chi} = b_i \quad (C-8)$$

Substitution of the expression for entrainment, equation (B-14),

Appendix B yields:

$$(d_{ij} + e_i c_j) \frac{d\psi_j}{d\chi} = b_i$$

or, as in equation (II-27),

$$a_{ij} \frac{d\psi_j}{d\chi} = b_i \quad (C-9)$$

Equations (C-9) form a set of four, non-linear, first order, ordinary differential equations.

N71-71002

FINAL REPORT
to the
NATIONAL AERONAUTICS AND SPACE ADMINISTRATION
in connection with
NASA Grant NGR 47-004-006

Part 7 of 21 Parts

Final Report
VPI&SU Project 313159

The Effect of Water Vapor on the Burning Rate of
Aluminum and Magnesium Wire

by

C. H. Long
Mechanical Engineering

Virginia Polytechnic Institute & State University
Blacksburg, Virginia

December, 1970

THE EFFECT OF WATER VAPOR ON THE BURNING RATE OF
ALUMINUM AND MAGNESIUM WIRE

C.H. Long
Professor, Mechanical Engineering
Virginia Polytechnic Institute
Blacksburg, Virginia

Work has been done on the burning of wires oriented horizontally in environments at high pressures when heating them to rupture point by passing a current through them. The burning rate, along with other phenomena, was measured as the flame moved along the two parts of the wire or ribbon.

It was proposed by Prof. C.H. Long in 1966 that an investigation should be conducted on vertical wires ignited at one end. These tests should be conducted at elevated pressures and temperatures, the burning phenomena observed, and the burning rate determined for various amounts of moisture and oxygen composing the environment in the chamber. This was done in dry oxygen at room temperature and pressures up to forty atmospheres and reported in September, 1967⁽³¹⁾ as Phase I of this project.

In 1968 the project was extended (Phase II) by mixing given quantities of moisture with the oxygen at pressures up to twenty atmospheres.

It was found that heating of the oxygen and the chamber wall to 280°F approximately, in order to allow all the moisture admitted to

evaporate into steam, had a very definite effect of increasing the burning rate of aluminum and magnesium wires up to approximately fifteen atmospheres while the addition of the moisture increased the burning rate of aluminum up to approximately six atmospheres but had no beneficial effect on the burning rate of magnesium.

I. INTRODUCTION

In contrast to the extensive literature on the combustion of conventional fuels, a relatively small number of studies on combustion of metals have been performed. Until only a few years ago, interest in this field was related primarily to such practical problems as the prevention of metal dust explosions in mines and industry, the attainment of high temperatures, and the production of intensive continuous or transient light emission as in commercial flashbulbs.

In recent years, research in this field has been intensified under the stimulus of new technological developments. The severity of the problem of metal-fire prevention has increased greatly with the use of metals in high-temperature and corrosive environments encountered in supersonic flight, rocket engines and jet propulsion as well as nuclear reactor technology. The use of metal fuels or metallized propellants in propulsion, on the other hand, has stimulated research both on ignition and on burning processes. The advantage of using certain metals, preferably aluminum, as fuels for propulsion and in other applications rests on their very large heats of combustion. Metals can be included in most conventional solid propellants in the form of powder or wires to increase the theoretical performance. In practice, the improvement of performance often falls significantly short of the prediction because of incomplete combustion.

Thus, aside from the intrinsic scientific interest there is considerable practical interest in the factors that influence the burning of metals. Because of their qualities as metal additives,

aluminum and magnesium have always been in the center of interest besides a variety of other metals.

The performance of all systems employing these metals can be improved when more information about the fundamentals of metal combustion is obtained. A knowledge of the mechanisms and physical parameters influential in the kinetics of metal combustion is required to predict and generate the conditions which will lead to increased combustion efficiency in the combustion chamber of a rocket motor.

Both analytical and experimental studies have been conducted in the past in an effort to understand and improve the ignition and combustion processes. Theoretical efforts to compute combustion rates have been deficient because of the use of inaccurate models or the application of limiting assumptions that may have been incorrect. A knowledge of the influence of gas pressure, composition and temperature on the burning rate of the metal is a necessary first step. The combustion of metals, as studied by many investigators under a wide variety of experimental situations, has been described alternatively as occurring on the metal surface, in the vapor phase or as a combination of both. A heterogeneous reaction occurring on the surface of condensed products in the flame zone was also taken into account. These distinctive features introduce additional complications into the already involved field of combustion in general. These aspects of metal combustion, different from those of hydrocarbons, together with the relatively small research effort are the reason for

this comparative lack of understanding in spite of our rapidly increasing interest.

Although the major portion of the experimental work on metal combustion has been accomplished by those working with powdered material, injected into gas burners, more recent work at Princeton with wires showed promise of this technique of providing more fundamental information about metal combustion than could be obtained with powders. The advantages of the study of metal combustion by burning wires is provided in part by the stabilization of the reaction in time and space. Other advantages of working with wires are the convenient way to collect the solid combustion products from the bottom of the combustion chamber and the easy way to operate in defined atmospheres. In fact, nearly all experiments carried out at higher pressures were conducted using wires. Usually, experimental results are strongly affected by the experimental conditions and techniques. Nearly all of the investigators in wire combustion use resistance heating to bring the wire to ignition temperature. This preignition period may have a pronounced effect on the thickness of the oxide coat covering the metal and on the subsequent combustion. Hence, some of the experimental techniques employed may be quite inadequate for gaining new information about the fundamental phenomena involved.

It is felt that the experimental technique developed in the Mechanical Engineering Department at Virginia Polytechnic Institute, Blacksburg, Virginia in recent years provides an excellent tool for investigation of the factors influencing metal combustion. Longitudinal burning is induced by igniting the wire locally on one

end a flame zone progresses cigarette-fashion from one end of the wire towards the other.

This work was carried out in an attempt to increase the understanding of basic metal combustion processes. The propagation rates of the burning zone were measured at various pressures in pure oxygen and oxygen-water vapor atmospheres. The experimental conditions were quite different from those occurring in the partical experiments, usually carried out with torch burners. It is hoped that a comparison of observations made under basically different conditions might help separate the effects of the environment from the phenomena of metal combustion.

II. Experimental

In Phase I of this investigation (See Report #6, Semi-Annual Report, NASA Grant NGR 47 004-006, Project 31669) Hans Sebald under Professor Long's supervision used William Proctor's² apparatus and determined the burning rates for aluminum and magnesium wires in dry oxygen initially at room temperature and at various pressures up to 38 atmospheres. Sebald also determined the effect of moisture on the burning rate at two pressures, 23.7 and 39.7 psia. For the instrumentation refer to Sebald's thesis and Grant Report #6. His results are shown on curves in Figure 1 and 3 up to pressures of twenty (20) atmospheres. Sebald also found that there was a considerable difference in the burning rate for both the aluminum and magnesium wire when it was burned in heated dry oxygen at these two pressures when compared with the rates obtained from burning the metals in cold dry oxygen. Figures 1, 2, 3, and 4, resulting from work of Phase I and Phase II, graphically portray the differences for burning both aluminum and magnesium in cold oxygen, hot oxygen and moisture laden oxygen.

In Phase II the first task undertaken was that of devising a means of obtaining pictures of the burning process under various conditions. Figures 1 and 3 indicate that the burning rate increase sharply as the pressure is raised above one atmosphere to three atmospheres. Then the rate drops and rises again as the pressure increases from three to ten atmospheres. After about fourteen atmospheres, the burning rate decreases to its approximate original value at twenty atmospheres. Then the burning rate starts

to climb again. It was hoped the pictures would show some physical difference in the combustion at various pressures and environments. Pictures were taken at speeds up to 64 frames per second in black and white and in color. A silent colored motion picture reel which accompanies this report shows the burning of both aluminum and magnesium at various conditions described therein. Different filters were used to show off both the smoke in one case and the flame dimensions in another.

As previously mentioned in Phase I Sebald evacuated the heated chamber, added oxygen until the pressure was atmospheric and then admitted steam until the pressure had increased the equivalent of the vapor pressure desired. Finally, the oxygen was again added until the chamber was filled to the total pressure for a given investigation. When this procedure was followed in Phase II it was found that moisture condensed on the windows and the true quantity of moisture present was questionable. It was also found that the wire would not reliably burn under these conditions. A new method of adding moisture was devised.

Investigation procedure for Phase II starting with a clean combustion chamber which had been vacuumed with a cleaner to remove particulate from the bottom of the chamber, a new fuse was fastened to the post fuse holder. (See Report #6). The wire was fastened into the holder at the top of the chamber and the assembly lowered into the chamber and secured. The chamber was evacuated and the pressure determined from the calibrated pressure transducer and Ellis Bridge. It was found that the pressure pickup had to be

fastened to the side of the chamber as close to the orifice as possible. All parts had to be heated and insulated to prevent moisture condensation which produced erroneous signals.

The steam and electric heating for the top and bottom of the chamber had previously been activated. No tests were run until the proper wall temperature, approximately 20 F above the vapor saturation temperature, had been reached.

The proper quantity of distilled water was then added and the vapor pressure read when all the water was evaporated. The valve at the chamber entrance was then closed and oxygen was added through heated lines slowly to bring the pressure to the final desired value. The oxygen pressure was kept above the chamber pressure at all times to prevent vapor from escaping.

The temperature readings for the combustor wall, top and bottom were recorded. The initial turbidity reading was made using the signal on the brush recorder chart from the photo cell placed at one window. The signal came from a light bulb used as a light source at the opposite window. The start position for the investigation was marked on the recorder paper. The twenty five (25) minute warm-up period followed.

During this period the switches on the resistor bank in the ignition fuse circuit were set and the rectifier supplying ignition power was started. The pressure transducer reading was observed for leak indication which would void the test. The camera was set into position and the turbidity light was turned off.

The ignition switch, the moving picture camera and the recorder

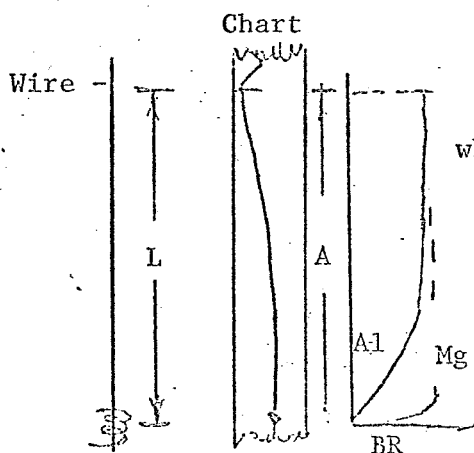
were started simultaneously. The ignition switch was opened when indication appeared on the recorder chart that the wire burning had passed the upper photocell. The final turbidity reading was taken immediately after the wire was burned.

The pressure was then released, the top was removed and the residue from the fuse and wire were collected. The vacuum sample paper was then attached to the vacuum cleaner and the combustion chamber was cleaned out. The sample paper with its white or yellow spheres, powder or filings were filed for further study.

As stated in the 1967 Report #6 the average burning rate was found by dividing the distance between the center line of the two photocell observation slits, in centimeters, by the distance between the peaks on the recorder chart divided by the paper speed. The paper speed was 12.5 cm/sec.

In order to arrive at a value for the ignition time, the time lapse between the energizing of the fuse and maximum light signal at the lower window was measured. The length of wire from window to fuse, L, was also measured.

For aluminum, the ignition time, in seconds, was found by the equation given below



$$\text{Ignition Time} = \left(A - \frac{L}{\frac{BR}{2}} \right)$$

where A = total time from switch closing to maximum peak at lower window

$$A = \frac{L \times 2.54}{12.5}$$

12.5 = paper speed, cm/sec

BR = average wire burning rate

L = distance from fuse to center of photocell window, cm

For the magnesium, the burning rate was not divided by two since it was felt magnesium reaches average velocity almost instantaneously.

Figures 5 and 6 show the variation of ignition time with pressure for hot dry wire burning and for some conditions where moisture was present.

III. Discussion of Results

The first section of the discussion will deal with the hot dry oxygen investigation and the runs where approximately 2.5% moisture was added to determine the effect of moisture, heat and pressure on the burning rate of aluminum and magnesium wires. The effect of variation of moisture on the burning rate at three specific pressures 6, 10 and 14 atmospheres, will then be discussed.

Other parameters which were measured and their effect on the burning rate of the two types of wire will then be discussed. These parameters are (1) smoke density as evidenced by the motion pictures visually and measured before and after the tests by a photocell and called turbidity, (2) the ignition lag time calculated from the charts used to measure the burning rates and (3) the color pictures of the residue collected after each test.

A. Burning Rates of Aluminum in Hot Dry Oxygen

Figure 1 indicates that the heating of the dry oxygen in the combustor with the walls at 280 F for 35 minutes before determining the burning rate caused the rate to increase from 11 cm/sec to 15 cm/sec at one atmosphere. The rate decreased to 15 cm/sec at two atmospheres but increased to 18.3 cm/sec at 14 atmospheres. Then, apparently, the effect of this parameter became nil as the burning rate approached 20 atmospheres. As seen by Sebald and previous investigators⁽⁴⁾ the burning rate between fifteen and twenty atmospheres decreases to the value of the rate at one atmosphere when burned in cold oxygen, 11 cm/sec.

B. Burning Rates of Aluminum in Hot Oxygen With Approximately 2.5% Moisture Present

The addition of 2.5% moisture increased the burning rate to 16.5

cm/sec at 6 atmospheres, 14% greater than when it was burned in cold oxygen and 6% greater than when it was burned in hot oxygen.

At seven atmospheres the effect of moisture was nil. Above this point moisture actually decreased the rate obtained with hot oxygen. Above 12 atmospheres moisture decreased the rate of burning even in cold oxygen or it at least canceled the effect of heating the oxygen prior to burning.

C. Burning Rate of Aluminum Wire at 6, 10 and 14 Atmospheres As Moisture is Varied

At six atmospheres pressure and between zero and 0.5% moisture, the burning rate of the aluminum increased from 15.5 cm/sec in hot dry oxygen to 16.0 cm/sec (Figure 2). The rate continued to increase 16.5 cm/sec at 2.0% moisture. In the presence of 3.5% moisture the rate dropped to the hot dry value and continued to drop to approximately 14 cm/sec at seven per cent moisture beyond which it was difficult to obtain ignition.

At ten atmospheres pressure the dry burning rate was 17 cm/sec. At 0.5% moisture the rate had increased to 17.8 cm/sec. At 1% moisture it was back to the dry value and beyond this it continued to decrease to 13.8 cm/sec at 5% moisture. In the presence of more moisture it was hard to ignite the wire at this pressure.

At fourteen atmospheres the burning rate increased rapidly with a trace (0.4%) of moisture to 19.5 cm/sec from 18 cm/sec in the hot dry oxygen. At 1% moisture the rate was reduced to the hot dry value and at 2.5% moisture the wire was difficult to ignite and only burned at 14.5 cm/sec when it did ignite.

Therefore, it is apparent there is a pressure, heat and moisture effect on the burning rate of aluminum wire in this range.

The pressure effect on the burning rate was a 41% increase from one to fourteen atmospheres and then a rapid vanishing of this effect as the pressure approached 20 atmospheres.

The heating effect caused an increase of 17% in the burning rate even beyond the fourteen atmosphere point and did not disappear completely at 20 atmospheres.

The moisture effect appears to vary with pressure. At six atmospheres moisture increased the rate 8.7% with 2% moisture present. At ten atmospheres the vapor increased the burning rate 4.3% in the presence of 0.5% moisture. At fourteen atmospheres a 0.4% trace of moisture increased the rate 13%.

D. Burning Rate of Magnesium In Hot Dry Oxygen

Heating the oxygen initially to 280 F decreases the burning rate of magnesium over that in cold oxygen at two atmospheres from six to four and nine tenths cm/sec. At four atmospheres the rate increased from 7.8 in cold oxygen to 8.6 cm/sec in hot oxygen. From this point on the heat increases the burning rate 25% up to 14 atmospheres and as much as 50% at 18 atmospheres. The sudden decrease in burning rate experienced with aluminum is not present with magnesium (Figure 3).

E. Effect of the 2 to 3% Moisture on the Burning Rate of Magnesium Wire

The moisture does not stimulate the combustion of magnesium wire as it does aluminum even at low pressures. As shown in Figure 4 it approximately cancels the effect of heating the oxygen initially.

F. Effect of Various Percentages of Moisture on the Combustion of Magnesium Wire

Even at low percentages of moisture the burning rates of magnesium wires are decreased as moisture is added. The magnesium was not difficult to ignite under any condition of pressure and moisture except at atmospheric pressure in the presence of water vapor.

G. Influence of Pressure and Moisture on Ignition Lag

Before beginning this discussion reference is made to the method by which the so-called ignition lag was determined and the fact that the magnesium absolute values are twice the aluminum values.

(a) Aluminum Wires (Figure 5)

It took less time to ignite the wire in 100% hot dry oxygen as the pressure increased from one to four atmospheres. The lag dropped from 2 seconds to 0.5 seconds. Then, as the pressure was increased to 12 atmospheres the lag increased again up to 1.75 seconds. Again, the lag fell sharply to 0.6 seconds at fifteen atmospheres and at twenty atmospheres rose again to one second.

As the moisture was increased this lag generally decreased about 33% in the 14-20 range of atmospheres. In the 8-14 range of pressure the moisture had a greater effect. It appeared to reduce the lag approximately 58%.

Below six atmospheres it is possible that moisture may increase ignition lag of aluminum wire. Above 14 atmospheres the effect of moisture is not significant.

(b) Magnesium Wires (Figure 6)

The ignition lag of magnesium wire decreased from 2 seconds at 1 atmosphere to approximately 0.75 second at 14 atmospheres. This

was an eighty-eight per cent decrease.

When the moisture in the environment was increased as much as 2%, the ignition lag increased as much as 47% at 14 atmospheres.

One interesting phenomena observed was on the 4% moisture curve which indicated that ignition lag increased with increase in pressure and it even exceeded the lag for wire ignited in hot dry oxygen at 14 atmospheres by 60%.

When the wire was left to temper in hot, wet oxygen for a fifty-five minute period instead of twenty-five minute period, the ignition lag was reduced 60%.

H. Effect of Pressure and Moisture on Turbidity (Smoke Formation) Resulting from Aluminum Wire Burning in Oxygen

One interesting observation made while determining the burning rate was the variation in the smoke density in the combustion chamber immediately before and after a test was performed. Figure 7 and 8 indicate the trends for the study made.

The general statement could be made that the turbidity reduces with pressure, at least up to 14 atmospheres, that moisture has the tendency to reduce smoke density and it appears there is a given percentage moisture which reduces smoke formation. This might be of significance with air pollution combustion problems.

I. Effect of Moisture on the Residue From Aluminum Wire Burning at Pressures up to 20 Atmospheres

(a) Aluminum

There does not seem to be any radical difference in the samples of residue collected from the bottom and the walls of the combustion

chamber after each test over the pressure range studied. The typical samples described by many authors who have reported on burning aluminum drops were seen over the range investigated. The small hollow spheres ranged in color from white to tan to yellow. Small, medium and large clinkers or hunks, exploded, dropped, or spattered parent metal, or pieces of partially oxidized metal were collected.

It might possibly be said that the spheres were smaller and had a yellow instead of a white tint when the wire was burned in dry hot oxygen while spheres from the wire burned moisture were white. Spheres were larger at higher pressure and as the moisture increased. This could be because the hot dry particles have a greater affinity for the iron in the bottom or sides of the chamber as they fall. There could also be some iron in the impurities of the wire. A better possibility is that AlO or Al was present when condensation occurred. AlO formed during combustion would appear yellow on condensation and Al vapor condensing on the Al_2O_3 would result in a yellow oxide coating.

(b) Magnesium

The residue for magnesium appeared to be spheres which had adhered to one another or even bubbles which had elongated and solidified. Also, it appeared new bubbles were being formed on the side of the spheres when they had suddenly solidified.

A large quantity of oxidized metal fragments was found. The moving pictures taken of the burning indicated that fragmentation was occurring.

It appeared also that the larger spheres were predominant at higher pressures as was the case with aluminum.

J. Observations from the moving pictures taken of the investigation

When viewing the moving picture, the motion of the flame up and around the wire is more apparent. The process causes the wire to vibrate irregularly. Possibly noise or accoustical instability could be studied further by extending these observations.

With a yellow filter, the smoke behavior and quantity can easily be observed. With a blue filter the flickering flame zone can be watched as it moves about the wire. It is hoped more funds will be made available for such a study of this oscillating flame.

The ignition of an aluminum wire was studied at fourteen atmospheres with 3% moisture present after the fuse was moved up into view in the range of the window. Studying the film record of such an event one sees first, the fuse become white hot, smoke and light increase as the aluminum inner fuse is melted and vapor formed and ignited. Finally, the ball of fire around the wire is seen as it attains its separate identity moving up the wire. The history of the burning of the pool of molten aluminum left from the fuse is also observed. Clouds of smoke from erratic burning are seen at intervals during the reaction.

IV. Summary

It was found that heating the environment had more effect on the burning rate than did increasing the moisture in the environment up to twenty atmospheres. Moisture had an effect on the burning rate of aluminum wire in the 4 to 15 atmosphere range. It had little or even adverse effect on magnesium burning. It is hoped this investigation can be continued to study the burning at higher pressures in the presence of moisture and oxygen at atmospheres up to 150 in value to see if the moisture effect reappears when the burning rate increases again above 20 atmosphere.

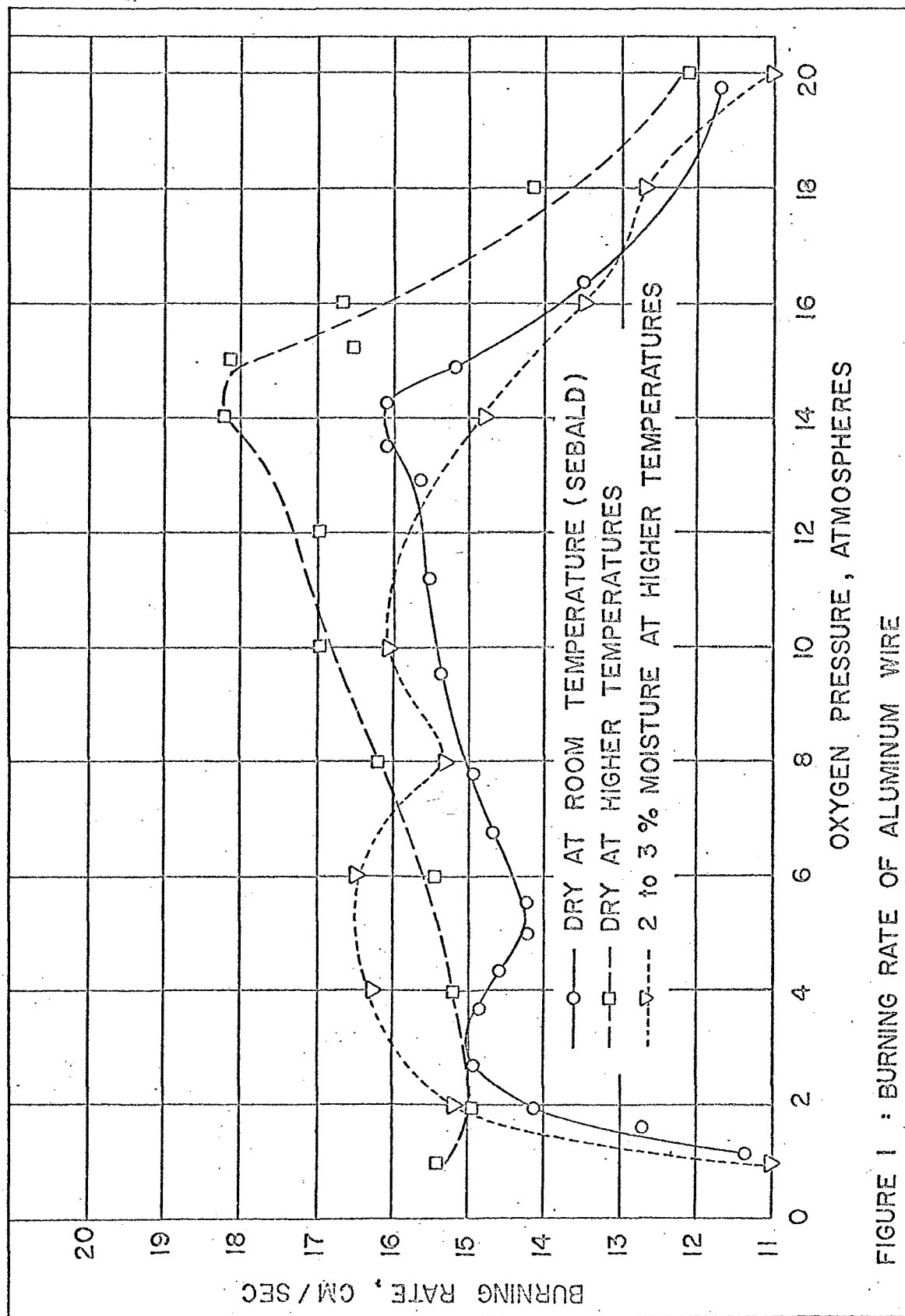


FIGURE 1 : BURNING RATE OF ALUMINUM WIRE

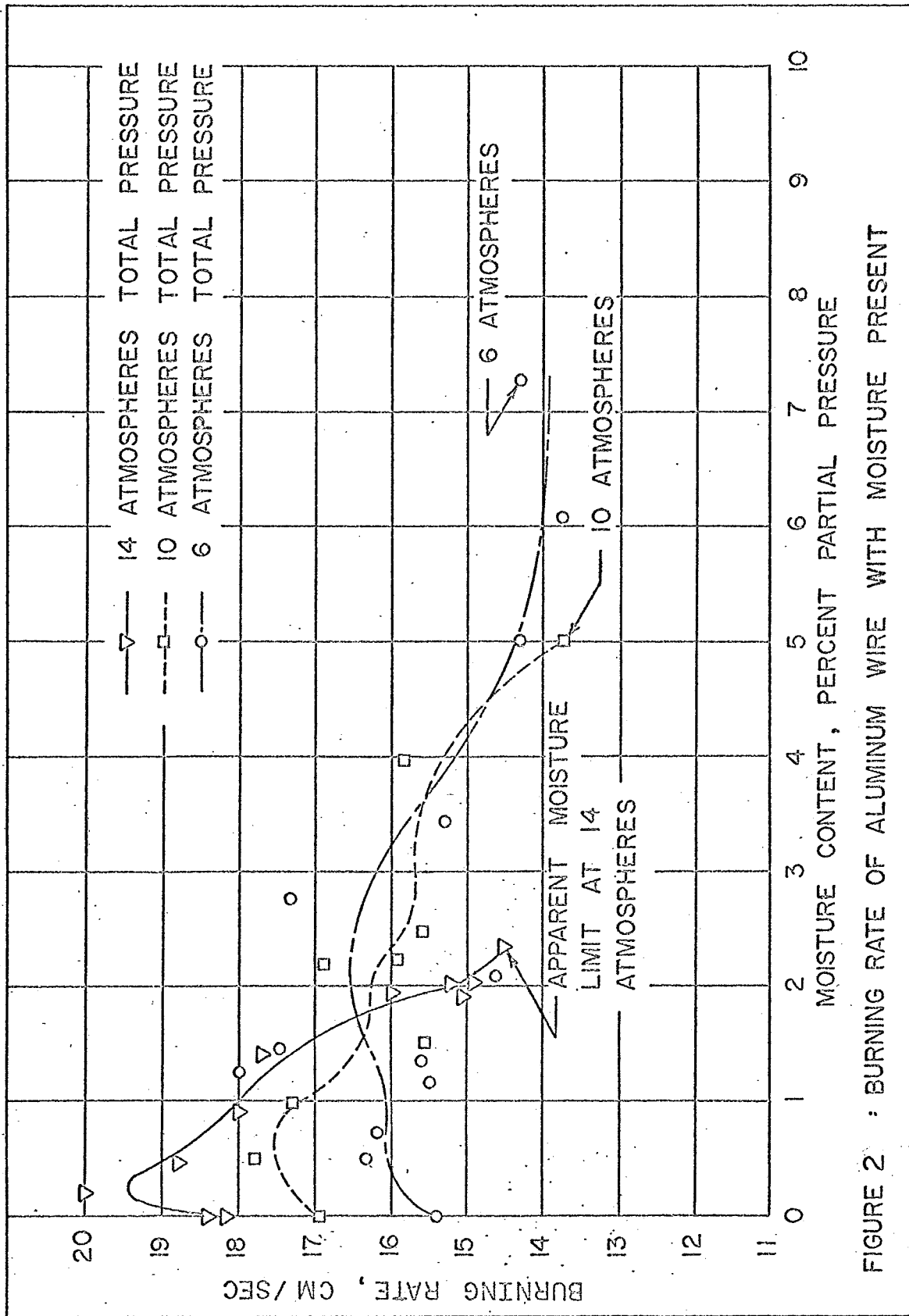


FIGURE 2 : BURNING RATE OF ALUMINUM WIRE WITH MOISTURE PRESENT

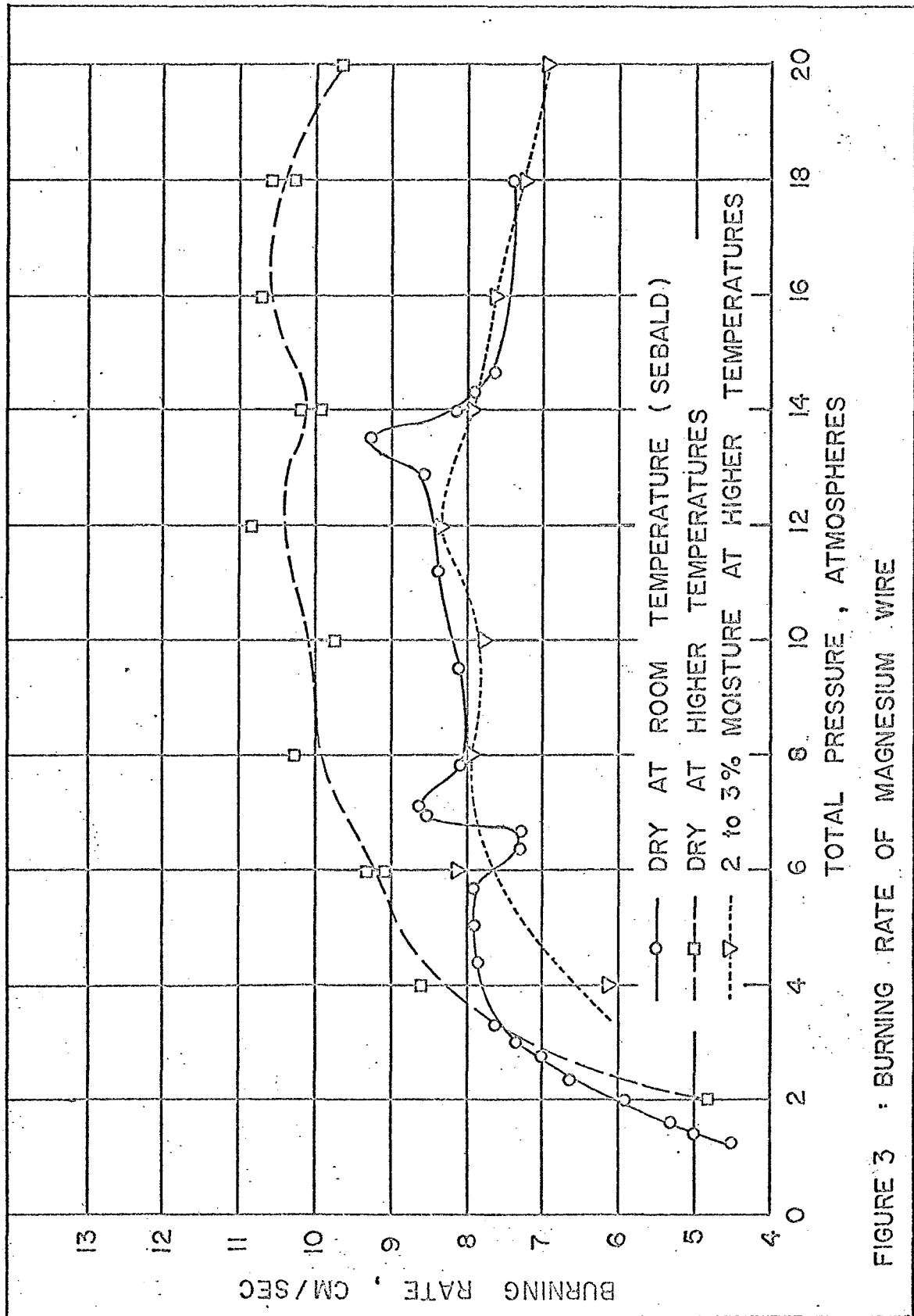


FIGURE 3 : BURNING RATE OF MAGNESIUM WIRE

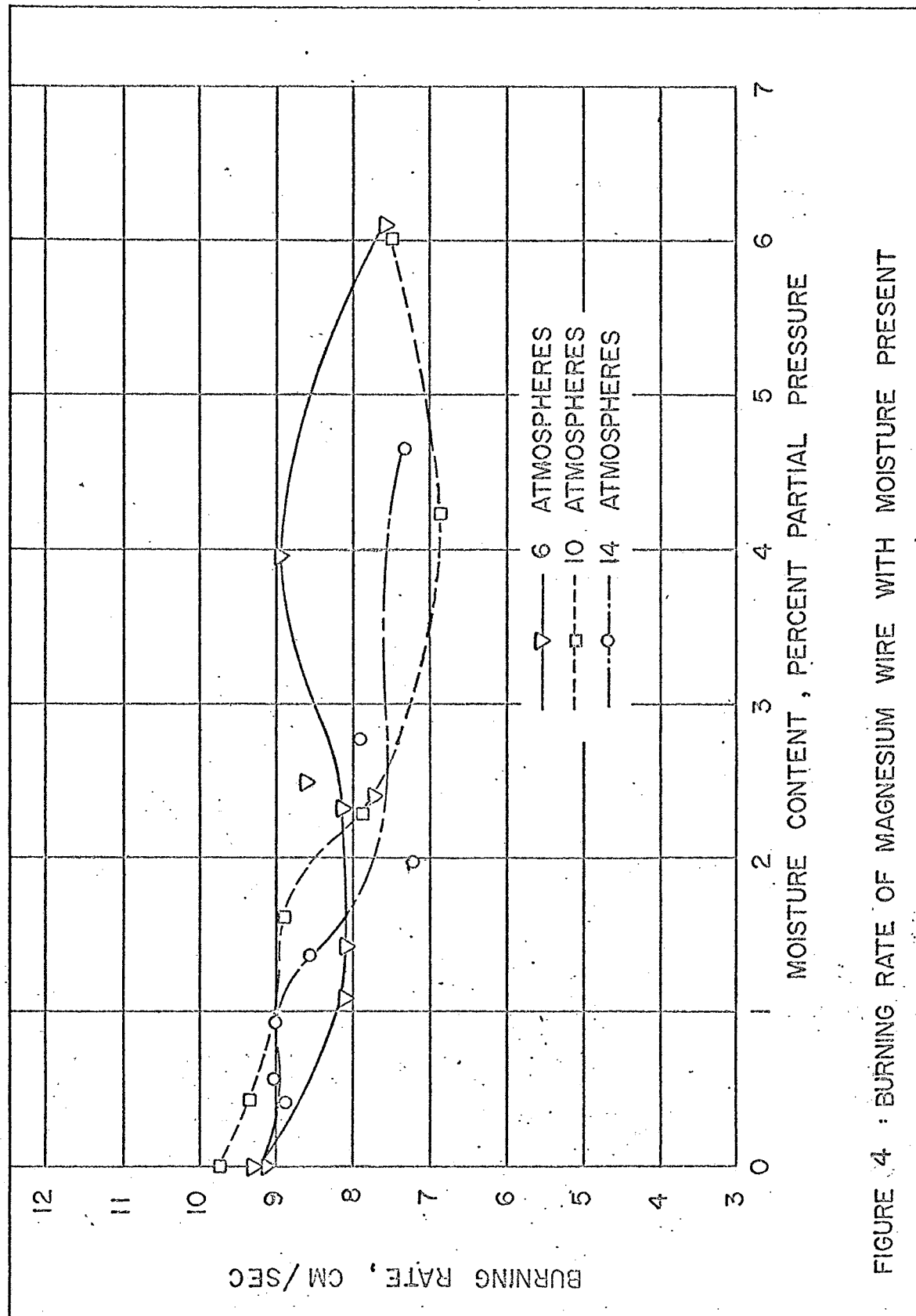


FIGURE 4 : BURNING RATE OF MAGNESIUM WIRE WITH MOISTURE PRESENT

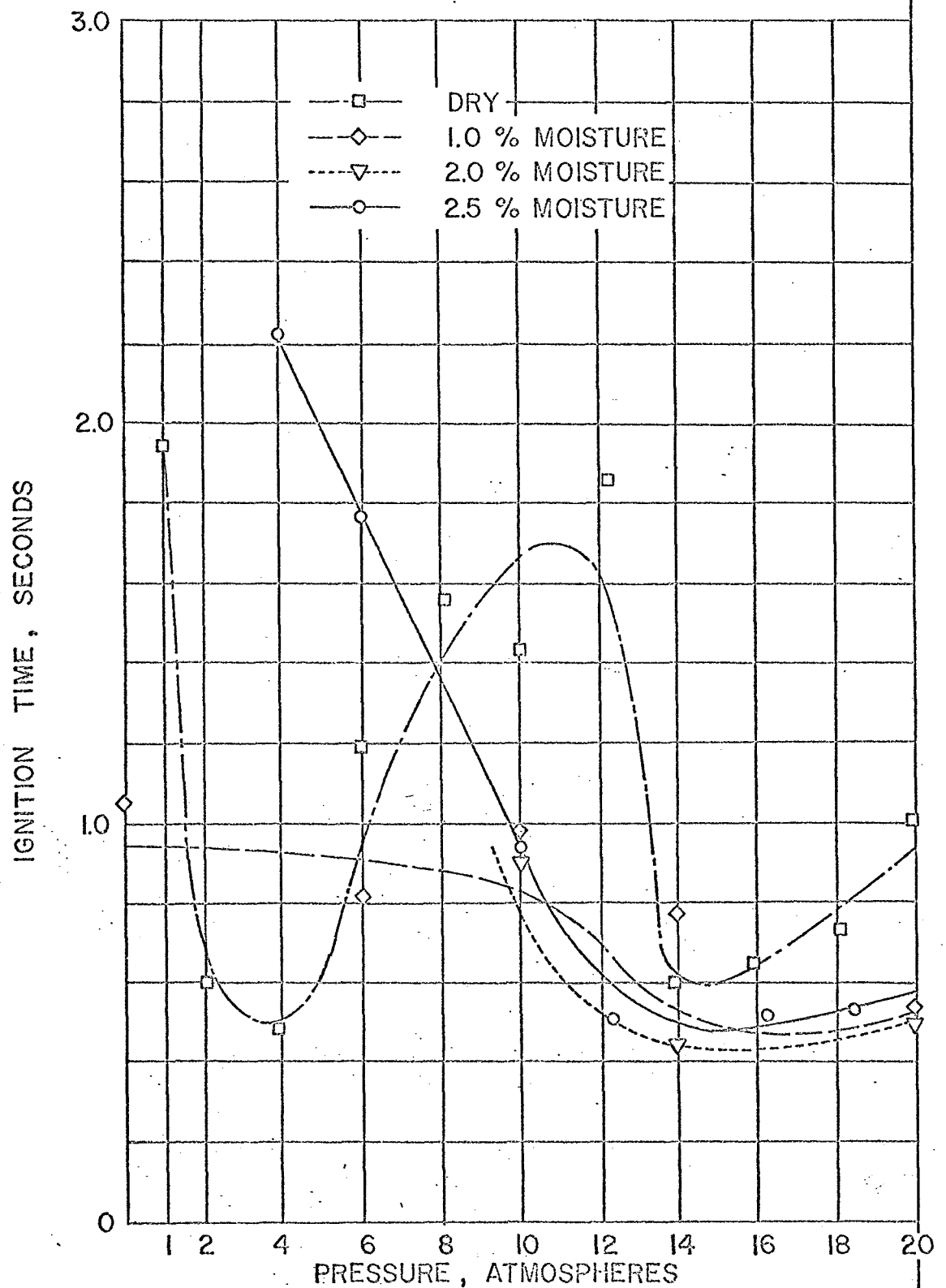


FIGURE 5 : INFLUENCE OF PRESSURE ON IGNITION TIME OF ALUMINUM WIRE

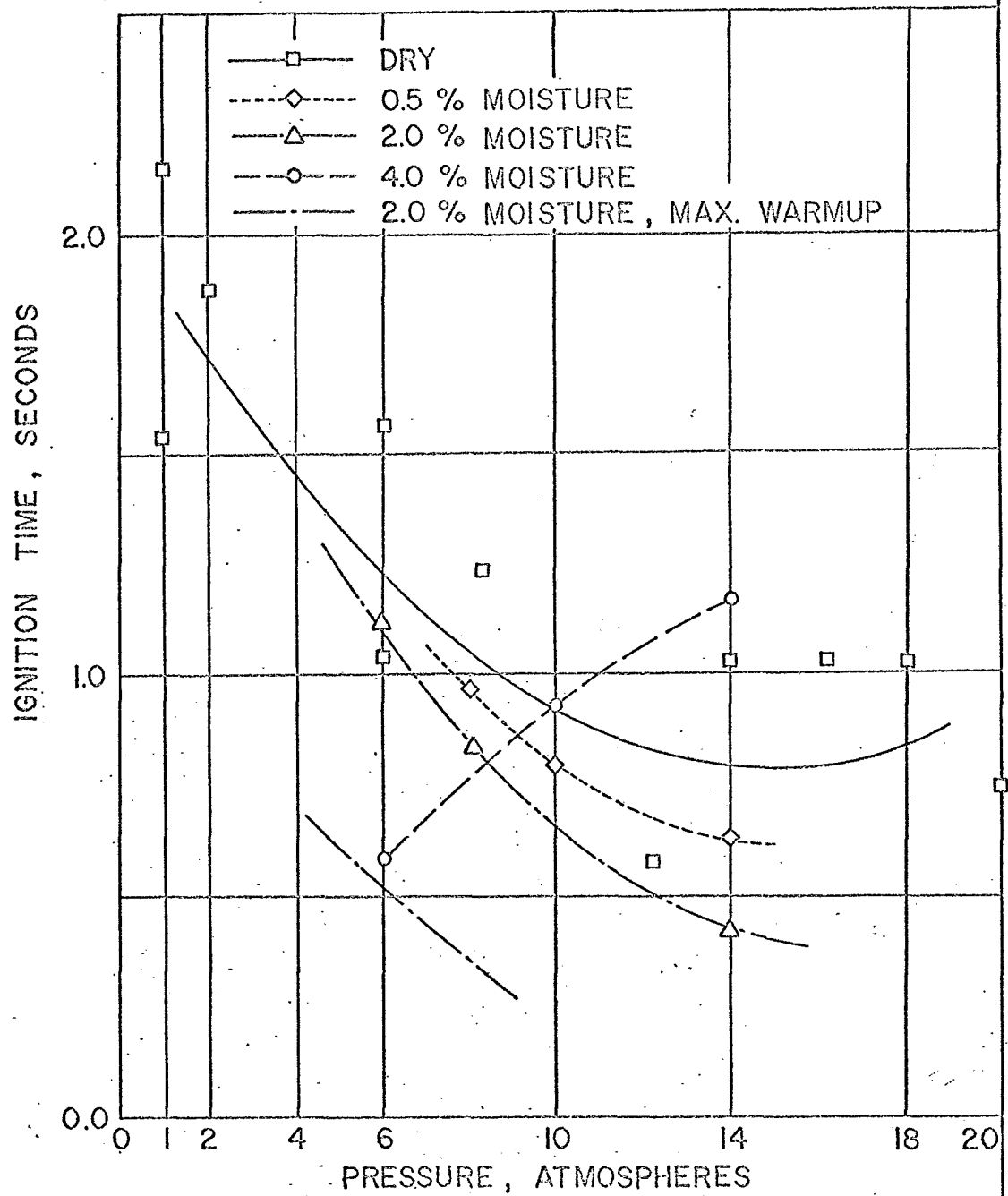


FIGURE 6 : INFLUENCE OF PRESSURE ON IGNITION TIME OF MAGNESIUM WIRE

—○— DRY
 —△— 2% MOISTURE
 —△— 6 ATMOSPHERES
 —○— 10 ATMOSPHERES
 —□— 14 ATMOSPHERES

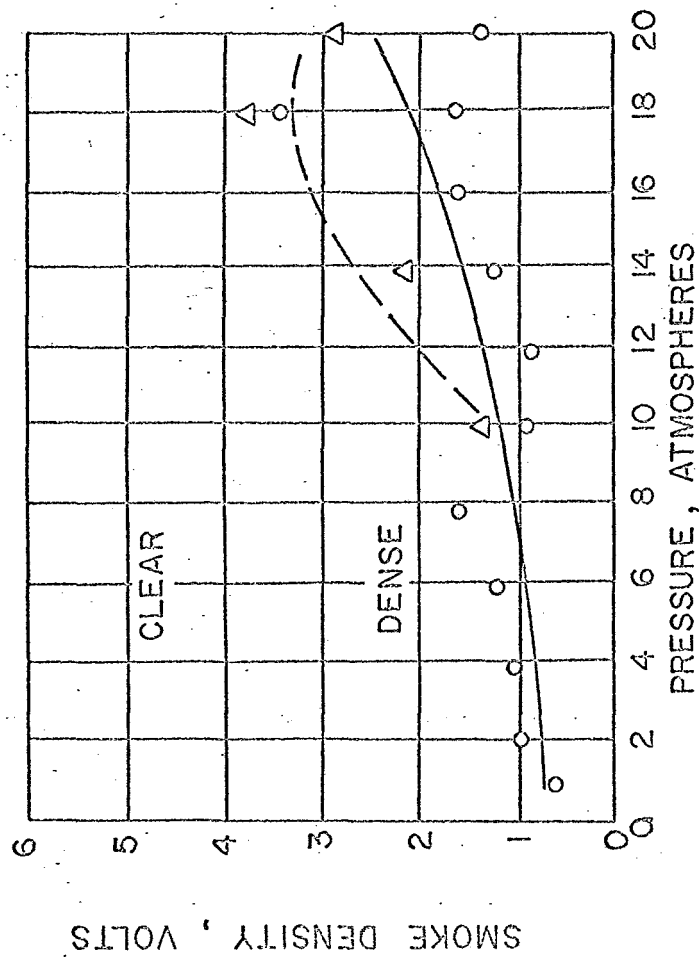
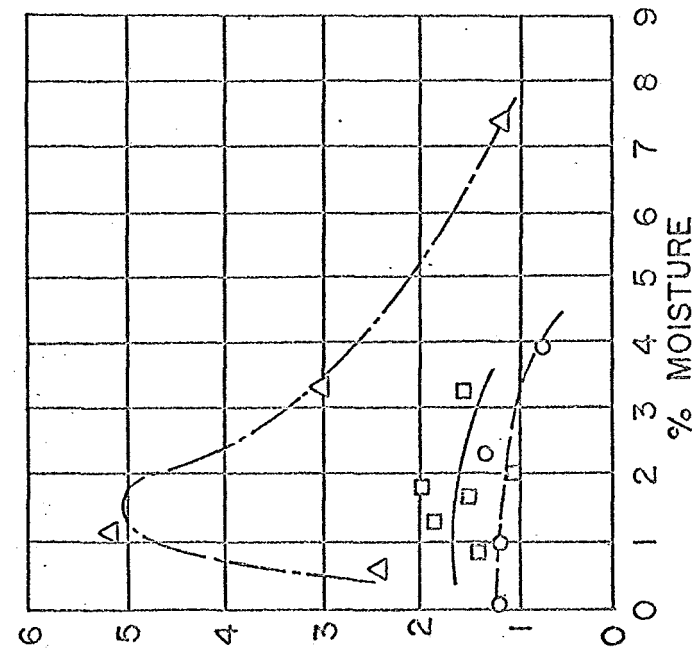


FIGURE 7 : EFFECT OF PRESSURE AND MOISTURE ON SMOKE FORMATION WHEN BURNING ALUMINUM WIRE

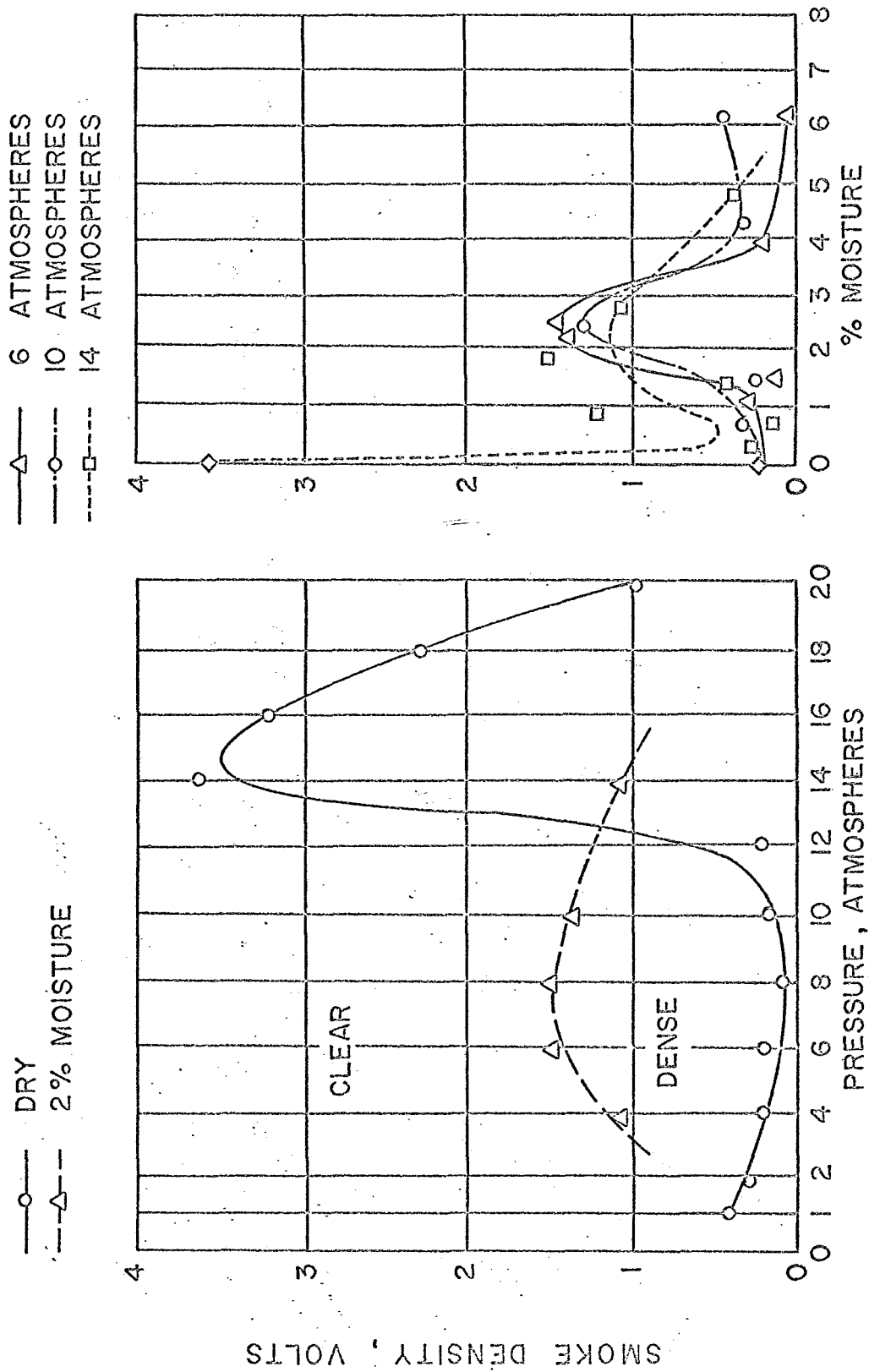


FIGURE 8 : EFFECT OF PRESSURE AND MOISTURE ON SMOKE FORMATION WHEN BURNING MAGNESIUM WIRE

BIBLIOGRAPHY

1. Friant, Ch. W., "Determination of the Burning Rate of Small Diameter Aluminum Wire," Master of Science Thesis in Mechanical Engineering, June 1964, V.P.I., Blacksburg, Virginia.
2. Long, C. H. and W. L. Proctor, "The Effect of Water Vapor Upon the Burning Rate of Aluminum and Magnesium Wires," Western States Combustion Institute, Denver, Colorado, April, 1966. WSC1-66-4.
3. Long, C. H. and Hans Sebal, The Burning Rate of Aluminum and Magnesium Wire In Pure Oxygen and Oxygen-Water Vapor Atmospheres at Higher Pressures, Western States Combustion Institute, Los Angeles, California, April, 1968.
4. Kirschfield, L., "Über die Verbrennungsgeschwindigkeit von Leichtmetalldrähten in Sauerstoff hohen Druckes," Metall, vol. 15, no. 9, September 1961, p. 873-878.
5. Bruzustowski, T. A., and T. Glassman, "Vapor-Phase Diffusion Flames in the Combustion of Magnesium and Aluminum: I. Experimental Observations in Oxygen Atmospheres," Progress in Astronautics and Aeronautics, vol. 15 (Heterogeneous Combustion), 1964, Academic Press, New York and London, p. 117-158.
6. Coffin, K. P., "Some Physical Aspects of the Combustion of Magnesium Ribbons," Fifth Symposium (International) on Combustion, 1955, Reinhold Publishing Corp., New York, p. 267-276.
7. Markstein, G. H., "Heterogeneous Reaction Processes in Metal Combustion," Eleventh Symposium (International) on Combustion, 1967, p. 219-234.
8. Macek, A., "Fundamentals of Combustion of Single Aluminum and Beryllium Particles," Eleventh Symposium (International) On Combustion, 1967, p. 203-217.
9. Markstein, G. H., "Combustion of Metals," AIAA Journal, vol. 1, no. 3, March 1963.
10. Kirschfeld, L., "Über die Verbrennungsgeschwindigkeit von Leichtmetalldrähten in Sauerstoff," Metall, vol. 14, 1960, p. 213-219.

11. Kuehl, D. K., "Ignition and Combustion of Aluminum and Beryllium," AIAA Journal, vol. 3, no. 12, December 1965.
12. Bruzustowski, T. A. and T. Glassman, "Vapor-Phase Diffusion Flames in the Combustion of Magnesium and Aluminum: I. Analytical Developments," Progress in Astronautics and Aeronautics, vol. 15 (Heterogeneous Combustion), 1964, Academic Press, New York and London, p. 75-116.
13. Harrison, P. L. and A. D. Yoffe, "The Burning of Metals," Proceedings of the Royal Society, 1961, vol. A261, London p. 357-370.
14. Kuehl, D. K., "The Ignition and Combustion of Small Diameter Aluminum Wires," Western States Section, the Combustion Institute, 1964 Fall Meeting (WSS/CI Paper 64-21), Salt Lake City, Utah.
15. Davis, A., "The Combustion of Particles of Metal Ingredients," Combustion and Flame, vol. 7, December 1963, no. 4.
16. Cassel, H. M. and T. Liebman, "Combustion of Magnesium Particles II: Ignition Temperatures and Thermal Conductivities of Ambient Atmospheres," Combustion and Flame, vol. 7, March 1963, no. 1.
17. Friedman, R., and A. Macek, "Ignition and Combustion of Aluminum Particles in Hot Ambient Gases," Combustion and Flame, vol. 6, March 1962, no. 1, p. 9-19.
18. Cassel, H. M. and T. Liebman, "Combustion of Magnesium Particles I," Combustion and Flame, vol. 6, September 1962, no. 3, p. 153-156.
19. Dean, L. E., R. C. Keith, T. L. Sumner and M. V. Taylor, "Ignition and Combustion of Aluminum in Small-Scale Liquid Rocket Engines," Journal of Spacecraft and Rockets, vol. 2, no. 5, September-October 1965, p. 753-757.
20. Brewer, L., and A. W. Searcy, "The Gaseous Species of the Al - Al₂O₃ System," Journal of the American Chemical Society, vol. 75, November 1951, no. 11, p. 5309-5315.
21. Glassman, T., "Combustion of Metals, Physical Considerations," Progress in Astronautics and Rocketry, vol. 1, (Solid Propellant and Rocket Research), 1960, Academic Press, New York and London, p. 253-258.

22. Fassell, W. M., C. A. Papp, D. L. Hildenbrand and R. P. Seruka, "The Experimental Nature of the Combustion of Metallic Powders," Progress in Astronautics and Rocketry, vol. 1, (Solid Propellant and Rocket Research), 1960, Academic Press, New York and London, p. 259-269.
23. Bruzustowski, T. A. and T. Glassman, "Spectroscopic Investigation Of Metal Combustion," Progress in Astronautics and Aeronautics, vol. 15 (Heterogeneous Combustion), 1964, Academic Press, New York and London, p. 17-39.
24. Mellor, A. M., and T. Glassman, "Vapor-Phase Diffusion Flames in the Combustion of Magnesium and Aluminum: III. Experimental observations in Carbon Dioxide Atmospheres," Progress in Astronautics and Aeronautics, vol. 15 (Heterogeneous Combustion), 1964, Academic Press, New York and London, p. 159-176.
25. K. P. Coffin, "Burning Times of Magnesium Ribbons in Various Atmospheres," NACA TN 3332, 1954.
26. Drew, Ch. M., A. S. Jordon and R. H. Knipe, "Study of Quenched Aluminum Particle Combustion," Progress in Astronautics and Aeronautics, vol. 15 (Heterogeneous Combustion), 1964, Academic Press, New York and London, p. 17-39.
27. Grosse, A. V. and T. B. Conway, "Combustion of Metals In Oxygen," Industrial and Engineering Chemistry, vol. 50, 1958, p. 663-672.
28. Bruzustowski, T. A., "Vapor-Phase Diffusion Flames in the Combustion of Magnesium and Aluminum," Ph.D. Thesis, Princeton University, Department of Aeronautical Engineering (1963).
29. Handbook of Chemistry and Physics, 46th Edition, 1965-1966, P. D-97-99.
30. Harrison, P. L., "The Combustion of Titanium and Zirconium," Seventh Symposium (International) on Combustion, 1959, Butterworth's Scientific Publications, London, p. 913-918.
31. Semi-annual Report #6 NASA Grant NGR 47-004-006 V.P.I. Multi-disciplinary Grant, 1967.

N71-71008

FINAL REPORT
to the
NATIONAL AERONAUTICS AND SPACE ADMINISTRATION
in connection with
NASA Grant NGR 47-004-006

Part 8 of 21 Parts

Final Report
VPI&SU Project 313367

The Transient Response of a Monotube Boiler

by

F. J. Pierce
Mechanical Engineering

Virginia Polytechnic Institute & State University
Blacksburg, Virginia

December, 1970

THE TRANSIENT RESPONSE OF A MONOTUBE BOILER

Object

This monotube boiler will be used in an experimental program on the transient response of this type steam source. The ultimate goal of the total project will be the development of a control algorithm for such a typical device with the ultimate fabrication and evaluation of a suitable fast response control system. Such a steam generating unit is a potential power source (perhaps with another working medium and energy source) for a fast response prime mover for highly transient local demands in some space applications.

Alternatively, the thorough understanding of and construction of a precise, fast response control system is necessary if such a steam source is to be seriously considered for use as an automotive prime mover where highly variable loading usually results in poor combustion efficiencies with the steam generating unit losing many of its low pollution emission characteristics.

The purpose of this NASA-MDG project was the construction of the heat exchanger portion of a small automotive-size steam generating unit. This boiler consists of an oil-fired combustion chamber within a closely wound helical coil of stainless steel tubing. Hot gases leaving the chamber pass through several rows of spiral tube coils to the exit flue. Feed water enters the spirals at the flue end and passes through a single tube until it emerges from the helical coil as superheated steam.

Substantial progress has been made toward the completion of this boiler. Stainless tubing has been wound into the required coils. The helical portion has been welded and successfully pressure tested. The stainless steel shell.

has been rolled and other sheet parts are in the shop. High temperature insulation has been purchased and construction work is actively underway. Information from numerous manufacturers indicated that the high intensity burner and variable displacement water pump are not available as stock items and will have to be fabricated at this facility.

Fabrication Details

It was intended that the tubing coils be wound on an existing jig which had already been used to successfully coil 1/4 in. steel pipe of 0.540 in. O.D. x 0.088 in. wall. However, the small lathe on which this jig was mounted did not have sufficient torque to bend 0.500 x 0.049 in type 321 stainless tubing. Apparently the smaller moment of inertia of the stainless tubing was more than balanced by the large increase in yield stress resulting from the cold work of bending. This problem was overcome through the design and construction of a special coil winder. This device consists of a circular steel table welded to a vertical shaft supported by ball bearings. It is driven by a 100 tooth worm gear at the lower end of the shaft which meshes with a single tooth worm driven by a 1 hp. motor. The worm is partially submerged in EP-90 to provide the continuous lubrication so necessary for this type of gear. To prevent the tube from swinging around the winder it is guided by a V-roller on a vertical pipe at the edge of the table.

This winder will produce an entirely satisfactory helical coil but spiral coils have excessive transverse spacing. This spacing is critical since it determines the minimum flow area for these combustion gases and hence the intensity of heat transfer. For a given steam generation rate and boiler efficiency the total tube length increases as the tube spacing increases. A longer tube results in increased size, cost, and reaction time, all of which are undesirable. Mechanical spacers to force the tubes together were rejected

for the hot-end coils since these spacers might overheat and fail. This large tube spacing was another result of the high rate of work hardening for which stainless steel is deservedly famous. The action taken was to anneal the coils in an electric furnace at 1600F for 1 hour. The coils were then re-wound on the jig to a smaller spacing.

Welding the coils presented another difficulty. Tungsten inert gas (TIG) arc welding would have been the preferred method but there is not enough space around the tubes to provide maneuvering room for a TIG welder. This method of welding could be used before the tubing is wound but there is no practical way to wind several coils at once. Since resistance or friction welding were not practical it was decided to use an acetylene torch and type 309 welding rod. This has not produced a weld as strong as the parent tube but the nominal stress is low (3200 psi) and a cold pressure test of 2400 psi (stress 9600 psi) caused no failure. Large boilers are normally subjected to a hydraulic test of twice the working pressure. The present coil boiler withstood three times working pressure.

The inner shell of the boiler casing has been made and other sheet metal parts are in fabrication. The stainless steel is annealed and no problems are expected.

The burner for this project must have a maximum heat release rate of 1.2 million B/hrft³ and a turn-down ratio of at least 10. It must burn fuel oil since that is on hand and the available gas line is too small. No manufacturer has been found who can meet these specifications so the burner is being made locally. Previous experience indicates that a carburetor type, which is started on gasoline and then switched to oil when hot, will be satisfactory. A 1-3/4 in. SU carburetor (from a Volvo automobile) has been modified to provide a balanced pressure in the float chamber. An igniter from a

domestic oil burner has been produced. These units deliver 10000v, to ground or 20000v between electrodes and should be a reliable and continuous ignition source. An existing blower has been tested and will deliver 310 cfm at 13 in H_2O which is probably satisfactory without two-staging.

The project is being continued with VPI&SU support.

N71-71009

FINAL REPORT
to the
NATIONAL AERONAUTICS AND SPACE ADMINISTRATION
in connection with
NASA Grant NGR 47-004-006

Part 9 of 21 Parts

Final Report
VPI&SU Project 313365

Development of a Research Program on Electrical
Phenomena in Ceramic Thin Films and Glasses

by

L. H. Slack
Metals & Ceramics Engineering

Virginia Polytechnic Institute & State University
Blacksburg, Virginia

December, 1970

"Development of a Research Program on Electrical
Phenomena in Ceramic Thin Films and Glasses"

A critical phase in the development of research on ceramic films and glasses was accomplished during the summer under this NASA-Multidisciplinary Grant. Two papers were written and some supporting experiments were carried out. Following are the references for the publications submitted.

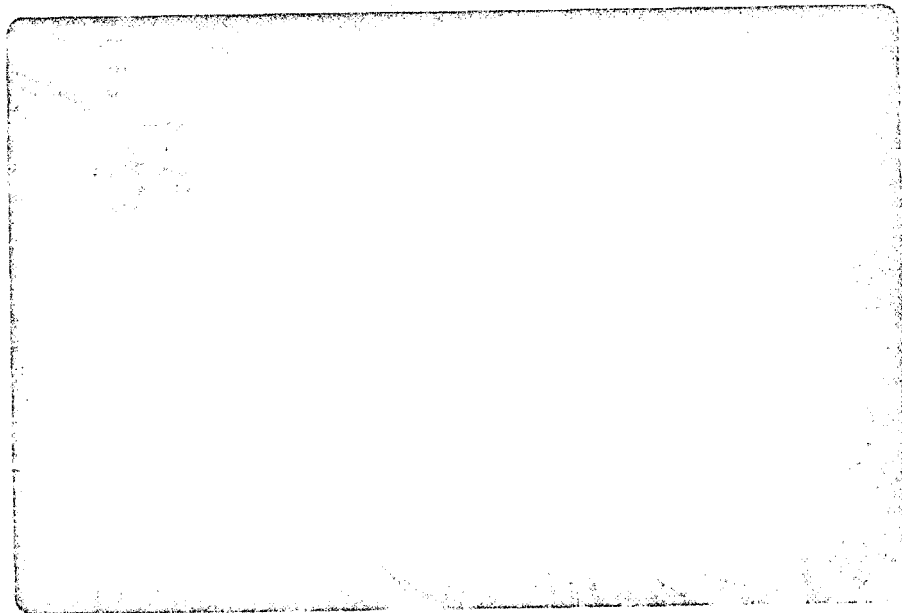
1. (with R. W. Frankson) "Nearly Temperature Independent Electrical Conduction in Manganese Oxide Films", J. Electrochem. Soc., submitted for publication.
2. (with T. J. Gray) "Thermoelectric Properties of Composites Formed by Crystallizing As_2SeTe_2 Glass", J. Am. Ceram. Soc., accepted for publication.

In the first project, on electrical conduction in oxide thin films, oxide films of manganese have been discovered which have resistances which are independent of temperature. The electrical and structural data suggested that the attainment of the zero temperature coefficient of resistivity coincides with the attainment of stoichiometric MnO . The as-deposited films are deficient in oxygen, and heat treated films contain excess oxygen. These research results have great relevance in microelectronic circuits which experience inadvertent temperature changes, and indicate that the mechanism of electrical conduction in MnO thin films is different than that observed in other oxide films.

The publication completed on the thermoelectric properties of semiconducting glasses was based on research completed previously. Recent research on semiconducting glasses has focused on the switching effects in these glasses. The establishment of the "on" memory state in these switches

has been found to be due to the growth of a crystalline filament as shown in the accompanying microphotograph. Eradication of this "on" state is accomplished by resistance heating and melting of this filament. Establishment of the dynamic switching state, in which the conductance of the glass device changes by a factor of 1000 during each electrical pulse, occurs when there is a small gap in the crystalline filament, also shown in the figure. These results are currently being prepared for publication.

The principal investigator and the Metals and Ceramic Engineering Department are grateful for this support.



See color copy Research Division Office File Copy 1/19/71

tjp

Figure. Photomicrograph of a conducting filament in the surface of a $\text{As}_{48}\text{S}_{52}$ glass after dynamic switching (Magnification = 335X).

FINAL REPORT

N71-71010

to the

NATIONAL AERONAUTICS AND SPACE ADMINISTRATION

in connection with

NASA Grant NGR 47-004-006

Part 10 of 21 Parts

Final Report

VPI&SU Project 313366

Systems Simulation of Composition and Temperature Dependence
of Dynamic Hot Corrosion of Metal Surfaces

by

D. R. Tenney

Metals & Ceramics Engineering

Virginia Polytechnic Institute & State University
Blacksburg, Virginia

December, 1970

Systems Simulation of Composition and Temperature
Dependence of Dynamic Hot Corrosion of Metal Surfaces

Introduction

To perform the shuttle mission, a reliable thermal protection system consisting of heat shields, shield supports and thermal insulation to protect the primary structure must be developed. It is generally recognized that more research and development is necessary to establish reliability of flight weight metallic heat shields. The goal of the NASA development technology effort is to have a heat shield which will survive the complex environment for 100 flights. Survival of a heat shield means that its rate of oxidation is slow enough that it will still have sufficient strength to carry the Δp pressure load encountered during flight even after 100 missions.

Depending on the vehicle configuration and reentry trajectory, it has been estimated that titanium alloys and nickel - or cobalt base super alloys may be used for 65 to 90 percent of the orbiter surface. These alloys form protective oxides on the surface which subsequently greatly reduce their rates of oxidation. The oxides slow down the rate of oxidation by providing a protective barrier between the metal and the oxidizing environment. Thus, to select the best alloy for a particular environment, the physical properties of the oxides formed on each alloy being considered must be known. Documented in the literature are several investigations which have been conducted to determine the oxidation behavior of many different metals and alloys in a variety of environments. These investigations, however, have been primarily concerned with the determination of the oxidation mechanism and the particular

rate law describing the rate at which the specimen oxidizes. There is a need to re-examine the data generated by this research with special consideration being given to the properties which make an oxide layer protective.

Progress

It is generally considered that oxidation resistance is the main factor controlling the reliability of heat shields for the thermal protection system of space shuttle. The objective of this study was to investigate those aspects of the oxidation process which have the greatest effect on reliability. Two important areas of this problem have been selected for this research project. The first of these areas is involved with the spallation of surface oxide layers during rapid heating or cooling. During such temperature changes, stresses are set up as a result of the metal and oxide having different coefficients of thermal expansion. Under certain conditions these stresses can be large enough at the oxide-metal interface to cause the generally brittle oxide to fracture at the interface and thus cause spallation. When oxide spallation occurs, "fresh" metal is exposed to the oxidizing environment resulting in rapid oxidation. Thus, each time the oxide layer is removed, there could be a significant decrease in substrate thickness. In the case of a heat shield, this decrease in substrate thickness means a loss of strength which could result in the shield not being strong enough to carry the Δp pressure load encountered during flight. It should be pointed out that the heat shields of the space shuttle will be subjected to large temperature changes and thus could be susceptible to this spallation problem.

The procedure used to study the problem of oxide spallation has been

to simulate the temperature changes occurring in an oxidized specimen during rapid heating. These simulations have been carried out on an analog computer employing the components purchased through this grant. The major purpose of these simulations was to determine the conditions under which the stresses in the oxide at the interface were high enough to cause the oxide to break loose from the metal surface.

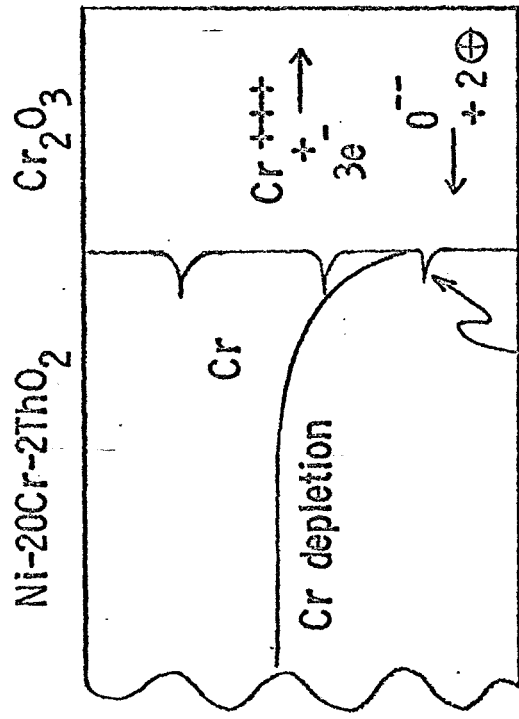
In treating the heat flow by conduction in the oxide and metal it was assumed that the heat flux in the oxide and metal were equal at the interface. It was also assumed that the geometry of the interface was planar such that all heat flow was perpendicular to the interface. A finite-difference approach is being used to solve the appropriate heat flow equations for various boundary conditions. This procedure allows one to use different thermal diffusivities for the oxide and the metal. Preliminary simulations have been completed but the results are not presently in a final form suitable for this report. Final simulations using better constants from the literature will be completed in the near future.

The second area of study is concerned with the redistribution of alloying elements in the alloy ahead of the metal-oxide interface. Preferential oxidation of one of the elements in the alloy will result in concentration gradients existing in the metal beneath the oxide layer. There will be a zone immediately below the oxide where the metal matrix is depleted of the selectively oxidized element and enriched with the other alloying elements.

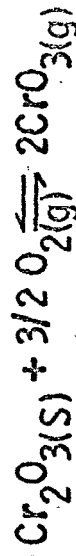
Analog simulation techniques can also be used to investigate the concentration gradients existing in a metal below the oxide layer. The objective of this effort is to be able to determine the concentration gradients existing in the metal as a result of the preferential oxidation of one of the elements

SCHEMATIC REPRESENTATION OF DIFFUSION PROCESSES IN THE ALLOY AND OXIDE PHASE DURING THE OXIDATION OF A NICKEL-CHROMIUM ALLOY

Selective oxidation
of chromium



O₂



$$K_P = \frac{(P_{\text{CrO}_3})^2}{(P_{\text{O}_2})^{3/2}}$$

Diffusion rates in Cr₂O₃ at 2200° F

$$D_{\text{Cr}^{+++}} = 1.27 \times 10^{-10} \text{ cm}^2/\text{sec}$$

$$D_{\text{O}^{--}} = 1.83 \times 10^{-14} \text{ cm}^2/\text{sec}$$

in the alloy. The procedure here is essentially one of using a finite-difference approach to solve the appropriate diffusion equation. Solutions for different temperatures and oxidizing environments which give different rates of oxidation will be considered. Conditions existing in the oxide-metal composite when different rate laws of oxidation are operating will also be studied.

The Ni-Cr system will be used as an example system for these studies. Shown in Figure 1 is a schematic representation of the diffusion processes in the alloy and oxide phases during the preferential oxidation of a Ni-Cr alloy. Although the model is for static oxidation work by this investigator this summer at NASA-Langley indicates that it is probably also an acceptable model for high speed flowing air tests conducted with a low oxygen partial pressure. It should be noted that there is selective oxidation of Cr giving rise to a protective layer of Cr_2O_3 on the surface and a Cr depletion region below the surface. (Under preferential oxidation conditions no NiO is formed because Cr_2O_3 is thermodynamically favored.) The Cr_2O_3 oxide layer is in general very adherent to the substrate and provides good protection for temperatures less than about 2400°F . The protection provided by the Cr_2O_3 oxide layer is generally considered to be due to the fact that the rate of diffusion of O^{--} through Cr_2O_3 is slower than that of Cr^{+++} . As shown at the bottom of the figure the rate of diffusion of Cr^{+++} in Cr_2O_3 at 2200°F is approximately 10,000 times larger than that of O^{--} . Because of this difference in diffusion rates the main oxidation reaction occurs at the outer surface and to a smaller degree along oxide grain boundaries. The rapid diffusion of Cr^{+++} to the surface results in the formation of a large depletion region below the main scale and in the formation of Kirkendall

porosity. (The extent of void formation as a function of time, temperature and other oxidation conditions is a problem the author plans to submit a proposal on in the near future.)

The loss of Cr from the outer surface is generally considered to take place as a result of the higher oxidation of Cr_2O_3 to form CrO_3 which is a volatile oxide. The reaction constant for this reaction is related to the partial pressures of CrO_3 and O_2 as illustrated at the right of the figure. Although this reaction constant is strictly valid only for equilibrium conditions it does serve to show the interdependency of two of the important parameters for a dynamic environment.

To simulate the concentration gradients in these alloys a model based on a mass balance between the supply of Cr to the oxide scale by solid-state diffusion and the loss of Cr from the scale by higher oxidation to form volatile CrO_3 must be used. This model is currently being developed but no simulations have yet been obtained. At the present time only the oxidation of Ni-Cr alloys is being studied. The reason for choosing the Ni-Cr system is that there is considerable data available in the literature on the kinetics of oxidation of various Ni-Cr alloys.

From a practical standpoint, the reliability of a heat shield is related to both of the areas mentioned above. These two areas are intimately related as can be seen by considering what happens when oxide spallation occurs. First, the composition of the metal exposed to the oxidizing environment following spallation can be significantly different from the composition of the starting alloy. The oxidation rate of this newly exposed metal may be much faster than that of the original alloy. This would result in rapid substrate thickness decrease in that area and thus in a loss of strength. This loss

of strength could also enhance the spallation problem in that area if localized flexing or buckling were to take place during subsequent flights.

The funds provided in this grant were used to purchase three components for a TR-20 analog computer in the department of Metals and Ceramic Engineering. Because of long delays by the supplier (Electronics Associates, Inc.), this equipment was not obtained until the middle part of October. Since that time, extensive use has been made of this equipment by our undergraduate and graduate students for simulation studies of metallurgical problems. The seniors in MCE 412 (Design) have used the analog for simulation of metallurgical processes while the graduate students taking MCE 515 have used the analog for the solution of selected diffusion and heat flow problems. These studies have suggested certain problem areas which are being included in a proposal to NASA-Langley currently being prepared by this investigator.

During the period of this grant (July 1 - Aug. 31, 1970) I was working at Langley Research Center in Hampton, Virginia as a NASA-ASEE Summer Faculty Fellow. It is only recently that I have been able to start making use of the equipment purchased on this grant. I am, however, currently preparing a research proposal to be submitted to Langley which will include a simulation study of the oxidation process of metallic heat shields. This simulation study will be performed on the analog computer which contains the components purchased through this grant.

N71-71011

FINAL REPORT
to the
NATIONAL AERONAUTICS AND SPACE ADMINISTRATION
in connection with
NASA Grant NGR 47-004-006

Part 11 of 21 Parts

Final Report
VPI&SU Project 313368

Velocity Measurements in Thin Liquid Films
Flowing on Solid Surfaces

by

W. C. Thomas
Mechanical Engineering

Virginia Polytechnic Institute & State University
Blacksburg, Virginia

December, 1970

VELOCITY MEASUREMENTS IN THIN LIQUID FILMS FLOWING ON SOLID SURFACES

An experimental technique was established for measuring the instantaneous flow characteristics in a thin, falling, laminar film. The hydrogen bubble technique was used to measure the velocity distribution, boundary layer thickness, and film thickness in liquid water films less than one-tenth of an inch thick. It was demonstrated that the technique could be effectively used for these extremely thin films by orienting the bubble generating wire diagonally across the film and observing from a direction normal to the "plane" of the flowing film. Experimental velocity distribution data was obtained during the investigation that will be a significant addition to that previously available. These data, as expected, can be used to infer viscous shear stress at the solid-liquid interface. An unexpected finding was the apparent velocity defect observed in the liquid at the liquid-atmospheric air interface. This appears to result from surface tension effects where the wire passes through the interface. This latter finding causes difficulties in inferring interfacial shear stresses from observed velocity profiles.

The project was an extension of a study initiated earlier with VPI Research funding. One graduate student completed his thesis research with VPI support. An additional graduate student was supported by the NASA-MDG phase of the project for two months and contributed to the success of the broader project. In the joint project, an analytical as well as an experimental study was carried out. Three different flow regimes for laminar falling films were identified and analyzed. The distinguishing characteristics of these regimes were classified as accelerating and boundary layer developing, accelerating and fully developed, and non-accelerating fully

developed film flow. Experimental data were obtained for each regime and compared with analytical results. The agreement was generally good. Further detailed information is available in a mechanical engineering master's thesis entitled: "Flow Characteristics of Thin Liquid Films," (Jan. 1970).

One subsequent proposal, "Heat Transfer from Spray-Wetted Tubes Exposed to Air Flow," which, in part, was an outgrowth of the project has been submitted to the National Science Foundation.

4 N71-71012

FINAL REPORT
to the
NATIONAL AERONAUTICS AND SPACE ADMINISTRATION
in connection with
NASA Grant NGR 47-004-006

Part 12 of 21 Parts

Final Report
VPI&SU Project 313240

A Theoretical Investigation of Low Mass Meteoroids

by

R. J. Adler
J. M. Alvarez
R. Hiromoto
M. Rasmussen
Physics

Virginia Polytechnic Institute & State University
Blacksburg, Virginia

December, 1970

A THEORETICAL INVESTIGATION OF LOW MASS METEORIDS

Abstract

Processes capable of ejecting small particles from the solar system were investigated. It was found that the comminution process produces very small particles in sizeable quantities. The Poynting-Robertson effect spirals these very small particles toward the sun where they evaporate and then spiral outwards due to radiation pressure. The lifetime of a Poynting-Robertson particle is $10^7 - 10^8$ years. A north-south component to the sun's magnetic field is capable of ejecting very small particles in a very short time (of the order of 10 - 100 years for a one micron particle). However, the existence of such a field is in doubt. Dynamical effects caused by the gravitational field of the planets were found to be negligible for a particle in the region of Earth's orbit.

Introduction

Past analyses of the Pegasus and Explorer satellite penetration data have uncovered the possibility of a low mass meteoroid cut-off. Figure 1 presents the penetration data from the two series of satellites together with some best fitted curves to the data.^(1,2) A straight line will not fit since the Pegasus and Explorer satellite data define essentially different slopes on log-log scales. It is the slope difference between the two sets of data which indicates that perhaps the low-mass meteoroid cut-off is close to the Explorer data.

Previous meteoroid data obtained in space does not show any trend toward cut-off. However, it should be noted that nearly all previous data were obtained by using meteoroid detectors consisting of piezoelectric elements attached to some rigid surface. The instabilities of piezoelectric elements used in this manner have been investigated.^(3,4) The investigations have shown that these detectors generate false impacts, which was not known at the time. Thus past meteoroid data obtained by these detectors has been discarded in this report.

There were other meteoroid experiments launched after Pegasus and Explorer. One of these was the penetration experiment on board the Ariel II satellite.⁽⁵⁾ Figure 1 shows the results of that null experiment. The Soviet Union has also launched some recent meteoroid experiments using special acoustically isolated piezoelectric meteoroid detectors of a new design. The data from these detectors is also in Figure 1.⁽⁶⁾ It is evident that the supposition of a low mass meteoroid cut-off (and a consequent

maximum flux) does not contradict this newer data.

The supposition of a minimum sized particle has yet to receive experimental verification. Once a cut-off is measured, however, a physical reason for it must be established. The purpose of this study is to investigate the physical processes which are responsible for meteoroid cut-off and perhaps help establish where further experimentation of this phenomena might be most fruitful.

The following sections present descriptions of the processes investigated along with some discussion of the effects.

A. Physical Processes Responsible for Cut-Off

Poynting-Robertson Effect:

A very striking effect predicted by the special theory of relativity is the Poynting-Robertson Effect. A particle in motion around the sun will experience pressure from the sun's radiation not only in the radial direction but also tangentially — against the particle's motion. This tangential drag will cause the particle to lose angular momentum and to eventually spiral into the sun. Following the development given by Robertson,⁽⁷⁾ we can sketch the derivation of this effect, with the expressed interest of getting a typical particle's lifetime in the solar system.

Consider a small, spherical particle of radius a , density ρ , moving with a unit four-velocity u^μ in the system S , in which the sun is at rest. In S , the sun's radiation falling on the particle can be considered to be a plane wave with the incident direction defined by the dimensionless null four-vector ℓ^μ , with $\ell^0 = 1$. The energy-momentum-stress tensor can be written as⁽⁷⁾

$$(A.1) \quad S^{\mu\nu} = d(\ell^\mu \ell^\nu)$$

where d is the energy density of the radiation.

Upon going to the nearly inertial proper frame of the particle, P , the four-velocity of the particle and the four-velocity of the incident radiation are given by

$$(A.2) \quad v^\mu = \delta^\mu_0, \quad \lambda^a = c\lambda^0 v^a \quad (a = 1, 2, 3)$$

where v is the direction of the incident radiation in P . We assume that the particle is in thermodynamic equilibrium; that is, the rate at which the radiation is absorbed is equal to the rate at which the particle isotropically re-emits radiation. This means that mass is constant in P , or

$$(A.3) \quad \frac{dmv^0}{d\tau} = 0$$

where τ is the proper time. Let us denote the radiation pressure by

$$(A.4) \quad \phi = \sigma\delta$$

where σ is a purposely ambiguous cross-section and δ is the energy density of the radiation in the system P . This force acts in the direction v^a . Therefore,

$$(A.5) \quad \frac{dmv^a}{d\tau} = \phi v^a = \frac{\phi}{c\lambda^0} \lambda^a$$

Putting (3) and (5) together, we have

$$(A.6) \quad \frac{dmv^\mu}{d\tau} = \frac{\phi}{\lambda^0 c} (\lambda^\mu - \lambda^0 v^\mu)$$

Going back to the sun's rest frame, S , we find the covariant generalization of (6) is

$$(A.7) \quad \frac{dmu^\mu}{d\tau} = \frac{fw}{c} (\ell^\mu - wu^\mu)$$

where $w = \ell_\alpha u^\alpha = \lambda^0$, $\delta = w^2 d$, and $f = \sigma d$ which is the force which the particle would experience if it were at rest in the sun's system. The proper time is τ .

We now take the low velocity approximation,

$$(A.8) \quad v^a = \frac{dx^a}{dt}, \quad n^a = \frac{\ell^a}{c}$$

where t is the coordinate time in S . This implies,

$$(A.9) \quad m \frac{dv^a}{dt} = f(1 - \frac{v \cdot n}{c})n^a - f \frac{v^a}{c}$$

where $v \cdot n = \underline{v} \cdot \underline{n}$. The first term is now the force due to radiation weakened by a Doppler factor. The second term is the so-called "tangential drag" although a drag arises from both the first and second terms of equation (9).

Let S be the solar constant (radiation falling on a square centimeter normal to the sun's rays at the mean distance b of the earth). This implies that

$$(A.10) \quad d = \frac{Sb^2}{cr^2}; \quad f = \frac{m\alpha c}{r^2}; \quad \alpha \equiv \frac{ASb^2}{mc^2} = \frac{2.5 \times 10^{11}}{ap}$$

where r is the sun-meteoroid distance, A is an effective cross sectional area, and a is the effective particle radius. Now let us write equation (9) in polar coordinates (r, θ) for a particle in the plane of the ecliptic.

$$(A.11) \quad \ddot{r} - r\dot{\theta}^2 = \frac{-\mu}{r^2} - \frac{2\alpha\dot{r}}{r^2}; \quad \frac{1}{r} \frac{d}{dt} (r^2\dot{\theta}) = -\frac{\alpha\dot{\theta}}{r}$$

where $\mu_0 = GM$, $\mu = \mu_0 - \alpha c$. From the second equation of (11) we find that the angular momentum per unit mass decreases according to

$$(A.12) \quad r^2\dot{\theta} = h - \alpha\theta$$

The first equation of (11) can be put into the form of an inhomogeneous Bessel's equation via a transformation to variables z and ϕ

$$(A.13) \quad \theta = \frac{h}{\alpha} - \phi ; \quad \frac{1}{r} = u = \mu \phi \frac{z}{\alpha^2}$$

Equation (A.11) then becomes

$$(A.14) \quad \frac{d^2 z}{d\phi^2} + \frac{1}{\phi} \frac{dz}{d\phi} + (1 - \frac{1}{\phi^2})z = \frac{1}{\phi^3}$$

and Equation (A.12) is now

$$(A.15) \quad \ddot{\phi} + u^2 \alpha \phi = 0$$

The asymptotic expansion of the solution of (A.14) for $\phi \gg 1$ is

$$(A.16) \quad \phi z \sim \frac{1}{\phi^2} \left\{ 1 - \frac{8}{\phi^2} + \dots + \frac{(-1)^n 2^{2n} n! (n+1)!}{\phi^{2n}} + \dots \right\}$$

Upon expressing ϕz in terms of r , we find

$$(A.17) \quad r = \alpha^2 \mu^{-1} (\phi^2 + 8 + \dots)$$

which in turn implies that (A.15) becomes

$$(A.18) \quad 2\alpha dt + r(1 + \frac{8\alpha^2}{\mu r} + \dots)dr = 0$$

Integrating this we find that

$$(A.19) \quad t = \frac{(r^2 - r_1^2)}{4\alpha} + \frac{4\alpha}{\mu} (r - r_1) + \dots$$

$$= 7.0 \times 10^6 (R^2 - R_1^2) (a\rho)$$

$$+ 5.0 \times 10^{-4} (R - R_1) (1.31 \times 10^5 a\rho - 7.53)^{-1}$$

where t is in years, R and R_1 in AU, and $\mu > 0$, $R > R_1$. Equation (A.19) holds as long as $\frac{\alpha c}{\mu_0} < .99$. For values of $a\rho$ so small that this inequality is violated, the radius is of the order of 10^{-5} cm., which is comparable

to the wavelength of radiation which the sun emits. Thus the cross section, σ , of the particle is a quantum mechanical rather than a geometrical cross section. When the radiation pressure overcomes the gravitational pull of the sun the radius of the particle must be $< 10^{-5}$ cm. in order for the particle to be blown out of the solar system.

As a simple numerical example, consider an asteroidal particle of radius 5.0×10^{-2} cm., density 3.5 gm/cc, lying in a circular orbit in the midst of the asteroid belt, ~ 3.0 AU. The time it takes for this particle to fall into the sun, assuming that it doesn't boil completely away, is $\sim 10^7$ years, which is comparatively short relative to the lifetime of the solar system.

B. Comminution Process

The comminution or grinding process was originally investigated by Piotrowsky⁽⁸⁾ and more recently by Dohnanyi^(9,10,11). The main ideas and equations of the comminution process are described below. The formulation described is the one presented by Dohnanyi in the three references quoted above.

Consider the collision of two objects of mass M_1 and M_2 where $M_1 < M_2$. The velocity of collision is assumed to be several kilometers per second. Two situations will occur at such high velocities:

1) M_1 will create a crater in M_2 and fragment itself into very small debris.

2) M_1 will completely fragment M_2 and itself. This will be referred to as a catastrophic collision.

For the first case it was assumed that the total mass, M_e , of the debris is given by

$$(B.1) \quad M_e = \Gamma M_1 \quad \Gamma \approx \left(5 \frac{\text{sec}^2}{\text{km}}\right) v^2$$

where v is the velocity of impact and is measured in km/sec. The expression for Γ is a rough fit to experimental data⁽¹⁰⁾ for basalt targets. The mass range of M_2 which can be catastrophically disrupted by M_1 is given by

$$(B.2) \quad M_2 \leq \Gamma' M_1$$

where

$$\Gamma' \approx 50\Gamma$$

according to Dohnanyi⁽¹¹⁾.

The products of the collisions and catastrophic events will have a certain mass distribution, and on the average, it is taken as

$$(B.4) \quad g(m; M_1, M_2) dm = C(M_1, M_2) m^{-\eta} dm$$

where $g(m; M_1, M_2) dm$ is the number of fragments of mass between m and $m + dm$ produced by the collision of M_1 with M_2 . The mass of the biggest fragment, M_b , is assumed to be

$$(B.5) \quad M_b = \Lambda M_1$$

where Λ is approximately given by

$$(B.6) \quad \Lambda = \Gamma/10$$

from experimental evidence.⁽¹⁰⁾ For collisions which M_2 survives, it must be that

$$(B.7) \quad M_e = \int_{\mu}^{M_b} mg(m; M_1, M_2) dm$$

where μ is the mass of the smallest fragment produced by the collision.

Evaluating (B.7) gives

$$(B.8) \quad C(M_1, M_2) = (2 - \eta) \Lambda^{\eta-2} M_1^{\eta-1} ; \quad M_2 > \Gamma' M_1$$

and for catastrophic collisions, the integration yields

$$(B.9) \quad C(M_1, M_2) = (2 - \eta) \Lambda^{\eta-2} (M_1 + M_2) M_1^{\eta-2} ; \quad M_2 \leq \Gamma' M_1$$

The differential equation of the collision process is next set up.

It is given by

$$\begin{aligned} \frac{\partial f(m,t)}{\partial t} dm = & \frac{\partial f(m,t)}{\partial t} dm \Big|_{\text{Erosion}} + \frac{\partial f(m,t)}{\partial t} dm \Big|_{\text{Catastrophic + Collisions}} \\ & + \frac{\partial f(m,t)}{\partial t} dm \Big|_{\text{Creation by Fragmentation}} \end{aligned}$$

where $f(m,t)dm$ is the number of particles per volume in the mass range dm . The various terms were evaluated by Dohnanyi⁽¹⁰⁾ who attempted to find a "steady state" equation for the process. In a later paper⁽¹¹⁾ he shows that if the number density function $f(m,t)$ is given by the equation

$$(B.11) \quad f(m,t)dm = Am^{-\gamma}dm$$

where A is a function of time and γ is a constant at time t , then the distribution is unstable for $\gamma > 11/6$ and will decay to a lower value of γ over a sufficiently long time. He considers the problem of comet fragments colliding with asteroids and asteroid fragments and concludes that such a process would produce a meteoroid environment characterized by different values of γ .

Also in his latest paper, Dohnanyi⁽¹¹⁾ states that collision processes are more efficient than radiation damping in producing very small particles. Small particles are produced by radiation damping since the Poynting-Robertson effect drives small particles close enough to the sun to cause them to evaporate to the point where they are small enough to be blown out of the solar system by radiation pressure. Thus what he envisions are particles

colliding with one another frequently enough so that the particles blown out of the solar system are small as a result of collisions and not because of evaporation near the sun.

C. Solar Interactions

Solar radiation on a particle can impart a small positive charge to the particle.⁽¹²⁾ The mechanism involved is the photoelectric effect and is capable of giving a particle a charge of a few electron volts. A charged particle is susceptible to the powerful Lorentz force.

The interaction of a charged particle with the sun has been discussed by Belton.⁽¹³⁾ His analysis showed that particles in the size range from 1 to 10 microns are all ejected from the solar system. The mechanism for their ejection is the following. The orbit of the particle, gently buffeted by the interplanetary magnetic field, first becomes circular, then begins to shrink under the effect of various drag forces like the Poynting-Robertson effect. Near the sun, the particle begins to evaporate and diminishes in size. The effects of the size change are counter to the drag forces. The drag forces are eventually overcome and then the particle moves on to larger and more eccentric orbits, eventually achieving a hyperbolic orbit.

A very dramatic Lorentzian effect is mentioned by Belton. The magnetometer on board Mariner II, IMPI and Mariner IV seemed to detect an interplanetary polar magnetic field directed southward with a magnitude of about 10^{-5} gauss. This B_0 , if it exists, represents a gigantic energy drain from the sun and poses considerable theoretical problems. The effect of such a field on orbiting particles is very pronounced and is much greater than the Poynting-Robertson effect. The lifetime of a particle charged to a few volts in a 1 AU circular orbit is about 30 years under the influence of such a field.

D. Dynamical Effects

These effects stem from the gravitational attraction⁽¹⁴⁾ which a planet exerts on the orbits of bodies crossing the orbit of the planet in question. Close approaches produce large changes in the orbital elements which can result in ejection or a shift to a shorter lived orbit. For particles crossing the orbit of earth or Venus the mean life of the particle orbit is about 10^8 yr. It is evident that the Poynting-Robertson effect is greater than dynamical effects for particles crossing the earth's orbit. Such is not the case for particles crossing Jupiter's orbit, however. The mean life of such a particle is about 10^6 years due to the dynamical effects of Jupiter.

Conclusions

All available evidence seems to indicate that very small particles (less than one micron) are produced by meteoroid collisions and erosion in sizeable quantities. Satellite detection of meteoroids seems to indicate that there are no very small particles in the solar system. Various physical mechanisms can explain the lack of very small particles.

The Poynting-Robertson effect is capable of eliminating small particles in a time frame of about 10^8 years. This lifetime is uncertain because evaporation of the particle near the sun may significantly change the particle's orbit and extend or shorten the lifetime considerably.

A polar component to the interplanetary magnetic field will affect a small charged particle very significantly. Particle lifetimes of about 30 years are the result of such a magnetic field. The existence of this field rests on rather uncertain satellite data and thus this potentially important effect is highly uncertain.

Dynamical effects due to the gravitational attraction of the planets lead to particle lifetimes of about 10^8 years for near-earth particles. These effects are felt to be generally smaller than either the Poynting-Robertson effect or electromagnetic effects.

It is important that the meteoroid cut-off be determined in some way since manned missions in interplanetary space will require meteoroid protection. Knowledge of the interplanetary meteoroid environment is presently obtained from only two sources; zodiacal light observation and observation of the asteroids. Definite knowledge of cut-off would make zodiacal light observation yield more information about the meteoroid population in interplanetary space.

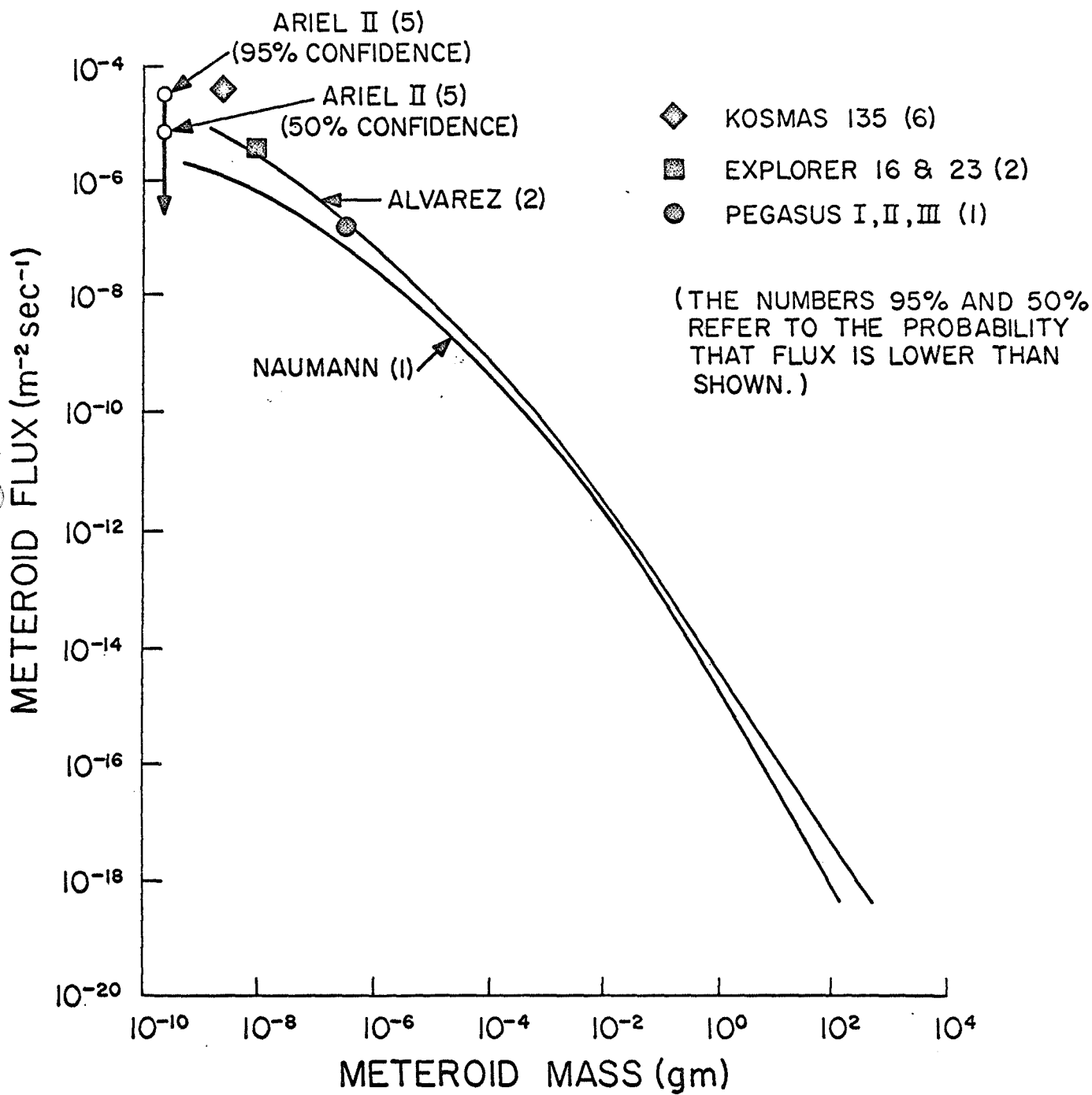
References

1. Naumann, Robert J., The Near Earth Meteoroid Environment, NASA TN D-3717, November 1966.
2. Alvarez, Jose M., Satellite Measurements of Particles Causing Zodiacal Light, NASA SP-150, p. 123-129.
3. Nilsson, C., Some Doubts about the Earth's Dust Cloud, Science 153, No. 3741, September 9, 1966, p. 1242-1246.
4. Holden, Dale G. and Beswick, Alfred G., Impact Detection Experiment, To be found in NASA TN D-4284 Explorer XXIII Micrometeoroid Satellite, June 1968, p. 45-57.
5. Jennison, R. C.; McDonnell, J. A. M.; Rogers, I.; The Ariel II Micrometeorite Penetration Measurements, Proc. of the Royal Soc., 300, 251-269 (1967).
6. Konstantinov, B. P.; Bredov, M. M.; Mazets, E. P.; Panov, V. N.; Aptekar', R. L.; Golenetskiy, S. V.; Guryab, Yu. A.; Il'yinskiy, V. N.; Micrometeoritic Investigations in the Near-Earth Space According to Observations on AES KOSMAS-163, from Preprint A.N. USSR, O. Lenina Fiziko Tekhnicheskiiy Institut, Imeni A.F. Ioffe, Leningrad, 1969 (translation).
7. Robertson, H. P. Dynamical Effects of Radiation in the Solar System, Royal Astronomical Soc., Monthly Notices, 97, 423-438 (1937).
8. Piotrowsky, S., Acta Astronomica, Ser. A, 5, 115 (1953).
9. Dohnanyi, J. S., Collisional Model of Meteoroids, Bellcomm. Rept. TR-67-340-3, 1967.
10. Dohnanyi, J. S., Collisional Model of Asteroids and Their Debris, Bellcomm. Rept., TR-68-710-4, 1968.

11. Dohnanyi, J. S., On the Origin and Distribution of Meteoroids,
Bellcomm. Rept., TR-69-105-3-2, 1969.
12. Rhee, J. W., Electrostatic Potential of a Cosmic Dust Particle,
NASA SP-150, p. 291-298.
13. Belton, Michael J. S., Dynamics of Interplanetary Dust Particles
Near the Sun, NASA SP-150, p. 301-306.
14. Opik, E. J., Stray Bodies in the Solar System, Part 1, Survival of
Cometary Nuclei and Asteroids. In Adv. in Astron. and Astrophys.,
Vol. 2, ed. by Z. Kopal, Academic Press, Inc., New York, p. 219-262.

Figure Caption

Fig. 1. Meteoroid Detection Satellite Results.



4 N71-71013

FINAL REPORT
to the
NATIONAL AERONAUTICS AND SPACE ADMINISTRATION
in connection with
NASA Grant NGR 47-004-006

Part 13 of 21 Parts

Final Report
VPI&SU Project 313242

Interaction of ^{50}Ti with Protons and Neutrons

by

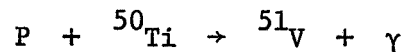
R. Onega
Physics

Virginia Polytechnic Institute & State University
Blacksburg, Virginia

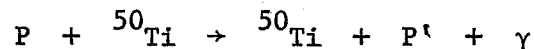
December, 1970

INTRODUCTION

The interaction of protons and neutrons with ^{50}Ti produces gamma rays. In the case of proton interactions with ^{50}Ti , both the proton capture process

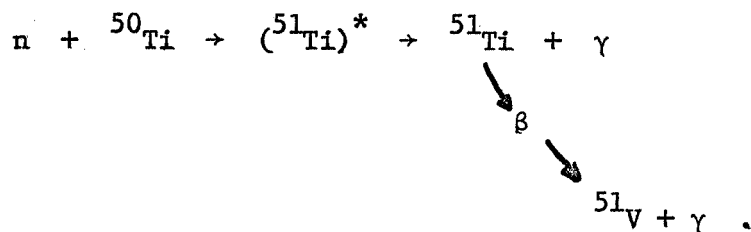


as well as the inelastic scattering process



occurs. The type of proton interaction with titanium depends upon the incoming proton energy. At some particular proton energies, resonances may be observed. These resonances arise due to energy level structures of the compound nucleus formed $({}^{51}\text{V})^*$. This nucleus subsequently decays and protons and/or gamma rays are emitted, leaving ${}^{51}\text{V}$ in the ground state.

When neutrons interact with ^{50}Ti , the $({}^{51}\text{Ti})^*$ compound nucleus is formed.



The compound nucleus immediately de-excites by releasing prompt gamma rays. The ${}^{51}\text{Ti}$, now in the ground state, beta decays into ${}^{51}\text{V}$ with a half life of 5.80 minutes. In this beta decay process gamma rays are also emitted.

The gamma ray environment in a space vehicle with some components containing ${}^{50}\text{Ti}$ will primarily be determined by the proton interaction with the titanium since the primary cosmic rays are mainly protons⁽¹⁾.

Secondary neutrons are produced by the interaction of the protons with matter. These neutrons undergo elastic and inelastic collisions and are then captured.

This report contains information on the neutron activation of ^{50}Ti as well as the proton interaction with titanium. The neutron activation has most recently been studied by Robinson et al.⁽²⁾ in 1963. There were three gamma rays which followed the beta decay of ^{51}Ti into ^{51}V . The ^{51}Ti was formed by the neutron activation of ^{50}Ti . Three gamma rays were found with energies of 0.319, 0.613 and 0.934 MeV. The relative intensities of these gamma rays are 100, 1.6 and 5.8 respectively. Prompt gammas are associated with this neutron capture process but were not investigated.

The $^{50}\text{Ti}(p,p'\gamma)$ reaction was studied by Gray et al.⁽³⁾. They studied this reaction at incoming proton energies of 18.2 MeV and 11.5 MeV. Most of their work was concerned with the outgoing elastically scattered protons, however, rather than the gamma rays. Most of the gamma rays emitted are in the low MeV region (≤ 3 MeV). The $^{50}\text{Ti}(p,p'\gamma)$ reaction was studied at an energy of 7 MeV by Belote⁽⁴⁾ et al.

Proton fluxes ranging from 10^3 eV to 200 MeV have been investigated⁽⁵⁾ in the magnetic field of the earth. These particles are also trapped in the magnetic field of Jupiter as well as the earth. Secondary particles originate when the protons interact with the nitrogen and oxygen in the earth's atmosphere or with other material.

The Capture of Neutrons by ^{50}Ti .

Since neutrons may be a constant environment in space due to various types of reactions of protons with material producing neutrons, a study of the capture of the neutrons by ^{50}Ti was undertaken.

The ^{50}Ti sample was inserted into the VPI reactor by means of a pneumatic transfer system. The transit time from the reactor to the counting facilities was about 5 seconds. The gamma ray spectrum due to the beta decay of ^{51}Ti was then investigated by means of a 4 cm^3 Ge(Li) detector as well as a NaI(Tl) crystal. Figure 1 is the gamma ray spectrum from the Ge(Li) detector. Only three gamma rays are observable, the 0.320, 0.613 and 0.933 MeV. The decay is such that the 0.320 and the 0.613 were in coincidence adding to give 0.933 MeV. There was, in addition, the cross over transition of 0.933 MeV.

Relative intensity measurements were performed and our results as well as those obtained by Robinson et al.⁽²⁾ are compared in Table I. The detector used in the investigation of the relative intensities was a 3" x 3" NaI detector in a lead shield to reduce background to a minimum.

Table I
Relative Intensities of ^{51}Ti Gamma Rays

Energy (MeV)	Relative Intensity (Robinson) ²	Relative Intensity (This Work)
0.320	100	100
0.613	1.6 ± 0.2	3.75 ± 0.4
0.933	5.8 ± 0.6	8.8 ± 0.8

The absorption cross section of ^{50}Ti for neutrons of 0.025 eV was 0.14b ⁽⁶⁾. The secondary neutrons impinging on ^{50}Ti could thus be a significant source of radiation due to the gamma rays following their capture.

Proton ⁵⁰Ti Interactions

The V.P.I. Van de Graaff accelerator has an energy range of 4 MeV. A titanium-50 target on a bismuth backing was placed in the beam tube of the accelerator. The proton beam was allowed to impinge on the target and the gamma rays were detected as function of energy. Since the γ rays could be attenuated by going through the bismuth backing, the NaI(Tl) detector was placed at a forward angle of about 45° with respect to the beam.

The gamma ray energy spectrum was taken with the proton beam at 1.5 MeV, 2.25 MeV and 3.0 MeV. The bismuth backing was then rotated 180° in the scattering chamber of the Van de Graaff accelerator and the background gamma ray spectrum was taken at these same three proton energies. Figure 2 shows the difference gamma ray spectrum for the 1.5 MeV incoming proton beam case. The gamma ray energy spectrum reached about 8.5 MeV for the 1.5 MeV incoming proton beam energy and about 10 MeV γ ray energy for the 3 MeV incoming proton energy.

Figure 2 indicates there was some structure in the gamma ray spectrum. This structure was due to the fact that as the (⁵¹Ti)* nucleus de-excited, gamma rays were emitted which were characterized by the difference of two nuclear energy levels.

CONCLUSIONS

The prompt gamma rays that were emitted following proton capture would present a very real hazard to people in capsules composed of titanium if the proton flux were significant. The same energy gamma rays would also be expected from the capture of neutrons. The energies of the gamma rays following the beta decay of the radioactive nuclei were always

much less in energy than the prompt gamma rays.

The dose rate was proportional to the energy of the gamma rays. This means that high energy gamma rays which were absorbed by a person are more damaging than low energy gamma rays. There were, however, other factors to be considered. The higher energy gamma ray had less probability of being absorbed. Foster and Wright⁽⁷⁾ show that the absorption coefficient for gamma rays in tissue reached a peak at about 0.6 MeV and then decreased on up to beyond 10 MeV. So low energy (~ 1 MeV) gamma rays do not cause as much biological damage but their absorption probability was greater than higher energy gamma rays.

The experiment indicates that it would be the prompt gamma rays which would be troublesome for space travel. They arise from both the (P, γ) and (n, γ) reactions on titanium.

BIBLIOGRAPHY

1. R. B. Leighton, "Principles of Modern Physics", McGraw-Hill Book Company, Inc. pages 680-708, (1959),
2. R. L. Robinson, N. R. Johnson and G. D. O'Kelley, Nuclear Physics, 47, pages 506-510, (1963),
3. W. S. Gray et al., Nuclear Physics, 67, 323 (1965),
4. T. A. Belote et al., Physics Letters, 14, 323 (1965),
5. K. A. Anderson, "Energetic Particles in the Earths Magnetic Field", from Annual Review of Nuclear Science, edited by E. Segre, Vol. 16, 1966, pages 291-344.
6. D. T. Goldman, J. R. Roesser, "The Chart of the Nuclides", distributed by the General Electric Company, Schenectady, N. Y., (1966),
7. A. R. Foster and R. L. Wright, Jr., "Basic Nuclear Engineering", Allyn and Bacon, Inc., Boston, Mass., 1968, page 119.

FINAL REPORT
to the
NATIONAL AERONAUTICS AND SPACE ADMINISTRATION
in connection with
NASA Grant NGR 47-004-006

Part 14 of 21 Parts

Final Report
VPI&SU Project 313243

Organo-Cobalt Oxygen-Carrying Complexes

by

L. Taylor
Chemistry

Virginia Polytechnic Institute & State University
Blacksburg, Virginia

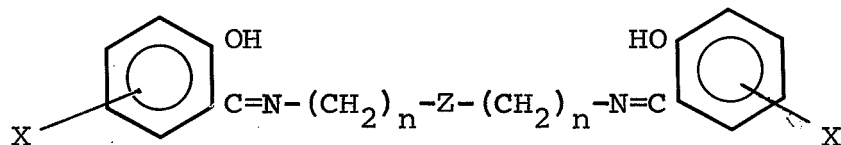
December, 1970

ORGANO-COBALT OXYGEN-CARRYING COMPLEXES

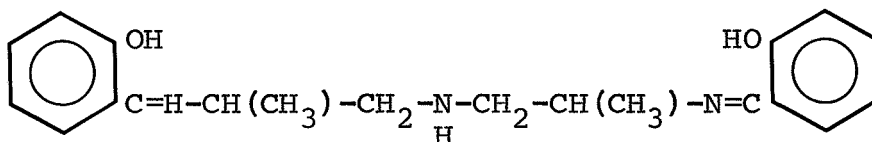
Initially the primary goals of this research were (1) to synthesize structurally related but electronically different cobalt(II) complexes which reversibly add oxygen and determine their stability to repeated cyclizations and (2) to completely describe the interaction or bonding between the oxygen molecule and cobalt complex by application of as many of the modern structural techniques as possible. Since these same cobalt(II) complexes were anticipated to be suitable synthetic models for Vitamin B₁₂ behavior, an additional goal became (3) to synthesize and characterize materials containing a cobalt to carbon sigma bond (i.e. the unique linkage found in the coenzyme of Vitamin B₁₂).

Our efforts since commencement of this research project (January 1, 1969) have been channelled toward (1) synthesizing the pentadentate ligands which are required for complexation with cobalt(II), (2) gaining a better understanding of the non-oxygenated complexes of cobalt(II) and nickel(II) with several of these pentadentate ligands, (3) the construction of a Faraday magnetic susceptibility balance, and (4) the interaction of alkyl halides with the reduced cobalt(II) complexes.

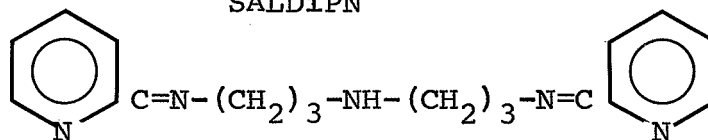
At the outset of this work only one of the desired pentadentate ligands was known, SALDPT ($n = 3$, $X=N-H$). We have now synthesized and characterized the following new ligands. Figure 1.



SALDPT	n=3	Z=NH	X=H
SALDiEN	n=2	Z=NH	X=H, 5-Br, 5-CH ₃ 3-CH ₃ O, 3-(CH ₃) ₂ CH
SALDAES	n=2	Z=S	X=H, 5-Br, 5-NO ₂ , 5-CH ₃ 3-CH ₂ O, 3-(CH ₃) ₂ CH
SALDAPS	n= 3	Z=S	X=H, 5-Br, 3-(CH ₃) ₂ CH
SALDAPE	n= 3	Z=O	X=H, 5-Br, 3-(CH ₃) ₂ CH



SALDiPN



PYDPT

Figure 1

These ligands have been prepared by the interaction of salicylaldehyde or pyridine-2-aldehyde with the corresponding polyamine, which in several cases had not been synthesized previously, in a Schiff base reaction.

It was felt that an adequate knowledge of the precursors was necessary for any results concerning the oxygen adducts and metal carbon bonded species to be meaningful. Therefore the physical, chemical and stereochemical properties of the non-oxygenated and non-carbon bonded complexes of cobalt(II) as well as nickel(II) were investigated. The latter metal ion was included in hopes that the results gained from this metal ion system would aid in unraveling the factors responsible for reversible oxygenation with certain cobalt systems(i.e. chemical and structural theories are considerably advanced for nickel complexes in relation to cobalt complexes and nickel systems are less susceptible to attack by oxygen).

This report is divided into a number of parts some of which are more detailed than others since much of the work is still being actively pursued.

Part I.

Nickel(II) Complexes of Schiff Base Ligands Derived from Substituted Salicylaldehydes and Diethylenetriamine and Bis(2,2'-aminopropyl)amine

Nickel(II) complexes of linear potentially pentadentate Schiff base ligands derived from variously substituted salicylaldehydes and diethylenetriamine and bis(2,2'-aminopropyl)amine have been prepared. The golden yellow materials have been characterized by elemental analysis, mass spectra, infrared-visible-ultraviolet spectra and magnetic susceptibility measurements, in the solid state and dissolved in pyridine. In the solid state

and in non-donor solvents the complexes appear to be pseudo square planar with magnetic moments ca. 1.2 B.M. The anomalous magnetism is explained in terms of either a singlet-triplet spin state equilibrium which arises from the weak in-plane field presented by the ligand or the coexistence of both high and low spin complexes in the solid state. In pyridine the complexes are pseudo-octahedral high spin nickel(II) species. A mono-pyridine adduct has been isolated for one of the complexes and it exhibits properties similar to the complexes dissolved in pyridine.

A more detailed account of this work is appended.

Part II.

Nickel(II) Complexes of Schiff Base Ligands Derived from Substituted Salicylaldehydes and Bis(2,2'-aminoethyl)sulfide

Nickel(II) complexes of the pentadentate Schiff base ligand derived from substituted salicylaldehydes and bis(2,2'-aminoethyl)-sulfide, SALDAES, have been prepared. Green complexes of general formula $\text{Ni}(\text{SALDAES})$, $(\text{Ni}(\text{SALDAES})(\text{H}_2\text{O}))$ and $(\text{Ni}(\text{SALDAES})(\text{py}))$ have been isolated. Magnetic and spectrophotometric studies have shown the stereochemistry of the hydrated and pyridine adducts to be high spin six-coordinate pseudo-octahedral. $\text{Ni}(\text{SALDAES})$ is postulated to be five coordinate in which the sulfur atom is very weakly bound to the nickel(II) ion. The weak attachment arises as a result of the steric requirements of the linear pentadentate ligand. The magnetic properties are anomolous and a spin-state

equilibrium between high and low spin states is postulated.

A more detailed account of this work is appended.

Part III.

Cobalt-Carbon Sigma Bond Formation Employing a High Spin Cobalt(II) Complex

A new series of vitamin B₁₂ coenzyme model compounds has been prepared starting with the high spin cobalt(II) chelate of the pentadentate Schiff base ligand derived from salicylaldehyde and bis(3-aminopropyl)amine (L. Sacconi and I. Bertini, J. Amer. Chem. Soc., 88, 5180 (1966)). The general method of preparation of these σ -bonded alkyl derivatives is the reduction of the cobalt complex with sodium borohydride in the presence of an alkyl halide. These compounds have been characterized by elemental and mass spectral analysis as well as infrared, visible and n.m.r. spectra. A six-coordinate pseudo octahedral structure is envisioned for these materials in the solid state. In poorly coordinating solvents an equilibrium between five and six coordinate complexes is postulated. These σ -bonded organic derivatives appear to be quite thermally and photochemically stable.

A more detailed account of this work is appended.

Part IV.

Nickel(II) Complexes of Additional New Pentadentate Ligands

Pentadentate Schiff base ligands derived from several substituted salicylaldehydes and (1) bis(3,3'-aminopropyl)sulfide, SALDAPS, and (2) bis(3,3'-aminopropyl)ether, SALDAPE, have been

complexed with nickel(II). Materials of composition Ni(SALDAPS) and Ni(SALDAPE) have been isolated and are in the process of being characterized. Preliminary magnetic and spectral data in the solid state and in pyridine solution indicate these complexes to have properties similar to those described in detail previously for Ni(SALDAES).

Nickel(II) complexes have also been prepared employing the pentadentate ligand arising from the condensation of pyridine-2-aldehyde and bis(3,3'-aminopropyl)amine, PYDPT. This ligand differs from the previous ones in that it coordinates as a neutral ligand rather than a dinegative one. Compounds have been isolated which may be formulated as $(\text{Ni}(\text{PYDPT})\text{X})\text{X}$ where $\text{X} = \text{ClO}_4^-$, PF_6^- , Cl^- , Br^- , I^- , NO_3^- and NCS^- . In addition mixed complexes are also obtainable such as $(\text{Ni}(\text{PYDPT})\text{X})\text{PF}_6$ where $\text{X} = \text{Cl}^-$, Br^- , NO_3^- and NCS^- . If X is a non-coordinating anion, water is incorporated into the coordination sphere. In all cases the geometry about the metal ion is pseudo-octahedral with the ligand providing five of the donor atoms and an anion or water molecule completing the six-coordinate structure. Magnetic and visible spectral data are in accord with this postulation. In good donor solvents the materials behave as 2:1 electrolytes; whereas, in poorer donor solvents 1:1 electrolyte behavior is observed. All efforts to prepare a five-coordinate nickel(II) complex were met with failure.

Part V.

Cobalt(II) Complexes of SALDiEN, SALDAES and PYDPT

Cobalt(II) complexes of the titled ligands have been

investigated preparatory to studying their interaction with molecular oxygen. Some work had previously been reported with SALDiEN which had indicated that Co(SALDiEN) was planar with the secondary nitrogen atom not coordinated to the cobalt ion. If little or no precautions are taken to exclude oxygen during the isolation procedure, results are obtained which would lead one to the above conclusion. However, total exclusion of all oxygen throughout the preparation and isolation steps yields a material whose magnetic and spectral properties suggest a pseudo-tetrahedral structure (i.e. magnetic moment ca. 4.5 B.M. rather than c.a. 1.0 B.M. as noted earlier). Five different salicylaldehyde derivatives have been made and complexed with cobalt(II) at least two and in some cases three times in order to prove the validity of this observation. Elemental analysis, infrared and mass spectra have been used to establish the composition of the complex as Co(SALDiEN). All derivatives exhibit a marked reactivity for oxygen when in solution or when suspended in some solvent. Whereas, in the solid state they are quite stable to air. Our work has been seriously hampered by lack of an excellent inert atmosphere box, but funds are being requested from another agency concerning obtaining one. These new results with Co(SALDiEN) are more in keeping with the known greater tendency for tetrahedral formation with cobalt(II) than with nickel(II) as predicted by Ligand Field Theory. (Ni(SALDiEN) is essentially square planar). Support for this observation can be found in the fact that increasing the atom chain that joins azomethine nitrogens on neighboring benzene nuclei promotes tetrahedral formation for complexes of cobalt(II)

but it does not promote this behavior concerning complexes of nickel(II) (i.e. nickel(II) complexes remain square planar).

Very similar results have been found concerning Co(SALDAES). While the solubility of these materials is considerably diminished over the former, their properties and reactivity are pretty much unchanged and therefore will not be discussed.

Complexes with the pentadentate ligand, PYDPT, show the same high reactivity with air in solution but a much less tenacity for air in the solid state. The composition of the isolable dark red or maroon crystals as predicted from elemental analysis and infrared spectra is $(\text{Co}(\text{PYDPT})\text{X})\text{X}$ where $\text{X}=\text{Cl}^-$, Br^- , I^- , NO_3^- , PF_6^- , SCN^- and SeCN^- . The chloride bromide and nitrate derivatives are extremely hygroscopic turning syrupy in the air over a twelve hour period. All the materials may be recrystallized under nitrogen. The magnetic properties of these materials are quite anion dependent. For poorly coordinating anions such as PF_6^- and I^- the complexes appear to be low spin (i.e. $\mu_{\text{eff.}} = 2.3 \text{ B.M.}$). High spin behavior is observed for the better coordinating anions. Those materials which are hygroscopic convert from high to low spin upon taking-up water. Redrying the complexes at 100°C in vacuo converts them back to high spin complexes whereupon taking up water they revert to low spin materials. Solution magnetic measurements via a n.m.r. technique suggests low spin behaviour for all derivatives except SCN^- and SeCN^- . Spectral and conductivity data support a pseudo-octahedral structure for these materials.

Further investigation concerning these cobalt complexes and their reaction with molecular oxygen is being actively pursued. Future plans include extending the study to ligands of other than a linear array of donor atoms and reinvestigating the known oxygen carriers employing electron spin resonance.

Pentadentate Ligands I. Nickel(II) Complexes of the
Linear Schiff Base Ligands Derived From Substituted
Salicylaldehydes and Diethylenetriamine and Bis(2,2'-
aminopropyl)amine

By W. M. Coleman and L. T. Taylor

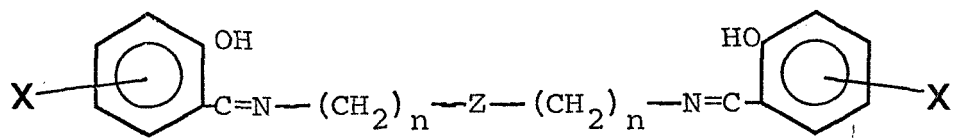
INTRODUCTION

Fig. 1
Pentadentate ligands are probably the least studied of the higher multidentate chelating agents.¹ The known structural types, Figure 1, include (1) linear, open chain, (2) branched chain where the bifurcation occurs at the donor atom, (3) a tetradentate macrocyclic ligand to which is attached a side chain containing a fifth donor atom (i.e. the ligand found in vitamin B₁₂ is an example), (4) a macrocyclic^{2,3} ligand in which all five potential donors are in the ring and (5) a "basket-like" macrocyclic ligand⁴. The linear branched chain ligands have been investigated to the greatest extent although much of this work is found in the older chemical literature. Sacconi⁵ has recently reinvestigated the metal complexes of the pentadentate ligand derived from salicylaldehyde and bis(3,3'-aminopropyl)-amine and has shown them to be high-spin five coordinate. We wish to report here our results concerning the nickel complexes of the pentadentate ligands derived from various substituted

-
1. H. A. Godwin, "Chelating Agents and Metal Chelates", F. D. Dwyer and D. P. Mellor, eds., Academic Press, New York, 1964, p. 167.
 2. J. D. Curry and D. H. Busch, J. Amer. Chem. Soc., 86, 592(1964).
 3. S. M. Nelson, P. Bryan, and D. H. Busch, Chem. Comm., 641(1966).
 4. V. Katovic', L. T. Taylor and D. H. Busch, J. Amer. Chem. Soc., 91, 2122 (1969).
 5. L. Sacconi and I. Bertini, J. Amer. Chem. Soc., 88, 5180 (1966).
-

salicylaldehydes and diethylenetriamine, structure Ia, hereafter

referred to as H₂XSALDIEN.



X = 5-H, 5-Br, 5-CH₃, 3-CH₃O, 3-(CH₃)₂CH

Ia, n = 2 Z = N-H

b, n = 3 Z = N-H

EXPERIMENTAL

Materials.--Diethylenetriamine(DIEN) and salicylaldehyde(SAL) were obtained from The Aldrich Chemical Company, Milwaukee, Wisconsin and used without further purification. Technical grade 3-methoxysalicylaldehyde (p-vanillin), also from Aldrich Chemical Company, was recrystallized from 95% ethanol in the presence of decolorizing charcoal. All other chemicals and solvents were of reagent grade or equivalent.

5-Bromosalicylaldehyde was prepared by adding bromine to an equivalent amount of a cold solution of salicylaldehyde dissolved in glacial acetic acid. White crystals were obtained upon recrystallizing the crude product from ethanol-water (60:40). 5-Methylsalicylaldehyde was prepared by a modification of the Reimer-Tieman⁶ reaction employing p-cresol and chloroform in a highly alkaline medium. 3-Isopropylsalicylaldehyde was prepared according to the general procedure of the Duff⁷ reaction starting with o-isopropylphenol. The bis(salicylaldehyde)nickel(II)

6. L. F. Fieser and M. Fieser, "Advanced Organic Chemistry", Reinhold Publishing Corporation, New York, 1961, p. 824.

7. J. C. Duff, J. Chem. Soc., 547 (1941).

complexes were obtained as green hydrated solids following the method of Holm.⁸

8. R. H. Holm, J. Amer. Chem. Soc., 83, 4683 (1961).

Uncomplexed pentadentate ligands were prepared by adding

one molecular equivalent of DIEN to two molecular equivalents of SAL dissolved in absolute ethanol at room temperature. After stirring for 15 minutes, the volume of the solution was reduced until only an oil remained which was identified via n.m.r. and infrared analysis as slightly impure $\text{H}_2\text{XSALDiEN}$.

Preparation of $\text{Ni}(5\text{-HSALDiEN})$.-- $\text{Ni}(\text{SAL})_2 \cdot 2\text{H}_2\text{O}$ (3.37 g, 0.01 mole) was suspended in 200 ml of absolute ethanol. The suspension was brought to reflux with stirring and DiEN (1.03 g, 0.01 mole) dissolved in a small amount of ethanol was added all at once. The color of the solution turned dark red-brown as the green solid quickly disappeared. The reaction mixture was refluxed for three hours. Upon allowing the flask to come to room temperature, yellow needles were precipitated which were filtered, washed with ether and dried in vacuo at 100°C for 12 hrs. More material could be isolated from the filtrate by cooling overnight (5°C).

Preparation of $\text{Ni}(5\text{-BrSALDiEN})$.-- $\text{Ni}(5\text{-BrSAL})_2 \cdot 2\text{H}_2\text{O}$ (4.95 g, 0.01 mole) was suspended in absolute ethanol and brought to reflux with stirring. DiEN (1.03 g, 0.01 mole) dissolved in a small amount of ethanol was added in one addition. An orange-red solution formed almost immediately. After refluxing for one hour, an orange precipitate formed which was isolated and dried as described above.

Preparation of $(\text{Ni}(5\text{-MeSALDiEN})) \cdot \text{H}_2\text{O}$.--To a refluxing suspension of $\text{Ni}(5\text{-MeSAL})_2 \cdot 2\text{H}_2\text{O}$ (2.76 g, 0.0075 mole) in 125 ml. of absolute ethanol was added in an addition DiEN (0.77 g, 0.0075

mole) dissolved in a small amount of ethanol. No immediate color change was noticed. Upon refluxing for three hours, the color of the solution gradually changed from light green to orange with dissolution of the green solid. Refluxing was continued for six more hrs. after which the reaction mixture was allowed to come to room temperature. Orange crystals formed which were isolated and dried as described above.

Preparation of $\text{Ni}(3\text{-MeOSALDiEN})$.-- $\text{Ni}(3\text{-MeOSAL})_2 \cdot 2\text{H}_2\text{O}$ (3.99 g, 0.008 mole) was suspended in 125 ml of absolute ethanol and brought to reflux with stirring. DiEN (0.82 g, 0.008 mole) in a small amount of ethanol was added to the suspension in one addition. The green solid quickly disappeared and a dark red-brown solution developed. The solution was refluxed for 3.5 hrs. then cooled overnight (5°C). A yellow solid precipitated which was isolated and dried as previously described.

Preparation of $\text{Ni}(3\text{-i-PropylSALDiEN})$.-- $\text{Ni}(3\text{-i-PropylSAL})_2 \cdot 2\text{H}_2\text{O}$ (12.75 g, 0.03 mole) was suspended to 100 ml. of ethanol-water (60:40) and brought to reflux with stirring. DiEN (3.08 g, 0.03 mole) dissolved in a small amount of ethanol was added in one addition. The solution immediately turned dark red brown as the bis(3-isopropylsalicylaldehydo)nickel(II) complex dissolved. The solution was refluxed for two hrs. and then cooled overnight (5°) whereupon an orange-brown precipitate appeared. This product was filtered and dried as described above.

Preparation of the Pyridine Adduct of $\text{Ni}(5\text{-BrSALDiEN})$.--
 $\text{Ni}(5\text{-BrSALDiEN})$ (1.0 g, 0.0019 mole) was suspended in 50 ml. of

spectrograde pyridine and the resulting mixture was refluxed for two hrs. The compound dissolved in pyridine on heating. The solution was then allowed to come to room temperature whereby a green powder was precipitated. The material was filtered and dried at room temperature and atmospheric pressure over KOH in a pyridine atmosphere.

Preparation of Ni(SALDiPN) .--Ni(SAL)₂·2H₂O (10.1 g, 0.03 mole) was suspended in 100 ml of absolute ethanol and brought to reflux with stirring. To this suspension DiPN⁹ (3.93) g, 0.03 mole)

9. DiPN, the abbreviation for bis(2,2'-aminoprypyl)-amine

in a little ethanol was added in one addition. The solution became orange in color immediately followed by precipitation of a yellow-orange material. Refluxing was continued for 1.5 hrs. The reaction material was allowed to come to room temperature after which the material was filtered and dried in vacuo at 100°C for 12 hrs.

Physical Measurements.--Infrared spectra were obtained in the region 5000-400 cm⁻¹ using a Perkin-Elmer Model 621 spectrophotometer. Solid state spectra were recorded as KBr pellets and as Nujol or hexachlorobutadiene mulls. Solution spectra were taken in spectroquality solvents using matched solution cells. Ultraviolet-visible-near infrared spectra were obtained with a Cary 14 recording spectrophotometer. Spectra of solid samples were obtained by a diffuse transmittance technique¹⁰ employing Nujol mulls impregnated on Whatman No. 1 filter paper.

-
10. R. H. Lee, E. Griswold and J. K. Kleinberg, *Inorg. Chem.*, 3, 1278 (1964).
-

Solution spectra were obtained utilizing spectroquality organic solvents.

Magnetic susceptibility measurements on solid samples were obtained by the Faraday method. Solution magnetic measurements were determined by an n.m.r. method¹¹ using a Varian A60 spectrometer. Diamagnetic corrections were made employing Pascal's

11. D. R. Evans, *J. Chem. Soc.*, 2003 (1959).
-

constants.¹² Special coaxial cells with precision spacing of the

12. B. N. Figgis and J. Lewis, "Modern Coordination Chemistry", J. Lewis and R. J. Wilkins, Eds., Interscience Publishers, Inc., New York, N. Y., 1960.
-

inner tube (Wilmad Glass Co.) were used. Measurements were performed at 10°C and 20°C using a Varian Model V6040 NMR variable temperature controller.

Mass spectra were obtained on a Hitachi-Perkin-Elmer RMU-7 double focusing mass spectrometer using a solid inlet probe. The solid probe temperature was maintained at a value to prevent decomposition of the samples. The source temperature was maintained at approximately the temperature of the solid probe. Analyzer tube and ion source pressures of less than 10^{-6} torr were employed. Where necessary mass to charge ratios were calibrated with perfluorokerosene.

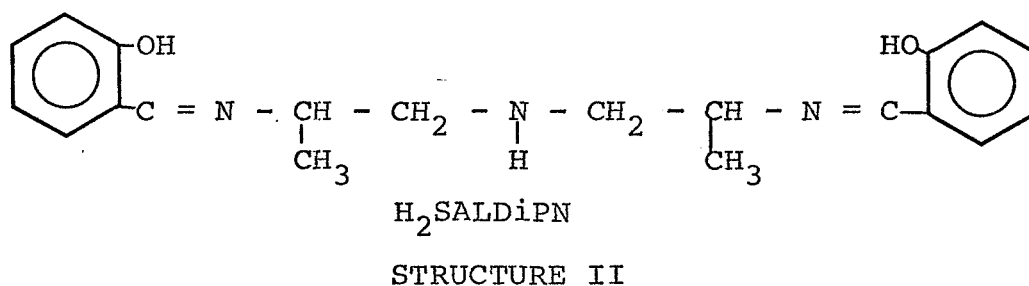
Elemental analyses were performed by Galbraith Microanalytical Laboratory, Knoxville, Tennessee and in this laboratory using a Perkin-Elmer Model 240 C, H & N Analyzer.

RESULTS AND DISCUSSION

Complexes of the following composition, $\text{Ni}(\text{XSALDiEN})$, have been isolated except for the 5-methyl derivative which contains a water molecule of hydration. Analytical data supporting the elemental composition of these materials is shown in Table I. Several preparative procedures have been successfully employed which include (1) treating the pre-formed ligand in situ with nickel(II) acetate 4-hydrate, (2) a metal template reaction of the appropriately substituted bis(salicylaldehydo)nickel(II) complex with DiEN and (3) reacting the previously isolated ligand with nickel(II) acetate 4-hydrate.

In each case the resulting neutral complexes are golden yellow in appearance being partially soluble in methanol, ethanol, water and dimethylsulfoxide and insoluble in methylene chloride, N,N-dimethylformamide, acetonitrile and 1,2-dimethoxyethane. Over a period of one day at room temperature they dissolve in pyridine; whereas, they are immediately soluble in hot pyridine. Melting with decomposition around 200°C indicates the products are relatively thermally stable.

A complex of analogous composition and properties was also prepared by substituting bis(2,2'-aminopropyl)amine for diethylene-triamine in its reaction with bis(salicylaldehydo)nickel(II) complexes. The color, solubility, thermal properties and general features of this compound were similar to Ni(XSALDiEN) . This material shall be referred to as Ni(SALDiPN) , structure II.



Positive ion mass spectra were determined under the least severe conditions that would allow an interpretable spectrum (i.e. minimum temperature and electron energy). Only Ni(5-HSALDiEN) ,

TABLE I

Analytical Data for the Nickel Complexes

<u>Compound</u>		<u>Analyses</u>		
		<u>C</u>	<u>H</u>	<u>N</u>
Ni (5-HSALDiEN)	Calcd.	58.89	4.95	11.45
	Found	58.72	5.26	11.19
Ni (5-BrSALDiEN)	Calcd.	41.11	3.26	7.99
	Found	40.98	3.17	7.72
(Ni (5-MeSALDiEN)) (H ₂ O)	Calcd.	57.97	6.04	10.14
	Found	57.71	6.04	9.66
Ni (3-MeOSALDiEN)	Calcd.	56.10	5.43	9.82
	Found	55.81	5.50	9.90
Ni (3-i-PropylSALDiEN)	Calcd.	63.73	6.92	9.29
	Found	63.23	6.26	9.31
Ni (SALDiPN)	Calcd.	60.63	5.86	10.61
	Found	60.51	5.72	10.41
(Ni (5-BrSALDiEN) (py))	Calcd.	45.43	4.15	9.22
	Found	45.62	3.64	9.26

(Ni(5-MeSALDiEN))·H₂O and Ni(SALDiPN) gave relatively intense peaks corresponding to the parent ion. The isotopic cluster for each parent ion is shown in TABLE II. The other derivatives probably have a very low vapor pressure and hence could not be transformed into the gas phase except with considerable decomposition. The mass spectra of most derivatives show a peak corresponding to the parent ion minus the nickel atom. Fragmentation patterns that would be expected from the basic ligand structure are observed in all the mass spectra. The mass spectra were measured above the basic molecular ion to the m/e value expected for the dimer but no such peak was observed which suggests the complexes are essentially monomeric in the gas phase rather than dimeric as has been postulated for some Schiff base complexes.¹³ Insufficient solubility in a suitable solvent precluded a molecular weight determination in solution.

13. E. P. Dudek, E. Chaffee and G. Dudek, Inorg. Chem., 3, 1278 (1964).

Infrared spectra were obtained both as Nujol and hexachlorobutadiene mulls and as KBr pellets on the complexes and free ligands. The major bands found in the infrared spectra of Ni(5-BrSALDiEN) and the corresponding free ligand are shown in Table III. A considerable shift to lower energy is observed in the C=N stretching frequency upon complexation with nickel which suggests the imine nitrogen atoms are coordinated. Only the 5-methyl derivative exhibits relatively intense

TABLE II

Mass Spectral Data on the Complexes^a

<u>Compound</u>	<u>Molecular Formula</u>	<u>Isotopic Cluster</u>
Ni(5-HSALDiEN)	C ₁₈ H ₁₉ N ₃ O ₂ Ni	367,369
Ni(5-MeSALDiEN)	C ₂₀ H ₂₃ N ₃ O ₂ Ni	395,397
Ni(SALDiPN)	C ₂₀ H ₂₃ N ₃ O ₂ Ni	395,397

^aIsotope patterns for C¹³ were observed for these complexes but are not included here.

TABLE III

Infrared Data (cm⁻¹) on Ni(5-BrSALDiEN) and
Protonated 5-BrSALDiEN^a

<u>Assignment</u>	<u>Free Ligand</u>	<u>Complex</u>
N-H str.	3305 vw, sh	3150 vw,b
C=N str.	1630 s,sh	1595 s,sh
C-H bend (aromatic nucleus)	825 s,sh	795 s,sh

^aAbbreviations: v = very, w = weak, s = strong, sh = sharp,
b = broad

absorption in the 3700-3100 cm^{-1} region. This has been attributed to the O-H symmetric and asymmetric stretching modes of water. The broadness of this absorption indicates the water is not coordinated.

A band assignable to a secondary nitrogen-hydrogen stretching vibrational mode could not be conclusively found in the infrared spectra of most of the complexes. A weak broad band centered at 3150 cm^{-1} was observed in the Nujol spectrum of $\text{Ni}(5\text{-BrSALDiEN})$. Several of the derivatives in various solvents including pyridine showed no meaningful absorption in the region of interest. The spectrum of $\text{Ni}(\text{HSALDiEN})$ in pyridine was investigated quite closely in an unsuccessful effort to find an N-H stretching mode. Langenbeck and coworkers¹⁴ had earlier reported a band around 3450 cm^{-1} in the spectrum of a pyridine

14. W. Langenbeck, M. Augustin, and H. J. Kerrinnes, J. Prakt. Chem., 26, 130 (1963).

solution of $\text{Ni}(\text{HSALDiEN})$ and had assigned the absorption to a N-H stretching mode. We have repeated this experiment a number of times and believe this band is characteristic of spectrograde pyridine. In fact, the infrared spectrum of pyridine shows an identically positioned band. This assumption is supported by the observation¹⁵ that secondary aliphatic amines usually

15. R. T. Conley, "Infrared Spectroscopy", Allyn and Bacon, Inc., Boston, Mass., 1966.

absorb weakly in the range 3350-3310 cm^{-1} . Deuteration in

slightly basic D₂O again revealed no bands in the anticipated N-D stretching region.

Free ligands were prepared for most of the derivatives although only the bromo-derivative showed a band in the region of interest assignable to a N-H stretching mode. Nevertheless, all free ligands gave essentially identical n.m.r. spectra except for those regions which can be attributed to the presence of various functional groups located at either the 3 or 5 position on the benzene ring. In every case the n.m.r. spectra are consistent with structure Ia.

These observations concerning the free ligands and the neutral complexes are consistent with the secondary amine participating in hydrogen bonding. Infrared measurements on various concentrations of free ligand and complex suggest intramolecular type hydrogen bonding. The absence of a sharp N-H stretching band in the complex indicates that the secondary nitrogen is perhaps not coordinated to the nickel ion.¹⁶

16. K. Nakamoto, "Infrared Spectra of Inorganic and Coordination Compounds", John Wiley and Sons, Inc., New York, N. Y., 1963.

Magnetic susceptibilities for Ni(XSALDiEN) and Ni(SALDiPN) were determined by the Faraday method and these results are presented in TABLE IV. The magnetic moments are higher than would be predicted for a low spin d⁸ nickel complex.¹⁷ Even if one

17. B. N. Figgis, "Introduction to Ligand Fields", Interscience Publishers, New York, 1968.

allows for the contribution made by temperature independent paramagnetism and the inherent error in trying to correct for diamagnetic susceptibilities, the moments are too high to consider the compounds completely diamagnetic. On the other hand the moments are lower than would be expected for high spin nickel(II). Several mechanisms may give rise to these anomalous moments. First, the complexes may be essentially diamagnetic low spin ones that are contaminated with (or in equilibrium with) a small percentage of some high-spin species (i.e. a low spin square planar or five coordinate material with a small fraction of a high spin octahedral, square planar, tetrahedral or five coordinate complex). Precedence¹⁸⁻²⁰ for such behavior is

-
18. B. T. Kilbourn, H. M. Powell and F. A. C. Darbyshire, Proc. Chem. Soc., 207 (1963).
19. R. H. Holm and K. Sawaminathan, Inorg. Chem., 2, 181 (1963).
20. L. Sacconi, "Transition Metal Chemistry", R. L. Carlin, ed., Vol. 4, Marcel Dekker, Inc., New York, 1968.

known. Secondly, a spin state isomerism²¹ between singlet and

21. S. M. Nelson and W. S. F. Kelley, Chem. Comm., 436 (1968); E. K. Barefield, S. M. Nelson and D. H. Busch, Quarterly Revs., 22, 457 (1968).
-

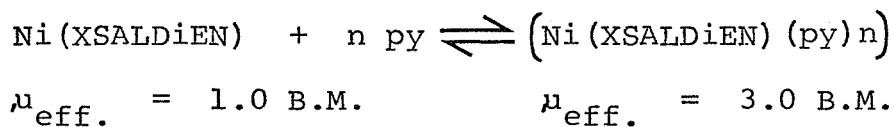
triplet states for a pseudo-square planar complex may be envisioned. In other words two energy levels of different multiplicity are positioned within kT of each other (i.e. the complex is near the "magnetic cross-over point") whereby population of both

states becomes probable. The latter rationalization is quite tenable in light of the fact that it has been shown²² that increas-

22. R. H. Holm, J. Amer. Chem. Soc., 82, 5632 (1960).

ing the carbon chain that joins Schiff base imine nitrogen atoms simultaneously weakens the in-plane ligand field. The magnetic properties of the complexes as a function of temperature are presently being studied in detail in order to test this hypothesis.

Magnetic susceptibilities on Ni(5-BrSALDiEN) and Ni(3-MeOSALDiEN) in pyridine show the complexes to be fully paramagnetic high-spin nickel(II) compounds, TABLE V. The change in spin state probably arises from pyridine coordinating to the complex in one or both axial positions. The magnetic susceptibilities are slightly dependent on both concentration and temperature within experimental error. An equilibrium such as follows which lies almost entirely to the right may account for these observations. The solubility of Ni(SALDiPN) in pyridine was not sufficient for a magnetic susceptibility measurement.



A pale green pyridine adduct has been isolated which retains pyridine up to 100°C at reduced pressure. Elemental analyses are in agreement with the composition, (Ni(5-BrSALDiEN)(py)). The mono-pyridinate has a magnetic moment typical of pseudo-octahedral nickel. Visible spectra in Nujol and chloroform

TABLE IV

Room Temperature Magnetic Data on the Nickel Complexes
in the Solid State^{a,b}

<u>Compound</u>	<u>$\chi_m \times 10^6$</u>	<u>$\mu_{eff.}$ (B.M.)</u>
Ni(5-HSALDIEN) ^c	270.5-234.3	0.80-0.75
Ni(5-BrSALDIEN) ^c	797.1-480.1	1.40-1.08
Ni(3-MEOSALDIEN) ^c	449.9-330.6	1.05-0.90
Ni(5-MeSALDIEN) (H ₂ O) ^c	633.7-384.5	1.24-0.97
Ni(3-i-PropylSALDIEN)	844.3-797.8	1.42-1.39
Ni(SALDIPN) ^c	1044.2-527.7	1.59-1.13
Ni(5-BrSALDIEN) (py)	4659.2-4410.8	3.34-3.25

^aMagnetic susceptibilities are corrected for diamagnetic ligands.

^bMagnetic susceptibilities show a slight inverse dependence on field strength. The numbers reported correspond to the maximum and minimum values measured at four different field strengths ranging from 6800 gauss to 11,800 gauss.

^cDuplicate measurements on independently prepared samples.

TABLE V

Magnetic Data on the Nickel Complexes in Pyridine

<u>Compound</u>	<u>Temperature °C</u>	<u>Conc. (g/ml)</u>	<u>$\mu_{\text{eff.}}$ (B.M.)</u>
Ni(5-BrSALDIEN)	26	0.0378	2.86
	20	0.0129	2.98
	10	0.0129	3.07
	26	0.0110	2.84
Ni(3-MeOSALDIEN)	20	0.0162	2.84
	10	0.0162	2.90
	20	0.0131	2.98
	10	0.0131	2.90

TABLE VI

Electronic Absorption Spectra (cm^{-1}) of the
Nickel Complexes

<u>Compound</u>	<u>Medium</u>	<u>Band Maxima^{a,b}</u>
Ni (5-HSALDIEN)	Nujol Methanol Pyridine	23,260; 30,770; 26,320 (7120); 30,300 10,870 (17.9); 25,970 (7100); 31,500 (5200)
(Ni (5-MeSALDIEN)) · H ₂ O	Nujol Methanol Pyridine	23,260; 24,940; 30,130 25,320 (5630); 30,130 (13,300) 10,360 (24.7); 25,000 (4950); 30,300 (3900)
Ni (5-BrSALDIEN)	Nujol Methanol Pyridine	23,030; 30,680 25,640 (8270); 30,537 (8770) 10,204 (69.7); 18,200 (18.8); 25,000 (7170); 30,540 (5580)
Ni (3-MEOSALDIEN)	Nujol Methanol Pyridine	22,730, 30,000 25,640 (2700); 30,300 (12130) 10,846 (9.9); 12,580 (5.2); 17,620 (9.2); 21,570 (3240)
Ni (3-i-PropylSALDIEN)	Nujol	25,310; 30,300
Ni (SALDIPN)	Nujol Methanol Pyridine	23,670; 24,840; 30,540 25,970 (4100); 30,540 (9700) 12,200 (404); 14,290 (70.8); 19,230 (606); 25,640 (3640)
(Ni (5-BrSALDIEN) (py))	Nujol Chloroform	11,630 vb; 18,500; 24,390 11,630 vb (70); 18,520 (100); 25,970 (7300)
Ni (SALEN)	Nujol	19,610; 23,530; 30,300
Ni (SALOPHEN)	Nujol	18,020; 19,610; 26,320

^aNumbers in parenthesis are molar extinction coefficients

^bAbbreviations: v = very, b = broad

support this contention. The bands at $11,630\text{ cm}^{-1}$ and $18,520\text{ cm}^{-1}$ may be assigned in O_h symmetry to the transitions ${}^3T_{2g} \leftarrow {}^3A_{2g}$ and ${}^3T_{1g}(F) \leftarrow {}^3A_{2g}$ respectively. Surprisingly the infrared spectra of the pyridine adduct shows an N-H stretching mode. The position of this band is shifted approximately 35 cm^{-1} to lower energy relative to the free ligand. It is tempting to suggest the pseudo-octahedral structure in the solid state is achieved by coordination of the secondary nitrogen and one pyridine moiety at the axial sites rather than both sites being filled by pyridine molecules.

In the solid state spectra of $\text{Ni}(\text{SALDiPN})$ and $\text{Ni}(\text{XSALDiEN})$ two bands are observed: $23,000\text{ cm}^{-1}$ and $30,500\text{ cm}^{-1}$. TABLE VI. Both bands are tentatively assigned as spin-allowed charge transfer transitions. The band at $23,000\text{ cm}^{-1}$ is in the region where d-d transitions peculiar to square planar nickel(II) are found but other observations rule against this assignment. First, square planar²² $\text{Ni}(\text{SALEN})$ ²³ has its d-d transition located around

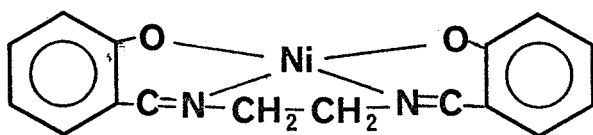
23. SALEN is N,N bis(salicylidene)-1,2-diaminoethane.

$19,000\text{ cm}^{-1}$. If $\text{Ni}(\text{XSALDiEN})$ is in fact square planar, its d-d transition should be of comparable or lower energy since lengthening the chain joining the imine nitrogen atoms is known to reduce the d-d transition energy. Secondly, the solid state spectrum of 5-BrSALDiEN shows a band around $23,000\text{ cm}^{-1}$. Thirdly, the extinction coefficients in methanol for these bands

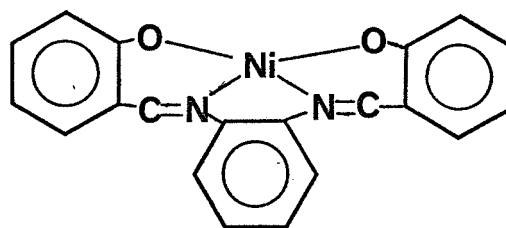
are much too large to have arisen from a d-d transition. We, therefore conclude that the band of interest is characteristic of the ligand and is not a d-d transition. The complexes are probably square planar but the d-d transition is masked because of the relatively low energy charge transfer band.

A change in coordination number when the complexes are placed in pyridine is further corroborated by the appearance of a new broad band in the $10,500\text{ cm}^{-1}$ region for $\text{Ni}(\text{XSALDiEN})$ and at $12,000\text{ cm}^{-1}$ for $\text{Ni}(\text{SALDiPN})$. The visible spectra of the complexes in pyridine and $(\text{Ni}(5\text{-BrSALDiEN})(\text{py}))$ in the solid state coincide quite well except for slight shifts in the band maxima.

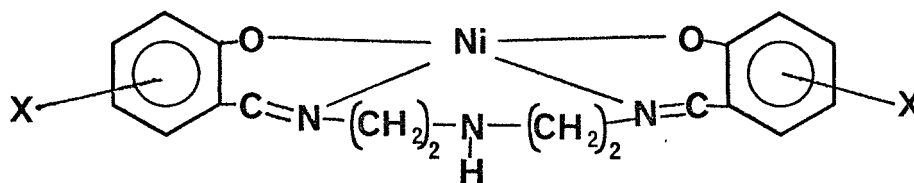
A comparison of the behavior in pyridine of $\text{Ni}(\text{SALEN})$ and $\text{Ni}(\text{SALOPHEN})$ with $\text{Ni}(\text{XSALDiEN})$ Structures III-V. reveals the



III



IV



V

following points. The former two complexes have been shown to be nearly planar and diamagnetic in the solid state.²² When dissolved in pyridine Ni(SALEN) remains diamagnetic whereas Ni(SALOPHEN) becomes partially paramagnetic (2.5 B.M.) at room temperature.²⁴

-
24. R. H. Holm, G. W. Everett, and A. Chakravorty, *Prog. Inorg. Chem.*, 7, 83 (1966); S. Yamada, E. Ohno, Y. Kuge, A. Takeuchi, K. Yamanouchi and K. Iwasaki, *Coordin. Chem. Revs.*, 3, 247 (1968).
-

Temperature dependent magnetic studies have shown that the moments decrease as the temperature increases. An equilibrium involving coordinated and non-coordinated pyridine has been postulated similar to our results with Ni(SALDiEN) in pyridine. The major difference being that the latter is fully paramagnetic in pyridine. The reason for this probably lies in the fact that the in-plane field strength of X-SALDiEN is expected to be diminished relative to SALEN or SALOPHEN. This may come about by two sources (1) the chain length between imine nitrogen atoms has increased, and (2) the secondary nitrogen atom may offer some degree of axial perturbation thereby effectively lowering the in plane field strength. Both effects may be interpreted in terms of the relative d orbital energies for a nickel(II) ion. Figure 2. The energy difference between the two highest energy orbitals, Δ , decreases in going from (1) a strong to a weaker in-plane field and/or (2) a very weak axial perturbation to a stronger axial perturbation. Energywise less and less CFSE is gained by

Fig. 2

electron pairing; therefore, the high-spin state becomes more favored. It should be easier for pyridine to unpair electrons for a weak in-plane field than for a strong in-plane field because Δ is smaller. Consequently, one might argue that (1) Ni(SALEN) is diamagnetic in pyridine because of the strong ligand field presented by SALEN, (2), Ni(SALOPHEN) is partially paramagnetic because SALOPHEN presents a weaker field arising from the lower coordinating ability of the imine nitrogen atoms which are in conjunction with the aromatic ring systems and (3) Ni(XSALDiEN) is fully paramagnetic and pseudo-octahedral in pyridine since XSALDiEN should present the weakest in-plane ligand field in that five atoms join the imine nitrogens. Alternatively the secondary nitrogen atom may present some small degree of axial perturbation, the degree being limited by the steric requirements of the ligands and the metal ligand distance. For metal-donor atom distances of 2,3-2.5 \AA , SALDiEN has been shown to function as a planar pentadentate ligand with a stable non-eclipsed conformation of its aliphatic chain²⁴. This conformation is not anticipated for

24. M. N. Akhtar, E. D. McKenzie, R. E. Paine and A.J. Smith, Inorg. Nucl. Chem. Letters, 5, 673 (1969).

first row transition ions since the metal to donor atom distance is approximately 2.0 \AA . The extent of this perturbation is difficult to measure but it would seem that it becomes more pronounced if a donor occupies the other axial position. That the pyridine adduct

of Ni(5-BrSALDiEN) shows a sharp N-H stretch in the infrared spectrum supports this postulate.

The suggested weaker in-plane field for Ni(XSALDiEN) lends evidence to our contention that the anomalous magnetic moments in the solid state may arise from a thermal population of singlet and triplet states.

Acknowledgment. This investigation was supported by VPISU-NASA Multidisciplinary Grant 47-004-006. The assistance of C. T. Spencer and T. C. Rhyne in making the magnetic and mass spectral measurements is gratefully acknowledged. Much of the instrumentation used to carry out this study was obtained by NSF Departmental Equipment Grants GP 8617 and GP 9530.

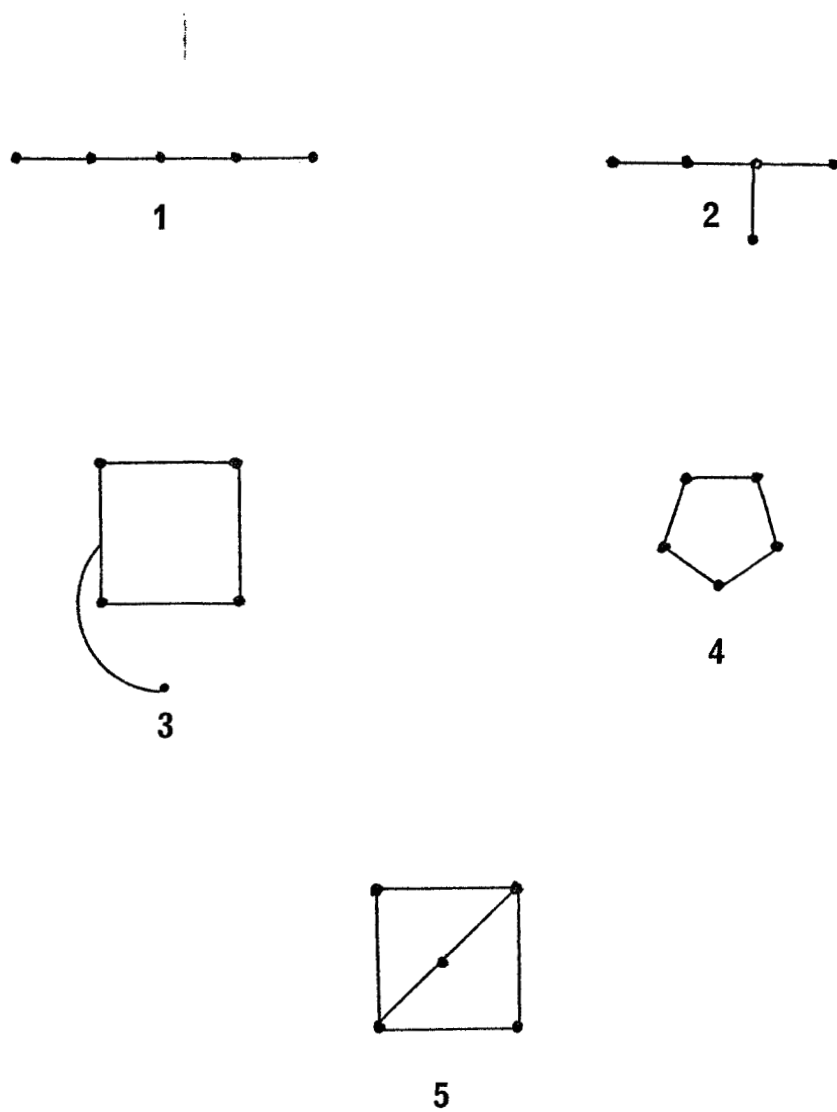


Figure 1. Types of Pentadentate Ligands

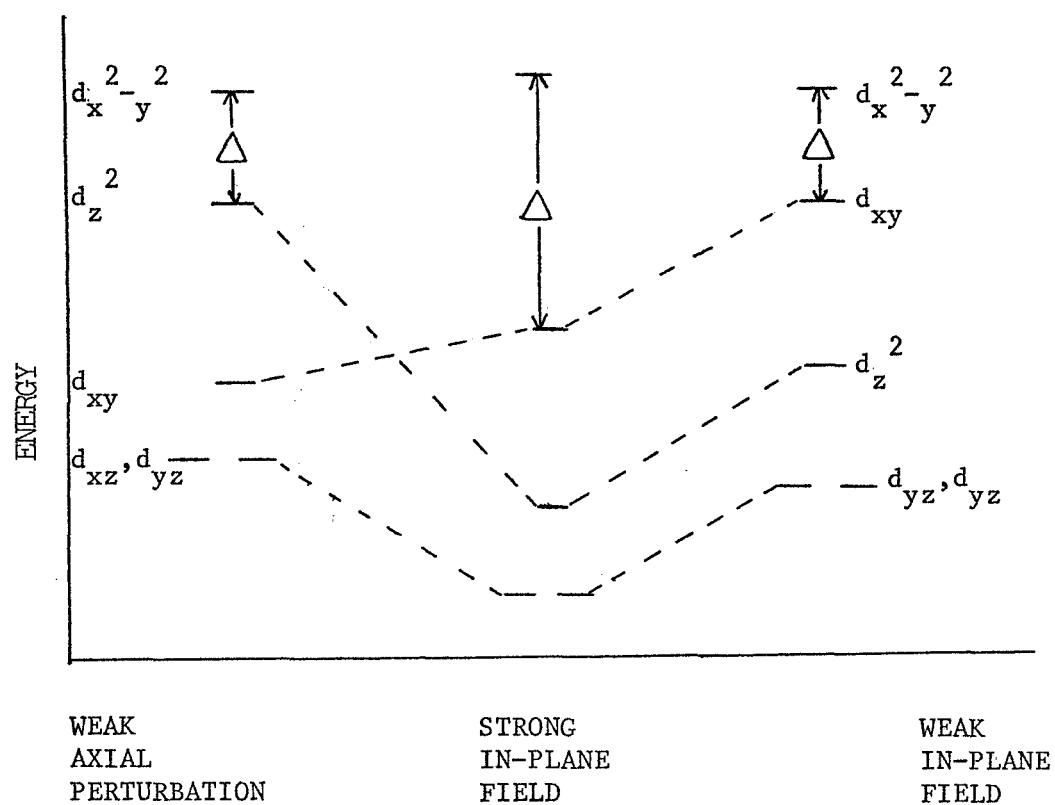


Figure 2. Relative d orbital energies for a nickel(II) ion in an essentially square planar environment.

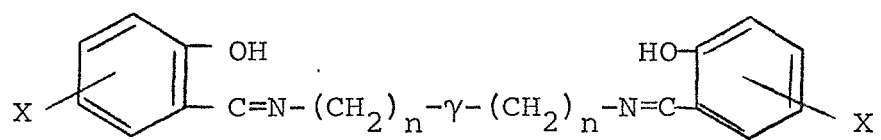
Pentadentate Ligands II. Nickel(II) Complexes of the
Linear Schiff Base Ligands Derived from Substituted
Salicylaldehydes and Bis(2,2'-aminoethyl)sulfide

By W. M. Coleman and L. T. Taylor

Introduction

Complexes of potentially linear pentadentate ligands derived from polyamines and monocarbonyl compounds have not been investigated to a great extent. High spin five coordinate complexes¹ have been shown to result from the interaction of first row transition metal ions with the pentadentate ligand derived from salicylaldehyde and bis(3,3'-aminopropyl)amine, structure Ia. Low spin, four coordinate distorted square planar complexes^{2,3} have been postulated for nickel(II) with ligands derived from substituted salicylaldehydes and diethylenetriamine, structure Ib and bis(2,2'-aminopropyl)amine. We have recently communicated⁵ preliminary results concerning the nickel complexes of Schiff bases formed from substituted salicylaldehydes and bis(2,2'-aminoethyl)sulfide, structure Ic. We wish to report a more complete description of these complexes here.

1. L. Sacconi and I. Bertini, J. Amer. Chem. Soc., 88, 5180 (1966).
 2. W. Langenbeck, M. Augustin and H. J. Kerrines, J. Prakt. Chem. 26, 130 (1964).
 3. W. M. Coleman and L. T. Taylor, unpublished results.
 4. M. K. Akhtar, E. D. McKenzie, R. E. Paine and A. J. Smith, Inorg. Nucl. Chem. Letters, 5, 673 (1969).
 5. W. M. Coleman and L. T. Taylor, J. American Chem. Soc., 92, 1449 (1970).
-



X=5-H, 5-Br, 5-CH₃, 3-CH₃ and 3-(CH₃)₂CH

Ia n=3, γ=N-H : H₂SALDPT

b n=2, γ=N-H : H₂SALDIEN

c n=2, γ=s : H₂SALDAES

Experimental

Materials - Technical grade 3-methoxysalicylaldehyde (o-vanillin) and salicylaldehyde (SAL) were obtained from the Aldrich Chemical Company, Milwaukee, Wisconsin and bis(2,2'-aminoethyl)-sulfide (DAES) was donated by the Dow Chemical Company, Midland, Michigan. The latter two were used without further purification, but o-vanillin was recrystallized from 95% ethanol in the presence of decolorizing charcoal. All other chemicals and solvents were of reagent grade or equivalent.

5-Bromosalicylaldehyde was prepared by adding bromine to an equivalent amount of a cold solution of salicylaldehyde dissolved in a glacial acetic acid. White crystals were obtained upon recrystallizing the crude product from ethanol: water (60:40). 5-methylsalicylaldehyde was prepared by a modification of the Reimer-Tiemann reaction employing p-cresol and chloroform in a highly alkaline medium. 3-Isopropylsalicylaldehyde was prepared according to the general procedure of the Duff⁶ reaction starting with o-isopropylphenol.

6. J. C. Duff, J. Chem. Soc., 547 (1941).

The preparation of the uncomplexed pentadentate ligands involved adding dropwise one molecular equivalent of DAES dissolved in 95% ethanol to a cold stirring solution of two molecular equivalents of salicylaldehyde also dissolved in a small amount of 95% ethanol. Soon after addition was begun bright yellow crystals formed in the reaction mixture which were filtered, recrystallized from hot 95% ethanol, filtered again, and dried

and dried in vacuo at room temperature for 12 hours. Their composition and structure have been established by elemental analysis, infrared and n.m.r. spectra.

Preparation of $\sqrt{\text{Ni(5-HSALDAES)}}$ -- Protonated 5-HSALDAES (3.26 g, 0.01 mole) was dissolved in 200 ml of absolute ethanol and brought to reflux. Nickel acetate, $\text{Ni}(\text{C}_2\text{H}_3\text{O}_2)_2 \cdot 4\text{H}_2\text{O}$, (2.49 g, 0.01 mole) dissolved in 125 ml of absolute ethanol was added dropwise. A green solid formed approximately after half of the nickel solution had been added. After addition was complete, refluxing was continued for two hours after which the flask was allowed to come to room temperature. A green powder was isolated by filtration and dried in vacuo at 100°C for twelve hours.

Preparation of $\sqrt{\text{Ni(5-BrSALDAES)}}$. -- To a solution of protonated 5-BrSALDAES (4.86 g, 0.01 mole) dissolved in 150 ml of hot N,N-dimethylformamide with stirring was added dropwise a solution of $\text{Ni}(\text{C}_2\text{H}_3\text{O}_2)_2 \cdot 4\text{H}_2\text{O}$ (2.49 g, 0.01 mole) dissolved in 125 ml of methanol. A green solid formed halfway through the nickel addition. The reaction mixture was refluxed for one hour and then allowed to come to room temperature. The green product was isolated and dried as described above.

Preparation of $\sqrt{\text{Ni(5-MeSALDAES)}}$. -- This material was prepared, isolated and dried following the procedure given above for $\text{Ni}\sqrt{\text{(5-BrSALDAES)}}$.

Preparation of $\sqrt{\text{Ni(3-MeOSALDAES)}}$. -- This material was prepared, isolated and dried following the procedure previously described for $\sqrt{\text{Ni(5-HSALDAES)}}$.

Preparation of $\text{Ni}(3\text{-i-PropylSALDAES})$. -- To a solution prepared by dissolving 3-isopropylsalicylaldehyde (4.86 g, 0.03 mole) in 50 ml of 95% ethanol, which also contained triethylorthoformate (4.44 g, 0.03 mole) and triethylamine (3.30 g, 0.03 mole), was added dropwise DAES (1.80 g, 0.015 mole) with stirring. The resulting mixture was yellow in color. A solution prepared by dissolving $\text{Ni}(\text{C}_2\text{H}_3\text{O}_2)_2 \cdot 4\text{H}_2\text{O}$ (3.74 g, 0.015 mole) in 200 ml of absolute ethanol was then added dropwise to the yellow solution. Refluxing was continued for three hours after nickel addition was complete. The reaction mixture was allowed to come to room temperature whereupon green crystals formed which were isolated and dried as previously described.

Preparation of $\text{Ni}(5\text{-HSALDAES})(\text{H}_2\text{O})$. -- To protonated HSALDAES (1.64 g, 0.005 mole) dissolved in methanol was added a solution of $\text{Ni}(\text{C}_2\text{H}_3\text{O}_2)_2 \cdot 4\text{H}_2\text{O}$ (1.44 g, 0.005 mole) dissolved in methanol. The mixture was refluxed for four hours. No precipitate formed upon mixing. After two hours a bright green precipitate formed. It was filtered, washed with ether, recrystallized from hot chloroform and dried in vacuo at room temperature for twelve hours.

Preparation of the Pyridine Adduct of $\text{Ni}(5\text{-HSALDAES})$. -- Approximately 1.0 g of $\text{Ni}(5\text{-HSALDAES})$ was dissolved in 10 ml of pyridine. The solution was heated for thirty minutes then allowed to come to room temperature followed by addition of water where upon a green solid precipitated. This material was filtered and dried in vacuo at 100°C for twelve hours.

Preparation of the Pyridine Adduct of $\text{[Ni(3-MeOSALDAES)]}$. --

Approximately 1.0 g of $\text{[Ni(3-MeOSALDAES)]}$ was dissolved in pyridine and stirred for thirty minutes. Water was then added to cause precipitation. The pale green material was isolated and dried as described above.

Physical Measurements. -- Infrared spectra were obtained in the region $5000\text{--}400\text{ cm}^{-1}$ using a Perkin-Elmer Model 621 spectrophotometer. Solid state spectra were recorded as KBr pellet and as Nujol or hexachlorobutadiene mulls. Ultraviolet-visible-near infrared spectra were obtained with a Cary 14 recording spectrophotometer. Spectra of solid samples were obtained by a diffuse transmittance technique⁷ employing Nujol mulls impregnated on Whatman No. 1 filter paper. Solution spectra were obtained utilizing spectroquality organic solvents.

Magnetic susceptibility measurements on solid samples were obtained by the Faraday method. Solution magnetic measurements⁸ were determined by a n.m.r. method using a Varian A60 spectrometer. Diamagnetic corrections were made employing Pascal's constants⁹. Special coaxial cells with precision spacing of the inner tube (Wilmad Glass Co.) were used. Measurements were performed at 10°C and 20°C using a Varian Model V6040 NMR variable temperature controller.

-
7. R. H. Lee, E. Griswold and J. K. Kleinberg, *Inorg. Chem.* 3, 1278 (1964).
8. D. F. Evans, *J. Chem. Soc.*, 2003 (1959).
9. B. N. Figgis and J. Lewis, "Modern Coordination Chemistry", J. Lewis and R. J. Wilkins, Eds., Interscience Publishers, Inc., New York, N.Y., 1960.
-

Mass spectra were obtained on a Hitachi-Perkin-Elmer RMU-7 double focusing mass spectrometer using a solid inlet probe. The solid probe temperature was maintained at a value to prevent decomposition of the samples. The source temperature was maintained at approximately the temperature of the solid probe. Analyzer tube and ion source pressures of less than 10^{-6} torr were employed. Where necessary mass to charge ratios were calibrated with perfluorokerosene.

Elemental analyses were performed by Galbraith Microanalytical Laboratory, Knoxville, Tennessee and in this laboratory using a Perkin-Elmer-Model 240 CH & N analyzer.

X-ray powder pattern data were obtained using a General Electric-XRD-5 Powder Diffractometer employing Cu-K α radiation

Results and Discussion

Complexes of composition $\text{Ni}(\text{XSALDAES})$ have been prepared by the dropwise addition of a solution of nickel acetate 4-hydrate to a solution of the pre-formed protonated Schiff base ligand¹⁰.

(10) Earlier (N. S. Gill, Ph.D. Thesis, U. of Sydney, Australia), complexes of indefinite composition had been reported employing a similar reaction.

Dark green complexes precipitate immediately which are insoluble in practically all organic solvents. $\text{Ni}(\text{HSALDAES})$ and $\text{Ni}(3\text{-i-PropylSALDAES})$ are partially soluble in chloroform and dichloromethane. Each complex is relatively thermally stable, melting above 250°C . Two pyridine adducts, $(\text{Ni}(\text{HSALDAES})(\text{py}))$ and $(\text{Ni}(3\text{-MeOSALDAES})(\text{py}))$, were prepared by precipitating the green materials from a concentrated pyridine solution by the addition of water. The compounds were soluble in a number of polar organic solvents and they retained pyridine even upon drying for twelve hours at 100°C in vacuo. An additional new complex could be prepared by carrying out the complexation reaction in methanol. This hydrated complex is postulated to have the formulation, $(\text{Ni}(\text{HSALDAES})(\text{H}_2\text{O}))$, TABLE I.

Mass spectra were measured on all the complexes under the least severe conditions. Many of the compounds gave a series of m/e peaks corresponding to the isotope pattern of the parent complex with no higher mass fragments, TABLE II, indicating negligible polymer formation in the gas phase. Isotopic clusters corresponding to the parent ion were observed for the methoxy, methyl, and isopropyl derivatives.

TABLE I

ANALYTICAL DATA FOR THE NICKEL COMPLEXES

<u>Compound</u>	<u>C</u>	<u>H</u>	<u>N</u>
$\triangleleft \text{Ni (5-HSALDAES)} \right\rangle$	Calcd. 56.13 Found 55.95	4.72 4.77	7.28 7.29
$\triangleleft \text{Ni (5-MeSALDAES)} \right\rangle$	Calcd. 58.13 Found 58.41	5.38 5.32	6.78 6.53
$\triangleleft \text{Ni (5-HSALDAES) (H}_2\text{O)} \right\rangle$	Calcd. 53.62 Found 53.69	5.01 4.91	6.95 6.53
$\triangleleft \text{Ni (5-BrSALDAES)} \right\rangle$	Calcd. 39.82 Found 39.90	2.98 2.87	5.16 5.17
$\triangleleft \text{Ni (3-MeOSALDAES)} \right\rangle$	Calcd. 53.95 Found 54.19	4.99 5.02	6.29 6.31
$\triangleleft \text{Ni (3-i-PropylSALDAES)} \right\rangle$	Calcd. 61.42 Found 61.51	6.46 6.46	5.97 6.16
$\triangleleft \text{Ni (5-HSALDAES) (PY)} \right\rangle$	Calcd. 59.50 Found 59.46	5.00 4.87	9.05 8.91
$\triangleleft \text{Ni (3-MeOSALDAES) (PY)} \right\rangle$	Calcd. 57.27 Found 57.09	5.20 5.43	8.02 7.79

TABLE II

Mass Spectral Data on the Complexes^a

<u>Compound</u>	<u>Molecular Formula</u>	<u>Isotopic Cluster</u>
Ni(5-MeSALDAES)	C ₂₀ H ₂₂ N ₂ SO ₂ Ni	412,414
Ni(3-MeOSALDAES)	C ₂₀ H ₂₂ N ₂ SO ₄ Ni	444,446
Ni(3-i-PropylSALDAES)	C ₂₄ H ₃₀ N ₂ SO ₂ Ni	468,470

^aIsotope patterns for C¹³ were observed but are not included.

Infrared spectra on all complexes were obtained as either Nujol mulls of KBr pellets. The spectra of Ni(XSALDAES) and the nickel(II) complexes of H₂SALDiEN are essentially the same. Of specific interest is the C=N stretching frequency in the complex which was observed to shift 25 cm⁻¹ to lower energy when compared with its position in the free ligand. This result is compatible with the imine nitrogen atom being coordinated to the metal.¹¹ The infrared spectra of (Ni(XSALDAES)(py)) show bands

11. P. X. Armendarez and K. Nakamoto, Inorg. Chem., 5, 796 (1966).
 12. "The Sadtler Standard Spectra", Sadtler Research Laboratory, Philadelphia, Penna., 1959.
-

assignable to pyridine. Comparison of these spectra with the Sadtler Catalogue spectrum¹² of pyridine confirm the presence of pyridine (i.e. bands at 1220 cm⁻¹, 1120 cm⁻¹ and 1060 cm⁻¹ could be attributed solely to pyridine). The appearance of a band at 3250 cm⁻¹ attributable to an O-H stretching mode in the spectrum of (Ni(5-HSALDAES)(H₂O)) lends evidence to its proposed formulation as an hydrate.

Magnetic susceptibilities were measured on Ni(XSALDAES) employing the Faraday method and the results are presented in TABLE III. The magnetic moments are anomolous and very similar to the results obtained with Ni(XSALDIEN)³, being in between the values expected for either high or low spin d⁸ nickel(II) complexes regardless of the coordination geometry about the metal. The several mechanisms which may account for the magnetic

TABLE III

Room Temperature Magnetic Data on the Nickel
Complexes in the Solid State

<u>Compound</u>	<u>$\chi_M \times 10^6$</u>	<u>$\mu_{\text{eff.}}$ (B.M.)</u>
Ni (5-HSALDAES)	482.8	1.11
[Ni (5-HSALDAES) (H ₂ O)]	3623.4	2.94
Ni (5-BrSALDAES)	436.1	1.02
Ni (5-MeSALDAES)	191.1	0.90
Ni (3-MeOSALDAES)	385.4	1.15
Ni (3-i-PropylSALDAES)	602.1	1.43
[Ni (5-HSALDAES) (py)]	2766.0	2.71
[Ni (3-MeOSALDAES) (py)]	2702.6	2.69

moments of these complexes which employ high strained linear pentadentate ligands have been previously discussed.³ In light of the fact that five-coordinate nickel(II) complexes are reported to exist as high or low spin complexes depending on the π -bonding character of the ligand donor atoms¹³, it seems highly tenable that a spin state isomerism between singlet and triplet states for a distorted five-coordinate complex may exist.¹⁴ A detailed temperature dependent magnetic susceptibility study is presently being pursued to test this hypothesis. In contrast $(\text{Ni}(\text{XSALDAES})(\text{py}))$

13. L. Sacconi, Transition Metal Chem., 4, 227 (1968) and references therein.

14. B. N. Figgis, "Introduction to Ligand Fields", Interscience Publishers, New York, 1966.

and $(\text{Ni}(\text{HSALDAES})(\text{H}_2\text{O}))$ give magnetic moments around 3.0 B.M. which are typical of pseudo-octahedral nickel(II).

The magnetic susceptibilities in pyridine solution support the contention that in pyridine the species are essentially spin free showing little dependence on temperature or concentration, TABLE IV. This could arise from pyridine completing the six coordinate structure. Visible spectral data in pyridine supports

this assumption in that the three Laporte forbidden transitions¹⁵ characteristic of pseudo-octahedral nickel(II) are observed in the region $10,300 \text{ cm}^{-1}$, $\nu_1(^3\text{T}_{2g} \leftarrow ^3\text{A}_{2g})$; $17,500 \text{ cm}^{-1}$, $\nu_2(^3\text{T}_{1g}(\text{F}) \leftarrow ^3\text{A}_{2g})$ and $25,000 \text{ cm}^{-1}$, $\nu_3(^3\text{T}_{1g}(\text{P}) \leftarrow ^3\text{A}_{2g})$. In some of the spectra

15. M. Kilner and J. M. Smith, J. Chem. Ed., 45, 94 (1968).

TABLE IV

Magnetic Data on the Nickel Complexes in Pyridine

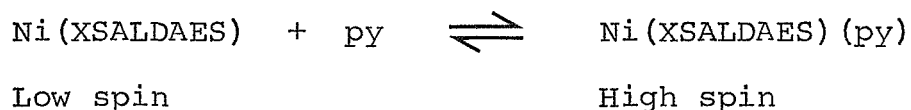
<u>Compound</u>	<u>Temp. °C</u>	<u>Conc. (g/ml)</u>	<u>μ_{eff} (B.M.)</u>
$\text{[Ni(5-HSALDAES)]}^+$	26	0.0439	2.67
	26	0.0128	2.73
	20	0.0128	2.81
$\text{[Ni(3-MeOSALDAES)]}^+$	20	0.0229	2.81
	10	0.0229	2.84
	20	0.0109	2.64
	10	0.0109	2.75
$\text{[Ni(3-i-PropylSALDAES)]}^+$	20	0.0152	2.75
	10	0.0152	2.92
	20	0.007	3.07

TABLE V

Electronic Spectra (cm^{-1}) of the Ni(XSALDAES) Complexes

<u>Compound</u>	<u>Medium</u>	<u>Band Maxima</u>
$\text{[Ni(5-HSALDAES)(H}_2\text{O)]}$	Nujol	8,403; 15,620; 24,390; 30,770
	CHCl_3	8,700(23); 16,000(30); 26,320(495) 30,300(350)
	Pyridine	10,420(9.71); 17,390(12.62); 25,970 (6700); 31,250(3970); 31,750(3980)
Ni(5-HSALDAES)	Nujol	16,060; 23,120; 30,080
	Pyridine	10,420(9); 17,390(12); 25,970(5590); 31,750(5280)
Ni(5-BrSALDAES)	Nujol	16,393; 22,220; 25,000; 30,300
	Pyridine	10,360(40); 17,780(40); 25,320(7720); 30,080(5280)
Ni(5-MeSALDAES)	Nujol	15,390; 22,730; 31,250
	Pyridine	10,310(37); 17,390(46); 25,160(8630); 30,300(6750)
Ni(3-i-PropylSALDAES)	Nujol	15,560; 20,830; 24,540; 30,300
	CH_2Cl_2	16,130(1360); 25,320(3710); 30,300(6400); 40,400(27,700)
	Pyridine	11,330(195); 17,360(260); 25,710(10,000) 28,990(11,100); 30,300(11,500)
Ni(3-MeoSALDAES)	Nujol	16,000; 22,990; 23,530; 25,320; 29,850
	Pyridine	10,100(9); 12,660(2); 17,390(9)
$\text{[Ni(3-MeoSALDAES)(PY)]}$	Nujol	11,630; 15,870; 24,390; 25,620; 29,410
	CHCl_3	12,500(60); 16,130(210); 24,390(3500); 25,640(4100); 30,300(6500)
$\text{[Ni(5-HSALDAES)(PY)]}$	Nujol	11,360; 16,950; 25,640
	CHCl_3	8,770(20); 10,640(20); 16,130(80)

the lowest energy band is split into two components which probably arises as a result of some low symmetry distortion from octahedral symmetry. The $\sqrt{3}$ transition has a rather high molar extinction coefficient for a d-d band although "intensity stealing" from the near-by charge transfer band (c.a. $30,000 \text{ cm}^{-1}$) may account for this. It is conceivable that the $25,000 \text{ cm}^{-1}$ band may be a composite d-d and charge transfer transition. The visible spectra of the pyridine adducts in the solid state and in non-donor solvents are in agreement with the results concerning Ni(XSALDAES) when dissolved in pyridine. It may, therefore, be concluded from magnetic and spectral measurements that (1) an equilibrium shifted far to the right such as the following exists in pyridine, and (2) the species in pyridine solution and the isolable pyridine adducts



are practically the same. The spectra of $(\text{Ni(XSALDAES)}(\text{H}_2\text{O}))$ in CHCl_3 and as a Nujol mull along with magnetic data indicate a pseudo octahedral environment for the nickel(II) ion here, also. These six coordinate structures may be envisioned to arise from the coordination of the five donor sites of the pentadentate ligand to the nickel(II) with pyridine or water completing the octahedral arrangement.

Visible spectra of Ni(XSALDAES) were also obtained as Nujol mulls and dissolved in CH_2Cl_2 when solubility permitted. Bands appeared around $16,000 \text{ cm}^{-1}$ and $23,000 \text{ cm}^{-1}$ in all cases. The

lower energy band may be characteristic of low spin five coordinate nickel(II)¹⁶ or it may arise from a square planar configuration in which the in-plane field is very weak.¹⁷ The higher energy band

16. L. Sacconi, Transition Metal Chem., 4, 227 (1968) and references therein.

17. R. H. Holm, J. Amer. Chem. Soc., 82, 5632 (1960).

is most probably ligand in origin since the free ligand also absorbs in this region. Stereochemical models show that the two phenolic oxygen atoms and two imine nitrogen atoms can easily coordinate in a regular planar manner or a twisted manner.

Whether the sulfur atom is in fact coordinated to the nickel(II) ion can only be confirmed by a single crystal ~~X~~-ray diffraction study. If the thioether atom does not in some way perturb the nickel ion, the magnetic and spectral properties of Ni(XSALDAES) and Ni(XSALDiEN), where the secondary nitrogen has been shown to not coordinate, should be identical. Major differences between both series of complexes are found in their visible spectra and x-ray powder patterns. Table VI compares ~~X~~-ray powder pattern data for Ni(3-MeOSALDAES) and Ni(3-MeOSALDiEN). Nickel complexes of identically substituted derivatives of SALDAES and SALDiEN gave ^{dis}similar results which indicate different structures for Ni(XSALDAES) and Ni(XSALDiEN). Solid state visible spectra also differ in that Ni(XSALDAES) has a significant low energy band around $16,000\text{ cm}^{-1}$ which is notably absent from the visible spectra of Ni(XSALDiEN). Both types of complexes become highly paramagnetic in pyridine giving rise to pseudo-octahedral species but

TABLE VI

X-Ray Data on the Ni Complexes

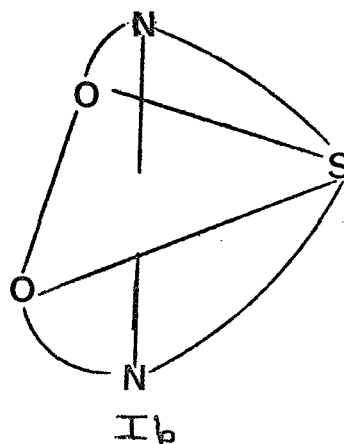
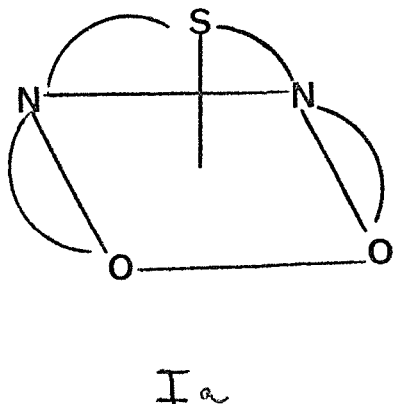
Ni(3-MeoSALDIEN)

d value	Intensity
14.730	28
12.627	18
11.191	40
10.281	25
7.254	8
6.326	17
5.906	40
5.391	14
5.277	23
5.096	19
4.796	12
4.529	15
3.619	25
3.520	40
3.401	30

Ni(3-MeoSALDAES)

d value	Intensity
10.782	45
8.845	58
8.192	25
6.026	25
5.438	22
4.575	19
4.270	15
4.114	22
3.934	60
3.850	43
3.633	48
3.363	38
3.220	12
2.921	20

judging from the position of the lowest energy band (which is an indication of the average ligand field strength presented by the donor atoms) the octahedral species are not identical. Band maxima appear at 10,900- and 17,000 cm^{-1} for Ni(XSALDiEN) and at 10,100- and 17,400 cm^{-1} for Ni(XSALDAES). If both structures were solely cis-planar NiN_2O_2 structures it is anticipated that their spectra in pyridine would give identically positioned band maxima. The ν_1 band is shifted 800 cm^{-1} to lower energy for Ni(XSALDAES) relative to Ni(XSALDiEN). This difference in pyridine may be attributed to a $\text{NiN}_3\text{O}_2\text{S}$ environment for Ni(XSALDAES) versus a NiN_4O_2 environment for Ni(XSALDiEN). The shift to lower energy is compatible in that a thioether linkage produces a smaller Dq than a secondary or pyridine nitrogen atom. These results may be rationalized in several ways concerning the structure of Ni(XSALDAES). The sulfur atom because of its orbital extension in space may only be perturbing excited states of the nickel ion without forming a direct ground-state metal-sulfur bond, or a five-coordinate species may be produced with formation of a metal-sulfur bond. The postulated five-coordinate Ni(X-SALDAES) may be ideally envisioned to have a square pyramidal or trigonal-bipyramidal structure.



Drieding and Fisher-Hershfelder-Taylor stereomodels do not rule out Figure 1a although 1b is reported to be preferred by a somewhat analogous pentadentate ligand. Regardless of the structure, the ligand must undergo severe steric strain in order for the sulfur atom to be situated near a coordination site. Alternatively, the true structure may be some compromise of two or more of the following structures: a) square planar, b) distorted square planar (metal ion raised above the plane defined by the four donor atoms or distorted tetrahedral structure), and c) trigonal bipyramid or square pyramid. Four-coordination is characteristic of (a) and (b) while five-coordination is exemplified by (c).

Cobalt Carbon Sigma Bond Formation Employing a High Spin
Five-Coordinate Cobalt(II) Complex

By W. M. Coleman and L. T. Taylor

Introduction

The significance of the cobalt-alkyl complexes as models for vitamin B₁₂ coenzyme has been discussed in some detail.¹⁻⁴

1. G. N. Schrauzer, Accounts of Chem. Res., 1, 97 (1966).
 2. G. N. Schrauzer, Adv. Catalysis, 18, 526 (1968) and references therein.
 3. G. N. Schrauzer, ACS-CIC Symposium "Bioinorganic Chemistry" Blacksburg, Va., June, 1970.
 4. G. Costa, G. Mestroni, G. Taugher and L. Itlefani, J. Organometal. Chem., 6, 181 (1966).
-

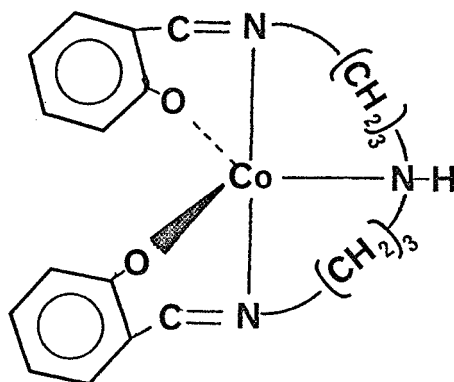
Those systems from which stable Co-C links can be produced have been limited exclusively to low spin cobalt(II) square planar complexes which employ tetradentate ligands with either all nitrogen donors or two nitrogen and two oxygen donor atoms.⁵ The two known

5. M. Green, J. Smith and P. A. Tasker, Dis. Faraday Soc., 47, 172 (1969).
-

exceptions in this regard are the square planar cobalt(II) complex of dimethylglyoxime (a bidentate ligand) and the five-coordinate vitamin B₁₂ coenzyme (cobalamin) which contains a pentadentate ligand. However, the spin state of the cobalt(II) in both cases is postulated to be low spin. In this report consideration is given to the nature of the cobalt-carbon bond formed from the previously reported⁶ high-spin five coordinate cobalt(II) complex of the pentadentate ligand derived from salicylaldehyde and bis(3,3'-aminopropyl)amine, hereafter

6. L. Sacconi and I. Bertini, J. Amer. Chem. Soc., 88, 5180 (1966).

referred to as Co(SALDPT), structure I.



STRUCTURE I

Experimental

Materials.--Bis(3,3'-aminopropyl)amine and salicylaldehyde were obtained from Aldrich Chemical Company, Milwaukee, Wisconsin and used without further purification. Palladium(II) chloride and NaBH₄ were obtained from Alfa Inorganic Inc., Beverly, Mass. The preparation of Co(SALDPT) was accomplished by several procedures which are recorded elsewhere⁶⁻⁸. No oxygen was allowed to come

7. R. H. Bailes and M. Calvin, J. Amer. Chem. Soc., 69, 1886 (1949).

8. C. Floriani and F. Calderazzo, J. Chem. Soc. (A).

in contact with the compound until the mother liquor had been washed away from the product with ether and allowed to dry to yield a golden yellow crystalline product. All other chemicals

including alkylhalides, and solvents were of reagent grade or equivalent.

Preparation of $\text{CH}_3\text{Co}(\text{SALDPT})$.-- $\text{Co}(\text{SALDPT})$ (1.0g, .0025 mole) was dissolved in 75 ml of methanol and the solution flushed with N_2 . Methyl iodine (1.07 g, .0075 mole) dissolved in 10 ml of MeOH was added, followed by two drops of a 10 per cent PdCl_2 solution in methanol along with 0.1 g of NaBH_4 . Immediately there was a rapid evolution of H_2 . After stirring for a short while 4 ml of a 50 per cent NaOH solution was added dropwise. Soon afterwards, a red solid appeared. Stirring was continued for one hour. The material was filtered and dried in vacuo at 100°C for twelve hours.

Preparation of $\text{Et-Co}(\text{SALDPT})$.-- $\text{Co}(\text{SALDPT})$ (1.0 g, .0025 mole) was dissolved in 75 ml of MeOH and the solution flushed with N_2 . Two drops of a 10 per cent PdCl_2 solution in MeOH was added. Then ethyl iodide (1.17 g, .0075 mole) dissolved in 10 ml of MeOH was added, followed by 0.1 g of NaBH_4 . There was an immediate evolution of H_2 . The solution was stirred for a few minutes then 3 ml of a 50 per cent aqueous NaOH solution was added. After a short while a red solid formed. It was isolated and dried as described above.

The remaining alkyl derivatives (i.e. n-propyl, n-butyl, n-pentyl, n-hexyl, n-heptyl, n-octyl and n-decyl) were prepared, isolated and dried as described above using the appropriate alkyl iodide or bromide in each case.

Physical Measurements.--Infrared spectra were obtained in the region 5000-400 cm^{-1} using a Perkin-Elmer Model 621 spectrophotometer. Solid state spectra were recorded as KBr pellets and as Nujol or hexachlorobutadiene mulls. Solution spectra were taken in spectroquality solvents using matched solution cells. Ultraviolet-visible-near infrared spectra were obtained with a Cary 14 recording spectrophotometer. Spectra of solid samples were obtained by a diffuse transmittance technique⁹ employing Nujol mulls impregnated on Whatman No. 1 filter paper.

9. R. H. Lee, E. Griswold and J. K. Kleinberg, *Inorg. Chem.*, 3, 1278 (1964).
-

Solution spectra were obtained utilizing spectroquality organic solvents.

Magnetic susceptibility measurements on solid samples were obtained by the Faraday method. Diamagnetic corrections were made employing Pascal's constants.¹⁰

10. B. N. Figgis and J. Lewis, "Modern Coordination Chemistry", J. Lewis and R. J. Wilkins, Eds., Interscience Publishers, Inc., New York, N. Y., 1960.
-

Mass spectra were obtained on a Hitachi-Perkin-Elmer RMU-7 double focusing mass spectrometer using a solid inlet probe. The solid probe temperature was maintained at a value to prevent decomposition of the samples. The source temperature was maintained at approximately the temperature of the solid probe. Analyzer tube and ion source pressures of less than 10^{-6} torr

were employed. Where necessary mass to charge ratios were calibrated with perfluorokerosene.

Nuclear magnetic resonance spectra were determined in deuterated chloroform and dimethylsulfoxide employing a Varian A60 NMR spectrometer with TMS as an internal standard.

Elemental analyses were performed in this laboratory using a Perkin-Elmer Model 240 carbon, hydrogen, nitrogen analyzer.

Results and Discussion

Highly crystalline, dark red sigma-bonded organocobalt derivatives have been prepared starting with the cobalt(II) complex of the pentadentate ligand derived from salicylaldehyde and bis(3,3'-aminopropyl)amine Co(SALDPT). The reactions have been carried out in methanol by chemically generating the highly nucleophilic cobalt(I) species in the presence of the appropriate alkyl halide. Reduction in methanol occurs only under highly alkaline conditions in the presence of PdCl_2 catalyst suggesting a relatively high Co(II)/Co(I) reduction potential¹¹ for

11. G. N. Schrauzer, J. W. Sibert and R. J. Windgassen, J. Amer. Chem. Soc., 90, 6681 (1968).

Co(SALDPT). Electrochemical studies involving Co(SALDPT) support this postulate. Accordingly, the Co(II)/Co(I) polarographic half-wave potential is observed at -2.8 v and the Co(I)/Co(o) potential of the same compound is at -3.1 v (in glyme, vs $\text{Ag}/0.10\text{M AgNO}_3$).¹² The similar reduction potentials in going

TABLE I
Analytical and Infrared Data on the Alkyl Derivatives

COMPOUND		ANALYSES			CH_3^a	CH_3^b
		C	H	N		
MeCoSALDIPN	Calc	61.30	6.38	10.22	1385	2965
	Found	61.34	6.13	10.06		3890
Et-CoSALDIPN	Calc	62.10	6.65	9.88	1380	2970
	Found	62.35	6.44	9.73		2870
Pr-CoSALDIPN	Calc	62.85	6.89	9.56	1380	2950
	Found	62.75	6.96	9.56		2860
Br-CoSALDIPN	Calc	63.56	7.13	9.27	1385	2955
	Found	63.37	7.18	9.22		2860
Pent-CoSALDIPN	Calc	64.22	7.35	8.99	1388	2955sh
	Found	63.95	7.28	8.88		2890
Hex-Co (SALDIPN)	Calc	64.84	7.55	8.73	1388	2960sh
	Found	64.59	7.49	8.68		2890sh
HEPT-Co (SALDIPN)	Calc	65.43	7.74	8.48		2960
	Found	65.19	7.60	8.36	1385	2890
OCT-Co (SALDIPN)	Calc	65.98	7.93	8.25		2960
	Found	65.75	7.79	8.11	1388	2890
DEC-Co (SALDIPN)	Calc	67.01	8.27	7.82		2960
	Found	66.92	8.06	7.72	1385	2890

^aAliphatic Carbon-hydrogen bending modes

^bAliphatic Carbon-hydrogen symmetric and asymmetric stretching modes

12. R. E. Dessy and R. W. Koch, Unpublished Results.

from Co(II) to Co(I) and Co(I) to Co(o) also suggest a high spin cobalt(II)² species in glyme.

The alkyl derivatives are relatively stable in sunlight, air and water undergoing little or no noticeable decomposition. They are thermally stable melting above 150°C and are quite soluble in chloroform and dimethylsulfoxide but insoluble in alcohols and water. Analytical data supporting their composition as RCo(SALDPT) are shown in Table I.

Calvin⁷ and later more definitively Sacconi⁶ have reported Co(SALDPT) to be a high-spin five-coordinated complexes since to date all vitamin B₁₂ model systems have been prepared starting with low-spin essentially square planar cobalt(II) complexes, we have taken great care to show that our Co(SALDPT) is the same as that reported earlier. In agreement with Sacconi, we find (1) that the yellow-brown crude Co(SALDPT) is hydrated, (2) the water may be removed by drying at 100°C for twelve hours under reduced pressure, (3) both crude and dried Co(SALDPT) are high spin with a magnetic moment equal to 4.15 B.M., and (4) the visible spectra are similar except for the absence of a band around 6000cm⁻¹ in our Co(SALDPT). In contrast to Sacconi we find that recrystallization from warm ethanol-water under nitrogen yields nicely formed green needles which differ in many respects from the crude material. Specifically, (1) visible spectra in solution and in the solid state are dissimilar, (2) the green product is essentially diamagnetic ($\mu_{\text{eff}} = 1.0$ B.M.), (3) X-ray powder

TABLE II

Data on Co(SALDPT)

<u>COMPOUND</u>	<u>COLOR</u>	<u>ANALYSES</u>			
		<u>C</u>	<u>H</u>	<u>N</u>	<u>X_m</u>
<u>Co(SALDPT)</u> (H ₂ O) $\overline{\overline{7}}$	yellow-brown	Calcd.	6.09	10.14	---
		Found	6.23	9.67	
Co(SALDPT)	yellow-brown	Calcd.	5.86	10.60	7017.3
		Found	6.11	9.95	
Co(SALDPT) ReX (EtOH, H ₂ O)	green	Calcd.	5.86	10.60	335.9
		Found	5.62	9.30	

patterns of both show them to be different structures and (4) 'CH & N analyses do not agree. Also, exposure of a saturated methanol solution of the green material to air precipitates a black material which is suspected to be the oxygen adduct. The crude yellow-brown material when treated in the same manner does not yield a black precipitate. Secondly, the infrared spectrum of our crude Co(SALDPT) differs significantly in the N-H stretching region. A single band at 3180 cm^{-1} is assigned to this vibrational mode. Sacconi⁷, in comparison, reports a band at 3250 cm^{-1} . The location of the N-H stretching mode at this frequency is inconsistent with the secondary nitrogen being coordinated. This finding is substantiated by the fact that the N-H stretching mode in the free ligand, SALDPT, which we have prepared, occurs at 3255 cm^{-1} .

On the other hand, the infrared spectra, mass spectra and reactivity with alkyl halides of "recrystallized" and crude material are identical. The exact structure of this new green material is presently under investigation. The results obtained to date possibly suggest magnetic isomers for these complexes. The analytical and magnetic data obtained in our laboratory on these materials is shown in Table II.

Infrared spectra of the ligand, precursor complex, and alkyl derivatives were obtained as KBr pellets and Nujol mulls. Of particular interest is the position of the N-H stretch and the C=N stretching vibrational mode. All of the alkyl derivatives behave as the methyl derivative, so it will be discussed with

TABLE III
INFRARED DATA (cm^{-1})

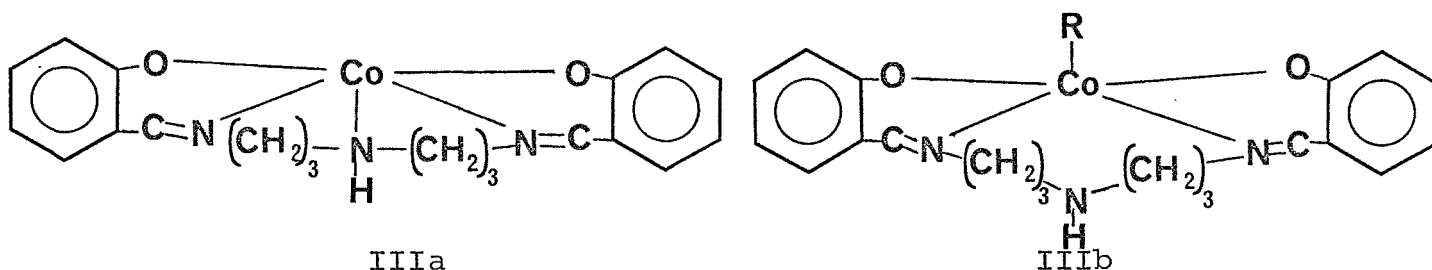
<u>Compound</u>	<u>Frequency</u>	<u>Assignment</u>
SALDIPN	3255	N-Hst
Co (SALDIPN)	3180	N-Hst
MeCo (SALDIPN)	3255	N-Hst
SALDIPN	1640	C=Nst
Co (SALDIPN)	1620	C=Nst
MeCo (SALDIPN)	1620	C-Nst

the understanding that the discussion could well apply to all derivatives. The pertinent data is presented in Table III. The drop of 20cm^{-1} in the position of the C=N stretch between the ligand and two complexes may be attributed to the fact that the imine nitrogen is coordinated which reduces the bond order of the C=N and lowers the stretching frequency.

One will notice that this shift of 20cm^{-1} is not as great as the shift of 35cm^{-1} observed with Ni(X-SALDIEN) and Ni(X-SALDAES) complexes. It has been shown previously that coordination of a donor atom in an axial position weakens the in-plane ligand field strength. In other words, the in-plane donor atoms are not coordinated as strongly as before. This strengthens our contention that the secondary N-H in the Co(SALDPT) is coordinated.

Of particular interest is the fluctuating position of the N-H stretching mode. When Co(SALDPT) is converted to RCoSALDPT, one observes that the N-H stretch returns to the position in the free ligand. This suggests that RCoSALDPT may be a five-coordinate species or a six-coordinate structure in which the secondary nitrogen is very weakly bound to the cobalt. In other words, both Co(SALDPT) and RCo(SALDPT) may possibly be five-coordinate; however, the difference is in the groups coordinated to the cobalt, structure IIIa and IIIb. It has been shown that alkyl ligands act as strong donors often giving rise to five-coordinate complexes by greatly weakening the donor-metal bond trans to it.¹³

-
13. H. A. O. Hill, J. M. Pratt and R. J. P. Williams, Disc. Faraday Soc., 47, 165 (1969).
-



The infrared spectra of all derivatives show peaks around 2965 and 2890 cm^{-1} which can be assigned to the aliphatic C-H stretching modes for a methyl group, TABLE I. Also a band around 1385 cm^{-1} can be assigned to a methyl bending mode. These bands are totally unique to the alkyl derivatives (i.e. they are not present in the spectrum of the parent complex) and coupled with the presence of a relatively strong secondary nitrogen-hydrogen stretching mode supports the formulation as $\text{RCo}(\text{SALDPT})$.

Mass spectra were determined on the alkyl derivatives employing conditions described earlier. For derivatives with $\text{R}=\text{CH}_3$, C_2H_5 , $\text{n-C}_3\text{H}_7$, $\text{n-C}_4\text{H}_9$ and $\text{n-C}_5\text{H}_{11}$, m/e peaks were observed for (1) the parent ion, (2) the parent ion less R and (3) the free ligand TABLE IV. In the cases for $\text{R}=\text{C}_6$, C_7 , C_8 , and C_{10} , no molecular ion was detected but m/e corresponding to the complex $\text{Co}(\text{SALDPT})$ was observed. However, in every case there were patterns associated with fragmentation of the appropriate alkane.

TABLE IV

Mass Spectral Data on the Alkyl Derivatives^a

<u>COMPOUND</u>	<u>MOLECULAR FORMULA</u>	<u>PROBE TEMP. °C</u>	<u>ISOTOPIC CLUSTER</u>
Me-CoSALDIPN	C ₂₁ H ₂₆ N ₃ O ₂ Co	-	411,412
Et-CoSALDIPN	C ₂₂ H ₂₈ N ₃ O ₂ Co	110	425,426
Pr-CoSALDIPN	C ₂₃ H ₃₂ N ₃ O ₂ Co	145	439,440
Bu-CoSALDIPN	C ₂₄ H ₃₂ N ₃ O ₂ Co	135	453,454
Pent-CoSALDIPN	C ₂₅ H ₃₄ N ₃ O ₂ Co	125	467,463

^aIsotope patterns for C¹³ were observed for the complexes but are not included here.

TABLE V
NMR Data on the Alkyl Complexes

<u>Compound</u>	<u>Range or Position (δ)</u>	<u>Assignment</u>
CH ₃ -Co (SALDIPN)	7.54-6.40	vinyl and aromatic protons
	4.24	proton on secondary nitrogen
	3.36-2.04	the CH ₃ bonded to the metal and the methylene protons on the backbone chain.
C ₂ H ₅ -Co (SALDIPN)	7.64-6.2	vinyl and aromatic protons
	4.24	proton on the secondary nitrogen
	3.32-2.00	α -methylene protons on the ethyl group plus the methylene protons on the backbone chain
	.4 (triplet)	methyl group on the ethyl group bound to the metal
C ₃ H ₇ -Co (SALDIPN)	7.12-6.20	vinyl and aromatic protons
	4.20	proton on secondary nitrogen
	3.34-2.00	α and β methylene protons on the propyl group plus the methylene protons on the backbone chain
	1.0 (doubled)	methyl protons on the propyl group attached to the cobalt

TABLE VI
Electronic Spectra (cm^{-1}) of the Alkyl Complexes

COMPOUND	MEDIUM ^{b,c}	ν			
		ν_1	ν_2	ν_3	ν_4
CH ₃ -Co (SALDPT)	Nujol	18,020sh	22,990sh	25,640sh	
	Chloroform (NL)	15,630sh		26,140	35,710
	Chloroform (L)	18,690sh			
C ₂ H ₅ -Co (SALDPT)	Chloroform (L)	15,680sh		26,670	
	Nujol	18,350sh	22,990sh	25,970sh	
	Chloroform (NL)	15,630sh		25,970	35,710
n-C ₃ H ₇ -Co (SALDPT)		18,520			
	Chloroform (L)	15,810		25,970	39,600
	Nujol	18,520sh	23,530sh	26,320sh	
n-C ₄ H ₉ -Co (SALDPT)	Chloroform (NL)	15,560		25,970	35,710
		18,080			
	Chloroform (L)	15,750		25,970	39,600
n-C ₅ H ₁₁ -Co (SALDPT)	Nujol	18,520sh	23,810sh	25,970sh	
	Chloroform (NL)	15,680		25,030	35,710
	Chloroform (L)	18,350			
n-C ₆ H ₁₃ -Co (SALDPT)		15,630		25,970	39,600
	Nujol	18,180sh	22,470sh	24,690	
	Nujol	18,180sh	22,470sh	25,320	
n-C ₇ H ₁₅ -Co (SALDPT)	Nujol	18,180sh	21,740sh	22,730sh	25,320
	Nujol	18,520sh	21,980sh	23,320	
	Nujol	18,180sh	22,470sh	25,320	
n-C ₈ H ₁₇ -Co (SALDPT)	Nujol	18,180sh	21,740sh	22,730sh	25,320
	Nujol	18,520sh	21,980sh	23,320	
	Nujol	18,180sh	22,470sh	25,320	
n-C ₁₀ H ₂₁ -Co (SALDPT)	Nujol	18,180sh	21,740sh	22,730sh	25,320
	Nujol	18,520sh	21,980sh	23,320	
	Nujol	18,180sh	22,470sh	25,320	

^b Solution exposed to no light;

^c Solution exposed to light

For instance, in the C_{10} derivative an $m/e = 142$ corresponding to $C_{10}H_{22}^+$ was observed along with the fragmentation expected from this alkane. Each spectrum was scanned above the parent m/e to check for dimer formation but no such peaks were observed which lends strong support to a composition of $RCo(SALDPT)$ in the gas phase.

Nuclear magnetic resonance spectra were obtained on the $R = CH_3$, C_2H_5 , and C_3H_7 derivatives in d_6 -dimethylsulfoxide. The set of data obtained from these spectra is presented in TABLE V. The assignment of the alkyl methylene protons lying closest to the metal was not possible because they fell in the range found for the methylene protons on the backbone chain. Investigation of the free ligand offered no assistance in elucidating the position of the protons under consideration. However, the appearance at relatively high field of a triplet in the case of the ethyl derivative and a poorly resolved doublet in the spectrum of the propyl derivative confirms the alkyl group is attached to the cobalt atom. The remaining assignments shown in Table V are consistent with the proposed ligand structure.

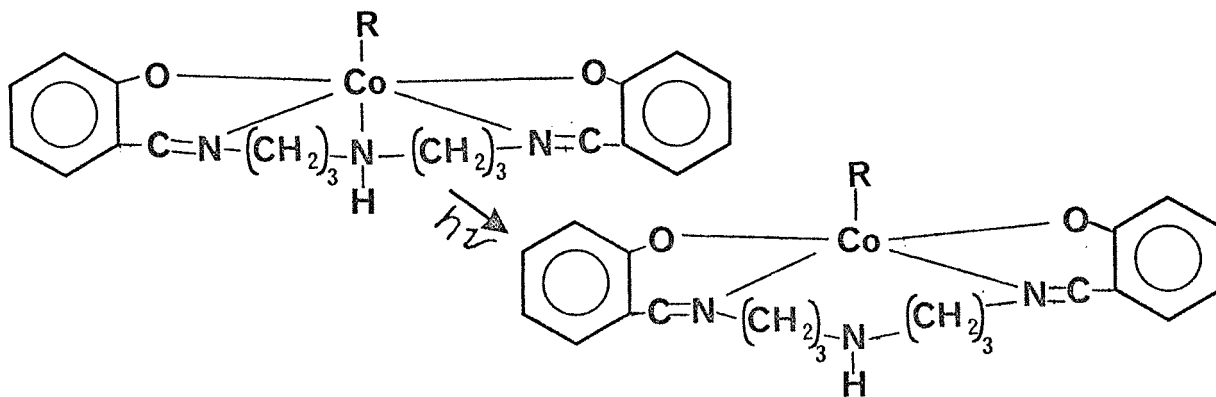
Visible spectra in the solid state of the alkyl derivatives are consistent with a pseudo-octahedral environment around a low spin $Co(III)$ ion, TABLE VI. Two Laporte forbidden $d-d$ transitions are predicted from the energy level diagram shown in Figure 1 for a regular octahedral $Co(III)$ complex. However, in our case, non-equivalent donor atoms give rise to a structure of lower symmetry, thereby causing a splitting of the ${}^1T_{1g}$ level. The ${}^1T_{2g}$ is not

split enough to be observed as predicted by theoretical results.

We observe three transitions in the visible region assignable to transitions from the $^1A_{1g}$ to the three excited states. This suggests a pseudo-octahedral environment for the metal ion. The apparent contradiction with the infrared data may be explained by assuming that the secondary nitrogen does not form a ground state bond with the metal atom but does offer some degree of perturbation.

When the alkyl derivatives are placed in $CHCl_3$ with a minimum exposure to any light, the visible spectrum exhibits the three previously discussed band maxima and a new band ca $15,500cm^{-1}$. Bands in this region have been assigned to transitions resulting from five coordinate geometry. It is postulated that in $CHCl_3$ solution, two species are present, one being five-coordinate and the other being six-coordinate.

If these same solutions are exposed to normal daylight an increase in intensity of the band at $15,500cm^{-1}$ is observed along with a decrease in intensity of the $18,500cm^{-1}$ band, which indicates that the species is possibly going more toward the five-coordinate species in $CHCl_3$ when exposed to light. A similar phenomenon is observed in dimethylsulfoxide. A probable reaction scheme is shown below.



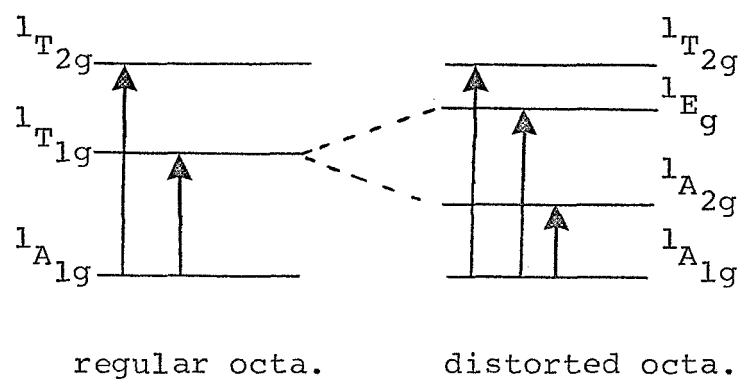


Figure 1

It may be argued that five-coordination could arise from dealkylation of the molecule in the presence of light. Gas chromatography was employed to test this possibility. A sample of Me-CoSALDPT was dissolved in CHCl_3 , stoppered and placed in the light for two days. Samples of the vapor above the solution were taken and analyzed. No peaks assignable to the presence of an alkane were observed in the gas chromatograms. Samples of the laboratory gas line were taken as standards and compared with the vapor above the solution.

The alkyl derivatives result only from the reaction of primary alkyl halides and not secondary or tertiary ones. Numerous reactions were attempted using secondary, tertiary, unsaturated, acyl and di-halides but without success. It can be shown from molecular models that a secondary alkyl halide results in a group which is too bulky to occupy the sixth position. Secondary and tertiary halides place methyl groups in positions which are very close to the region of the benzene aromatic cloud of electrons. The benzene rings are forced to bend out of the CoN_2O_2 plane and from the secondary nitrogen in order for it to coordinate. Hence this prevents the formation of a sigma alkyl carbon-cobalt bond with large and bulky organic groups.

There is a distinct dependence on the halide anion insofar as the rate is concerned. Chloro derivatives seem to give no reaction at all. Bromo derivatives react very slowly. However, iodo derivatives react very rapidly; in fact, the product forms almost immediately as soon as the pH is adjusted.

N71-71015

FINAL REPORT
to the
NATIONAL AERONAUTICS AND SPACE ADMINISTRATION
in connection with
NASA Grant NGR 47-004-006

Part 15 of 21 Parts

Final Report
VPI&SU Project 313113

Electrocatalysis of the Oxidation of Organic
Fuel Materials Using an Oxidation-Reduction
Couple as Catalyst

by

J. G. Mason
Chemistry

Virginia Polytechnic Institute & State University
Blacksburg, Virginia

December, 1970

ELECTROCATALYSIS OF THE OXIDATION OF ORGANIC
FUEL MATERIALS USING AN OXIDATION-REDUCTION
COUPLE AS CATALYST

One of the major problems in fuel cell technology is the slow electrochemical rate of oxidation of organic fuel materials at normal temperatures. It is highly desirable to explore quantitatively the methods by which such slow reactions may be catalyzed. One method which has been proposed but not quantitatively tested is the use of a reversible oxidation-reduction couple as a catalyst. Catalysis would occur via the sequence of reactions at the electrode:

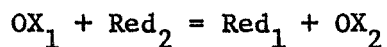


In this sequence M_o and M_r represent the oxidized and reduced forms of a reversible redox system and S_r and S_o the reduced and oxidized forms of the organic substrate. It is seen that if M_o reacts rapidly with S_r , regeneration of the M_r takes place and the oxidation of the fuel occurs at the rate at which M_r is oxidized. Since by the definition of reversibility, this reaction is rapid, catalysis is the net result.

The purpose of this research was therefore to explore the feasibility of catalysis of the oxidation of organic fuel materials by redox couples. In order to do this, the research was separated into two parts, one dealing with the effect of noble metal surfaces on inorganic oxidation reduction reactions; the other, kinetic studies of the oxidation of organic substrates by a simple electrochemically reversible couple. The first study was felt necessary since heterogeneous catalysis of numerous inorganic redox reactions by noble metal surfaces had been reported and a mechanism proposed but not quantitatively verified. The second was needed because of limited available data on the rates of oxidation of organic materials by inorganic systems. The first study related to both reactions (1) and (2); the second to reaction (2).

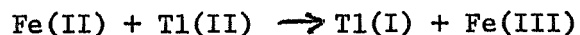
I. Heterogeneous Catalysis of Inorganic Redox Reactions by Noble Metal Surfaces.

Spiro and Ravno [J. Chem. Soc., 78, (1965)] tabulated all available data on the effect of platinum surfaces on the kinetics of redox reactions. They postulated that the catalytic effect was due to the surface functioning as an electrode in most cases. For the reaction



if the electrochemical rate of the conversion of OX_1 to Red_1 was faster than the chemical rate of OX_1 with Red_2 at the potential established at the electrode surface catalysis would result which would be potential dependent and limited by the slower of the two electrochemical reactions. If both systems were electrochemically reversible, the catalytic rate would depend upon the mass transport of material to the surface, however, if one couple were irreversible electrochemically, the rate would be potential dependent and be determined by the irreversible couple. In either event the rate of reaction would be predictable from current - voltage curves for the two systems involved obtained independently. No quantitative data were presented to support this conclusion. Of all the reactions listed, only the oxidation of iron(II) by thallium(II) had only semiquantitative results reported for the catalytic action of platinum. This system was chosen for detailed initial study.

The uncatalyzed reaction had been thoroughly studied by Ashurst and Higginson (J. Chem. Soc., 3044, 1953) and the following mechanism proposed:



Consistent with this mechanism was retardation of the reaction by Fe(III) produced during the reaction as well as Fe(III) added initially. Gilks and Waird [Discuss. Faraday Soc., 29, 102, (1960)] reported that the addition of a large square of platinum eliminated

the retardation by Fe(III) observed during one run by catalyzing the Fe(II) - Tl(II) reaction but only one run was published. The approach adopted by us was first detailed verification of the uncatalyzed rate data of Ashurst and Higginson followed by verification of the reported effect of Gilks and Waird.

Table I shows some of the results obtained for the uncatalyzed reaction. These results quantitatively verify the results previously reported. The methods for obtaining the rate data were those employed by the previous workers. Attempts to reproduce the catalysis using a platinum foil electrode are shown in Table II where Experiments A-L record different methods of cleaning the foil between runs. The specific rate constant k , refers to the initial second order rate constant obtained before any departure from second order kinetics was observed. In our hands a reproducible platinum surface using platinum foil was not obtained.

At this point, a different approach was attempted. A pyrex cylinder was prepared and coated with Englehard Bright Platinum solution, (or Bright Gold) air dried, then vacuum dried at 600°C. The cylinder was wired as an electrode by connecting a platinum wire to the surface coating and inserted in a large reaction vessel designed for rapid mixing. Mixing was achieved by constant speed magnetic stirring. After several preliminary conditioning runs, rate data became highly reproducible. Electrodes prepared in this way could be used for other reactions, then used again for checks on the thallium(III)-iron(II) reaction with excellent reproducibility.

Figure I shows representative rate curves obtained at such surfaces as a function of surface area. It is obvious that at long times curvature occurs in an upward direction when the data are plotted as a simple second order kinetic function.

The data were analyzed by determining the instantaneous catalyzed rate

Summary of Kinetic Data for the
Uncatalyzed Reduction of Thallium(III) by Iron(II)

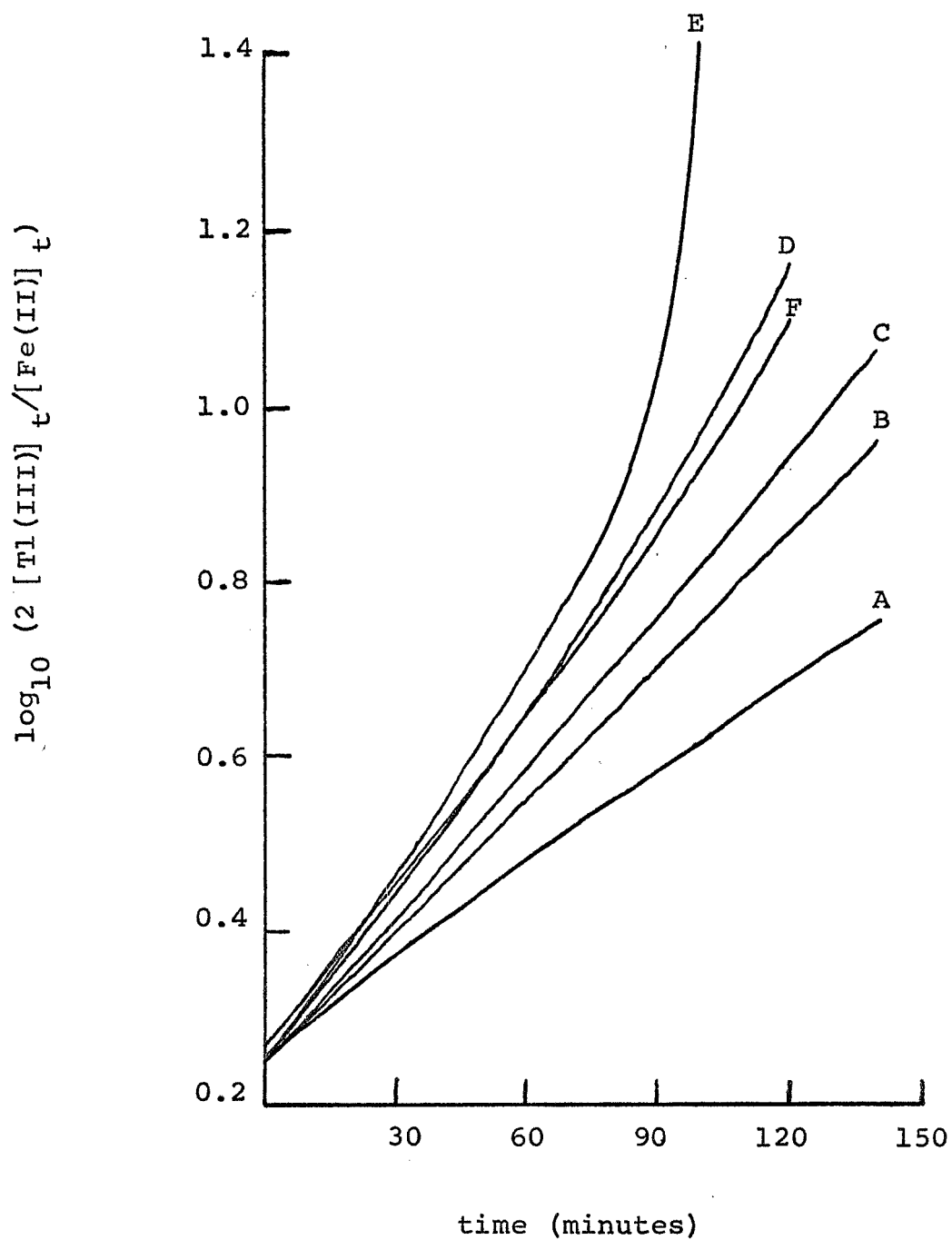
<u>Exp't.</u>	<u>[Fe(II)]</u>	<u>[Fe(III)]</u>	<u>[Tl(III)]</u>	<u>[H⁺] x M</u>	<u>k₁</u>	<u>k₃/k₂</u>
A	5.96	0.07	5.83	0.795	1.75	19.4
B	5.93	0.00	6.14	0.665	1.85	23.6
C	5.81	0.22	6.13	0.665	1.82	20.2
D	6.14	0.13	5.70	0.680	1.89	24.0
E	5.65	0.63	5.97	0.680	1.69	19.4
F	6.34	0.14	5.67	0.680	1.67	19.4
G	5.98	0.31	5.47	0.680	1.67	19.4
H	5.98	5.60	5.47	0.680	1.65	19.4
I	5.98	10.89	5.47	0.680	1.68	19.4
J	5.98	16.17	5.47	0.680	1.67	19.4
K	5.60	0.10	6.20	0.680	1.67	19.4
L	11.07	0.34	3.10	0.680	1.67	19.4

$$Tl(I)_{init} = 3.0 \pm 0.3 \times 10^{-4} M$$

$$k_3/k_2 = 19.4, k_1 = 1.80 M^{-1} \text{ min}^{-1}$$

The Velocity Constant, K_1 ,
Obtained with a Platinum Foil Electrode

<u>Exp't.</u>	<u>[Fe(II)]</u>	<u>[Fe(III)]</u>	<u>[Tl(III)]</u>	<u>[Tl(I)]</u>	<u>[H⁺]xM</u>	<u>k₁</u>
A	5.26	0.41	6.13	0.32	0.665	2.46
B	5.67	0.51	6.13	0.32	0.665	1.96
C	5.55	0.62	6.13	0.32	0.665	1.88
D	6.14	0.12	5.70	0.29	0.572	2.17
E	6.11	0.15	5.70	0.29	0.680	2.65
F	6.01	0.26	5.70	0.29	0.680	1.99
G	5.98	0.28	5.70	0.29	0.680	1.96
H	5.97	0.29	5.70	0.29	0.680	1.95
I	5.71	0.55	5.84	0.30	0.680	2.58
J	5.71	0.55	5.84	0.30	0.680	2.16
K	5.67	0.59	5.84	0.30	0.680	2.08
L	5.67	0.59	5.84	0.30	0.680	2.08

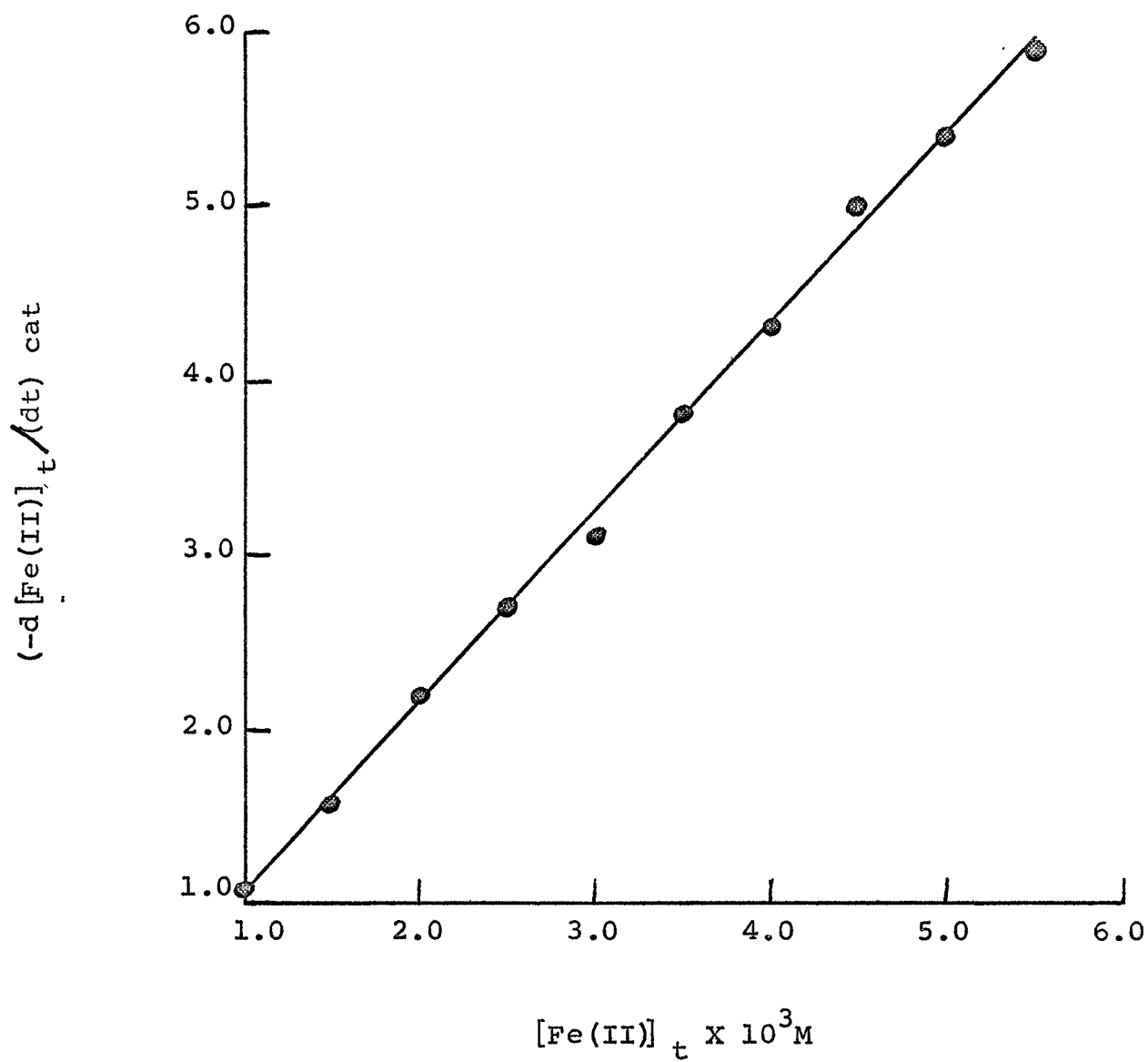


Second Order Plot for Several
Catalyzed Reactions on Platinum

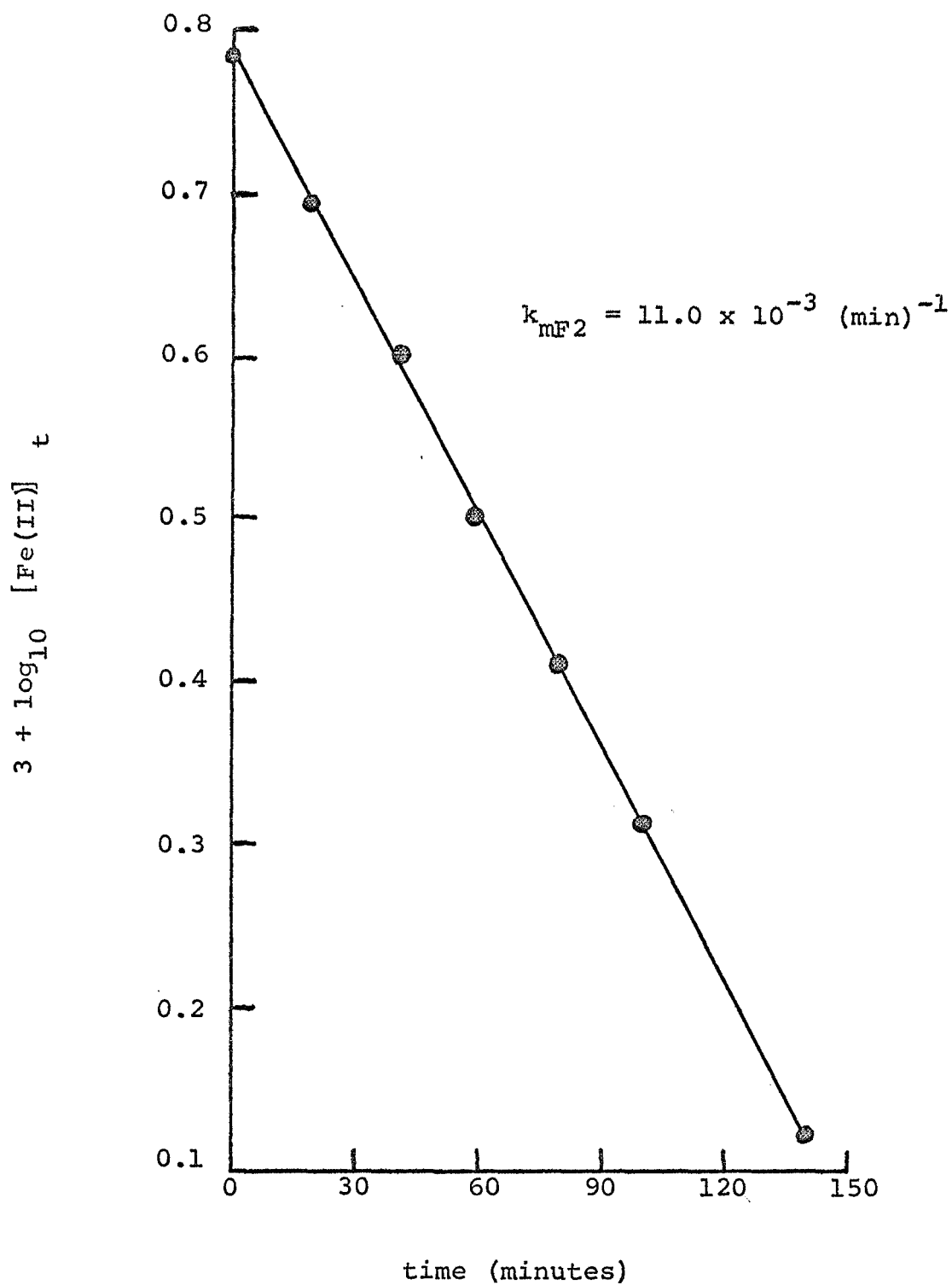
by subtraction of the instantaneous uncatalyzed rate from the instantaneous observed rate. The rate law for the catalyzed reaction was then sought. Figure II shows a plot of the instantaneous catalyzed rate of disappearance of Fe(II) versus the [Fe(II)]. The linearity of this result establishes the reaction to be first order in Fe(II) and independent of Tl(III) under these reaction conditions (which were Tl(III) in greater than stoichiometric amounts). Similar experiments with excess Fe(II) established a first order dependence on Tl(III). The rate determining step in this forced convective system appeared to be mass transport to the catalyst surface, the rate being determined by the species with the slower mass transport rate.

To test this, current voltage curves were obtained for the species individually and electrolyses were performed in the limiting current region. The rate of electrolysis was monitored chemically and the mass transport rate constant evaluated as shown in Fig. III. For a given surface area, it was established that the rate constant for catalysis was within 5% of the mass transport rate constant for the rate determining ion. The current - voltage curves showed total irreversibility of both couples and that at the potentials established at the electrode surface during the catalyzed runs only 10% of the observed rate would be predicted from current - voltage curves. Additional experiments using an electrolysis cell with Fe(II) in one compartment and Tl(III) in another with a large salt bridge connecting the two and electrodes identical to those used in kinetic runs established a very slow electrochemical reaction. The conclusions are that the reaction is catalyzed at the electrode surface, the catalysis is chemical not electrochemical, and although the electrochemical system is irreversible, the catalyzed rate is mass transport controlled. In all cases the observed rate constant was proportional to the surface area as shown in Fig. IV.

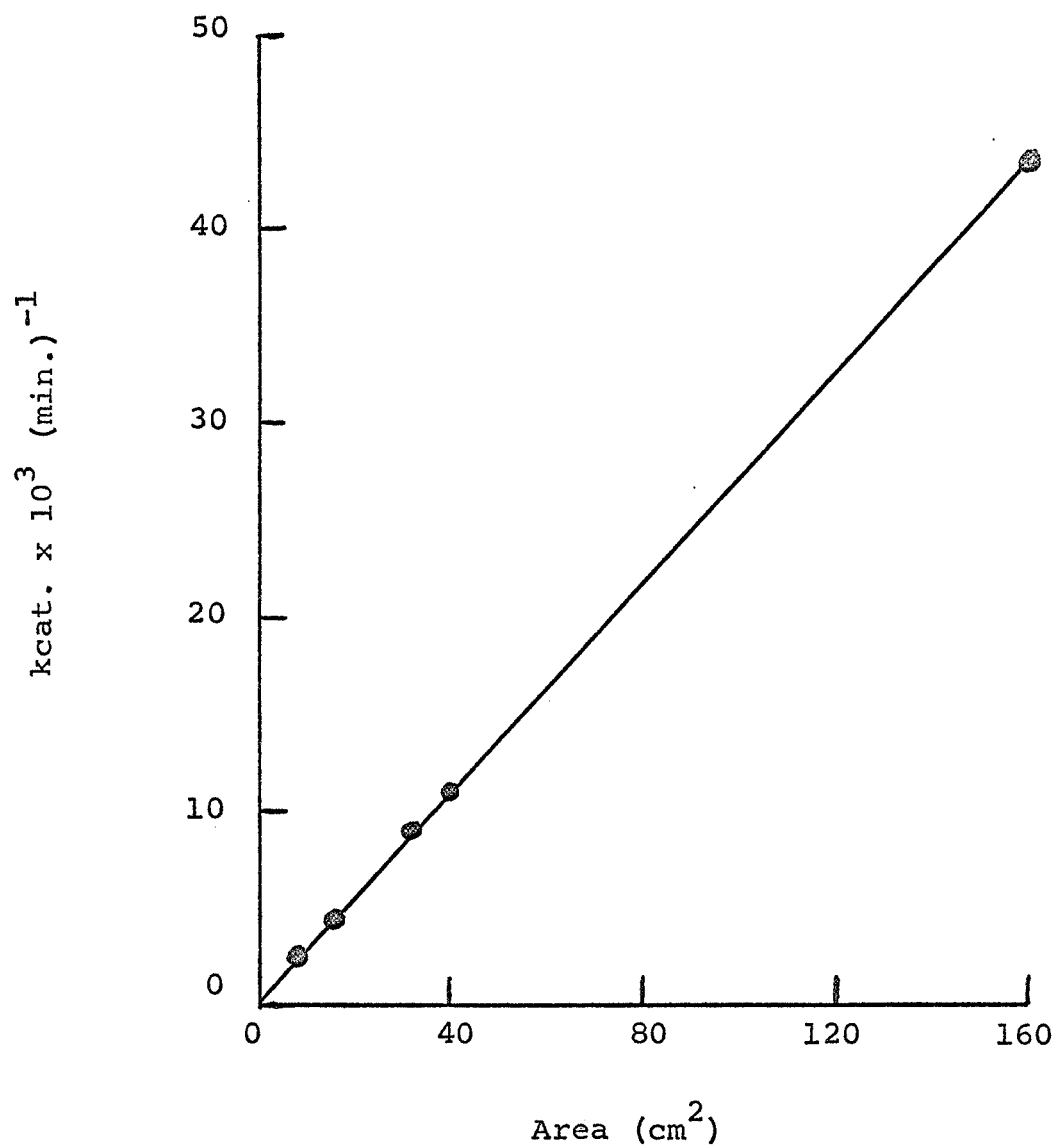
Similar investigations were conducted on the Fe(II)-b-benzoquinone, cerium(IV) - mercury(I), cerium(IV) - thallium(I), and cerium(IV) - water reactions. With the



Instantaneous Catalyzed
Rate versus $[Fe(II)]_t$



Evaluation of k_{mF2} at 1.150 volts



The Rate Constant, k_{cat} ., versus
Geometric Surface Area

exception of the cerium(IV) - water reaction, all reactions showed totally irreversible electrochemical behavior with mass transport controlled catalysis. In cases when both the catalytic rate constant and the mass transport rate constant could be evaluated these rate constants were identical as shown in Table III.

II. The Kinetics of the Oxidation of Alcohols Using Electrogenerated Halogens

This part of the research was an attempt to obtain quantitative information concerning the oxidation of alcohols in acid solution using electrogenerated chlorine and bromine. Isopropanol and cyclohexanol were chosen for investigation because previous work had been the subject of some debate.

The experimental technique for the determination of the rate constants was the coulometric generation of Cl_2 or Br_2 at a platinum electrode in a solution containing the alcohol, acid, and the appropriate sodium halide. Rate data were obtained by stopping the generation of the halogen and monitoring the decay of halogen amperometrically. In this way pseudo-first order rate constants were obtained which were converted to second order rate constants by plotting the pseudo first order rate constants vs. the alcohol concentration. As this work is part of a thesis (M.S.) still in preparation, fewer details will be given as the final results are not firm.

A. Cl_2 Oxidation of 2-Propanol.

The rate law found is

$$\frac{-d(\text{Cl}_2)}{dt} = k_2 [\text{Cl}_2][\text{alcohol}]$$

The rate is unaffected by Cl^- or acid. The products as analyzed by gas chromatography indicate acetone, but no chloro ketone. The rate is sufficiently rapid to prevent buildup of undesirable amounts of Cl_2 .

B. Chlorine Oxidation of Cyclohexanol

The rate law is

$$\frac{-d[\text{Cl}_2]}{dt} = k [\text{Cl}_2][\text{alcohol}]$$

Table III. Summary of the Catalytic
and Mass Transport Rate Constants

General Reaction: $A + 2B \longrightarrow \text{Products}$

Rxn.	A	B	$k_{\text{cat}_A} \times 10^4$	$k_{\text{mA}} \times 10^4$	$k_{\text{cat}_B} \times 10^4$	$k_{\text{mB}} \times 10^4$
A	Tl(III)	Fe(II)	1.6	1.6	2.7	2.7
B	Q	Fe(II)	5.5	5.5	---	4.0
C	Hg(I)	Ce(IV)	3.7	---	3.2	3.2
D	Tl(I)	Ce(IV)	5.0	---	3.2	3.2
E	H ₂ O	Ce(IV)	---	---	k_e	3.2
F	Sn(II)	Fe(III)	---	---	---	---

with complications occurring at high alcohol concentration where the rate becomes faster than described. This is attributed to a buildup of ketone in the reaction mixture and shown to be a function of the time of generation used prior to making kinetic measurements. Additions of cyclohexanone produce the same effect on the consumption of Cl_2 . Product analysis of reaction mixtures by gas chromatography reveal several products but no chlorinated ketone. Extensive oxidation appears to have occurred.

C. Bromine Oxidation of 2-Propanol.

Bromine oxidation has been found to be a complex function of the bromide ion concentration and the acidity. The rate law is

$$\frac{-d[\text{Br}_2]}{dt} = \frac{k_2 [\text{Br}_2][\text{alcohol}]}{1 + K[\text{Br}^-]}$$

where both K and k_2 are functions of acidity. The reaction is retarded by acid. The K in the denominator does not correspond to the expected K for the equilibrium $\text{Br}_2 + \text{Br}^- \rightleftharpoons \text{Br}_3^-$ as measured in these solutions by distribution measurements. The formation constant for Br_3^- has been found to be independent of acidity. Detailed experiments are currently in progress.

FINAL REPORT

4 N71-71016

to the

NATIONAL AERONAUTICS AND SPACE ADMINISTRATION

in connection with

NASA Grant NGR 47-004-006

Part 16 of 21 Parts

Final Report

VPI&SU Project 313128

Thermal and Electrical Transport in a Tungsten Crystal
for Strong Magnetic Fields and Low Temperatures

Geometrical Interpretation of the
Magnetoelectricity of a Fermi Ellipsoid

Predicting the Galvanomagnetic Coefficients
of Tungsten from Fermi Surface Data

by

J. R. Long
Physics

Virginia Polytechnic Institute & State University
Blacksburg, Virginia

December, 1970

THERMAL AND ELECTRICAL TRANSPORT
IN A TUNGSTEN CRYSTAL FOR STRONG
MAGNETIC FIELDS AND LOW TEMPERATURES

Jerome R. Long

Scheduled for publication in Physical Review B on 15 ~~January~~^{FEBRUARY} 1971.

THERMAL AND ELECTRICAL TRANSPORT IN A TUNGSTEN CRYSTAL
FOR STRONG MAGNETIC FIELDS AND LOW TEMPERATURES*

Jerome R. Long

Department of Physics,

Virginia Polytechnic Institute and State University,

Blacksburg, Virginia 24061

Direct-current electrical and thermal transport coefficients were experimentally determined in a very pure tungsten crystal at six temperatures in the range 1.4 K to 4.1 K and at magnetic fields up to 22 kOe. The field was applied along a [100] axis and each of the coefficients measured along an equivalent $\langle 100 \rangle$ direction. Kinetic coefficients computed from the data were interpreted in terms of a Sondheimer-Wilson type, multi-band, relaxation time model. The results were generally consistent with the extensive literature on the fermiology of tungsten. Galvanomagnetic data was approximately independent of temperature, a result implying elastic scattering and a common relaxation time for all transport effects, but the field dependence and magnitude of the thermal and Righi-Leduc resistivities were both distinctly less than that predicted by the Wiedemann-Franz law when a reasonable value of the lattice conductivity was assumed. A density of states computed from the Nernst-Ettinghausen coefficient was consistent with values reported from specific heat measurements, but displayed an anomalous temperature dependence similar to that of the Righi-Leduc coefficient.

I. Introduction

The temperature and magnetic field dependence of six galvanomagnetic and thermomagnetic transport coefficients of a tungsten monocrystal are reported here. The dc measurements were performed at liquid helium-4 temperatures in magnetic fields up to 22 kOe directed along a [100] axis transverse to the plane of the effects in the body centered cubic crystal.

Provided the magnetic field is applied along an axis of three, four, or six-fold rotational symmetry, and the electrical and thermal fluxes are constrained to the plane normal to that axis, only six kinetic transport coefficients are required to determine all of the thermogalvanomagnetic phenomena in a metallic crystal. The transverse-even effects vanish, and the six kinetic coefficients are calculable in terms of only six measurable non-kinetic coefficients. This is a consequence of the Onsager relations.^{1,2}

A study of transport phenomena is motivated by two distinct, but coupled, goals. First, one would like to use the transport effects as a tool for investigating the structure and dynamics of the electron-lattice defect system in a class of materials. Secondly one wishes to understand mechanisms present in the transport process and to determine the relative importance of those mechanisms which are active in a given material under a specific set of conditions. The measurements reported here were primarily directed toward the second of these goals. The successes of fermi-surface studies³ over the past decade have made it possible to seek a much more detailed interpretation of transport processes on the fermi surface than was possible earlier. Improvements in experimental facilities and sample quality are also very significant.

Much of extant transport data was obtained when our knowledge of fermi-surfaces was poor. In addition, the large impurity content of most samples resulted in a masking of the intrinsic scattering mechanisms at low temperatures, a situation which may actually favor the first of the above stated goals, but which severely limits the second. Tungsten is representative of the above situation.

Tungsten, a transition metal of the sixth group and period, has been available in monocrystalline form with relatively high purity for a longer time than most other metals. The behavior of electrical and thermal transport coefficients of tungsten in a magnetic field was investigated as early as 1936 by Justi and Scheffers⁴ and by Gruneisen and Adenstedt.⁵ An extended series of measurements of the thermal and electrical magnetoresistivities by de Haas and de Nobel⁶ and de Nobel^{7,8} are particularly relevant to the thermal measurements reported here. Except for the relatively high temperature work of van Witzenburg and Laubitz,⁹ work on the very high purity tungsten now available has not considered the problem of thermal transport. The electrical resistivity has been studied by Berthel¹⁰ and by Volkenshteyn et al.,¹¹ while the galvanomagnetic effects were measured by Fawcett,¹² by Fawcett and Reed¹³ and by Volkenshteyn et al.¹⁴ The low temperature magnetothermoelectric, Nernst and Righi-Leduc effects reported here do not appear to have been studied previously.

References to the extensive experimental literature on the closed, compensated fermi-surface of tungsten may be found in the de Haas- van Alphen work of Girvan, Gold and Phillips¹⁵ while theoretical APW band structure calculations were done by Loucks¹⁶ and by Mattheiss¹⁷

following the model of Lomer¹⁸.

In section II, following these introductory paragraphs, the phenomenological definitions and elementary microscopic theory of the magneto-transport coefficients are reviewed. Section III deals with pertinent experimental aspects of the work. The results and an elementary interpretation of each type of measurement are then presented. A more detailed interpretation of certain parts of this work will be found in a following paper. All of the measurements reported pertain to transport effects with a monotonic dependence on the magnetic field. Oscillatory phenomena due to size effect¹⁹ or Landau quantization²⁰ were not measured.

II. Theory

The Onsager formulation^{1,2} of the thermodynamics of irreversible processes has resulted in a rigorous phenomenological framework for defining the magnetotransport coefficients. The kinetic coefficients of the thermogalvanomagnetic effects are tensors defined by the kinetic equations²¹

$$\begin{aligned} \underline{J} &= \underline{\sigma} \underline{E} + \underline{\epsilon}'' \underline{\nabla} T \\ \underline{U} &= -\underline{\pi}'' \underline{E} - \underline{\lambda}'' \underline{\nabla} T \end{aligned} \quad (1)$$

which express the fluxes \underline{J} , the electric current density and \underline{U} , the heat current density as linear combinations of the affinities \underline{E} ,

the effective e.m.f. (which includes the thermodynamic force associated with the chemical potential of the electronic carriers and plays the role of the measurable electric field) and ∇T , the temperature gradient. The kinetic coefficients so defined are $\underline{\hat{\sigma}}$, the electrical conductivity; $\underline{\hat{\lambda}}$ the thermal conductivity; $\underline{\hat{\epsilon}}$, the thermoelectric tensor and $\underline{\hat{\pi}}$ the Peltier tensor. Only one of the tensors $\underline{\hat{\epsilon}}$ and $\underline{\hat{\pi}}$ is independent, since by the Onsager-Kelvin relation, $\underline{\hat{\pi}} = T \underline{\hat{\epsilon}}$. For effects measured in the [100] plane normal to the magnetic field, the independent tensors $\underline{\hat{\sigma}}$, $\underline{\hat{\lambda}}$ and $\underline{\hat{\epsilon}}$ each reduce to 2 x 2 form with two independent elements in each tensor. The total number of independent coefficients is thus six. The $\underline{\hat{\sigma}}$ tensor is, for instance

$$\underline{\hat{\sigma}} = \begin{pmatrix} \sigma_{xx} & \sigma_{xy} \\ \sigma_{yx} & \sigma_{yy} \end{pmatrix} = \begin{pmatrix} \sigma_{11} & \sigma_{12} \\ -\sigma_{12} & \sigma_{11} \end{pmatrix}$$

if the magnetic field is applied along a three-fold or higher $z \rightarrow 3$ direction and the affinities and fluxes are measured in orthogonal $x \rightarrow 1$ and $y \rightarrow 2$ directions.

The phenomenological kinetic coefficients are most important because kinetic coefficients relate directly to the results of microscopic theory where it is customary to calculate \underline{J} and \underline{U} . The conventional microscopic theory of transport phenomena assumes validity of a Boltzmann transport equation and the fundamental problem is then to solve the equation for the distribution function f_k for specific conditions of symmetry, thermodynamic affinities and other parameters. One then calculates

$$J_m = \frac{e}{4\pi^3} \int V_{m,k} f_{m,k} dk ; U_m = \frac{1}{4\pi^3} \int V_{m,k} (\epsilon_{m,k} - \epsilon) f_{m,k} dk \quad (2)$$

where $V_{m,k}$ is the velocity of an electronic carrier of charge e , energy $\epsilon_{m,k}$, chemical potential ϵ and wave vector k . A calculation of the currents by (2) leads to expressions in which the kinetic coefficients defined by (1) may be identified as the coefficients of E and ∇T .

A tractable comparison of all six experimentally determined kinetic coefficients with microscopic theory is possible at present only for rather simplified models. The most useful of these has been the Sondheimer-Wilson²² model which assumes conduction by independent quadratic bands of carriers of either sign, each achieving equilibrium by a relaxation process and each contributing additively to the total current. The Sondheimer-Wilson (S-W) results²³ as modified by Grenier^{24,25} are summarized in gaussian units as follows:

Magnetoconductivity

$$\sigma_{11} = ec \sum_i \frac{n_i a_i H_i}{H^2 + H_i^2} \quad (3 a)$$

Hall Conductivity

$$\sigma_{12} = ec \sum_i (\pm) \frac{n_i H}{H^2 + H_i^2} \quad (3 b)$$

Magnetothermopower

double print

$$\xi_{ii}''' = \frac{\pi^2 k_B^2 c T}{3} \sum_i (\pm) \frac{Z_i a_i H_i}{H^3 + H_i^2} \quad (3 c)$$

Nernst or Nernst-Ettinghausen Coefficient

$$\xi_{12}'' = - \frac{\pi^2 k_B^2 c T}{3} \sum_i \frac{Z_i H}{H^3 + H_i^2} \quad (3 d)$$

Thermal Magnetoconductivity

$$\lambda_{ii}''' = \lambda_g''' + \lambda_{e_{ii}}''' = \lambda_g''' + L_1 T \sigma_{ii} \quad (3 e)$$

Righi-Leduc Conductivity

$$\lambda_{12}''' = L_2 T \sigma_{12} \quad (3 f)$$

In these expressions H is the magnetic field applied normal to \underline{d} and \underline{U} and T is the Kelvin temperature. The symbols π , e , c and k_B are constants having their conventional meaning. The other symbols represent properties of the crystal. The i th band contains N_i carriers, which if hole (electron) like takes the $+$ ($-$) sign as indicated in Eqs. (3b) and (3c). The mobility μ_i of the carriers is represented by the relaxation field $H_i = c/\mu_i = m_i^* c / e \tau_i$ where τ_i is the relaxation time and m_i^* is the cyclotron effective mass. For a band of cyclotron frequency ω_{ci} , H_i is the applied field for which $\omega_{ci} \tau_i = 1$. The magnitudes of the thermoelectric coefficients are determined by Z_i , the density of states of the i th band. The quantity a_i is a mass anisotropy factor which takes the value unity for

a spherical fermi surface.^{24,25} The thermal conductivities are given in terms of the electrical conductivities, where L_j is the Lorenz number. Strict validity of these S-W expressions is limited to elastic scattering in which case $L_j = L_0 = \pi^2 k_B^2 / 3e^2 = 2.445 \times 10^{-8} \text{ V}^2 \text{ K}^{-2}$. The electronic component $\lambda_{e''}$ of the thermal conductivity is supplemented by λ_j'' , the lattice thermal conductivity²⁶ which will be considered separately from the S-W theory of the electronic effects.

The physical conditions which lead to Eqs. (1), (2) and (3) imply control of \underline{E} and $\underline{\nabla T}$ as independent variables, a condition not readily attained in the laboratory. The practical experimental arrangements are the following: (a) one immerses the sample in an isothermal bath and controls \underline{J} and $\underline{\nabla T}$ in which case a set of isothermal coefficients are defined by the equations

$$\begin{aligned} \underline{E} &= \underline{\rho} \underline{J} - \underline{E} \underline{\nabla T} \\ \underline{U} &= -\underline{\pi} \underline{J} - \underline{\lambda} \underline{\nabla T} \end{aligned} \quad (4 \text{ a})$$

or (b) one connects one end of the sample to a thermal reservoir, while thermally isolating the bulk of the sample in a high vacuum. These transverse adiabatic conditions imply control of \underline{J} and \underline{U} in which case a set of "adiabatic" coefficients are defined by the equations.

$$\begin{aligned} \underline{E} &= \underline{\rho}' \underline{J} + \underline{E}' \underline{U} \\ \underline{\nabla T} &= -\underline{\pi}' \underline{J} - \underline{\gamma}' \underline{U} \end{aligned} \quad (4 \text{ b})$$

In this work, both sets of experimental conditions were utilized in order to measure two elements each of $\underline{\rho}$, the isothermal resistivity tensor, $\underline{\gamma}$, the "adiabatic" thermal resistivity tensor and $\underline{\epsilon}'$, the "adiabatic" thermoelectric tensor.

Microscopic theory calculates kinetic coefficients, but an experiment does not measure them. A popular practice found in the literature of transport phenomena is to "invert" the expressions obtained from a microscopic theory into the form of the experimental coefficients. In the present work, the experimental coefficients have, instead, been inverted into kinetic form. Presentation of the measurements in kinetic form offers several advantages. Any simplifying approximations made in the inversions are determined by the experimentally observed magnitudes of the coefficients and do not involve additional assumptions in the microscopic theory. Experimental results presented in kinetic form should be more directly comparable to any new theoretical results. Finally, the physical interpretation of kinetic coefficients is usually more direct.

In general, the kinetic coefficients are obtained from the isothermal and "adiabatic" coefficients by means of Heurlinger²⁷ relations of the form $\underline{\sigma} = \underline{\rho}^{-1}$; $\underline{\lambda}'' = \underline{\gamma}^{-1} (1 + \underline{\epsilon}'^2 \underline{\rho}^{-1} \underline{\gamma}^{-1} T)$ and $\underline{\epsilon}'' = \underline{\rho}^{-1} \underline{\epsilon}' \underline{\gamma}^{-1}$. For electronically compensated metals, it is usually possible to demonstrate, as in the present case, that some of these relations may be greatly simplified without significant error. One finds it particularly helpful that, when

$$H \gg H_d, \text{ then } \underline{\lambda}'' \approx \underline{\gamma}^{-1} = \underline{\lambda} \text{ and } \underline{\epsilon}_{12}'' \approx \underline{\epsilon}_{12}' / \underline{\rho}_{11} \underline{\gamma}_{11}.$$

III. Experimental

The tungsten monocrystal was spark planed into a rectangular parallelepiped with sides nominally 19 mm long x 4 mm wide x 2 mm thick oriented normal to the <100> directions. It was purchased from Aremco Products, Inc. The residual resistivity ratio was found to be $\rho_{300K} / \rho_{1.3K} \approx 3 \times 10^4$.

All of the electrical and thermal measurements were performed using the four terminal dc methods of Grenier et al.^{24,25,28}. The magnetic field was generated by a Ventron-Harvey-Wells L128A-FFC4 system and the dc potentials were detected with a Keithley 147 in conjunction with a Honeywell 2768 potentiometer. The sensors used in the bridge measurement of temperature differentials were Allen-Bradley 1/10 W, 33 Ω carbon resistors calibrated by He⁴ vapor pressure thermometry. The 67 Ω heater wound on a copper bobbin attached to the lower end of the crystal was made of W. B. Driver Cupron as were the leads connected to the crystal, thermometers and heater.²⁹

In the thermomagnetic measurements, heat current densities from .44 mW/cm² at the lowest temperature to 4.6 mW/cm² at the highest temperature were used in order to adjust the maximum longitudinal temperature differential to about 0.1 K. A complete set of measurements was performed at the temperatures 4.1 K, 3.8 K, 3.4 K, 2.6 K, 1.9 K and 1.38 K. An electric current density of 7.1 A/cm² was used.

The most persistent source of error in the absolute determination of transport coefficients is the measurement of the effective spacing of the electrical and thermal probes to the sample. Some difficulty

was encountered in obtaining contacts to tungsten suitable for both electrical and thermal currents under cryogenic high vacuum conditions. The contacts used were made by Bi-Cd soldering to a lug consisting of a 0.5 mm wide by 5 mm long strip of .003" gold foil which was attached to the crystal with a dot of Dupont #4922 silver preparation. The main virtue of this type of contact is that it may be completely removed by aqua regia, and leaves the crystal in pristine condition for any other measurement. The properties of these contacts were generally satisfactory except that they did not provide a very ideal point contact. The probe separations of 8.34 mm for the longitudinal set and 3.86 mm for the transverse set were thus systematically uncertain by about $\pm 3\%$. Analysis of the effect of all combined systematic errors on the calculated kinetic coefficients led to a confidence of about $\pm 4\%$ in the absolute values of the coefficients σ_{11} , λ''_{11} and ϵ''_{12} . The coefficients σ_{12} and λ''_{12} are only reliable to $\pm 8\%$, while the absolute precision of ϵ''_{11} may be as poor as $\pm 15\%$. Errors in field and temperature dependences, relative values, and ratios are much less, the precision in this case being about $\pm 1\%$.

The magnetic field was oriented with respect to the crystal in situ for the experiment by finding the [100] minimum¹² in the electrical magnetoresistance. In that position the transverse-even voltage was null.

IV. Results and Discussion

A. Galvanomagnetic (Magnetoelectric) Tensors $\vec{\rho}$ and $\vec{\sigma}$

Zero Field Measurements

The temperature dependence (or lack of) of $\rho_{||}(0, T)$, the electrical resistivity in zero applied magnetic field, is the standard indicator of the nature of the dominant scattering mechanism in a metal and for tungsten has been the subject of several recent studies.^{10,11,30} For the crystal and conditions of this work, $\rho_{||}(0, T)$ was nearly residual, increasing by only 5% at 4.1 K over a minimum value of $(1.8 \pm 0.2) \times 10^{-10} \Omega\text{-cm}$ at 1.3 K which will be taken as the residual value. It is thus inferred that large angle elastic scattering by point impurities and defects was dominant over intrinsic processes in the limitation of charge transport. Size effect was certainly also a factor.¹⁹ A study of the intrinsic scattering and a check of Matthiessen's³¹ rule from the temperature dependence of $\rho_{||}(0, T)$ was beyond the capabilities of the measuring system.^{10,11,30} It is generally concluded that the dominant low temperature intrinsic scattering mechanism in tungsten is the electron-electron U-process,^{32,33} but this conclusion has been based on data taken at somewhat higher temperatures than those used here.

High Field Measurements

In this work the term high field is taken to mean $H \gg H_i$ for all bands. Such is the usual condition in standard magnetoresistance studies of the fermi-surface topology of metals^{34,12} and is distinct from other uses of the term "high field" as applied to quantum

oscillatory³⁵ and magnetic breakthrough³⁶ effects. The results of the high field measurements of ρ_{11} and ρ_{21} are shown in Fig. 1 for the data up to $H=22$ kOe at 1.3 K and 4.1 K.

The magnetoresistivity $\rho_{11}(H,T)$ was found to be precisely quadratic in H at all temperatures. The deviation from pure H^2 behavior for H in the $\langle 100 \rangle$ direction as reported by Fawcett¹² was not observed.

Volkenshteyn et al.¹⁴ have pointed out that "the influence of temperature on the galvanomagnetic properties of metals has received very little study in the region of high fields." The temperature dependence of the ρ_{11} data reported here was small and could only be approximately determined. The criterion applied in obtaining an expression was to fit the data to the nearest integral power of T . From previous studies of $\rho_{11}(0,T)$, a T^2 relation was expected but a T^3 relation gave a better fit to the scattered values of the small quantity $\rho_{11}(H,0) - \rho_{11}(H,T)$. The data is approximated by either of the expressions

$$\rho_{11}(H,T) \approx \rho_{11}(0,T) + 2.86 \times 10^{-14} H^2 [1 - 7.9 \times 10^{-4} T^3] \quad (5a)$$

$$\rho_{11}(H,T) \approx \rho_{11}(0,T) + 2.87 \times 10^{-14} H^2 [1 - 3.4 \times 10^{-3} T^2] \quad (5b)$$

Although it is not well justified,³⁷ it is interesting to examine Eqs. (5) on the basis of a relaxation time model. For a compensated metal in a strong field, $\sigma_{11} \gg \sigma_{12}$, when the geometry is such that there is no transverse-even voltage. From Eq. (3a) one thus obtains

$$\lim_{H \gg H_1} \rho_{11}(H,T) \approx \lim_{H \gg H_1} \frac{1}{\sigma_{11}} = \frac{H^2}{c^2 \sum_i n_i a_i m_i^* / \tau_i}$$

where $\rho_{11}(0,T)$ is negligible. If Matthiessen's rule is assumed valid, then it is possible to simply add the reciprocals of the relaxation times τ_{0i} of the large angle elastic processes (presumably due to point defect

scattering plus some size effect) contributing to the residual resistivity, and $\underline{\gamma}_{ti}$ of the intrinsic processes leading to a temperature dependent resistivity. Dominance of the residual resistivity implies that $\underline{\gamma}_{oi}/\underline{\gamma}_{ti} \ll 1$. If one makes the further assumption that all of the N bands in the sum over bands are identical except for charge compensation, then

$$\lim_{H \gg H_i} \rho_{ii}(H, T) \approx \left(\frac{H}{c}\right)^2 \frac{\gamma_o}{N n a m^*} \left(1 - \frac{\gamma_o}{\underline{\gamma}_{ti}}\right)$$

Comparison of this approximation with Eqs. (5) implies either $\underline{\gamma}_o/\underline{\gamma}_{ti} \approx 7.9 \times 10^{-4} T^{3/2}$ or $\underline{\gamma}_o/\underline{\gamma}_{ti} \approx 3.4 \times 10^{-3} T^2$ or some intermediate relation. Application of the same arguments to $\rho_{ii}(0, T)$ implies that

$$\rho_{ii}(0, T) = \lim_{H \ll H_i} \rho_{ii}(H, T) \approx \frac{m^*}{e^2 N n a \underline{\gamma}_o} \left(1 + \frac{\gamma_o}{\underline{\gamma}_{ti}}\right)$$

which with the previous result would indicate that

$$\underline{\rho}_{ii}(0, T) \approx \underline{\rho}_{ii}(0, 0) + 1.4 \times 10^{-13} T^{3/2} \underline{\Omega}\text{-cm}$$

or

$$\underline{\rho}_{ii}(0, T) \approx \underline{\rho}_{ii}(0, 0) + 6.1 \times 10^{-13} T^2 \underline{\Omega}\text{-cm}$$

where $\underline{\rho}_{ii}(0, 0) = 1.8 \times 10^{-10} \underline{\Omega}\text{-cm}.$

The foregoing analysis is clearly too simple, and should be regarded, primarily, as a vehicle for presenting the experimental observations. It is curious, however, that little support can be found in this work for the dominance of electron-electron scattering as concluded from the T^2 law found by others.^{10,11,30} The coefficient of $T^{3/2}$ found here is, roughly, a factor of 45 smaller than the coefficient indicated by the work of

Volkenshteyn et al.¹¹ and the approximate fit, Eq. (5b) of the data to a T^2 relation is inferior to the fit Eq. (5a) to a T^3 relation. A T^3 law is indicative of phonon-electron s-d scattering also commonly found in many transition metals.^{30,38}

The Hall resistivity ρ_{21} (Fig. 1) exhibited a somewhat complicated field dependence and, within the precision of the measurements was independent of temperature with a magnitude approximately 1% that of ρ_{11} . The observed behavior of ρ_{21} is readily understood by again applying the conditions $\sigma_{11} \gg \sigma_{12}$ and $H \gg H_i$ to the inversion of Eqs (3a) and (3b). Then,

$$\lim_{H \gg H_i} \rho_{21} = \lim_{H \gg H_i} \frac{\sigma_{12}}{\sigma_{11}^2} = \frac{H^3 \sum_i (\pm) n_i - H \sum_i (\pm) n_i H_i^2}{ec \left(\sum_i n_i a_i H_i \right)^2}$$

On the basis of this model, any observable temperature dependence of ρ_{21} must come from the temperature dependence of the relaxation time contained within the quantities of each band. Therefore, if the metal is perfectly compensated ($\sum_i (\pm) n_i = 0$ but $\sum_i (\pm) n_i H_i^2 \neq 0$ except when all H_i are equal), it is only necessary that the relaxation time of each band have the same functional temperature dependence in order that ρ_{21} be independent of temperature. In the present case, compensation was complete to the extent that the term linear in H was roughly 9 times as great as the cubic term at a field of 10 kOe. The very weak temperature dependence of ρ_{21} is thus quite reasonable. The positive sign and somewhat greater than linear field dependence of ρ_{21} implies that $\sum_i (\pm) n_i$ was positive but that $\sum_i (\pm) n_i H_i^3$ was negative. Holes were thus in the majority and also the more mobile carriers.

Results of the inversion of the measured quantities ρ_{11} and ρ_{21} into the kinetic quantities σ_{11} and σ_{12} are summarized (Table 1) in terms of Eqs. (3a) and (3b). Inverse square dependence of σ_{11} on magnetic field is expressed in terms of the quantity $\sum_i n_i a_i H_i$ derived from $H^2 \sigma_{11}$ and Eq (3a). The temperature dependence of $\sum_i n_i a_i H_i$ was covered in the discussion of ρ_{11} . The results for σ_{12} are expressed by putting Eq. (3b) in the form

$$\lim_{H \gg H_i} \sigma_{12} = ec \left\{ \frac{1}{H} \sum_i (\pm) n_i - \frac{1}{H^3} \sum_i (\pm) n_i H_i^2 \right\}$$

and tabulating the quantities $\sum_i (\pm) n_i$ and $\sum_i (\pm) n_i H_i^2$. Comparison of the quantity $\sum_i (\pm) n_i = 4.4 \times 10^{17} \text{ cm}^{-3}$ with the number $^{15} \sum_i (+) n_i = \sum_i (-) n_i = 7.4 \times 10^{21} \text{ cm}^{-3}$ obtained from de Haas-van Alphen measurements, indicates an excess of only 0.006% of hole-like over electron-like carriers. This result supports the view that minute impurities are the sole cause of any deviation from perfect compensation of a metal which satisfies the Fawcett³⁹ criteria for compensation.

B. Magnetothermal Tensors $\underline{\gamma}$ and $\underline{\lambda}$

The thermal magnetoresistivity $\underline{\gamma}_{11}$ and the Righi-Leduc resistivity $\underline{\gamma}_{21}$ are shown as functions of temperature and magnetic field in Fig. 2. In the event that thermal and electrical transport in the crystal were entirely limited by large angle elastic (point defect) scattering, which is the common assumption at helium temperatures, and in the absence of an appreciable conduction by the lattice, one would expect

that the curves of Fig. 2 could be made to resemble quite closely those of Fig. 1 by simply multiplying all of the quantities of Fig. 2 by $L_0 T$. That is, $\hat{\rho}$ and $\hat{\gamma}$ might be connected by a straight forward application of the Wiedemann-Franz-Lorenz (WFL) relation. Such is not the case.

The most obvious dissimilarity between the $\hat{\rho}$ and $\hat{\gamma}$ data is the tendency of the Righi Leduc resistivity to pass through a maximum, the maximum apparently moving to fields above the range of these measurements at the lowest temperatures. In addition, the product $T\hat{\gamma}_{21}$ increases by approximately 65% as T is reduced from 4.1 K to 1.4 K, while $\hat{\rho}_{21}$ is essentially independent of temperature. This temperature dependence of $\hat{\gamma}_{21}$ does not appear explainable in terms of any conventional model. It has been discussed in a brief communication⁴⁰ and will be discussed further in a following paper in terms of the kinetic coefficient λ''_{12} .

The peaking of $\hat{\gamma}_{21}$ is characteristic of a crystal in which the application of a magnetic field has reduced the conduction of heat by electronic carriers to a point comparable to that of the conduction of heat by the lattice. Larger fields must be applied to achieve this peaking at lower temperatures because the lattice conductivity is smaller at lower temperatures. A further discussion of the peaking of $\hat{\gamma}_{21}$ can be found in a study of antimony^{28,41} where the effect was considerably more pronounced.

The direct effect of an apparently appreciable lattice conductivity (which is, itself, essentially independent of the magnetic field) at the fields of these measurements was the reduction of the pure quadratic field dependence of $\hat{\rho}_{11}$ to an effective $H^{1.6}$ depen-

dence of γ_{ii} , Fig. 2. At fields of 60-80 kOe and above the γ_{ii} of this crystal should have saturated to values characteristic of the lattice conductivity and independent of H. An example of the complete saturation of γ_{ii} due to lattice conduction was reported at much lower fields in the antimony papers^{28,42} and the tendency to saturation as observed here in tungsten at liquid helium temperatures was studied extensively for tungsten in the scattering regime of liquid hydrogen temperatures by deNobel.⁶⁻⁸

The term saturation as applied here to the effect of lattice conduction on γ_{ii} should not be mistaken for the ordinary saturation of both ρ_{ii} and γ_{ii} in uncompensated metals or saturation due to magnetic breakthrough in normally compensated metals.^{34,36}

Lattice conduction will be discussed further in a following paper.

It can be seen, Fig. 2, that γ_{ii} depends on temperature approximately as $T^{-1.5}$ over the range of temperatures studied, rather than with the T^{-1} dependence predicted by the WFL relation. The product $T\gamma_{ii}$ is considerably more dependent upon temperature than ρ_{ii} . While ρ_{ii} increases by about 7% as T varies from 4.1 K to 1.3 K at 22 kOe, the product $T\gamma_{ii}$ increases by 70% over roughly the same interval. Although lattice conduction accounts for some of this variation, it is not nearly sufficient to account for all of it.

The assumption of a single relaxation time common to both electrical and thermal processes is implicit in Eqs. 3. The excess temperature dependence of $T\gamma_{ii}$ is not consistent with the assumption of a single relaxation time. The common inference, that a single relaxation time is dominant when the residual part of the zero field

resistivity $\rho_{ii}(0, T)$ is dominant appears to be valid only for electrical processes. Small angle scattering which has a rather minor effect upon ρ_{ii} can be very effective upon γ_{ii} via the vertical process.⁴²

The failure of γ data to conform to a straightforward Sommerfeld version of the WFL relation does not rule out the possibility of fitting the data to more general relations of the form of Eqs. (3e) and (3f), as will be seen in a following paper. If this is to be done, the data must be converted into λ'' form. The conversion involves the lengthy tensor manipulation $\lambda'' = \gamma^{-1} (\hat{1} + \epsilon^{-1} \gamma^{-1} T)$.

In general, these manipulations may seriously compound errors in the measured quantities. For compensated metals at high fields and low temperature, however, it turns out that, to a precision of 1% or better,

$$\lambda''_{ii} \approx (1 - \epsilon_{21}^{\prime 2} T / \rho_{ii} \gamma_{ii}) / \gamma_{ii} \quad \text{and} \quad \lambda''_{i2} \approx \gamma_{21} (1 - 2 \epsilon_{21}^{\prime 2} T / \rho_{ii} \gamma_{ii}) / \gamma_{ii}^2$$

with the correction term $\epsilon_{21}^{\prime 2} T / \rho_{ii} \gamma_{ii}$ usually being small. For the present tungsten data at 20 kOe, the correction ranges from 0.3% at 1.4 K to 1.7% at 4.1 K. The kinetic thermal conductivities λ''_{ii} and λ''_{i2} can thus be computed from the experimental data with nearly the same precision as the electrical conductivities σ_{ii} and σ_{i2} .

C. Magnetothermoelectric tensors $\underline{\underline{\epsilon}}$, $\underline{\underline{\epsilon}}'$ and $\underline{\underline{\epsilon}}''$

The "adiabatic" thermoelectric tensor $\underline{\underline{\epsilon}}'$, as defined by Eqs. (4b), was measured. Raw $\underline{\underline{\epsilon}}'$ data is of little interest because it contains the effect of the thermopower of the electric field probes²⁹, and is not simply related to any microscopic theory. The isothermal thermoelectric tensor $\underline{\underline{\epsilon}}$, as defined by Eqs. (4a), is related to $\underline{\underline{\epsilon}}'$ by

the relation $\vec{\epsilon} = \vec{\epsilon}' \vec{Y}^{-1}$. The $\vec{\epsilon}$ tensor is conceptually more familiar, its component $\epsilon_{11}(0, T) \equiv S$ being the absolute thermo-electric power as involved in the measurement of temperature with a thermocouple. The correction for the Seebeck effect of the leads is simply related to $\vec{\epsilon}$ through the relation $\vec{\epsilon} = S_{\text{leads}} \hat{1} + \vec{\epsilon}' \vec{Y}^{-1}$. Components of the tensor $\vec{\epsilon}$ corrected for the effect of the leads are shown as functions of field at two temperatures in Fig. (3). The thermocouple effect of the leads does not appear in ϵ_{12} , but was sufficiently large in ϵ_{11} at the lower fields to render the low field ϵ_{11} data useless. Both quantities were negative with ϵ_{11} essentially independent of field and one order of magnitude smaller than ϵ_{12} . Substitution of Eqs. (3) into the Heurlinger relation $\epsilon_{11} = (\epsilon_{11}'' \sigma_{11} + \epsilon_{12}'' \sigma_{12}) / (\sigma_{11}^2 + \sigma_{12}^2)$ shows that the high field value of ϵ_{11} should be independent of field if $\sum_i (\pm) n_i$ is negligible compared to $\sum_i (\pm) n_i H_i^2 / H^2$. This was found to be approximately true in the analysis of σ_{12} , and the thermal effect is characterized by larger H_i values.

A comparison of the data with Eqs. (3) requires that it be put in the form of the kinetic tensor $\vec{\epsilon}''$, as defined by Eq. (1). The tensor is related to the corrected $\vec{\epsilon}$ tensor by the operation $\vec{\epsilon}'' = \vec{\epsilon} \vec{P}^{-1}$. The inequalities $\rho_{11} \gg \rho_{21}$, $\gamma_{11} \gg \gamma_{21}$ and $\epsilon_{12} \gg \epsilon_{11}$ found in the compensated metal at high field and low temperature allow some simplification. Thus, to first order $\epsilon_{12}'' = \epsilon_{12} / \rho_{11} = - \epsilon_{21} / \rho_{11} \gamma_{11}$ and $\epsilon_{11}'' = (\epsilon_{11} \rho_{11} - \epsilon_{12} \rho_{21}) / \rho_{11}^2$.

The kinetic Nernst Coefficient ϵ_{12}'' can, therefore, be computed from the experimental data with reasonable precision, since it involves only a single product of three large measured coefficients and does not involve a correction for the thermocouple effect of the leads. The computation of ϵ_{11}'' however, is very crude. Not only does the computation involve the difference of comparable small quantities, but the term in ϵ_{11}'' involving S_{leads} is

roughly 50% of the total effect.²⁹ Nevertheless, the field and temperature dependence of ϵ''_{11} computed at six temperatures was found to be self consistent.

From Eqs. (3c) and (3d) it is, perhaps, expected that, when $H \gg H_c$, the quantities ϵ''_{11}/T and ϵ''_{12}/T should be independent of temperature. They are not. Their actual behavior is indicated in Fig. (4). Each coefficient has the expected field dependence, ϵ''_{11} decreasing as $1/H^2$ and ϵ''_{12} decreasing as $1/H$. Therefore, the excess temperature dependence implies that the density of states factors $\sum_i (\pm) Z_i a_i H_i$ and $\sum_i Z_i$ are temperature dependent. A fit of the high field results to Eqs. (3c) and (3d) requires that $\sum_i (\pm) Z_i a_i H_i$ and $\sum_i Z_i$ vary from $-3.26 \times 10^{37} \text{ erg}^{-1} \text{ cm}^{-3} \text{ Oe}$ and $+1.95 \times 10^{34} \text{ erg}^{-1} \text{ cm}^{-3}$ respectively at 1.4 K to $-3.61 \times 10^{37} \text{ erg}^{-1} \text{ cm}^{-3} \text{ Oe}$ and $+2.31 \times 10^{34} \text{ erg}^{-1} \text{ cm}^{-3}$ respectively at 4.1 K.

The temperature dependence of $\sum_i (\pm) Z_i a_i H_i$ is accountable in terms of the relaxation field H_i which is expected in the thermoelectric effect to display an excess temperature dependence if the ϵ''_{11} data is to be consistent with the temperature dependence found in the thermal magnetoresistivity γ_{11} , presumably due to vertical scattering processes.

The relaxation field does not appear in the high field limit of ϵ''_{12} . Like the high field Hall conductivity σ_{12} , the high field Nernst coefficient should be independent of the scattering and measure a property of the band structure. The Nernst coefficient is, in principle, an alternative measure of the free electron density of states as classically determined from the temperature coefficient of the electronic specific heat C_e . The observed temperature dependence of $\sum_i Z_i = 3C_e / \pi^2 k_B^2 T$ is thus not directly explicable in terms of the Eqs. (3). This will be discussed further in a following paper. The results for $\sum_i Z_i$ when expressed in terms of a specific heat γ ($C_e = \gamma T$) imply a systematic decrease of γ from

$13.8 \times 10^{-4} \text{ J-Mole}^{-1}\text{-K}^{-2}$ at 4.1 K to $11.7 \times 10^{-4} \text{ J-Mole}^{-1}\text{-K}^{-2}$ at 1.4 K, (Fig. 5). These values are well within the range of values of γ reported from specific heat measurements on tungsten.⁴³

V. Conclusion

The high field magnetotransport effects at liquid helium temperatures in this rather pure tungsten crystal are, in most respects, amenable to analysis in terms of the asymptotic ($H \gg H_i$) form of a multiband Sondheimer-Wilson theory, Eqs. (3). The theory must be empirically modified to allow for a temperature dependent relaxation time which is not unique, but different for electrical and thermal processes. Exceptions to this conclusion are the Righi-Leduc coefficients γ_{21} and λ''_{12} and the Nernst coefficient ϵ''_{12} which display temperature dependences which are not explicable in terms of the SW equations without still further modifications. This and the appreciable lattice conduction found in the thermal resistivity data will be considered in a following paper. The relationship between these results and fermi surface data must also be considered.

It has recently been noted by Ehrlich⁴⁴ that thermal umklapp scattering may be mistaken for electron-electron scattering. This may bear on Eq. (5), the discussion following that equation and other parts of this work.

Acknowledgement

The author is indebted to the administration and staff of the Laboratory for Research on the Structure of Matter of the University of Pennsylvania and to Dr. Robert K. MacCrone for their support of and interest in the early phases of this work.

References

* The experiments and preliminary analysis in this work were conducted in the Laboratory for Research on the Structure of Matter of the University of Pennsylvania with support by the Advanced Research Projects Agency of the United States Department of Defense under contract SD-69. The work was completed at Virginia Polytechnic Institute with support by the National Aeronautics and Space Administration.

- 1) L. Onsager, Phys. Rev. 37, 405 (1931); Phys. Rev. 38, 2265 (1931).
- 2) H. B. Callen, Phys. Rev. 73, 1349 (1948); Phys. Rev. 85, 16 (1952).
- 3) D. Shoenberg, Low Temperature Physics LT9 (Plenum Press, Inc., New York, 1965), Pt. B., p. 680.
- 4) E. Justi and H. Scheffers, Phys. Z. 37, 700 (1936); 38, 891 (1937).
- 5) E. Gruneisen and H. Adenstedt, Ann. Physik 29, 597 (1937).
- 6) W. J. deHaas and J. de Nobel, Physica 5, 449 (1938).
- 7) J. de Nobel, Physica 15, 532 (1949).
- 8) J. de Nobel, Physica 23, 261 (1957); 23, 349 (1957).
- 9) W. van Witzenburg and M. J. Laubitz, Canad. J. Phys. 46, 1887 (1968).
- 10) K. H. Berthel, Phys. Stat. Sol. 5, 159 (1964); 5, 399 (1964).
- 11) N. V. Volkenshteyn, L. S. Starostina, V. Ye. Startsev and Ye. P. Romanov, Fiz. Met. Metalloved. 18, 888 (1964) [English transl.: Phys. Met. Metallog. 18, No. 4, 85 (1964)]
- 12) E. Fawcett, Phys. Rev. 128, 154 (1962).
- 13) E. Fawcett and W. A. Reed, Phys. Rev. 134, A723 (1964).

- 14) N. V. Volkenshteyn, V. A. Novoselov and V. Ye. Startsev, Fiz. Met. Metalloved. 22, 175 (1966); 24, 677 (1967). [English transl.: Phys. Met. Metallog. 22, No. 2, 15 (1966); 24, No. 4, 92 (1967)].
- 15) R. F. Girvan, A. V. Gold and R. A. Phillips, J. Phys. Chem. Solids 29, 1485 (1968). The data reported in this largely corroborates and extends an earlier study reported by D. M. Sparlin and J. A. Marcus, Phys. Rev. 144, 484 (1966).
- 16) T. L. Loucks, Phys. Rev. 139, A1181 (1965); 506 (1966).
- 17) L. F. Mattheiss, Phys. Rev. 139, A1893 (1965).
- 18) W. M. Lomer, Proc. Phys. Soc. 80, 489 (1962).
- 19) D. E. Soule and J. C. Abele, Phys. Rev. Letters 23, 1287 (1969)
This paper reports measurements of the oscillatory magnetomorphic effect in tungsten.
- 20) H. J. Trodahl and F. J. Blatt, Phys. Rev. 180, 706 (1969).
- 21) J. M. Ziman, Electrons and Phonons, (Oxford Univ. Press, London, 1960), p 496.
- 22) E. H. Sondheimer and A. H. Wilson, Proc. Roy. Soc. A190, 435 (1947).
- 23) A. H. Wilson, Theory of Metals (Cambridge Univ. Press, London, 1953), p 218.
- 24) C. G. Grenier, J. M. Reynolds and N. H. Zebouni, Phys. Rev. 129, 1088 (1963).
- 25) C. G. Grenier, J. M. Reynolds and J. R. Sybert, Phys. Rev. 132, 58 (1963).
- 26) See ref. 21, p 501 and ref. 23, p 320.
- 27) T. Heurlinger, Ann. Phys. Lpz. 48, 84 (1915); Phys. Z. 17, 221 (1916).
- 28) J. R. Long, C. G. Grenier and J. M. Reynolds, Phys. Rev. 140, A187 (1965).

- 29) The data was corrected for magnetoresistance and thermoelectric effects in the cupron wire. The choice of cupron (constantan) wire was unwise. Measurements verified that the W. B. Driver alloy Evanohm is a better choice for such applications. Samples of the constantan type alloys at 4.2 K showed a negative magneto-resistance varying as $H^{-1/2}$ at low fields and saturating in fields of order 10 kOe to a value about 2% less than the zero field resistivity. No magnetoresistance was observed in Evanohm. Measurements of the isothermal thermoelectric coefficient of samples from several spools of both alloys against superconducting lead revealed the large value $\epsilon = -0.364$ T for constantan alloys and the copper like value $\epsilon = -0.05$ T for Evanohm. The constantan samples also exhibited some magnetic field dependence of ϵ , but no field dependence of ϵ was exhibited by the Evanohm samples.
- 30) L. Colquitt, Jr., J. Applied Phys. 36, 2454 (1965).
- 31) See reference 23, p. 310.
- 32) See reference 21, p. 412 and W. G. Baber, Proc. Roy. Soc. A158, 383 (1937).
- 33) M. J. Rice, Phys. Rev. Letters 20, 1439 (1968).
- 34) E. Fawcett, Advances in Physics 13, 139 (1964).
- 35) See, for instance, E. N. Adams and T. D. Holstein, J. Phys. Chem. Solids 10, 254 (1959).
- 36) See, for instance, M. H. Cohen and L. Falicov, Phys. Rev. Letters 7, 231 (1961).
- 37) See reference 23, p 195, p 264.
- 38) See reference 23, p 271.
- 39) E. Fawcett, Phys. Rev. Letters 7, 370 (1961).

- 40) J. Long, Phys. Letters 25A, 677 (1967).
- 41) R. S. Blewer, N. H. Zebouni and C. G. Grenier, Phys. Rev. 174, 700
(1968).
- 42) See ref. 21, p 386.
- 43) See ref. 16; the table on p 1187 of the first paper.
- 44) A. C. Ehrlich, Phys. Rev. B (to be published).

Table I: Coefficients of the Asymptotic Conductivities. Comparison of the experimental results with the strong field limits of Eqs. 3a and 3b yielded the tabulated quantities shown at three temperatures.

Quantity Shown and Units	Kinetic Coefficient from which quantity is derived	Quantity at Selected Temperatures		
$T(K)$		4.1	2.6	1.4
$\sum_i n_i a_i H_i (10^{24} \text{ cm}^{-3} \text{ Oe})$	$\lim_{H \rightarrow \infty} H^2 \underline{\sigma}_{11}$	2.32	2.24	2.19
$\sum_i (\pm) n_i (10^{17} \text{ cm}^{-3})$	$\lim_{H \rightarrow \infty} H \underline{\sigma}_{12}$	4.4	4.4	4.4
$\sum_i (\pm) n_i H_i^2 (10^{26} \text{ cm}^{-3} \text{ Oe}^2)$	$\lim_{H \rightarrow \infty} H^3 \underline{\sigma}_{12}$	-3.86	-3.57	-3.43

Figure Captions

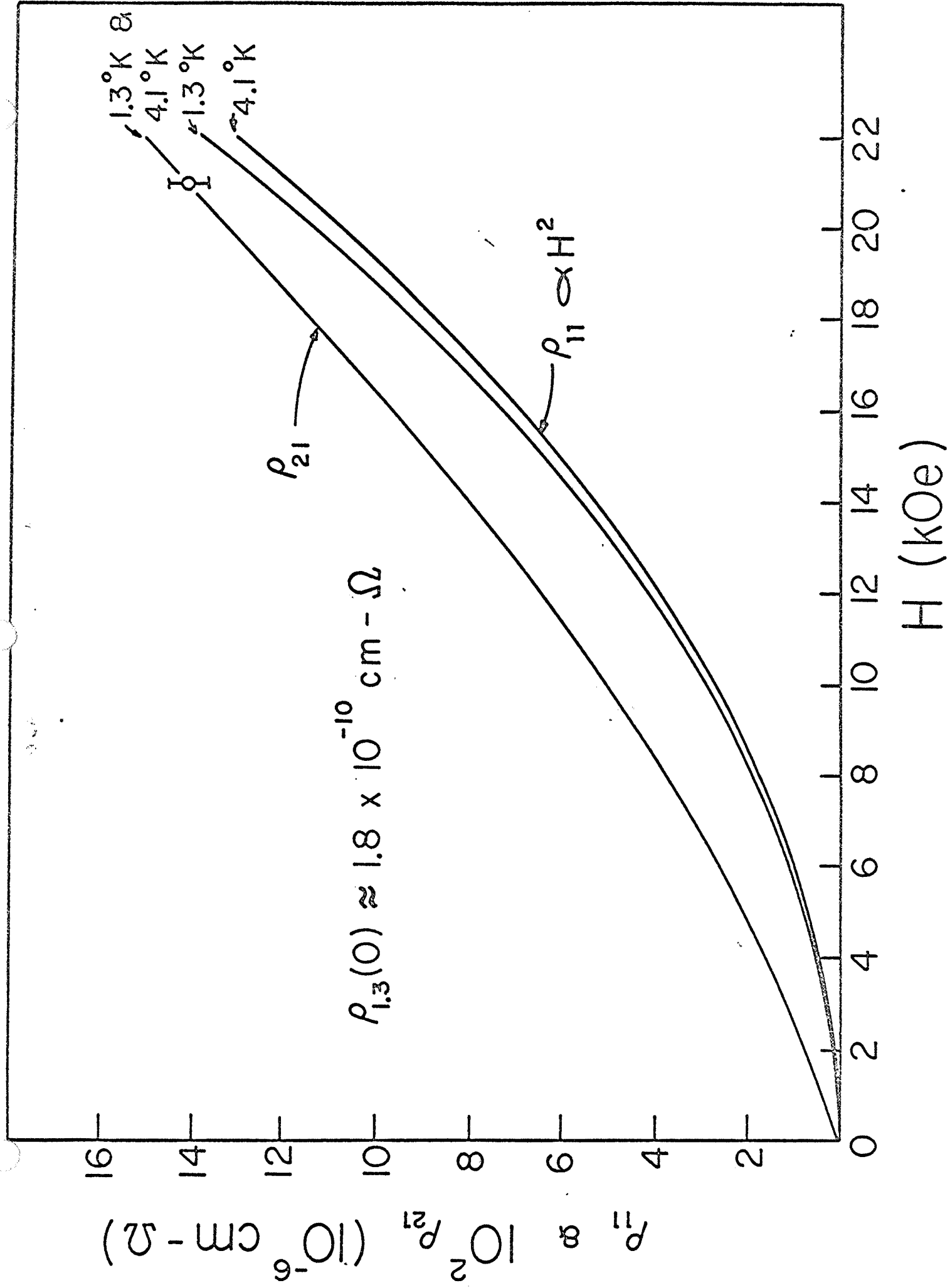
Figure 1: The electrical resistivity tensor. The magneto-resistivity ρ_{11} and the Hall resistivity ρ_{21} are shown as functions of field and temperature. Note the temperature dependence of ρ_{11} and that ρ_{21} is roughly 1% of ρ_{11} in the upper field range.

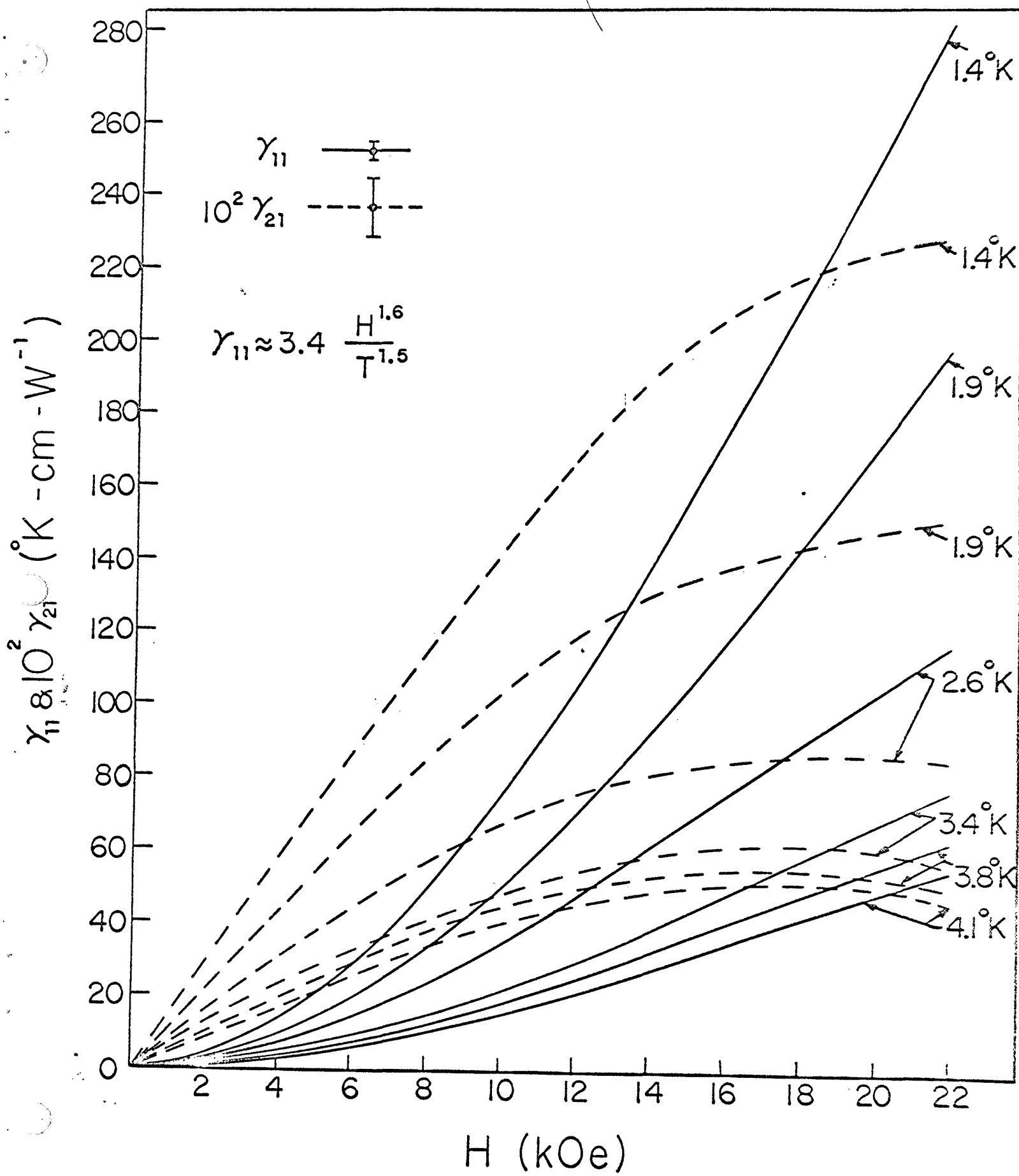
Figure 2: The thermal resistivity tensor. The thermal magneto-resistivity γ_{11} and the Righi-Leduc resistivity γ_{21} are shown as functions of field and temperature. Note that γ_{11} is less than quadratic in H and that γ_{21} tends to pass through a maximum at a value that is roughly 1% of γ_{11} .

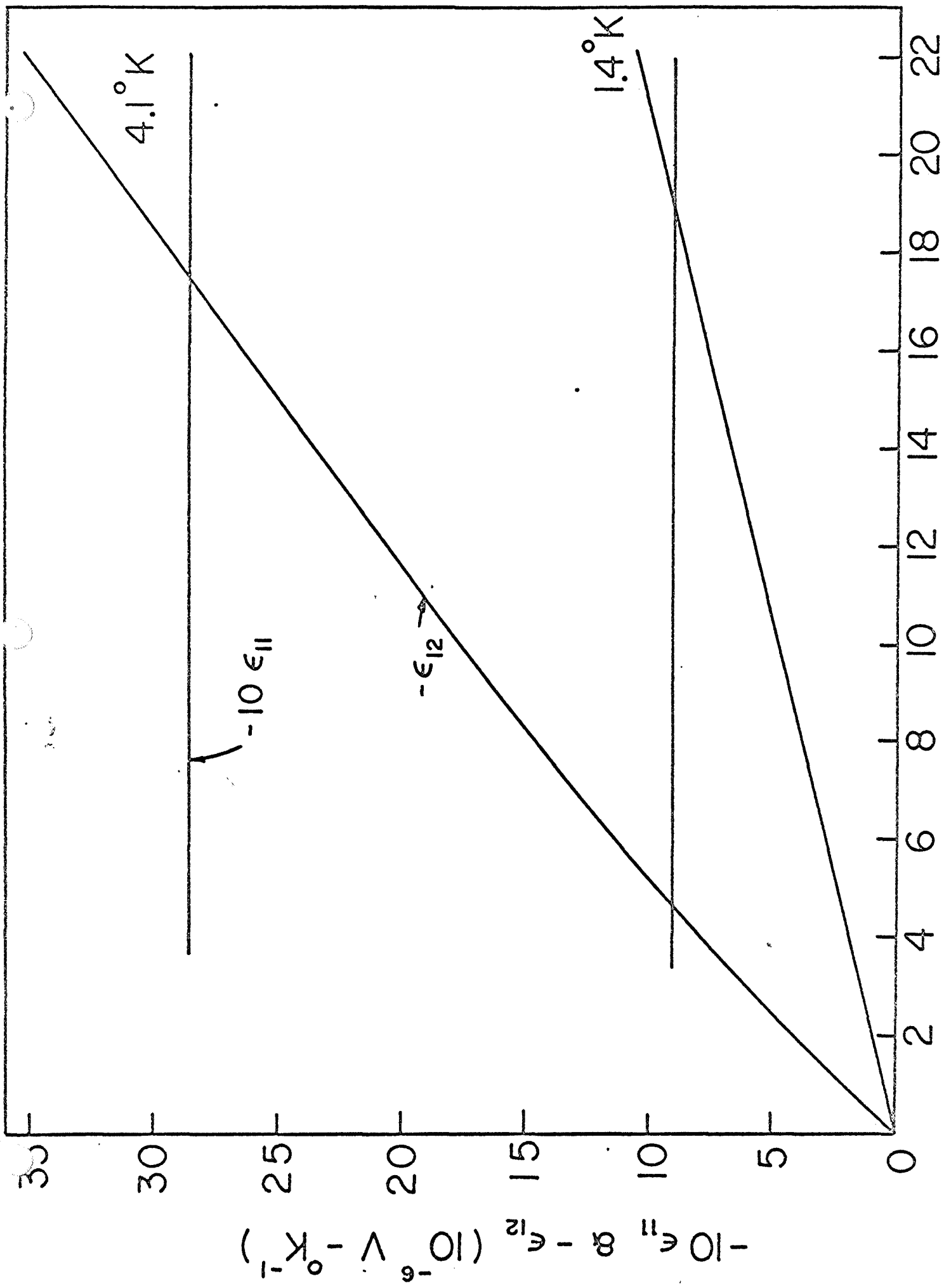
Figure 3: The isothermal thermoelectric tensor. The coefficient ϵ_{11} is the ordinary thermocouple coefficient, the absolute thermoelectric power, and ϵ_{12} is the isothermal Nernst coefficient. Note that ϵ_{11} is essentially independent of H. Results at the lowest fields were not reliable and are omitted. These are quantities derived from the experimental coefficients $\hat{\epsilon}'$ and are corrected for the ϵ of the leads.

Figure 4: The kinetic thermoelectric coefficients. The thermoelectric coefficient ϵ''_{11} and the Nernst coefficient ϵ''_{12} are shown as functions of field and temperature T. The simplest interpretation of Eqs. 3c and 3d leads one to expect that $\hat{\epsilon}''/T$ should be independent of T. The precision of ϵ''_{12} results is much greater than that of ϵ''_{11} results.

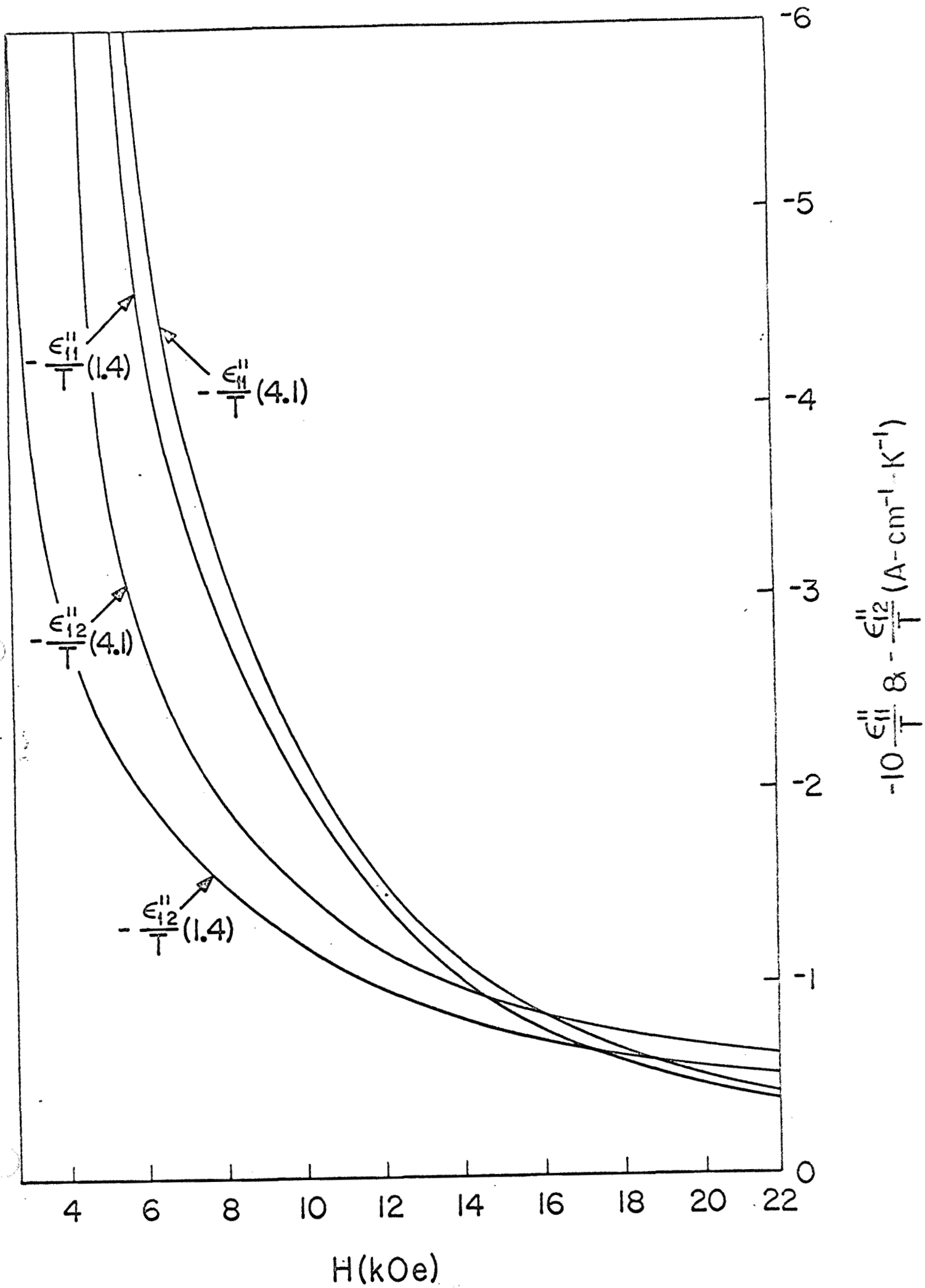
Figure 5: The Nernst specific heat coefficient. The ϵ''_{12} data interpreted in terms of Eq. 3d leads to a prediction of the temperature coefficient γ of the electronic specific heat. The value of γ spans the range of published specific heat results and displays a monotonic temperature dependence.

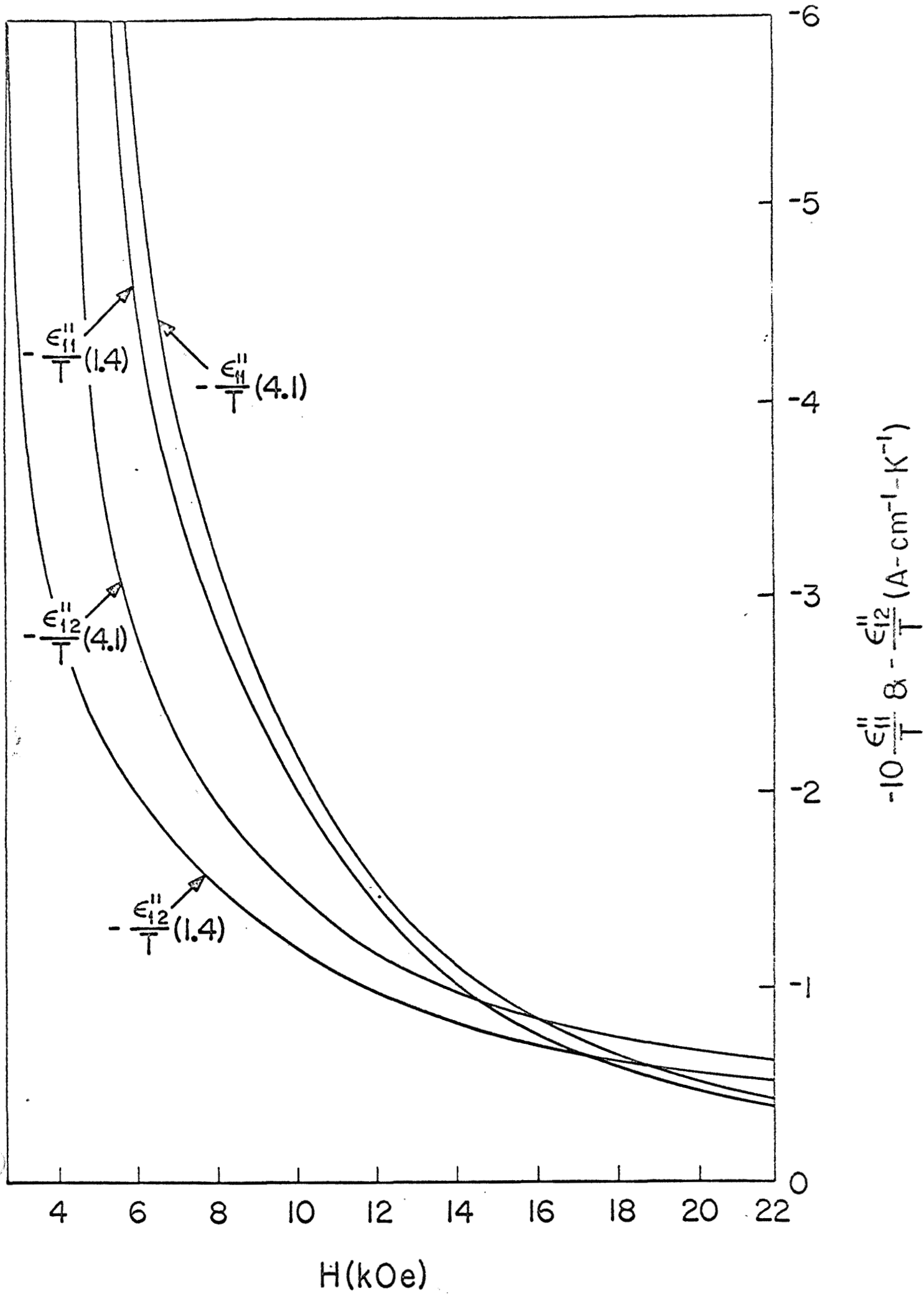


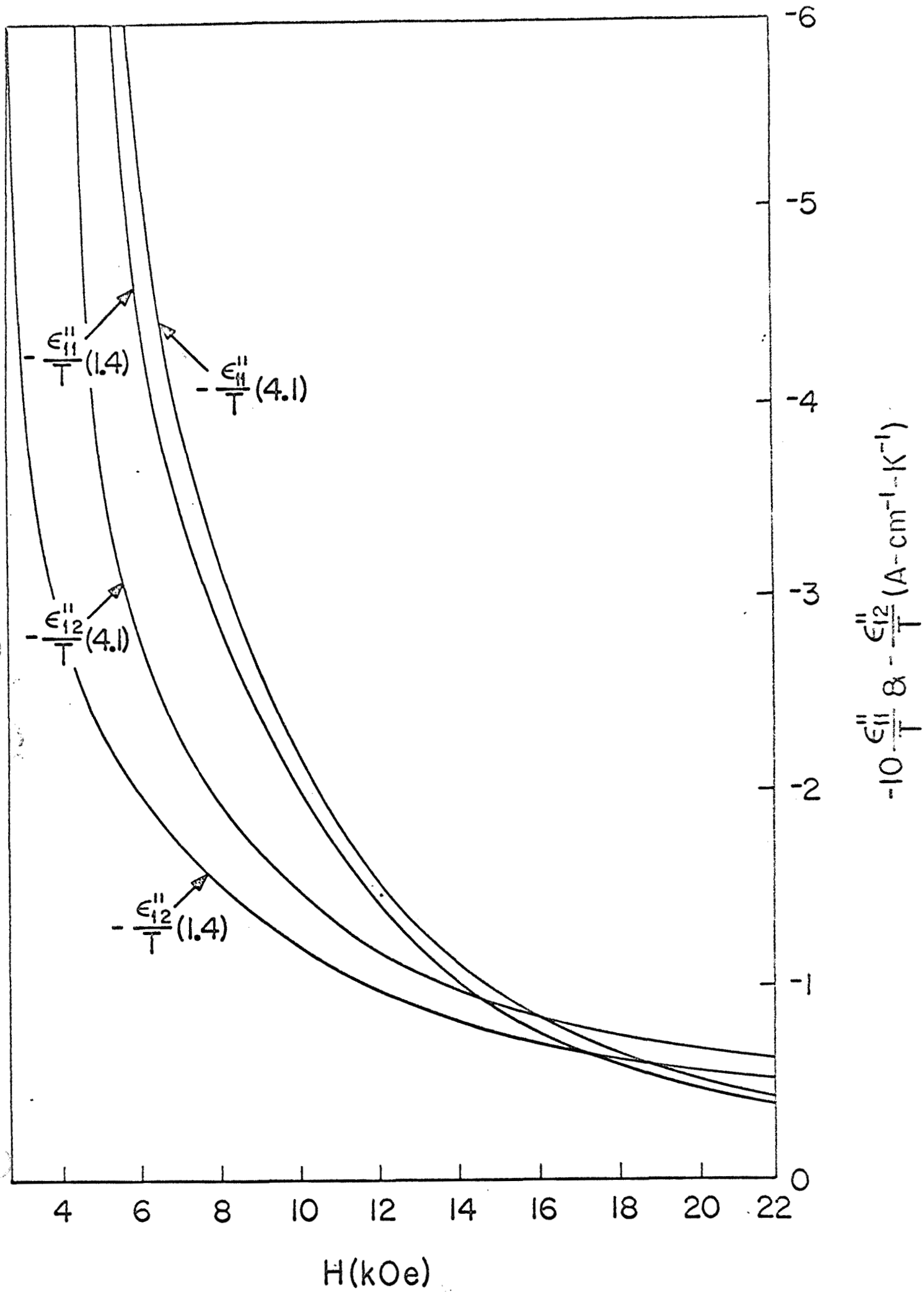


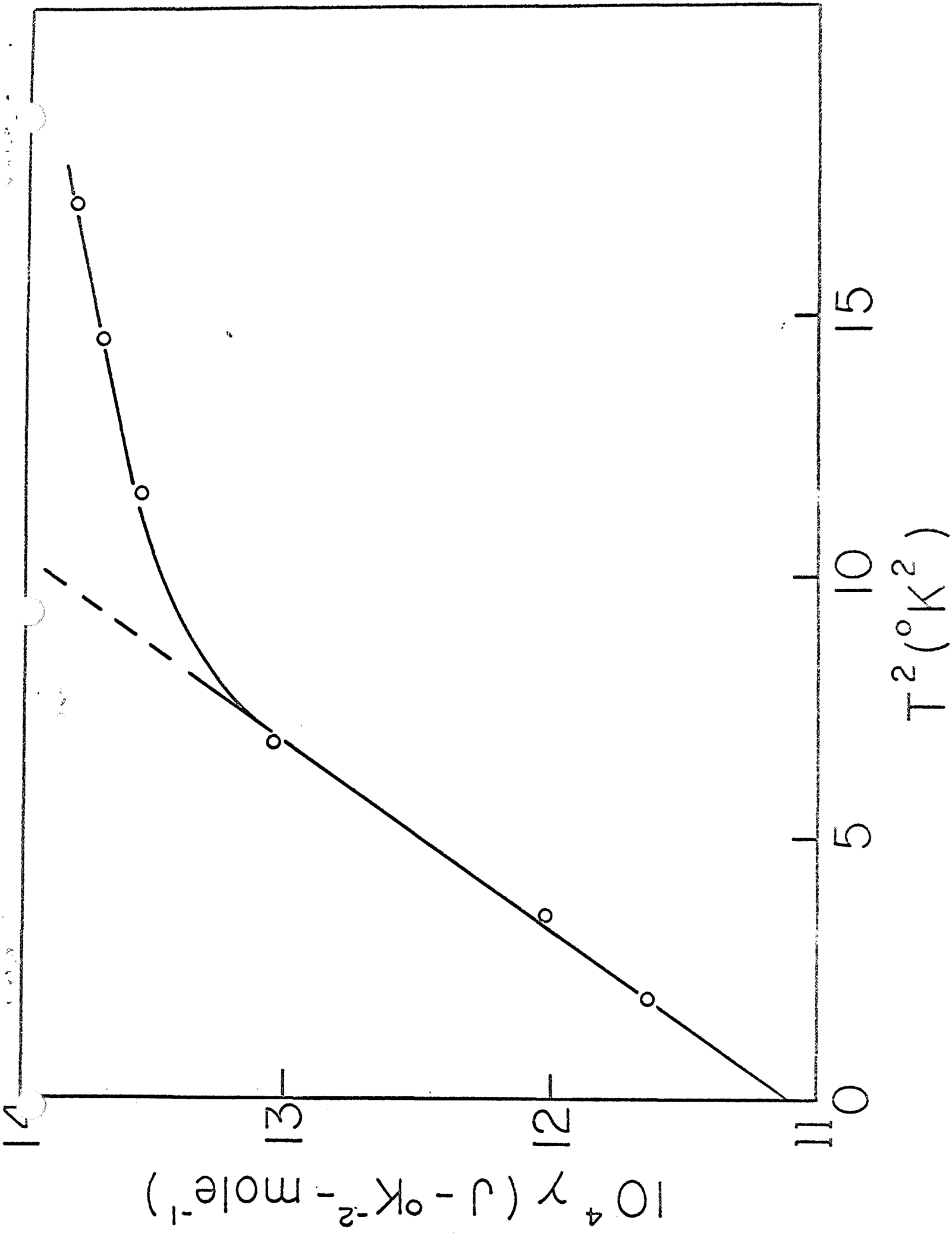


H (kOe)









GEOMETRICAL INTERPRETATION OF
THE MAGNETOCONDUCTIVITY
OF A FERMI ELLIPSOID

Jerome R. Long

Scheduled for Publication in the 15 ~~January~~^{MARCH}, 1971 Issue of Physical Review B

ABSTRACT

The Sondheimer-Wilson approximation to the magnetoconductivity tensor of metals has recently been extended by Mackey and Sybert to the model of an arbitrarily oriented Fermi ellipsoid with an anisotropic relaxation time. A study of their results shows that a straightforward geometrical interpretation can be attached to the parameters which appear in the transverse magnetoconductivity and Hall conductivity expressions derived from this quasi-classical model at arbitrary strengths of the applied magnetic field. It is suggested that the geometrical relationships may be more general than their limited derivation and could lead to quantitative predictions of the galvanomagnetic coefficients of some metals with a complex Fermi surface.

INTRODUCTION

A tractable analytical calculation of the magnetoconductivity tensor of metals appears to require rather drastic specializations and simplifying assumptions. One such case is the calculation by Sondheimer and Wilson¹ of the transverse magnetoconductivity tensor due to independent bands of electronic carriers represented by spherical sheets of Fermi surface with an isotropic scalar relaxation time. Grenier et al² extended the Sondheimer-Wilson results to ellipsoidal surfaces, and Mackey and Sybert³ have recently succeeded in adapting the Sondheimer-Wilson approach to arbitrarily oriented ellipsoids with a tensor relaxation time. The latter is about the most general case

that has been worked to conclusion. Non-ellipsoidal Fermi surfaces have been treated by other formalisms, but the results obtained are limited. The Jones-Zener expansion⁴ is useful only at very weak magnetic fields, while the vector mean free path method⁵ leaves the results in quadratures. Another possibility is the graphical method, in which the correct Fermi surface is simulated by a planar faced model⁶, but this method, like that of Jones and Zener, seems to be an inherently weak field approximation. How does one calculate the magnetoconductivities of non-ellipsoidal Fermi surfaces in a manner suitable for comparison with experiments not restricted to weak or strong field limits?

The breaking of a similar impasse which existed for energy band calculations was largely due to recognition of the physical significance of certain geometrical features of the Fermi surface. Perhaps it is also true for transport effects, that features of the results obtained for an ellipsoidal surface have a geometrical interpretation which transcends the ellipsoidal limitations of the calculation.

In this paper, it is shown that there exists a simple geometrical interpretation of the results of Mackey and Sybert when applied to tilted ellipsoids symmetrically arrayed about the direction of the applied magnetic field. Reasonable quantitative success has been obtained in developing a band model based upon this geometrical interpretation which predicts the galvanomagnetic coefficients of tungsten at effectively arbitrary field strength⁷.

THEORY

It is well known that an appropriate description of the dispersion relation of a degenerate energy band at the Fermi energy is, in some cases, given in terms of a mass tensor. It may also be appropriate, as proposed by Herring and Vogt⁸, to describe some scattering processes in terms of a relaxation time tensor. Mackey and Sybert³ have derived a very compact form for the isothermal electrical magnetoconductivity tensor $\hat{\sigma}$ of a model metal of the above type. In gaussian units, their results for a single electron band with spatial charge density ne are

$$\hat{\sigma} = nec (\hat{H}^s - \hat{H})^{-1} \quad (1)$$

$$\hat{H}^s \equiv (c/e) \hat{\tau}^{-1} \hat{m} \quad (2)$$

where \hat{H} is the magnetic part of the applied field tensor. For a uniform steady field H , one can always, as is customary, describe $\hat{\sigma}$ in a laboratory coordinate system oriented such that

$$\hat{H} = \begin{bmatrix} 0 & -H & 0 \\ H & 0 & 0 \\ 0 & 0 & 0 \end{bmatrix} \quad (3)$$

In this same system, \hat{m} and $\hat{\tau}$ are the mass and relaxation time tensors. The laboratory system is not generally the principal axis system, but is obtained from the principal axis system by an orthogonal

transformation \hat{X} . Explicitly

$$\hat{m}_p \equiv \begin{bmatrix} m_1 & 0 & 0 \\ 0 & m_2 & 0 \\ 0 & 0 & m_3 \end{bmatrix}; \quad \hat{m} = \hat{X}^{-1} \hat{m}_p \hat{X} \quad (4)$$

$$\hat{\gamma}_p \equiv \begin{bmatrix} \gamma_1 & 0 & 0 \\ 0 & \gamma_2 & 0 \\ 0 & 0 & \gamma_3 \end{bmatrix}; \quad \hat{\gamma} = \hat{X}^{-1} \hat{\gamma}_p \hat{X} \quad (5)$$

For the specific example of an ellipsoid tilted away from the laboratory 3 (field) direction by a rotation through an angle ψ about the 1 principal axis, the preceding definitions imply

$$\hat{H}^s = c/e \begin{bmatrix} m_1 \gamma_1^{-1} & 0 & 0 \\ 0 & [m_2 \gamma_2^{-1} \cos^2 \psi + m_3 \gamma_3^{-1} \sin^2 \psi] & [(m_2 \gamma_2^{-1} - m_3 \gamma_3^{-1}) \sin \psi \cos \psi] \\ 0 & [(m_2 \gamma_2^{-1} - m_3 \gamma_3^{-1}) \sin \psi \cos \psi] & [m_2 \gamma_2^{-1} \sin^2 \psi + m_3 \gamma_3^{-1} \cos^2 \psi] \end{bmatrix} \quad (6)$$

It was shown by Onsager⁹ that, if the laboratory 3 direction defines an axis of at least three-fold rotational symmetry in the metal, that the only non-zero elements of the magnetoconductivity tensor are $\sigma_{11} = \sigma_{22}$, $\sigma_{12} = -\sigma_{21}$ and σ_{33} , as in the isotropic case. A specific example which satisfies this condition is that of three tilted ellipsoids symmetrically placed about the 3 - direction. The discussion that follows will focus upon σ_{11}^T and σ_{12}^T , the total transverse magnetoconductivity and Hall conductivity

due to the three ellipsoids. Following Mackey and Sybert, the results are

$$\sigma_{11}^T = 3nec a_i H_i / (H^2 + H_i^2) \quad (7)$$

$$\sigma_{12}^T = -3necH / (H^2 + H_i^2) \quad (8)$$

$$H_i^2 \equiv H_{11}^S [H_{22}^S - (H_{23}^S)^2 / H_{33}^S] \quad (9)$$

$$a_i \equiv H_i / 2H_{11}^S + H_{11}^S / 2H_i \quad (10)$$

where the subscript i would denote the i th such band of carriers in a multi-band model. The above result is formally identical to that of Mackey and Sybert, but the elements of their \hat{H}^S are different due to their use of a $\hat{\gamma}$ which was diagonal in the laboratory coordinate system.

The object is to now indicate the geometrical significance on a Fermi surface of the quantities H_i and a_i . Direct substitution for the elements of \hat{H}^S in terms of the principal axis tensors \hat{m}_p and $\hat{\gamma}_p$ yields

$$H_i = c/e (m_1 m_2 m_3 / \gamma_1 \gamma_2 \gamma_3)^{1/2} (m_2 \gamma_2^{-1} \sin^2 \psi + m_3 \gamma_3^{-1} \cos^2 \psi)^{-1/2} \quad (11)$$

$$a_i = \frac{1}{2} \left(\frac{\gamma_i m_i^{-1}}{\gamma_3 m_3^{-1} \sin^2 \psi + \gamma_2 m_2^{-1} \cos^2 \psi} \right)^{1/2} + \frac{1}{2} \left(\frac{\gamma_3 m_3^{-1} \sin^2 \psi + \gamma_2 m_2^{-1} \cos^2 \psi}{\gamma_i m_i^{-1}} \right)^{1/2} \quad (12)$$

The actual scattering anisotropy should be expected to fall between two limiting cases of these last expressions.

Limiting Case 1.): Complete Scattering Isotropy

Isotropic scattering is defined here as that scattering which is independent of the direction of the $\frac{\mathbf{k}}{m_i}$ vector on the Fermi surface. It is characterized by the condition $\gamma_1 = \gamma_2 = \gamma_3 \equiv \gamma_i$. The interpretation of H_i and Q_i is unambiguous for this case of the ellipsoidal model.

The semi-axes of each ellipsoid are given by $(2m_1 \xi_0)^{1/2}$, $(2m_2 \xi_0)^{1/2}$ and $(2m_3 \xi_0)^{1/2}$, where ξ_0 is the Fermi energy. The extremal intersection between one of the ellipsoids and a family of planes normal to the direction of the applied field is an elliptical extremal orbit, the enclosed area A_e of which determines the de Haas-van Alphen frequency. Elementary mensuration formulae give

$$A_e = 2\pi \xi_0 (m_1 m_2 m_3)^{1/2} (m_2 \sin^2 \psi + m_3 \cos^2 \psi)^{-1/2}$$

For a quadratic dispersion law, the cyclotron effective mass is given by

$$m_i^* = (2\pi)^{-1} (\partial A_e / \partial \xi_0) = (2\pi)^{-1} A_e / \xi_0$$

Therefore,

$$H_i = cA_e / 2\pi e\gamma_i \hbar = m_i^* c / e\gamma_i \quad (13)$$

a standard result.²

The equivalent result for a_i is not standard. Consider the ratio $P_{orb.} / P_{cir.}$. In this ratio, $P_{orb.}$ is the perimeter of the extremal orbit, and $P_{cir.}$ is the perimeter of a circle which would enclose the same area A_e as that enclosed by the extremal ellipse. Application of elementary mensuration formulae in order to determine this ratio yields the very simple result

$$a_i = (P_{orb.} / P_{cir.})^2 \quad (14)$$

This result leads one to interpret a_i as a geodesic factor in the magnetoconductivity which partially describes the shape of the path a typical carrier traverses upon the Fermi surface as the momentum of the carrier is reversed by collisions.

Limiting Case 2.): Complete Scattering Anisotropy

Completely anisotropic scattering is defined here as that scattering in which the tensor $\hat{\gamma}_p$ is scaled in direct proportion

to the tensor \hat{m}_p . It is characterized by the condition

$$\gamma_1/m_1 = \gamma_2/m_2 = \gamma_3/m_3 \equiv \gamma_i^*/m_i^*$$

where m_i^* is the cyclotron effective mass as defined earlier, and

γ_i^* is now defined by the above condition as the effective

relaxation time of the band for the stated field configuration. In

this case, one immediately obtains the results

$$H_i = m_i^* c / e \gamma_i^* \quad (15)$$

$$a_i = 1 \quad (16)$$

The assumption of completely anisotropic scattering on an anisotropic Fermi surface has led, as a little reflection will show it should, to the standard result for isotropic scattering on a spherical Fermi surface.

From the two limiting cases, one can now speculate an interpolation form for the intermediate case. The simplest possibility is

$$H_i = m_i^* c / e \gamma_i^* \quad (17)$$

$$a_i = (P_{orb.} / P_{cir.})^\gamma; \quad 0 \leq \gamma \leq 2. \quad (18)$$

CONCLUSION

The perimeter rule, Eq. (18) is the focal point of this work. It is interesting that the coefficient a_i has such an interpretation. Interest in Eq. (18) should not be great, however, unless it can be shown that Eqs. (17) and (18) along with Eqs. (7) and (8) are applicable to more complex, and unsolved problems. Eqs. (17) and (18) with $\gamma=1$ have been applied to the complex Fermi surface of tungsten¹⁰, and this will be detailed in the following paper⁷. The quantitative success achieved in that application was sufficient to prompt this separate report.

REFERENCES

*Partially supported by National Aeronautics and Space Administration grant NGR 47-004-006.

- 1.) A. H. Wilson, Theory of Metals, (Cambridge University Press, Cambridge, England, 1953), pp. 208 ff.
- 2.) C. G. Grenier, J. M. Reynolds and J. R. Sybert, Phys. Rev. 132, 58 (1963).
- 3.) H. J. Mackey and J. R. Sybert, Phys. Rev. 180, 678 (1969).
- 4.) J. M. Ziman, Electrons and Phonons, (Oxford University Press, London, 1960), pp. 501 ff.
- 5.) G. Fair and P. L. Taylor, Bull. Am. Phys. Soc. 15, 252 (1970).
- 6.) R. S. Allgaier, Phys. Rev. 165, 775 (1968) and C. C. Evans, T. A. Reglein and R. S. Allgaier, Phys. Rev. B (to be published).
- 7.) J. R. Long, Bull. Am. Phys. Soc. 15, 252 (1970) and the following paper.
- 8.) C. Herring and E. Vogt, Phys. Rev. 101, 944 (1956).
- 9.) L. Onsager, Phys. Rev. 37, 405 (1931); 38, 2265 (1931).
- 10.) See, for instance, R. F. Girvan, A. V. Gold and R. A. Phillips J. Phys. Chem. Solids 29, 1485 (1968).

PREDICTING THE GALVANOMAGNETIC
COEFFICIENTS OF TUNGSTEN
FROM FERMI SURFACE DATA

Jerome R. Long

Scheduled for Publication in the 15 ~~January~~^{MARCH}, 1971 Issue of Physical Review B

ABSTRACT

In the context of specific scattering processes, the galvanomagnetic coefficients of a metal crystal should be expressible in terms of features of the Fermi surface. For energy surfaces more complex than ellipsoids, however, analytical solutions of the transport equations with the most tractable scattering assumptions have not been found, except in quadratures or in an asymptotic limit of the applied magnetic field. A procedure is introduced here for the purpose of predicting approximate values of arbitrary field galvanomagnetic coefficients of a metal with non-ellipsoidal Fermi surface sheets. The procedure is based upon a semi-empirical extension of the solution for ellipsoids. An application of the procedure to the Fermi surface of tungsten and measurements of the low field galvanomagnetic coefficients of a tungsten crystal are described. The prediction is generally successful. No attempt is made to adjust parameters or obtain best fits to curves. The intent is to show how closely one can estimate by a simple, first trial method.

INTRODUCTION

Certain transport effects, particularly the Hall effect and the magnetoresistance, are frequently treated as tools for investigating the Fermi surface of metals, with scant attention being given to transport processes per se.¹ Conversely, one frequently cited justification of Fermi surface determinations is that transport properties of the electronic carriers in a nearly perfect, large metal crystal can be derived from the shape of the Fermi surface. There are considerable mathematical difficulties, however, in solving a kinetic transport equation and current integrals for the complicated dispersion relations indicated by most Fermi surfaces. Only for ellipsoids and elastic scattering have reasonably complete results been obtained. A particularly compact and general treatment of the galvanomagnetic coefficients for ellipsoidal energy surfaces was given by Mackey and Sybert². In the preceding paper³, it was shown that there exists a simple geometrical interpretation of the Sondheimer-Wilson parameters⁴ which appear in the results of a Mackey-Sybert calculation of the magnetoconductivity tensor for tilted ellipsoids with anisotropic relaxation time. The implication is that the geometrical interpretation may apply to non-ellipsoidal surfaces.

It is the purpose of this paper to apply the results of the preceding paper to the Fermi surface of tungsten. A semi-empirical scheme is developed for obtaining, from Fermi surface data, a quantitative estimate of the contribution of a given Fermi surface sheet to the magnetotransport coefficients. The scheme appears to be restricted to cases where the magnetic field is applied along a symmetry axis of the crystal.

In a previous paper, the results of high field measurements of six electrical and thermal transport coefficients in a tungsten crystal were presented.⁵ The coefficients were measured in magnetic fields up to 22 kOe directed along a $\langle 100 \rangle$ axis at temperatures in the liquid helium - 4 range. That data was obtained under high field conditions (the product $\omega_c \tau$ of the cyclotron frequency and the phenomenological relaxation time much greater than unity) and is not a very stringent test of the proposed scheme. In order to provide a better test, measurements of the magnetoresistivity and Hall resistivity of the same crystal were extended into the low ($\omega_c \tau < 1$) field range. The semi-empirical procedure was, thus, subjected to trial over a continuous field range from 5 Oe to 22 kOe.

Tungsten is an excellent metal for testing the proposed scheme. The major portions of the Fermi surface of tungsten are non-ellipsoidal, with the electron "jack" having non-central orbits⁶, but the topology of its individual sheets is simple, there being no multiple connections or open orbits.

THEORY

The galvanomagnetic effects were measured in a tungsten crystal⁵ for which the electrical resistivity in zero magnetic field was found to be essentially independent of temperature at 4K. It is thus assumed that electrical conduction in the crystal was limited by large angle elastic scattering characterized by a relaxation time. The Sondheimer-Wilson theory⁴ as modified by Mackey and Sybert² would, therefore, be expected to be applicable to the galvanomagnetic effects in the crystal, were its Fermi surface ellipsoidal, and any phenomena due to Landau quantization neglected. In that case, the magnetoconductivity $(\sigma_{11})_i$ and Hall conductivity $(\sigma_{12})_i$ due to the i th such ellipsoid or band of equivalent ellipsoids would be given in gaussian units by^{3,5}

$$(\sigma_{11})_i = ec n_i a_i H_i / (H^2 + H_i^2) \quad (1a)$$

$$(\sigma_{12})_i = (\pm) ec n_i H / (H^2 + H_i^2) \quad (1b)$$

The quantities e , c , and H are the electronic charge, speed of light and applied magnetic field. The i th band contains n_i carriers per cm^3 , which if hole (electron) like takes the $+(-)$ sign as indicated in Eq. (1b). H_i and a_i are defined from the point of view of the preceding paper³. $H_i \equiv m_i^* c / e \tau_i^*$, where τ_i^* and m_i^* are the effective relaxation time and cyclotron mass of the i th band for the specified orientation of H . The geometrical definition of a_i is $a_i = (P_{orb} / P_{cir})^{1/2}$ where P_{orb} is the perimeter of

the extremal orbit on the ellipsoid and P_{cir} is the perimeter of a circle which would enclose the same area (same de Haas-van Alphen frequency) as that enclosed by the extremal ellipse. The exponent ranges from the value two for isotropic scattering to zero for scattering with the same anisotropy as the dispersion law.

The Sondheimer-Wilson theory assumes completely independent bands. This implies that the net conductivities of a multiband metal to which Eqs. (1) are applied are given by $\sigma_{11} = \sum_{\text{bands}} (\sigma_{11})_i$ and $\sigma_{12} = \sum_{\text{bands}} (\sigma_{12})_i$.

EXPERIMENT

Extension of the galvanomagnetic data into the low field range was accomplished with essentially the same apparatus and procedure as that used in measuring the high field coefficients⁵. Due to the small ($10^{-10}\Omega\text{-cm}$) magnitude of the resistivities in the low field range, a few changes were necessary in order to make the measurements with the available conventional dc equipment.

All thermometers and heaters used in the thermal measurements were omitted, and instead of a single #36 strand, the electric current probe was made up of several parallel #30 strands in order to carry currents up to 10A. Despite this modification and the immersion of the sample in liquid helium, significant Joule and Thomson heating were observed at the higher currents. This was apparently due to the insulating effect of bubbles formed in the helium I, particularly at the relatively high resistivity conducting adhesive contacts⁵ between the strands of copper wire and the sample. Heating effects and the magnetoresistance due to the self field of the sample current⁷ thus limited the maximum useable current density to about 90 A/cm^2 ($I \approx 7\text{A}$). Corrections for these extraneous effects were obtained by current reversal and by measuring the change in resistivity as a function of current in zero applied field.

The zero field resistivity being nearly residual at 4.2K, all of the measurements were performed at this temperature for reasons of simplicity and economy. The heating effects could be reduced by working in helium II, but this did not allow higher current densities because of the self field effect.

The advantages of enhancing the small signal by increasing the current density having been exhausted, the apparatus was further simplified by eliminating the six dial potentiometer and feeding the voltage probes directly into a Keithly 148 nanovoltmeter mounted at the dewar head. With repeated measurements it was then possible to verify signal changes of less than one nanovolt. Each data point, Figs. (2) and (3) is an average of many trials, particularly at the lowest fields.

RESULTS

The kinetic coefficients σ_{11} and σ_{12} were computed from the measured magnetoresistivity ρ_{11} and Hall resistivity ρ_{21} through the usual inversion relations $\sigma_{11} = \rho_{11} / (\rho_{11}^2 + \rho_{21}^2)$ and $\sigma_{12} = \rho_{21} / (\rho_{11}^2 + \rho_{21}^2)$. In order to display both conductivities in the Lorentzian form indicated by Eqs. (1), the results are shown, Figs. (1) and (2), as the quantities $H\sigma_{11}$ and σ_{12} plotted against $\ln H$. The $H\sigma_{11}$ curve is seen to peak at about 85 Oe, while the σ_{12} data has a truncated peak centered at about 50 Oe and is positive at all fields. The positions of the peaks tempt one to say that a "typical" carrier satisfies the condition $\omega_c \tau = 1$ somewhere in the field range 50-85 Oe. The band-by-band analysis will show the limitations of such an estimate. The positive sign of σ_{12} at all fields is a clear indication that occupied hole states were in greater number, however slightly, and also more mobile than occupied electron states. This is consistent with the high field data⁵, which found $\sum_i (\pm) n_i > 0$, but $\sum_i (\pm) n_i H_i^2 < 0$.

The data points, Figs. 1 and 2, are approximated by an unbroken curve. The ordinates of each unbroken curve are the algebraic sums of the ordinates of the six broken curves. Each of the six broken curves was calculated from Eqs. (1). The parameters n_i , a_i , and H_i appearing in Eqs. (1) were determined, as will be discussed in the following section, by a procedure utilizing details of the tungsten Fermi surface constructed from de Haas-van Alphen data by Girvan, Gold and Phillips⁶ (GGP), a model closely attuned to the theoretical work of Loucks⁸ and Mattheiss⁹. The parameters are tabulated in Table 1 and specify a model of six independent bands.

ANALYSIS

The following semi-empirical rule was developed for the purpose of selecting a portion of the k-space volume enclosed by a non-ellipsoidal Fermi surface to be associated with a given i th band: when the magnetic field is directed along a given high symmetry direction of the Brillouin zone, each class of extremal cyclotron orbit for that field direction may be associated with a distinct band. (Association of a band with an extremal orbit is supposedly justified for the transverse magnetic field transport effects upon the grounds that carriers in the vicinity of an extremal orbit are weighted heavily in the computation of the current, because they tend to have a large common velocity component in the direction of the applied electric field.) If a given sheet α of the Fermi surface has only a single, central extremal orbit 0_α for the chosen field direction, then the k-space volume of the band associated with 0_α may be taken as the sum of the total volumes of all sheets within the reduced zone which are equivalent (in the applied field) to the α sheet. If a sheet β has multiple extremal orbits for the chosen field direction, then the k-space volume of the band associated with the j th orbit $0_{\beta j}$ may be taken as the sum of all volumes in the zone which are equivalent to the volume contained between a pair of planes that are parallel to the plane of the orbit, and pass through inflection points on the surface marking transitions from the contour of the j th extremal orbit to the $(j - 1)$ th and $(j + 1)$ th extremal orbits on the same sheet β of the Fermi surface.

Seven distinct classes of extremal area cyclotron orbit exist on the GGP surface when the magnetic field is directed along a $\langle 100 \rangle$ axis, the orientation used in the measurements reported here. The bands are denoted by a modified version of the orbit notation of GGP.

The hole Fermi surface includes six ellipsoids centered at the points N in the zone. Orbits on these ellipsoids are denoted by GGP as ρ . When the magnetic field is along $\langle 100 \rangle$, two of the ellipsoids have their long axis parallel to the field. A nearly circular orbit characterizes the band formed by these two ellipsoids. The band is denoted $\rho_1 N$, Fig. 3. The two remaining pairs of ellipsoids have their long axis normal to the field and display nearly identical elliptical orbits of nearly equal cyclotron mass¹⁰. It was assumed that a single band, denoted $\rho_2 N$, Fig. 3, is formed by these two pairs of ellipsoids, thus reducing the number of independent bands from seven to six.

Most of the holes belong to the octahedron centered at the zone vertex H. The symbol ν was assigned by GGP to orbits on the octahedron. According to the extremal orbit criterion, the contribution of the hole octahedron to the data reported here should be characterized by the nearly square orbit, Fig. 3, which girdles the edges of the octahedron for $H \parallel \langle 100 \rangle$. The notation $\nu^1 H$ has been assigned to this band to distinguish it from the $\langle 111 \rangle$ orbit denoted ν by GGP.

The $\langle 100 \rangle$ electron bands of tungsten are denoted by the symbols τ , π and σ . These correspond to the orbits on the Γ centered jack denoted τ , π and σ by GGP. The τ orbit, also called the four-ball orbit is central, while the π , or knob, and σ , or neck, orbits are both non-central, Fig. 3.

Having apportioned the k-space volume enclosed by the Fermi surface into six bands, the carrier concentration n_i of each band, Table 1, was simply given as the product $1/4\pi^3 \times$ (k-space volume of the i th band).

Values of the coefficient a_i , Table 1, depend on two sequential assumptions. The first of these was that the geometrical definition (perimeter rule) of a_i as derived for ellipsoids³ is applicable to a non-ellipsoidal surface. Secondly, the exponent γ in the interpolation form of the perimeter rule was assumed to be unity. This choice seemed probable, since $0 \leq \gamma \leq 2$, and was the easiest to work with. One could use γ as a fitting parameter if he took the perimeter rule very seriously.

The method used to calculate the quantities $H_i = m_i^* c / e \tau_i^*$ of each of the six bands depended upon an assumption that the same effective relaxation time τ^* applied to all bands. There was no basis for this assumption other than computational simplicity, and ignorance of a better choice. Upon the assumption of a common τ^* , all of the H_i were scaled by means of effective mass data¹⁰ and expressed in terms of a single unknown. The unknown chosen was H_6 of the high mass four ball orbit τT on the electron jack; then, $H_i = (m_i^* / m_6^*) H_6$.

From the prescription outlined above, it was possible to calculate the product $a_i n_i H_i$ for each band within the common factor H_6 ; then, $\sum_i a_i n_i H_i = 13.65 H_6 \times 10^{21} \text{ 0e-cm}^{-3}$, Table 1. The factor H_6 depends upon τ^* , which is, at least, a function of the impurity concentration in a particular sample. At least one data point was, therefore, required. From high field measurements⁵ on the same crystal, it was determined that $\sum_i a_i n_i H_i = 2.32 \times 10^{24} \text{ 0e-cm}^{-3}$ in the context of

Eqs. (1) for $H \gg H_i$. It was thus found that $H_6 = 170$ Oe. A set of numbers was then available, Table 1, which was used to calculate the individual band and net behavior of $H\sigma_{ii}$ and σ_{12} at all fields, Figs. 1 and 2.

DISCUSSION

The qualitative similarity between the predicted and measured behavior of $H\sigma_{ii}$, Fig. 1, is very satisfactory for such a simplified calculation. That the gross features of the weak field coefficients and the strong field coefficients are simultaneously consistent with Eqs. (1) should be well established by these results, since the position of the weak field relaxation peak was set by the solution for H_6 as a force fit of $\sum_i a_i n_i H_i$ to the strong field measurements. There is no support for the theoretical contention⁴ that the condition $\omega_c \tau \gg 1$ invalidates a description of the monotonic conductivities in terms of Eqs. (1) or other results based on a classical transport equation. At 22 kOe, the highest field utilized⁵, $\omega_c \tau$ of the massive electrons on the π orbit reaches the value $H/H_6 \approx 130$.

The quantitative discrepancies between the predicted and measured behavior of $H\sigma_{ii}$ can be understood somewhat by studying the predicted behavior of the individual bands, Fig. 1. Each band peaks at $H = H_i$, with the peak height being proportional to $a_i n_i$. Although there are six bands, it should be clear from Fig. 1 that $H\sigma_{ii}$ is dominated by the $v'H$ and π -bands and that only very drastic changes of any of the other four bands would produce a significant adjustment of the calculations. The most obvious adjustment is a reduction of H_6 by about 1/3. A change in H_6 is reasonable, as there were never any theoretical

grounds for the initial assumption of an equal relaxation time for all sheets of the fermi surface, and the scattering dynamics of the τ -orbit would appear to be significantly different from the dynamics of the other more nearly circular orbits. A simultaneous reduction of $a_6 n_6$ by about 20% is also indicated. Such a reduction would imply either a failure of the perimeter rule or of the method used for apportionment of the jack volume among its three extremal orbits.

The Hall conductivity, Fig. 2, is a much better test of the calculated parameters than $H\sigma_{11}$ because the calculated σ_{12} is a resultant of six terms of alternating sign and comparable magnitude, whereas $H\sigma_{11}$ is not sign sensitive and was dominated by only two bands. The peak heights of the individual bands in σ_{12} are proportional to n_i/H_i , so the assigned values of H_i are tested by both peak magnitude and position. The bands of high mobility are obviously weighted more heavily in σ_{12} than in $H\sigma_{11}$ and are more sensitive to the n_i assignments, without ambiguity due to a_i .

Agreement between the calculated resultant σ_{12} and data is thus remarkably good. The fit at low and high field extremes is good and the qualitatively large overestimate of the peak height is no larger than the height of the least effective of the six bands. Furthermore, the σ_{12} results appear reasonably consistent with the $H\sigma_{11}$ results. In discussing $H\sigma_{11}$, a 1/3 reduction of H_6 was suggested. The same adjustment in the σ_{12} calculation removes approximately half of the excess peak in the resultant σ_{12} . A reduction in the value of n_6 is not implied. The indicated 20% reduction of $a_6 n_6$ in the $H\sigma_{11}$ calculation would, therefore, come at the expense of a_6 , thus apparently weakening the perimeter rule.

The calculation of the H_i seemingly in error, with a reduction of H_0 indicated, it is fortunate that a sensitive independent check of this calculation is available. From the field dependence of σ_{12} at high fields, the result $\sum_i (\pm) n_i H_i^2 = -3.86 \times 10^{26} \text{cm}^{-3} \cdot \text{Oe}^2$ was obtained.⁵ The calculated parameters of table 1 yield a smaller number; $-1.49 \times 10^{26} \text{cm}^{-3} \cdot \text{Oe}^2$. A reduction of H_0 is obviously inconsistent with the large experimental value of $\sum_i (\pm) n_i H_i^2$. An alternative adjustment of the parameters which is more consistent with all of the data would be to increase, rather than decrease H_0 , while simultaneously transferring many of the electrons from the four ball π band to the σ band on the adjacent necks of the jack, Fig.3. This alternative would also allow retention of the large value of a_0 calculated by the perimeter rule and tend to produce the shoulder which can be seen in the peak of the $H\sigma_{11}$ data at about 200 Oe.

The semi-empirical calculation of the kinetic galvanomagnetic coefficients σ_{11} and σ_{12} having been more successful than expected, it was of interest to see how well the Table 1 transport parameters could predict the behavior of the thermoelectric coefficients measured at high fields.⁵ For fields $H \gg H_i$ the expressions equivalent to Eqs.

(1) for kinetic thermoelectric coefficients ϵ''_{11} and ϵ''_{12} are

$$\epsilon''_{11} = (\pi^2 k_B^2 c T / 3 H^2) \sum_i (\pm) Z_i a_i H_i \quad (2a)$$

and

$$\epsilon''_{12} = (-\pi^2 k_B^2 c T / 3 H) \sum_i Z_i \quad (2b)$$

where all symbols are either standard, or as defined for Eqs. (1), except Z_i which is the density of states of the i th band. The high field measurements⁵ of ϵ''_u and ϵ''_n at approximately 4.2K temperature were substituted into the above expressions to obtain the numbers $\sum_i Z_i = 2.3 \times 10^{34} \text{ erg}^{-1} \text{ cm}^{-3}$ and $\sum_i (\pm) Z_i a_i H_i = - 3.6 \times 10^{37} \text{ erg}^{-1} \text{ cm}^{-3} \text{ Oe.}$

In order to calculate these same quantities in terms of Table I parameters it was necessary to arrive at a set of numbers for the Z_i .

These were estimated from Table I parameters in terms of the free electron expression $Z_i = m_i^* (3\pi^2 n_i)^{1/3} (\pi \hbar)^{-2}$. It was thus calculated that $\sum_i Z_i = 2.1 \times 10^{34} \text{ erg}^{-1} \text{ cm}^{-3}$ and $\sum_i (\pm) Z_i a_i H_i = - 0.38 \times 10^{37} \text{ erg}^{-1} \text{ cm}^{-3} \text{ Oe.}$ The calculated $\sum_i Z_i$ is as close as should be reasonably expected for a free electron (band effective mass approximation) calculation. It is, appropriately, less than the measured value which contains renormalization terms. The negative sign of $\sum_i (\pm) Z_i a_i H_i$ is a consequence of the large masses of the jack electrons on the four ball orbit, which far exceeds the slight hole majority which gives σ_{12} its positive sign. The large ratio of measured to predicted $\sum_i Z_i a_i H_i$ is also understandable in terms of the H_i factor. It was seen in the high field measurements⁵ that temperature independent large angle scattering was only dominant in the galvanomagnetic data and that the thermal effects were, apparently, controlled by a shorter and temperature dependent relaxation time. A set of larger H_i than those in σ_{11} and σ_{12} should thus be expected to determine $\sum_i Z_i a_i H_i$. Eqs. (2) should not be expected to work very well when inelastic processes are significant.

CONCLUSIONS

The low field magnetoconductivity and Hall conductivity for a transverse field applied along a $\langle 100 \rangle$ axis of the tungsten crystal were calculated from high field transport and de Haas-van Alphen data according to the proposed semi-empirical prescription. The gross features of the calculated coefficients were found to be in good agreement with an experimental determination of the coefficients. It bears emphasizing that no attempt was made to adjust parameters or obtain a best fit to curves. The intent of Figs. 1 and 2 is to show how closely one can estimate by a simple first trial method. Discrepancies between data and calculation appear to have been principally due to failure of the assumption of a common relaxation time and errors in the apportionment of the k -space volume of the electron jack.

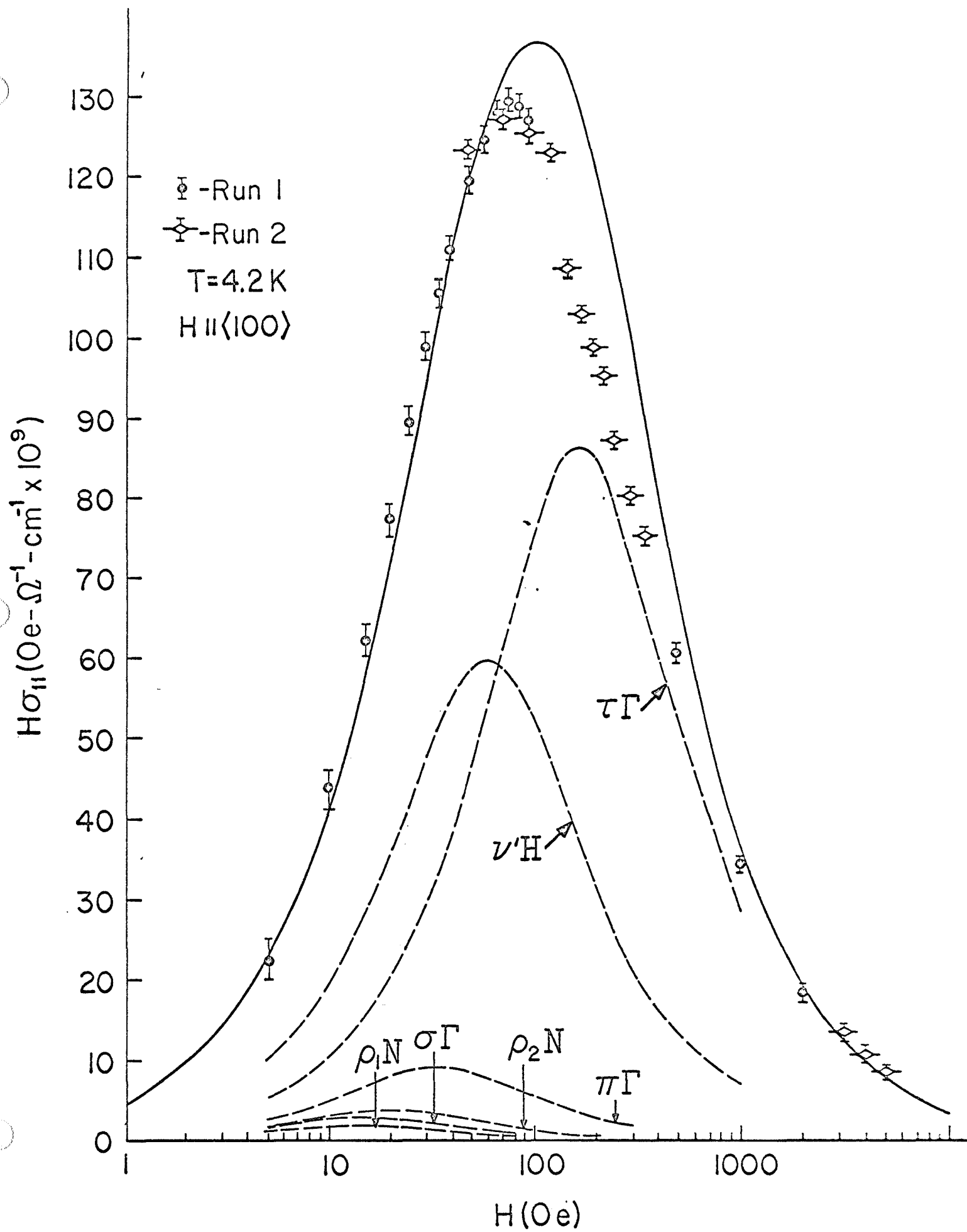
A definite evaluation of the methods used to apportion the carriers among a set of bands and to calculate the effect of the shape of the Fermi surface was not possible, but the results seem sufficiently encouraging to merit additional work for other field orientations and other metals. It is hoped that such results might serve to guide those who would attempt to obtain solutions of the transport equation. At the least they may provide a simple rule of thumb for estimating the transport properties of the carriers in a given region of a Fermi surface.

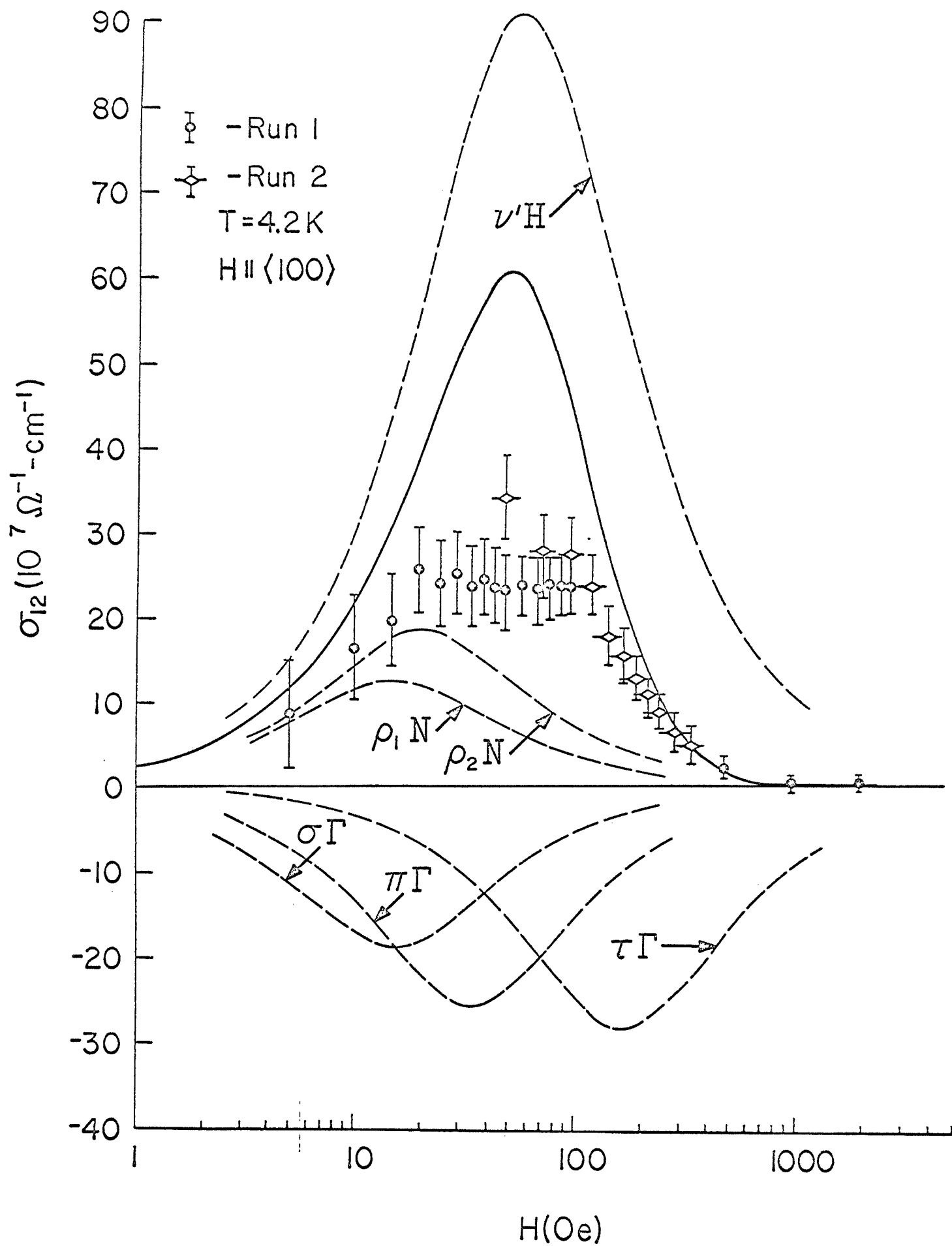
FIGURE CAPTIONS

Figure 1: The product of the applied magnetic field H and the transverse magnetoconductivity σ_{11} of the tungsten crystal plotted as a function of $\ln H$. Each broken, peaked curve was calculated, Eqs. (1a), from Fermi surface data, Table 1, and represents a band formed by a class of carriers on the Fermi surface. The unbroken curve, which approximately fits the data points is the sum of the broken curves. Peak heights are proportional to $n_i a_i$.

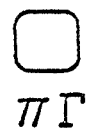
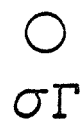
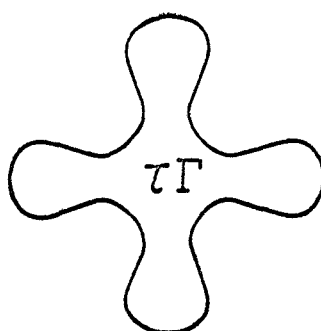
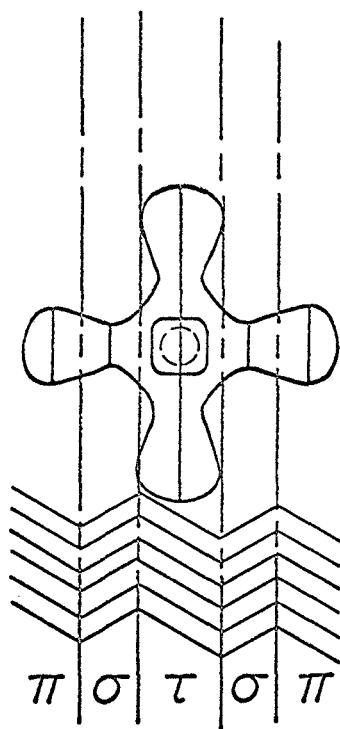
Figure 2: The Hall conductivity σ_{12} of the tungsten crystal plotted as a function of the natural logarithm of the applied magnetic field H . Each broken, peaked curve was calculated, Eqs. (1b), from Fermi surface data, Table 1, and represents a band formed by a class of carriers on the Fermi surface. The unbroken curve is the algebraic sum of the broken curves. Peak heights are proportional to n_i/H_i .

Figure 3: The six distinct extremal cyclotron orbit shapes on the Fermi surface of tungsten when a magnetic field is applied along a cubic axis. A conduction band is associated with each orbit in the calculation of the galvanomagnetic coefficients, Eqs. (1). The upper left view shows the partitioning of the volume of the electron jack into three volumes, corresponding to the π , σ and τ orbits on the jack.

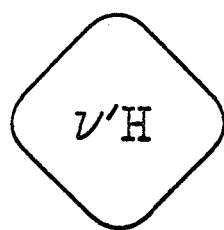




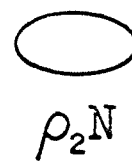
ELECTRON JACK



HOLE OCTAHEDRON



HOLE ELLIPSOIDS



REFERENCES

*The experiments and preliminary analysis in this work were conducted in the Laboratory for Research on the Structure of Matter of the University of Pennsylvania with support by the Advanced Research Projects Agency of the United States Department of Defense under contract SD-69. The work was completed at Virginia Polytechnic Institute with support by the National Aeronautics and Space Administration.

- 1.) E. Fawcett, *Advances in Physics* 13, 139 (1964).
- 2.) H. J. Mackey and J. R. Sybert, *Phys. Rev.* 180, 678 (1969).
- 3.) J. R. Long, *Phys. Rev. B* (preceding paper).
- 4.) A. H. Wilson, *Theory of Metals*, (Cambridge University Press, Cambridge, England, 1953), pp. 208 ff.
- 5.) J. R. Long, *Phys. Rev. B* (to be published).
- 6.) R. F. Girvan, A. V. Gold and R. A. Phillips, *J. Phys. Chem. Solids* 29, 1485 (1968). A good bibliography of the Fermiology of tungsten may be assembled from the references in this paper. These authors refer to an extremal orbit as non-central if the k-space coordinates of the orbit centers are not given by crystal symmetry.
- 7.) K. H. Berthel, *Phys. Stat. Sol.* 5, 159 (1964).
- 8.) T. L. Loucks, *Phys. Rev.* 143, 506 (1966).
- 9.) L. F. Mattheiss, *Phys. Rev.* 139, A1893 (1965).

- 10.) W. M. Walsh, Jr., Resonances Both Temporal and Spatial (edited by J. F. Cochran and R. R. Haering) Gordon and Breach (1969).

This reference contains data on effective masses of tungsten as obtained by cyclotron resonance. When a choice was possible, the cyclotron resonance masses were chosen in preference to those obtained from dHvA temperature dependence. Agreement between the two methods is good.

Table 1. Multiband parameters for $H \parallel \langle 100 \rangle$. Sondheimer-Wilson parameters of the magnetoconductivity and Hall conductivity of a tungsten crystal calculated from experimentally determined details of the Fermi surface of tungsten. The parameters are defined by Eqs. (1) of the text.

i	Surface Sheet	Orbit	m_i^*/m_0	H_i	H_i (Oe) for $H_6 = 170$ Oe	a_i	N_i (10^{21}cm^{-3})	$a_i n_i H_i$ (10^{21}cm^{-3})	$a_i n_i H_i$ ($10^{21} \text{Oe-cm}^{-3}$) for $H_6 = 170$ Oe
1	Hole Ellipsoid	$\rho_1 N$.25	$.25 H_6 / 2.86$	14.8	1	.234	.0204 H_6	3.47
2	Electron Jack	$\sigma \Gamma$ Neck	.25	$.25 H_6 / 2.86$	14.8	1	.35	.0304 H_6	5.17
3	Hole Ellipsoid	$\rho_2 N$.35	$.35 H_6 / 2.86$	20.4	1.03	.468	.0578 H_6	9.83
4	Electron Jack	$\pi \Gamma$ Knob	.58	$.58 H_6 / 2.86$	34.5	1.05	1.1	.234 H_6	39.8
5	Hole Octahedron	$\nu' H$	1	$H_6 / 2.86$	59.5	1.1	6.75	2.595 H_6	441.5
6	Electron Jack	$\tau \Gamma$ four ball	2.86	H_6	170	1.8	5.96	10.72 H_6	1824.
Sum							14.86,	13.65 H_6	2320.

FINAL REPORT

N71-71012

to the

NATIONAL AERONAUTICS AND SPACE ADMINISTRATION

in connection with

NASA Grant NGR 47-004-006

Part 17 of 21 Parts

Final Report
VPI&SU Project 313244

Effect of Weightlessness on the Timing of Gene Expression
and Specific Enzyme Synthesis During the Division
Cycle of Higher Organisms

by

R. R. Schmidt
Biochemistry

Virginia Polytechnic Institute & State University
Blacksburg, Virginia

December, 1970

EFFECT OF WEIGHTLESSNESS ON THE TIMING OF GENE EXPRESSION
AND SPECIFIC ENZYME SYNTHESIS DURING THE DIVISION
CYCLE OF HIGHER ORGANISMS

Animal Cell Studies:

The original aim of the research was to use an isopycnic density-gradient technique to select synchronous daughter cells of human cells (heLa cells), from asynchronously-growing populations, for use in cell cycle studies. The aim of these studies was to determine if the timing of enzyme synthesis during the cell cycle was controlled at the gene transcriptional level (a) by a "temporal mechanism" which allows genes to be transcribed only in sequence as in budding yeasts (1), or (b) by solely "oscillatory endproduct repression", the primary mode of control is non-compartmentalized cells such as bacteria (2). The final stage of research was to determine the effect of weightlessness on whichever of these control mechanisms was operative in the human cells.

Initial success was achieved in culturing the human cells, and separating daughter cells from asynchronous populations on density-gradients of Ficoll. However, success was short-lived because the daughter cells taken from these Ficoll gradients would not grow. Variations in cultural conditions (e.g., CO₂-tensions, different buffers, serum content, etc.) and gradient composition (e.g., purified Ficoll, different osmolarities of salts, etc.) failed to remedy the problem. Considerable time (several months) and expense went into this phase of the project. Because of these problems, we decided to temporarily abandon the work with human cells in

favor of working with synchronous cells of Chlorella which would grow after being subjected to Ficoll density-gradient fractionation. In a recent issue (January, 1970) of Science (Vol. 167, pp. 80-82), Fox and Pardee also reported that animal cells fractionated upon Ficoll gradients would not grow. This problem was corrected by addition of serum to the Ficoll gradients, a treatment which we did not try.

Chlorella Cell Cycle Studies:

1. The first phase of research was to determine if Chlorella, a highly compartmentalized eucaryote, regulated enzyme synthesis at the gene level by a mechanism similar to that in budding yeast (temporal mechanism) or to that in bacteria (oscillatory endproduct repression).

Experimental results: Isocitrate lyase was inducible (derepressible) throughout the cell cycle, even though its basal activity (un-induced) remained constant and then increased as a single-step at the end of the cell cycle. The rate of induction of this enzyme also increased 4x in a single-step as did the level of cellular DNA. These data indicate gene potential is continuous during the cell cycle and gene transcription with resultant enzyme synthesis is regulated by "oscillatory endproduct repression" as in bacteria.

2. The second phase was to determine the factors affecting the synthesis of enzymes which function in different subcellular organelles.

Experimental results: (a) Carboxydismutase, a chloroplast enzyme, was synthesized as a single-step during the first 0.5 of the cell cycle when neither the chloroplast nor nuclear DNA appeared to be replicating, indicating that the transcription of the structural gene of this enzyme is not obligately coupled to gene replication. Comparison of rates of

synthesis of the enzyme in daughter cells, having been synchronized by light-dark periods to those selected with Ficoll gradients from continuously-lighted cultures, indicated that the timing of synthesis of this enzyme is also probably controlled by oscillatory endproduct repression.

(b) In contrast to carboxydismutase, the cytoplasmic enzyme, aspartate transcarbamylase (ATCase), increased in a single-step paralleling the step-increase in total cellular DNA in the last 0.5 of the cell cycle. Although exogenous uracil could be utilized to support nucleic acid synthesis, added uracil failed to repress the stepwise increase in ATCase activity. The addition of 6-azauracil to cells, during the period of the cycle in which ATCase activity remained constant, resulted in a rapid decrease in ATCase activity instead of the anticipated increase due to derepression. These data suggest that ATCase synthesis may be fully-repressed during this period of the cycle. Moreover, since ATCase activity also was shown to decay rapidly in crude cell sonicates or in partially purified preparations in absence of either uridine monophosphate (UMP) or carbamylphosphate, the resultant loss of ATCase activity in vivo upon addition of 6-azauracil (a blocking agent of UMP synthesis) could be due to a reduction in endogenous UMP. The addition of cycloheximide (a protein synthesis blocking-agent) to cells during the period of constant ATCase activity, also resulted in decay of the enzyme's activity, suggesting the rate of ATCase synthesis and breakdown equaled each other during this period of the cell cycle.

3. The third phase involved the test of a proposal by Schmidt (3) which stated that the continuous but alternating exponential rates of synthesis of certain nucleotide biosynthetic enzymes during the cell cycle represented the sum of activities of isoenzymes synthesized in stepwise fashion at

discrete but overlapping periods of the cell cycle. To test Schmidt's model, it was decided to attempt to measure the independent activities of isoenzymes during the cell cycle to determine if synthesis of individual enzymes is indeed stepwise as proposed. Rather than try to measure the separate activities of "proposed" isoenzymes of nucleotide enzymes which would be difficult to distinguish from each other without physical separation, an attempt was made to select isoenzymes with specific cofactor or coenzyme requirements so that they could be independently assayed in the presence of each other. Reports that certain higher plants, fungi, and bacteria contain both NAD^+ - and NADP^+ -dependent glutamate dehydrogenases prompted us to determine if Chlorella might have isoenzymes of this enzyme with specific coenzyme requirements that could be employed in cell cycle studies.

Experimental results: One NADP^+ -dependent and one NAD^+ -dependent glutamate dehydrogenase were discovered in Chlorella by use of disc-gel electrophoresis. These were independently assayed during the cell cycle and were found to increase at differential rates but in approximately a stepwise manner during the cell cycle.

4. A modified procedure for measuring the level of total cellular DNA with minimum interference from non-DNA cellular components was developed.
5. A procedure for the isolation of intact chloroplasts (from Chlorella) on linear, sucrose density gradients was developed.

LITERATURE CITED

1. Tauro, P., Schweizer, E., Epstein, R., and H. O. Halvorson. In, The Cell Cycle--Gene-Enzyme Interactions (G. M. Padilla, G. L. Whitson, and I. L. Cameron, eds.), Academic Press, P.Y., pp. 101-117 (1969).
2. Donachie, W. D., and M. Masters. Ibid., pages 37-74.
3. Schmidt, R. R. Ibid., pages 159-176.

FINAL REPORT
to the
NATIONAL AERONAUTICS AND SPACE ADMINISTRATION
in connection with
NASA Grant NGR 47-004-006

N71-71018

Part 18 of 21 Parts

Final Report
VPI&SU Project 313248

Variable Parameter Network Design

by

H. VanLandingham
R. K. S. Wang
Electrical Engineering

Virginia Polytechnic Institute & State University
Blacksburg, Virginia

December, 1970

VARIABLE PARAMETER NETWORK DESIGN

Summary

The objective of this project was to develop design techniques for RC active networks which are suitable for integrated circuit construction. The principal difficulty encountered in the design of continuous-time active networks is the inaccuracy of response resulting from a combination of temperature drift, effecting a change in the gain of the active device, and sensitivity of response to the gain of the active device. Clearly, two approaches toward reduction of these inaccuracies are indicated: 1) to provide a constant temperature environment, as is commonly done, and 2) to design the network such that device gain changes do not appreciably affect the network response.

In this project the latter approach was taken toward the design of "gain insensitive" networks. The key idea to accomplish this task was to use variable-parameter elements, e.g. voltage-controlled variable resistors, in appropriate feedback configurations to compensate for active device variations.

Introduction

The advent of integrated circuit techniques has given a great impetus to the use of active circuits. The design of these microcircuits is continually being improved, i.e. the networks are being constructed in such a manner as to be less and less sensitive to the gain variations of the active components. It was proposed in this project to investigate the feasibility of self-compensating networks through the use of FET's in appropriate feedback structures. After preliminary consideration two situations were looked at: 1) the case where a reference was provided from external circuitry, and

2) the case where a self-reference was developed using basically either thermocouple or thermister circuits. Only simple network structures were considered due to the lack of manpower available for the investigation.

Problem Investigation

After sufficient expertise has been developed in constructing basic networks with appropriate compensation, the network illustrated in Figure 1 was proposed as a solution to the gain-temperature drift.

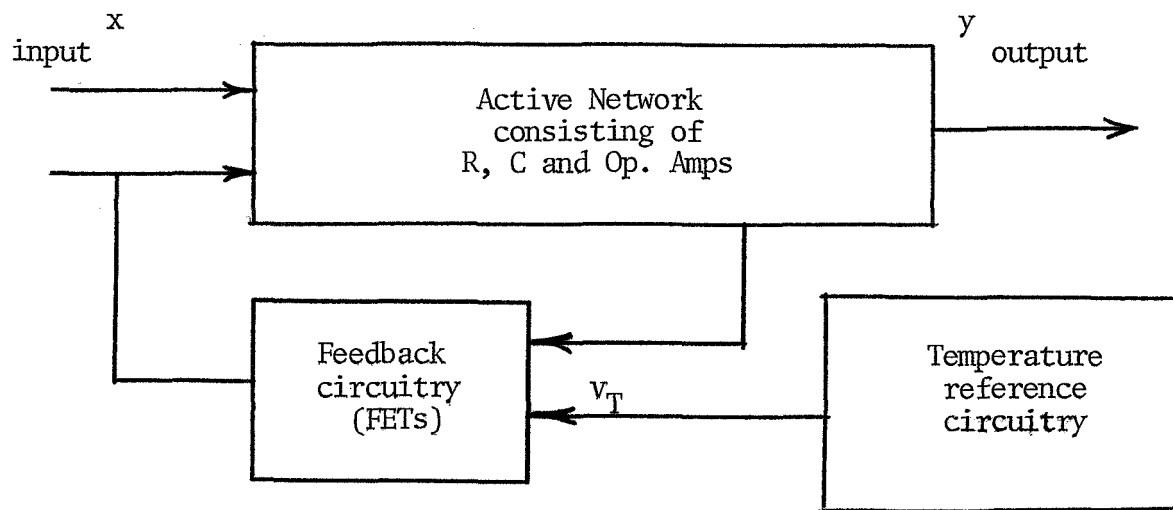


Figure 1 Self-Compensating Active Networks

The Figure 1 is almost self-explanatory, however, a few words on the operation may be necessary. The main block shown represents a general (low order) active network, such as an inverter, integrator, etc.

The feedback block represents an interconnection of voltage-variable resistors (FET's) and the main active network. This feedback circuitry has, in addition, an independent input from the third block. This input (voltage) differs from some nominal value only when the ambient temperature changes.

As such then, this voltage v_T is an encoded temperature measurement.

The operation is simply explained. When the ambient temperature changes, both v_T and the relation between x and y (input and output functions of the original active network) change in some predetermined manner. The complete design is to have the increase, say, in v_T be such that the change in the relation between x and y is adjusted back to the original relation, i.e. self-compensation.

As an example of Figure 1, consider the network of Figure 2. The ideal output is given for y ; however, for frequency variations above 10^6 Hz, the gain of the operational umplifier will influence the output $y(t)$ as well. In such a situation a given temperature change would change the relation between x and y ; therefore, if R_i could be adjusted electronically in a way to compensate for this relation change, the total network would be self-compensating or insensitive to temperature variations. The solution is then to replace R_i with an FET, whose resistance is a function of the input

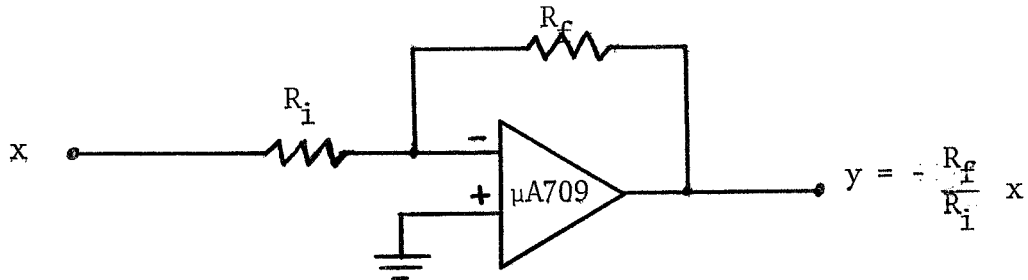


Figure 2 Simple Inverter Network

voltage. This input voltage is in turn derived from v_T of Figure 1 appropriately to return the network to its specified operation. The complete network is shown in Figure 3. Note that the equivalent gain K must be known

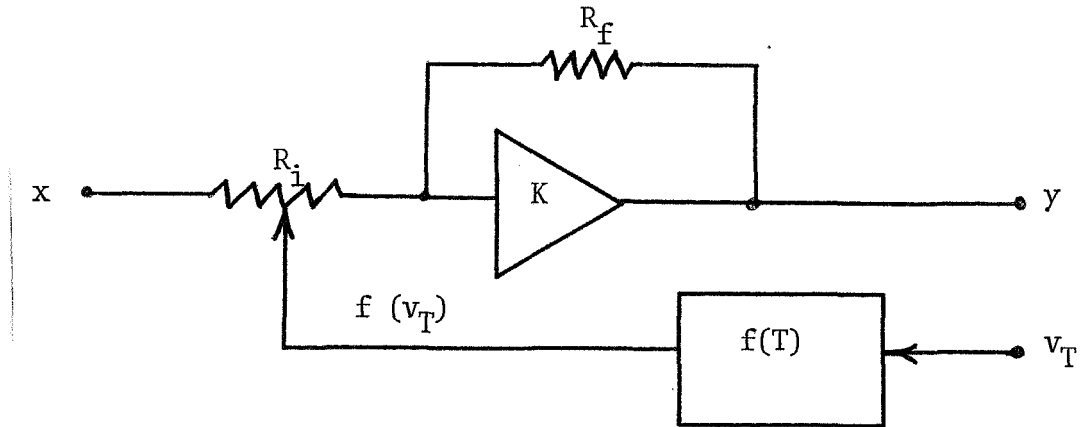


Figure 3 Compensated Inverter Circuit

as a function of the temperature. In practice, this poses no significant problem since this is a simple measurement to obtain and is closely repeated from amplifier to amplifier.

Conclusion

Although the project is continuing on an unsupported basis, the developed results obtained in the duration of the NASA support were encouraging. That is, the feasibility of such a compensating network does, in fact, significantly reduce the transfer function sensitivity to the active element gain. This has been demonstrated for only simple network configurations but these are precisely those networks which serve as building blocks for larger, more complex networks.

REFERENCES

1. Huelsman, L., Theory and Design of Active RC Circuits, McGraw-Hill, New York, 1968
2. Sallen, R. P. and Key, E. L., "A Practical Method of Designing RC Active Filters", IRE Trans. on Circuit Theory, March 1955
3. Kerwin, W. J., Ames Research Center Seminar Notes, Moffett Field, California, 1968

FINAL REPORT

N71-71019

to the

NATIONAL AERONAUTICS AND SPACE ADMINISTRATION

in connection with

NASA Grant NGR 47-004-006

Part 19 of 21 Parts

Final Report
VPI&SU Project 313245

Normal Flora of the Adult Human

by

J. L. Johnson
W. E. C. Moore
Anaerobic Laboratory

Virginia Polytechnic Institute & State University
Blacksburg, Virginia

December, 1970

NORMAL FLORA OF THE ADULT HUMAN

The purpose of this research was to determine the number of distinct types of anaerobic diphtheroids (proprionibacteria) that commonly occur as members of the normal flora of the human body.

There is a range of phenotypic variation among strains of anaerobic diphtheroids that are frequently found on the skin and in the intestinal tract of clinically health individuals. Very similar organisms are found in soft tissue infections of the brain, lung, and other body organs or blood, sometimes as the only species present. Several well-documented cases demonstrate that these organisms can be primary pathogens, although the conditions under which they infect and the possible genetic differences between pathogenic strains and normal flora strains were unknown.

Manned space flight requires modification of environmental conditions and changes in sanitation practices. Resulting changes in normal bacterial flora present potential health problems, some of which have been indicated in earth-bound chamber studies. Therefore, it was desirable to determine whether normal flora organisms of this group are the same as those that are associated with infections. Available phenotypic data were insufficient for this determination because pathogenicity was not clearly correlated with any individual phenotypic characteristics of the strains.

The results of genetic studies on over 80 strains of organisms in this group are summarized in Table 1. DNA was isolated from each strain and the genetic

Relative similarity of DNA preparations of propionibacteria

Competitor DNA from strains that conform to previous descriptions of	Reference DNA from strains of							G + C % of DNA (by thermal melting point)
	<i>P. freudenreichii</i>	<i>P. jensenii</i>	<i>P. thoenii</i>	<i>P. acidipropionici</i>	<i>P. acnes</i>	<i>P. avidum</i>	<i>P. granulatum</i>	
<i>P. freudenreichii</i>	85-*	< 40	< 40	< 40	< 20	< 20	< 20	66
<i>P. shermanii</i>	100							
<i>P. jensenii</i>								
<i>P. raffinosaceum</i>		85-						
<i>P. peterssonii</i>	< 40	100	50	< 40	< 20	< 20	< 20	66
<i>P. technicum</i>								
<i>P. zeae</i>		78						
<i>P. thoenii</i>	< 40	50	85-	< 40	< 20	< 20	< 20	65
<i>P. rubrum</i>			100					
<i>P. acidipropionici</i>	< 40	< 40	< 40	85-	< 20	< 20	< 20	65
<i>P. arabinosum</i>				100				
<i>P. acnes</i>	< 20	< 20	< 20	< 20	90-100	50	< 20	59
<i>P. avidum</i>	< 20	< 20	< 20	< 20	50	85-100	< 20	62
<i>P. granulatum</i>	< 20	< 20	< 20	< 20	< 20	< 20	85-100	63

* relative similarity value. The relative similarity value expresses (in per cent) the relative effectiveness of unlabeled DNA fragments from a competitor strain (as compared with the effectiveness of DNA fragments from the homologus [reference] strain) to inhibit duplex formation between immobilized reference DNA and labeled (reference) DNA fragments.

similarity among the strains was determined by competitive recombination experiments as described in earlier reports.

These data demonstrate that among the range of phenotypic variants there are seven distinct genetic groups (species). Within each of these genetically distinct species there is a range of phenotypic variants that has led to confusion and has made interpretation of previous information difficult.

As a result of this work, we found that

1) 6-8 previously described "species" are actually Propionibacterium acnes

2) Four, genetically distinct species, P. acnes, P. avidum, P. granulosum, and P. jensenii are associated with the human body [some microbiologists have reported that only P. acnes is associated with the body.] The strains from infections are genetically like those from the normal flora.

3) Three species in this genus, P. freudenreichii, P. thoenii, and P. acidipropionici, have not been found associated with the human body -- they are found primarily in dairy products.

We have correlated certain phenotypic properties with the individual genetic groups and can now differentiate the species with a high degree of accuracy on the basis of these properties. This information has been prepared for publication in the 8th edition of Bergey's Manual of Determinative Bacteriology.

In related work, we have found that there are two major serologic groups of the species P. acnes. Strains in this group differ in cell wall composition and can be differentiated with fair reliability on the basis of commonly available phenotypic tests.

In summary, we have demonstrated that there are four distinct species of propionibacteria that are found as members of the normal skin or intestinal flora. These organisms are the same as those associated with human infections, sometimes as the only organism present. Phenotypic characteristics that differentiate the genetic groups have been defined. Thus for the first time, changes in numbers of these organisms on the skin or in the intestinal tract can be interpreted on an accurate basis. Such changes may occur as a result of modified metabolic activity or modified sanitation practices and do concern potential health problems.

EFFECTS OF BEHAVIORAL RESPONDING ON SKIN CONDUCTANCE LEVEL¹

JOSEPH GERMANA

Virginia Polytechnic Institute, Blacksburg, Va

Summary.—The effects of behavioral response requirements on skin conductance level (SCL) were studied. Initial Ss were placed in either a "non-respond" (NR) or a "respond" (R) condition. No clear effects were observed other than large differences in individual response to both conditions. Subsequent use of a within-Ss replication design showed, however, that behavioral requirements have a tonic effect on SCL and that anticipatory changes in SCL may occur prior to the R condition. The results support the hypothesis that autonomic and behavioral events are essentially integrated and, in addition, suggest the efficacy of the within-Ss replication design in treating individual differences.

A central assumption underlying psychophysiological research is that there exists some essential, meaningful basis for correlated physiological-behavioral activity; that there exists, for example, a fundamental neurophysiological integration of autonomic and somatic events. Support for this assumption has been provided by neurophysiologists (cf. Gellhorn, 1967) and by psychophysiologicalists (cf. Germana, 1969).

Recent studies conducted in this laboratory (Germana, 1968; Germana & Chernault, 1968) have attempted to investigate the fundamental nature of autonomic-behavioral correlation. We have been attempting, in a sense, to "strain" this correlation by manipulating *elemental* behaviors in human Ss. Behaviors such as single or multiple finger-movement and number-naming are regarded as elemental to the extent that they are discrete behavioral events which probably involve minimal cognitive and emotional process. The results of these studies support the view that autonomic and behavioral activities are highly correlated in a wide variety of situations including those involving elemental behavior.

Germana (1968) has found, for example, that instructed changes in these kinds of behavior (e.g., a change in the number of required finger movements) may be as effective as stimulus novelty in producing re-emergence of the orienting reflex. In another study, we investigated GSRs to signal and non-signal stimuli (Germana & Chernault, 1969). Employing the elemental behaviors mentioned above, it was found that signal stimuli (those with instructed behavioral associates) produced GSR patterns characterized by multiphasic activity (superimposed responses) and by a persistence or tonic feature (longer re-

¹This research was supported by a grant from the National Aeronautics and Space Administration, NGR 47-004-006, Project 313181. I thank G. Chernault for his assistance in conducting these experiments.

cruitment time). Both characteristics were subject to habituation. In contrast to this prior study, which was concerned with the "fine-grain" analysis of GSRs to signal stimuli, the present experiment was designed to investigate the effects of behavioral response requirements on skin conductance level (SCL). It represented, therefore, an attempt to study the tonic effects of behavioral involvement, "responsibility," on an autonomic measure. The study is presented through its initial failures in the hope that a methodological contribution can also be made.

METHOD

Subjects

Thirty-two male undergraduate students enrolled in an introductory psychology course participated in the study. The records of five additional Ss were discarded because of apparatus failure, previous participation in a psychophysiological study, or because of consistent failure to follow instructions.

Apparatus

A Grass Model 7 polygraph, equipped with 7P1 preamplifier, was used along with *Ag/AgCl* electrodes and K-Y surgical jelly to record skin conductance. Electrodes were firmly taped to the distal phalanges of the index and ring fingers of the right hand after these surfaces had been cleansed with alcohol. Preamplifier sensitivity was maintained at a relatively low 2 mv./cm. and polygraph paper speed at a slow .25 mm./sec. for all Ss.

The experimental stimuli consisted of 35-mm. slides containing a single-digit number in written form. Additional slides were used, on occasion, to present black-out intervals and asterisk stimuli. Impulses from a Lafayette timer, occurring every 10 sec., controlled advance of a Kodak Carousel projector and were recorded on the polygraph.

General Procedure

Ss were placed in a "non-respond" (NR) and/or a "respond" (R) condition. In the NR condition, Ss were instructed to simply "attend" to the stimuli and were told that they did not have to respond behaviorally to the slides. In the R condition, Ss were required to say each number after it had been presented. They were instructed, however, not to respond while the number was being presented but were told to withhold the response for a subsequent blank, light interval. All intervals were of 10-sec. duration. This delay between stimulus and behavioral response has been employed in prior studies as a technique for separating GSRs occurring to stimulus items from those resulting from Ss' behavior. In addition, this procedure seems to be effective in extending the preparation for overt behavior.

The first eight Ss were randomly assigned to two groups. Group NR Ss were not required to respond to the number stimuli, whereas Group 1R Ss were required to say each number once during the subsequent light interval.

RESULTS AND DISCUSSION

The data showed no readily apparent differences between the two groups but did demonstrate considerable within-group variation, i.e., individual difference in response to each condition.

It was suggested that an increased "behavioral demand" might provide a clearer picture of the effects of behavioral responding on SCL. We therefore ran an additional four Ss under a multiple-response (XR) condition and simultaneously doubled the number of trials. These Ss were required to respond by saying each number five times during the subsequent blank, light interval. The results for these Ss are presented in Fig. 1. No differences were apparent between this condition and the previous conditions of the experiment but individual differences in response characteristics were, again, evident.

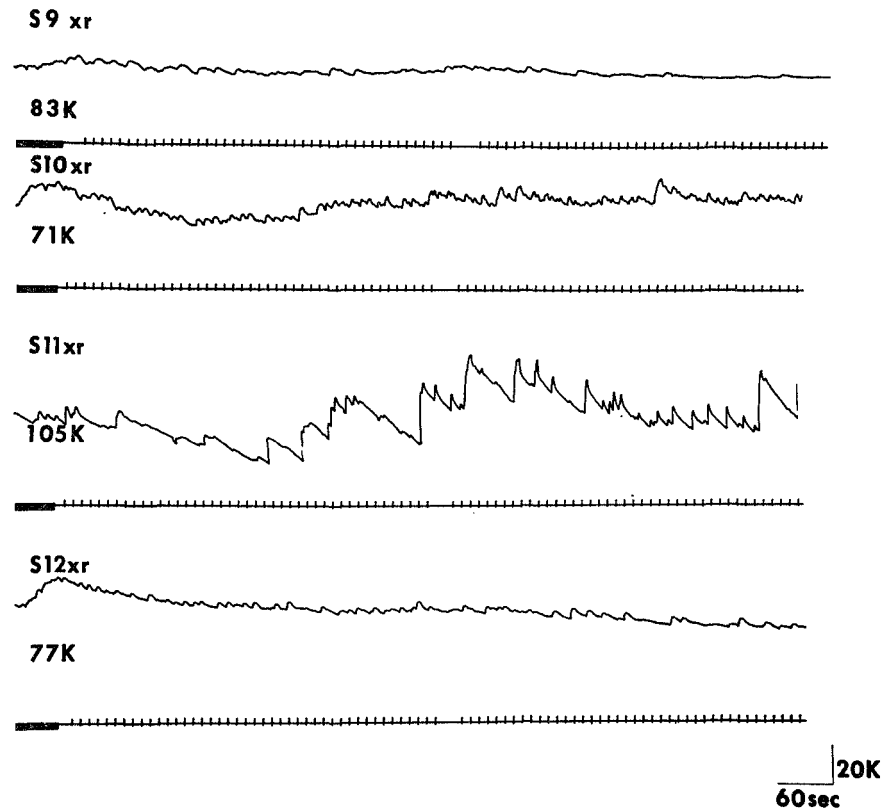


FIG. 1. Skin conductance recordings of four Ss in the "multiple response" (XR) condition. Increases in skin conductance are represented as upward deflections. Solid bar on the time line represents period of instruction and subsequent event marks denote slide tray advances. Resistance level at the beginning of the instructions is noted for each S. Calibration provided at lower right.

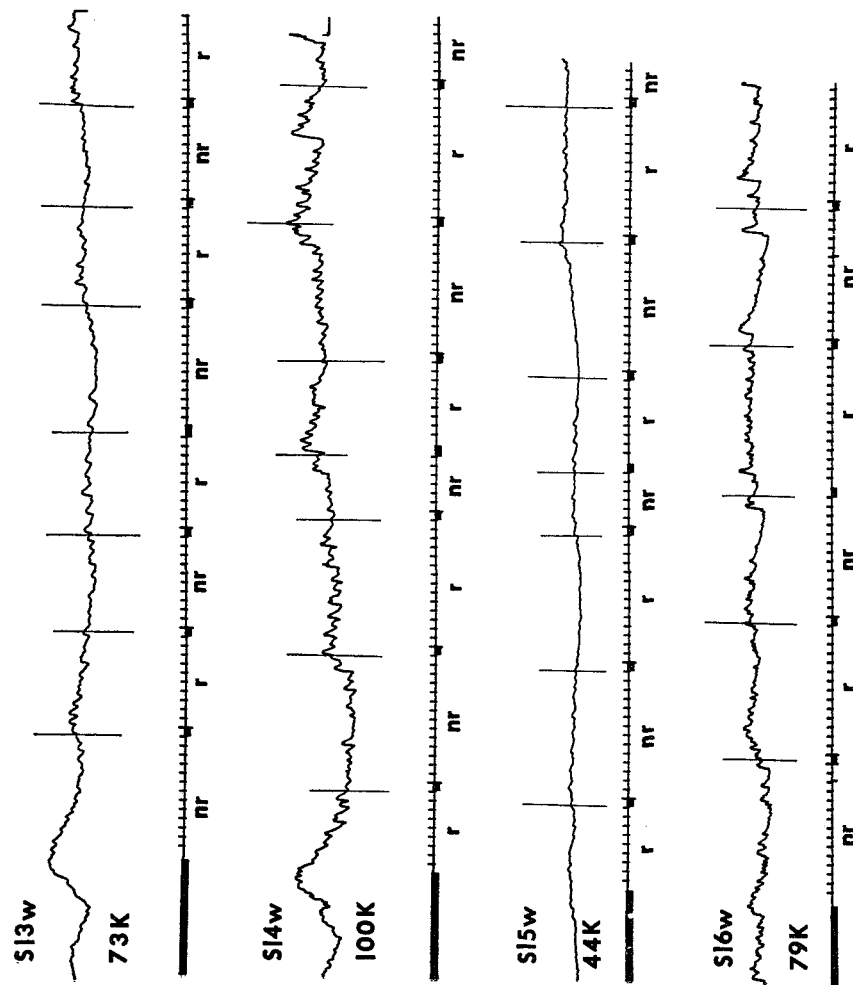


FIG. 2. Skin conductance recordings of four Ss employed in a within-Ss replication (W) design. Ss were alternately placed in the "non-respond" (NR) and "respond" (R) conditions. Designations and calibration the same as in Fig. 1.

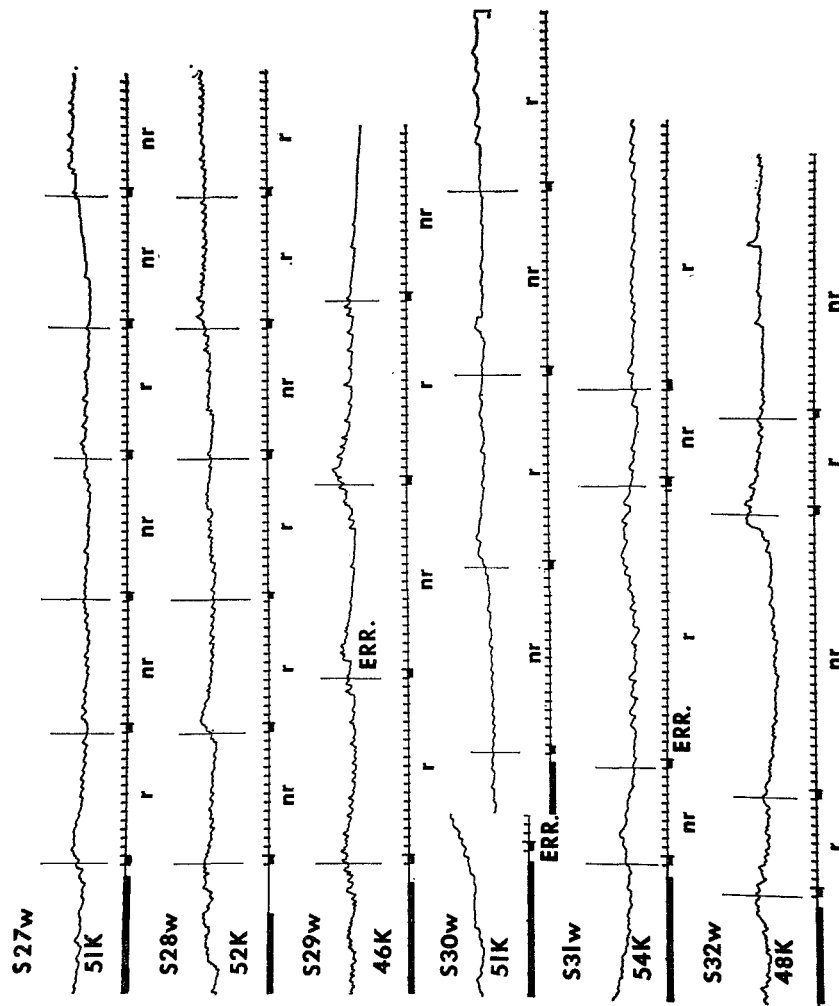


FIG. 3. Skin conductance recordings of six Ss employed in a within-Ss replication (W) design. Ss were administered "non-respond" (NR) and "respond" (R) conditions of variable characteristics. Designations and calibration same as in Fig. 1. Behavioral errors are designated "ERR."

The magnitude of these individual differences suggested still another research strategy—a within-Ss replication design in which each S was administered both NR and R conditions several times. Fig. 2 presents the results of four Ss who were alternately assigned to the NR and R conditions. Ss were instructed to respond by saying each number five times when in the R condition and to simply “attend” to the stimuli when in the NR condition. The two conditions were signalled by black-out and asterisk stimuli which preceded each series of number slides. The significance of the black-out and asterisk stimuli was changed between Ss.

It is evident that the R condition tended to elevate SCLs and contrasted with the NR condition in this respect. The tonic effect of behavioral responding is most clearly demonstrated in the records of the three Ss (S_{13} , S_{14} , S_{16}) who began the experiment with higher resistance levels. On several occasions, anticipatory or preparatory changes toward increased SCL developed during the later portions of the NR condition.

These successful demonstrations led to a reexamination of the effects of behavioral responding on the SCLs of 10 Ss who were administered only the R condition. A variety of procedures was employed: direct rather than delayed responding to the stimuli, a shorter, 5-sec. inter-stimulus interval, different behavioral responses, and an increased number of trials. The results, however, were comparable to those presented in Fig. 1, i.e., the only clear effect was the marked difference in individual response.

Lastly, six Ss were run under the within-Ss replication design: two Ss (S_{27} and S_{28}) were administered consecutive NR or R conditions, two Ss (S_{29} and S_{30}), conditions of longer duration, and two Ss (S_{31} and S_{32}), conditions of variable duration. Again, the two conditions were signalled by the black-out and asterisk stimuli and the R condition required S to say each number five times.

The results of these treatments are presented in Fig. 3. It was again generally apparent that the R condition produced a tonic effect on SCL. Anticipatory changes in SCL occurred but were not generally characteristic. It may be suggested that the variable nature of the treatments retarded the development of these preparatory effects.

Also of interest are those instances in which Ss committed behavioral errors (labeled ERR). S_{29} continued to respond during the initial period of the first NR condition, S_{30} made a similar error of commission and had to be re-instructed, and S_{31} failed to respond on the initial trials of the first R condition. In each case, the behavioral error was accompanied by the anticipated change in SCL.

Conclusion

The results of the study obtained under the within-Ss replication design indicate that behavioral response requirements have a tonic effect on SCL and

that preparatory changes in SCL may be demonstrated when fixed orders and intervals are used between NR and R conditions. These findings, therefore, provide additional support for the general hypothesis that autonomic and behavioral activities are essentially integrated and that this integration is not reserved for emergency or emotion-provoking situations. Instead, the correlation of autonomic and behavioral events may be demonstrated when elemental behaviors are required.

Secondly, the present findings suggest that the within-Ss replication design may be an effective technique for treating individual difference effects and should, perhaps, be employed more frequently. Questions concerning the power and generality of results provided by this and related techniques as well as questions concerning their applicability have been thoroughly treated by Sidman (1960).

REFERENCES

- GELLHORN, E. *Principles of autonomic-somatic integrations*. Minneapolis: Univer. of Minnesota Press, 1967.
- GERMANA, J. Response characteristics and the orienting reflex. *Journal of Experimental Psychology*, 1968, 78, 610-616.
- GERMANA, J. Central efferent processes and autonomic-behavioral integration. *Psychophysiology*, 1969, in press.
- GERMANA, J., & CHERNAULT, G. Patterns of galvanic skin responses to signal and non-signal stimuli. *Psychophysiology*, 1968, 5, 284-292.
- SIDMAN, M. *Tactics of scientific research*. New York: Basic Books, 1960.

Accepted March 31, 1969.

N71-71020

FINAL REPORT
to the
NATIONAL AERONAUTICS AND SPACE ADMINISTRATION
in connection with
NASA Grant NGR 47-004-006

Part 20 of 21 Parts

Final Report
VPI&SU Project 313181

Psychophysiological Correlates

by

J. Germana
Psychology

Virginia Polytechnic Institute & State University
Blacksburg, Virginia

December, 1970

RESPONSE CHARACTERISTICS AND THE ORIENTING REFLEX¹

JOSEPH GERMANA

Virginia Polytechnic Institute

Habituation of the orienting reflex (OR) is typically treated as a kind of stimulus learning. The results of 3 experiments employing the GSR indicate, however, that (a) stimuli which have behavioral associates produce greater ORs than those which do not, (b) "new" behavioral associations produce greater ORs than "old" associations, i.e., selective habituation occurs to response characteristics and, (c) level of ORs across habituation trials is a direct function of the amount of response information to be encoded. It appears, therefore, that the "neuronal model" of a stimulus includes the characteristics of associated responses.

The orienting reflex (OR) constitutes a diffuse complex of somatomotor (e.g., postural) and autonomic (e.g., cardiovascular, sense organ) responses with three defining characteristics: (a) The adequate stimulus for the OR is one which is, to some extent, "new" or "novel," i.e., the OR occurs in response to stimuli which have not been repeatedly presented to the organism. (b) The OR is a nonspecific reaction, i.e., it occurs in response to changes, of at least "just noticeable" value, in any parameter (frequency, amplitude, duration, rate of presentation) of a stimulus belonging to any sense modality. (c) The OR selectively habituates or extinguishes to a stimulus which is repeatedly presented. *Selective* habituation is demonstrated by the reemergence of the OR which occurs when one of the parameters of a previously habituated stimulus is changed.

¹The research reported here was supported by a research grant, Project No. 31687, from the National Aeronautics and Space Administration. The author wishes to thank G. Chernault and S. Klein for their assistance in conducting the experiments. Major portions of this paper were presented at the meeting of the Pavlovian Society of North America, Baltimore, September 6, 1968.

Pavlov (1927) noted the biological significance of the OR and further observed that this reaction plays an important role in the initial formation of conditioned responses, and that the OR to extraneous stimuli is capable of temporarily inhibiting a well-established conditioned response and disinhibiting one which is in the process of extinction.

In addition to the importance which results from its complex interactions with conditioned responses, the OR possesses independent significance since habituation may, in itself, be viewed as a simple form of learning (Hernandez-Peon & Brust-Carmona, 1961; Thorpe, 1963). The response changes (progressive decrements) which take place as a function of repeated exposure to the stimulus cannot be ascribed to fatigue or receptor adaptation. Highly selective or specific habituation argues against both possibilities. The operations and consequent response changes which define OR habituation and reemergence would seem to necessitate at least the temporary storage of relevant information within the central nervous system.

These last considerations have led several investigators (cf. Lynn, 1966)

to speculate on the central neural systems which are responsible for the production and habituation of the OR. Because of their circumscribed experimental operations and probably because Pavlov originally described the OR as the "what is it?" reflex, these investigators have limited their attempts to neural schemata which are more or less capable of handling the *stimulus* learning features of OR habituation.

Sokolov (1960, 1963a, 1963b), e.g., has suggested a central "modeling system" which acts in functional parallel with both the classical afferent system and the amplifying system responsible for the production of the OR. Most or all of the discriminable aspects of the stimulus are encoded within this system, i.e., a "neuronal model" of the stimulus is constructed on the basis of repeated presentation of the stimulus during the habituation series. When a stimulus coincides with a previously established model, inhibitory impulses are sent from the modeling to the amplifying system, attenuating the response of the last system to the extent that concordance has been achieved between model and stimulus.

Although Sokolov's conceptualization is capable of interpreting those features of the extensive OR data which demonstrate that a kind of stimulus learning takes place during habituation, his concept of the "neuronal model" is limited to this extent. Other investigators (Berlyne, 1960; Kvasov & Korovina, 1965) have suggested, however, that at least some of the OR components (increments in general muscle tension, postural responses) should properly be viewed as constituting the question "what's to be done?" This view suggests that those central structures which are directly or indirectly responsible for the production of the OR may be as concerned with

possible behavioral requirements as they are with purely sensory events. In addition, Anokhin (1961, 1965) has proposed that a model of specific behaviors and associated reinforcement outcomes is constructed on the basis of the afferent feedback which is produced by behavior and the results of behavior.

It is interesting to note that although Sokolov (1963b) has provided a substantial amount of data concerning the effects of endowing stimuli with "signal significance," i.e., pairing them with behavioral responses, he has not included response characteristics in his conception of the "neuronal model" of the stimulus.²

The research to be reported was designed to systematically explore the possibility that the "neuronal model" of a stimulus includes not only the parameters of the stimulus, but also the characteristics of associated responses.

An important methodological feature of these studies should be noted here. In all three studies, Ss were instructed not to respond behaviorally during the presentation of the experimental stimuli but were provided with a subsequent blank or "response" interval during which they performed any instructed behavior. Both the stimulus and response periods were of 10-sec. duration. This procedure was employed to insure that the GSRs to the experimental stimuli would clearly antecede the behavioral responses and would, therefore, be unconfounded with the autonomic activity that directly accompanies overt behavioral responding.

² Sokolov (1963b, p. 287) defines the neuronal model as "a certain cell system whereby the information is stored concerning the properties of a stimulus which has been applied many times."

EXPERIMENT I

The first study in the series explored the effects of a behavioral association on the ORs to stimuli and, in addition, generally tested for selective habituation to response characteristics.

Method

Subjects.—Thirty-two male and female undergraduates enrolled in an introductory psychology course volunteered to participate in the study.

Apparatus.—A Grass Model 7 polygraph, equipped with 7P5 preamplifier, was used along with Ag/AgCl electrodes and EC-2 electrode cream to record GSRs.

The experimental stimuli consisted of 35-mm. slides containing any single number from one to eight in written form. The stimuli were presented by a Kodak Carousel projector and the duration of stimulus and response intervals were determined at 10 sec. each by a Lafayette timer. Impulses from the timer were automatically recorded by the polygraph.

Procedure.—One-half of the Ss was required to respond, in Stage I, by simply saying the odd numbers after they had been presented. They were instructed not to repeat the even numbers. The remaining 16 Ss were required to respond to the even but not to the odd numbers. Again, Ss were instructed not to respond while the stimuli were being presented. Four odd and four even slides were presented.

In Stage II, a different random order of the eight stimuli was used. One-half of each Stage I group ($N=8$) was instructed to respond to the class of stimuli (odd or even numbers) to which they had responded in Stage I, whereas the remaining Ss were instructed to respond to the class of stimuli to which they had not been responding. These constituted the unswitched (U) and switched (S) groups, respectively.

Results and Discussion

The GSRs to the 16 experimental stimuli were measured in change in conductance units. Change scores were computed as the difference between the conductance level immediately preceding the GSR and the peak amplitude value of the GSR. Only resistance changes 500 ohms or greater were considered and this same

criterion was used to separate multiple GSRs, i.e., if the first GSR was separated from a second response by an *increase* in resistance greater than 500 ohms, the two responses were considered as different and only the magnitude of the first response was computed. Only GSRs with an onset latency of 1–5 sec. were used. This last procedure, combined with the multiple-response cutoff criterion, provided some assurance that only initial responses to the stimuli were investigated. These might reasonably be identified as ORs.

The square root transformation was applied to the change in conductance scores.

The results of this study are presented in Fig. 1. It is apparent that the respond (R) stimuli, those which were followed by simple behavioral responses, consistently produced greater GSRs than the nonrespond (NR) stimuli. In addition to demonstrating the R–NR and habituation or trials effects, the Stage II data indicated that the GSRs to R and NR stimuli across trials were, in part, determined by the Group conditions, i.e., whether Ss were producing “new” or “old” responses.

A Groups (S–US) \times Response Condition (R–NR) \times Trials analysis of the Stage I data revealed significant R–NR, $F(1, 30) = .451/.077 = 5.86$, $p < .05$, and Trials, $F(3, 90) = 2.493/.063 = 39.57$, $p < .001$, effects.

The same analysis applied to the Stage II data yielded significant R–NR, $F(1, 30) = .310/.050 = 6.20$, $p < .05$, Trials, $F(3, 90) = .353/.071 = 4.97$, $p < .01$, and Groups \times Response Condition \times Trials, $F(3, 90) = .414/.080 = 5.18$, $p < .01$, effects.

To further test the hypothesis that the Stage II, Trial 1 R–GSRs of the S group constituted a significant increment over their terminal R–GSRs of Stage I, a t test was applied to the

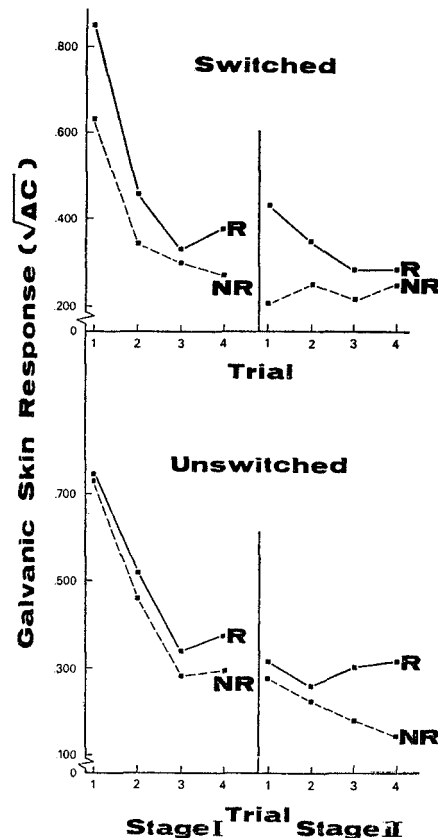


FIG. 1. Mean GSRs to respond (R) and nonrespond (NR) stimuli across habituation trials. (In Stage II, switched Ss performed responses different from those of Stage I, whereas unswitched Ss performed the same responses in both stages.)

difference between these means, yielding a paired $t(15) = .259/.094 = 2.76$, $p < .01$. The same test carried out on the US means resulted in a $t(15) = .044/.094 = .47$.

The latter finding suggests, in a general way, that selective habituation occurs to response characteristics.

EXPERIMENT II

The second experiment investigated the relationship between degree of Stage II response change and the extent of reemergence of the OR. It constituted, therefore, a further test of

selective habituation to response characteristics.

Method

Subjects.—Thirty male and female undergraduates from an introductory psychology course volunteered to participate.

Apparatus.—The same apparatus was used to measure GSRs, to present experimental stimuli, and to time the stimulus and response intervals.

An additional polygraph channel, equipped with the Grass 7P1 preamplifier, was used along with the SP1 accelerometer to measure the finger movement responses which were the instructed behavior in this study.

Alternating light and dark intervals of 10 sec. each constituted the stimulus and response intervals, respectively.

Procedure.—In Stage I, one-half of the Ss was instructed to respond to each light stimulus by making one up-down movement of the left index finger during the subsequent dark or response interval. The remaining 15 Ss were instructed to respond by producing 10 such movements. The accelerometer, taped to the left index finger, recorded these finger movements.

Subsequent to eight Stage I trials, Ss were instructed to respond with either 1, 5, or 10 movements. The instructions differed only in terms of the number of requested responses. One-third ($N = 5$) of each Stage I group was instructed to make 1 response, one-third was told to produce 5 movements, and one-third was instructed to make 10 responses. Thus, three Stage II conditions were established: 10 Ss continued to respond with the Stage I response (1 or 10 movements); 10 Ss were requested to make a mean response change of 4.5 movements (changes from 1 to 5 or 10 to 5 responses); and 10 Ss were instructed to make a response change of 9 movements (1 to 10 or 10 to 1). In this way, Stage I response frequency was counterbalanced and a direct test of the effects of response change on the reemergence of the OR on two Stage II trials was afforded.

Results and Discussion

The results of this study are presented in Fig. 2. It is apparent that Stage I response frequency did not affect GSR magnitude in any consistent fashion and that habituation took place across trials. A Groups \times Trials analysis revealed only a significant

Trials or habituation effect, $F(7, 196) = .349/.087 = 4.01$, $p < .001$.

The data for the two Stage II trials demonstrated graded reemergence of the OR on the basis of degree of Response Change. A Stage I Frequency \times Response Change \times Trials analysis of the Stage II data yielded significant Response Change, $F(2, 24) = .920/.262 = 3.51$, $p < .05$, and Trials, $F(1, 24) = .173/.054 = 3.20$, $p < .10$, effects.

These findings suggest that highly selective habituation occurs to response characteristics and that the central structures which are responsible for the production and habituation of the OR are sensitive to response as well as stimulus parameters.

EXPERIMENT III

If habituation may be regarded as the result of progressive encoding of both stimulus and response characteristics, then it would follow that habituation can be affected by the amount of

stimulus and response information that will be encoded. The last experiment attempted to manipulate the overall level of ORs across habituation trials by varying the amount of response information to be encoded.

Method

Subjects.—Forty male and female students volunteered.

Procedure.—The Ss were randomly assigned to four groups of 10 Ss each: Group 0 Ss were not requested to make any response to the light stimulus; Group 5 Ss were instructed to respond by saying any number from 1 to 5 (one-half was requested to say any number from 6 to 10), but were not to repeat the same number on two successive trials; Group 10 Ss were required to respond by saying any number from 1 to 10, also with the provision that they were not to make the same response on any two successive trials. A last 10M group was added to investigate the effects of mixing response classes. These Ss were required to respond by saying any number from 1 to 5 (or 6 to 10) or the letters A to E, with the same restriction on successive repetition. Again, all Ss were told not to make the instructed response during the 10-sec. stimulus light period but were to withhold their responses for the 10-sec. dark response interval. The GSRs of all Ss to the signal light stimuli were measured on 10 habituation trials.

Results and Discussion

Figure 3 shows that although habituation took place for all groups, the overall level of GSRs across the habituation series was a positive function of the amount of response information.

A Groups \times Trials analysis of variance was applied to these data. Significant Groups, $F(3, 36) = 1.777/.579 = 3.07$, $p < .05$, and Trials, $F(9, 324) = .895/.092 = 9.73$, $p < .001$, effects were obtained.

A Duncan multiple-range test (Edwards, 1960) applied to the group means revealed that only the 10–10M difference was not significant beyond the .05 level.

It should be noted that an interpre-

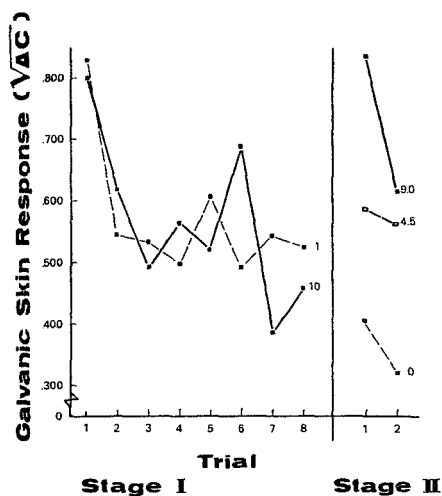


FIG. 2. Mean GSRs across habituation trials of Ss performing either 1 or 10 finger movements in Stage I and requested to make a mean response change of 0, 4.5, or 9.0 movements in Stage II.

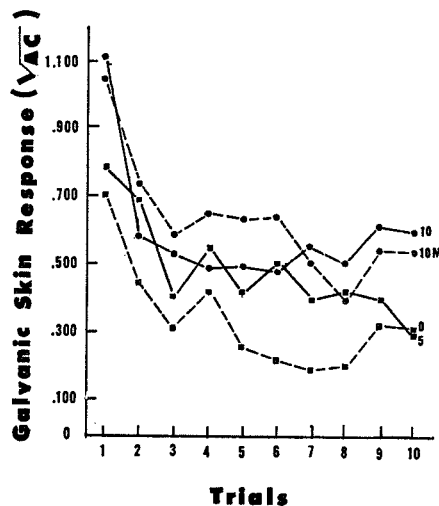


FIG. 3. Mean GSRs across habituation trials of Ss performing no responses (0), 1 of 5 possible responses (5), 1 of 10 possible responses (10), or 1 of 10 possible mixed-class responses (10M), on each trial.

tation other than that based on response encoding may be applied to these results. It may be suggested, e.g., that level of GSRs across habituation trials primarily reflects the generality of the preparation to respond behaviorally. The Ss in Group 0 were not required to make any preparation for overt behavior, Group 5 Ss, on the other hand, were required to prepare for one of five *possible* responses, while both the 10 and 10M Ss were required to make a preparation for 1 of 10 possible responses. The hypothesis that magnitude of GSR in the present situation may have been affected by the degree of experienced "responsibility," i.e., by the degree of generality of behavioral preparations, receives support from the fact that Trial 1 GSRs show apparent group differences in Exp. III but not in Exp. II.

Additional support for such an interpretation may be found in the ancillary observation that "response" requirements typically resulted in postinstruc-

tional shifts in base levels toward increased skin conductance whereas the "no response" condition did so to a lesser extent. It was primarily for this reason that the square root transformation was performed, since this treatment operates better than any other nonempirical transformation to free GSRs from base-line influences.

GENERAL DISCUSSION

Whenever it can be demonstrated that a system is capable of detecting differences between past and present events, then it would seem necessary to conclude: (a) that the system is receiving information concerning the present event; (b) that it already possesses information, in some form, of the past event; and (c) that it possesses some mode of comparison. If it is necessary, then, to postulate at least temporary storage of stimulus parameters in order to explain the demonstration of habituation which is selective to those characteristics, then it is equally necessary, on the basis of the data reported here, to postulate the encoding of response characteristics. It appears, therefore, that the "neuronal model" of a stimulus must include the characteristics of associated responses.

A peculiar feature of this last statement is the implication that progressive S-R learning (habituation) involving molar behavior may be shown to have occurred in the absence of any modification of that behavior *beyond its original production*. The results of Exp. II demonstrated, e.g., that Ss progressively associated a particular response to the experimental stimulus in Stage I. That such learning had, in fact, taken place was demonstrated by Stage I habituation and by the graded reemergence of the OR in Stage II when Ss were asked to produce a different behavior to the stimulus. The behavioral responses of Stage I, however, were invariant in their "correctness" from Trial 1 to Trial 8, providing no indication of a trial-by-trial learning.

Returning to the suggestion that many of the autonomic-somatic components of

the OR may, either directly or indirectly, represent the question "what's to be done?" it may be stated that the central structures responsible for the production of the OR are as concerned with response characteristics as they are with stimulus parameters. This rephrasing of the "what is it?" question is reminiscent of Sperry's (1952) treatment of perception and his encouragement to view the brain as a mechanism for governing motor activity.

REFERENCES

- ANOKHIN, P. K. A new conception of the physiological architecture of conditioned reflex. In J. F. Delafresnaye (Ed.), *Brain mechanisms and learning*. Oxford: Blackwell, 1961.
- ANOKHIN, P. K. The role of the orienting-exploratory reaction in the formation of the conditioned reflex. In L. G. Voronin et al. (Eds.), *Orienting reflex and exploratory behavior*. Washington: American Institute of Biological Sciences, 1965.
- BERLYNE, D. E. *Conflict, arousal, and curiosity*. New York: McGraw-Hill, 1960.
- EDWARDS, A. L. *Experimental design in psychological research*. New York: Holt, Rinehart & Winston, 1960.
- HERNANDEZ-PEON, R., & BRUST-CARMONA, H. Functional role of subcortical structures in habituation and conditioning. In J. F. Delafresnaye (Ed.), *Brain mechanisms and learning*. Oxford: Blackwell, 1961.
- KVASOV, D. G., & KOROVINA, M. V. The reflex organization of perception and the propriomuscular apparatus of the analyzers (of the sense organs). In L. G. Voronin et al. (Eds.), *Orienting reflex and exploratory behavior*. Washington: American Institute of Biological Sciences, 1965.
- LYNN, R. *Attention, arousal and the orientation reaction*. New York: Pergamon Press, 1966.
- PAVLOV, I. P. *Conditioned reflexes*. (Anrep trans.) London: Oxford, 1927.
- SOKOLOV, E. N. Neuronal models and the orienting reflex. In M. A. Brazier (Ed.), *The central nervous system and behavior*. New York: Josiah Macy, Jr. Foundation, 1960.
- SOKOLOV, E. N. Higher nervous functions: The orienting reflex. *Annual Review of Physiology*, 1963, 25, 545-580. (a)
- SOKOLOV, E. N. *Perception and the conditioned reflex*. New York: Pergamon Press, 1963. (b)
- SPERRY, R. W. Neurology and the mind-brain problem. *American Scientist*, 1952, 40, 291-312.
- THORPE, W. H. *Learning and instinct in animals*. London: Methuen, 1963.

(Received December 9, 1967)

PATTERNS OF GALVANIC SKIN RESPONSES TO SIGNAL AND NON-SIGNAL STIMULI

JOSEPH GERMANA AND GEORGE CHERNAULT

Virginia Polytechnic Institute

ABSTRACT

Two studies investigating the specific features of galvanic skin responses (GSRs) to signal and non-signal stimuli are reported. The results of Exp. I indicate that stimuli which have instructed behavioral associates (signal significance) produce GSRs which are both multiphasic and relatively persistent in nature. Multiple GSRs are produced by the initial presentation of a signal stimulus and the persistence of the overall response appears to have at least a short-term effect on baseline. Exp. II was designed to investigate the possible independence of these two characteristics through the manipulation of response certainty. The results suggest that multiplicity and persistence may be separable features of the response to signal stimuli in which the latter may be a correlate of response novelty.

DESCRIPTORS: Galvanic skin response (GSR), Signal and non-signal stimuli, Response novelty. (J. Germana)

In his pioneering brain stimulation studies, Hess (1954) concluded that diencephalic organization is best described in terms of the integrated activity of the autonomic and somatic nervous systems. The frequent correlation of somatic and autonomic responses led him to suggest the terms, "ergotropic" and "trophotropic" for the integration of behavioral responses with sympathetic and parasympathetic activities, respectively.

Gellhorn (1967) has comprehensively reviewed the vast neuroanatomical and neurophysiological data which support the concept of autonomic-somatic integration, while various psychophysiologicalists have provided evidence of another kind through their studies of autonomic-behavioral correlations.

Ehrlich and Malmo (Ehrlich, 1960, 1964; Ehrlich & Malmo, 1965; Malmo, 1963), for example, have demonstrated high correlations between heart rate and the occurrence of operant behavioral responses. More recently, Obrist and Webb have provided evidence for an interrelationship between cardiac and somatic activities in classical (Obrist 1968; Obrist & Webb, 1967) and operant (Webb & Obrist, 1967a,b) conditioning.

MacNeilage (1966a,b) has provided data which support Jasper's (1958) earlier finding that blocking of sensorimotor and parietal electrocortical activity is related to the preparation for movement. The results of studies by

This research was supported by a grant from the National Aeronautics and Space Administration, NGR 47-004-006, Project 31687.

Address requests for reprints to: Joseph Germana, Department of Psychology, Virginia Polytechnic Institute, Blacksburg, Virginia 24061.

Campos and Johnson (Campos & Johnson, 1966, 1967; Johnson & Campos, 1967) are in acknowledged agreement.

Pursuing still another line of investigation, Germana (in press) has shown that the central structures which are responsible for the production and habituation of the orienting response are concerned not only with stimulus parameters but with *behavioral* response characteristics, as well. The findings of these experiments may be summarized in the statement that the "neuronal model" of a stimulus includes associated response characteristics.

The above studies support the view that autonomic and behavioral activities are highly integrated in a variety of situations and therefore suggest the possibility of identifying patterns of autonomic activity which reflect the organization and initiation of behavioral responses. The studies reported here were specifically designed to investigate patterns of GSRs to stimuli which do and do not possess instructed behavioral associates, i.e., signal and non-signal stimuli.

A general feature of these studies should be noted here. In both experiments, a procedural separation of stimulus and response events was imposed, i.e., Ss were told not to produce the instructed behavior *during* the presentation of the stimulus but were required to withhold their responses for a subsequent, "response" interval. Both intervals were of 10-sec duration. This procedure was employed to avoid the confounding of GSRs to stimulus and response events.

EXPERIMENT I

Method

Subjects. Twenty-five male and female undergraduates volunteered to participate in the study.

Apparatus. A Kodak Carousel projector was used to present the light, *stimulus* and dark, *response* intervals. A Lafayette timer delivered impulses to the projector every 10 sec.

A Grass Model 7 polygraph, equipped with the 7P1 preamplifier, was used along with Ag-AgCl electrodes and EC-2 electrode cream to record GSRs. Preamplifier sensitivity was set at .5 mv/cm for all Ss.

In addition, a Grass SP1 accelerometer was used in conjunction with the 7P5 preamplifier to record the finger movements of ten Ss.

Paper speed was always set at 2.5 mm/sec and impulses from the timer were automatically recorded on the event channel of the polygraph.

Procedure. Ten Ss were randomly assigned to the 0 Response condition—these Ss did not have to respond behaviorally to the experimental stimuli but were instructed to attend to them.

Five Ss were randomly assigned to the Number (N) Response condition. These Ss were instructed to respond by saying any number from one to ten during each response interval, with the added provision that they not make the same response on two successive trials.

An additional ten Ss were required to respond to the light stimulus by producing ten up-down movements of the left index finger (FM condition) during

the subsequent dark or response interval. The accelerometer, taped to this finger, transduced these movements. Five of these Ss made anticipatory errors on Trial 1, i.e., they made at least one finger movement during the stimulus interval; the remaining five Ss were successful in withholding their responses.

Five trials were administered to all Ss.

Treatment of the data. Polygraphic recordings of skin resistance throughout the 10-sec stimulus and response intervals were traced-out, by hand, on onion-skin paper. A common origin was taken at the onset of the stimulus. This method of analysis: permitted the "fine-grain" examination of individual skin resistance changes; provided a continuous representation, in contrast to an arbitrary time-sampling; and avoided the "averaging-out" of variable but consistent GSR features. The effects of habituation were investigated by contrasting the responses on the initial and last trials (Trials 1 and 5).

Results and Discussion

The results of the Trial 1 analysis are presented in Fig. 1. It is readily apparent that the GSRs to stimuli with signal significance (Panels C & D) are both multiphasic and relatively persistent in nature, differing from GSRs to non-signal stimuli (Panels A & B) in these two respects. It is also apparent that at least four of the five Ss in the FM condition who made an anticipatory error on Trial 1 (Panel E) did not show these characteristic GSRs. Thus, the features of GSRs to signal stimuli, presented in C & D, seem to reflect the *preparation* for, rather than the occurrence of, behavior.

The Trial 5 data are presented in Fig. 2. Again, a marked difference in GSRs to signal and non-signal stimuli may be noted. It would appear that, although there was a reduction in both the multiplicity and persistence of signal GSRs, these GSRs could still be differentiated from those occurring to non-signal stimuli. Whereas basal resistance was characteristically increasing (downward tracing) for the 0 Ss, basal levels remained around pre-stimulus level when signal stimuli were presented. It would appear, therefore, that what we have termed "response persistence" may primarily represent a baseline effect of longer duration than phasic GSRs. The possibly contradictory term, "tonic response," might best describe this effect.

It should be noted that all FM Ss were comparable on this trial, i.e., the recordings presented in Panel E are those of Ss who made an anticipatory error on Trial 1 but not on Trials 2-5.

The results of this study indicate that stimuli which possess signal significance, those that have behavioral associates, produce GSRs which are both multiphasic and persistent or tonic in nature and that, although habituation of both features may take place, these characteristics may nevertheless serve to differentiate signal and non-signal responses. It may be concluded, therefore, that the organization and initiation of behavioral responses have specific effects on GSRs.

Two major hypotheses concerning the multiphasic and tonic features of GSRs to signal stimuli may be entertained. The first hypothesis is that these two features are interdependent, in fact, inseparable insofar as persistence or tonicity is simply the end result of superimposed GSRs.

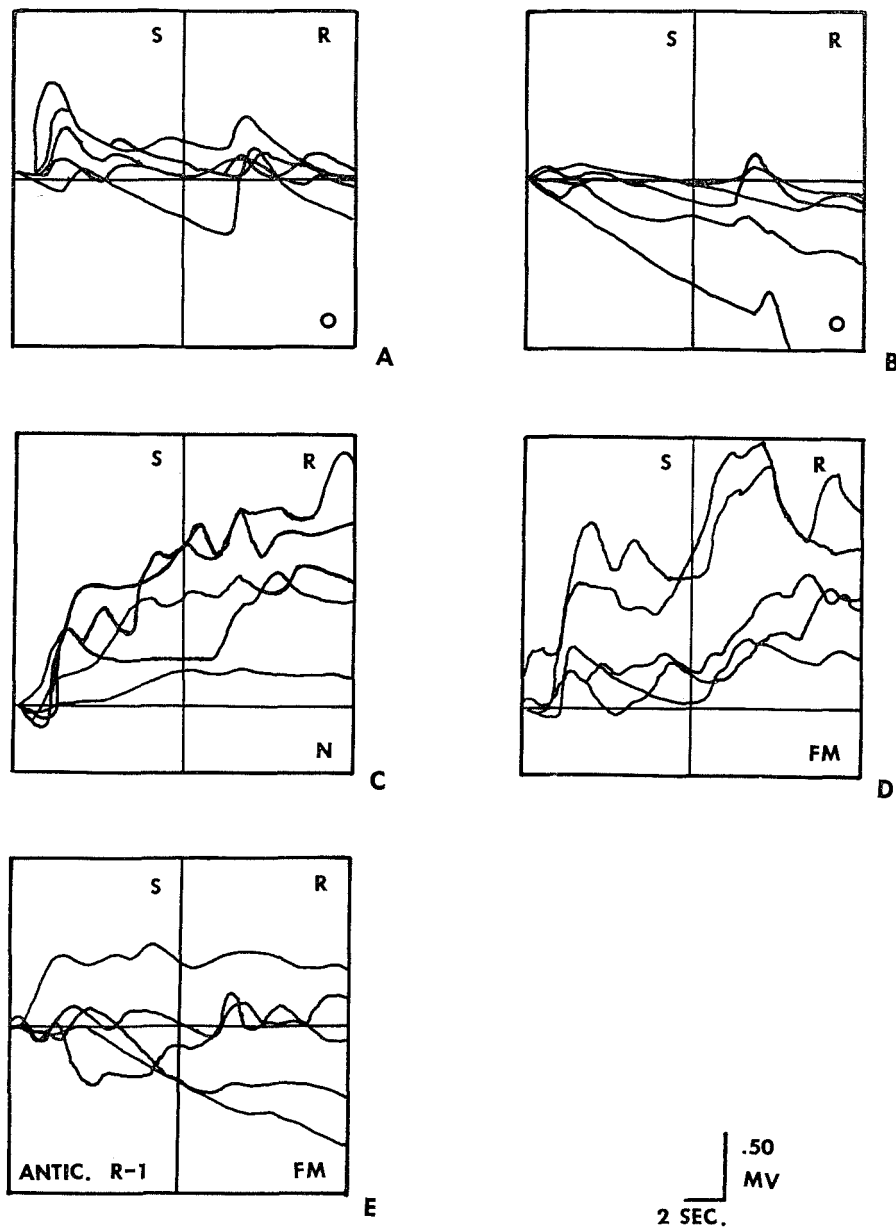


FIG. 1. Trial 1 skin resistance recordings throughout the 10-sec stimulus and response intervals. Downward tracings represent increased skin resistance. Panels A & B present the responses of Ss in the 0 Response condition (no instructed behavioral requirement). C & D present the data from Ss in the Number Response (N) and Finger Movement (FM) conditions, respectively. The responses of five Ss in the FM condition who made an anticipatory error on Trial 1 are presented in E. Calibration: .50 mv or 500 ohms/cm.

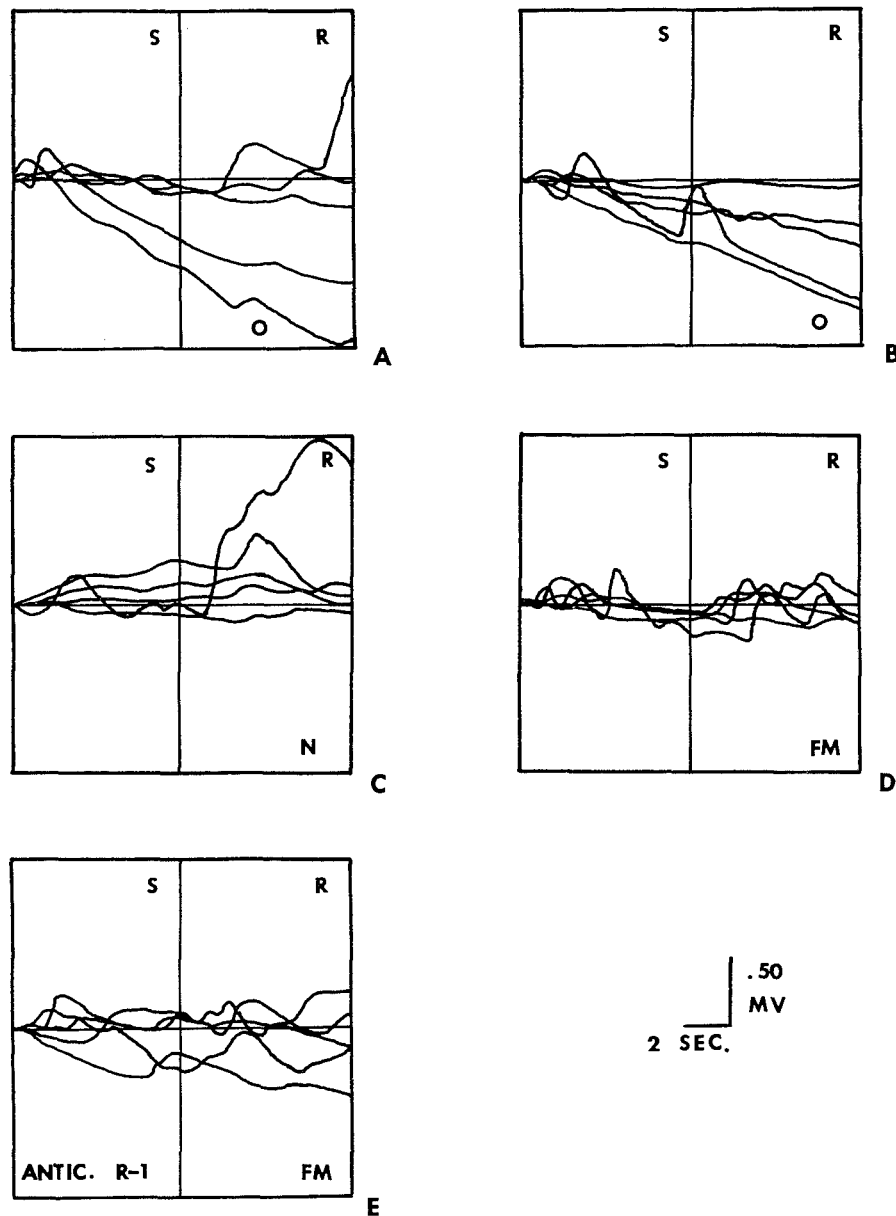


FIG. 2. Trial 5 skin resistance recordings throughout the 10-sec stimulus and response intervals. Downward tracings represent increased skin resistance. Panel representation is as in Fig. 1. It should be noted that the Ss in E did not make an anticipatory error on Trial 5. Calibration: .50 mv or 500 ohms/cm.

A second hypothesis views the two features as representing different events in the organization of behavioral responses. It may be suggested, for example, that tonicity represents the primary process of preparation for overt behavior whereas GSR multiplicity reflects an instability in the behavioral organization resulting from response uncertainty.

The converse hypothesis is equally appealing on intuitive grounds. The multiphasic feature of GSRs to signal stimuli may represent the organization of behavioral responses over time, in which case, preparation for overt response may be reviewed as consisting of discrete, successive events. Tonicity or persistence may primarily reflect the effect of response uncertainty.

The second experiment was designed to investigate the inter- or independence of these features of signal GSRs in a situation in which response certainty was directly manipulated.

EXPERIMENT II

Method

Subjects. Fourteen male and female undergraduates enrolled in an introductory psychology course participated in fulfillment of a course requirement.

Apparatus. The same apparatus was used to record GSRs, to present experimental stimuli, and to time stimulus and response intervals.

The experimental stimuli consisted of eight 35-mm slides, each containing a series of seven single-digit numbers selected from a table of random numbers.

The slide tray was programmed so that each of these eight experimental stimuli was followed by three blank, light intervals. The blank period immediately following the stimulus slide was designated as the "response" interval—Ss were previously instructed to respond during this interval. The next blank interval was used by *E* to inform the *S* whether the response which had been given was "correct" or "incorrect." The third blank, light period was used to instruct *S* either to respond with a certain number on the next trial or to guess which number on the next trial was the "correct" one. The projector was timed for 10-sec advance.

Procedure. All Ss were administered eight learning trials on which the response pattern to be acquired consisted of a simple alternation. Ss were reinforced by confirmation when they responded with extreme left or extreme right number responses *given in appropriate order*. Ss were informed, in advance, that they were participating in a learning study and that there was a pattern of "correct" responses.

The first four trials were "forced" for all Ss, i.e., they were told what response to make on each trial, whereas the last four trials were "free"—Ss were told, at the appropriate time, to guess which of the seven numbers presented on the next trial was the "correct" one.

On the first four trials, all Ss were to respond by saying the number, "nine." This number appeared on the extreme left, right, left, and right on Trials 1-4. It did not appear in these positions on Trials 5-8.

Ten Ss were assumed by *E* to be completely "in-phase," i.e., it was as-

sumed that their alternation pattern began with a left response. Thus, the four "nine" responses were regarded as "correct" and these Ss were so informed. Four of these Ss gave complete evidence of having learned the alternation on the subsequent "free" or test trials—four correct responses on the four test trials. The remaining six Ss in this group made only 0, 1, or 2 correct responses on Trials 5–8.

Four other Ss were assumed to be "180 degrees out-of-phase." It was assumed by *E* that their alternation pattern began with the extreme right number. Thus, the four "nine" responses forced on Trials 1–4 were regarded as "incorrect" and these Ss were so informed. As might be anticipated, these Ss gave no evidence of having learned a right-left alternation—zero correct responses on "free" Trials 5–8.

The purpose of this somewhat elaborate procedure was to insure identical stimulus and response experiences on the first four trials but to nevertheless manipulate reinforcement history on these trials and, therefore, response certainty on Trials 5–8. It was assumed that response certainty was greater on Trial 5 for those Ss who had received four reinforcements and who later gave complete evidence of learning (4L Ss), on the one hand, than for either those Ss who had received no reinforcements and who made "incorrect" responses on Trials 5–8 (0 Ss) or for those Ss who had received four reinforcements but who gave little or no evidence for learning (4NL Ss).

The same analysis as that carried out in Exp. I was made of the skin resistance records of all Ss.

Results and Discussion

Figure 3 presents the polygraphic tracings for all Ss on Trial 5, the first "free" or test trial. The data from the 0 and 4L Ss are presented in Panels A & B, respectively. Panel C consists of the data from four Ss who received the initial four reinforcements but who made only 0 or 1 correct response on Trials 5–8. The recordings presented in D are also from Ss who gave incomplete evidence for learning but these two Ss were unusual in one of two respects. The *S* demonstrating the larger increment in skin conductance made his one correct response on Trial 5 whereas the other *S* presented here gave correct responses on two test trials (7 and 8).

Although it might appear that the GSRs of the 0 Ss were more multiphasic than the GSRs of the other Ss, closer inspection reveals this feature to be an artifact of response clustering around base-line. In fact, the truly salient feature of all these data is that persistent or tonic responses occurred for 4L and 4NL(D) Ss without increase in multiphasic activity, suggesting a possible independence of the two features of signal GSRs.

The lack of increased multiphasic activity in the records of 0 Ss argues against the hypothesis that this feature represents an instability in response organization resulting from response uncertainty. The trend toward more tonic responses in 4L and 4NL(D) records, however, argues against the converse hypothesis—that tonic activity reflects response uncertainty.

The results of the present study lend support only to the general hypothesis

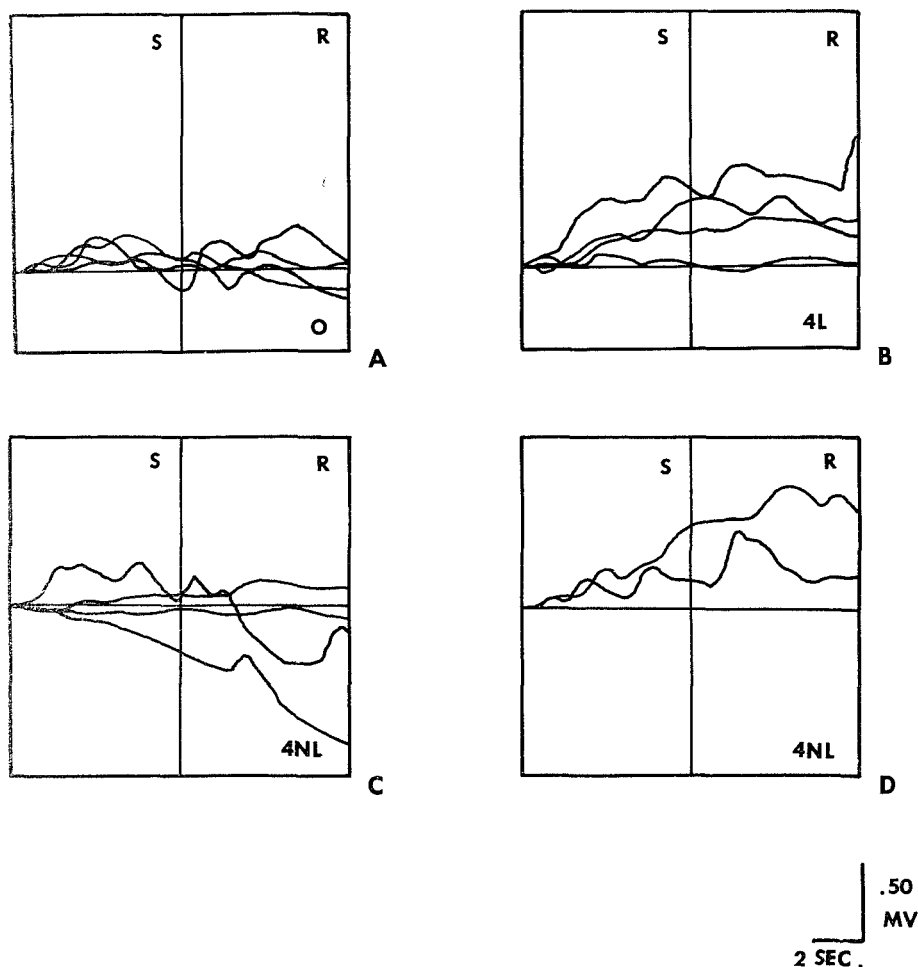


FIG. 3. Trial 5 skin resistance recordings throughout the 10-sec stimulus and response intervals. Downward tracings represent increased skin resistance. Panel A presents the responses of four *Ss* who received no reinforcements prior to Trial 5 and who demonstrated no behavioral evidence for learning on four test trials. B presents the data from four *Ss* who received four reinforcements prior to Trial 5 and produced correct responses on all four test trials. The responses of *Ss* who received four reinforcements but made only 0, 1, or 2 correct responses on the test trials are presented in C & D. Calibration: .50 mv or 500 ohms/cm.

that the multiphasic and tonic features of GSRs to signal stimuli may be independent.

Previous research (Germana, in press) suggests another interpretation of GSR persistence or tonicity. One finding of this prior study was that orienting responses to stimuli reemerge when some physical feature of associated behavioral responses is changed. If it may be assumed that the "correctness" of a response serves to differentiate it from other responses, thereby contributing to response novelty in the early stages of learning, then it may be sug-

gested that the greater tonicity in the 4L and 4NL(D) records reflects the effect of response novelty. The decreased tonicity of signal GSRs from Trial 1 to Trial 5 in Exp. I supports the response novelty interpretation. The effects of response novelty would appear in the *S*'s preparation for that response.

Further support for this interpretation is provided by the many psychophysiological studies of learning which have found that trial-by-trial increments in activation occur as *S*s enter the "learning stage" of conditioning (Germana, 1968). These trial-by-trial increments in GSR, heart rate, and EEG desynchronization may reflect the effects of increased differentiation of the "correct" response from all other responses.

REFERENCES

- Campos, J. J., & Johnson, H. J. The effects of verbalization instructions and visual attention on heart rate and skin conductance. *Psychophysiology*, 1966, 2, 305-310.
- Campos, J. J., & Johnson, H. J. The effect of affect and verbalization instructions on directional fractionation of autonomic response. *Psychophysiology*, 1967, 3, 285-290.
- Ehrlich, D. Changes in tegmental electrogram and in heart rate during bar-pressing in the rat. Paper presented at the meeting of the Eastern Psychological Association, New York, April, 1960.
- Ehrlich, D. Motivational and operant conditioning effects on rat heart rate. Paper presented at the meeting of the American Psychological Association, Los Angeles, September, 1964.
- Ehrlich, D., & Malmo, R. B. Reinforcement effects on heart rate and EEG in rat lever pressing. Paper presented at the meeting of the Eastern Psychological Association, Atlantic City, April, 1965.
- Gellhorn, E. *Principles of autonomic-somatic integrations*. Minneapolis: University of Minnesota Press, 1967.
- Germana, J. Response characteristics and the orienting reflex. *Journal of Experimental Psychology*, in press.
- Germana, J. The psychophysiological correlates of conditioned response formation. *Psychological Bulletin*, 1968, 70, 105-114.
- Hess, W. R. *Diencephalon: Autonomic and extrapyramidal functions*. New York: Grune & Stratton, 1954.
- Jasper, H. Reticular-cortical systems and theories of the integrative action of the brain. In H. F. Harlow & C. N. Woolsey (Eds.), *Biological and biochemical bases of behavior*. Madison: University of Wisconsin Press, 1958. Pp. 37-61.
- Johnson, H. J., & Campos, J. J. The effects of cognitive tasks and verbalization instructions on heart rate and skin conductance. *Psychophysiology*, 1967, 4, 143-150.
- MacNeilage, P. F. EEG amplitude changes during different cognitive processes involving similar stimuli and responses. *Psychophysiology*, 1966, 2, 280-286. (a)
- MacNeilage, P. F. Changes in electroencephalogram and other physiological measures during serial mental performance. *Psychophysiology*, 1966, 2, 344-353. (b)
- Malmo, R. B. On central and autonomic nervous system mechanisms in conditioning, learning, and performance. *Canadian Journal of Psychology*, 1963, 17, 1-36.
- Obrist, P. A. Heart rate and somatic-motor coupling during classical aversive conditioning in humans. *Journal of Experimental Psychology*, 1968, 77, 180-193.
- Obrist, P. A., & Webb, R. A. Heart rate during conditioning in dogs: Relationship to somatic-motor activity. *Psychophysiology*, 1967, 4, 7-34.
- Webb, R. A., & Obrist, P. A. Heart-rate changes during complex operant performance in the dog. Proceedings, 75th Annual Convention, American Psychological Association, 1967. (a)
- Webb, R. A., & Obrist, P. A. Comments on heart rate changes during complex operant performance in the dog. Paper presented at the meeting of the American Psychological Association, Washington, D. C., September, 1967. (b)

CENTRAL EFFERENT PROCESSES AND AUTONOMIC-BEHAVIORAL INTEGRATION

JOSEPH GERMANA

Virginia Polytechnic Institute

ABSTRACT

Neurophysiological and psychophysiological studies have provided a substantial amount of data concerning the integration of autonomic and somatic responses. It is clear that this integration is primarily achieved within the central nervous system and that coordinated autonomic-behavioral activity is reflected, at the periphery, in the anticipatory and preparatory phases of movement. It is suggested that the central efferent organization of these preparatory responses is directly responsible for emotional experience. The demonstration that autonomic events are highly correlated with behavioral responses is regarded as providing further support for the view that the primary concern of the central nervous system is the production of adaptive behavior.

DESCRIPTORS: Autonomic-behavioral integration, Emotion, Psychophysiology. (J. Germana)

On several occasions in the recent past, the neural and behavioral sciences have been provided with the reflective insights of their most prominent investigators. Given the opportunity to temporarily divorce themselves from their specific research programs, these scientists have attempted general overviews of central nervous function. It is possible to identify a major theme in many of these statements, that is, that the regulation of behavior is the primary function of the central nervous system; that the control of overt movement is the intrinsic concern and function of organized neural tissue at all phylogenetic levels.

The preeminence of behavior in the neural scheme is reflected in the following representative viewpoints. Sherrington, for example, observed that "recognizable mind" seems to have arisen in connection with the motor act. "Where motor integration progressed and where motor behavior progressively evolved, mind progressively evolved" (1952, p. 213).

Sperry (1952) has urged us to view the brain as an organ for the transformation of patterns of sensory experience into patterns of motor response, and notes that an investigation of the terminal operations and finished products of the nervous system may be more enlightening than any amount of analysis of sensory input. He states that "... the principal function of the nervous system is the coordinated innervation of the musculature. Its fundamental anatomical plan and working principles are understandable only on these terms" (p. 298).

This paper was supported by National Aeronautics and Space Administration Grant NGR 47-004-006, Project 313181.

Address requests for reprints to: J. Germana, Department of Psychology, Virginia Polytechnic Institute, Blacksburg, Virginia 24061.

In acknowledged agreement, Herrick (1961) states that our search for the nervous mechanisms that regulate behavior has focused on sensory experience but the significant or key factors may be at the other end of the behavioral process, i.e., "... the patterns of central operations involved are determined primarily by the ends to be reached by the appropriate behavior" (p. 69). In his discussion of the evolution of the nervous system, he notes that the nerve cells of the most primitive systems: "... form a network that serves to keep all parts of the body in communication and so facilitates orderly coordination of the bodily movements. In higher animals with more complicated structure and behavior special collections of nerve cells are set apart to provide more efficient coordination and integration. These ganglia and brains take a great variety of forms in different animals depending on the patterns of behavior manifested" (p. 255).

Highly correlated with these general views of nervous function are those approaches to specific psychological processes (e.g., perception, cognition) which emphasize the role of efferent responses organized within the central nervous system.

MOTOR THEORIES

As a general feature, "motor theories" postulate the necessary occurrence of efferent processes of some kind. They may be further differentiated, however, on the basis of whether the necessary efferent events are regarded as central or peripheral in nature. In the former case, the organization of efferent processes within the central nervous system: (a) constitutes or directly leads to the psychological event of concern, and (b) independently results in discharge of peripheral end-organs. Peripheral theories, on the other hand, state that end-organ activity is a necessary antecedent of psychological process insofar as experience is directly dependent on feedback sensations or "reafference" from the periphery.

The motor theories of thought and consciousness proposed by Max (1935, 1937) and Jacobson (1932) may serve as examples of peripheral theories and may be contrasted with the views of Sherrington (1952) and Herrick (1961) noted earlier. Herrick states, for example, that conscious experience arises within an inhibitory state, i.e., "... a stage of uncompleted movement expressed as attitude ... and the next step is the release of some pattern of behavior" (1961, p. 314). He observes the essential similarity between his concept of an "inhibitory state," on the one hand, and the concepts of "anticipatory phase" (Sherrington, 1952) and "posture" (Coghill, 1941), on the other.

Sperry's treatment of perception is particularly noteworthy in this respect. He observes that: "If there be any objectively demonstrable fact about perception that indicates the nature of the neural processes involved, it is the following: Insofar as an organism perceives a given object, it is prepared to respond with reference to it. ... The presence or absence of adaptive reaction potentialities of this sort, ready to discharge into motor patterns, makes the difference between perceiving and not perceiving ... the preparation for response *is* the perception" (1952, p. 301). Festinger, Ono, Burnham, and Bamber (1967) have reviewed

effluent theories of perception and their experiments support the role of "efference readiness" in visual perception.

Perhaps the clearest examples of peripheral and central approaches regarding the role of efferent processes in psychological responses can be found in theories of emotion. The James-Lange theories are, of course, examples of peripheral efferent approaches in which the experience of emotion is dependent upon afferent feedback from effector organs. In contrast to these are the primarily central theories, e.g., Cannon (1931), Hebb (1949), Lindsley (1951), and others recently reviewed by Goldstein (1968). The essential features of these theories are: (a) that the emotional experience is primarily regarded as a central event, and (b) that the autonomic and behavioral concomitants of emotion result from the downward discharge of central efferent structures. If it is assumed, in addition, that the same structures mediate the experience and the peripheral discharge, then it would appear reasonable to suggest that the experience of emotion is the direct result of the central organization of efferent activities.

Some interesting suggestions have been made, in this respect, by Nina Bull (1951, 1962). She has proposed that an "attitude" or postural adjustment intervenes between stimulus and emotional response. The attitude is reflexively organized and feedback stimuli from its autonomic and somatic components give rise to the conscious experience of emotion. The theory represents an attempt to reconcile peripheral and central theories of emotion but would itself be formally classified as a peripheral approach. The theory does, however, contain some interesting suggestions for central efferent theories. First, it postulates the correlated activity of autonomic and somatic effector organs in which the integration is provided by central mechanisms (Bull has made special note of the role of the limbic system in emotional behavior). Secondly, the theory postulates the central organization of an anticipatory or preparatory stage (attitude) which precedes the specific emotional responses of the organism. If the theory were modified so that it treated the central organization of attitudinal responses as the direct basis for emotional experience, it would then constitute a central efferent theory comparable to those which have been proposed in perception, cognition, and consciousness.

The viewpoints or suggestions shared by *central efferent* theories, as proposed for various psychological processes, would seem to be the following:

1. Central activities independently give rise to experience and to the specific autonomic and behavioral responses which occur at the periphery.
2. These central activities constitute the organization of autonomic and behavioral responses.
3. Central efferent organization is initially reflected at the periphery as an anticipatory, preparatory state, or posture.
4. The autonomic and somatic responses which constitute such a preparation for specific behaviors should demonstrate high intercorrelation since they have common central origins and are concerned with the same end-product (adaptive behavior).

Of these hypotheses, the last two are most clearly open to direct experimental observation and data have become available on these points.

NEUROPHYSIOLOGICAL AND ANATOMICAL EVIDENCE FOR AUTONOMIC-SOMATIC INTEGRATION

In his pioneering brain stimulation studies, Hess (1954) systematically investigated diencephalic organization and these data are perhaps the earliest and most directly relevant to the question of autonomic-somatic integration. There are two general findings which are of concern here. The first consists of the frequent association of autonomic and behavioral responses simultaneously occurring to electrical stimulation of the same site. Examples of these associations are: pupillary dilatation accompanied by orienting behavior, blood-pressure increments and other autonomic activity associated with rage responses, and respiratory and blood-pressure changes correlated with the assumption of sleep postures.

In view of the high degree of autonomic-somatic overlap that appeared in his diencephalic maps, Hess proposed the terms, "ergotropic" and "trophotropic," for those activities and areas which involve the association of behavioral responses with sympathetic and parasympathetic responses, respectively. In general, the posterior hypothalamus yielded ergotropic, whereas the anterior portions yielded trophotropic responses. The organization of these "zones" was, however, complex.

The second feature of these studies which is of interest is the distinction made by Hess (1954) between voluntarily aimed movements and the dynamic support upon which these specific movements are superimposed. Recognizing the fact that the pyramidal-extrapyramidal distinction is primarily an anatomical one, Hess proposed the terms, "ereismatic" and "teleokinetic," for the supportive or postural, and specifically aimed phases of motion, respectively. The distinction would seem comparable to those cited earlier, e.g., between anticipatory and consummatory phases of motion (Sherrington, 1952).

Gellhorn (1964, 1967) has comprehensively reviewed the literature relating to autonomic-somatic integration and demonstrates, in concise fashion, the essential validity of the ergotropic-trophotropic distinction. The "ergotropic syndrome," according to Gellhorn (1957) consists of: sympathetico-adrenal events (e.g., a rise in blood pressure and heart rate, dilatation of the pupil, secretion of sweat, etc., and adrenomedullary secretion), increased somato-motor activity, and cortical responses, reflected as EEG desynchronization. In general, trophotropic responses constitute converse changes.

Gellhorn states that each response complex is graded, depending upon the nature and intensity of the stimulus, and the pre-existing state of excitability of the ergotropic and trophotropic systems. He has observed, for example, that general patterns of ergotropic discharge may be discerned. When stimuli of moderate intensity are administered to the organism, only the "neurogenic" or sympathetic responses may occur, without involvement of the adrenal medulla. More intense stimuli typically produce both the sympathetic and adrenomedullary responses. Those occasions on which only humoral response may occur have not yet been clearly defined.

In addition, Gellhorn (1967) clearly reveals the full extensity or generality of

autonomic-somatic integration. It is apparent, for example, that ergotropic and trophotropic responses can be activated through spinal reflexes. So-called viscerosomatic and somatovisceral reflexes may be mediated at this level. A most interesting demonstration of these effects is the fact that the activity of the gamma-efferent system, which acts as a basic reinforcer of somato-motor activity, is also influenced by autonomic parameters and vice versa. Gellhorn notes that "... the intimate relation between the activity of the ergotropic system and that of the gamma impulses (and between trophotropic discharges and inhibition of the gamma system) contributes effectively to the maintenance of the reciprocal inhibition between the two systems" (1967, pp. 34-35).

More complete integration of autonomic and somatic responses occurs at the supraspinal level. It is clear that the hypothalamus plays a major role in the organization of ergotropic and trophotropic responses and that the posterior hypothalamus is primarily ergotropic, the anterior trophotropic in nature, as Hess observed.

A full treatment of the autonomic and somatic functions is clearly beyond the scope of the present paper. The reader is referred to the extensive treatments of this topic provided by Gellhorn (1957, 1964, 1967; and Gellhorn & Loofbourrow, 1963) and to the reviews provided by Ingram (1960) and Patton (1966). Perhaps it is sufficient here to note that the hypothalamus may occupy a functionally focal position for these responses since it is neurogenically capable of interacting with limbic and neocortical mechanisms, with thalamic and reticular structures, and because of its intimate relationship with the hypophysis.

Two further points relating to autonomic-somatic integration are evident. Extensive brain stimulation studies have shown that autonomic responses may be produced through stimulation of a wide variety of central structures and, in addition, there appears to be a considerable amount of autonomic-somatic overlap existing outside of the hypothalamus.

Gellhorn (1967), for example, lists stimulation of the following structures as producing ergotropic responses: motor and sensorimotor areas of the neocortex (and other areas including those designated as "associational"), various areas of the limbic system, subcortical structures such as the globus pallidus, the caudate nucleus, the medial thalamus, the reticular formation, and the cerebellum.

An interesting demonstration of the supraspinal representation of an autonomic response has been provided by Wang (1964) in his studies of electrodermal phenomena. As a result of his extensive investigations, Wang concludes that excitatory areas may be found in: sensorimotor cortex, anterior limbic and infra-limbic cortex, anterior hypothalamus, a region of the dorsal thalamus, and the lateral reticular formation. In addition, he has suggested that a regulatory sweat center exists in the basal ganglia. The existence in this list of known points of origin and fiber tracts of the extrapyramidal motor system, which plays a demonstrable role in tonic, postural responses (Jung & Hassler, 1960), is readily apparent.

Ingram's (1960) conclusion is particularly appropriate for the present discussion. He states that: "Interactions between the somatic and autonomic mechanisms must not be overlooked. It has been clearly shown that these interactions

are not only present but exceedingly important . . . somatovisceral and viscerosomatic circuits are also modulated by influences from higher regions" (p. 975).

PSYCHOPHYSIOLOGICAL EVIDENCE FOR AUTONOMIC-BEHAVIORAL CORRELATION

The field of psychophysiology is explicitly concerned with the correlation of physiological and behavioral processes in experimental situations which involve the direct manipulation of the behavioral event or process (independent variable) and measurement of physiological correlates as dependent variables. Since it also aspires to minimal extraneous disturbance of the organism, maintaining the organism in its intact state and assuring that its physiological functions are within normal ranges, psychophysiological research has traditionally, though not exclusively, employed methods of surface recording of autonomic function. A central assumption of these studies is that there exist some anatomical and physiological bases for autonomic-somatic integration and that behavior events, beyond the simplest reflex level, have meaningful physiological associates. Because it has made this assumption and has employed its distinctive methodology, psychophysiology has provided a substantial amount of data of direct concern to the present study.

Many of these findings have been presented within the framework of activation theory and have been reviewed by Duffy (1962). It is clear from this and other discussions (e.g., Malmö, 1962) that increments in activation are essentially comparable to ergotropic responses, i.e., they consist of sympathetico-adrenal, somato-motor, and EEG responses. High activation levels may be equated with maintained ergotropic dominance.

Activation has been shown to have direct effects on the intensive aspects of behavior (e.g., the force and speed of response) but its effects on the directional aspects of behavior appear to be more complex in nature. Substantial support has been provided, however, for the notion that high levels of activation (Duffy, 1962) and short-term increments in activation (Germana, 1967a, 1967b) produce competing response errors in some situations.

The present paper will limit its discussion to three research problems which have provided data directly relevant to the question of autonomic-behavioral correlation. These data concern: the physiological events which precede and accompany the occurrence of overt behavior, the role of behavior in the production and habituation of the orienting reflex, and the psychophysiological correlates of behavioral learning.

Activational Correlates of Behavior

In some early studies, R. C. Davis and his collaborators (e.g., Davis, 1957; Davis, Buchwald, & Frankmann, 1955; Davis, Lundervold, & Miller, 1957) clearly demonstrated the high degree of sensitivity of the autonomic and somatic systems to a wide variety of stimuli. Activational or ergotropic responses were shown to accompany each type of stimulus employed, yielding, as Davis, Lundervold, & Miller (1957) noted, a pattern of autonomic and somatic responses which closely resembled the physiological changes which occur during exercise or in the "emergency reaction." It was also found: that somatic muscular activity is a con-

sistent response to stimulation (Davis, Buchwald, & Frankmann, 1955); that a behavioral requirement produces the strongest autonomic and somatic responses (Davis, Lundervold, & Miller, 1957); and, that activational responses occur to warning stimuli which precede behavioral responses (Dawson & Davis, 1957).

Concerning these last "preparatory responses," Jasper (1958) reported that blocking of sensorimotor and parietal electrocortical activity was primarily related to the preparation for movement rather than to movement, *per se*. Mac-Neillage (1966a, 1966b) has recently provided data which support this conclusion.

In an interesting study of autonomic-behavioral correlation, Pinneo (1961) demonstrated clear functional relationships between level of induced muscle tension, on the one hand, and generalized electromyographic, skin conductance, cardiac, respiratory, and EEG responses, on the other. The study suggests, therefore, that there exists a close matching between the intensity of required behavior and activational or ergotropic responses.

Ehrlich and Malmo (Ehrlich, 1960, 1964; Ehrlich & Malmo, 1965; Malmo, 1963) have shown that increments in heart rate immediately precede and accompany the occurrence of operant behavioral responses. In a similar vein, Obrist and Webb have recently demonstrated high positive correlations between cardiac and somatic activities during classical (Obrist, 1968; Obrist & Webb, 1967) and operant (Webb & Obrist, 1967a, 1967b) conditioning.

Germana and Chernault (1968) have reported distinct patterns of galvanic skin responses (GSRs) to signal and non-signal stimuli. In these studies, it was shown that signal stimuli (those which have required behavioral associates) produce GSRs which are more persistent (tonic) than those elicited by non-signal stimuli. In addition, signal GSRs appear to be multiphasic in nature. Both the persistence and multiphasic characteristics of signal GSRs showed habituation over trials. It should be emphasized that the experimental procedure insured that these characteristic GSRs occurred in response to the signal stimuli and directly preceded any instructed behavior. They were, in this sense, preparatory to behavior.

Some recent studies in our laboratory (Germana, 1969) have investigated the effects of behavioral requirements on skin conductance levels. Each *S* was administered multiple, successive "non-respond" (NR) and "respond" (R) conditions. In the NR condition, *Ss* were required to simply "attend" to each number stimulus whereas in the R condition they were required to respond by saying the number five times. The results clearly showed that the R condition tended to elevate skin conductance level and that on numerous occasions anticipatory changes occurred in preparation for the R condition.

The studies presented in this section demonstrate that the preparation for and the initiation of behavior produce changes in autonomic functioning which may be described as activational or ergotropic.

Behavior Characteristics and the Orienting Response

The orienting response (OR) consists of a diffuse complex of autonomic and somatic events which seem to be highly comparable to those which have been designated as "activational" or "ergotropic" in this paper. Increments in skin conductance, heart rate, pupillary dilatation, general muscle tension, etc., as well

as postural responses, have been shown to be consistent components of the OR. The OR is a non-specific reaction insofar as it may be produced by a *novel* stimulus belonging to any sense modality and, in addition, it may be shown to habituate or extinguish with repetition of that stimulus. When any characteristic of the stimulus is changed the OR "reemerges."

Pavlov (1927) originally described the OR as the "what is it?" reflex, implying that the organism was reflexively attempting, through this reaction, to discern the nature of the stimulus. A considerable amount of evidence has accumulated to support such an interpretation. Sokolov (1960, 1963a, 1963b), for example, has shown that the OR is accompanied by a decrease in visual and auditory thresholds and has suggested that the components of the OR may directly (pupillary dilatation) or indirectly (EEG desynchronization, cardiovascular responses) serve to increase sensitivity.

Without questioning the essential validity of these data, it may, nevertheless, be appropriate to recall, at this time, some earlier statements concerning the role of efferent processes in perception. If, for example, Sperry's (1952) view that the brain is primarily an organ for transforming patterns of sensory information into patterns of motor impulses is well-taken, it may be reasonable to suggest that the essential question being asked by the organism, through the OR, is "what's to be done?" rather than the purely academic, "what is it?" According to this viewpoint, the organism is primarily concerned with its behavior or the behavioral requirements of the situation and asks "what is it?" only insofar as it is concerned with "what's to be done?"

Such an interpretation has already been proposed for some of the OR components, e.g., increased general muscle tension (Berlyne, 1960; Kvasov & Korovina, 1965). According to the general view expressed in this paper, however, the total OR complex may be divided into components which indirectly aid the organism in determining possible behavioral requirements by increasing the sensitivity of receptor mechanisms (e.g., pupillary dilatation, behavioral orienting toward the stimulus) and those responses which represent a general preparation to respond (increased muscle tension, EEG desynchronization, cardiovascular responses). Such an interpretation receives support from those studies, reported earlier, which have shown that activational or ergotropic responses precede and accompany behavior.

Habituation of the OR has traditionally been reviewed as a kind of stimulus learning. Sokolov (1960, 1963a, 1963b), for example, has shown that a "neuronal model" of the stimulus is established on the basis of repetitive experience with that stimulus. The "neuronal model" is multi-dimensional in form, i.e., it includes the amplitude, frequency, duration, and rate of presentation characteristics of the stimulus. That a kind of learning has taken place during habituation, that a "model" of the stimulus has been constructed, is shown by the fact that the OR reemerges when any characteristic of that stimulus is changed. Although differing in some respects, other attempts to specify the central events underlying habituation are similar to Sokolov's to the extent that they have concentrated on the stimulus learning features of the phenomenon (cf. Lynn, 1966).

Germana (1968b) has shown, however, that the "neuronal model" of a stimulus

includes the characteristics of associated behavioral responses. In these studies, it was shown: that stimuli which have behavioral associates (signal stimuli) produce greater ORs than non-signal stimuli; that "novel" behavioral associates produce greater ORs to signal stimuli than "old" associations; and, that the overall level of ORs across the habituation series is a direct function of the amount of "response information" to be encoded. Perhaps the most interesting finding of these studies is the demonstration that the degree of reemergence of the OR is directly related to the amount of *behavioral change* that is required.

The results of these studies indicate that those central structures which are responsible for the production and habituation of the OR are at least as concerned with behavioral characteristics as they are with stimulus parameters. It is clear, for example, that *response novelty* may be as effective as stimulus novelty in producing the OR. These findings lend some support to the contention that the organism is primarily concerned with behavioral requirements and that its attempts to facilitate the sensitivity of sensory systems in the OR situation may be essentially reducible to its overall attempt to produce adaptively efficient behavior.

Psychophysiological Correlates of Behavioral Learning

Germana (1968a) has reviewed the research literature concerning the psychophysiological correlates of learning. The studies which were considered in this previous paper employed the traditional psychophysiological technique of recording physiological events, as *behavior* was being manipulated (in this case, through classical and instrumental conditioning procedures). In addition, these studies provided some objective behavioral criteria for identifying stages of learning so that physiological records of individual *Ss* could be examined at comparable points in the learning process.

It is clear from this discussion that these GSR, EEG, and heart rate studies have consistently supported the existence of an "activational peaking" effect. The effect consists of the following sequence of events: during the initial stages of learning, activational responses to the CS systematically increase over the level of responsiveness characteristic of the pre-conditioning or habituation stage. These increments continue until some level of CR performance is achieved, after which activational responses decrease in magnitude.

Several features of the "activational peaking" effect should be emphasized. First, only the activational responses which occur to the CS demonstrate the effect, in contrast to the responses which occur to the reinforcing stimulus which tend to show only habituation. Secondly, trial-by-trial increments in activation can be demonstrated in those situations (serial, paired-associate learning, concept formation) which involve the learning of a discrete response(s) to a stimulus, or series of stimuli. In these situations, the trial-by-trial increments occur when the *S* is committing the final response errors which immediately precede his achievement of the learning criterion. Lastly, activational peaking may not occur when the *S* has already learned one response to each stimulus and is then required to associate new responses to the same stimuli.

In view of these last findings and because activational responses occur in a wide

variety of situations and tend to be quite general in nature, it is probably unreasonable to suggest that the increments in activation which occur during learning reflect either the specific encoding or an engrammic support process. It should also be noted that the initial incremental arm of the "activational peaking" effect occurs in direct contrast to the OR habituation which would be expected on the basis of stimulus repetition.

It has been suggested (Germana, 1968a) that the activational responses which demonstrate the peaking effect may constitute general preparations to respond and act in this capacity to facilitate "correct response" emission. Lacking in this interpretation, however, is the identification of the specific features of the situation which "trigger" the successive increments in activation. If it may be assumed that the primary effect of learning is to differentiate the "correct" response(s) from all other possible responses, then it may be postulated that the successive differentiation of the "correct" response serves to increase its novelty in the initial stages of conditioning. Response novelty, as noted earlier, produces ORs which are graded on the basis of the degree of response change. It may be suggested, therefore, that the process of response differentiation contributes a novelty feature to the CS, resulting in successive increments in activation. Following differentiation habituation decrements then occur.

SUMMARY AND CONCLUSIONS

The neurophysiological and psychophysiological studies which have been reviewed consistently support the hypothesis that the central integration of autonomic and somatic systems normally results in a high degree of intercorrelation between autonomic and behavioral responses. It is clear, therefore, that the distinction between nervous systems is primarily an anatomical convenience which applies well at the periphery, i.e., in terms of innervated effector organs, but which constitutes a gross over-simplification of central organization. It is undoubtedly more precise to speak in terms of response complexes which possess both autonomic and somatic components, as Hess and Gellhorn have done, and it is more realistic to view the two systems as complexly coordinated into response patterns. When it can be shown that behavioral involvement, occurring even at the simplest level of complexity or difficulty, produces autonomic involvement and distinct patterns of autonomic discharge, then it would seem appropriate to recognize that integrated autonomic-somatic activity is not reserved for "emergency" or exercise conditions.

In contrast, it is apparent that activational or ergotropic responses are readily produced as preparations for overt behavior which take the form of "postural," "anticipatory," or "ereismic" adjustments. These preparations for behavior, with their central, autonomic, and somatic components are most clearly evident in situations which involve: (a) a transition from behavioral inactivity to overt behavior (Germana, 1968b, 1969); (b) a transition to more intense, sustained, or complex behavior (Pinneo, 1961); (c) the presentation of a novel stimulus (Berlyne, 1960; Sokolov, 1963a); and, (d) the acquisition of a new response to a stimulus (Germana, 1968a).

It is suggested, therefore, that integrated autonomic-somatic activity may

occur predominantly in situations which involve intensive (situations a and b) or extensive (situations c and d) preparations for overt behavior. In these last situations, the organism is, by definition, ignorant of specific appropriate behaviors and, for this reason, can make only a general as opposed to a specific preparation to respond.

It is interesting to note that the above-mentioned situations are precisely those in which human Ss might report anxiety or apprehension. If conflict situations, which again demand an extensive preparation for more than one behavioral response, are added, then it would seem reasonable to suggest that preparations for behavior constitute the basis for these emotional experiences. This hypothesis, it will be noted, is quite similar to the "attitude" theory proposed by Nina Bull (1951, 1962). Having seen in preceding sections of this paper that the autonomic-somatic components of behavioral preparations are primarily organized within the central nervous system, however, it would seem more reasonable to suggest that the central organization of "attitude" directly constitutes the emotional experience. To rephrase Sperry (1952), ". . . the preparation to respond constitutes the emotion." The basic problem with peripheral theories is that what they immediately rob from the central nervous system, they must return twofold. That is to say, they must first postulate that the system is capable of organizing extremely complex and well-differentiated peripheral responses and, secondly, that the system is capable of interpreting the total pattern of reafference. Although it would appear that the system can do both tasks quite well, it is nevertheless more direct and parsimonious to postulate that central efferent organization itself constitutes experience.

In discussing the integration of autonomic and somatic responses, it was not intended to ignore the fact that the autonomic nervous system clearly performs functions which may not be directly related to behavior. But, the demonstration that the autonomic system is not closed to external events, that it, too, is concerned with adaptive behavior and functions in tandem with the somatic system, lends further support to the notion that the brain is primarily a motor organ.

REFERENCES

- Berlyne, D. E. *Conflict, arousal, and curiosity*. New York: McGraw-Hill, 1960.
- Bull, N. The attitude theory of emotion. *Nervous and Mental Disease Monographs*, 1951, 81, 3-159.
- Bull, N. *The body and its mind*. New York: Las Americas, 1962.
- Cannon, W. B. Again the James-Lange and the thalamic theories of emotion. *Psychological Review*, 1931, 38, 281-295.
- Coghill, G. E. The educational methods of F. Matthias Alexander: An appreciation. In F. M. Alexander, *The universal constant in living*. New York: Dutton, 1941. Pp. xxi-xxviii.
- Davis, R. C. Response patterns. *Transactions of the New York Academy of Sciences*, 1957, 19, 731-739.
- Davis, R. C., Buchwald, A. M., & Frankmann, R. W. Autonomic and muscular responses, and their relation to simple stimuli. *Psychological Monographs*, 1955, 69 (Whole No. 405), No. 20.
- Davis, R. C., Lundervold, A., & Miller, J. D. The pattern of somatic response during a repetitive motor task and its modification by visual stimuli. *Journal of Comparative & Physiological Psychology*, 1957, 50, 53-60.

- Dawson, H. E., & Davis, R. C. The effects of an instructed motor response upon somatic responses to a brief tone. *Journal of Comparative & Physiological Psychology*, 1957, 50, 368-374.
- Duffy, E. *Activation and behavior*. New York: Wiley, 1962.
- Ehrlich, D. Changes in tegmental electrogram and in heart rate during barpressing in the rat. Paper presented at the meeting of the Eastern Psychological Association, New York, April 1960.
- Ehrlich, D. Motivational and operant conditioning effects on rat heart rate. Paper presented at the meeting of the American Psychological Association, Los Angeles, 1964.
- Ehrlich, D., & Malmö, R. B. Reinforcement effects on heart rate and EEG in rat lever pressing. Paper presented at the meeting of the Eastern Psychological Association, Atlantic City, April 1965.
- Festinger, L., Ono, H., Burnham, C. A., & Bamber, D. Efference and the conscious experience of perception. *Journal of Experimental Psychology Monograph*, 1967, 74(Whole No. 637), 1-36.
- Gellhorn, E. *Autonomic imbalance and the hypothalamus*. Minneapolis: University of Minnesota Press, 1957.
- Gellhorn, E. Motion and emotion. *Psychological Review*, 1964, 71, 457-472.
- Gellhorn, E. *Autonomic-somatic integrations*. Minneapolis: University of Minnesota Press, 1967.
- Gellhorn, E., & Loofbourrow, G. N. *Emotions and emotional disorders*. New York: Hoeber, 1963.
- Germana, J. Isolation of an habituational position effect in paired-associate learning. *Psychological Reports*, 1967, 20, 27-30. (a)
- Germana, J. Effects of activation level on paired-associate learning. *Psychological Reports*, 1967, 21, 329-332. (b)
- Germana, J. The psychophysiological correlates of conditioned response formation. *Psychological Bulletin*, 1968, 70, 105-114. (a)
- Germana, J. Response characteristics and the orienting reflex. *Journal of Experimental Psychology*, 1968, 78, 610-616. (b)
- Germana, J. Effects of behavioral responding on skin conductance level. *Psychological Reports*, 1969, 24, 599-605.
- Germana, J., & Chernault, G. Patterns of galvanic skin responses to signal and non-signal stimuli. *Psychophysiology*, 1968, 5, 284-292.
- Goldstein, M. L. Physiological theories of emotion: A critical historical review from the standpoint of behavior theory. *Psychological Bulletin*, 1968, 69, 23-40.
- Hebb, D. O. *Organization of behavior*. New York: Wiley, 1949.
- Herriek, C. J. *The evolution of human nature*. New York: Harper, 1961.
- Hess, W. R. *Diencephalon: Autonomic and extrapyramidal functions*. New York: Grune & Stratton, 1954.
- Ingram, W. R. Central autonomic mechanisms. In J. Field, H. W. Magoun, & V. E. Hall (Eds.), *Handbook of physiology. Neurophysiology*. Vol. II. Washington, D. C.: American Physiological Society, 1960. Pp. 951-978.
- Jacobson, E. The electrophysiology of mental activities. *American Journal of Psychology*, 1932, 44, 677-694.
- Jasper, H. Reticular-cortical systems and theories of the integrative action of the brain. In H. F. Harlow & C. N. Woolsey (Eds.), *Biological and biochemical bases of behavior*. Madison: University of Wisconsin Press, 1958. Pp. 37-61.
- Jung, R., & Hassler, R. The extrapyramidal motor system. In J. Field, H. W. Magoun, & V. E. Hall (Eds.), *Handbook of physiology. Neurophysiology*. Vol. II. Washington, D. C.: American Physiological Society, 1960. Pp. 863-927.
- Kvasov, D. G., & Korovina, M. V. The reflex organization of perception and the proprio-muscular apparatus of the analyzers (of the sense organs). In L. G. Voronin, A. R. Leontiev, A. R. Luria, E. N. Sokolov, & O. S. Vinogradova (Eds.), *Orienting reflex and exploratory behavior*. Washington: American Institute of Biological Sciences, 1965. Pp. 178-186.

- Lindsley, D. B. Emotion. In S. S. Stevens (Ed.), *Handbook of experimental psychology*. New York: Wiley, 1951. Pp. 473-516.
- Lynn, R. *Attention, arousal and the orientation reaction*. New York: Pergamon Press, 1966.
- MacNeilage, P. F. EEG amplitude changes during different cognitive processes involving similar stimuli and responses. *Psychophysiology*, 1966, 2, 280-286. (a)
- MacNeilage, P. F. Changes in electroencephalogram and other physiological measures during serial mental performance. *Psychophysiology*, 1966, 2, 344-353. (b)
- Malmo, R. B. Activation. In A. J. Bachrach (Ed.), *Experimental foundations of clinical psychology*. New York: Basic Books, 1962. Pp. 386-422.
- Malmo, R. B. On central and autonomic nervous system mechanisms in conditioning, learning, and performance. *Canadian Journal of Psychology*, 1963, 17, 1-36.
- Max, L. W. An experimental study of the motor theory of consciousness: III. Action-current responses in deaf mutes during sleep, sensory stimulation and dreams. *Journal of Comparative Psychology*, 1935, 19, 469-486.
- Max, L. W. An experimental study of the motor theory of consciousness: IV. Action-current responses in deaf mutes during awakening, kinaesthetic imagery, and abstract thinking. *Journal of Comparative Psychology*, 1937, 24, 301-344.
- Obrist, P. A. Heart rate and somatic-motor coupling during classical aversive conditioning. *Journal of Experimental Psychology*, 1968, 77, 180-193.
- Obrist, P. A., & Webb, R. A. Heart rate during conditioning in dogs: Relationship to somatic-motor activity. *Psychophysiology*, 1967, 4, 7-34.
- Patton, H. D. Higher control of autonomic outflows: The hypothalamus. In T. C. Ruch, H. D. Patton, J. W. Woodbury, & A. L. Towe (Eds.), *Neurophysiology*. Philadelphia: Saunders, 1966. Pp. 238-251.
- Pavlov, I. P. *Conditioned reflexes*. London: Oxford, 1927.
- Pinneo, L. R. The effects of induced muscle tension during tracking on level of activation and performance. *Journal of Experimental Psychology*, 1961, 62, 523-531.
- Sherrington, C. S. *Man on his nature*. London: Cambridge University Press, 1952.
- Sokolov, E. N. Neuronal models and the orienting reflex. In M. A. Brazier (Ed.), *The central nervous system and behavior*. New York: Josiah Macy, Jr. Foundation, 1960. Pp. 187-239.
- Sokolov, E. N. *Perception and the conditioned reflex*. New York: Pergamon Press, 1963. (a)
- Sokolov, E. N. Higher nervous functions: The orienting reflex. *Annual Review of Physiology*, 1963, 25, 545-580. (b)
- Sperry, R. W. Neurology and the mind-brain problem. *American Scientist*, 1952, 40, 291-312.
- Wang, G. H. *The neural control of sweating*. Madison: University of Wisconsin Press, 1964.
- Webb, R. A., & Obrist, P. A. Heart-rate changes during complex operant performance in the dog. Proceedings, 75th Annual Convention, American Psychological Association, 1967. (a)
- Webb, R. A., & Obrist, P. A. Comments on heart rate changes during complex operant performance in the dog. Paper presented at the meeting of the American Psychological Association, Washington, D. C., September 1967. (b)

PATTERNS OF AUTONOMIC AND SOMATIC ACTIVITY DURING
CLASSICAL CONDITIONING OF A MOTOR RESPONSE

JOSEPH GERMANA
Virginia Polytechnic Institute

Journal of Comparative and Physiological Psychology
1969, Vol. 69, No. 1, 173-178

PATTERNS OF AUTONOMIC AND SOMATIC ACTIVITY DURING CLASSICAL CONDITIONING OF A MOTOR RESPONSE¹

JOSEPH GERMANA²

Virginia Polytechnic Institute

Skin conductance (SC), heart rate (HR), and muscle-action potentials (MAP) were recorded from 10 *Ss* during habituation and subsequent classical conditioning of a voluntary motor response. Responses to the CS, occurring in all three physiological measures, demonstrated a pattern of activity which has been termed "activational peaking" (AP). Activational responses to the CS increased during initial conditioning trials but returned to the level of responsiveness characteristic of habituation with subsequent CS-US pairings. The SC and MAP basal activity during four-trial segments also demonstrated AP. These findings extend the generality of the AP effect and provide support for the hypothesis that AP constitutes a pattern of changes in the preparation for behavior.

A recent review of the psychophysiological literature (Germana, 1968a) revealed broad replication, across *Ss*, tasks, and measures, of a pattern of activational responses, e.g., electroencephalographic (EEG) desynchronization, galvanic skin response (GSR), and heart-rate (HR) acceleration, which occurs during *behavioral* conditioning or learning. This pattern, termed "activational peaking" (AP), consists of the following sequence of events: (a) During the initial stages of conditioning, activational responses to the CS show systematic trial-by-trial increment up to the trial or group of trials which define some *behavioral* criterion of response acquisition; (b) subsequent elaboration of the CR is accompanied by decrements in these activational responses toward the preacquisitional habituated level.

Germana (1968a) has discussed some of the immediately available interpretations of this effect (e.g., that it reflects an engrammatic support process) and has found them inadequate in one or more

respects. It was suggested that activational responses generally occur during intensive and extensive preparations for overt behavior and that AP represents the case in which preacquisitional preparations for behavior are more extensive than those which occur when the CR has become fully elaborated within *S's* behavioral repertoire, i.e., when the CR becomes fully reflexive. Some preliminary support for this hypothesis has been provided by the finding that habituated orienting responses reemerge when changes in overt behavior are required (Germana, 1968b).

The present study was designed to explore the changes in somatic muscle-action potentials (MAP) or electromyographic activity which occur during conditioning, since these may more directly reflect preparations for behavior, and compared these responses with those occurring in two measures of autonomic activity, GSR and HR. In addition, the experiment investigated changes in the tonic or background activity occurring in these effector systems and contrasted these with the responses apparently bound to the CS. It was anticipated that extensive preparations for behavior would be relatively persistent and would therefore be reflected in basal activity scores. Previous observations in this laboratory (Germana, 1969a; Germana & Chernault, 1968) have shown that preparations for behavior have persistent or tonic effects on physiological base lines.

¹This research was supported by Grant NGR 47-004-006, Project 313161 from the National Aeronautics and Space Administration. The assistance of G. Chernault and D. F. Johnson is gratefully acknowledged. Major portions of this paper were presented at the meeting of the Eastern Psychological Association, Philadelphia, April 1969.

²Requests for reprints should be sent to Joseph Germana, Department of Psychology, Virginia Polytechnic Institute, College of Arts and Science, Blacksburg, Virginia 24061.

METHOD

Subjects

Ten male undergraduate students volunteered to participate.

Apparatus

Physiological and behavioral responses were recorded on a Grass Model 7 polygraph. The 7P1 preamplifier was used, along with *Ag/AgCl* electrodes and K-Y surgical jelly, to record skin conductance (SC). The electrodes, 8.5 mm. in diameter, were taped to the central volar region of the distal phalanges on the index and ring fingers of the right hand after these surfaces had been cleansed with alcohol. The 7P4 tachographic preamplifier presented a beat-by-beat read-out of HR in beats/minute (b/m). Plate electrodes were attached in the standard Lead II configuration. The 7P5 wide-band ac preamplifier was used to record raw MAP and these signals, in turn, constituted the input to the 7P10 preamplifier which cumulatively integrated MAP voltage over time. Silver disc electrodes were affixed with Grass EC-2 cream to record the activity of the brachioradialis muscle of the left forearm. The elbow was used as a reference site.

The Grass remote event marker was placed in *S*'s left hand so that the button could be depressed by a flexion movement of the thumb. The com-

plete polygraph record therefore presented four measures of physiological activity (SC, HR, raw and integrated MAP) and a permanent trace of *S*'s button-pressing response.

A Kodak Carousel projector was used to present blank-light stimuli and slides containing three asterisks. The slide tray was programmed so that each of nine asterisk slides, which served as CSs, was preceded by four blank-light stimuli and was timed for 5-sec. advance by a Lafayette timer. Impulses for slide-tray advance also reset the MAP integrating channel to base line so that measures of total MAP activity in successive 5-sec. stimulus intervals could be obtained and stimulus events could be denoted on the polygraph record.

Procedure

The classical conditioning paradigm which was employed has been termed the "motor method of speech reinforcement" or, more briefly, the "motor-speech" method. It involves the pairing of a discriminable CS, on the one hand, with a verbal command US, delivered by *E*, and a consequent voluntary UR, on the other (cf. Hartman, 1965). Although there exist some questions concerning the representativeness of this procedure, it was employed in the present experiment because it was anticipated that: (a) The task would be characterized by high inter-*S* homogeneity of acquisition rate; (b) it would result in rapid CR

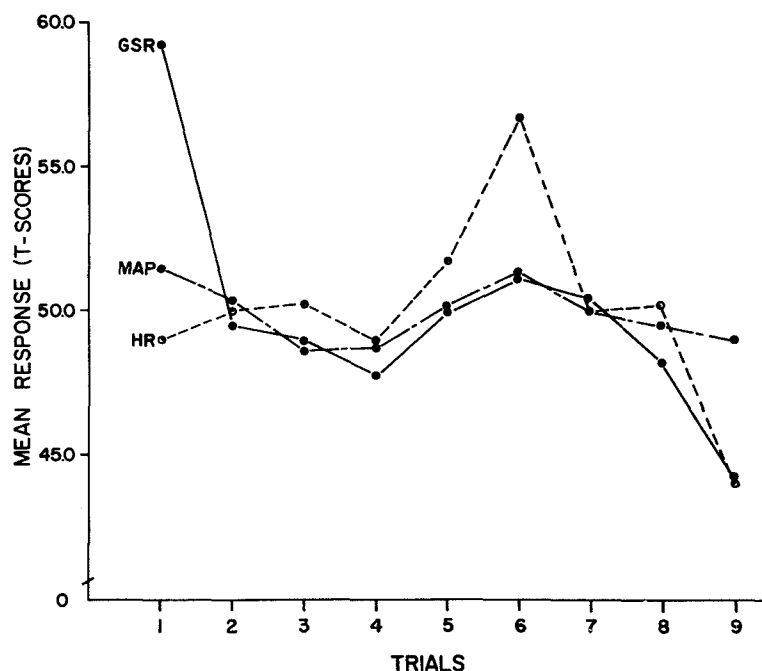


FIG. 1. Magnitude of GSR, HR acceleration, and MAP response (in *T*-score units) to the CS during habituation (Trials 1-3) and subsequent conditioning (Trials 4-9).

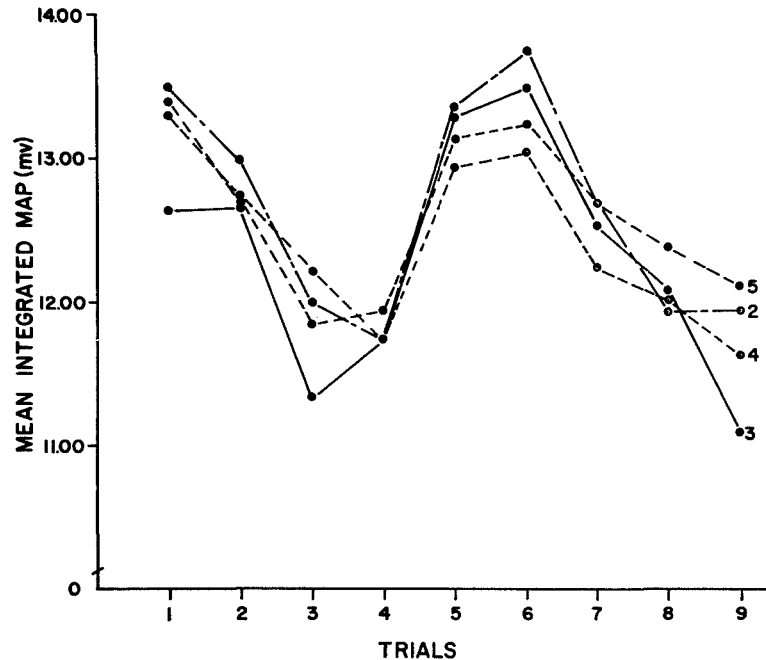


FIG. 2. Mean integrated MAP response during habituation (Trials 1-3) and subsequent conditioning (Trials 4-9) as a function of trial segment.

formation; and (c) positive results would extend the generality of the AP effect across learning tasks.

After the electrodes had been affixed to *S*, he was simply informed that blank-light stimuli and slides containing asterisks would be presented and that on some occasions he would be told to press the button in his left hand. He was further instructed to avoid extraneous movement and to depress the button, when requested, in a quick discrete fashion.

Each *S* received nine trials—a trial consisted of four blank stimuli followed by an asterisk slide (Segments 1-5). The *S* was not requested to depress the button on the initial three habituation trials but the verbal command US, "press," was administered immediately after the termination of the asterisk-slide CS (Segment 5) on the remaining six conditioning trials.

RESULTS

Responses to the CS

The GSRs occurring to the asterisk CS were transformed into square-root change in conductance units, HR accelerative response was measured as the maximal continuous or unbroken acceleration in b/m to the CS (the criterion for discontinuity was a deceleration of two or more

b/m), and total MAP occurring in the 5-sec. CS period was directly measured from the integrated read-out in millivolts. It should be noted that the integrated MAP includes any phasic responses to the CS and the ongoing or tonic level of activity occurring during this period.

Figure 1 presents the specific responses to the asterisk CS, i.e., those occurring during Segment 5, on the three habituation and six conditioning trials. The GSR, HR, and integrated MAP responses were converted into *T* scores for comparison. It is apparent that whatever habituation occurred on the first four trials was effectively reversed after the first conditioning trial, that the AP pattern was present in all three measures, and that the "peak" response occurred on Trial 6 (following two conditioning trials).

A Measures \times Trials analysis of variance was applied to these data and yielded a ($F = 2.914$, $df = 8/144$, $p < .01$) trials effect. Neither the measures ($F < 1$) nor interaction ($F = 1.205$, $df = 16/144$) effect was significant. Subsequent trend analysis

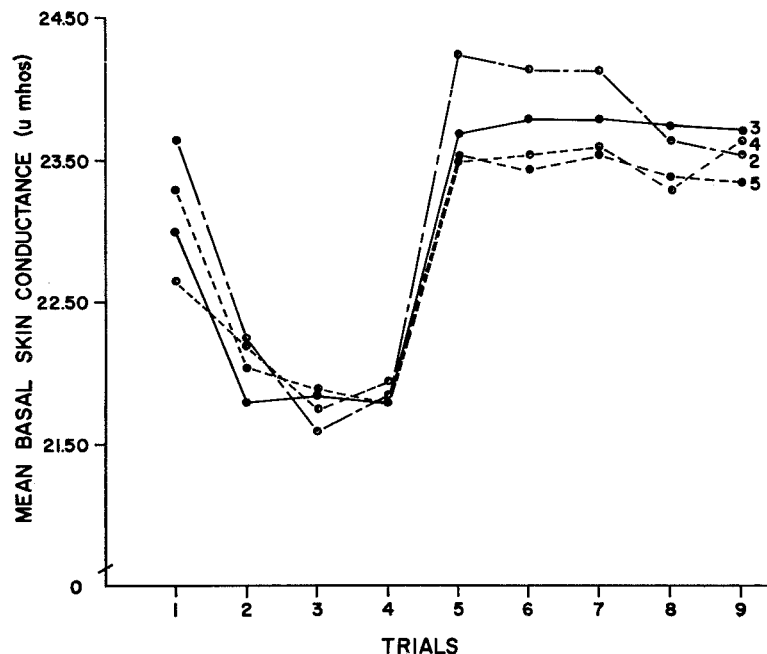


FIG. 3. Mean basal SC during habituation (Trials 1-3) and subsequent conditioning (Trials 4-9) as a function of trial segment.

of the trials effect resulted in significant linear ($F = 6.028$, $df = 1/144$, $p < .05$) and cubic ($F = 13.642$, $df = 1/144$, $p < .001$) components.

Intersegmental Analysis of Basal Activity

Basal SC in micromhos, HR in b/m, and total integrated MAP in millivolts were measured for Trial Segments 2-5. Segment 1 measures were excluded from analysis since they were directly confounded with the overt behavioral response.

Figure 2 shows integrated MAP activity during these four segments on all nine trials. The patterns consist of habituation and subsequent AP and are clearly comparable for all segments. Again, peak activity occurred on Trial 6. A Segments \times Trials analysis yielded a ($F = 29.298$, $df = 8/216$, $p < .001$) trials effect. Trend analysis revealed significant linear ($F = 41.958$, $df = 1/216$, $p < .001$) and cubic ($F = 105.120$, $df = 1/216$, $p < .001$) components. The segments effect resulted in

$F = 1.677$ ($df = 3/216$); the interaction effect yielded an $F < 1$.

The basal SC data presented a somewhat similar picture. As shown in Figure 3, habituation occurred on the first four trials but was completely reversed after the first presentation of the US and evocation of the UR. No clear peak is apparent in the data. Analysis of variance, however, revealed a significant trials effect ($F = 72.454$, $df = 8/216$, $p < .001$) with significant linear and cubic components ($F = 226.186$ and 225.983 , $df = 1/216$, $p < .001$, respectively). The analysis yielded a significant segments effect ($F = 5.609$, $df = 3/216$, $p < .05$) and an insignificant interaction ($F < 1$) effect.

Figure 4 presents the basal HR data, characterized only by a tendency toward habituation across all nine trials. No evidence for AP is apparent. Analysis of these data yielded a ($F = 4.156$, $df = 8/216$, $p < .001$) trials effect which, when subjected to trend analysis, demonstrated only a significant linear component ($F = 24.489$, $df = 1/216$, $p < .001$). The segments effect ($F =$

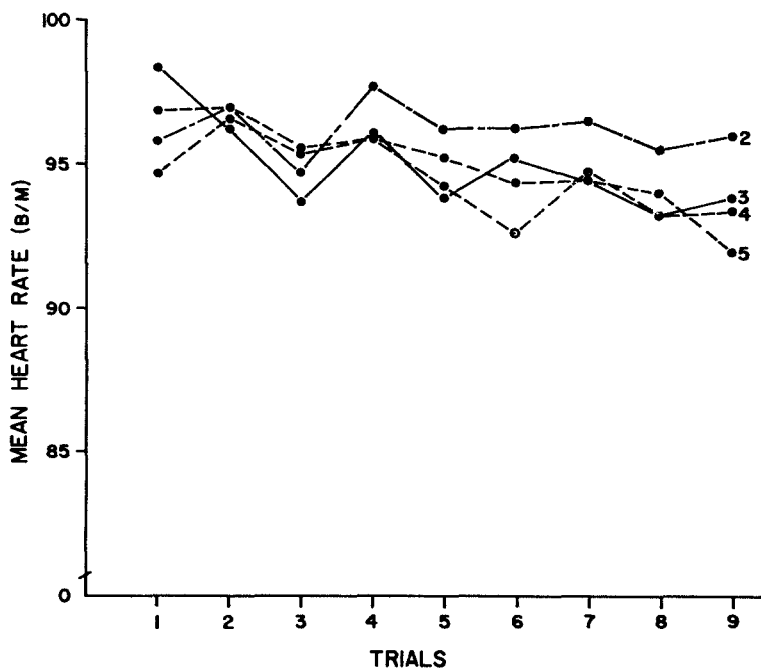


FIG. 4. Mean basal HR during habituation (Trials 1-3) and subsequent conditioning (Trials 4-9) as a function of trial segment.

4.071, $df = 3/216$) was also significant at this level but the interaction effect resulted in an $F < 1$.

DISCUSSION

The results of the present study provide additional support for the AP effect and extend its generality over learning tasks. Responses occurring during the presentation of the CS demonstrated AP in all three physiological measures and basal activity measures of SC and MAP yielded the same pattern of habituation and subsequent AP for all analyzed trial segments. No explanation is available at the present time for the lack of an AP effect in the basal HR data.

The finding that background somatomotor activity demonstrated AP during conditioning provides necessary, though not sufficient, support for the hypothesis that AP constitutes a pattern of changes in behavioral preparations. Additional, though indirect, support for this interpretation is provided by the fact that AP occurred in all measured trial segments.

Lastly, the findings of the present study constitute a demonstration of the integration of autonomic and somatic activity and provide some support for the concept of "cardiac-somatic coupling" presented by Obrist and Webb (Obrist, 1968; Obrist & Webb, 1967; Webb & Obrist, 1967a, 1967b). A partial discrepancy between HR and MAP activity apparently occurred in the intersegmental analysis. Extensive reviews of the neurophysiological and psychophysiological literature concerning the subject of autonomic-somatic integration have been provided by Gellhorn (1967) and Germana (1969b).

REFERENCES

- GELLHORN, E. *Principles of autonomic-somatic integration*. Minneapolis: University of Minnesota Press, 1967.
- GERMANA, J. The psychophysiological correlates of conditioned response formation. *Psychological Bulletin*, 1968, **70**, 105-114. (a)
- GERMANA, J. Response characteristics and the orienting reflex. *Journal of Experimental Psychology*, 1968, **78**, 610-616. (b)
- GERMANA, J. Effects of behavioral responding on

- skin conductance level. *Psychological Reports*, 1969, **24**, 599-605. (a)
- GERMANA, J. Central efferent processes and autonomic-behavioral integration. *Psychophysiology*, 1969, in press. (b)
- GERMANA, J., & CHERNAULT, G. Patterns of galvanic skin responses to signal and non-signal stimuli. *Psychophysiology*, 1968, **5**, 284-292.
- HARTMAN, T. F. Dynamic transmission, elective generalization, and semantic conditioning. In W. F. Prokasy (Ed.), *Classical conditioning*. New York: Appleton-Century-Crofts, 1965.
- OBRIST, P. A. Heart rate and somatic-motor coupling during classical aversive conditioning in humans. *Journal of Experimental Psychology*, 1968, **77**, 180-193.
- OBRIST, P. A., & WEBB, R. A. Heart rate during conditioning in dogs: Relationship to somatic-motor activity. *Psychophysiology*, 1967, **4**, 7-34.
- WEBB, R. A., & OBRIST, P. A. Heart-rate changes during complex operant performance in the dog. *Proceedings of the 75th Annual Convention of the American Psychological Association*, 1967, **2**, 137-138. (a)
- WEBB, R. A., & OBRIST, P. A. Comments on heart rate changes during complex operant performance in the dog. Paper presented at the meeting of the American Psychological Association, Washington, D. C., September 1967. (b)

(Received December 13, 1968)

Differential effects of interstimulus interval on habituation and recall scores¹

JOSEPH GERMANA, Virginia Polytechnic Institute, Blacksburg, Va. 24061

Habituation of the orienting reflex (OR) may be viewed as a simple or model form of learning. Previous research (Germana, 1968) has demonstrated that habituation of the OR may take the form of conventional stimulus-response learning and suggested the present comparison between habituation and a behavioral recall measure. Habituation to a 10-digit number was an inverse function of interstimulus interval (ISI), whereas recall of the same stimulus, tested after habituation, did not significantly vary across the range of ISIs employed. It was suggested that the effects of ISI on habituation were primarily determined by increased difficulty of encoding rate of stimulus presentation at increasingly longer ISIs and that behavioral recall does not reflect this temporal dimension of stimulus learning.

Habituation represents a general neurophysiological and behavioral process which may constitute "a model phenomenon for the study of (the) neuronal substrates of behavior [Thompson & Spencer, 1966, p. 16]." It consists of systematic response decrement which occurs as a function of repeated stimulation and which cannot be simply attributed to either receptor adaptation or fatigue. Habituation of the orienting reflex (OR), e.g., is defined by the decrement in both the autonomic and somatic components of this response which results when a stimulus of fixed or unaltered characteristics is repeatedly presented to the organism.

Several investigators (e.g., Grossman, 1967; Hernandez-Peon & Brust-Carmona, 1961; Thompson & Spencer, 1966; and Thorpe, 1963) have concluded that any broad definition of learning will include the phenomenon of habituation or that habituation may be regarded as a simple form of negative learning, i.e., learning not to respond.

Support for this view has been provided by the extensive research on the OR which has revealed that habituation is highly selective to the characteristics of the experimental stimulus. Selective habituation is demonstrated by re-emergence of the OR when a change, of at least just-noticeable value, occurs in the intensity, frequency, or temporal parameters of the stimulus.

Sokolov (1960; 1963a, b) has shown, e.g., that: (a) a decrease in stimulus intensity, (b) a change in pattern of component stimuli, (c) the omission of a stimulus previously presented at regular intervals, or (d) the administration of a dishabituating stimulus will cause reemergence of the habituated OR. These findings effectively argue against the hypotheses that receptor adaptation or fatigue are responsible for habituation of the OR or that habituation involves only neuronal refractoriness (cf. Gray, 1966; Lynn, 1966).

Sokolov has postulated the existence of a central "modeling system" within which the discriminable aspects of the habituated stimulus are encoded. He has described the "neuronal model" of a stimulus as "polyvalent," in the sense that it includes the intensity, frequency, duration, and rate of presentation characteristics of the experimental stimulus. Recent data (Germana, 1968) have revealed, however, that the characteristics of associated behavioral responses are also included in the "neuronal model" of the stimulus.

This last finding suggests that habituation may take the form of conventional stimulus-response learning and that measures of the processes mediating habituation and other behavioral learning may be comparably affected by various experimental parameters. Barrett & Ray (1968) have shown, e.g., that electroconvulsive shock interferes with both habituation and recall in mice. The present study was designed to investigate the effects of interstimulus interval (ISI) on habituation, generalized habituation, and verbal recall scores in human Ss.

SUBJECTS

Sixty-four male and female undergraduates, enrolled in an introductory psychology course, volunteered to participate.

APPARATUS AND PROCEDURE

Subjects were randomly assigned to eight ISI groups: 5, 15, 30, 45, 60, 90, 120, and 240 sec. All Ss received four trials, on each of which the complete 10-digit number, 3760549182, was presented for 5 sec, and a fifth trial, on which the different number, 6194273058, was presented. Five seconds after the presentation of this last number, Ss were asked to recall "the first number that had been presented."

Slides containing these number stimuli

were presented by a Kodak Carousel projector which was programmed for 5-sec advance by a Lafayette timer. Thus, ISIs were filled with blank-light, slide-tray advances occurring every 5 sec. It was anticipated that this method, combined with instructions to "attend" to the stimuli, would maintain S's attention to the site of stimulus presentation. In addition, it was regarded as a moderate method of reducing rehearsal. An active rehearsal-prevention procedure could not be employed because such a method would disrupt skin conductance which was monitored throughout the experiment.

The galvanic skin responses (GSRs) to the five experimental stimuli were measured for all Ss in order to test for habituation on Trials 1-4 and for generalization of habituation on Trial 5. GSRs were recorded from the distal phalanges of the index and ring fingers of the right hand. Ag/AgCl electrodes, prepared with K-Y surgical jelly, were firmly taped to these surfaces after they had been cleansed with alcohol. A Grass Model 7 polygraph, equipped with 7P1 preamplifier, was used to record these responses.

RESULTS

GSRs were converted into square-root change in conductance units since this measure acts to normalize the distribution of scores and, in addition, tends to free GSRs from baseline conductance effects.

Recall scores were computed in the following way. A single digit was counted as correctly recalled if it occurred in the correct position or if it followed in correct sequence from the previously given number. Number of correct digits were summed and constituted the recall score, out of a possible 10, for each S.

Figure 1 presents mean GSR on Trials 1-4 as a function of ISI. Separate analysis of variance showed that the ISI groups were not significantly different on Trial 1 ($F < 1$). It is apparent, however, that degree

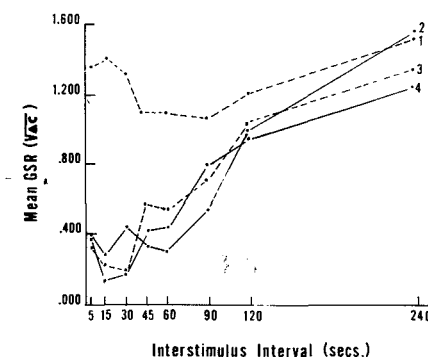


Fig. 1. Mean galvanic skin response (GSR) to the same 10-digit number on Trials 1-4 as a function of interstimulus interval (ISI).

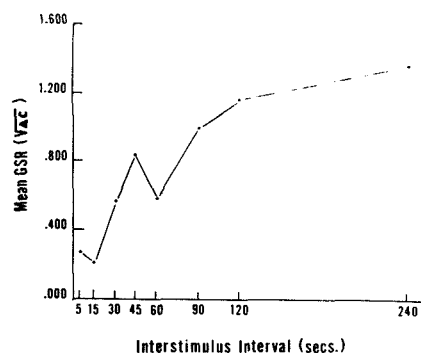


Fig. 2. Mean galvanic skin response (GSR) to a different 10-digit number on Trial 5 as a function of interstimulus interval (ISI).

of habituation on Trials 2-4 was an inverse function of ISI and that little or no habituation was demonstrated when an ISI = 240 sec was employed. A groups by trials analysis of these data yielded a significant groups or ISI effect [$F(7,56) = 10.341$, $p < .001$]. Both the trials and interaction effects resulted in an $F < 1$.

Figure 2 shows mean GSR on Trial 5 as a function of ISI. Habituation generalized to the different stimuli presented on this trial, but amount of generalized habituation was also an inverse function of ISI. Analysis of the Trial 5 data demonstrated that the groups or ISI effect was significant [$F(7,56) = 3.861$, $p < .01$].

The recall data, on the other hand, presented a different picture of information storage. Briefly, it was found that the ISI values employed in the study had no consistent effect on recall score. Analysis of the recall data yielded an $F < 1$ for the ISI effect. Mean number of digits correctly recalled was 6.50.

The possibility exists, however, that recall, measured after the presentation of the different 10-digit number on Trial 5, may have been subject to retroactive inhibition which, in some way, masked an

ISI effect. For this reason, and to test for the effects of repetition on recall of the present material, an additional 64 Ss were given only one exposure to the same stimulus employed on Trials 1-4 in the preceding experiment. Recall was tested after time intervals equal to the ISIs previously used and these intervals were also filled with blank-light, slide-tray advances occurring every 5 sec.

Mean recall score after one exposure was 5.34 but, again, there was no consistent effect of ISI. Since the fluctuations of recall means across intervals were similar to those found in the first study, an ISI by number of repetitions analysis of variance was applied to the combined recall data of the two experiments. The analysis yielded only a significant number of repetitions effect [$F(1,112) = 5.641$, $p < .05$], indicating that recall was reliably improved after four exposures. Subsequent trend analysis of the ISI effect ($F < 1$), carried out to the quintic component, yielded no significant effects.

DISCUSSION

The results of these studies indicate that ISI produces different effects on habituation and recall scores. Habituation was shown to be an inverse function of ISI and little or no habituation occurred over four trials when an ISI of 240 sec was employed. Behavioral recall of stimulus content, on the other hand, was not similarly affected within the range of ISIs investigated.

These findings, however, do not necessarily imply that habituation and recall involved independent storage mechanisms or trace systems which are subject to different rates of decay.

As previously noted, the "neuronal model" of a stimulus contains a representation of the discriminable aspects of that stimulus, including its temporal characteristics: duration and rate of presentation. On this basis, it may be suggested that the primary factor underlying the inverse relationship between ISI and habituation was relative difficulty in establishing an accurate representation of

stimulus rate with increasingly longer ISIs. In contrast to measures of habituation, measures of recall or recognition do not directly test this temporal dimension of stimulus learning. Thus, the differential effects of ISI on habituation and recall scores may simply result from the fact that these two measures are not equally comprehensive.

REFERENCES

- BARRETT, R. J., & RAY, O. S. Attenuation of habituation by electro-convulsive shock. Paper read at the meeting of the Psychonomic Society, St. Louis, October-November, 1968.
- GERMANA, J. Response characteristics and the orienting reflex. *Journal of Experimental Psychology*, 1968, 78, 610-616.
- GRAY, J. A. Attention, consciousness and voluntary control of behavior in Soviet psychology: Philosophical roots and research branches. In N. O'Connor (Ed.), *Present-day Russian psychology*. New York: Pergamon, 1966. Pp. 1-38.
- GROSSMAN, S. P. *A textbook of physiological psychology*. New York: Wiley, 1967.
- HERNANDEZ-PEON, R., & BRUST-CARMONA, H. Functional role of subcortical structures in habituation and conditioning. In J. F. Delafresnaye (Ed.), *Brain mechanisms and learning*. Oxford: Blackwell, 1961. Pp. 393-412.
- LYNN, R. *Attention, arousal and the orientation reaction*. New York: Pergamon, 1966.
- SOKOLOV, E. N. Neuronal models and the orienting reflex. In M. A. Brazier (Ed.), *The central nervous system and behavior*. New York: Josiah Macy, Jr., 1960. Pp. 187-239.
- SOKOLOV, E. N. *Perception and the conditioned reflex*. New York: Pergamon, 1963a.
- SOKOLOV, E. N. Higher nervous functions: The orienting reflex. *Annual Review of Physiology*, 1963b, 25, 545-580.
- THOMPSON, R. F., & SPENCER, W. A. Habituation: A model phenomenon for the study of neuronal substrates of behavior. *Psychological Review*, 1966, 73, 16-43.
- THORPE, W. *Learning and instinct in animals*. London: Methuen, 1963.
- NOTES
1. This research was supported by Grant NGR 47-004-006, Project 313181, from the National Aeronautics and Space Administration. The assistance of G. Chernault, M. Smith, J. Baird, and D. F. Johnson is gratefully acknowledged.
 2. Address reprint requests to: J. Germana, Department of Psychology, Virginia Polytechnic Institute, Blacksburg, Va. 24061.

N 71-71021

FINAL REPORT
to the
NATIONAL AERONAUTICS AND SPACE ADMINISTRATION
in connection with
NASA Grant NGR 47-004-006

Part 21 of 21 Parts

Final Report
VPI&SU Project 313151

The Effects of Restricted Movement on Protein
Metabolism and Body Composition

by

S. J. Ritchey
Human Nutrition and Foods

Virginia Polytechnic Institute & State University
Blacksburg, Virginia

December, 1970

THE EFFECTS OF RESTRICTED MOVEMENT ON PROTEIN METABOLISM AND BODY COMPOSITION

A series of experiments were conducted to examine the effects of restricted movement on protein metabolism and on body composition. Conditions of restricted movement and short periods of forced exercise were utilized to simulate conditions imposed upon man during space travel.

Experimental Procedures

Laboratory rats were used in all experiments. The animals were housed in individual screen-wire cages in an animal room having controlled temperature and humidity. The diet was usually a commercial preparation and was fed ad libitum unless the particular experimental regime demanded a variation.

Restricted movement was obtained by placing animals in small restraining devices which permitted little or no movement. After certain difficulties in early preliminary tests, the restraining cages worked very well and the desired conditions were obtained. A satisfactory scheme for feeding the animals in the restraining cages was not available although numerous attempts were made. Thus, the animals were freed for purposes of getting feed and water at regular intervals during each day of the experiments.

In certain experiments exercise was forced upon groups of animals by placing the animals in a tank of warm water for controlled periods of time. Animals were observed during this time to prevent drownings.

Changes in the composition of the whole body and certain tissues were determined. The amounts of water, fat and nitrogen in tissues or in excreta were determined by methods of the A.O.A.C. (1960).

Results and Discussion

The results from the various experiments are discussed in the following sections.

Effects of short periods of exercise. Adult male rats were divided into four groups. Each group had comparable average weights at the beginning of the experiment. The four groups were treated as follows for 18 days:

- A. Unrestricted movement, swimming for 10 minutes daily.
- B. Unrestricted movement, no forced exercise.
- C. Restricted movement, swimming for 10 minutes daily.
- D. Restricted movement, no forced exercise.

Results from this experiment are given in Table I.

Table I. Average weight change and food consumption of adult rats restricted in movement and forced to exercise

<u>Treatment</u>	<u>Weight change (g/day)</u>	<u>Food Consumption (g/day)</u>
A. Unrestricted, exercised	0.5±0.6 ¹	9.7±0.9
B. Unrestricted	0.4±1.2	9.6±1.4
C. Restricted, exercised	0.2±0.6	9.9±0.8
D. Restricted	-0.2±1.3	9.8±1.7

¹Mean ± SD, ten animals in groups A and C, eleven animals in groups B and D.

The animals restricted in movement lost weight (Group D) or did not gain as much weight as the unrestricted animals (Groups A & B). Forced exercise by swimming had no significant effect on weight changes of rats restricted, although Group C continued to gain weight while Group D lost weight. The effects of even more strenuous or longer periods of exercise on changes in weight can be speculated on, but in this experiment, significant changes did not occur.

Losses in weight as a result of restricted movement. Results from the above experiment illustrated the loss of weight (Group D) when animals were restricted in movement. Data from several experiments indicated this loss during restriction. A five-day experiment (Table II) in which animals were restricted demonstrated clearly this result.

Table II. Average changes in weight during a five-day experiment.

<u>Treatment</u>	<u>Weight change (g)</u>
Restricted	-7.8 ¹
Controls	10.5

¹Mean of 4 animals per group.

Adaptation to restriction. Although animals lost weight rapidly during the initial days during restriction (Table II), the animals seemed to adapt to restriction and would gain weight if the experiment were prolonged. This phenomenon is illustrated by changes in weight of animals restricted and unrestricted, but paired for food intake, in Figure 1. Data from other experiments demonstrated a similar result. Animals reached the low point in weight at about day 15 and gained weight from that point.

Feed intake and weight loss. In those experiments where food consumption was not controlled, large differences in weight changes between control animals (unrestricted) and restricted animals occurred. Experiments were conducted to examine the relationship between activity, food consumption, and weight changes. Pair-feeding technique was used to equalize food consumption between restricted and control animals.

Table III. Changes in weights of rats restricted in movement and control animals given same amounts of total food.

<u>Treatment</u>	<u>Daily Food Consumed (g)</u>	<u>Weight Gain (g)</u>
Restricted	10.6 ¹	7.2
Controls	11.0	28.2

¹Mean of 10 animals per treatment.

The results indicated clearly that restriction itself resulted in changes in weight (Table III). The same conclusion can be based on data in Table I, another experiment in which food intake was controlled between paired groups of animals.

Table IV. Changes in weight and carcass composition during restriction compared to pair-fed and ad libitum controls.

<u>Treatment</u>	<u>Weight changes</u>			<u>% Nitrogen</u>		
	<u>Day 0</u>	<u>Day 4</u>	<u>Day 8</u>	<u>Day 0</u>	<u>Day 4</u>	<u>Day 8</u>
Restricted	211.8 ¹	186.8	140.0	2.88	2.83	2.75
Pair-fed	212.4	193.0	173.0	2.88	2.84	2.81
Ad-Libitum	211.6	219.6	198.6	2.88	2.79	2.84
	<u>% Water</u>			<u>% Fat</u>		
Restricted	77.1	77.1	80.1	4.08	3.56	0.88
Pair-fed	77.1	73.9	75.5	4.08	4.40	3.12
Ad-Libitum	77.1	75.2	75.5	4.08	4.42	2.80

¹Mean of 5 animals per treatment.

Changes in body composition. Analyses of the composition of animals, such as the experiment in Table I, showed no differences in amounts of nitrogen, fat and moisture. However, since the major loss in weight of these animals (Table I) seemed to be as a result of losses in body fat, total weight changes of individual animals regardless of treatment was compared to the percentage of

carcass fat (Figure 2). A highly significant positive correlation ($r = 0.798$) was found between the two parameters. As gain in weight increased, the percentage of carcass fat increased.

Data from an experiment designed to show the changes in composition during the restriction confirm the effect on carcass fat. These data (Table IV) show, as expected, that weights drop markedly in the initial days of restricted movement (day 4-day 8). However, the percentage of nitrogen was not altered. Restriction causes the amount of carcass fat to drop markedly and the amount of water to increase above the control groups.

Short term restriction followed by rehabilitation. Animals restricted in movement lost considerable weight during a 7-day restriction period, but regained this weight rapidly when returned to a normal metabolism cage (Table V). During a 91-day recovery period, the restricted animals attained weights above the pair-fed controls and almost as much as ad libitum fed animals. There seemed to be no long-term effects of restriction, but these data are not conclusive.

Effects on protein metabolism. There seemed to be no real effects on protein metabolism and losses of nitrogen from the body during restricted movement. Data from several experiments were similar to those reported in Table IV. No differences in nitrogen retention between control and restricted animals were found. Attempts to accomplish nitrogen balance experiments were abandoned because of physical problems encountered with the restriction units. The collection of excreta and thus the quantitative analyses for nitrogen losses were impossible using these units.

Summary and Conclusions

In a series of experiments it was demonstrated that restricted movement causes a dramatic loss in weight. The loss in weight was attributed in part to lowered energy intake, but even when the effects of feed intake were removed

by pair-feeding technique, there was a loss explained only by the restriction in movement. Short periods of forced exercise did not alter this trend.

The primary effect of the weight loss was a drastic loss in body fat accompanied by an increase in body water. Nitrogen content was not changed.

Animals adapted to restricted movement after fifteen to eighteen days. There seemed to be no long-term effects of restriction, although the experiments were not conclusive in this respect. Neither was there an apparent effect on protein metabolism, although short-term nitrogen balance experiments were not conducted because of certain limitations imposed by the restricted regime.

Table V. Changes in weight during restriction and long-term rehabilitation following restriction.

	Treatment		
	<u>Ad Libitum</u>	<u>Restricted</u>	<u>Pair-Fed</u>
Initial weight	208.7 ¹	208.1	208.2
Wt., end of 7-day restriction	230.7	159.2	170.3
Recovery - Day 14	253.8	204.0	215.6
Day 21	284.8	252.4	259.7
Day 35	330.0	318.9	313.3
Day 49	357.7	345.8	343.6
Day 63	394.0	378.6	368.3
Day 77	408.7	400.3	388.0
Day 91	434.5	417.2	407.4

¹Mean of 9 animals per treatment.

Publications:

Heald, Judith W. The Effects of Restricted Movement and Forced Exercise on Protein Metabolism and Body Composition of Adult Rats. Master of Science Thesis, Virginia Polytechnic Institute, December, 1968.

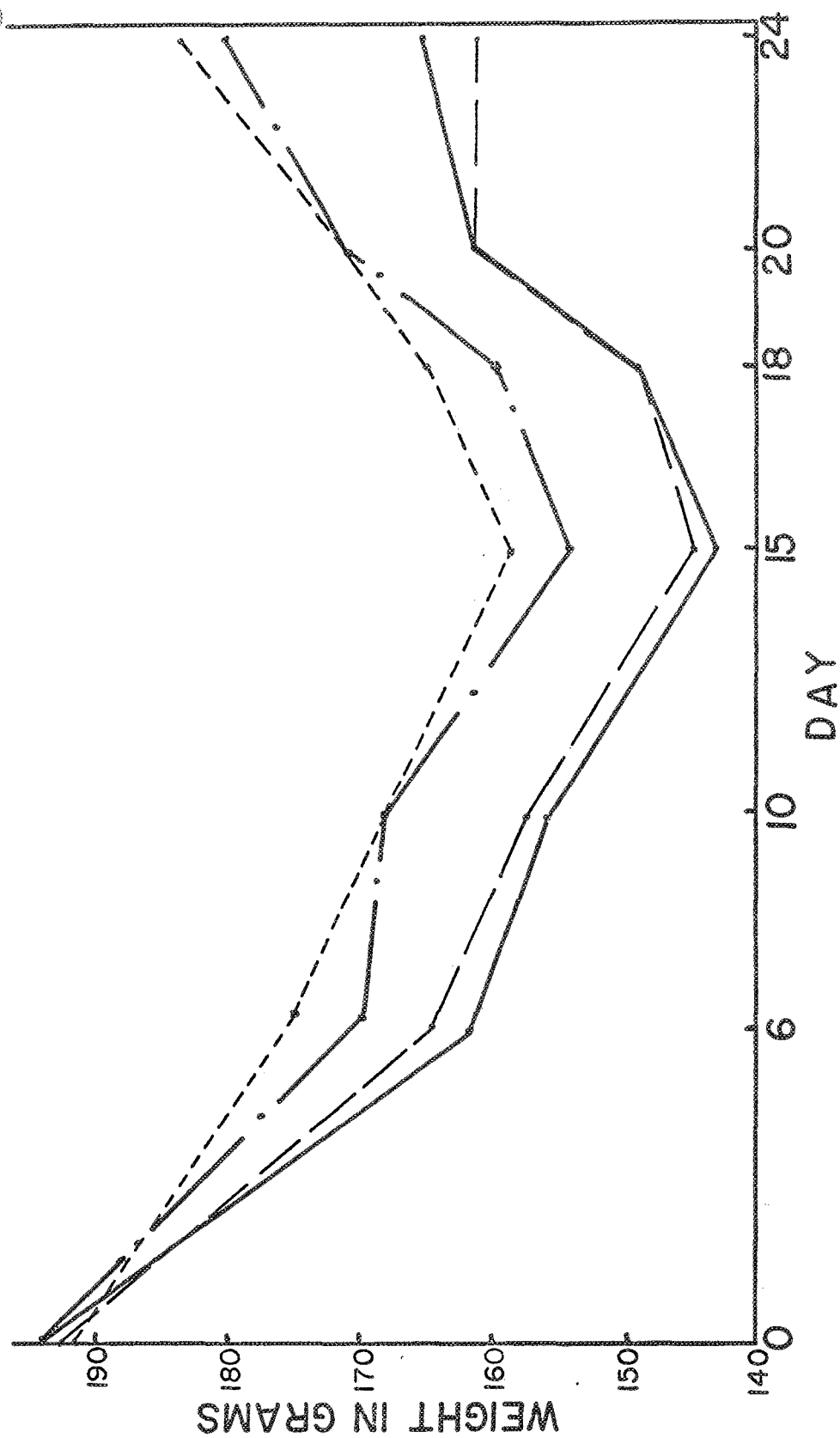


Fig. 1 Average weights of animals on various treatments throughout the 24 day study.
 Group A, Unrestricted and exercised (days 10-20) - - - - -; Group B, Unrestricted - - - - -;
 Group C, Restricted and exercised (days 10-20) - - - - -; Group D, Restricted - - - - -.

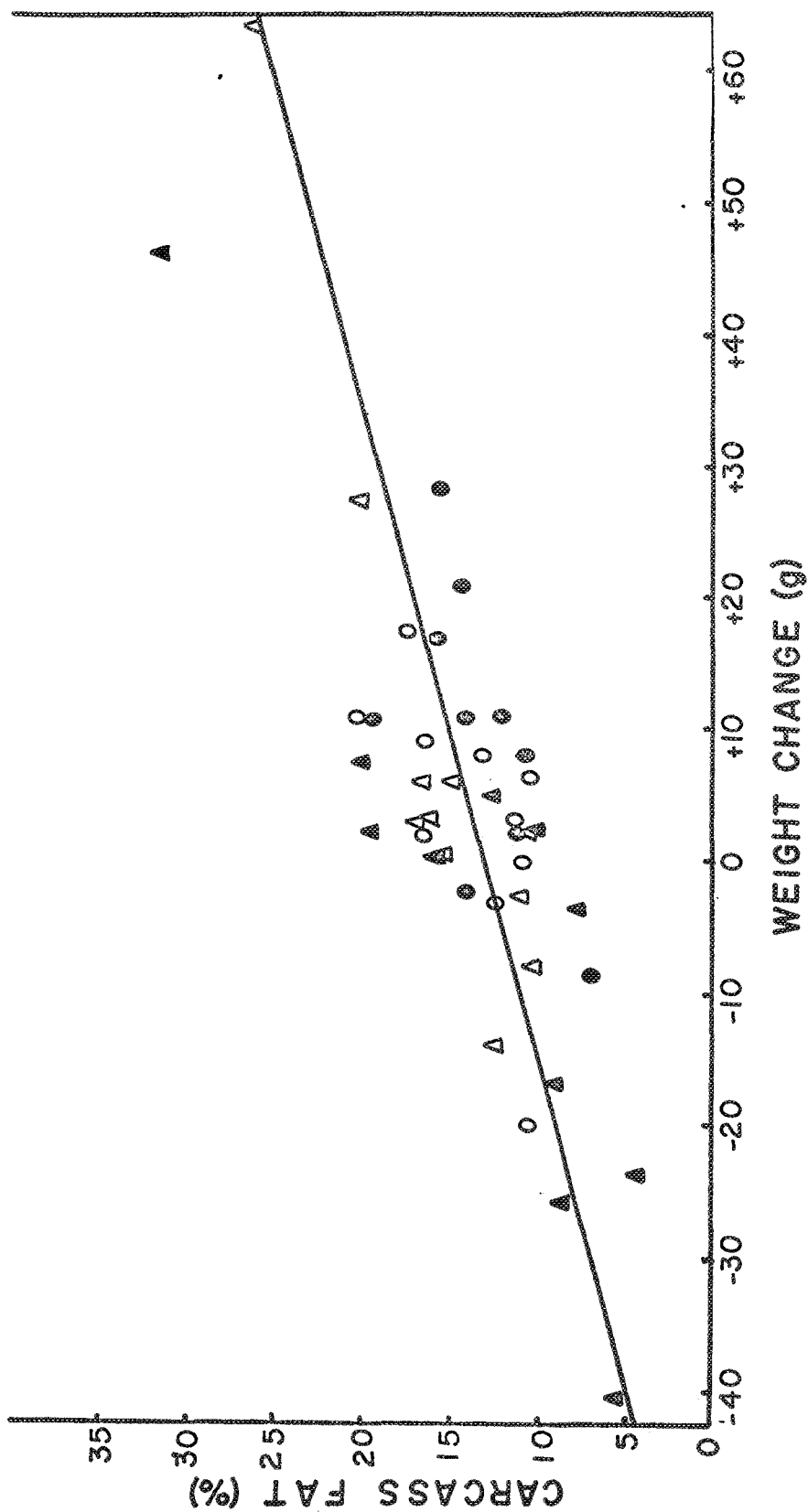


Fig. 2 Relationship between carcass fat and weight change following eighteen days of restriction in movement. Group A, Unrestricted and exercised \bullet ; Group B, Unrestricted \circ ; Group C, Restricted and exercised \blacktriangle ; Group D, Restricted \triangle . $r = +0.798$; $y = 13.4 + 0.21x$.